Active Production of Large Aspheric Optics for Astronomy

A Thesis Submitted for the Degree

of

Doctor of Philosophy of the University of London

by

Sug-Whan Kim

Optical Science Laboratory

Department of Physics and Astronomy

University College

University of London

1993

ProQuest Number: 10045766

All rights reserved

INFORMATION TO ALL USERS
The quality of this reproduction is dependent upon the quality of the copy submitted.

In the unlikely event that the author did not send a complete manuscript
and there are missing pages, these will be noted. Also, if material had to be removed,
a note will indicate the deletion.

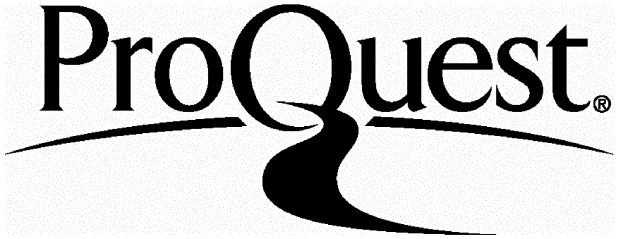

ProQuest 10045766

Published by ProQuest LLC(2016). Copyright of the Dissertation is held by the Author.

All rights reserved.
This work is protected against unauthorized copying under Title 17, United States Code.
Microform Edition © ProQuest LLC.

ProQuest LLC
789 East Eisenhower Parkway
P.O. Box 1346
Ann Arbor, MI 48106-1346

To My Parents, The Past
To Jung-Sook, The Present
To Sae-Young, The Future
All in Our Creator's Mind

Active Production of Large Aspheric Optics for Astronomy

Abstract

This thesis is devoted mainly to tackling the unsolved problem of producing secondary mirrors for 8 m telescopes, which will be up to 2-2.5 m in diameter and in excess of 1000 waves aspheric. This can not be done by traditional methods. The project directly addresses the problem and forms part of the UK's R&D contributions to the Gemini USA/UK/Canada/Brazil/Chile/Argentina project to produce two 8 m telescopes. Its aim was to develop a new active method. The thesis starts with a review of astronomical implications of 8 m telescope projects currently being undertaken or planned world wide and continues with discussions on technological challenges specifically in main optics production.

The first stage of producing the mirror is generation of the aspheric surface profile by diamond milling. This has been directly addressed by developing a new computer-controlled profiler based on the existing manual hardware of the Grubb-Parsons 2.5 m machine. An essential part of the development also includes a computer-controlled contact profilometer. The system performance is presented, including calibration, error profile and convergence of error compensation.

The main part of the project was to develop polishing using a full size active lap, by which the pressure distribution and hence ablation rate are modulated in real time. The progress of the project is described, starting with a review of other approaches being developed world wide. The overall philosophy and design of active components are presented. Following this, experiments with a sub-diameter polisher and a prototype active lap of 85 cm in diameter, as built, are also described, including methods of testing, ablation algorithm and control theory. The final part of this section discusses the performance of the active polishing lap in terms of functionality at component and system levels.

The conclusion briefly summarises the evaluation of the active method and its impact on large optics production. It also gives ideas for future improvements of performance, research work still needed and viable applications for the technique.

Glossary

AAT	Anglo Australian Telescope
AFH	Ablation Film Hysteresis
ANSYS 4.4	A Finite-Element Analysis Software Package from SWANSON LTD.
ASCII	American Standard Code for Information Interchange
AGC	Angled Grubb-Geetron Coordinate
AXAF	Advanced X-Ray Astronomy Facility
CCOS	Itek's Computer Controlled Optical Surfacing
3D	Digital Design and Development Ltd.
DVM	Digital Volt Meter
ESO	European Southern Observatory
FE	Finite Element
FOV	Field Of View
FRT	Friction Response Time
FWHM	Full Width Half Maximum
GP	Grubb-Parson Ltd.
GPA	Global Process Algorithm for Active Polishing
GUI	Graphic User Interface
HST	Hubble Space Telescope
INT	Isaac Newton Telescope
IR	Infrared Wavelength
ISSA	Institute of Space Science and Astronomy in Korea
JNLT	Japanese National Large Telescope
KAO	Korean Astronomical Observatory
LA	LosAngeles
LDR	Large Deployable Reflector
LLNL	Lawrence Livermore National Laboratory
LVDT	Linear Variable Displacement Transducer
MMT	NOAO's Multi-Mirror Telescope
MRP	Moving Reference Profile
MOST	Ministry of Science and Technology in Korea

MTF	Modulation Transfer Function, from Force to Friction
MTP	Carl Zeiss's Membrane Tool Polisher
NC	Numerically Controlled
NOAO	National Optical Astronomical Observatory in USA
NPL	National Physical Laboratory in UK
NTT	ESO's New Technology Telescope
ORS	Oversee Research Student Award
OSL	Optical Science Laboratory in UCL
PASS	PASS.EXE, Profile Analysis System Software
PC	Personal Computer
PROG	PROG.EXE, Profile Generation System Software
P-to-V	Peak-to-Valley
RGC	Rectangular Grubb-Geetron Coordinate
RTA	Real-Time Ablation Algorithm for Active Polishing
QSO	Quasi Stellar Object
SERC	Science and Engineering Research Council
SIRTF	Space Infrared Telescope Facility
SPIE	Society of Precision Instrument Engineers
UCL	University College London
UCLES	UCL high resolution Eschell Spectrograph
UHRF	Ultra High Resolution Facility for UCLES
UKIRT	UK Infrared Telescope
UKLT	UK Large Telescope
ULE	Ultra Low Expansion
VGA	Video Graphic Array
VLT	ESO's Very Large Telescope Project
UV	Ultra-Violet Wavelength
WHT	William Herschel Telescope
WYKO	WYKO LTD., producing a fringe analysis system

Contents

Abstract 3

Glossary 4

1 Introduction 20

1.1 Astronomical Background 20

1.2 Technological Background 26

1.3 Historical Background 29

1.4 Author's Contribution 30

1.5 Aim and Summary of The Thesis 34

2 Optical Surface Profile Generation 37

2.1 Introduction 37

2.2 New Philosophy of Profile Generation 39

2.2.1 Grubb-Parson's Method of Profile Generation 39

2.2.2 Computerisation of Profile Generation 42

2.3 PROG.EXE: PROfile Generation Software 45

2.3.1 Fundamentals of PROG.EXE 45

2.3.2 `AXIS` Procedure 51

2.3.3 `MANUAL` Procedure 52

2.3.4 `FACING` and `EDGING` Procedures 53

2.3.5 BEVELLING Procedure 54
2.3.6 PROFILING Procedure 55
2.3.7 Debugging and Testing 63
2.4 Contact Profilometry and Profile Calibration 67
2.4.1 Talylevel and Profile Gauge Measurements 67
2.4.2 Simple Contact Profilometer Using LVDT 68
2.4.3 PASS.EXE: Profile Calibration System Software 76
2.4.4 Profile Calibration and Error Compensation 83
2.5 Discussion 84

3 Optical Surface Polishing **91**

3.1 Introduction 91
3.2 Existing Methods of Polishing 92
3.2.1 Conventional Polishing 92
3.2.2 Recent Developments in World-Wide 94
3.2.2.1 Stressed Lap Polishing in University of Arizona . . . 94
3.2.2.2 CCOSs in Litton Itek and Contraves Goerz 97
3.2.2.3 Stressed Mirror Polishing in University of California, Berkeley 97
3.2.2.4 Ion-Ablation Process in Eastman Kodak 98
3.2.2.5 Linear Membrane Polishers in Zeiss and University of Turku 99
3.2.2.6 Pressurising Rod Polisher in REOSC 101
3.2.2.7 Full Size Passive Polisher in Grubb-Parson 102
3.3 New Philosophy of Active Polishing 103
3.3.1 Background of the new philosophy of genuine active polishing 103
3.3.2 New philosophy of genuine active polishing 104

3.4 Initial System Design of Active Lap 118
3.4.1 Specification of The 85 cm Scaled Gemini Secondary Mirrors . 118
3.4.2 Initial Design of Active Lap System 119
3.5 Discussion 124

4 Development of Active Elements **127**

4.1 Introduction 127
4.2 Force Sensing Element 128
4.2.1 Design Philosophy 128
4.2.1.1 Basic Requirements 128
4.2.1.2 Transducer Survey 131
4.2.1.3 Strain Gauge Selection 134
4.2.1.4 Strain Elements 136
4.2.2 Structural Analysis and Design 141
4.2.2.1 Structural Analysis 141
4.2.2.2 Design and Considerations for Prototyping 144
4.3 Force Actuator 146
4.3.1 Background 146
4.3.2 Design Philosophy 147
4.3.2.1 Basic Requirements 147
4.3.2.2 Solenoid Actuator 149
4.3.2.3 Electromagnetic Coupling Actuator 154
4.3.2.4 Linear Motor-Spring Actuator 156
4.3.3 Design and Structural Analysis 159
4.3.3.1 Stepper Motor Selection 159
4.3.3.2 Spring Unit Design 162
4.4 Active Polishing Module 165

4.4.1 Background . . . 165
4.4.2 Active Polishing Module . . . 166
4.4.2.1 Prototype Load Cells . . . 166
4.4.2.2 Prototype Actuator and Enclosure . . . 168
4.4.3 APOLO: Active Polishing Module Controller . . . 168
4.4.4 APOLO.EXE: Active Polishing software . . . 170
4.4.4.1 Control Elements . . . 170
4.4.4.2 Overall Structure . . . 171
4.4.5 Test and Optimisation . . . 173
4.4.5.1 Calibration and Some Experiments . . . 173
4.4.5.2 Temperature Effect . . . 174
4.4.5.3 Lateral Force Effect . . . 177
4.5 Discussion . . . 185

5 Sub-Diameter Tool Polishing and Polishing Variables 189

5.1 Introduction . . . 189
5.2 Ablation Rate . . . 190
5.2.1 Experiment Programme . . . 190
5.2.2 Apparatus . . . 192
5.2.2.1 Scatter Plate Interferometer . . . 192
5.2.2.2 Equal Thickness Interferometer . . . 200
5.2.3 Measurements, Data Reduction and Results . . . 203
5.3 Friction Coefficient . . . 213
5.3.1 Experiment Programme . . . 213
5.3.2 Apparatus . . . 214
5.3.2.1 Use of A Spring Balance Force Sensor . . . 214
5.3.2.2 Use of The Prototype Load Cell 2 . . . 215

5.3.3 Measurement, Data Reduction and Results 217
5.4 Behaviours of Abrasive Films 226
5.4.1 Experiment Programmes 226
5.4.2 Apparatus 228
5.4.3 Measurement, Data Reduction and Analysis 228
5.4.3.1 Case Study 232
5.4.3.2 AFH Analysis 234
5.4.3.3 FRT Analysis 237
5.5 Discussion 242
5.5.1 Implication of Ablation Experiment with Thick Abrasive . . . 242
5.5.2 Implication of Friction Measurement 245
5.5.2.1 Friction Coefficient-Sliding Velocity-Pressure 246
5.5.2.2 Friction Coefficient Stability-Sliding Velocity-Time . 247
5.5.3 Combined Implication of Ablation and Friction Experiments . 248
5.5.4 Implication of AFH and FRT Analysis 250
5.5.5 Criticism on The Existing Theories and Developments of Large Optics Polishing 252
5.5.6 Some Guide Lines for Future Trends in Large Optics Polishing 255
5.5.7 Problems with The Experiments Made 256
5.5.8 Suggestions for Future Experiments 257

6 85 cm Scaled Experimental Active Lap 260

6.1 Introduction 260
6.2 Progress towards The Manufacturing Design 261
6.2.1 Mechanical Design 261
6.2.2 Load Cells and Actuators 276
6.2.3 Control Electronics 278

6.2.4 Software Specification 285
6.2.4.1 Functional Specification 285
6.2.4.2 Ergonomic Specification 286
6.2.5 Ablation Algorithms 288
6.2.5.1 Detailed Structure of RTA 289
6.2.5.2 Detailed Structure of GPA 293
6.2.6 Optical Testing 307
6.3 Construction, System Debugging and Calibration 308
6.3.1 Construction of The Lap 308
6.3.2 System Debugging 311
6.3.2.1 Debugging for Electro-Mechanics 311
6.3.2.2 Active lap system calibration 324
6.4 Real-Time Control of The Active Lap 331
6.4.1 Real-Time Actuator Update 332
6.4.2 Construction of Pressure Map 338
6.4.2.1 Linear Interpolation Method 338
6.4.2.2 A-L Coupling Coefficient Method 342
6.4.2.3 L-L Coupling Coefficient Method 345
6.4.3 Control of Global Actuators 351
6.5 Work Progress for The Active Lap and The 85 cm Scaled Gemini Secondary 354
6.6 Discussion 361

7 Conclusion **365**

7.1 Summary 365
7.2 Performance 366
7.3 Implications 366

7.4 Applicability and Contribution 367

7.5 Future Work 369

Acknowledgements **373**

Bibliography **376**

Appendix **386**

A Publications **387**

A.1 ESO Conference Proceedings in 1992 387

B Active Elements **391**

B.1 FE Analysis for Various Web Models 391

B.2 Software Half Bridge 393

C Calculation of Polishing Variables **401**

D Structural Coupling Coefficient of Active Lap **404**

D.1 Actuator-Load Cell Coupling Coefficient 404

D.2 Load Cell-Load Cell Coupling coefficient 405

List of Tables

2.1 Coefficients of the two best fit 5th order polynomials 80

2.2 Comparison of profile generations between the f/3 concave sphere and the scaled f/7 Gemini secondary 90

4.1 The results of FE static analysis 142

4.2 The comparison of the designed load cell to the ELF-1000 model . . . 145

4.3 The calibration of the prototype load cell 1 173

5.1 The results of fringe analysis 211

5.2 Friction coefficient against sliding speed for both the abrasives 222

5.3 Friction stability time against sliding speed for both the abrasives . . 222

5.4 The third measurements for behaviour of abrasive films with sub-diameter tool polishing 230

5.5 The statistics of the cases and their reducibility 233

5.6 Frequencies of 'Strong' and 'Weak' AFHs in Reducible AFH data set. 234

5.7 Averaged AFH times for 'Strong' and 'Weak' AFHs for the thin and thick abrasives 235

5.8 AFH times for the different load cases 235

5.9 Recovery rate for the Weak and Strong AFHs 236

5.10 Recovery rate for the different load cases 236

5.11 Unit load FRTs for different load cases in separation of loading and unloading 237

5.12 Unit load FRTs for different load cases in combination of loading and unloading data sets 238

6.1 Classification scheme of various GPA strategies 294

6.2 The ablation scaling factors for different magnitudes of surface error . 300

List of Figures

2.1 Photograph of the Grubb 8 ft grinding and polishing machine 40

2.2 Schematic diagram of the 8 ft machine 41

2.3 New method of profile generation using the 8 foots machine 43

2.4 Coordinate systems used for PROG.EXE 49

2.5 Concept of the MRP method 51

2.6 Overall structure of PROG.EXE version 1.0 52

2.7 Movement of tool for facing 53

2.8 Movement of tool for edging 54

2.9 Movement of tool for AGC mode bevelling 56

2.10 Movement of tool for RGC mode bevelling 57

2.11 Tool movements and quill configuration for concave surface. 62

2.12 Tool movements and quill configuration for convex surface. 62

2.13 Target control including overshooting protection for concave profile . 64

2.14 Target control including overshooting protection for convex profile . . 65

2.15 Structure of the PROG.EXE version 1.2 67

2.16 The concept of the Mark 1 profilometer. 68

2.17 The first alternative method for calibration of the LVDT using the 2 large flats. 72

2.18 The second alternative for calibration of the LVDT using the 1 mm slip gauge and the steep frame. 72

2.19 The three results of the thermal experiment for the LVDT behaviour. 74

2.20 The residuals of least square fit on the default calibration data 76

2.21 Overall flow chart of PASS.EXE 79

2.22 Prediction error plotted against the range of measurement 81

2.23 Prediction error curves with the splitted calibration data. 82

2.24 Surface error profiles generated with and without error compensation 83

3.1 A brief flow diagram of the algorithms for the active polishing. 115

3.2 Schematic diagram of the initial design for the active lap. 119

3.3 Global rocking actuators that transforms the active lap to the Draper machine action. 122

3.4 Schematic diagram of the active lap control electronics. 123

4.1 Two ways of using pressure transducers for the active lap 131

4.2 Use of the small flat line load cell 134

4.3 Cylindrical load cell and its bar analogy 137

4.4 Two flexural structures for measuring direct load to strain gauge . . . 138

4.5 Flexural split-bar 139

4.6 Cantilever and guided lever as strain element 140

4.7 The manufacturing design for prototype load cell 145

4.8 Solenoid as linking device of the two plates 150

4.9 Neoprene rubber as linking device 150

4.10 Central washer as linking device 150

4.11 Use of the electro-magnetic coupling actuator 154

4.12 Linear motor-spring actuator 157

4.13 FE analysis results for the 3 spring models 163

4.14 Use of the disk spring and design of the enclosure 164

4.15 The active polishing module 169

4.16 The active polishing module controller 169

4.17 The structure of APOLO.EXE 172

4.18 Effects of off-axis load to the web 178

4.19 The apparatus for measuring the off-axis load 180

4.20 An example of the friction measurement 181

4.21 The experiment of the forced tipping 182

4.22 The measurements of the forced tipping 183

4.23 A second full bridge for self-compensating load cell 184

5.1 The interferometry setup for testing the f/3 concave mirror with Burch's configuration of the scatter plate interferometry. 193

5.2 The ablation rate experiment setup including the modified configuration for scatter plate interferometry. 195

5.3 The proposed 'Modified Hindle Test' for testing the f/7 scaled secondary mirror of the Gemini telescopes 199

5.4 Fiezou fringe set-ups with the detector angle of about 45° and 0° . . . 202

5.5 Photograph of fringe file TB800.VID 205

5.6 Resulting OPD display of the first three grooves 206

5.7 Growth of the pitch in size 207

5.8 The apparatus using a spring balance force sensor. 215

5.9 The apparatus using the prototype load cell 2. 216

5.10 Friction coefficients with different loads against sliding velocity for the thin and thick abrasive. 219

5.11 Average friction coefficient over the sliding velocity against different load 220

5.12 Examples of the friction stability with time for the two abrasives . . . 221

5.13 An example of typical frictional behaviour of the thick abrasive . . . 231

5.14 Averaged FRT plotted against magnitude of load pulses for the thin and thick abrasives 240

5.15 Time variation of ablation rate in continuous polishing(A) and in intermittent polishing(B) 244

5.16 A proposed new experiment set-up 258

6.1 A modified design of the active lap 262

6.2 Exploded view of the active lap with the final design 263

6.3 Hexagonal packing of the 61 load cells 266

6.4 Circular packing of the 61 load cells 267

6.5 The new design of the global actuators for rocking compensation and global pressure control 269

6.6 An alternative model of active lap, using dye-cast Al boxed frames. . 274

6.7 A modified circuit for 88 half bridges, using only 2 instead of 176 dummy resistors 277

6.8 A block diagram of the active lap control system 281

6.9 Definitions of various work piece surfaces in polishing 289

6.10 A work flow of RTA 291

6.11 Flow chart of the 1AaBa-2A-3A-4Aa strategy of GPA, using the ablation coefficient map C(X,Y) 296

6.12 Flow chart of the 1Bb-2B-3B-4B strategy of GPA, showing data base approach to plan the polishing variables 304

6.13 Experiments to give 3 different lateral forces to load cell 313

6.14 Sensitivity difference (High-Low) against bridge number, measured at 21.8^oC and 24.4^oC 314

6.15 Offset difference (High-Low) against bridge number measured at the 2 temperatures 315

6.16 Schematic diagram of the new actuator spring. 318

6.17 FE model of the active lap for A-L coupling analysis 334

6.18 Vertical deflection of the flex plate 335

6.19 Conic selection area for the active load cells to be involved for interpolation 341

6.20 FE model of the active lap for L-L coupling analysis. 347

6.21 A vertical deflection contour map of the flex plate with +40N at load cell 7 348

6.22 The main part of the active lap and the scaled 85 cm Gemini secondary mirror 355

6.23 Expected pressure maps with the active lap on the mirror 357

6.24 Observed pressure map with the active lap offset in stroke 358

6.25 Observed pressure map with one of the global actuators lifting the lap on the mirror 359

B.1 Stress distribution of load cell with the web of $2cm \times 1cm \times 0.1cm$ . . 392

B.2 Stress distribution of the web of $2cm \times 1cm \times 0.1cm$ 394

B.3 Stress distribution of the web of $1cm \times 0.5cm \times 0.1cm$ 395

B.4 Stress distribution of load cell with the web of $1cm \times 0.5cm \times 0.1cm$. 396

B.5 Stress distribution of the rounded-edge web of $1cm \times 0.5cm \times 0.1cm$. 397

B.6 Stress distribution of the notched web 398

B.7 Software half bridge consisted of two quater bridges 400

C.1 Geometry of sub-diameter polishing tool in polishing 401

C.2 Error propagation in calculation of ablation rate coefficient 403

Chapter 1

Introduction

1.1 Astronomical Background

Since the invention of the astronomical telescope by Galileo Galilei in the early 17th Century (Hecht, p 192 [49]), there has been an ever increasing demand for larger telescopes for astronomical observation, which eventually lead to the construction of the 5 m optical telescopes at Mt. Palomar in the 1950s. It was a unique facility, that produced many discoveries and useful data throughout the 1960s. During the same period, however, the performance of the 5 m telescope has been significantly downgraded mainly due to the rapid growth of Los Angeles and the inevitable consequence of city light pollution. In the 1970s, a number of 3-4 m class telescopes were constructed and became operational at much better sites, serving astronomical communities in different countries world-wide. They include the 3.8 m AAT and UKIRT, 4.3 m WHT, 4 m NOAO telescopes, etc. These have been the most exploited in the major international observatories throughout the 1970s and 1980s.

They have proved themselves to be extremely powerful tools in the discovery and analysis of phenomena such as the evolution and distribution of galaxies, the Lyman α forest of QSO absorption lines, gravitational lenses, blue arcs in clusters of galaxies, active galaxies, QSOs themselves and the distribution of dark matter in spiral galaxies. There is no doubt that they have been and will remain to be productive and powerful facilities throughout the 1990s and indeed toward the early 21st Century. However, the astronomical knowledge obtained from the operation of

the 4 m class telescopes has played an important role in giving birth to necessity for still larger telescopes during the 1980s. Oertel [80] has put it in a very persuasive way in September, 1989.

> *" ... If, however, astronomers are to probe more deeply in time, ... we must have observational tools that extend our reach in terms of sensitivity and spectral and spatial resolution. During the past 2 decades, advances in sensitivity ... depended ... on improvements in detectors. In the visible, and increasingly in the infrared, ... existing devices already approach theoretical limits in terms of both detective quantum efficiency and readout noise. Additional gains must be achieved through increased aperture.*
>
> *... therefore proposing ... to construct two 8 m telescopes ... . Both ... to achieve an image quality that matches the best conditions offered by the Earth's atmosphere, and the instrumentation ... for imaging and spectroscopy in both the optical and the infrared. ... The combination of increased aperture, superb image quality, infrared compatibility, superior sites and state-of-the art instrumentation will guarantee ... to explore ... the types of fundamental questions about the origin and evolution of the Universe ... "*

During the 1980s, a number of 8 m class telescope projects have been proposed and some have started construction. Such examples include ESO VLT [3] [31], JNLT [67], UKLT [24], the NOAO telescopes [81], the Columbus telescope [16] [102], the Magellan telescope [51], etc. For the same period, the Keck 10 m telescope [77], the world largest optical telescope, has been constructed and became preliminarily operational in the early 1990s. Most of them are to be built either at Mouna Kea in Hawaii or in Chile where there are the world best sites over the atmospheric inversion layer, providing extremely good seeing and minimum levels of water vapour.

In principle, it is true that the larger aperture the telescope has, the more effective, in terms of gains, it is. However, in reality, it is found, looking at the current state of the relevant technologies gathered over the last two decades, that 8 m class telescopes are at the practical limit of the optimal balance between scientific

requirements, cost, risk, feasibility of transportation, fabrication of instrumentation and main optics components, etc. [80].

• Astronomical Programme of 8 m telescopes

The 8 m class telescopes will in no doubt bring major impacts on every corner of astronomical programs. Specifically three key astronomical programmes are identified and briefly summarised below [67] [80] [82]. These are expected to benefit greatly, taking full advantage of the 8 m class telescopes compared to their 4 m class predecessors.

Star and Planet Formation:

The infrared imaging, with adaptive optics and large collecting areas, enables searches and spatially resolved spectroscopy of disks around young stellar objects and sub-stellar objects near young stars. Again, the large aperture makes it possible to measure reflex radial velocity variations of solar type stars up to the distance of the Pleiades cluster and to detect planets as small as Jupiter. These capabilities would permit a still deeper knowledge of the properties of circumstellar disks around young stars, i.e. disk kinematics and its gas contents, proto-planetary materials, massive planets and sub-stellar objects at early evolutionary phase, brown dwarfs, etc.

Structure and Evolution of Our Galaxy:

The large optical collecting area and wide FOV extend medium-resolution multi-object spectroscopy to faint and weak-line stars and to very old stars at large galactocentric distances. The high resolution combined with the large optical collecting area enables determination of stellar and gas kinematics, through IR spectroscopy. An example of this is the search for the central cusp. The multi-object spectroscopy of main sequence stars in globular clusters can benefit enormously from its large collecting area, high-angular resolution and wide FOV. Again the large collecting area can extend high resolution, high signal-to-noise spectroscopy to the most metal poor stars.

This will allow more detailed study in the following areas.

- nature and distribution of mass i.e. stars, dark matter, mass of the outer halo in galaxies
- history of star formation in the early stages of galaxies

- chemical composition and kinematics of outer galactic disks
- structure of the nucleus of Our Galaxy; nature and extent of the central mass concentration
- age of galaxies
- chemical enrichment history and the formation of the elements

Formation and Evolution of Galaxies:

The large optical/IR collecting area and seeing-limited performance enable imaging and spectroscopy of large samples of the faintest and most distant galaxies. It also allows the application of high-resolution spectroscopy to absorption lines to significant samples of distant QSOs. This permits our access to deeper understanding of evolution of galaxies and the intergalactic medium, by providing much better information on composition, dynamics, and morphology at early epochs.

• Role of Ground Based 8 m Telescope in Space Age

The ground based 8m class telescopes can provide parallel observation in support of space missions, such as the Advanced X-Ray Astronomy Facility (AXAF) and the Large Deployable Reflector (LDR), operating outside the optical/IR wavelengths. This will make it possible, for the first time since the beginning of astronomical observation, to simultaneous observe in all wavelength regions from γ -ray and X-ray to radio waves. In optical/infrared regions, the role of the 8 m class ground based telescopes can be more clearly understood, when compared with the Hubble Space Telescope (HST) and the Space Infrared Telescope Facility (SIRTF) that share some of the same wavelengths with them.

Comparison with HST and SIRTF:

In optical and near-IR wavelengths, the HST, of 2.4 m in diameter, is undoubtedly the most powerful tool for astronomical programs that require high spatial resolution. Such examples include accurate photometry in crowded fields, imaging active galactic nuclei, and the morphological classification of distant galaxies, etc [80]. However, according to Nelson *et.al.* [78], for moderate to high resolution spectroscopy, the large aperture of an 8 m telescope gives much better sensitivity than HST at all wavelengths for the limiting magnitude actually achievable in

reasonable exposure times. Tyson [109] has pointed out that, given the expected angular diameter of faint galaxies, 8 m class ground based telescopes are superior to HST for detection of elliptical galaxies at visible wavelengths and for photometry, surface photometry, and detection of spiral galaxies at all wavelengths. For survey work, the 8 m telescope provides a much wider FOV than that of the HST.

Oertel [80] explained that, in the far-IR wavelengths, SIRTF of 0.9 m in diameter (still in planning) will be cooled to about 7^oK in orbit. The thermal background noise from both telescope and earth atmosphere will be virtually eliminated. For this reason, in principle, SIRTF is very much exceeded the 8 M ground based telescopes in sensitivity for both imaging and spectroscopy at 10 μm. However, in reality, SIRTF is diffraction-limited to 2.75 arcsec in spatial resolution whilst an 8 m ground based telescope has a diffraction limit of 0.3 arcsec. At a first class site such as Mauna Kea in Hawaii, the 8 m ground based telescopes equipped with active/adaptive optics technology can achieve near diffraction-limited imaging for a considerable fraction of observing time. Thus, the 8 m telescope will be much more effective than SIRTF in high spatial resolution for far-IR imaging and spectroscopy. In addition, it is practically impossible for SIRTF to have a high resolution spectroscopic instrument for 10 μm observation whereas the 8 m ground based telescope has no practical restriction for using it.

The recent advent of the active/adaptive optics technology can actively compensate wave-front distortions caused by atmospheric turbulence. About 0.3-0.25 arcsec imaging using this has been quite successfully demonstrated by the NTT operation in ESO. Application of this technology will certainly bring up the spatial resolution of the 8 m ground based telescopes, at first class sites, beyond that of HST, especially in the infrared (Diffraction limited imaging in the near IR with a 8 m telescope is now a realistic goal.) An additional advantage of the ground based 8 m telescopes is the capability of interferometric operation, proposed for the ESO VLT project [3], which the space telescopes are unable to offer. Moreover, the 8 m ground based telescopes have a very big advantage over the space telescopes in terms of cost, maintenance, upgradebility and re-engineering for their major components and instruments. This is clearly demonstrated by comparing the recent findings of the defects on the HST main optics and the launch of the new project to install small auxiliary optics to correct it. Finally, an 8 m telescope will have about 10 times the collecting area of

HST. The full area gain will be realised in photon-starved observation such as high resolution spectroscopy.

• Brief Outline of Gemini Telescope Project

Recently, the two 8 m telescope projects - NOAO and UKLT - have been combined to launch a new project called 'Gemini Telescope Project' [83] [90]. The aim to build two 8 m telescopes in Hawaii and in Chile remains the same as the original proposal of the 8 m NOAO telescopes. At the time of finalising this thesis, it has been confirmed that in total 6 countries join the project; USA (50 %), UK (25 %), Canada (15 %), and Brazil, Chile, Argentina (10 %).

Osmer [82] [83] and Randall [90] have described various aspects of the Gemini project, including the scientific requirements, which can be summarised as follows.

- Full sky coverage and excellent sites.

  The proposed sites of Mauna Kea in Hawaii and Cerro Pachon in Chile cover both hemispheres and provide full-sky coverage with excellent IR properties and seeing conditions.

- Optical system and imaging performance.

  The Gemini primary mirrors will be 8 m in effective diameter and very fast at f/1.8. They will have three configurations depending on choice of the three secondary mirrors - f/6, f/16 and f/20. The f/16 secondary mirror is designed to give IR optimised operation, allowing 3.5 arcmin field of view and 1-30 μm primary spectral range extendible to 0.4-1000 μm. Near diffraction limited imaging of 0.1 arcsec FWHM is aimed to be achieved at the wavelength of 2.2 μm using active optics and tip-tilt correction. The f/6 secondary is used for wide-field optical/UV observations, providing 45 arcmin field of view with the primary spectral range of 0.3-1.2 μm, but usable up to 2.2 μm. The image quality is to achieve 0.25 arcsec FWHM for this configuration. The f/20 secondary is used to give optical/UV Nasmyth focus - highly gravity stable platform for sensitive instruments - with 3 arcmin field of view covering 0.3 to 2.2 μm spectral range. The image quality is aimed at 0.25 arcmin FWHM.

- Flexibility in observation and instrument changes.

It will support additional service observation and remote observation in conjunction with traditional observation by users at the telescope location. It will be operating in principle of rapid interchanges between various instruments at both the Cassegrain and Nasmyth foci to take full advantage of varying weather conditions during an observing night.

As seen above, the specifications of the main optics for the Gemini telescopes are extremely tight, introducing a number of technological challenges to be solved for real construction. Thus, this thesis is intended to form an integral part of the UK contribution to the technology development for the fabrication of main optics for the 8 m Gemini telescopes.

1.2 Technological Background

• Traditional large telescopes

Traditional telescopes utilise optics of moderate size, typically less than 3-5 m in diameter for the primary mirror, and moderate asphericity, some tens of waves. The thickness-to-diameter ratio of the main optics is typically around 1/6. Their optical configuration is slow focal ratio; for example, f/3-5 primary mirrors and associated f/8, f/15, f/36 secondary mirrors. This leads to long tubes either in open trusses or in closed cylinders with small secondary mirrors (, though it can be large if it covers a large field angle). Due to the heavy weight of the primaries, the telescopes need heavy support structures, such as in the equatorial mount. All in all, the telescopes become heavy and bulky, requiring large infrastructure such as buildings and domes, which again are designed and built with inadequate understanding of the dome-seeing. In performance, the telescopes inevitably suffer from low resonance frequencies and are easily influenced by external perturbations, such as wind pressure, vibration, etc. The control electronics have to consume more power to drive the heavy structure, generating greater heat inside the dome, that again causes poor dome-seeing. Simply scaling up traditional telescopes to 8 m in diameter would not only be extremely costly, but also lead to the poor performance of the telescopes, so that they do not take full advantage of technological advances over the last few decades and of the world-best sites.

• **New generation large telescopes**

In contrast, the trend in new generation telescopes is clearly set to be in favour of the larger apertures of about 8 m in diameter, diffraction limited IR imaging with real-time active compensation of atmospheric influence, and considerable reduction in relative cost. A fair example of such trend can be found in the proposed design of the Gemini telescopes. Its primary mirror has the thickness of 17 cm over the diameter of 8.5 m (i.e. the thickness-to-diameter ratio of 1/20) The optical configuration is very fast e.g. f/1.8 primary mirror and associated f/6-7, f/16, f/20 secondary mirrors. This leads to a very short tube in Serrurier truss, with light and compact support structure of alt-azimuth mount. In summary, the telescopes are comparatively light-weight and compact, requiring relatively small buildings and enclosures that will be designed and build with deeper understanding of dome seeing, collected over the last two decades. The telescopes will have high resonance frequencies and much greater stability that reduces the effects of external influences. The control system will need reduced power when driving the lighter structure, producing less heat and hence smaller dome-seeing. Since the volume and weight of the telescope is critically dependent on the mass of the primary mirror, the light-weight mirror is of crucial importance when aiming to achieve all the prospectus described above for the 8 m telescopes.

• **Main optics fabrication for the new generation large telescopes**

There are three structural forms for a light-weight mirror; honeycomb mirror, thin meniscus mirror, and segmented mirror. The Keck telescope has a segmented primary mirror that consists of 36 zerodur 1.8 m hexagonal segment mirrors, whilst ESO VLT and Gemini telescopes will have single thin meniscus mirrors, as their primary mirrors. Each form has its own problems for mirror fabrication. For example, the figuring process for honeycomb mirrors is likely to produce the print-through of the honeycomb pattern onto the reflecting surface, which acts as high-spatial frequency defects. However, it is stiff and normally used on the passive support system. The single thin meniscus mirror is flexible and therefore needs an active support system that deflects the mirror in an controlled manner. Although it has been used for the MMT and the Keck telescope, the multi/segmented mirror has more serious problems than the single mirror. Firstly, the IR emissivity of the building and tele-

scope structure between the primary segments is reflected by the secondary and acts as high background IR noise, degrading the IR performance. Secondly, each mirror segment has bevelled edges that makes the IR emissivity problem extremely difficult to remove. Thirdly, it is extremely difficult to compensate the phase difference between a number of segmented or multi mirrors, which is crucial for optical interferometric observation. For these reasons, it is believed that the Gemini telescope and ESO VLT have intended to use single thin monolithic meniscus mirror, even though it requires an active support system. The advantage of single large mirror is clearly demonstrated with the current conversion programme of the MMT from six 1.8 m primary mirrors to a single borosilicate honeycomb monolithic primary mirror telescope of 6.5 m in diameter.

• Influence from recent evolution in related fields

Meanwhile, since the 1950s, rapid advance has been made in microprocessors, electro-optical sensors and actuators, computers and software. This new technology has been revolutionary in many respects our daily life, scientific research and instrument engineering. The recent developments in large optics fabrication have also been gradually moving toward to taking full advantage of this new technology.

• Technological problem that this PhD study tackles to solve

To date, major developments in large telescope optics production technology are mainly concerned with how to fabricate primary mirrors. It is because traditionally, the secondary mirrors have been produced without much difficulty, mainly due to their moderate size and asphericity. However, the Gemini telescopes will require the f/7 secondary mirrors to be about 2.5 m in diameter, highly aspheric(hyperbolic in asphericity of larger than 1000 waves), convex mirrors. (Recently, it has been informed that the Gemini telescopes will have the f/6 secondary mirrors, instead of f/7.) They will be the worlds largest and most aspheric secondary mirrors ever built in telescope history. In spite of this fact, the production of these secondary mirrors have been comparatively neglected in the course of the progress of the Gemini project, until now. The difficulty of producing this is two-fold; how to figure, and to test it. As explained in Chapter 3 and 6, in more detail, its extreme size and asphericity pushes mirror fabrication technology to limit, offering technical challenges in many respects. This thesis directly addresses these problems and is aimed

at the development of a new technology that benefits not only figuring the proposed Gemini secondary mirrors but also delivering the most advanced method to large telescope optics fabrication in terms of surface quality, removal rate, control of ablation, testing, and cost.

1.3 Historical Background

In 1984, Grubb-Parson & Co. Ltd., UK's unique and world leading manufacturer of large optics for astronomical telescopes for many decades, was closed by its parent company NEI Parson Ltd. The collective expertise gained over 5 decades was totally dispersed, demonstrated by their two main optics fabrication facilities, the 20 ft and 8 ft grinding and polishing machines, being stored unattended in a closed factory. Dr. David Brown, the UK's unique expert and the technical manager of the former Grubb-Parson, moved to University of Durham with the entire suite of their test optics. He had been employed as a consultant for some period of time by OSL to produce a technical record about large optics production, before he died suddenly in 1987. His death seemed to be an irrecoverable loss in UK large optics production that is still one of active research areas elsewhere world-wide. David Walker and Richard Bingham realised that it is imperative for the UK to maintain its expertise, not only to retain a capability for manufacture, but also in order to contribute properly to any international collaboration and to access the viability of technical proposals for large optics such as large telescope optics.

In 1987, OSL took serious steps to carry forward work in large optics production. The 1 m polishing machine and the 8 ft diamond milling and polishing machine were bought from the NEI Parson. By kind cooperation of University of Durham, OSL acquired the former Grubb's wavefront shearing interferometer and a large and unique suite of test optics. These include a 30 inch diameter flat and sphere, and the 40 and 60 inch meniscus lenses for testing secondary mirrors. This collection enhanced OSL to a unique position in the production of large optics for astronomical telescope in UK. Indeed, its capability of producing optics up to 2.5 m in diameter is about three times as large as others can do within UK. After an intensive programme of maintenance, both machines became fully operational in the way that the former

Grubb-Parsons ran the machines.

In 1988, by the time when the author joined OSL, an ambitious research programme had just started for a new development in the active production of large aspheric optical surfaces. It was aimed at providing

- better quality of large highly aspheric optics for astronomical telescopes
- cost reduction in manufacturing them
- manufacturing technology less tied to skilled craftsmen
- further development of the former Grubb-Parson's technology (full size passive flexible lap polishing), which had already been unique in this field world-wide.

The main contents of the project are to develop hardware and software for

- computerised diamond-milling for optical surface profile generation
- automated profilometric testing for ground optical surfaces.
- full size active polishing
- optical testing for large and highly aspheric optical surface.

1.4 Author's Contribution

The author contributed to the project as briefly summarised below.

• Development of computer-controlled diamond-milling facility for optical surface profile generation

The main contribution is the Profile Generation Software, versions of PROG.EXE, which drives the Grubb 8 ft machine to diamond-mill any shape of optical surface up to 2.5 M in diameter. Specially, it is capable of actively compensating errors in real-time while generating profiles. The work inevitably involves configuration and test of control electronics, and experiments with the former Grubb 8 ft machine.

• Development of computer-controlled contact profilometer for measurement for ground surface profile

Two profilometers were developed and are called Mark 1 and 2. The main contribution was the calibration of the LVDT and the Profile Analysis System Software, versions of PASS.EXE for Mark 1. The work also involves configuration and test for the LVDT sensor, its control electronics and commercial software supplied with the sensor. This proved the inadequacy of the commercial software for OSL's profilometry application. This encouraged our own development of PASS.EXE, of which the main function is to provide error information of ground surface profile that PROG uses to actively correct it in a real-time grinding operation.

• Development of overall philosophy and concept of full size active polishing

The current developments in production technology for large astronomical optics world-wide were reviewed, providing a close look at their advantage and disadvantage in depth. In collaboration with Dr. David Walker, who pioneered the concept of full-size active polishing in 1989, the author has refined and expanded it to establish a working structure of the full-size active polishing, which is thought to be superior to other methods.

• Development of load cell and force actuator specially tailored for requirements for full-size active polisher

Two of the most critical elements of the active lap were designed, developed, prototyped and experiments performed in house - this being specially tailored to suit the full-size active polisher, with pressure on reduction of production cost. FE analysis with ANSYS 4.4A is extensively used to design them. The characteristics of the prototype load cells and actuators was fed into the development of a sub-diameter active polishing module.

• Development of sub-diameter active polishing module comprising a load cell, an actuator, close-loop feed back control electronics and software

Prior to committing ourselves to development of the full-size active polisher, an active polishing module was developed with the purpose of being able to foresee technical difficulties in building the full-sized active polisher. Use of this module is also in mind for experiments for ablation rates and behaviour of abrasives in different polishing conditions. The prototype active elements were investigated experimentally as integrated parts of the module. It revealed the various characteristics of

them and eventually lead to the novel solution for minimising thermal and off-axial force effects. All these are taken into account when the full-size active lap was designed and built.

• Initial and manufacturing design of the full size active lap

The initial design for the active lap addresses technical requirements for the active lap and its major components. It evolves later to the manufacturing design for the machine and its parts in general. The design involves not only the hardware of the active lap but also the control software and ablation algorithm. FE analysis plays again a very important role to define the specification of the main mechanical structure.

• Developing optical testing for large highly aspheric optics surfaces, e.g. experimenting scatter plate inteferometry and the WYKO fringe analysis system

In preparation of development of optical testing for the 85 cm scaled Gemini secondary, scatter plate interferometry was experimented in conjunction with the WYKO fringe analysis system at the premises of the 1 m polishing machine in OSL. The findings from the experiments were fed into the development of the proper scatter plate test setup for the 85 cm scaled Gemini secondary.

• Experiments for ablation rate and behaviour of abrasive films with different polishing conditions

This work started from developing the experimental apparatus, comprising the prototype load cell 2, the control electronics and software, a Fizeau fringe test setup and the WYKO fringe analysis system. It is used to determine the ablation rate and to understand the behaviour of abrasive films under different pressure, sliding velocity and mixture ratio of water and cerium oxide. The results are compared with other studies and found to be extremely influential in how to control the active lap and hence fed to the ablation algorithms.

• Development of ablation algorithm consisted of Real-Time Ablation Algorithm(RTA) and Global Process Algorithm(GPA) for full size active polishing

The active polishing is to be controlled by an ablation algorithm that should function

to correct not only the surface figure, but also the algorithm, itself. The algorithm developed here is divided into 2 sub-algorithms - RTA and GPA. RTA is designed to control in real-time the ablation over the mirror surface while the machine runs. Specially, the core process of RTA that relates the ablation rate to the polishing variables are determined and adjusted by GPA in between each polishing run. They are the equations that define ablation rate and target pressure. It is found that there exist different forms of ablation algorithm, depending on which variable and how to control them. A classification scheme is developed for them and the most attractive forms of RTA and GPA are explored in detail.

• Test, calibration and modification for the installed active lap at component and whole system levels

The active elements - load cells and actuators - are calibrated and experimented with to see their performance as assembled on the lap. The results lead to substantial modification of the actuator and its spring. In doing so, the control electronics, mechanical components, low and high level control software also have to be tested and their problems are reported to be fixed accordingly. The measurement of the static pressure demonstrates that the active lap samples correctly different pressure distributions throughout the 1/3 diameter stroke on the 85 cm scaled Gemini secondary. The control theory for the active lap for construction of pressure map and actuator (stepper motor and global actuators) update in real-time are developed and suggested in the light of a deterministic algorithm approach.

• Providing other colleagues with consultations for the concept and technical informations of the active lap

Multi-disciplinary inputs were necessary to cope with the technical complexity of the project. Parts of the active lap were designed and built by the author's colleagues, some of whom are specialised professionals and others are postgraduate students. Examples include the mechanical components, the on-lap electronics, the low level control software, the high level GUI software, etc. Their work is cited properly where necessary throughout this thesis. In doing this work, they all needed technical inputs which the author provided via consultations and project group meetings.

• Publications

During about 5 years research, the author has written the publications i.e. internal

and external as author/co-author as follows.

1. User Guide for Profile Generator version 1.0 at OSL,
   1989, (OSL Internal Publication).

2. Production of large Optical Components for Astronomy,
   1989, OE report, No. 70, p8, (External Publication).

3. Specifications for The Active Lap Control Software,
   1991, (OSL Internal Publication)

4. The Production of Highly Aspheric Secondary Mirrors Using Active Laps,
   1992, ESO Conference on Progress in Telescope and Instrumentation Technologies, Edi. M.-H. Ulrich., ESO Conference and Proceedings No. 42, pp 215-218. (External Publication, Appendix A.1).

The author has also provided technical informations in help for the project manager, Dr. David Walker, to generate a number of project and design study reports. Examples include

1. Design Study Report; Progress on The Active Lap for production of The Secondary Mirror(s) for The 8 m Telescopes,
   1991, D.D. Walker., submitted to the UKLT project team.

2. Final Report SERC Grant GRT/43676 - *Research in Producing Astronomical Optics Using Active Laps*,
   1992, D.D. Walker., submitted to SERC.

1.5 Aim and Summary of The Thesis

The aim of the research was firstly to develop a new computerised method of producing large astronomical optics. Secondly, it was specifically intended to be used for producing a 1/3 scaled model of the proposed f/7 2.5 m hyperbolic Gemini secondary mirrors. (When the project started, the Gemini secondary mirror was specified to be f/7. This was changed to f/6 after we had profiled the mirror. Thus, the development was proceeded at f/7.)

The development consists of

- a fully operational surface profile generating facility including software
- detailed concept of full-size active polishing
- active front-end elements for full-size active polisher
- a 85 cm scaled full size active polishing lap, including optical testing
- ablation rate and behaviour of abrasive film under different polishing conditions
- theory and necessary data for the two main functions of real-time active lap control - construction of pressure map and actuator update
- classification of ablation algorithm
- detailed structure of a complete ablation control algorithm.

The fully operational active lap works with the computer-based ablation algorithm that takes considerable time to be fully matured after the first run. Completion of the 85 cm scaled Gemini secondary using the active lap would ideally be some time after the algorithm is fully matured. The full-size active polishing is indeed a long-term project. This five and a half years work the author has spent did not take the project to completion. Thus, neither a fully operational active lap nor completion of the scaled Gemini secondary mirror is within the scope of this thesis. This thesis documents the development of concept and theory and construction of the active production facilities up to a stage of initial tests. The thesis is, therefore, intended to present the first few results of tests for functionality of the active lap at component and system levels.

Chapter 2 deals with the development of the active profile generation and measurement systems. Chapter 3 is concerned with the review of the current technologies world-wide in large optics fabrication and establishes the new concept of full-size active polishing. It is followed by the development of the load cell, actuator and a sub-diameter active polishing module in Chapter 4. The experiments for ablation rate and behaviour of abrasive film are described in Chapter 5. Chapter 6 discusses

the interim and manufacturing designs, construction, calibration and testing for the 85 cm scaled full-size active lap. It also presents the results of the preliminary tests for functionality of active lap on the 85 cm scaled model of the proposed Gemini secondary mirror. Chapter 7 summarises the implications of the developments made in this thesis. The application of the full-size active lap and the technologies involved are discussed and future work with the lap are envisaged .

Chapter 2

Optical Surface Profile Generation

2.1 Introduction

The production of large astronomical optics consists of three main processes. The first is the generation of surface profile, to produce a milled optical surface ready for the second process, grinding with loose abrasives. This is followed by polishing. By surface profile generation, it is meant a process of making a right shape and dimension for a requested optics and removing the bulk of the unwanted material from a glass blank to produce a surface profile near to the desired profile. Like other manufacturing processes, this process can comprise two activities in itself; how to generate the profile and how to detect and to correct errors on it. In this case, they form an iterative process one after the other until it reduces the surface error below an acceptable level. These are the main subjects that concerns this Chapter.

The glass blank, that an optics shop normally starts working for an astronomical optics, is a thick circular disk of material such as Cervit or Zerodur (These are zero expansion ceramic glass materials). Even though a blank fabrication process called *'Spin Casting'* [117] can reduce dramatically the material to be removed for concave primary mirrors, its dimensions are not normally what is exactly wanted and its surface finish is by no means near to optical quality. Optical polishing can not be applied directly from this stage because there is still too much glass material to

remove. Thus, the first thing to do is to make the blank suitable for polishing. It starts with making both the surfaces of the disk flat and parallel to each other. The edge has to be cut out to a requested diameter. Both the outskirts of the disk are trimmed with bevelling. Then the bulk of glass material is milled off to generate a surface profile close to the desired one. With this milling, the final surface profile generated leaves about 20-30 μm above the required profile [54]. This is to allow for sub-surface damage and machine marks. A series of lapping with loose abrasives is applied to reduce the surface error down to 2-3 μm. Here the surface error means a combined effect of the overall departure from the theoretical one, local slope error and high frequency spatial ripples. The traditional method that GP and, indeed, others elsewhere have used is, however, long and tedious. GP simply cut coarse steps with the manually controlled milling tool. Then they used loose abrasive lapping to remove the coarse steps and to converge on the required profile. This was crude and very slow. It contributes largely to the time required, and hence cost for large optics production. Larger and highly aspheric optics production would be greatly benefited if the surface profile generation could be completed quickly. Our development in computerised milling process is intended to go straight to the profile in milling to 25-50 μm accuracy.

Since 1950, the fast evolution of microprocessors and electro-optical sensors for measuring various physical parameters has made unmanned feed-back and forward controls very much reliable. This Chapter is mainly concerned with development of a new computer-controlled surface generation facility (Phase 1 Development) based on these technological advances. Section 2.2 introduces a new method OSL developed as well as the traditional GP's method and its problems. The core of the OSL's method, profile generation software, is presented in Section 2.3. The calibration of generated profiles and detection and compensation of errors are dealt with Section 2.4. The implication of the development is discussed in Section 2.5.

2.2 New Philosophy of Profile Generation

2.2.1 Grubb-Parson's Method of Profile Generation

• Grubb-Parson's 8 ft grinding and polishing machine

Horne has briefly explained how GP ground and polished the 98 inch INT and the 150 inch AAT primaries [54]. The 8 ft grinding and polishing machine OSL acquired, was used for making the INT primary by GP. The way in which GP ground the primary can be understood more easily from Figure 2.1 and Figure 2.2.

The rotating platform on which the blank is mounted is powered by a 20 HP electric motor and rotates at a period of typically 43 sec/rev. The quill carries a vertically moving steel column along the horizontal platform. It is supported by a frame that consists of two heavy steel columns linked with another heavy steel arch. The quill and the horizontal platform have a lead screw each. The one on the platform holds the quill whilst the other on the quill keeps the vertically moving steel column. A 5 HP grinding spindle of 2000 rpm is mounted on the column. At the end of the spindle, there is a cutting tool to which surface fine diamond powder is glued. As the two lead screws rotate, the quill moves across the work piece and the cutting tool up and down to diamond-mill the blank. The two lead screws are rotated either with handles powered by man or with mechanical gear boxes and mains power motors. One turn of both the lead screws causes a tool movement of 0.25 inch in both axes. When fine movements are required, the lead screws are rotated with the handles and the mechanical readings used.

• Operation of the 8 ft machine for milling optical surfaces

With the 8 ft machine described above, continuous-horizontal movements of the quill over the radius were made with the electric motors to flatten both surfaces. Then, at a required radius, continuous-vertical movements were made to the thickness of the blank for edging. These two processes resulted in sharp edges on the top and bottom surfaces. The quill was tilted so as to push the cutting tool to the edges with an angle. This bevelling led to an angled edge and reduced effective diameter but decreases the possibility of contamination by broken pieces of the sharp edge of the blank when polishing. A number of coarse step cuts along the diameter were then made to remove the bulk of glass material when starting the profile generation.

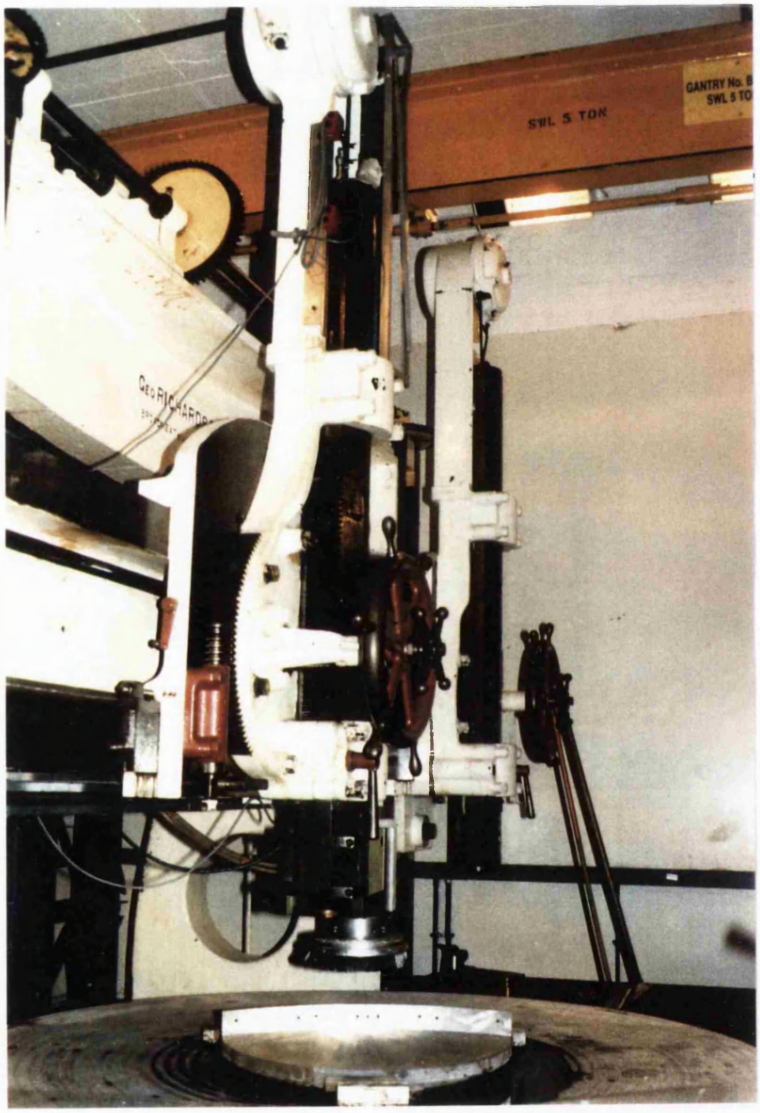

Figure 2.1: Photograph of the Grubb 8 ft grinding and polishing machine

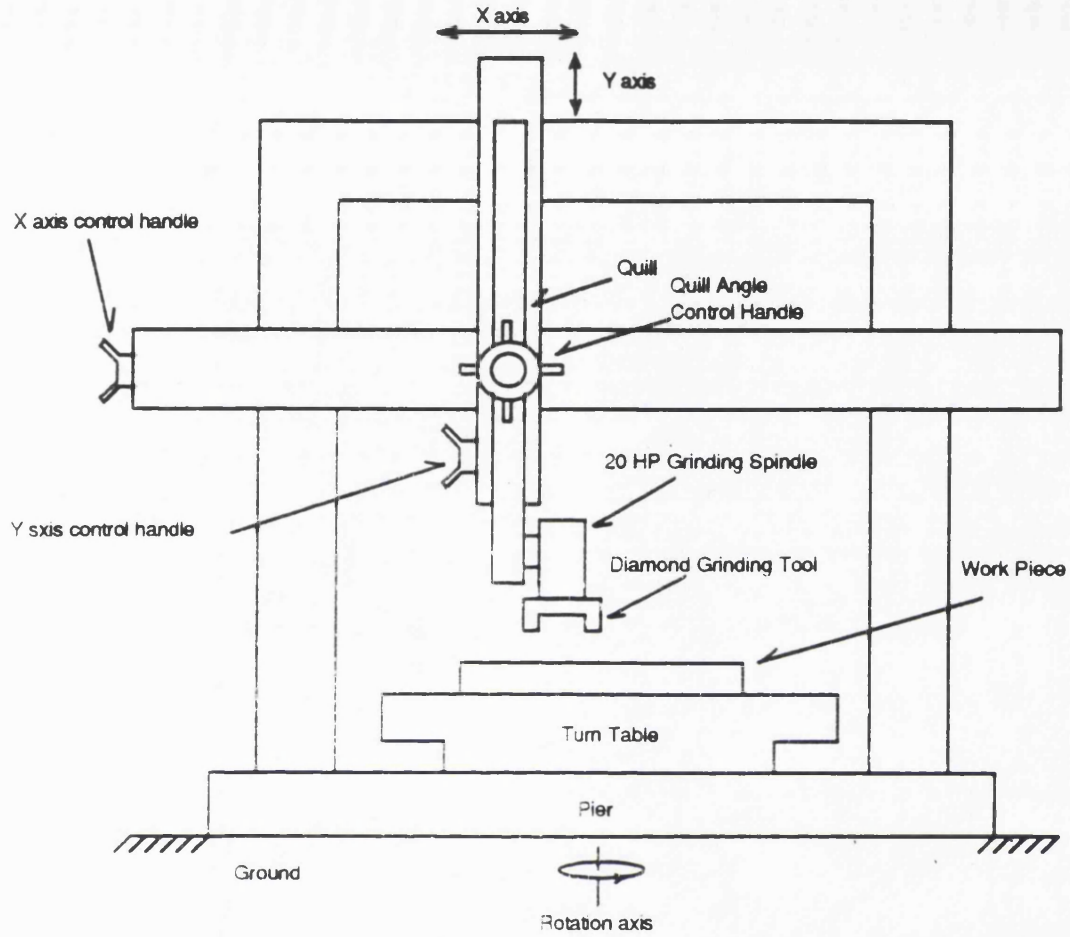

Figure 2.2: Schematic diagram of the 8 ft machine

A number of finer step cuts were made along the requested profile. The handles for both the X and Y movements had to be manually operated in conjunction with mechanical dial gauge. Great care was necessary in monitoring the readings and fine operation by an optician who controls the handle played a crucial roles in this stage.

Traditionally, the role of the profile generation has been to produce a closest spherical surface to the desired aspheric surface. Aspherising was normally achieved after the completion of the spherical surface by polishing since the asphericity required for traditional telescopes was small. GP had followed this tradition and used to achieve about 25 μm error in diamond-milling the spherical surface profile. A series of lapping with loose abrasive such as water-carborundum mixture was applied for fine grinding. As the lapping went on, finer and finer abrasives were used until they finished the profile generation with the accuracy of 2-3 μm in the surface profile.

• **Error detection of milled surface profile**

A spherometer was GP's favourite instrument to detect surface errors. At their best, GP were able to detect the error of 2-3 μm [54]. It was entirely due to the limitation of the mechanical instrument. From that to one tenth of the wavelength in accuracy, which is the realm of polishing, optical means are used such as shear beam interferometry. Once they located errors on the ground surface, they were either ground or lapped off depending on the nature of the error. For example, if there were deep scratches, then the profile generation by the fine step cuttings were iterated. If there was a hump of which height is less than 10 μm, sub-diameter lapping was applied on it. This is the way in which not only GP but others have traditionally used for profile generation. Despite the good quality in output, this is indeed a long and tedious process that requires a optician's patience as well as skill and hence increases production cost of large astronomical optics.

2.2.2 Computerisation of Profile Generation

• **Modernisation of the 8 ft machine**

The 8 ft machine has been substantially renovated since it was acquired by OSL. As seen in Figure 2.3, two linear encoders [43] are fitted (e.g. one on the horizontal platform and the other on the quill) to monitor the X and Y coordinates of the cutting tool. Two mechanical gear boxes and two stepper motors [103] are mounted near the left end of the horizontal platform. These are to provide the cutting tool with fine X and Y movements. The motors run at half step mode for finer stepping and minimum resonance. The motor driver controller generates signals for full/half step mode, stepping pulses, direction, etc. under the commands from a 3D MITC6 intelligent stepper motor control card [26] (see Glossary for 3D). The card sends the command signals under the supervision of profile generation software, run on a IBM PC/AT compatible clone. The encoders are also interfaced to the PC via a 3D MITC3 72 way programmable digital I/O card [26]. The optician can move the cutting tool by low level commands that the 3D MITC6 card understands directly. This requires rather simple software, that conveys input command strings to the card. Alternatively, an intelligent software package would prompt the user to define high level operating parameters instead. Then it translates them to command strings

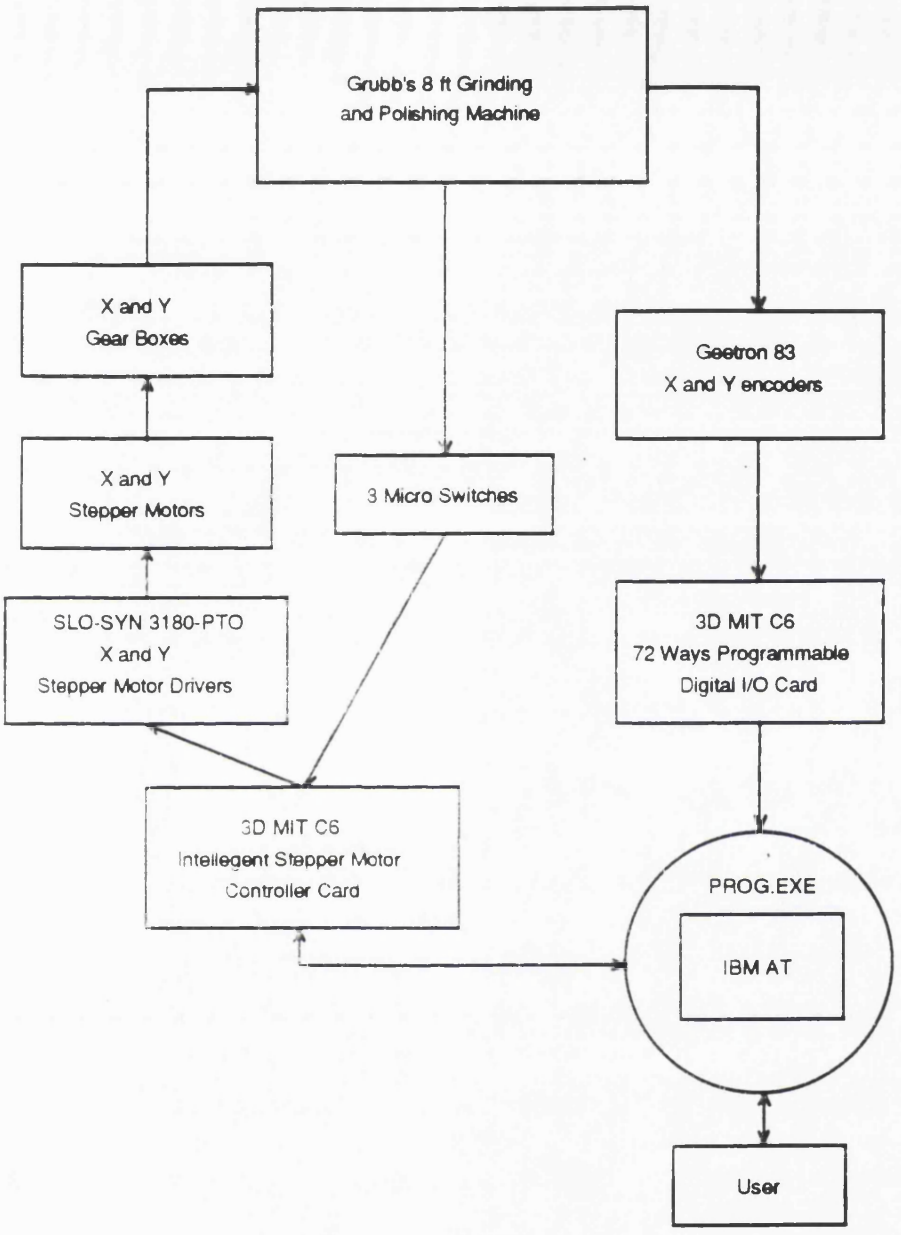

Figure 2.3: New method of profile generation using the 8 foots machine

sent to the 3D MITC6 card at right time and positions.

There are a number of micro switches, as a safety system, that limits the X and Y movements of the quill and the cutting tool. A pair of the switches are placed at each end of the movements, i.e. a total 8 for 4 pairs at 4 directions. The first switch that the quill meets with excessive movement in any direction would be continuously monitored by the software. The 'motion halt' command would be issued, when the switch is touched. The second switch is a back-up safety device that turns directly the main DC power to the motor and its driver off when it is touched by the quill.

This would be the only way in which the surface is not damaged when the first switch monitoring fails to stop the quill motion.

• Detection and compensation of surface profile error

Detection of the surface error can be made by using a profilometer. Modern LVDTs have readily achieved sub-micro metre resolution and the error better than a few micro metres, in determining position within the range of few millimetre to few tens centimetre. It can be used to build a simple but effective profilometer to detect surface errors of about 1-5 μm. There would be profile analysis software that reads the signals from the profilometer. The software would make use of the profilometer to sample a number of points, e.g. 20 points along the generated profile. The measured profile would then be compared to the theoretical one. The difference between the two profiles forms an error profile. Taking this into account, the next profile generation would be capable of reducing the error. In principle, the iterative process of the profile generation and the error detection can continue until the error is reduced to about 1-5 μm. When the iteration stops is a trade off between the profile accuracy to be achieved, the calibration accuracy of the sensor and the subsurface damage.

• Advantages of this new method of surface milling

There are two distinctive advantages of the new philosophy over the traditional method. Firstly, surface profiles, of any asphericity, can be milled directly once flattening of the blank surface is completed. Or the milling can be made after the coarse step cutting along the aspheric profile is finished, if there is not much time left for profile generation. Thus, the new philosophy allows the direct asphersation of a surface by diamond-milling whilst the traditional method does this by polishing after completion of the closest sphere. The advantage of lapping a sphere is that it is guaranteed rotationally symmetric. Direct milling for an asphere has a potential danger that it may mill in astigmatism. However, this kind of surface error can be corrected with full size active polishing that is described mainly in Chapter 3 and 6. Nevertheless, as said in the Chapter 1, there has been rapid increase in the asphericity of large optics for modern telescopes. The completion of a closest sphere and subsequent aspherisation by polishing would greatly increase the production time and cost for this. It is this that the new philosophy is capable of reducing.

Secondly, this way of error compensation means that the absolute calibration of the 8 ft machine does not have to be made. The error profile is an integrated expression of the ways in which the 8 ft machine behaves during cutting. It includes tool vibration, backlash, bending of the horizontal platform, change in tilt angle of the quill, variation of pitch in lead screws, tilt of the encoders with respect to the horizontal platform and the quill, change in contact area on the cutting tool while grinding, tool wear, etc. To calibrate all these factors individually is enormously complicated and eventually ended up with the integrated expression on the surface profile. This is what the new philosophy intends to measure directly and compensate instead.

2.3 PROG.EXE: PROfile Generation Software

2.3.1 Fundamentals of PROG.EXE

• Initial work for PROG.EXE

3D supplied a rudimentary software for controlling the MITC6 card. The function of the software is to translate high level ASCII commands to equivalent 8 bits Binaries and send them to the MITC6 card. However, its graphic interface did not properly function with the VGA black and white monitor OSL had at that time. Since the time for the Phase 1 development to demonstrate OSL's ability to produce large optics was running out rapidly, even a simple software package needed to be urgently developed to start diamond-milling a Cervit blank of about 85 cm in diameter. A software later called MOTOR24.EXE was developed. It functions much like the one 3D supplied, but is more user-friendly. Examples include the ability to show the command history that a user input and a new set of direction commands i.e. LE(LEFT), RI(RIGHT), UP(UP) and DO(DOWN) were added. The graphic interface is replaced with a text-dialogue interface. The concept of MOTOR24.EXE was later used to write the AXIS procedure of PROG.EXE. Another software package that 3D supplied for reading the encoder included a bug, producing entirely the wrong readings. This was repaired later and forms the encoder reading routine of PROG.EXE.

• Initial specification for PROG.EXE

Walker [110] has initially outlined the specification for PROG.EXE, summarised it as follows.

1. It must be user-friendly since traditional opticians are not familiar with the use of computer and software package in production.

2. The number of mnemonic commands are to be minimised. They should be short, i.e. ideally maximum two characters and easy to use.

3. Units are the same everywhere and are consistent e.g. micrometre.

4. The programme may consist of about six procedures that can be menu- selected. They are movement with low level command, movement with defined target, facing, edging, bevelling and general profiling with target lists.

5. By the general profiling with target lists, it means the fine step cutting along the profile is made by reading target coordinates listed in a target file that an optics design software package such as KIDGER 3.71 produces.

6. When motions are made, the two axes must move simultaneously so that the tool motion is tangent, not first X and second Y movements or vice versa.

7. For the profile generation, it must be capable of making several cuts across the diameter of the blank without being monitored continuously by the operator.

8. It must be able to generate all normal optical surfaces including aspheres.

9. It must be able to be stopped with single key stroke e.g. F1-key in case of emergency.

10. Once fine step cutting starts, backward movement of the tool must not be allowed in the horizontal (X) coordinate.

11. The micro limit switches must be monitored all the time when any movements are made.

12. When the machine is in action, all necessary information including warnings and precautions must be displayed to help the operator.

• General features of resulting PROG.EXE version 1.0

All these specifications are met with PROG.EXE version 1.0, which is fully operational, except the item 5 and 6. It was necessary to modify them to improve the performance of the machine operation. Some general aspects regarding the specification are worth being presented here. Firstly, the user-friendly features are enhanced by no mnemonic command that user has to learn, except about 9 original ASCII commands 3D supplied. All necessary information is displayed whichever stage the user works with. Users do not have to worry about how to direct and route the programme, in other word how to control the programme, to achieve a task. The programme execution is already oriented for this and its flow is fixed. All users have to do is to simply follow it by choosing and defining the parameters prompted at each page of display.

Determination of target coordinate:

The proposed method of determining the next target coordinate during fine step cutting could produces some difficulties listed below.

- Fine step cuttings with 10 μm interval over the radius of optics of 1.25 m, that the 8 ft machine can handle, need about 125000 pair of array variables. The conventional DOS memory of 640 KB can not handle this together with a programme of fair size reside in it.

- There would have to be a coordinate transformation which converts the fixed target coordinates to the Grubb-Geetron coordinate system.

- Since it is inadvisable to cut a depth larger than 100-200 μm, the generation of a profile consists of a number of fine step cuttings over the different radii. This requires accessing different parts of the target list file to achieve series of fine cuttings with different radii depending on the depth of a profile from the flattened surface.

- The excessive use of hard disk access could reduce its life expectancy.

- The programme must be capable of accessing the data file that any optics design software produces. This requires knowledge on various output file formats that each optical design software uses.

All these increase the complexity and size of the programme so as to push the memory use beyond its limit. Thus the idea is replaced with a new method called *'Equation Pointing'* instead. A set of equations that can describe all normal optical surfaces is put into the programme. It uses them to calculates the next target coordinate each time a step movement is completed. This Equation Pointing was proved successful in removal of all the problems described above, and hence to simplify the software. The equations are presented later in this chapter.

Resolution of tool movement and machine backlash:

The 1 step pulse corresponds to the actual distances of 0.529 and 0.539 μm with the standard deviation of 0.001 and 0.005 μm in the X and Y axes respectively. The difference of 0.01 μm/step was taken into account in the calculation of step pulses as distance between target points in the X and Y axes. The measured backlashes at an arbitrary position are 3.205 and 0.682 mm in the X and Y axes respectively. It can be noted that the Y backlash is much smaller than the X backlash. This can be explained by gravity preloading the vertical traverse . The backlashes are expected to vary over the ranges of XY movements. The precise calibration of the backlash over the movement range was not necessary since it was intended to move in only one direction during fine step cutting. For other parts of tool movement, it is compensated in the first order by using the measured backlashes where necessary.

Units:

Units for distance or length are in μm everywhere unless otherwise indicated. The unit for velocity is 3D's C6 unit, which the 3D MITC6 card can understand. The velocity expressed with this unit increases but not linearly. 1 3D's C6 unit equals roughly about 53 μm/sec for the X axis and 54 μm/sec for the Y axis. It is always, except the facing and low level motor control, initialised as minimum values of 145 μm/sec and 148 μm/sec for both the X and Y axes.

Tool movement in general:

The diagonal movement of the tool does not always have to be used. Even if it is intended, there will be step wise movements if required movement in one axis is much longer than that in other axis. If it has to be made all the time, the only way is to control the stepping speed in conjunction with the distance to move. However, control of the stepping speed is dangerous during fine step cutting along the profile.

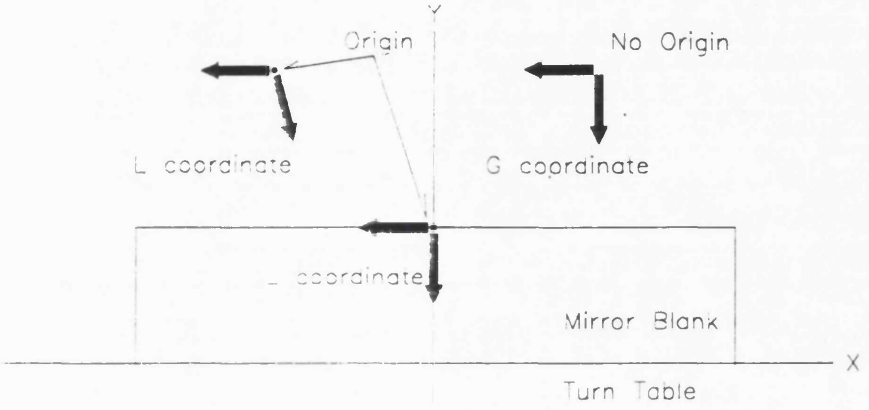

Figure 2.4: Coordinate systems used for PROG.EXE

If something goes wrong, it will produce irrecoverable damage to the optical surface. For this reason, the stepping speed must be set to the lowest level during fine step cutting. As a result, the two movements are mixed in use depending on where the tool is and what stage of profile generation is at.

Coordinate systems:

Two coordinate frames are defined, as depicted in Figure 2.4.

1. Machine coordinate frame (G coordinate system) :

This is absolute, but not fixed in space with respect to the machine. It is defined by the machine X and Y encoders. Since they are incremental, the origin of the frame can be defined anywhere within the space defined by the precision fiducial microswiches at the ends of the X and Y traverses. This limits its use to simple task, such as facing, edging and parts of bevelling.

2. Cutting coordinate frame (L coordinate system) :

This is the coordinate frame used to define the equation of a specific cut in the profiling procedure. The origin is defined at an arbitrary (but fixed) distance above the turn table. The cutting coordinate frame is in fact a machine coordinate frame that has a fixed origin clearly defined. This coordinate frame is used for parts of

the bevelling procedure and the profiling procedure.

Coordinate transformation:

When cutting fine steps, the quill may have to be tilted from time to time. This changes the coordinate system in which the tool moves whilst the mirror sits in the fixed rectangular coordinate system. Since the profile is in the fixed rectangular coordinate, the direction and the distance to the next target have to be transformed into the tilted coordinates. The coordinate transformation is written as follow.

$$X_a = X - Y \tan\theta \tag{2.1}$$

$$Y_a = Y / \cos\theta \tag{2.2}$$

where X = X coordinate in the rectangular i.e. mirror coordinates

Y = Y coordinate in the rectangular i.e. mirror coordinate

X^a = X coordinate in the angled i.e. quill coordinate

Y^a = Y coordinate in the angled i.e. quill coordinate

θ = quill angle

Concept of 'Moving Reference Profile':

A concept called *'Moving Reference Profile(MRP)'* was developed for multiple-cutting fine steps along the surface profile that the user defines. It allows users to define not only the reference surface profile that user wants to generate but the way in which the reference profile itself moves in the XY coordinate. The MRP method defines only half the profile as measured from the vertex toward the Cartesian positive direction. Figure 2.5 shows the MRP concept.

A reference point of a profile, defined in the cutting coordinate frame, is shifted down between one cut and the next cut, by an amount equal to the depth of cut. Examples of such reference point include the centre of a sphere, a focal point of a parabola, etc. Therefore, the equation which defines the tool path during a specific cut, is always defined by the fixed origin in the cutting coordinate frame. However, during the entire process of milling a workpiece, the reference point of the profile , so as the profile itself, progresses down into the workpiece in successive steps.

Overall structure of PROG.EXE version 1.0:

The overall structure of PROG.EXE is drawn in Figure 2.6. It starts with configuration of the interface cards followed by a main menu prompt, asking for control

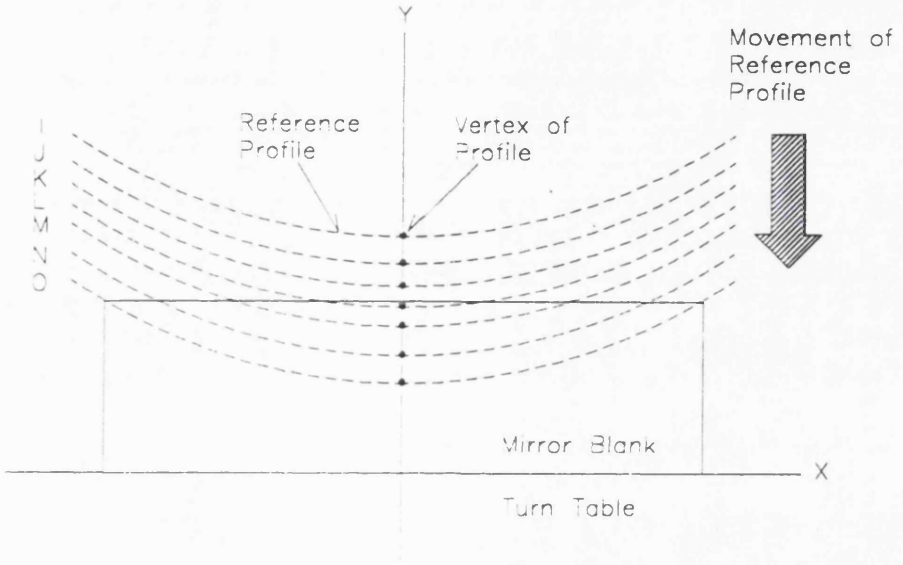

Figure 2.5: Concept of the MRP method. A reference profile can be defined as I and then moved through J, K, L, M, N until O to mill the glass surface.

command input. There are 9 non-mnemonic plain language commands, which are in fact the names of the tasks. Typing a command moves to one of the tasks described more details in the following subsections. Individual tasks consists of generally two stages, definition of parameters and execution. Interrupt by key trapping can stop the machine operation and bring back to the main menu at any time during programme execution. Direct interlinks between the tasks are provided where necessary. When a task is completed, the task ending message comes with a set of menus to direct a user.

2.3.2 AXIS Procedure

All the low level ASCII commands can be directly implemented to the 3D MITC6 card in this procedure. This is a descendant of MOTOR24.EXE, which functions similarly. The axis of intended movements is chosen first and then movements can

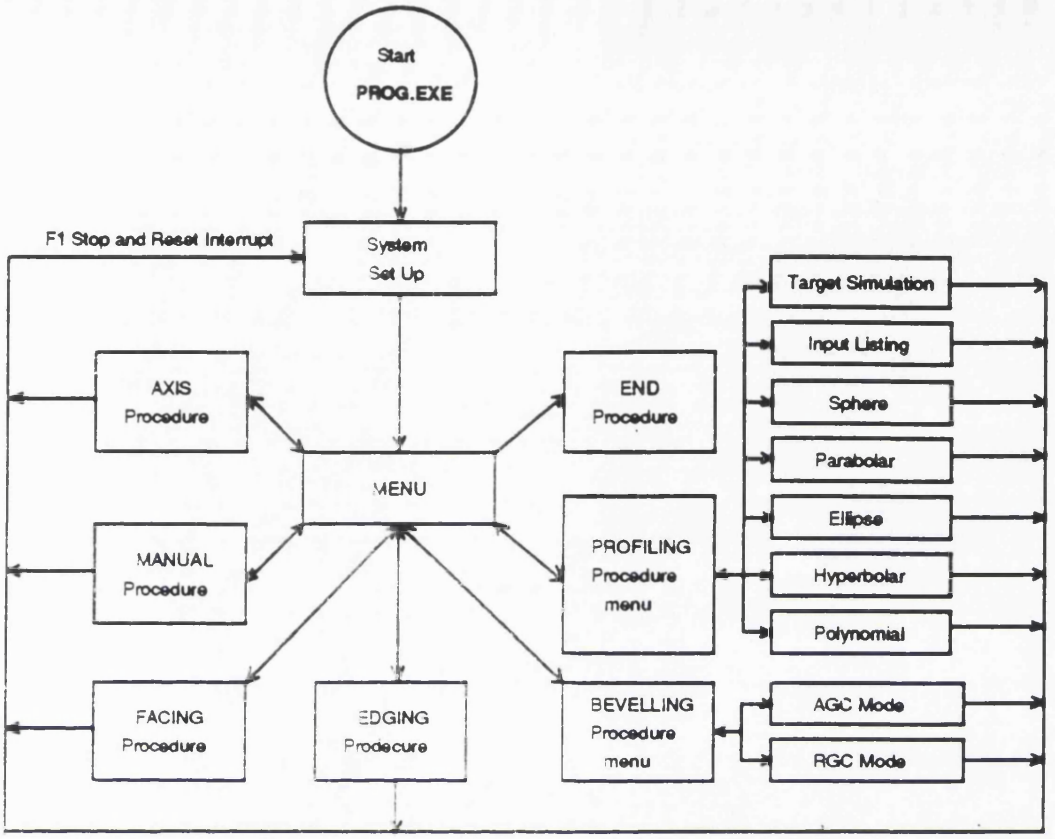

Figure 2.6: Overall structure of PROG.EXE version 1.0

be made. Only one axis can be selected for movement at a time. The status of the control parameters in the card are updated continuously as long as the user is working with this procedure. The 3D MITC6 card memorises the control status made by the last command input even if the main power is off and on again. For this reason, all the tasks except the MANUAL procedure pass the initialisation when they start.

2.3.3 MANUAL Procedure

This procedure makes movements in the X and Y axes by defining target coordinates. Comparing the target and present coordinates gives the direction and distance for movement. These are then exported to the 3D MITC6 card to trigger the movement. Here two parameters are set prior to iterative definitions of targets for successive movements. They are the quill angle in degrees and the target box size in microns. By the target box size, it means the amount of error that the movement toward a

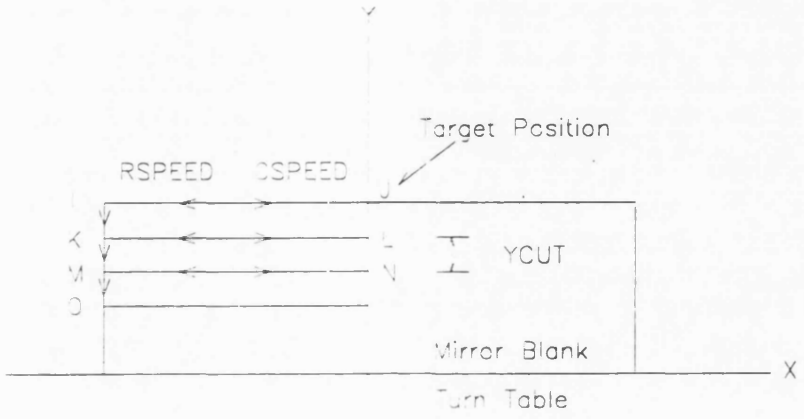

Figure 2.7: Movement of tool for facing.
The tool moves along the track defined by the point sequence I-J-I-K-L-K-M-N-M-O. It is shown here how 3 cuttings are made. CSPEED denotes the cutting speed whilst RSPEED the returning speed. DYCUT is the vertical depth of a cut. The target is the point J.

target must achieve. The tool moves until it is within the square error box centred by the target. It can be made with as many movements as wanted until escaping to the main command prompt with the interrupt. The motor control parameters such as first and final rates, acceleration, etc. are not initialised if directly accessed via the main control prompt from the `AXIS` procedure.

2.3.4 `FACING` and `EDGING` Procedures

Figure 2.7 and Figure 2.8 show how the tool movement is controlled for these tasks. The G coordinate is used for these procedures, so that a fixed origin does not have to be defined. Speeds for both cutting and returning in the `FACING` procedure are allowed up to 40 units, equivalent to about 1915 μm/sec and 1940 μm/sec for the X and Y axes respectively. However, edging needs to be done at the slowest speed possible, to prevent grinding spirals on the side surface of the blank. The grinding

spindle must be configured with the quill angle of 0 degree for both the tasks. For facing, PROG.EXE prompts for an input of 5 parameters; target position, vertical cut i.e. depth of a cut in microns, number of cuts, cut and return speeds in 3D units. Edging requires just three parameters to be input since speed control is no longer necessary. They are target position, horizontal cut i.e. width of a cut in micron and number of cuts.

2.3.5 BEVELLING Procedure

There are two ways of bevelling the blank. One is to move the angled quill downward toward the edge of the blank. No X movement of the quill is used for this. This is called 'Angled Geetron Coordinate(AGC) mode bevelling'. The other is to use the zero-angled quill with the MRP concept. This of course uses both the X and Y movements. The tool moves along the inclined reference line, which again moves down each time a cutting is completed. This is called 'Rectangular Geetron

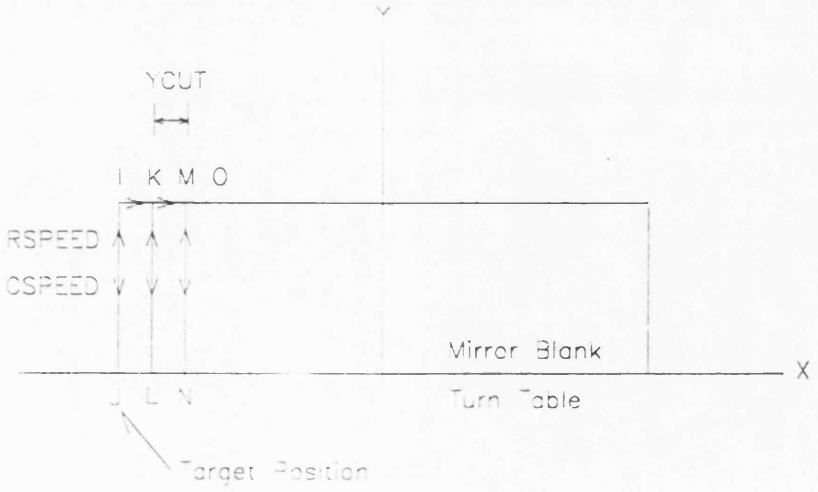

Figure 2.8: Movement of tool for edging.

The tool moves along the track defined by the point sequence I-J-I-K-L-K-M-N-M-O. It shows how the 3 cuttings are made. XCUT denotes the horizontal depth of a cut. The target is the point J.

coordinate(RGC) mode bevelling'. The AGC mode bevelling is for optics larger than 80 cm in diameter, if there is no auxiliary platform to pull up the Y coordinate of the mirror blank. This is because once the quill is tilted, its limited capability of travel along the quill makes it impossible for the tool to reach the edge of the blank just sitting on the turn table. RGC mode bevelling is capable of generating bevelled edges in any size of optic, since it uses both the X and Y movements of the tool.

Both methods use the L coordinate so a fixed origin must be defined prior to cutting. In AGC mode bevelling, there are 4 other parameters to be defined; quill angle in degrees, total depth of vertical cut in microns, period of revolution of the turn table in seconds and depth of a cut in microns. RGC mode bevelling requires 6 parameters to be defined. They are bevelling angle in degrees, vertical depth of a cut in microns, number of cuts, period of revolution of the turn table in seconds, target box size in microns and X incremental step in microns. Figure 2.9 and Figure 2.10 explain these parameters as well as how the tool moves for the 2 modes of bevelling.

2.3.6 PROFILING Procedure

This starts with a stage to define an origin of the coordinate system, followed by the profiling sub-menu. It directs individual tasks to generate various surfaces such as sphere, parabola, ellipse, hyperbola and polynomial. There are 3 groups of parameters to be defined.

Geometric Parameters:

These defines properties of the reference surface profile to be generated.

- `type of surface`
  defines whether a concave or convex profile is to be generated.
  appears in all the sub-procedures to generate profiles.

- `radius of curvature`
  defines the radius of curvature of a sphere.
  appears only in the sub-procedure to generate a sphere.

- `focal length`
  defines the focal length of a parabola.

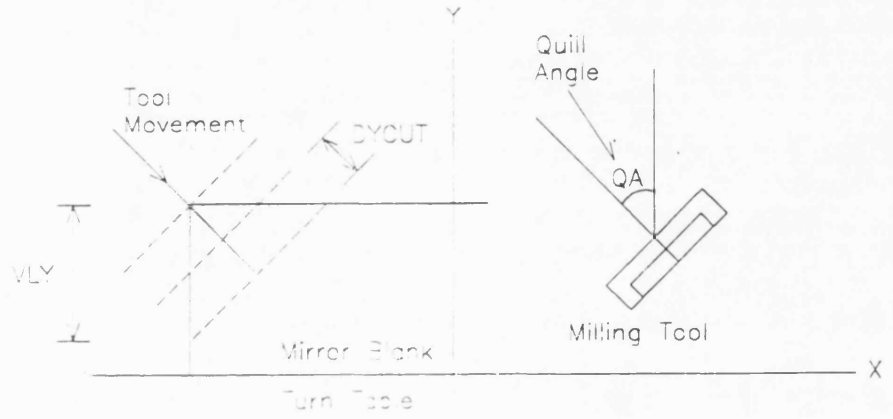

Figure 2.9: Movement of tool for AGC mode bevelling.
The tool moves along the angled line with step increment denoted by DYCUT until the total depth cutting reaches to what is expressed as VLY. The arrow indicates the direction of the tool movements.

appears only in the sub-procedure to generate a parabola.

- `Y distance of vertex from intersect of asymptote` and
  `coefficient of inclination of asymptote`
  defines the geometric property of a hyperbola.
  appear only in the sub-procedure to generate a hyperbola.

- `semi major radius on the Y axis` and
  `semi minor radius on the X axis`
  defines the geometric property of a ellipse.
  appears only in the sub-procedure to generate a ellipse.

- `How many terms does your polynomial have ?`

`powerN(1) =` `coefficientA(1) =` (2.3)

`powerN(n) =` `coefficientA(n) =` (2.4)

defines the geometric property of a polynomial.

appear only in the sub-procedure to generate a polynomial.

System Parameters:

These defines how the 8 ft machine and a mirror blank are configured and how to move the tool. They appear the same in every sub-procedures for generating profiles.

- `radius of mirror blank`

  defines the radius of a mirror blank over which the profile is generated.

- `quill angle`

  defines the angle with which the quill is tilted.

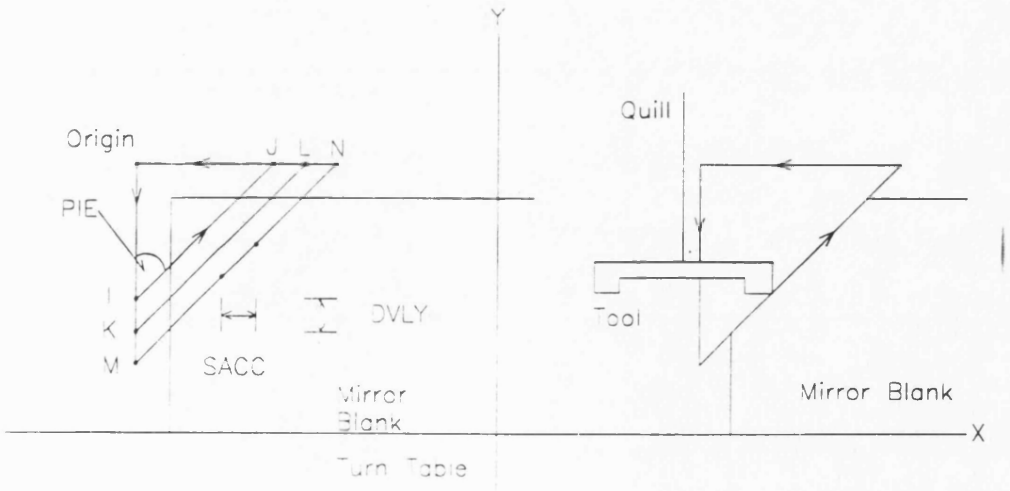

Figure 2.10: Movement of tool for RGC mode bevelling.

The tool moves along the track defined by the points sequence Origin-I-J-Origin-K-L-Origin-M-N. The profile IJ is incremented with DVLY to the line KL and then again to the line MN. YSECT means the intersection between the profile and vertical axis. SACC is the horizontal cutting step. The arrow indicates the direction of the tool movements.

- `target box size`
  defines the error box size surrounding a target point into which the tool is to move in.

- `interval between movements`
  defines time delay between stopping a tool movement and starting the next movement in step cutting.

- `cutting mode`
  defines whether several cuttings or single cutting is to be made.

Operating parameters:

These define the way in which the reference profile moves and the step cutting is controlled.

- `initial vertex`
  defines the initial position that the vertex of the profile starts movements.

- `final vertex`
  defines a final position that the movement of the vertex is terminated.

- `X step size for moving the vertex`
  defines a horizontal step of increment for the vertex movement.

- `Y step size for moving the vertex`
  defines a vertical step increment of the vertex movement.

- `X step size for cutting`
  defines a horizontal step for each step movements along the profile. PROG.EXE uses this to calculate the corresponding vertical step to the next target.

These appear the same in all the sub-procedures for generating profile.

However, in addition to these, the sub-procedure for a polynomial surface requires 3 more parameters to be defined, depending on whether concave or convex surface is to be generated.

- `initial X position of cutting`
  defines where the tool starts a cutting.

- **final X position of cutting**
  defines where the cutting should be ended.

- **horizontal step of changing the initial initial X point**
  defines a step size with which the **initial X position of cutting** moves for the next cutting.
  appears only for the **Concave surface**.

- **horizontal step of changing the final X point**
  defines a step size with which the **final X position of cutting** moves for the next cutting.
  is only for the **Convex surface**.

Traditional algebraic equations are used to describe the surfaces and to calculate targets along profiles. In all the equations, (X, Y) denotes the coordinate of a target and (H, K) is the location of a reference profile. These are the positive X half of complete equations since the tool moves only in the positive half of the X coordinate. The equations calculate the Y coordinates of targets. Those for the X coordinate are not actually used for target calculation.

- **Sphere**

Concave Sphere:

$$Y = (K - R) + \sqrt{R^2 - (X - H)^2} \tag{2.5}$$

$$X = H + \sqrt{R^2 - (Y - (K - R))^2} \tag{2.6}$$

Convex Sphere:

$$Y = (K + R) - \sqrt{R^2 - (X - H)^2} \tag{2.7}$$

$$X = H + \sqrt{R^2 - (Y - (K + R))^2} \tag{2.8}$$

where R is the radius of the curvature.

- **Parabola**

Concave parabola:

$$Y = \frac{X^2}{-4P} + \frac{XH}{2P} + K + \frac{H^2}{4P} \tag{2.9}$$

$$X = H + 2\sqrt{P(-Y + K)} \tag{2.10}$$

Convex parabola:

$$Y = \frac{X^2}{4P} - \frac{XH}{2P} + K - \frac{H^2}{4P} \tag{2.11}$$

$$X = H + 2\sqrt{P(Y - K)} \tag{2.12}$$

where P= forcal length of parabola

- **Ellipse**

Concave ellipse:

$$Y = K - A + \frac{A}{B}\sqrt{B^2 - (X - H)^2} \tag{2.13}$$

$$X = H + \frac{B}{A}\sqrt{A^2 - (Y - (K - A))^2} \tag{2.14}$$

Convex ellipse:

$$Y = K + A - \frac{A}{B}\sqrt{B^2 - (X - H)^2} \tag{2.15}$$

$$X = H + \frac{B}{A}\sqrt{A^2 - (Y - (K + A))^2} \tag{2.16}$$

where A=semi major radius on the Y axis

B=semi minor radius on the X axis

- **Hyperbola**

Concave hyperbola:

$$Y = K + A - \frac{A}{B}\sqrt{B^2 + (X - H)^2} \tag{2.17}$$

$$X = H + \frac{B}{A}\sqrt{(Y - (K + A))^2 - A^2} \tag{2.18}$$

Convex hyperbola:

$$Y = K - A + \frac{A}{B}\sqrt{B^2 + (X - H)^2} \tag{2.19}$$

$$X = H + \frac{B}{A}\sqrt{(Y - (K - A))^2 - A2} \tag{2.20}$$

where A=Y distance of the vertex from intersect of asymptote
B=coefficient of inclination of asymptote

- **Polynomial**

$$Y = \sum_{i=1}^{n} a_i X^{b_i} \tag{2.21}$$

(2.22)

where a_i = coefficient for the ith order term of polynomial
b_i = power constant for the $i$the order term of polynomial.

Tool movement for concave profiles:

The tool movements for both the concave and convex spherical profile are illustrated in Figure 2.11 and Figure 2.12. For the concave profile, the cutting point P is on the left edge of the tool. The tilt angle of the quill can be used at either 0^o or θ^o counter-clockwise as seen from the push-pull arms(see Figure 2.1) but is not greater than 10^o. The quill must be tilted if the radius of curvature is small and the cutting tool is large, so that the opposite edge of the tool does not touch the right-hand side of the profile. The cutting point P starts the movement from the neutral point N which is always 1 mm above the flat surface of the work piece. It moves to the point A, followed by homing in on to the starting position C1 for cutting. The fine step movements are made along the calculated profile toward the point Cn where the step cutting is terminated. The point P moves back to N. The new position of the reference profile is defined, in the normal situation, one step down toward the work piece. The next cutting step is made along the profile at its new location.

Tool movement for convex profiles:

The convex profile requires the right edge of the tool to be the cutting point P.

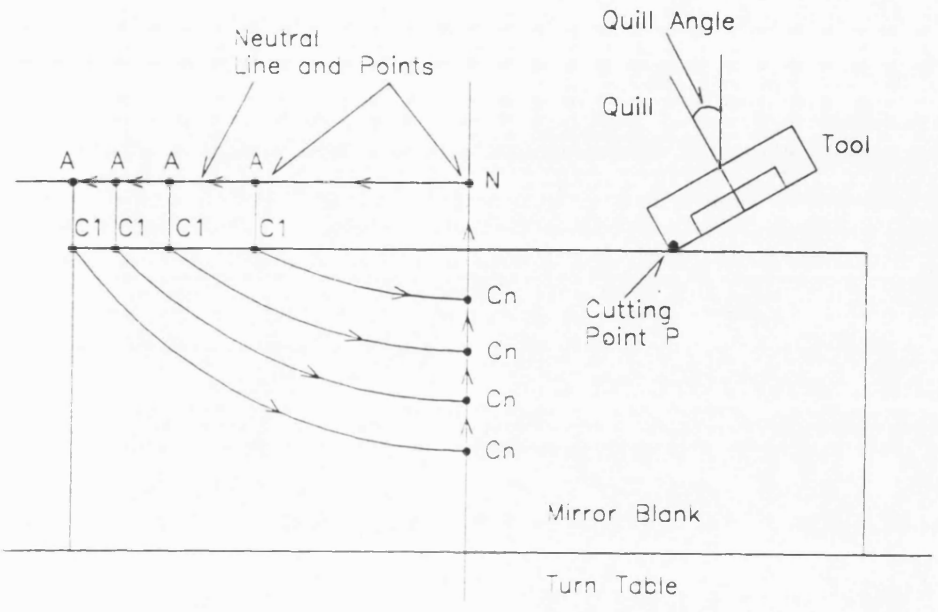

Figure 2.11: Tool movements and quill configuration for concave surface.

It starts from the neutral point N, moving to the point B through the point A. It then homes in on to C1 where the fine step cutting starts following the profile. The cutting is terminated when the present Y coordinate of P is above the top surface

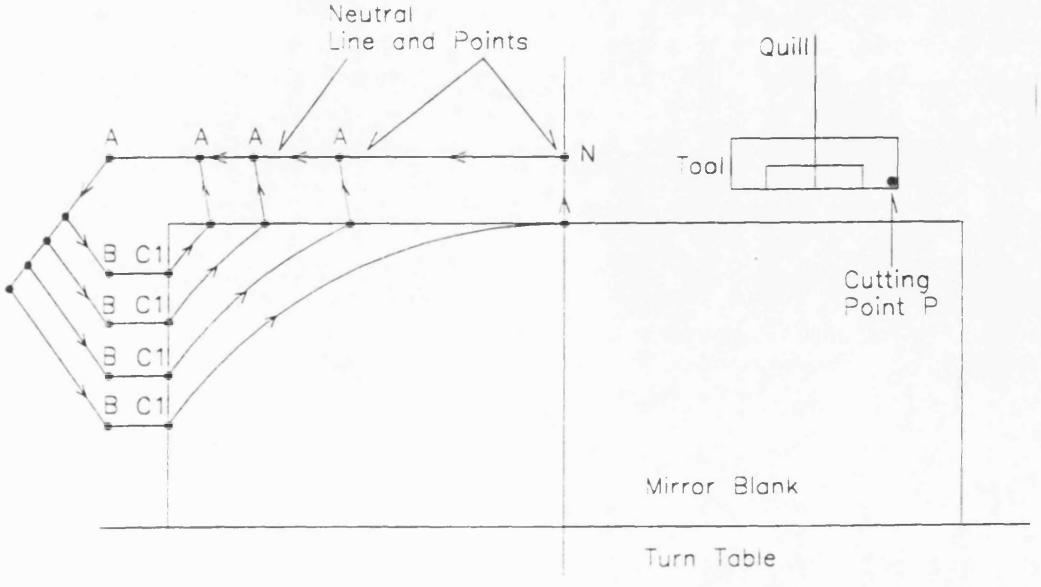

Figure 2.12: Tool movements and quill configuration for convex surface.

of the work piece. The tool moves back to the neutral line which is 1 mm above the surface. The location of the reference profile is again calculated for the next cutting step. The quill must have the tilt angle of 0^o for generating the convex profile. The quill tilted with θ^o in counter-clockwise would force the other part of the cutting tool to grind the surface which is already step-cut by the tool point P. This would completely re-shape the surface to a completely different one.

Strategy to stop overshooting for tool movement for concave and convex profiles:

The accuracy with which a tool movement is achieved in air was found to be about $\pm 20\ \mu m$ in both axes. If it falls before the target, the next movement is automatically re-targeted to the original one. However, if it overshoots beyond the target in any axes, it would, without additional safeguards, trigger the backward movements toward the target. Because of the finite accuracy of a tool movement, the backward movement is likely to cause surface damage. Also, reversing the X motion takes much longer than doing the Y motion due to smaller Y backlash compared with the X backlash (This would be another cause of the surface damage), For this reasons, when a tool movement is within or overshot beyond the target box size in either X or Y coordinate, the backward movement is prohibited. The next movement is directed to the next target. The details of target control including this is explained in Figure 2.13 and Figure 2.14.

Auxiliary sub-procedures in the profiling procedure;

Two auxiliary routines are incorporated into this procedure. The `TARGET SIMULATION` routine is designed to give user the list of target coordinate that the user defined with the input parameters. The other, `INPUT PARAMETER LISTING` routine, is to provide a list of input parameters before starting the tool movements for the fine step cutting. Since the parameter input stage consists of several pages of display, this is a safety device to ensure that the right parameters are input.

2.3.7 Debugging and Testing

The performance of PROG.EXE was continuously monitored when OSL milled a 85 cm diameter cervit blank, which is actually a central hole of the 3.8 m AAT, to produce the f/3 concave test sphere and the scaled f/7 Gemini secondary. Some

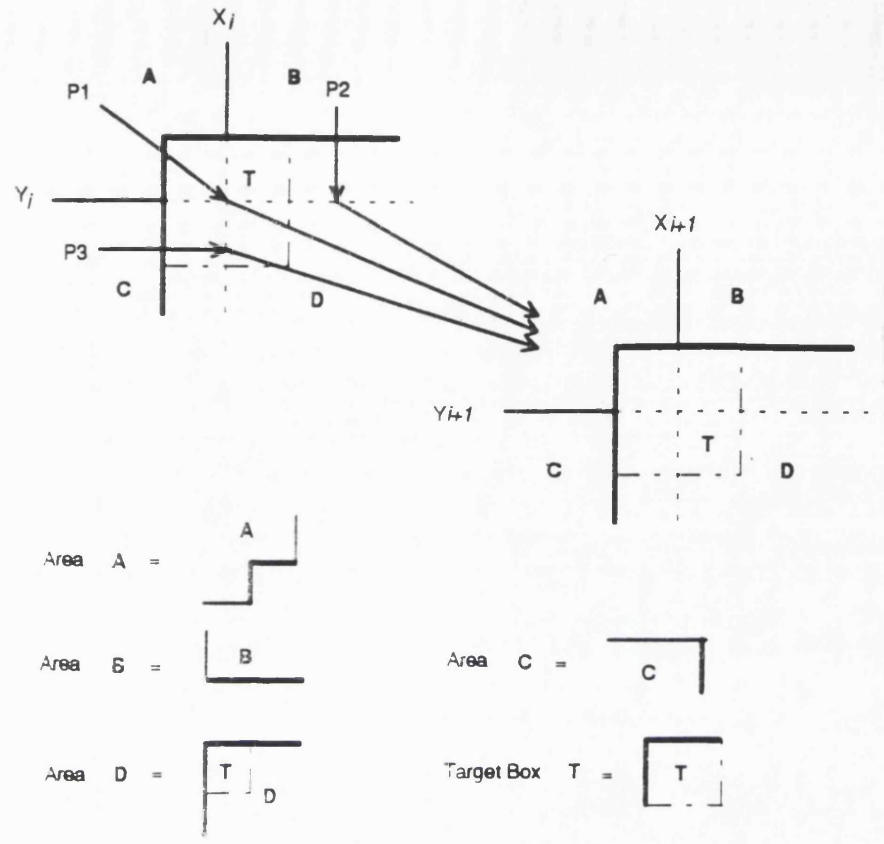

Figure 2.13: Target control including overshooting protection for concave profile

improvements and modifications were made as follows.

- **Potential risk of producing a deep scratch while the machine is running**

  If the slope of a profile changes from larger to smaller than the quill angle while profiling, the Y axis movement is given backlash. Then the combination of X (no-backlash) and Y movements (backlash) tends to generate a deep scratch on the mirror until the Y backlash is removed so that one-way movement without backlash is resumed. Fortunately, this has virtually no possibility of existence in real profiling. All the optical surfaces to be generated have smaller slope over the diameters than the quill angle of 10 degree, which is perhaps the largest OSL optics shop uses in practice. Thus, there was no need for treating this.

- **Redundant procedures**

  The two sub-procedures for target simulation and input parameter listing are redundant so far. They have been hardly used but remain intact for now.

The fate of these sub-procedures will be determined by its use in the future generation of other types of surface profile.

- **Success of milling the 85 cm scaled f/7 Gemini secondary mirror**
  The Sphere and Hyperbola sub-procedures were tested in producing the 85 cm scaled f/7 Gemini secondary mirror. It was proved successful. There was no opportunity to test other procedures in real production. The success of PROG.EXE in profiling spheres and hyperbolae means that the error must be in the equation bank, if generating other type of surface profile has gone wrong. Debugging these type of errors is easier than any other sort of structural bug in the programme. This is indeed one of the advantage of using equations rather than handling target list files within PROG.EXE.

- **Unstable encoder signal**
  Flickering in the encoder display and the coordinate value in the PC display was observed. Its frequency was observed to be rather high e.g. much faster than 10 Hz, once it started, and the location could be in any digit. It was

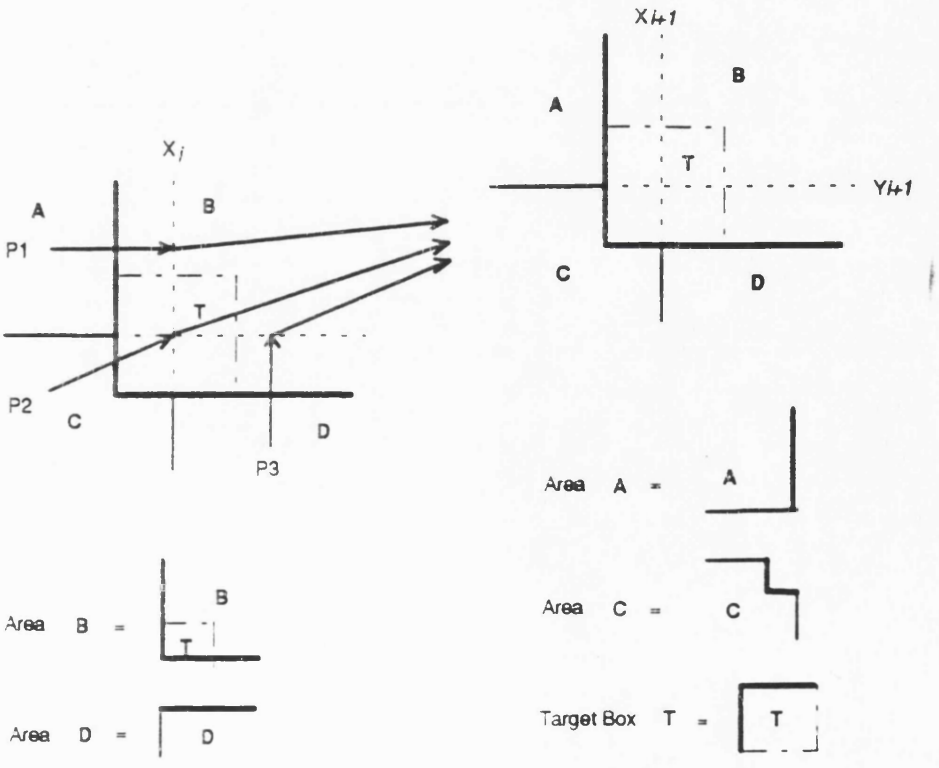

Figure 2.14: Target control including overshooting protection for convex profile

foreseen that there would be a potential problem, induced from this. The digit of 1000 μm in the Y encoder may start suddenly flickering between 1 and 2 at any time when generating a profile but the real position of the tool is unchanged. Assuming that a cutting step was made with the Y coordinate of 2000 μm which suddenly surged down to 1000 μm, PROG.EXE will then force the next step cutting to produce the unwanted groove of 1 mm in depth on the mirror. If this happens, re-profiling the entire surface has to be made again. In any cases like this, the intended profiling job is completely destroyed, reducing the efficiency greatly.

This was greatly improved by damping the encoder mounting bracket. The residual flickering was then completely removed with an averaging technique. 10 readings from the encoder are averaged to produce a coordinate value. Doing this three times gives three coordinate values which are compared. If any of these have difference larger than 10 μm from other values, it goes back to encoder reading without giving the coordinate value. If all three values are within 10 μm in difference, they are averaged to produce a coordinate value that is actually used. The problem is resolved completely with this method.

- **A structural bug in PROG.EXE version 1.0**

  With PROG.EXE ver 1.0, sometimes during step-cutting it exited the operator to the operating system with the error message of 'insufficient memory'. The frequency of this happening was unpredictable. The program is suspected to be too big, consuming too much DOS conventional memory and leaving no memory for allocating working variables in action. The PROG.EXE version 1.2 is re-structured to be smaller stand-alone modules, each of which is invoked independently by calling their names at the DOS prompt as shown in Figure 2.15. Lower level modules are included in higher level modules. For example, the `MANUAL` module includes the `AXIS` module and the `FACING`, `EDGING`, `BEVELLING` and `PROFILING` modules have the `MANUAL` and `AXIS` modules in them. This solved the problem and the error has not been observed since then.

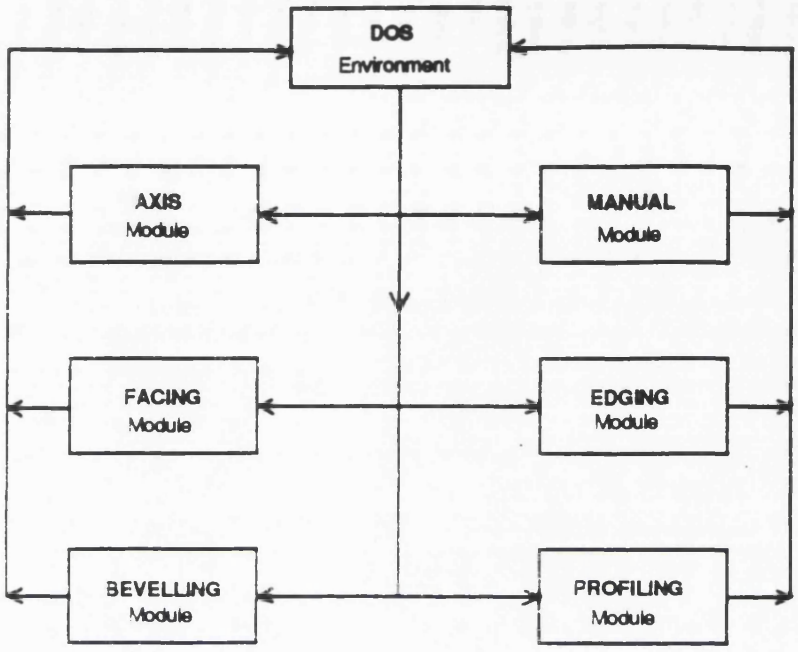

Figure 2.15: Structure of the PROG.EXE version 1.2

2.4 Contact Profilometry and Profile Calibration

2.4.1 Talylevel and Profile Gauge Measurements

When the scaled f/7 secondary was milled over its entire surface for the first time, two simple methods were used for quick inspection of the surface quality. Firstly, a Talylevel, which is in fact a clinometer, was mounted on the quill at 415 mm from the centre of rotation. The Talylevel gave the Y variation of about 0.1417 μm in the X travel of 1 mm. This equals to about 59 μm of the downward movement of the quill in the Y axis for the X travel of 415 mm to the centre of the rotation.

Secondly, a simple profile gauge made of Al bar is NC-milled to have a conjugate concave hyperbola on its one side. It is then placed over the mirror surface. There should not be a gap between the two profiles, if the grinding process was ideal. However, there was a gap occupying an area of about 20 cm in diameter in the central part of the profile. It was wide enough for the slip gauge of about 50-70 μm in thickness to slide in and out.

Assuming that the NC-milled gauge was itself accurate, the two quick checks agreed

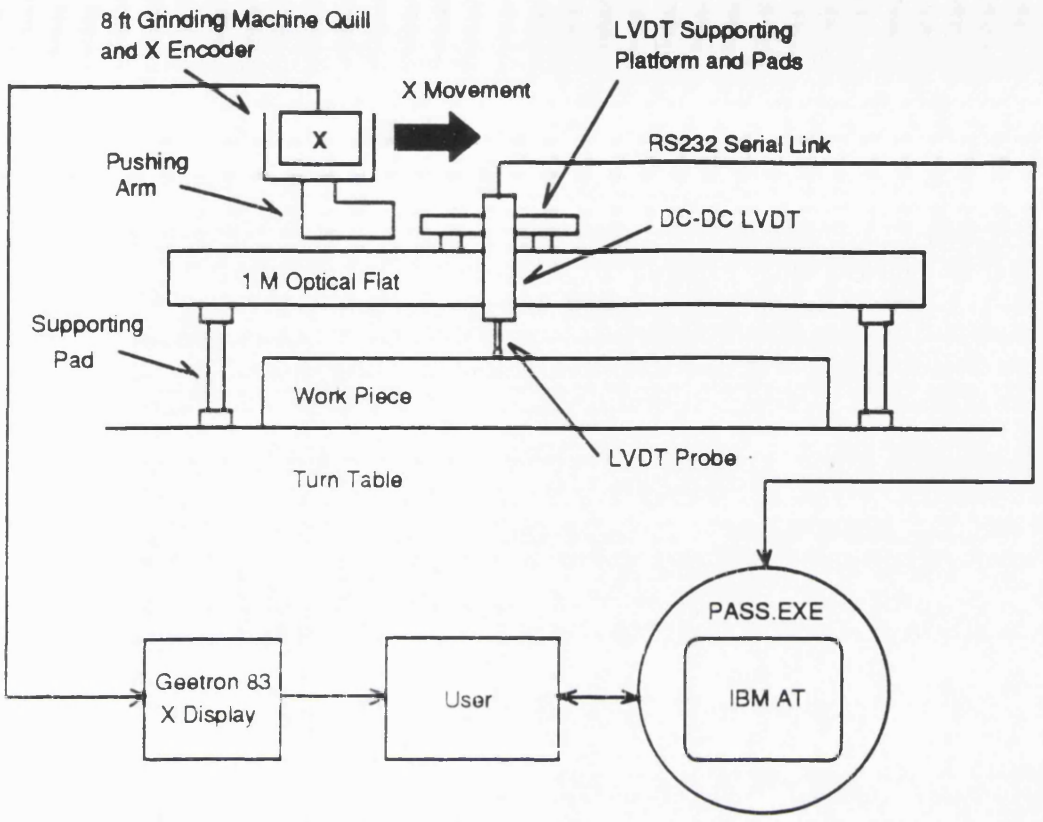

Figure 2.16: The concept of the Mark 1 profilometer.

well with the first approximation in telling that the profile generated without sorts of error compensation has a turn-down centre of about 60 μm in depth. In other words, this has to be a turn-up edge of the same height, if the centre is overlapped by the theoretical convex hyperbola. Unfortunately, neither of them was able to give any detailed error features in profile generation. This raised greatly urgent necessity for a simple but effective profilometer for estimating the detailed error data.

2.4.2 Simple Contact Profilometer Using LVDT

• Concept of Mark 1 profilometer

The proposed concept of the profilometer (hereafter called 'Mark 1') is presented in Figure 2.16. It is to use a large optical flat of about 1 m in length sitting on 3 mechanical pads. It serves as a reference profile. One edge of the flat must be placed to cross the centre of the milled surface. An LVDT [27] is used to measure depths along its diameter between the flat and the milled surfaces, which are then converted to the profile. An LVDT is a simple and convenient transducer to construct a simple

probe. Its resolution of about 1 μm is well within that needed to assess the milled profile, remembering that some 20 μm of glass has to be removed with loose abrasive lapping due to sub-surface damage. The LVDT slides over the flat surface along the edge of the flat surface crossing the centre of the ground surface. The signal from the LVDT is relayed via a RS232 serial link to an IBM AT clone. A preliminary measurement with the LVDT showed that about 80 readings have to be averaged to produce a stable value in ADU. 3D has supplied their general purpose data acquisition software called OASIS. However it could not be used for measuring the profile. Firstly, its calibration routine is rudimentary. It uses only 10 cardinal points and the linear regression is applied in between 2 adjacent cardinal points. Secondly, OASIS is not capable of manipulating stored data for generating profile data in the format users want. This means that either OASIS has to be modified or another software package is necessary to generate the profile data. For these reasons, a customised, new software package called PASS.EXE had to be developed.

• Measuring the horizontal position of the probe

The hyperbola has a sag of about 2.2973 cm at the edge i.e. at R=41.5 cm. This gives the accuracy of about 18 μm in the first approximation when decoding the X position of the LVDT, i.e. the probe more specifically, if the surface profile has to be measured with 1 μm in accuracy. The accuracy is not difficult to achieve with the Geetron X encoder. Thus the quill and the Geetron X encoder are employed to move the LVDT and to decode its X position instead of acquiring a separate encoder. The accuracy of about 18 μm gives another difficulty in matching the edge line of the flat surface to the centre of the ground surface. Mark 1 has to be taken away and put back before and after grinding the surface. Positioning the flat should be within about 18 μm in deviation from the centre of the surface. Brooks [9] showed that this can be achieved without much difficulty.

• Tilt compensation

The top and bottom surfaces of the large flat are not accurately parallel. Furthermore, to adjust the height of the three mechanical pads in the order of microns does not seem to be practical. This gives rise to the importance of removing the inclination effects of the milled profile with respect to the reference flat from the measured profile. It can be solved by measuring the depths of the two edge points of the profile, setting the inclination line to be removed from the measured profile.

This method assumes that the milled profile is circular-symmetric, so that the profile measurement is made up to the radius, not to the diameter.

• Limitation of the Mark 1 profilometer

The limitation of Mark 1 is obvious. It is not capable of measuring surface profiles larger than 1 m. The length of the flat mirror is just about 1 m. The Geetron X encoder does not cover the diameter of 2.7 m which is the maximum capacity of the Grubb 8 ft machine. A new encoder will have to be used if a larger mirror is to be made or the entire diameter has to be measured.

• Calibration of LVDT probe

Preliminary calibration:

The specification for the LVDT, with a non-linearity of about ± 0.5 % of full scale, was not good enough. The LVDT had to be precisely calibrated to measure the profile within the accuracy of at least 10 μm. The engineering slip gauges were stacked to produce reference heights covering the full scale of the LVDT. The LVDT probe was placed on the top surfaces of the stacks. A PC then grabbed the signal and stored it in the hard disk. The two preliminary measurements for calibration showed that the large deviation of about 2000 μm from linearity for the X range of 0-500 and 55000-60000 μm. For the X range of 500-55000, the graph fluctuates about ± 90 ADU. These patterns were identical in the two separate measurements and this was later demonstrated again with the default calibration shown in Figure 2.20. From this feature, it was concluded as follows.

- It is better to use the X range of 500-55000 μm when in use. Thus, the linear regression has to be made only with the data in this range. The residual within the range is only regarded as meaningful in use.

- The residual of about $\pm 90 - 100$ P-to-V ADU is too large to be ignored. The calibration should be able to take this into account in converting ADUs to microns. Otherwise, it would be impossible to measure the profile with the accuracy of better than 10 μm.

- The linear regression for the 2 data sets over $500 < X < 55000$ μm gives

$$LVDT = 1.156815 T_{gauge} - 2020.96 \tag{2.23}$$

$$LVDT = 1.157477 T_{gauge} - 2116.05 \tag{2.24}$$

(2.25)

where LVDT=number in ADU

and T_{gauge}=thickness of slip gauge in micron.

In the first approximation, this gives about 0.86 μm for 1 ADU.

- The fitted equation gives the residuals of about $\pm 78 - 86 \mu m$ P-to-V.

Problems with the calibration above:

There is a problem with the calibration above. The gauge is not the 'reference slip gauge', meaning that the error in thickness of each gauge may be in the order of a few microns. When 2-4 gauges are stacked to achieve a height, it is quite likely for the cumulative error to reach about 10 μm. Thus, the calibration can not guarantee the error better than about 10 μm, unless the reference slip gauges or single gauges are used for each heights. Two alternative ways of calibration were discussed in detail, although subsequently rejected.

First alternative calibration:

Firstly, as seen in Figure 2.17, the flat mirror B is placed on the 2 slip gauges of same height, perhaps about 500 μm each, which are placed on the flat mirror A. The LVDT is read while moved on the top surface of the mirror B. This is to determine the inclination of the surface B to A. Then a slip gauge of 1 mm in thickness is added to the slip gauge S1. The LVDT signal is read again while moving across the flat surface B. The subtraction of the first set of reading from the second would give the slope caused by the 1 mm slip gauge. If the both ends of the flats only are read, the subtraction will result in 2 numbers of which subtraction is again a number in ADU corresponding to the height of 1 mm. The probe is adjusted to give the number corresponding to the first height of 1 mm at the position P1 where each cycle of measurement starts. Then move the LVDT to the point P2 and read the signal. To subtract the 2 readings will give the second number corresponding to the second height of 1 mm. If this sort of cyclic measurement is made 55 times over the LVDT operational full scale, then the precision calibration can be made.

Second alternative calibration:

Secondly, it is in fact the similar idea to what is suggested in Figure 2.18 but with only 1 flat surface. The LVDT is screwed into a steel bridge supported by 2 columns

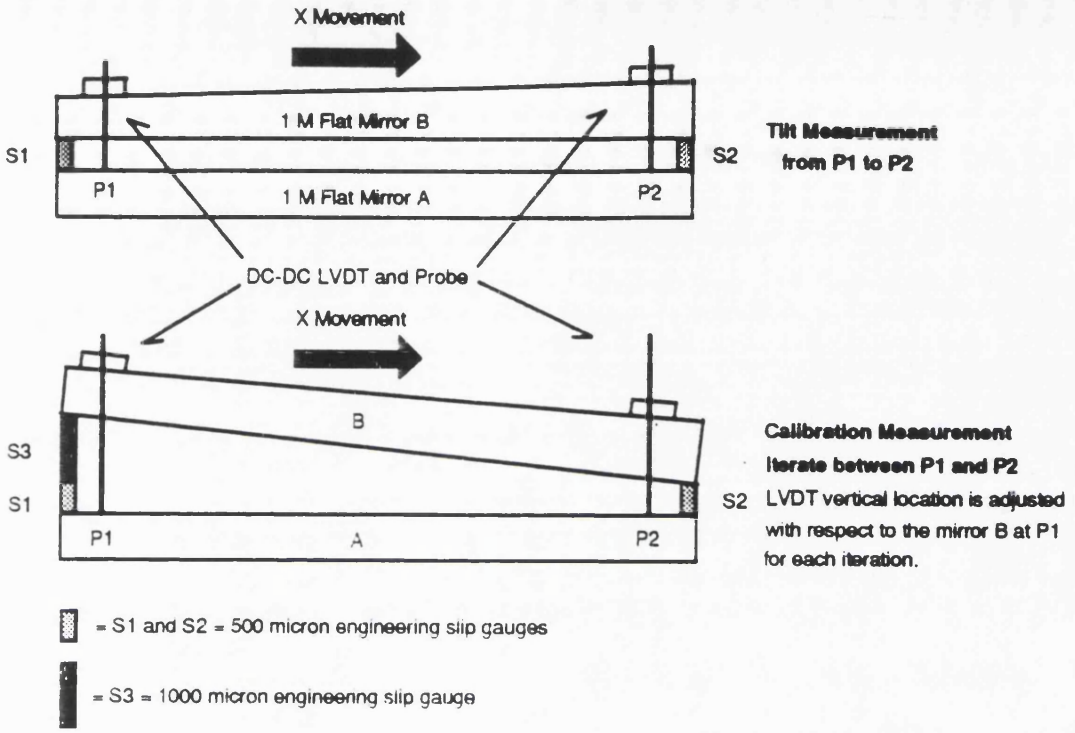

Figure 2.17: The first alternative method for calibration of the LVDT using the 2 large flats.

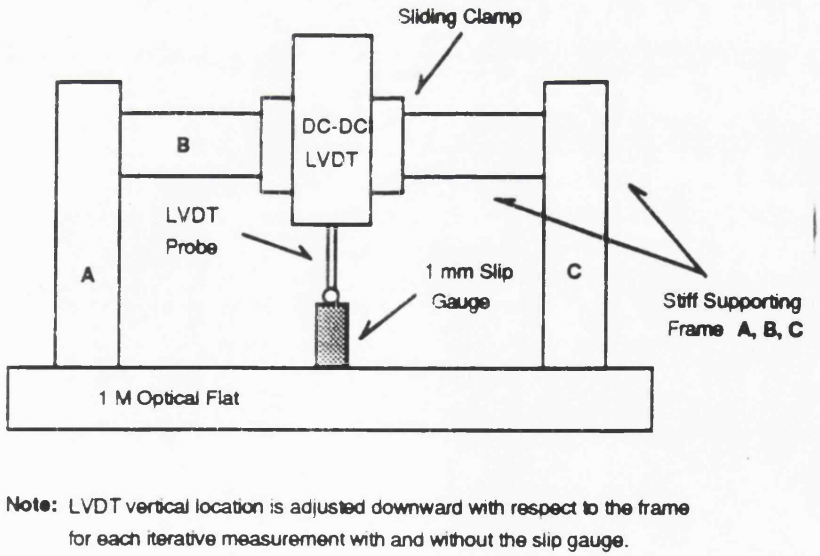

Note: LVDT vertical location is adjusted downward with respect to the frame for each iterative measurement with and without the slip gauge.

Figure 2.18: The second alternative for calibration of the LVDT using the 1 mm slip gauge and the steep frame.

placed on the flat mirror. The slip gauge of 1 mm in thickness can be placed in

and out in-between the columns. The LVDT is read with its probe on the empty flat surface to start. Next time, it is read with the probe on top of the 1 mm slip gauge. The difference in ADU corresponds to 1 mm. Then the LVDT is screwed further down through the bridge to give the difference with the probe on the empty flat surface. The next reading with the probe on top of the slip gauge can be subtracted from the previous one again. This gives the second number in ADUs which corresponds to 1 mm. This type of cyclic measurement can be done 55 times to cover the operational full scale of the LVDT. The second method is easier. No heavy 1 m scale flats have to be handled in measurement.

Problems with the two alternative calibrations:

However, both the alternatives would accumulate the error of each measurement cycle. Brooks showed that it is not difficult to manually adjust the LVDT position through a sliding clamp to give a specific number in ADUs [9]. The error accumulation would not be so severe if the LVDT is stable enough for the duration of the calibration measurement. The two alternatives certainly would take much longer than the way of the preliminary calibration described. The trade-off is whether the error accumulation exceeds about 10 μm. It depends on how stable the LVDT is against various working conditions during the measurement.

Repeatability and daily signal drift of the LVDT probe:

The repeatability was tested with and without lateral force onto the LVDT probe. It is within about ± 2 and ± 3 in ADUs respectively. The signal drift of the LVDT was also measured as shown in Figure 2.19. For the data A and B, sampling the signal starts when the power is on at 12:00 AM and continues until approximately the 12:00 AM next day every 1 minute, in the temperature controlled OSL optics shop. Figure 2.19 shows the good agreement between the measurements A and B.

- The signal drops about 40-50 ADUs within a couple of hours after the LVDT is powered.
- Except the first drop, the LVDT signal varies about 30 ADUs P-to-V for the duration of the sampling. The room temperature varies about $2.5 - 4.0^{o}$ C for the same period of time. This gives in the first approximation about 4 μm per degree C as temperature effect. It has been claimed that, in worst case, the thermal effects on both the zero point and the span are 2.5 μm per

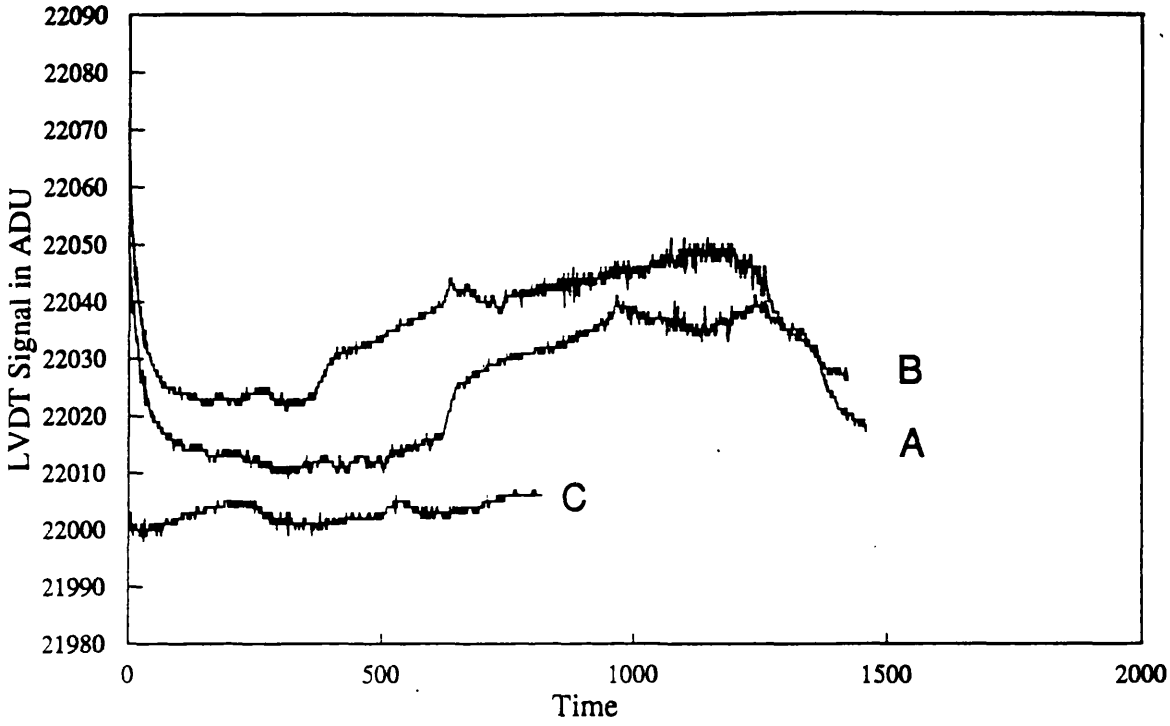

Figure 2.19: The three results of the thermal experiment for the LVDT behaviour.

degree C and 7.5 μm per degree C respectively [27]. These give about 5 μm per degree C as the combined thermal effect when the probe length is about 22000 ADU(cf. the full scale of 65535 ADU) for the measurement. The result of about 4 μm per degree agreed well with the claim.

- The daily variation of the room temperature seems to be responsible for this. The third measurement (data C) is made with the double-skinned foam and polythene blanket thermally insulating the LVDT and its probe from the room temperature. The result shows a large improvement that the P-to-V is about 9-10 ADU as shown in the graph C in Figure 2.19. The room temperature varies about 4.5°C for the same period of time. The improvement made is a factor of about 3.

A few findings from these experiments are as follows.

- The LVDT must be energised for at least about 2 hours before starting any serious measurements. Alternatively it should be left powered-on all the time.

- The combined error, repeatability plus thermal behaviour, is about ± 8 ADUs with thermal insulation. This suggests that it can be further reduced if the LVDT is in a proper thermal controller.

- This imposes a condition that the thermal controller must be able to stabilise the temperature around the LVDT within $\pm 0.5^{o}$ in order to keep the thermal effect less than 4-5 μm.

- Thus, it seems unreasonable to use the LVDT to measure profiles with accuracy better than about ± 8 ADUs i.e. ± 7 μm in practice.

Reasons to reject the two alternative calibrations:

If each measurements has the error of about ± 7 μm, the accumulation of errors, during 55 cyclic measurements, is likely to exceed about ± 10 μm. This means that the two alternative ways proposed are worse than the first method used for the two preliminary calibrations. It is not because the principles of the two alternatives are inapplicable, but the LVDT, itself, is not reliable under the environmental changes during the measurements suggested. The possibility of increasing the error is further enhanced with the longer period of time required to complete the alternative calibrations.

Default calibration for the Mark 1 profilometer:

For these reasons, the original method was applied for the third calibration that has been used as the default calibration data since then. The following points were considered for this calibration.

- The number of slip gauges must not exceed 3 in stacking to limit the maximum error to 10 μm.

- The time period for completing the calibration must not exceed about 1 hour. The preliminary calibrations suggest that the signal drift with time at room temperature does not seriously influence the calibration if it is completed in short time period e.g. 1 hour during daytime.

- The gauge combination of 30000 μm is used, as a comparison point, to monitor any abnormal behaviours of the LVDT during the default calibration. The

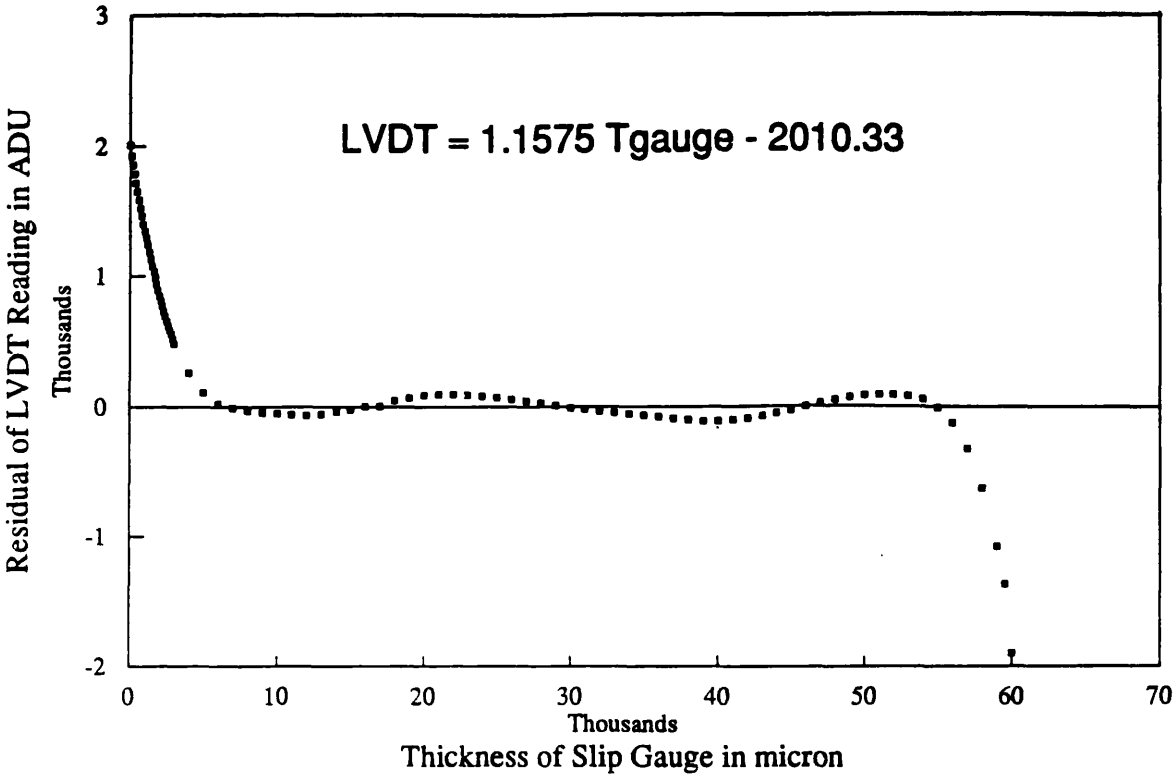

Figure 2.20: The residuals of least square fit on the default calibration data

result shows that the LVDT signal remains stable within ± 1 ADU i.e. about $\pm 0.86\ \mu m$.

- When the measurement is completed from 0 to 60000 μm, few reference heights are rapidly sampled as a back up monitoring. It shows that the signal is stable within $\pm 5\ \mu m$ i.e. about $\pm 4.3\ \mu m$.

Thus the default calibration is expected to have the inaccuracy of at least about $\pm 5 - 10\ \mu m$ at best. Figure 2.20 shows the residuals of the least square fit as the default calibration of the LVDT. The least square fit can be expressed in microns as follows.

$$LVDT = 1.157472 T_{gauge} - 2010.33 \qquad 5000 < T_{gauge} < 50000 \qquad (2.26)$$

2.4.3 PASS.EXE: Profile Calibration System Software

• Software specifications

Software is the core of the Mark 1 profilometer. It is developed to satisfy the

specifications briefly outlined below.

- Again, it must be user-friendly and hence it is better to give the user no control over the way in which the programme works. Instead, the programme has a fixed flow to achieve the task i.e. mapping errors in surface profile. It prompts the user what to do at any stage during programme execution. Users are to follow instructions displayed at every stage of its running.

- It may consist of 4 sub-procedures i.e. `CALIBRATION`, `CONFIGURATION`, `MEASUREMENT` and `ANALYSIS`.

- The `CALIBRATION` procedure produces the calibration file. The file name has the extension of `CAL`.

- The `CONFIGURATION` procedure reads a specified calibration data to the PC memory. It also defines the tilt angle between the flat and the ground surface.

- The surface profile is measured with the `MEASUREMENT` procedure. There must be the `EDIT` subprocedure for modifying the data measured by mistake. The profile data is stored in the files of which the name has the extension of `DAT`.

- The measured profile is compared to the theoretical one that user defines in the `ANALYSIS` procedure. The result is written to files with the extension of `ERR`.

- All the files produced are ASCII text files. It gives easy access via other software package the user might like to use later.

- Except the `CALIBRATION` procedure, the spinal flow of PASS.EXE is fixed. The user starts with the `CONFIGURATION` procedure, continues through the `MEASUREMENT` procedure and ends with the `ANALYSIS` procedure. The `MEASUREMENT` procedure cannot be accessible unless the `CONFIGURATION` procedure is completed. The `ANALYSIS` procedure can not be entered if there is no profile data available, that has been produced either by the `MEASUREMENT` procedure, or by reading from the profile data file on the hard disk.

- The coordinate systems that PROG.EXE uses must be employed. The error file, in particular, must have consistent sign conventions with them since

PROG.EXE version 2.0 is intended to use this files for active error compensation while generating profiles.

- The equations used to design theoretical profiles with PASS.EXE must be same as those used with PROG.EXE. This is to provide the user with consistency, leaving no confusion in the use of equations.

• Structure of PASS.EXE

The overall flow of working with PASS.EXE is presented in Figure 2.21 which shows clearly some features of the specification. The working version of PASS.EXE meets successfully the specification.

• Implementation of calibration data into PASS.EXE

In the development of PASS.EXE, one of the most important issues was a way in which the calibration data is used to convert observed data in ADU to microns. There are two methods for this, i.e. interpolation or model fitting. The question was which is better for PASS.EXE.

Error estimation to determine which method is better:

The first approach is to see if the error estimation previously made can give any clues about this. There are two types of error in measurements of any physical quantities. They are the statistical and systematic errors. Examples of the statistical error include non-repeatability due to electrical noise on the LVDT signal. The model fitting starts with the assumption that the measurement has statistical error which may be Poisson or Gaussian. It is to smooth the observed data to minimise the deviation, i.e. the statistical error. Thus it can average out the statistical error if the observation has enough quantity of data. In contrast, the interpolation assumes that data is free from the statistical errors involved in measurement. Any statistical error, if it exists, would be magnified with the interpolation. Meanwhile, the systematic error such as the thermal effect to the LVDT can not be corrected with either these 2 methods. The error estimation shows that the thermal effect combined with stacking 2-3 slip gauges (i.e. systematic error of about $\pm 5 - 7\ \mu m$) is the dominant error source rather than the repeatability (statistical error) of about $\pm 2\ \mu m$. It implies that there would not be much advantage in using polynomial fitting, in reducing the overall error. Alternatively, nor does this give any supports in favour of the interpolation either. Thus, the error estimation can not be the right measure to

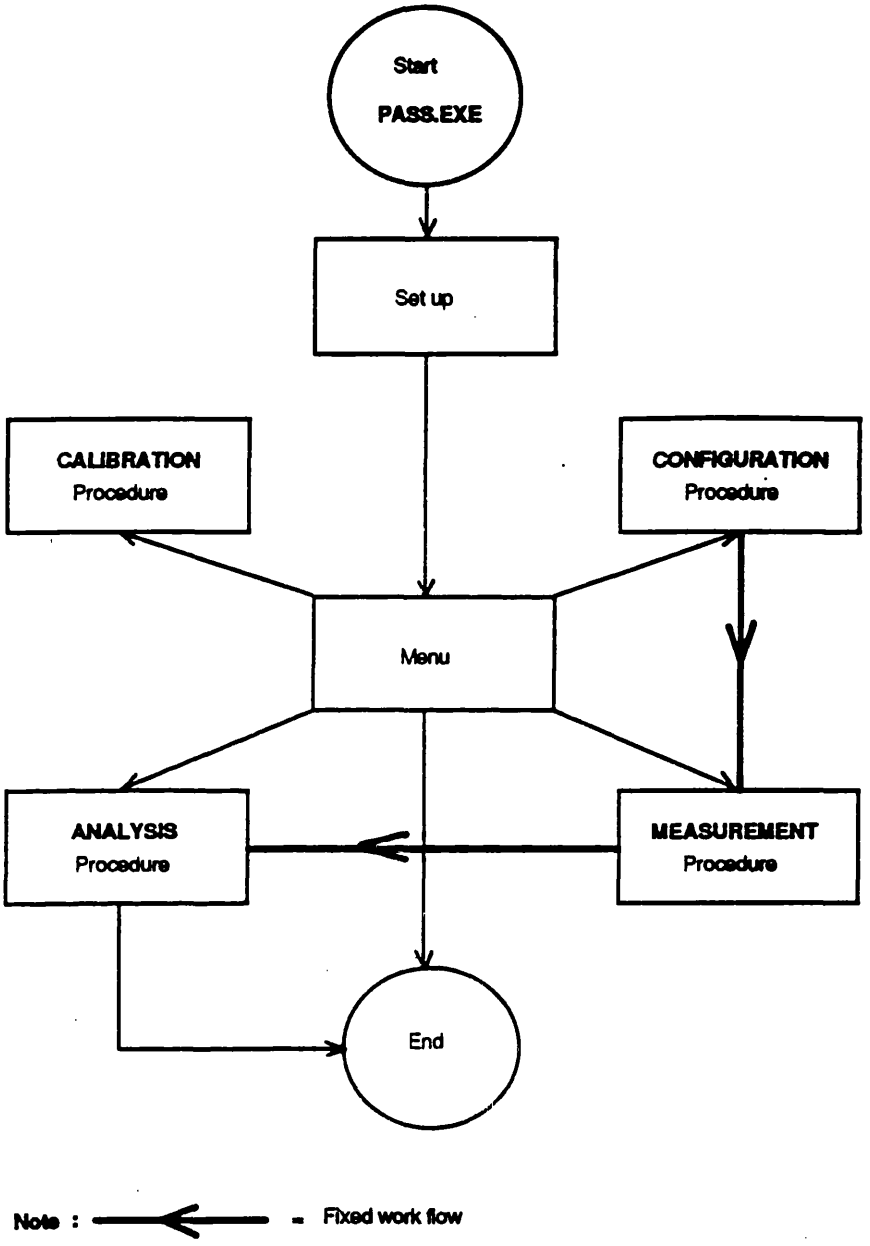

Figure 2.21: Overall flow chart of PASS.EXE

determine which method has to be used.

Direct application of the two methods to predict an observed data:
The second resort is to apply the methods to the calibration data to predict a data set of a separate observation and observe the magnitude of error in the prediction. 2 methods for interpolation and 1 for model fitting were compared with this process. They are the polynomial interpolation, cubic spline interpolation and general least square fitting of polynomial (Press *et.al.*, pp 77-101 and 498-546 [88]). In particular, the Lagrange's classical formula (Press *et.al.*, p 80-83 [88]) is implemented

Term	PRED3B.BAS	POLCOE3.BAS
X^0	-1002.1786	-952.2662
X^1	0.8676	0.8460
X^2	2.7381×10^{-5}	2.9849×10^{-5}
X^3	-1.1052×10^{-9}	-1.2162×10^{-9}
X^4	1.9783×10^{-14}	2.1916×10^{-14}
X^5	-1.2923×10^{-19}	-1.4394×10^{-19}

Table 2.1: Coefficients of the two best fit 5th order polynomials

straight-forwardly for the polynomial interpolation since the error estimation from the interpolation algorithm, itself, is not needed. As discussed by Press *et.al.* (p 77-101 [88]), using all the 89 calibrated points to extract the point of interest X did not help to reduce the error in prediction. Thus, the *localised* polynomial interpolation devised selects the nearest 3-4 calibration points to the point of interest, X, and exports them to the Lagrange's formula. The interpolation over the full range is then constructed with a number of segmented 3-4 order polynomial interpolations stacked and overlapped in series.

Mills, OSL software programmer, has used STARLINK data reduction softwares called `DIPSO` and `FIGARO` to provide the two best fit 5th order polynomials using the calibration data. Their coefficients are shown in Table 2.1. The routine for the localised polynomial interpolation was written in Quick Basic 4.5. The FORTRAN routine for the cubic spline interpolation (Press *et.al.*, p 77-101 [88]) was translated into the equivalent Quick BASIC routine. The results compared in Figure 2.22 show the followings.

- The interpolation, i.e. polynomial and cubic spline, gives much smaller errors than the best fit 5th order polynomials. The error of the interpolation is a bit higher, but much closer to the estimated error, than that of the polynomial fitting.

- Both interpolations give a almost identical error curve and its amplitude reaches up to about ± 10 μm for $5000 < X < 55000$ μm. The amplitude is a bit larger than the error estimation of individual measurements of about ± 7 μm, but agreed very well with the overall error of about ± 10 μm caused by stacking.

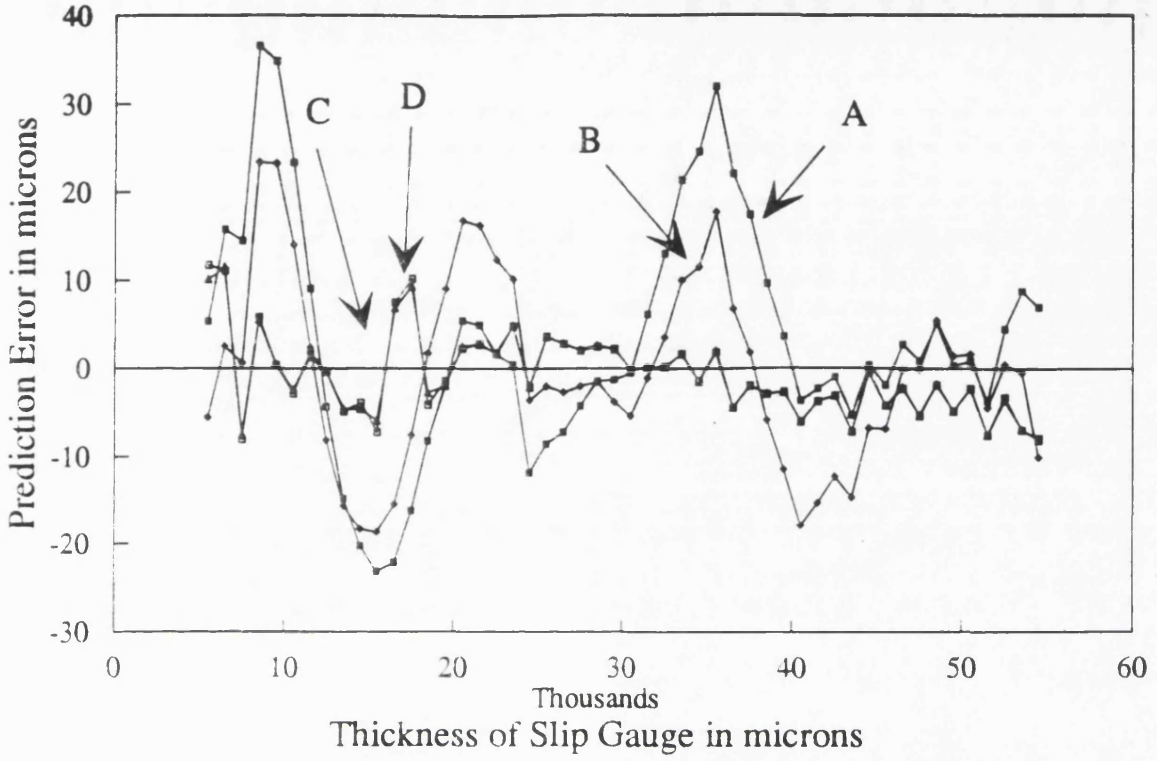

Figure 2.22: Prediction error plotted against the range of measurement.
The curves are the difference of the prediction from the observation. The curve B comes from the best fit 5th order polynomial using only 6 representative cardinal points i.e. X=5000, 12000, 22000, 40000, 51000 and 55000 μm. The curve A is obtained by the best fit 5th order polynomial using 51 cardinal points in $5000 < X < 55000$ μm. The localised polynomial and cubic spline interpolations give the curve C and D respectably.

Final choice in favour of polynomial interpolation:

Thus, the interpolations have better performance than the model fitting in terms of error. Because of its ease in programming, the localised polynomial interpolation is selected for converting the LVDT signal in ADU to physical length in microns. The Quick BASIC routine for the localised polynomial interpolation became an essential part of PASS.EXE.

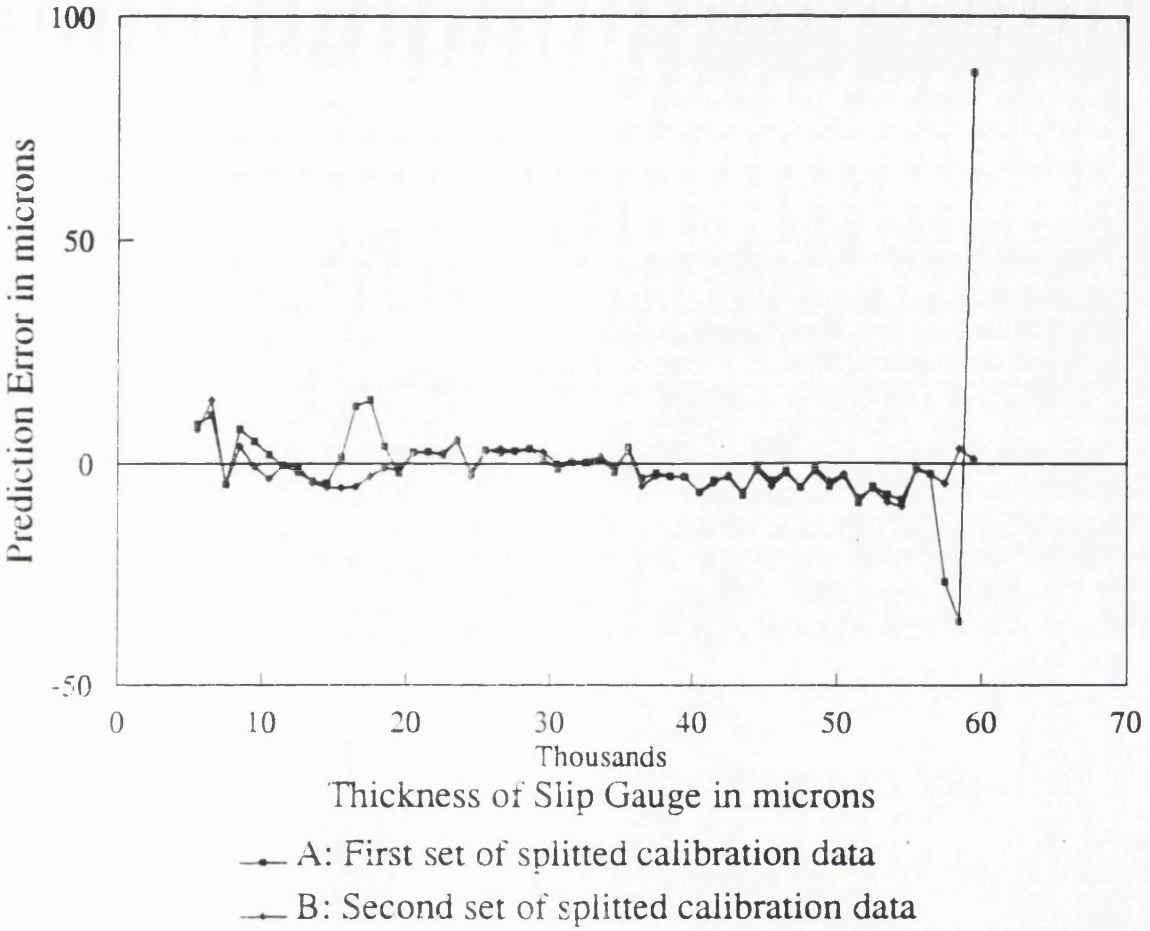

Figure 2.23: Prediction error curves with the splitted calibration data.

• Sampling interval of the default calibration data

It needed to be checked if the sampling interval of the calibration data was fine enough. The method is to split the calibration file into 2 groups and use them with the localised polynomial interpolation to predict the observed data collected independently. Two groups should be able to give almost the same error if the sampling interval is acceptable [75]. The result is Figure 2.23. Again the graphs are the difference of the prediction from the observation. The majority of the predicted points lies within the error amplitude of about $\pm 10\ \mu m$. The error curves are very similar to each other, except the 3 points at X=6500, 16500 and 17500. This proves that the sampling interval is fine enough.

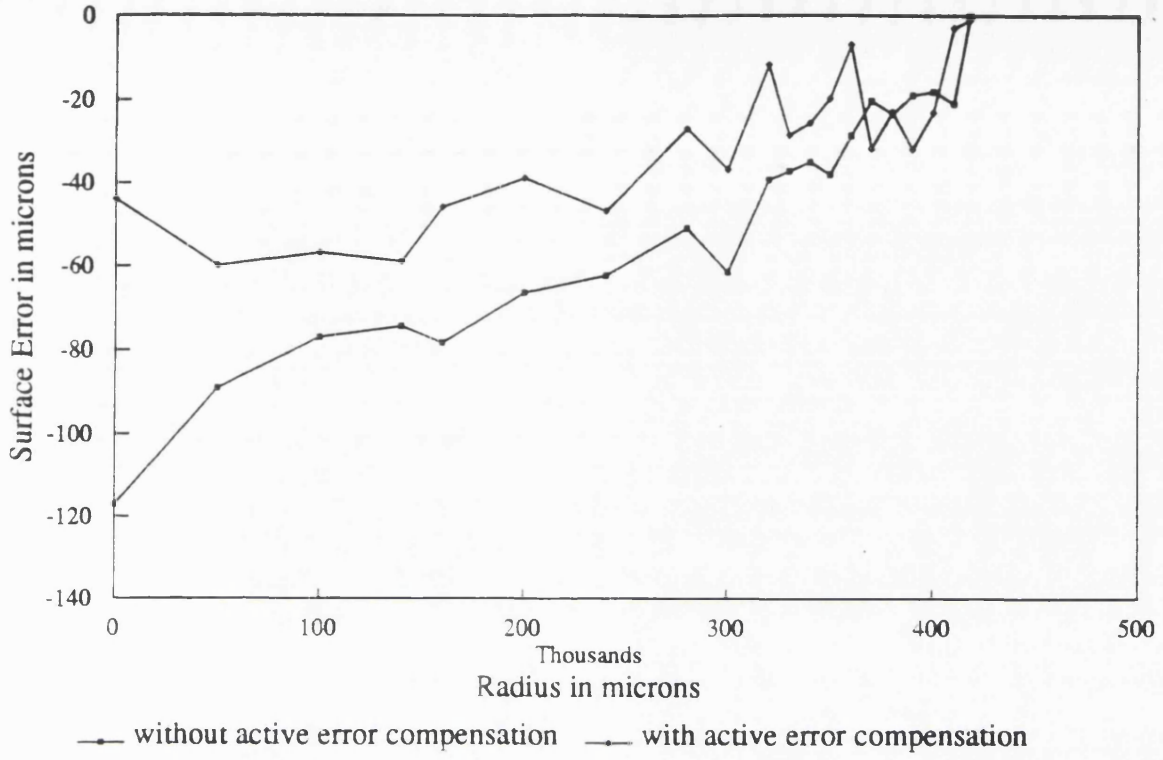

Figure 2.24: Surface error profiles generated with and without error compensation

2.4.4 Profile Calibration and Error Compensation

Humm, OSL optics technician, built a thermally controlled cylinder and the LVDT was permanently housed in it. The real time error compensation routine was incorporated into the existing PROG.EXE version 1.2 to form the version 2.0. When the entire surface of the blank was NC-milled for the first time, the profile was measured with Mark 1. The resulting error shown in Figure 2.24 was then fed into the PROG.EXE version 2.0 to compensate the error in NC-milling the surface the next time. The error-compensated profile was then measured to give the second error data also shown in Figure 2.24. The profile error is clearly seen to be greatly reduced. The maximum error amplitude decreases from about ± 60 μm (P-to-V) to about ± 30 μm (P-to-V). Thus, the error correction factor of around 2 has been achieved.

In principle, this iterative process can be continued until the error amplitude falls to about ± 10 μm P-to-V. However, Horne (p 215 [54]) has pointed out that Grubb Parson normally stopped milling when the machine marks produce surface roughness

of about 25 μm. Holland (p 54 [52]) also has said that the surface roughness by milling can reach to about 5-25 μm at best. Meanwhile, the sub-surface damage has been reported about 30 μm in brittle grinding [69]. Thus, the quality of milled surfaces due to the combined effects of the machine marks and the sub-surface damage is not accurate within the error of ± 30 μm at all. For this reasons, NC-milling was no longer employed in further smoothing the surface profile.

2.5 Discussion

• Summary and implication of development made in this Chapter

The process of generating surface profiles in OSL has been completely modernised with the new electronics and software developed. It has been very successful in operation to NC-mill a number of optics and related components. Examples include the f/3 spherical concave mirror of 85 cm in diameter, the 30 cm UHRF collimator lens, the flat epoxy wedge of the active lap and the f/7 scaled Gemini secondary. In particular, the active real-time error compensation is incorporated in the PROG.EXE version 2.0. The Localised Polynomial Interpolation is again employed to calculate the error at a target X position using the error data read from the .ERR file.

The implication of the success can be listed as follows.

- The process of removing the bulk of glass material to generate underlying surface profile is successfully computerised.
- It is able to directly NC-mill any aspheric surfaces in the accuracy of about ± 60 μm without the active error compensation.
- An error convergence factor of about 2 in profile generation has been achieved with the active error compensation in diamond-milling.
- It would normally need two cuts to complete the generation of surface profiles i.e. the first cut without error compensation and the second cut with error compensation.
- It would be impractical to NC-mill beyond the error of ± 25 μm because of the subsurface damage. However, OSL's ability of grinding the profile is limited

wholly by the inaccuracy of the default calibration which is about $\pm 10\ \mu m$.

- Surface faults such as astigmatism, caused by the incorrect mirror rotation, can be measured with the profilometer and corrected with the iterative millings in active error compensation. If it is no use in removing the surface fault, it can be traced and lapped/polished off using the active lap.

• The Mark 1 profilometer and its limitations

The NC-milled surface requires lapping with fine caborundum-water slurry. For the f/7 Gemini secondary, the lapping with finer and finer carborundum- water slurry has continued to achieve the surface profile to $\pm 4\ \mu m$ in P-To-V error. Most of the machine marks and sub-surface damage have been removed in this stage. The Mark 1 profilometer has been in continuous use to monitor the quality of the lapped surface profiles. A few aspects in the use of the Mark 1 were found during the early stage of the lapping.

- It does not have its own X encoder so that the X position of the LVDT can not be decoded properly. Instead, the Geetron X encoder is used but with unknown tilt angle between the Geetron X encoder and the absolute flat where the LVDT moves along. Thus decoding the X position of the LVDT is not very accurate. This uncertainty induces the error in producing the profile error data.

- It was envisaged that the way in which the tilt angle of the flat with respect to the mirror surface is compensated does not cause any harm to the profile measurement. However, this is right only if there is no asymmetric profile caused by the incorrect table rotation and the LVDT probe crosses exactly the centre of the mirror surface. These were later found to be rather difficult, in particular, with handling either the large absolute flat or the mirror. As a result of that, the measured profiles are not consistent occasionally, showing substantial changes in the slopes of subsequently measured 2 profiles.

- The 1 m polisher is in a separate room from the large optics shop where Mark 1 is placed. Mark 1 is too large to be used on the polisher. However, the mirror should be lapped on the polisher to leave the 8 ft Grubb machine free to be engaged in other polishing work. There has been a large amount of effort

in carrying the mirror to the large optics shop everytime when a lapping is finished. This combined with difficulty of handling the heavy mirror reduces the efficiency of lapping.

• The Mark 2 profilometer and its advantage over Mark 1

As the lapped surface approached a quality where the polishing can be started with, this has created the necessity for a second profilometer for cross-checking the profiles. The second Invar-type profilometer was built and named Mark 2 [114]. It has several AG 2.5 LVDTs that are more accurate and repeatable [95]. They are plugged in series at precisely determined locations on Invar rod. Mark 2 is capable of standing on the mirror surface using its two legs at the both ends of the rod. The legs are separated 83 cm which is the diameter of the mirror surface. Therefore they are fixed tightly with the mirror edges only when it crosses the centre of the mirror surface. Mark 2 has a number of advantages over its predecessor.

- The LVDTs are more reliable, i.e. better repeatability and small thermal effect. The LVDT is AC-energised and all the electronic components are taken into the PC interface card. Thus, the LVDT suffers very little from its own thermal behaviour. This means that, if the thermal expansion inside the LVDT is small and the temperature change in the room is kept small, then it gives fairly good accuracy. With the thermal change of $1°C$, the zero point change is less than 3 μm and the sensitivity alters less than 3 μm in the full scale of 60000 μm. It has a non-repeatability of less than 0.15 μm and a non-linearity better than 180 μm over the 60000 μm. In fact, the LVDTs operate with predetermined heights within the Invar rod so that the actual movements of the LVDT probes are fairly small, perhaps smaller than 100 μm centred at the middle of the full scale. It gives no possibility of the non-linearity in practice since the probe does not travel a large distance. Again, since Mark 2 needs less than about 30 sec to sample the height data across the diameter, there would be no substantial change in the room temperature, i.e. larger than $\pm 0.5^o$. This makes the thermal error within ± 3 μm. The total error of Mark 2 in the worst case is estimated to be about ± 5 μm which is twice better than Mark 1.

- The mirror can be measured while being mounted on the 1m polishing machine. There is no need to put much effort into carrying it to the large optics shop to

be measured. Mark 2 is light and portable. It is easily placed onto the mirror.

- The profile can be easily measured over the entire diameter so that any asymmetric features can be detected.

- Because the profilometer sits on the surface to be measured, there is no tilt between them so does not effect the measured profile.

• Performance and comparison of the two profilometers

The surface profiles measured with Mark 1 and 2 have revealed rather interesting features. Firstly, the overall appearance of the profiles were very similar to each other. Secondly, however, the one with Mark 1 showed larger amplitudes in P-to-V and slope variations in successive measurements of profile. The validity of the default calibration was put under suspicion. Mark 1's performance was again examined with the slip gauges. There were systematic differences of about 50 μm, meaning that for some reason the default calibration is no longer valid. The difference increases with the height of the probe. This gave rise to suspicion of thermal controller malfunctions. The temperature increase inside the Mark 1 cylinder seems to cause thermal expansion of the critical components of the LVDT. The LVDT was again tested against the slip gauges with the thermal controller off. The P-to-V amplitude of the measured profile decreased substantially but with the profile slope variation improved little. Thirdly, Mark 2 does not have the profile slope variation and the measurement is repeatable.

New method for tilt compensation:

The continuous experiment finally confirmed that the thermal controller functions well and the default calibration is valid. Measurements with both Mark 1 and 2 show consistency in profile appearance and P-V amplitude but not in slope. This indicated that the tilt compensation using only two edge points of the work piece is not good enough. A better way for tilt compensation was explored as follows. It measures the entire profile from one end to another with the same spatial interval. No data process is made at this stage. Assuming that the profile is symmetric, the data is folded at the centre of the work piece. Then, for example, the data from the left half of the X range, i.e. diameter, would be subtracted from those of the right half. The difference plotted against the radius would give a straight line, if there is

a systematic tilt. The slope that has to be compensated would be half the slope of the line.

This method would work on the basis of three facts. Firstly, the profile is assumed symmetric. Small scale local deviations from the symmetry can be treated so that the suggested tilt compensation would not suffer from it. However, if there exists large scale asymmetry covering a considerable range of the profile, this method would not work. Secondly, the work piece centre must coincide with the centre of the turn table for precision alignment with the absolute flat. Thirdly, it requires an X encoder which can measure across the work piece diameter. The current Geetron encoder has the measurement coverage of about 1.5 m from one edge of the turn table. In addition, the quill movement can go only up to about 23 cm beyond the centre of rotation. These mean that the proposed tilt compensation does not work with the large optics such as the Gemini secondary of about 2.5 m in diameter. The scaled Gemini secondary is likely to be the one that Mark 1 can handle with its maximum capacity. This will be implemented in a new version of PASS.EXE in the future. Mark 2 has been used more often to measure the profile of the scaled Gemini secondary throughout the loose abrasive lapping, and continued until the error equals to about ± 4 μm in P-to-V.

Impact from finite size of the probe head of the Mark 1 and 2 profilometers:

The LVDT ball heads of Mark 1 and 2 have the diameter of 0.82 and 3 mm respectably. The slope of the theoretical surface of the scaled secondary is about 6.16^o at R=40.8 cm which is the radius of the ground secondary. Because of the different area of the ball heads in contact with the work piece surface due to the slope variation, it forces an underestimation of the height, with respect to the centre of the profile by about 2.4 μm and 8.7 μm at R=40.8 cm for Mark 1 and 2 respectably. This error is compensated for in the software for Mark 2. But for Mark 1, the error is smaller than the calibration error and hence no correction needed to be made.

• Future improvements for the profile generation system developed here

Although the profile generation system developed here has been operating successfully in producing the surface profiles, some prospects have been seen for improvements in its performance.

- In fact, a major set of the algebraic equations PROG.EXE uses for target calculation can be replaced with a so-called 'conic equation'. The single conic equation can be used to calculate targets along all conic surfaces i.e. sphere, parabola, hyperbola and ellipse. This will substantially simplify the stage of `Geometric parameter` where the user inputs the geometric parameters to define a specific surface within PROG.EXE. It will help users greatly, who understand the surface with the conic parameters rather than the coefficients of the algebraic equations. There would be no need for the conversion between the conic parameters and the algebraic coefficients.

- Since the LVDT has to move along the X axis, it is necessary to run both PROG.EXE and PASS.EXE at the same time. If PASS.EXE run exclusively, then user has to step up and down to move the quill manually. Although it does not affect the efficiency of profile measurements very much, it is worth looking at possibilities to combine the two functions, i.e. move the quill and measure the profile with software.

  One way is to incorporate either AXIS.EXE or MANUAL.EXE into PASS.EXE. The other way is to use a multi-tasking operating system, running both the softwares and switching between them. Following the second way, the SYSTEM.INI file of Microsoft Windows 3.0 is modified to allow swapping two non-window applications such as MANUAL.EXE and PASS.EXE. The two programmes then run without any conflicts under the supervision of Windows 3.0. However, the LVDT signal jumps up and down about 500 μm. It is found to be nothing to do with the interpolation process but the communication between the PC and the LVDT. In fact, it has been reported that Windows 3.0 sometimes causes problems with multiple use of serial communications via RS 232 [74]. Several alternatives are worth being tested. Examples includes the DOS 5.0 task swapper, Windows 3.1, OS/2, Windows NT, etc. This has been never materialised because of the low priority since the development of Mark 2. Currently, PASS.EXE runs exclusively when the profile measurement is made.

Mark 2 has been used frequently as the primary profilometer and Mark 1 occasionally as the back-up profilometer.

Item	f/3 concave sphere	f/7 scaled Gemini secondary
Surface	Sphere	Hyperboloid
Diameter	83 cm	83 cm
Grinding	120 hours in 20 days	120 hours in 20 days
Method	Passive NC-milling	Active NC-milling
Profile Error	No active compensation	Active compensation
Loose-Abrasive Lapping	About 10 days	21 hours in 26 days
Surface Accuracy	Not recorded	±4 micron P-V
Profilometry	Spherometer	Mark 1 and 2 profilometers
Polishing	182 hours in 56 days	Not done yet
Polishing Tool	Full size passive lap	Full size active lap

Table 2.2: Comparison of profile generations between the f/3 spherical concave and the f/7 hyperbolic convex Gemini secondary. Both are 83 cm in diameter.

• Concluding remarks for this Chapter

Brooks, the OSL optician, claims that the new profile generation system increases the efficiency between 5-10 times, compared with the traditional way that GP had used. In addition, there is substantial increase in efficiency of the profile generation by adding the new profilometer and active error compensation to the computerised diamond-milling. Table 2.2 shows the technical differences used in generating the profiles of the f/3 spherical concave and f/7 hyperbolic convex Gemini secondary as well as the statistics of time spent.

Chapter 3

Optical Surface Polishing

3.1 Introduction

Polishing and figuring are the most critical stages in the fabrication of any size of optics. Polishing is the removal of subsurface damage and surface defects, to provide a smooth surface at the 1 nanometre level. Figuring is the control of the overall surface profile ('figure') of a polished surface. The quality of polishing defines the stray light performance of the surface. The figure defines the imaging performance. The process here is to achieve sub-micron accuracy, typically $\lambda/5$ to $\lambda/10$ i.e. about 1/10 to 1/20 μm, in manufacturing. As seen in Chapter 1, the new generation of large telescopes, being built and planned, require large and highly aspheric optics. Some are even thin and flexible optics. And yet the surface figure of about $\lambda/10$ is to be challenged by all means. Conventional polishing can not cope with this evolving face in telescope optics requirements.

In this Chapter, a new philosophy is developed for that. An initial design for the instrumented active lap and proposed tests with the lap are presented accordingly. This inevitably needs to address some technical aspects foreseen in view of real construction and polishing operation. The lap design and test method proposed in this Chapter will evolve towards construction and testing of the active lap described where appropriate in Chapter 5 and 6.

This Chapter starts with a review of existing methods and their problems in polishing the telescope optics in Section 3.2. The new philosophy of active polishing

developed is presented in detail in Section 3.3. The initial design of the overall system is described in Section 3.4., mainly concerned with the active lap hardware. The implications and the proposed tests with the lap are briefly discussed in Section 3.5.

Optics testing is an essential part of the polishing activity, that verifies the surface faults and feeds necessary information to the next polishing run. Hence, broad conceptual developments are described as a part of the overall polishing process. This led to some preliminary experiences in building a testing facility, which is described in Chapter 5. However, details of the major developments OSL has achieved in optics testing is not of special interest to this thesis, but will be described in another colleague's Ph.D. thesis.

3.2 Existing Methods of Polishing

3.2.1 Conventional Polishing

• Description of conventional polishing

Conventional polishing described by Texereau [106] and Horne (pp 148-217 [54]) uses a rigid lap made of either wood or glass or metal, e.g. cast aluminium. Typically squares of pitch are stuck onto its bottom surface. The pitch is pressed for considerable time before a polishing run starts so that the pitch flows for its surface to conform to the optical surface with no gap in between. An example of abrasive slurry is the mixture of water and cerium Oxide. It is poured in between the two rubbing surfaces i.e. optics and pitch surfaces. The work piece rotates with a turn table. For small optics, a full size rigid lap held by hands or automatically moves with zig-zag motion across the work piece. The motion, if it is tangential, must move forward and backward along the longitude. The typical stroke is about 1/3 of the diameter of the work piece, but is modified by the optician to control the figure of the workpiece. However, for large optics, the full size lap becomes larger accordingly and its motion must be driven by electric motors. Examples include the two push-pull arms attached to the two eccentrics drives that GP had used. Using various combinations of the arm lengths and rotation speeds of the eccentrics, varieties of

the lap motion can be achieved. The rotation of the work piece and the lap strokes give the rubbing surfaces pseudo-random contacts as much as possible over the polishing time. It is also to remove any non-symmetric effects from polishing. The polished surface is tested with various optical testing methods such as knife-edge testing and shearing interferometry. Surface errors such as deep scratches, incorrect figure and zonal defects are corrected either by subsequent polishing using the full size lap or by local touching with a smaller lap.

Thus, in the conventional polishing, the lap varies in size, depending on the surface quality and defects. The large lap, approximately work piece size, has superior removal rate of material and ability to smooth the surface. Hence it is normally used to control overall surface figure. However, because of its rigidity, it lacks the ability to ablate localised zonal spots and is used with a small stroke. Realising this, various companies have developed in-house process for small aspheric optical components, by providing a compliant layer (e.g. rubber) within the lap. Sometimes, the smaller lap, about $\frac{1}{5} - \frac{1}{10}$ of work piece in diameter, is used. But the small lap tends to produce high frequency spatial ripples and zones. A sub-diameter lap, a hybrid of the two laps above, is sometimes used. It is about 1/3-1/4 of the work piece in size so as to give a compromised way in polishing between the two extreme ends.

• Traditional method of aspherisation

Aspherising is normally carried out by changing pitch distribution and the stroke on the lap for successive polishing runs after a best-fitting sphere is figured. This has long been used to successfully produce telescope and related optics of small and moderate size and asphericity up to few tens wavelengths. It is indeed a slow time-honoured process that relies entirely on skilled opticians. Most of the production time is taken by optical testing and fine local correction. Thus it is very costly and irrecoverable once the experience is lost.

• Fundamental problems with the traditional polishing and aspherising

Facing on the larger optics for 3-4 m and even larger 8-10 m class telescopes with severe asphericities of few hundreds to thousands wavelengths, a fundamental problem rises from the conventional polishing. Figuring highly aspheric surfaces has to cope with the continuous and rapid change in radius of curvature across the work

piece. The conventional lap, either full size or sub-diameter, is too rigid. Time scale of pitch deformation is much longer than typical polishing time. These imply that the lap does not conform with the surface, unable to maintain good contact everywhere throughout its stroke. Thus the polishing takes place preferentially, inevitably producing large or small surface errors. The result is that the workpiece tends to revert towards the sphere. The local touching with a smaller but rigid lap is not quite helpful for that. Because of the rapid change in the radius of curvature, there would still be non-contact within the area of local touching, unless the lap size is substantially smaller than the area of error i.e. of local touching. Using a very small rigid lap compared to the local touching area might be able to remove the errors to some extents. However, it tends to impose high frequency zonal defects and spatial ripples onto the surface, which produces larger stray lights, thus degrading imaging quality of telescopes. To overcome these, several approaches have been developing recently world wide and described in the next Section.

3.2.2 Recent Developments in World-Wide

3.2.2.1 Stressed Lap Polishing in University of Arizona

• Summary of the stressed lap polishing

Martin *et.al.* [71] have described the stressed lap polishing that Steward Observatory, University of Arizona, is developing and its application to the 1.8m f/1 ellipsoidal mirror fabrication. Here, the sub-diameter lap of about 1/3 of the work piece in diameter is actively distorted by 12 moment generating actuators. They apply no net force, but a bending moment to the lap, working independently from the polishing machine. These are to continuously change the lap shape to fit the mirror surface as it moves across the work piece. The shape is expressed by a sum of the first three Zernike polynomial terms which are bending i.e. defocus, astigmatism and coma. They use a high acceleration of lap movement up to 1 m/sec^2 for rapid coverage of the surface. This is to average out uncontrolled variation of removal rate of which time scale is typically several minutes. The mirror profile is controlled by modifying the locus traced out by the lap.

• Problems with the stressed lap polishing of Martin et.al [71]

At the start of our work, we recognised potential problems with the stressed lap polishing.

- It is impossible to control the lap shape to optical precision. Their off-line calibration shows that the best accuracy of the lap bending is about 3 μm rms. This misfit, even if it can be easily filled with the abrasive film, can cause different ablation conditions on the mirror surface in polishing. They admitted that the working version is several times worse due to unexpected hysteresis in the polishing lap. In addition, the calibration is made with an entirely static condition, in which the lap is placed on the 32 spring-loaded displacement transducers. All the transducers take part in supporting the lap during the calibration. This is indeed irrelevant to the dynamic situation of the real polishing. As the lap moves not only on the hard mirror surface but also on the abrasive fluid and the mirror surface, the number and the reaction forces of the supporting point vary in real time. Thus the boundary condition, with which a desired load distribution is computed to make a lap shape, changes continuously in polishing. This does not seem to be taken into account.

- Even if the tool surface can be fitted to the mirror surface to optical precision somehow, it cannot still be sure that there is a predictable way of controlling the ablation rate with this approach. Obviously, the wear rate is related to friction condition which is formed by some controllable parameters such as the polishing pressure, the sliding velocity and the integrated polishing time. Therefore, the friction, either instantaneous or integrated, is more important than the lap deformation for ablation control.

- They use a sum of the three lowest order bending modes to represent the lap shape. Thus, it is unable to deal with the higher order feature of the lap shape and therefore of the mirror surface. This agrees well with the fact that each actuator is responsible for the area of about 22 cm in diameter, leading to only about 3-4 actuators along the diameter of the lap. Therefore it is not capable of achieving higher order bending modes, limiting the ability to correct localised-zonal errors. In particular, as the sizes of lap and work piece and the asphericity increase, the lap cannot fit the mirror surface adequately

without the ability of generating higher-order bending modes. They seem to be aware of that but find no solution as yet.

- It does not monitor the polishing pressure. They are unable to control the friction which is the primary parameter for ablation control. Moreover, there is no sensor to monitor the lap deformation in real time. Thus they can not close the control loop with no information to feed-back. It leaves no ability to build a computer-based algorithm for ablation control. They realised this problem and have a plan to make use of a force measuring device for a larger version, perhaps about 2.5 m in diameter in the future.

- As a result, it is still unknown what happens during strokes and hence polishing. In fact, the whole idea is to give opticians a working environment where polishing aspherics with the stressed lap seems very much similar to polishing spheres with the conventional lap. The main aspect in figuring cycles remains very much the same as those of the conventional polishing except using a set of fixed Zernike polynomial coefficients to deform the lap surface. The metrology information of the previous polishing must be fed back to *opticians* who determine the polishing conditions for the next run, relying on their personal experiences. The optician's experience and feeling are the core of the ablation control algorithm. In addition, the vital information, i.e. pressure, is missed and nor is the rest of the information in a useful form for the optician to quantitatively plan for the next polishing run. It is not aimed to directly control removal rate and thus it does not have an advanced algorithm to control ablation rate during a polishing run and to predict necessary changes in polishing conditions for the next polishing. Opticians have to plan almost all aspects of the next polishing run.

- The small and sub-diameter tools cause the edge problem that, when it is overhung, figuring the edge properly is extremely difficult.

They stated that stressed lap polishing started in November 1989 on the surface of 4 μm rms. and of the subsurface damage of about 30 μm. After 120 hours polishing, the measured surface was very smooth on small scales but revealed substantial large scale errors. In February 1990, the surface figure error was still 22 μm P-to-V after

removal of focus and tilt, including some 5 microns of azimuth error caused by the support. It was still far out from an optical surface. (The final parts of Chapter 7 describes the progress of this method after February 1990.)

3.2.2.2 CCOSs in Litton Itek and Contraves Goerz

Jones & Rupp [62] and Zimmerman [120] have described the computer-controlled optical surfacing process(CCOS) that Litton Itek Optical Systems is developing and its application to produce an off-axis parabola. A similar method is also being developed by Contraves Goerz Corporation [100]. It has been used for producing several f/1.5, 1.5 m diameter on-axis paraboloids. A sub-diameter lap of about 0.1 to 0.2 m in diameter is driven in a orbital motion whilst scanning over the work piece. Typically, the lap is about $\frac{1}{10} - \frac{1}{5}$ of the work piece in size. The lap surface can conform to the mirror surface by using a multi e.g. 5 axis CNC machine for the lap movement (Itek). The ablation is controlled with different dwelling times induced by impact velocities of the lap to different positions on the work piece.

However, firstly, as the physics of polishing is not well understood, there are no firm theoretical or even empirical foundations supporting the dwelling time alone as a primary parameter for ablation control. Unless the polishing pressure is either known or maintained equally everywhere during polishing as well, the convergence factor of successive polishing is expected to be low. Secondly, above all, the most serious problem is its natural tendency to produce high spatial frequencies and zones. Thirdly, the removal rate is rather low, requiring precision grinding prior to polishing. It is interesting to note that Itek has been using the stressed mirror polishing, instead of their own technique, for fabricating the Keck telescope segments as described below.

3.2.2.3 Stressed Mirror Polishing in University of California, Berkeley

Mast and Nelson [73] have explained the use of the stressed mirror polishing that the University of California at Berkeley has developed for the fabrication of the 1.8 m hexagonal off-axis Keck primary mirror segments. Litton Itek and Tinsley Laboratory have been using this technique to figure them. It pre-stresses to warp

a circular optic where grinding and polishing aim to produce a good but stressed sphere. The work piece is then cut to form a hexagon as it is stressed. The designed aspheric surface can be obtained from releasing the stress given to the edge of the work piece. Here, the polishing, itself, is no different from conventional polishing, to figure a sphere using a sub-aperture rigid lap. Thus, it has all the properties of the conventional polishing discussed above.

In the relatively short period i.e. 6 weeks, the polished surface reached the error of 0.25 μm rms. However, it was also found that the excessive stress relief, when cutting, caused surface warping of about 0.2-1 μm which is entirely unacceptable. They stopped polishing with the error of about 0.25 μm rms, which is roughly matched to the warping amplitude. The warped surface could not be re-figured since it was already cut into a hexagon. The only solution was to use a mechanical device called a *'Warping Harness'* specifically developed to deform the warped hexagonal surface to the designed one. Intensive research, including FE analysis and use of a strain gauge, was required to develop the Warping Harness. Thus, the Keck segments were successfully produced only with the auxiliary mechanical device, meaning that the stressed mirror polishing, itself, is not successful as a optics fabrication metrology.

3.2.2.4 Ion-Ablation Process in Eastman Kodak

Wilson [117] has described a completely different method called ion-ablation process that Eastman Kodak is developing. It bombards an ion-beam onto the work piece. The material of the substrates is sputtered on the atomic level by a momentum transferred from the ion-beam. An advantage of this is that the influence of the work piece to the figuring is low. In other word, for example, the tool does not have to fit the local surface feature and there is no problem with the edge figuring. Eastman Kodak has constructed the ion ablation machine that is capable of figuring optics up to 2.5 m in diameter. An application of this technique was a 1.3 m ULE frit-bonded, ultra lightweight, off-axis primary mirror segment. The ion ablation process started with the surface error of 5.02 and 0.62 λ in P-to-V and rms. respectively. After four iterations of figuring(about less than 100 hours in processing time) and testing, it was improved to 0.17 and 0.015 λ in P-to-V and rms. respectively. Three different beam diameters were used to correct various surface errors. It is claimed that its

convergence ratio is greater than 2.5 whilst that of others ranges from 1.1 to 1.3.

However, the overall ablation rate is very small compared to other methods. This requires either precision grinding or the other polishing techniques for rapid material removal in preparation of the surface to start the ion ablation process. In addition, this method does not improve the surface error in the successive polishing runs. In other words, if a bad surface is input, then the result will still be a bad surface. Realising this problem, the starting surface error of the 1.3 m ULE primary was prepared by the conventional polishing. This implies that the ion ablation process alone can not be solely used to successfully and economically figure the large aspheric. Realising this problem, Kodak acquired a precision grinding machine (from Cranfield Precision Engineering) which is capable of doing this.

Unfortunately, recent information via NOAO shows that the method has not been very successful. Litton Itek's test on one of the Keck segments figured with this method showed that the ablation turned out to be only 2/3 of that predicted. More seriously, the process left furrows in the surface, presumably due to overlapping of the ion beam on successive pass and use of different beam sizes. It seems unlikely that, with typical ion beam profile, it will be easy to eradicate this effect completely. It has been heard that Lick have elected not to entrust the Keck secondary to the ion ablation process but to work it in-house by other polishing methods. Their opinion is that it is on the margin of practicality for this mirror's comparatively modest asphericity. It seems likely that this technique is incapable of successfully figuring optics of more severe asphericities.

3.2.2.5 Linear Membrane Polishers in Zeiss and University of Turku

Beckstette *et.al.* [4] have explained the use of the Zeiss membrane tool process (MTP) to fabricate the f/1 50cm mirror as a part of their development for the SOFIA f/1 3m primary. Korhonen *et.al.* [66] has been developing independently a cousin of Zeiss MTP. They have realised that the primary variable for ablation control would be the polishing pressure, not the absolute profile of the tool shape. This lead to the use of Preston's law, stating that the instant wear rate is proportional to relative velocity and polishing pressure, as the underlying principle of their approaches.

The MTP tool consists of mainly a thin membrane and a set of actuators at its

rear side. The membrane carries the pitch squares and oscillates along a diagonal of the machine table on which the mirror rotates. It has to be designed flexible enough to accommodate the desired variation of curvature of the asphere and stiff enough to give a smooth print-through function of the actuator forces (even when an actuator falls off the edge or falls down a central hole). The actuator set generates the necessary polishing pressure in real time under a stream of instructions from a computer.

They claimed a number of advantages of this method, including some examples as follows.

- It is able to actively remove errors with low and medium spatial scales. The smallest spatial scale error that can be actively be reduced is determined by the actuator size.
- There is no need to change the tool shape to remove low frequency error in contrast to the stressed lap polishing. In fact, the tool can be designed to be flexible enough to accommodate any variations in curvature of the asphere.
- The tool covers the entire diameter so that the bending moment can be applied at the tool edge. This can remove the inherent edge problem of the small lap.
- Larger tool can be easily made. This provides a good volume removal which is necessary to ablate off the large surface errors and the subsurface damage made by diamond-wheel-milling.
- No tool preparation time is required in planing the next polishing run. The metrology data is processed and directly fed into the control computer which determines the necessary changes in polishing condition.
- It minimises the possibility of producing a hole in the surface during fine correction with a small area lap. Because of this, traditional opticians and even CCOS tend to remove less material than predicted during 1 iteration step.

But, this method is by no means perfect. It contains some problems.

- The physical law governing glass polishing is still unknown despite the efforts made by a few centres. And none of the existing wear laws have been proved entirely valid in glass polishing, including Preston's law.

- The tool motion is an one-dimensional oscillation in radius while the mirror rotation is tangential. This leads to the relative velocity vector in similar directions all the time, which violates integrated random movement of the polisher on the mirror surface.

- The removal rate is still lower than the full size polisher. The total area coverage is still less than 1/5 of the work piece. This requires longer polishing time and hence increases the production cost.

- There is no measurement to monitor the polishing pressure, being unable to close the control loop with no feed back pressure information monitored in real time. As a result, they do not know the real pressure distribution in polishing action.

- Because it has no on-lap force/pressure measuring element, the calibration of MTP must be made in off-line and static condition which is irrelevant to the dynamic condition in polishing operation. MTP has the same problem as with the stressed lap polishing, as far as calibration is concerned.

- Regardless the validity of the Preston's law, the use of an ablation relation make it easy to build up an optimised ablation algorithm which determines a desired pressure distribution for a ablation rate in real time. However, they do not seem to develop this sort of ablation algorithm.

3.2.2.6 Pressurising Rod Polisher in REOSC

REOSC has been awarded the contract for figuring the ESO VLT primaries. Their method uses a large flexible lap with rollers which push down to give some control of the pressure distribution on its back. Obviously, they seem to understand that the large lap is clearly faster (therefore more economic in polishing the 8 m primary mirrors) and has a smoothing effect which tends to minimise the high frequency

defects. REOSC has always polished large astronomical optics in its cell. Espiard [38] showed a photograph of the parts of their polishing facility for ESO VLT primary mirrors. (Unfortunately, neither the photograph showed, nor he explained clearly their polishing lap itself.) It indicates that ESO VLT primary mirrors will be again polished in its cell comprising the active support system. It seems that REOSC tends to use a pressurising rod polisher on the reflecting surface while the thin meniscus VLT mirror is actively distorted on the active supporting system to give more ablation at high areas.

It looks like a cross breed between Zeiss MTP and the stressed mirror polishing. However, it could have one distinctive advantage over Zeiss MTP and the stressed mirror polishing that it will be able to monitor polishing pressure if the active support system has some sorts of array of force/pressure transducers supporting the VLT mirrors on its back. If this is the case, REOSC alone will have the method comparable to Our Development, in terms of removal rate, smoothness of resulting surface and ablation control, which are discussed throughout this thesis. However, one should note that this will inevitably suffer from more or less the same problem with the stressed mirror polishing that produced the deformation of the Keck segments due to excessive stress release after the polishing.

3.2.2.7 Full Size Passive Polisher in Grubb-Parson

In contrast to all others, Dr. David Brown in Grubb-Parson had used full size passive polishing in figuring a number of large telescope optics such as the 3.9 m AAT and the 4.2 m WHT primary mirrors. This was based on a full sized passive flexible lap which, as it overhung the mirror towards the ends of the stroke, deformed under its own weight in a predictable manner. In order to figure the initial sphere to the desired paraboloid (or hyperboloid), he calculated, in advance of a polishing run, the parameters needed to ablate preferentially the edge of the mirror with respect to the centre. This method worked very well in producing the moderate asphericities of the 4m class primary mirrors.

The full size polishing has two inherent advantages. One is that it polishes more rapidly than any sub-diameter methods, by virtue of the increased area of contact. This speed advantage may be a factor of 2-10. This can substantially affect the

economics and lead-time for producing a large mirror. The other is its superior smoothing action for the surface being polished, reducing high frequency errors. This will very much help not only for collecting 80 % of the light in 0.3 arc second, but also remaining 20 % falling closer to the 0.3 arc second boundary.

However, Dr. Brown's passive way has a number of problems, when encountering larger mirrors of severe asphericities or with convex secondary mirrors. For larger asphericities, it becomes very difficult to predict in advance the surface ablation with sufficient precision. In any case, it does not work for the turned-up asphericity of convex secondary mirrors since the ablation must be greater in centre than in the edge. The polishing process is almost identical to the traditional one with one additional process to calculate the deformation of the lap according to its strokes. Like the traditional one, the preparation for a polishing run is long and tedious. The metrology data can not be processed and fed to an algorithm that can identify what and how to change for the next polishing run. No physical parameter is measured in real time during a polishing run, leading to no real-time controllability over the physical parameters affecting ablation. With this method, the speed advantage of the full size polishing is simply consumed by the long and tedious process of the conventional polishing technique.

3.3 New Philosophy of Active Polishing

3.3.1 Background of the new philosophy of genuine active polishing

As seen in the previous section, the current development emphasis, world-wide, is in figuring primary mirrors for 8-10 m class telescopes to the required aspheric concave profile. However, the production of the convex secondary mirrors for these telescopes has been comparatively neglected during the course of the projects. These will also be highly aspheric. For example, the f/7 secondary for an 8 m f/1.8 primary would typically have nearly a thousand waves of asphericity. In addition, the sign of the asphericity turns the edge of the mirror up with respect to the a sphere. This combination of sign and magnitude of asphericity is surpassed by the difficul-

ties of testing convex surfaces and makes figuring the secondary for 8 m telescopes extremely challenging and costly. The new philosophy of active polishing developed in this Section has the primary application of figuring the secondary mirrors. But, it is equally be applicable to figuring the primary mirrors with severe asphericities.

The review in the previous section showed that all the methods suffer from one or more problems. Among them, the 4 methods: MTP in Zeiss, the stressed lap polishing, the REOSC's pushing-roller and Itek's CCOS can be categorised into *'pseudo-active polishing'* for the reasons they have in common. Firstly, they alter continuously the ablation parameters (allegedly !) during a polishing run. For example, Itek uses a multi-axis arm to carry the small tool in orbital motion with velocity control. The other three methods use force actuators. This gives them some degree of controllability in polishing, resulting in a better convergence factor than 'passive polishing'. Secondly, they measure *no ablation parameters* while the machine is running. This results in no real-time ablation information feeding back during polishing action. This open-loop nature of the process limits the further gain in the controllability. Thirdly, they have neither concrete theoretical foundation nor an ablation algorithm for real-time ablation control. The ablation control remains confused due to use of different control elements i.e. tool shape, pressure, dwelling time, etc. Fourthly, except REOSC's pressurised roller polisher, the polishing tools are small, covering only a fraction of the mirror surface. This lowers the volume removal rate. Except the Zeiss MTP, the other sub-diameter tools create the well-known edge problems. All the sub-tool polishings are likely to produce the high frequency errors, which we want to avoid, on the mirror surface.

3.3.2 New philosophy of genuine active polishing

In the middle of 1989, realising the facts described above, Walker [111] put forward the initial philosophy for full size active polishing. It was a full sized lap with 2 dimensional arrays of force actuators and force/pressure sensors, which aims to actively control the ablation rate in polishing. However, it was not detailed in technical aspect. Later, during late 1989 and throughout 1990, this has been substantially enhanced and finally developed to the proposed new philosophy for the *'genuine active polishing'* summarised here after.

- **Definition of active polishing:**

  The phrase 'active polishing' means that the ablation is actively-continuously controlled in a predictable manner while the machine is running. This requires real-time control of the primary variables that affect mostly ablation in polishing. Thus, the new philosophy adopts the use of the force actuators from the pseudo active polishings. The actuator operation has to be more advanced and inter-related to what is actually happening in terms of resulting ablation during polishing. The actuators would be distributed over the lap surface to control local surface figure, with real-time modulation of the primary ablation variables i.e. polishing pressure for the active polishing here proposed.

- **Profile generation by diamond-milling and loose abrasive lapping:**

  The rapid fabrication of the large fast aspheric optical surface requires direct generation of the desired aspheric profile by diamond-wheel grinding. It should be capable of achieving better than about 20-30 μm P-to-V in surface error which is roughly the magnitude of subsurface damage. Currently, several companies, such as Eastman Kodak, have the precision grinding machines capable of doing that up to 2.5 m in diameter, which would be the typical size of the secondary of the 8-10 m class telescope. Diamond-wheel grinding up to 8-10 m would still be necessary for aspheric profile generation for the 8-10 m single piece primary despite the spin casting reducing dramatically the amount of material to be removed. Then, in principle, the same active polishing tool with ceramic tiles instead of the pitch squares can be used for lapping with loose abrasive (e.g. water-carborundum slurry of different grades) to rapidly converge to the surface error of about 1-4 μm P-to-V. The lapping would have no different aspects in operation from the active polishing, except for the use of different abrasive slurry and lap surface material.

- **Profilometry:**

  A profilometer has to be employed to rapidly verify the generated surface profile with the accuracy of, perhaps, better than 1 μm. If it has an accuracy of somewhat between 0.1-0.2 λ over the distance of up to few metres, it could be used for testing in the early stage of active polishing. Our early experience indicates that LVDT based profilometers can only achieve 1 μm accuracy over

1-2 m distance at its best and it is still behind what is optimally required as profilometer. A profilometer based on laser interferometry would be a good candidate since it is able to detect sub-μm height difference easily. The main obstacle, though, is the distance over which the accuracy has to be achieved, e.g. 8-10 m for primary and 2-3 m for secondary. To know the position of the profilometer probe with sub-μm accuracy over 8-10 m distance in both horizontal and vertical axes may or may not be viable even with the laser interferometry . In that case, one solution would be a scaled version up to 2-3 m used in range synthesis mode to cover 8-10 m. This is the same idea as the aperture synthesis testing described later.

- **Control of polishing pressure:**

  A typical polishing pressure that GP used with their aspheric polisher is about 0.1-0.2 psi. It is generated entirely by the weight of the lap and the push-pull arms, sitting on the mirror in strokes. They had two ways to control the polishing pressure. One is to use laps of different size and thickness and therefore alters the weight of the lap. The other is to change the distribution of the pitch squares on a single full size lap, altering the effective area of contact which affects the polishing pressure. Since this method has no fixed device which force is added to or subtracted from, it is unable to directly control the overall polishing pressure. In contrast to this, the Draper type machine (Horne, p 166 [54]) has the fixed reference which gives direct control of the overall polishing pressure from zero upward, unrelated to the lap weight.

  For the active polishing we propose, the former approach was initially suggested since it had been used for several aspheric polishers such as the GP's full size passive polisher and the stressed lap polisher. However, more advantages are seen with the Draper machine than with the GP's aspheric polisher. Examples include its ability to reduce the potential risk of rocking the lap in operation and ease of control for absolute polishing pressure in real time. A further advantage is that, because of its ability to control the absolute pressure, over-weight of the lap is no longer be a serious problem. Indeed, the active lap is likely to be over-weighted due to extra components for the on-lap electronics and actuators. The argument is finally settled on by the idea that the active

polishing must be able to run mainly the Draper machine mode but with ease of conversion to the GP's aspheric polisher when needed in operation.

- **Full size lap for active polishing:**
  Since the ablation parameters are intended to be controlled in real-time with the active polishing, full size polishing has more advantages than any sub-diameter tool polishing. Firstly, it has faster overall ablation rate for a given pressure with the machine of necessary power simply because of the increase in polishing area at a time. For example, it has about 9 times higher ablation rate than the stressed lap polishing which uses typically 1/3 diameter of the work piece. Secondly, much lower pressure can be used than with the small tool polishing. This reduces greatly the possibility of producing print-through with honeycomb substrates. Thirdly, the well-proven advantage of full size polishing is its natural smoothing action. It minimises high frequency errors and thus gives the ability to make the entire optical surface extremely smooth.

- **Stiffness of the active lap structure:**
  However, the traditional full size lap is too rigid to maintain good surface contact throughout the stroke. The polishing often results in very smooth surface at the expense of a large deviation from the desired surface profile, being incapable of correcting local slope errors. Thus, the requirement is that the tool, particularly the lap surface with the pitch facets, must be flexible enough to accommodate local change in slope. At the same time, it must be stiff enough to filter the localised actuator forces to a smooth force distribution over the mirror surface. A mechanical low pass filter needs to be embodied in between the actuators and the pitch surface. The pitch surface of the active lap must be easily converted between the concave and convex surfaces without major engineering work, when needed.

- **Theory of polishing:**
  The physical nature of the glass polishing is still veiled by the complicated friction condition, involving the hard fluid nature of glass, soft fluid nature of pitch, abrasive compounds and water. There have been three theories suggested since the beginning of this century; mechanical wear, plastic flow, and chemical attack. The recent understanding is that not one but two or three

processes may be responsible simultaneously in polishing. But there is still no knowledge on how they share and change the responsibilities with the varying polishing condition. This leads to the fact that no quantitative expression better than Preston's law [4] is found in relating the polishing parameters to the ablation. Preston's law [4] has been used for this reason.

Nevertheless, to know a quantitative expression between the ablation rate and the various physical quantities is crucial for the success of the active polishing. Thus, the active polishing accepts only the broad concept of Preston's law [4] (i.e. the wear rate is related to the polishing pressure, the relative velocity of the two sliding surfaces and the integrated polishing time) as a starting point. As the active polishing continues over a period, it would then be able to evolve to a more accurate relation with a learning ability i.e. human operator or advanced algorithm implemented within the overall working process. An experiment is needed to examine Preston's law and to find alternatives if any exist. The experiment undertaken and the analysis on the result are described in the first half of Chapter 5.

- **Behaviour of abrasive film:**

  All the polishing methods described above have one aspect in common which is completely neglected. The behaviour of the abrasive film in a polishing run has never been studied in sufficient detail for application to real- time ablation control. Most early studies collected and reviewed by Cornish [19] are not concerned with the ablation control but rather the nature of glass polishing. The existing methods alter the ablation parameters with the 2 assumptions. Firstly, the abrasive film remains homogeneous in its physical and chemical characteristics over the working surface at a given time. Secondly, the physical properties of the modulation of any ablation parameters are identically copied onto the ablation behaviour on the mirror surface without any influences of the abrasive film.

  Traditionally, opticians alter the grade of abrasive compound and the mixture ratio of the water and the abrasive compound at various stages of polishing. The aim has been to control the ablation not in a single polishing run but a series of polishings. However, there has been no quantitative understanding on

what and how the change in the characteristics of the abrasive slurry affects the ablation on the mirror. In addition, during the figuring process, they do not normally change the contents of the abrasive slurry. Particularly in a polishing run, the same abrasive slurry is continuously used, being supplied when optician feels that it is dried out. In this way, one normally does ignore the information on

- how long a supply of the abrasive slurry could last in a polishing run.
- how its characteristics varies over the time span of the supply in terms of friction.
- how the lasting time changes with the ambient temperature.

Furthermore, there is no validation if the assumption is correct. And, it would be quite likely that the presence of the abrasive film would certainly influence at least the modulation characteristics of the ablation parameters during its propagation through the abrasive film. The behaviour of the abrasive slurry in view of controlling the ablation, not of knowing the physical nature of polishing process, may be one most interesting to the active polishing, since it aims to control the ablation parameters at the modulation speed of fractions of a second.

The success of the active polishing may critically depend upon how well it is understood, organised in the process and used in a polishing run. This makes it crucial to undertake an experiment specially designed to reveal the information questioned. The second half of Chapter 5 is dedicated to describing the experiment and its implication.

- **Variables and metrology data for active polishing:**
  Active polishing needs to define clearly what physical parameters and metrology data are to be involved and the way in which they should be organised in the process. They can be divided into 4 groups as seen below.

  1. **Group 1: Real-time operation parameters**

     polishing pressure, relative position and orientation between the lap and the mirror, polishing time, overall friction, ambient temperature and humidity.

The parameters in this group are to be monitored and some are actively-controlled in real-time throughout strokes.

2. **Group 2: Induced parameters**

   The relative velocity and orientation are used to determine the distribution of sliding velocity over the mirror surface, which we call *'velocity map'*. This enables us to calculate the instant friction and ablation maps. The integration of the instant ablation map over the duration of polishing gives the predicted-integrated ablation map. The history of the time interval between two successive polishing contacts at a point on the mirror surface can also be traced and quantified. This history would be useful to determine the difference in ablation rate, if it exists, between the continuous and intermediate polishings.

3. **Group 3: Parameters from the optical testing**

   Optical testing gives optical surface topography. It is used to determine the observed-integrated ablation map which is to be compared with the predicted one. The surface temperature of the mirror may have to be stabilised before optical testing since it affects not only the thermal expansion of the material but also generating air turbulence in the optical path if a temperature difference exists between the mirror surface and air. The time interval in between the completion of a polishing run and the beginning of the following optical testing may have to be kept constant. It allows for the wet mirror surface to be thermally relaxed and fully dried before the optical testing. Keeping the constant room temperature and humidity, as in normal optics workshop, helps to maintain the same condition in the series of optical tests during the polishing process.

4. **Group 4: Off-line metrology data**

   The optician has to pre-determine the 3 operating parameters i.e. stroke, desired polishing pressure and polishing time, when beginning a polishing run. An off-line sub-process would have to be developed for this. The glass materials and the polisher are normally fixed once mirror fabrication starts. The kind, age, grade and pH of the abrasive slurry used in a series of polishing runs also have to be carefully determined. It is rec-

ommended that these parameters remain constant as much as possible in the polishing series, by using the same abrasive slurry always made with the same grade of the abrasive compound, the same water-abrasive compound ratio and the same time before a polishing run begins.

- **Real-time closed-loop control while the machine runs:**
  All the real-time operation parameters have to be sensed and displayed on a VDU in real time. For the first time in the history of optics polishing, it closes the real-time process, which has long been open in nature, providing opticians with a process-control feedback. Not only that, it also provides opticians with a live-feeling about what is happening on the mirror while the machine is running.

  This needs some sort of force/pressure sensors distributed over the tool surface. This sensors have to be adequately calibrated, not individually but as parts of the whole system of the lap. The sensor and actuator positions also have to be precisely encoded on the fixed mirror coordinate system. It is to calculate relative velocities of each sampling position on the tool and the mirror. If possible, the frictional force exerted onto the entire lap is to be measured throughout strokes. It would enable us to estimate the overall ablation at a given time since the friction is the closest physical parameter to the ablation. The ambient temperature and humidity histories collected over the polishing process would certainly be useful to refine a real-time ablation process.

  The use of closed-loop feedback control requests the appropriate electronics, which performs sensing the pressure and their locations, compares it to a desired pressure and activates the actuators to compensate for the differences. The main tasks of the electronics would be the signal multiplexing and the A/D conversion, the real-time distributed actuator control, Graphic User Interface (GUI) and the bi-directional communication.

- **Control system outline:**
  All the metrology data described above must be in a usable form to be processed and fed back for improving the system performance. This requires a master intelligence which performs GUI, coordinate transformation, ablation rate calculations, improving algorithm, updating actuator control commands

etc. The master is linked to a slave intelligence via some sorts of bi-directional data communication link. The slave would perform the sensing ablation parameters e.g. pressure, position and controlling actuators, sending information to and receiving instructions from the master. All the real-time data is processed and can be stored in a mass storage device, if required. A software would read the results of the optical testing made before and after a polishing run, calculate the integrated ablation map, integrate the ablation parameters monitored and compare them to the two surface maps. This would generate a surface error map which makes it possible to examine and improve the real-time ablation algorithm.

- **Tool movement:**

  For tool movement, the conventional strokes using two eccentrics and two push-pull arms is considered more beneficial since it gives more random motions. The lap is mounted to the push-pull arm in such a way that provides easy conversion between rotation-free and driven rotation. This can give complete control over the tool movement in X and Y translation and rotation, with respect to the mirror. In fact, all the tool movements can be under computer-control in conjunction with other ablation parameters. However, it is not necessarily one of the initial functions that the active polishing should have in the development stage.

  The stroke has been typically 1/5-1/10 diameter for the traditional full size polishing because of its inability of conforming with the local surface curvature. Since the active polishing lap is the flexible structure, it would have a wider choice of the stroke distance, ranging from 1/10 to 1/3 diameter stroke(conventional sub-diameter polishing). In addition, the suggested computer control, if built in, makes it possible to work with variable stroke when required in a polishing run.

- **Rotation of workpiece:**

  Conventional polishing uses a fixed rotation speed for the mirror for a polishing run. The rotation of the mirror is accepted for the active polishing for the reason that it eliminates certain types of error such as astigmatism by maintaining the circular symmetry in polishing action. As suggested previously

with the stroke and the lap rotation, the computer control of the rotation speed would not be an immediate requirement to be implemented for the active polishing. Nevertheless, the variable rotation speed with the computer control would certainly increase the efficiency of the ablation control in a polishing run. This can also give the active polishing the ability to violate the rotational symmetry on purpose.

- **Workpiece support:**

  It would be ideal if, during fabrication, the blank should stay in the same support system as in telescope operation. For example, an active support system would be used for a thin meniscus mirror. It can then be used to stress actively the blank for the polishing conditions that the active polishing would prefer during a polishing run. In contrast to that, the mirror blank must be as stress-free as possible on its back, when polishing, if it has a passive supporting system.

- **Tool preparation time:**

  Significant time of conventional polishing is spent for the tool preparation e.g. altering pitch distribution, replacing major parts of the tool such as the cast aluminium frame of the lap body. Active polishing can minimise the tool preparation in both the time and resources. For example, the pitch squares can be stuck onto the mirror side surface of the lap once in for all and do not have to be replaced unless damaged. The major parts of the active lap do not need any replacements unless they are damaged by accidents. Thus, this would give substantial saving in time and resource during mirror fabrication.

- **Scalability of the active polishing lap:**

  The active polishing lap and its auxiliary equipment have to be designed for ease in scaling up to the full sized 2.5 m lap for a real secondary mirror. The pressure sensors and the actuators should be easily multiplicated, using the existing one. The electronics should be designed with a simple plug-in board strategy to increase sensing and controlling channels. Bi-directional communication should be designed to be able to increase speed, to cope with increasing data flows. The on-lap slave intelligence should be as fast as possible, this being able to take over some of the tasks for the master to speed up other

tasks. The major mechanical components such as the lap body frame must be easily replaceable. In doing so, it would be crucial to design the entire lap and the components with the modular approach. This can ease the maintenance as well.

- **Computer based ablation algorithm:**
  The whole process of active polishing would proceed under supervision of a computer-based algorithm. It consists of the Real-Time Ablation Algorithm(RTA) and the Global Process Algorithm(GPA), each of which interacts closely with others in operation. A brief explanation of these is made below and can be more clearly understood with Figure 3.1.

  1. **RTA:** This can be divided into five work blocks that are cycled to perform the close-loop control in real time. It would start with measuring the polishing pressure, velocity, contact between the lap and the mirror, the polishing time over the mirror surface. Direct display of these variables would be continuously updated in the form of 2 dimensional map in the fixed mirror coordinate. Then the measured data would be used to estimate the instant and therefore integrated ablation maps. It would enable us to compare the predicted surface contour to the target one. If the comparison does not result in satisfaction with a tolerance defined, a new target pressure map would be define and compared to the measured pressure map. This defines the pressure map that the actuator operation is to compensate to in a real-time control cycle. However, if the comparison shows the predicted surface within the tolerance, the polishing run would be stopped, being proceeded onto GPA.
  2. **GPA:** This would start with optical testing that provides an observed surface contour. It is used to obtain the observed integrated ablation map or the observed surface error map between the final target and observed surfaces normalised to the centre of rotation over the mirror surface. This gives adjustment to the 2 work blocks in RTA for the next polishing run. They are the prediction of the integrated ablation map and the definition of the new target pressure map to be updated in real-time.

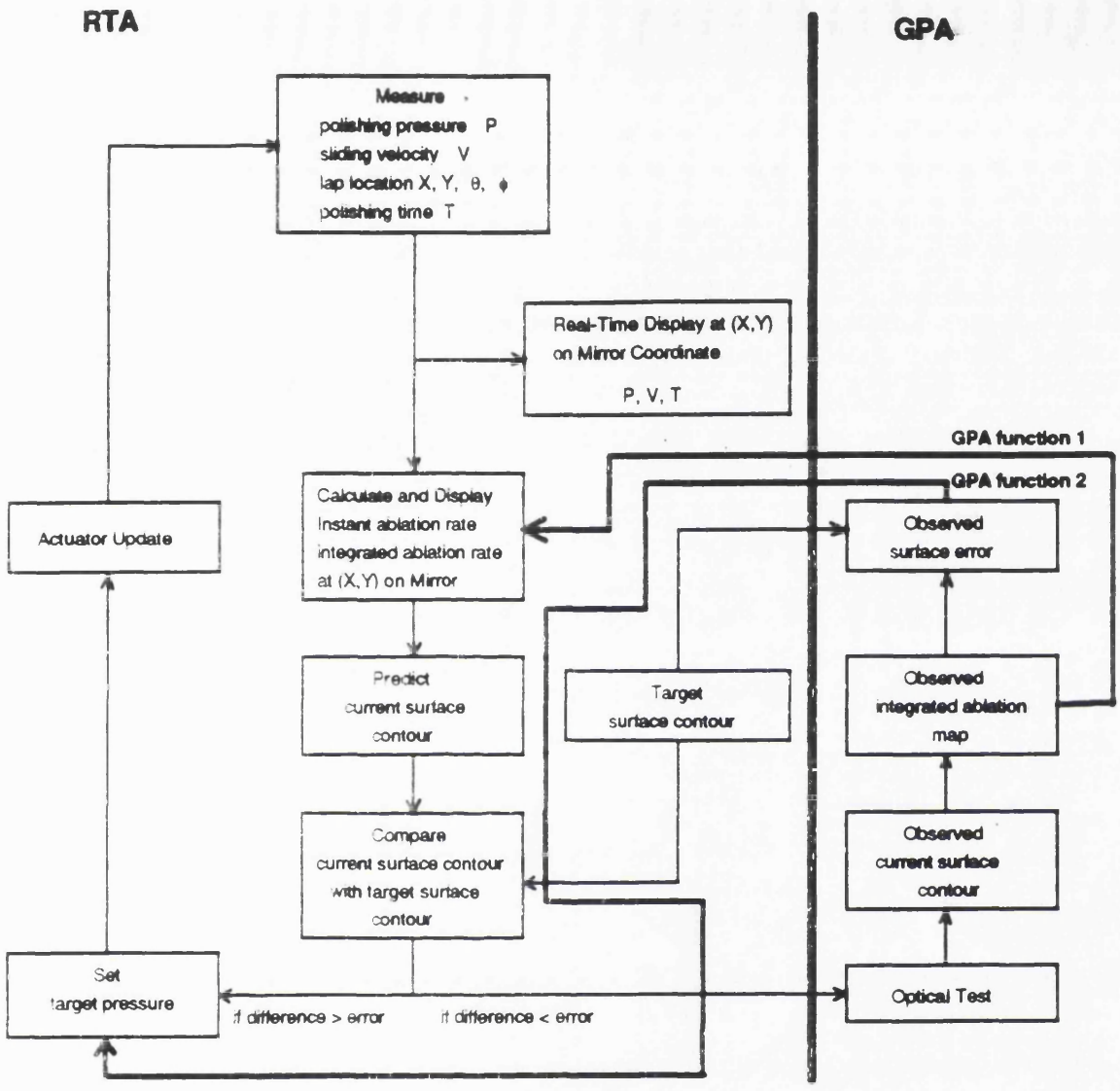

Figure 3.1: A brief flow diagram of the algorithms for the active polishing.

Thus, for the first time in the history of optics manufacturing, the proposed active polishing utilises *computer-based algorithm*, which is potentially capable of learning and evolving by itself. It is this approach that gives the our active polishing the potential for a superior convergence factor.

- **Control of polishing variables:**

  The methodological strategy for the active polishing would be to alter mainly the three variables i.e. polishing pressure, relative velocity and polishing time for the ablation control. The polishing pressure alone would be actively-controlled first whilst other two remain constant in behaviour with the successive polishing runs. If this approach is proved good enough to control the

ablation, no other parameters would have to be actively-controlled. This is what is expected to be the main active polishing mode. However, if it does not converge to a certain precision in predicting and controlling the ablation, the relative velocity would have to be under the active control with the computer-controlled driven rotation and stroke as well.

When the active polishing begins to figure a mirror for the first time, the polishing time could normally be set to a fixed time period. After a few iterations of polishing and testing runs, the active polishing run can be stopped when the predicted surface map approaches closely to the final target surface map within the error of, for example, 2 % rms over the mirror surface. To this extent, the polishing time can be actively-controlled if required. All the other variables and the work conditions are to remain constant throughout polishing a mirror.

- **Optical testing for the active polishing:**
  The lesson from the Hubble space telescope [99] mirror suggests that at least two independent optical testing methods have to be employed to cross-validate the results of each other. The common requirement for the testing method is that it must be able to produce the resulting surface topography in digital format i.e. either binary or ASCII. This enables the GPA software to read and process it further. Two methods appear to be of most interest.

  The first is the well-known knife edge test. In contrast to ordinary interferometry, it needs virtually no quality, costly optics for testing a concave mirror but yet gives extreme sensitivity and no obscured sign in analysing the result. It is also easy to set up. One drawback is that the knife image of the mirror being under test has been traditionally observed with the naked eye, leaving no quantitative result to be processed. Instead of the eye, the use of a CCD camera and frame grabber at the focal plane gives the digitally recorded image that would be analysed with a separate software. The second is scatter plate interferometry. This also requires no quality, costly and large optics. For this reason, it has been popularly used to test large astronomical optics. The characteristics of the test and the preliminary experiment with this method are described in detail in Chapter 5.

The application of the two methods of testing primary mirrors is quite straightforward since they focus the light to the focal plane. However, the secondary mirrors reflect and diverge the incident parallel light beam, which is somehow focused to be observed. An auxiliary focusing element is needed to form a real image in preferably a null configuration. The classic solutions are the Hindle test using a large spherical mirror and the modified Hindle test using a large meniscus lens with spherical surface. Both the spherical mirror and lens need to be of a diameter exceeding that of the secondary under test. The large mirror or lens exceeding about 2 m diameter is hardly practical. It is very costly, increasing the overall cost of the mirror fabrication and thus the telescope.

Instead. the aperture synthesis technique can be explored. It uses small, perhaps slightly larger than half the diameter of the secondary, but still a single piece meniscus lens of no power, placed off-axis in between the detector/light source and the convex surface under test. It illuminates a part of the mirror surface which is at least radially larger than the radius of the mirror to be tested. The mirror has to rotate for other parts to be in the illuminating area. Each part of the mirror covered with the lens is separately tested using the two methods above. The software can synthesise the results to form the surface topography of the entire convex surface.

- **Work overhead:**

  In fact, the whole figuring process should be designed to minimise the work overhead so that the increased work efficiency reduces the manufacturing cost. A typical example of such a overhead would be the mirror handling for the testing. For the minimum overhead, the test set-up must be designed to allow the mirror to stay on the polishing machine all the time once the figuring begins. When a polishing run is completed and the lap is taken off, the set-up should allow immediate testing without further work on the machine. The active lap has the inherent tendency to the minimal overhead. For instance, it has no need to change the distribution pattern of the pitch facets and the major lap components such as the lap body.

- **Environmental factor:**

  The common problems faced with the large optics testing would be environmental variation during testing e.g. vibration and air turbulence in the optical path. All measures have to be made to ensure that those variations are minimised for testing. For instances, the polishing machine and the test setup might have to be vibration-isolated. The optics shop may be better if it is located in an underground basement. The optical path has to be insulated for rapid stabilisation of the air column. All thermal sources such as motors and cooling fans must not be in proximity to the test setup.

3.4 Initial System Design of Active Lap

3.4.1 Specification of The 85 cm Scaled Gemini Secondary Mirrors

In order to demonstrate the new philosophy of the active polishing, an instrumented active lap was intended to be built and used to make an approximately 1/3 scaled model of the f/7 hyperbolic secondary for the 8 m Gemini telescopes. Bingham [7] has come up with the full size design for the secondary. It has a clear diameter of 2.13 m with a radius of curvature at the vertex of 9582 mm and, of course, the blank would be larger. The height difference at the edge from a sphere which osculates at the vertex is 404 μm. Hence the scaled model would ideally utilise a 85 cm cervit blank that OSL has. It could be generated to a radius near 4191 mm and then aspherised by 202 μm with respect to a 4191 mm sphere. Alternatively, the desired aspheric profile could be directly NC-milled and then the instrumented lap is constantly used for the entire lapping and polishing processes. The scaled secondary can be mathematically expressed with the equation below [7].

$$Z = \frac{CS^2}{1 + \sqrt{1 - \epsilon C^2 S^2}} \tag{3.1}$$

where Z= depth of curve at radial distance S from centre of mirror in mm

C= reciprocal of radius of curvature at vertex=4791^{-1} in mm

ϵ= asphericity coefficient=-1.8639(dimensionless)

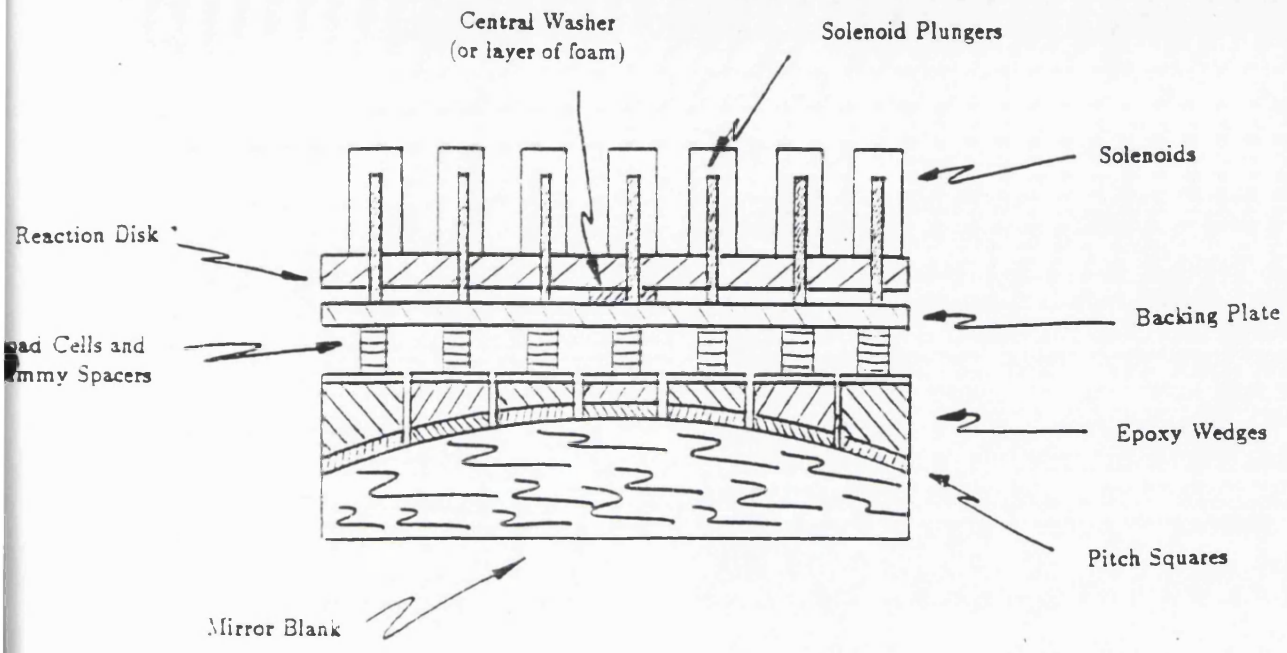

Figure 3.2: Schematic diagram of the initial design for the active lap.

3.4.2 Initial Design of Active Lap System

The instrumented lap could be built as follows. A schematic diagram of the lap is presented in Figure 3.2. The main mechanical elements comprise two flat, plane-parallel aluminium disks of about 1 M diameter. The upper disk is a *'reaction plate'* and the lower is a *'flexible-backing plate'* for the lap. They are attached together with a bolt through a central washer, leaving a gap elsewhere, of a few mm. A 2-dimensional array of solenoids, as force actuators, are mounted to the upper face of the reaction plate. The plungers pass down through clearance holes in the disk, pulling on the upper face of the flexible backing plate. About 16 solenoids in total are distributed in two rings. Energising the solenoids tends to bow the disks together. However, in practice, the force should not be sufficient to distort the disks, but strong enough to modulate the pressure distribution exerted onto the workpiece, and hence the polishing rate.

In this application, the solenoids must operate with extremely small strokes with the plungers almost bottomed. A force of several kgf per solenoid can readily be extracted. When fully energised, the dissipation would be about 10 watts each. The total dissipation with the servo working is expected to be about 100-200 watts. Most of this is dissipated well above the lap, expected to be smaller than the frictional

heat of polishing and hence would not affect the polishing conditions. If a null lens is permanently placed above the polishing machine for the test set-up, the heat dissipation during a polishing run can eventually warm up the lens, altering its surfaces. The testing must be followed with a time interval that allows the air and lens surface temperatures to be cooled down in this case. Or alternatively, an insulating plate can be placed under the lens during polishing.

Either the whole system, or the individual disks alone, can be FE-modelled so that an optimum thicknesses of the disks can be found. For example, the thickness of the flexible plate can be optimised to give a natural sag of about twice the desired mirror asphericity. An aluminium plate of 1m diameter and 8 mm thickness can self-sag by about 0.39 mm. The thickness is not critical but simply defines the flexibility of the plates, with which the actuator force propagates toward the mirror surface. The flexible plate serves as the low pass filter for the actuator forces. Altering the thickness changes the frequency characteristics of the force distribution exerted by the actuators. The use of an FE model for the whole system also allows us to analyse the force propagation in the flexible plate.

Polishing pressures that GP used are typically about 0.1-0.2 psi, leading to a total mass of about 80 kg for a 1 m lap. This helps to defines the thickness of the reaction plate to about 20 mm. If there is a margin with the manufactured lap, then the top of the lap can be loaded with lead weights to trim the total mass and the uniform pressure distribution. If the total weight of the lap is proved to be too heavy due to extra components such as actuator, force sensor, electronics, etc., the thicknesses of the two plates would have to be adjusted to reduce it. Alternatively, the system can be made with the concept of the Draper machine.

Below the flexible plate, there is another plate of 1 m in diameter and 0.5-2 mm in thickness. This is connected to the flexible plate by an array of spacer units on a slightly-decentred 100 mm pitch of about 70 in total. Some 20 of them are active force/pressure sensors to sample the pressure exerted on the workpiece and the rest of them are dummies. An important condition is that the active sensor must have very small compliance to prevent the returning pitch facets from impacting onto the edge of the mirror. At the same time, they must have the same compliance as the dummies. Otherwise, the sampled pressure would be over or under estimated

depending on which i.e. active or passive has the higher stiffness. If the active sensor and dummy are built with different mechanical design, the compliance of the active sensor can be determined experimentally, matching the dummies. If they remain in a same design, they naturally tend to have same compliance, within manufacturing tolerance. The active sensor would have to be designed to produce axial compliance with high lateral stiffness. In practice, the thin plate can stop the contamination of the polishing slurry to the force/pressure sensor and its related electronic components. However, it also contains the lateral polishing force, while disturbing the axial force distribution to an unknown extent. This must be solved for a sampled pressure distribution to be realistic.

The whole assembly, being plane-parallel, is of general applicability. It could be constructed in a modular manner so that all parts except for the plates would be re-used on a larger version. It also gives ease of accommodating any mirror sags with a given diameter. It could be achieved with an array of slightly-under 100 mm square reinforced epoxy wedges, which could either be cast using the generated mirror as a mould or be directly NC-milled as the mirror surface is generated. These wedges are attached to the underside of the thin plate, in line with the array of the force/pressure sensors and dummies above. They carry the pitch facets for polishing.

The whole lap is pushed and pulled over the workpiece using the existing push-pull arms of either the 8 ft machine or the 1 m polishing machine with abrasive slurry. Rocking of the lap as a whole, as it moves, could increase pressure on one side at the expense of the other side on the mirror. Furthermore, it completely degrades the pressure distribution sampled without encoding the rocking angle in real time. Thus it needs to be actively stabilised in real time using a quadrapod of actuators that provides compensating forces reacting against a horizontal plate attached to the push- pull arms of the machine near the central pivot. This scheme is presented in Figure 3.3, which brings the whole system to the regime of the Draper machine.

The lap motion, i.e. the motion of the arms, is derived from the 2 eccentrics which have very slightly different rates of rotation and stroke distances. This gives a pseudo-random element to the lap stroke, which is important for avoiding zones. The lap motion would be coarsely encoded in X, Y and θ with respect to the centre of the workpiece, while taking into account a constant rotation rate of the workpiece

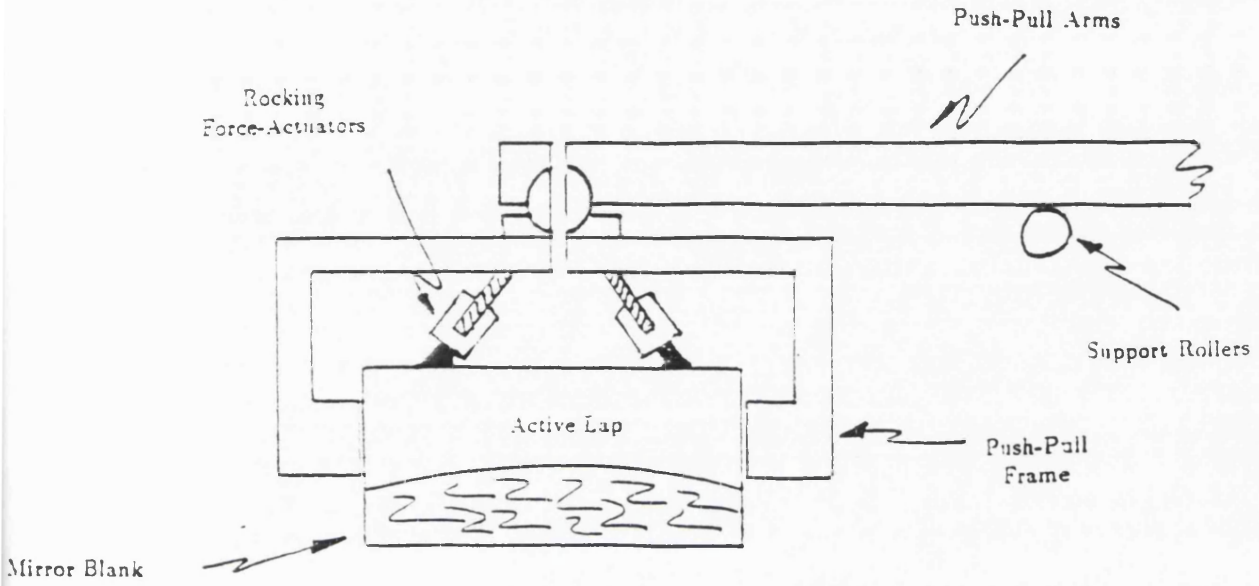

Figure 3.3: Global rocking actuators that transforms the active lap to the Draper machine action.

in polishing. This can provide a complete set of coordinates for each actuators, force/pressure sensors and dummies and pitch facets in real time. A force sensor is mounted at one end of each arm, preferably the one opposite to the eccentrics. Hence two force sensors in total can measure the total lateral polishing force i.e. friction which is expected to be directly related to total instant ablation rate.

There are light-weight electronics racks mounted to the upper side of the reaction disk. Figure 3.4 shows a schematic diagram of the electronics. The analogue signals from force/pressure sensors would be analogue-multiplexed onto one flash ADC and then serialised for transmission to a master intelligence, i.e. a 386/486 PC clone. A micro processor, a slave intelligence, needs to be on the lap, polling around the force/pressure sensors and the encoders, then serialising and sending them to the PC via a bi-directional communication link. The PC would perform coordinate transformations to keep track of which pitch facet, actuator and force/pressure sensor are over which part of the mirror. It converts the force readings in ADU to a physical unit, then construct and display a pressure map. It uses the encoder readings to derive a velocity map which, together with the pressure map, gives an instant ablation map. The PC compares the pressure map to a desired pressure distribution to

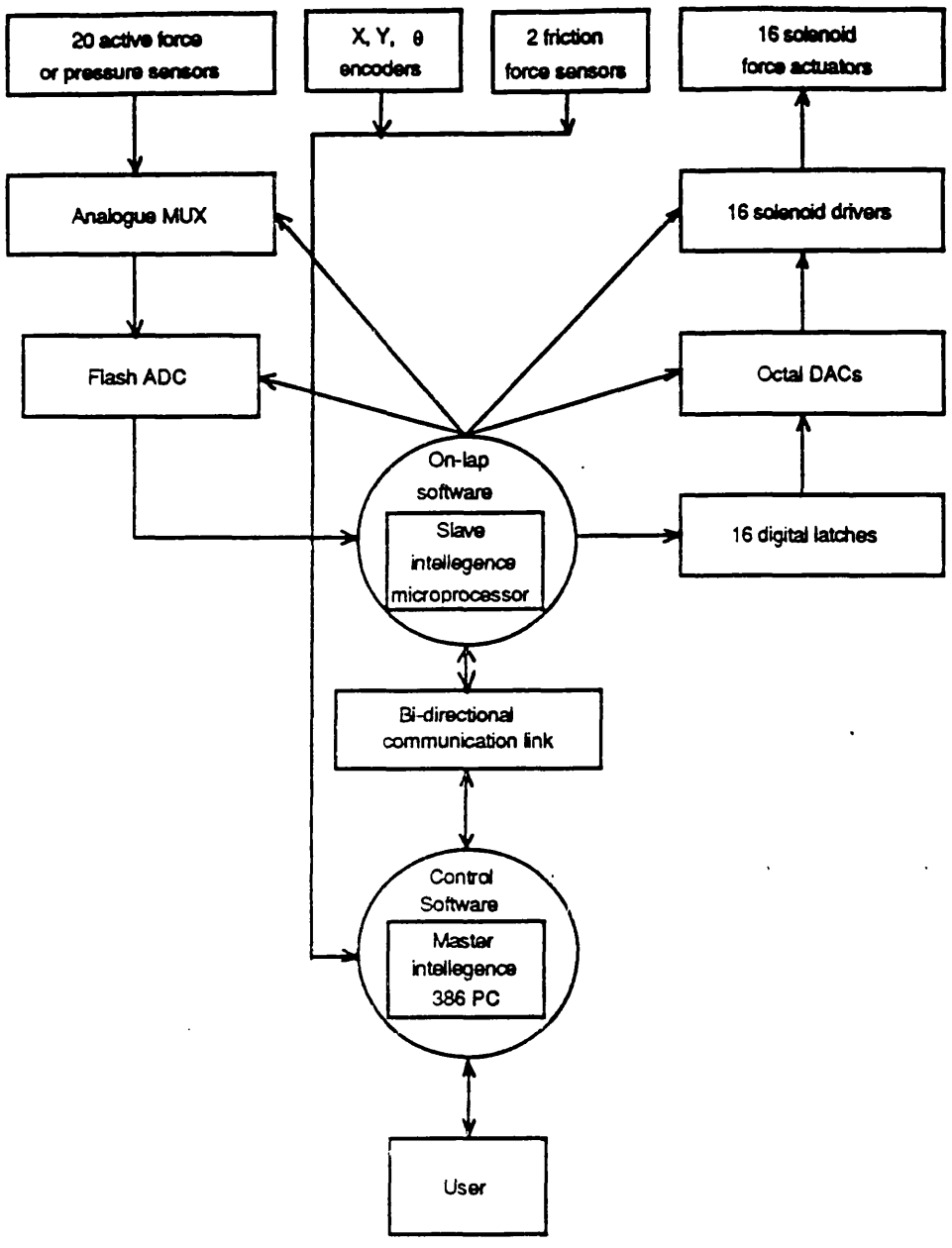

Figure 3.4: Schematic diagram of the active lap control electronics.

compute the compensating forces for the solenoids to exert. The serial force input data, transmitted from the PC, are sequentially update a digital latch associated with each solenoid. The data are then converted to analogue form by octal-DACs and used to control constant-current power drivers.

The lap, as usual, is free to rotate. Thus, the communication link, power supply and ground must be designed to cope with the lap rotation. A solution could be that the power supply and ground are taken through slip-rings and re-stabilised at the lap if necessary. If electrical noise becomes a problem, Ni-Cad cells would be

used instead to provide the low-level power for the analogue signal electronics. In particular, the lap rotation and stroke give the bi-directional communication link a special problem. The lap stroke forces the line of sight between a emitter and a receiver to form a cone. There would be two cones facing each other in operation. The bi-directional signals emitted from the sources can easily affect the receivers of the opposite pairs, becoming noise to each other. The difficulty is enhanced by combination with the lap rotation. Solutions for this problem depends largely on the types of communication link, which is subjected to further design in Chapter 6.

3.5 Discussion

• Advantages of the full size active polishing over other methods

The philosophy of the full-size active polishing developed here has a number of advantages over other methods currently under development elsewhere. They are summarised as below.

- inherent tendency to produce the surface with minimal zonal errors
- general applicability, specially to figuring convex secondary mirrors
- real-time numerical monitoring and control of the figuring process
- fast overall rate of polishing in removal rate
- highest convergence factor with close-loop process control and ablation algorithms
- minimal work overhead
- lowest pressure polishing possible, reducing possibility of producing print-through of the honeycomb substrates.

• Role of the full size active polishing in active-adaptive optics

In particular, recently, the intensive research in active-adaptive optics has been underway to correct low and medium spatial frequency wavefront errors for thin-meniscus mirrors in telescope operation. This gives a rise in importance of removing

high-frequency errors during the fabrication process. It means that the smoothness of the surface must be more emphasised in polishing than local surface figure. A large polishing tool, preferably full size, is more useful to tackle this. Thus the full-size active polishing with ability to sense polishing pressure provides a better solution than any other for the fabrication process for large highly aspheric telescope optics.

• Proposed experiments with the active polishing lap

Proposed experiments with the instrumented lap are as follows. While the instrumented lap is under construction, the 85 cm cervit blank OSL has would be generated and polished to the closest sphere to the desired convex hyperboloid using the methods OSL has now established. They are the computerised profile generation and the passive polishing with full size and sub-diameter tools. The mirror would continuously be supported by a passive pneumatic support system throughout the process. There would then be experiments on this mirror to quantify the ablation rate as a function of variables, such as the polishing pressure exerted by the lap and its sliding velocity. This can provide the essential ground-work for subsequent development of the active lap.

After the completion of the construction for the instrumented lap, it would be used to regain the sphere. The active lap would be pressed to ensure perfect contact between the pitch and the mirror. This would be monitored with the force/pressure sensors. The null condition i.e. uniform pressure can be achieved by a combination of loading the lap with weights and applying small bias forces to the solenoids. The software servo loop between solenoids and force/pressure sensors can be trimmed so that a specified force distribution in mirror coordinates can be applied by the moving lap. A key factor in this process is to allow for the overhang of the lap at the ends of the stroke.

There would then be a series of experiments using the active lap. The lap would move with the pressure distribution continuously adjusted by software control to introduce a known aberration such as coma into the spherical mirror. It should then be possible, in retrospect, to remove the aberration in a predictable manner. The ablation rate function would be kept updated and improved each time after a polishing run and testing cycle. The lap would then be used with fine abrasive to re-

work the mirror into the severe aspheric form of the model secondary. Periodically, the mirror would be roughly polished with Cerriumoxide to permit testing, followed by more abrasive work. When the figure is close to optimum, the lap would be striped of pitch and fresh-uncontaminated pitch squares with abrasive would be applied. After pressing, final polishing and figuring with Cerriumoxide can then proceed.

Chapter 4

Development of Active Elements

4.1 Introduction

Following the system design in the previous chapter, two questions are raised immediately.

- How can the polishing pressure be sensed ?
- How can the required pressure be applied ?

The questions are mainly concerned with *two active front-end elements* (i.e. force sensor and actuator) of feed-back control, that must be designed and optimised not in isolation but as integral parts of the active lap. This chapter describes the progress made to reach the answers.

Initially, it was intended to procure them if they were readily available in the market and fell in the required specifications and the budgetary limitation. However, it was later decided to develop customised force sensors and actuators with our own designs. The reasons are described later in this chapter.

To design them is the main subject of section 4.2 and 4.3. FE analysis played an important role in designing both the elements. Implementation of the designs by prototyping an active module is described in section 4.4, including various measurements for testing and optimisation. Section 4.5 summarises the implications of the development and evaluates the performance of the module. There are also some findings valuable for construction of the active lap.

4.2 Force Sensing Element

This section describes how the force transducer called the *'load cell'* is designed and optimised for the active polishing, including transducer survey and examination of various design options using FE analysis.

4.2.1 Design Philosophy

4.2.1.1 Basic Requirements

- **Geometry, size and mass**

  Unlike the traditional passive lap, it is relatively hard to make the active lap low in profile since it consists of more components than the passive one. Examples include force sensors and actuators, control electronics, etc. However, as the height increases, the lap becomes more unstable and would suffer greatly from an increasing rate of rocking when polishing. The rocking during polishing also tends to ablate the edge of the mirror preferentially, producing a turned down edge with respect to the required surface. In addition, the lap structure would be exposed to greater force parallelograms, giving rise to unnecessary shear components. These give an important condition that every component of the active lap should be as low in profile as possible. The lap thickness was aimed at approximately 10 cm maximum at the vertex of the convex mirror profile. This would give about 1 cm or less as the height of the ideal force sensor unless there were ways to use high profile force sensors for the active lap.

  The typical size of the pitch facet that the OSL optics shop would normally use for this type of mirror is $8cm \times 8cm$. If the force sensor were similar to that in size, it would then be possible to sense not only the force at a particular position on the mirror but the behaviour of a pitch facet under the force given to it. This leads to the size of about 8 cm in either diameter or length. The mirror blank is about 85 cm in diameter so that the full size lap can comfortably accommodate about 70 force sensors, allowing about 30% of the total area as marginal space. This does not leave much room for its mass.

Even 500 gm for each sensor would take 35 kg which is about 44% of the lap mass of 80 kg (see Section 3.4 for the lap mass). This was clearly unacceptable. It would be better if the force sensor is about 250 gm mass.

- **Range of force**

  Since about 70 force sensors would experience the lap weight of 80 kg, each force sensor would have the static load of about 1.1 kgf. However, there are various sources that can generate dynamic loads much greater than the static load. Examples include rocking and local contacts between the pitch facets of the lap and the mirror surface. The action of placing the lap on the mirror also tends to produce a shock load to some of the force sensors. This intuitively leads to a positive dynamic load of about 400% that must be within the measurable range. When the lap is overhung at the end of each stroke, some force sensors outside the mirror surface would experience a negative force which is a fraction of the positive dynamic force. Thus, the full dynamic range of measurement would be -0.5 to 4.4 kgf.

- **Response time and compliance**

  The force sensor should have the minimum compliance, perhaps much less than 100 μm. Firstly, this is to protect the mirror from the impact of pitch squares on its edge when returning from the end of previous strokes. As the compliance increases, the impact is more likely to happen and the impact energy becomes greater, thus resulting in damage at the edge of the mirror. This again contributes to producing the turned down edge.

  Secondly, the lower the compliance is, the faster response time and the higher the resonance frequency the force sensor would have. Using the mass of 250 gm, the force range of about 5 kgf and the assumed compliance of about 25 microns, the resonance frequency of about 2.8 KHz can be calculated with the equation below.

$$k = \frac{F}{D} \tag{4.1}$$

$$\omega_o = \sqrt{\frac{k}{M}} \tag{4.2}$$

$$\omega_u = \frac{\omega_o}{5} \tag{4.3}$$

where k = spring constant

F = force range

D = compliance

ω_o = resonance frequency

M = mass

and ω_u = useful frequency [36]

This leads to the useful frequency of about 560 Hz within which the force sensor is able to respond linearly [36]. This is well over the frequency of 10 Hz with the load of 5 kgf which is likely to be the worst case in force modulation by an actuator for the active polishing.

- **Impacts to and from other components and working environments**
  - The force sensor should be insensitive to change in operation conditions such as self heating, room temperature, magnetic field of force actuator, etc. Alternatively, it could be compensated for these effects
  - It should not suffer from significant hysteresis
  - It should be able to produce linearity in signalling axial force even under the presence of lateral and shear forces.
  - It should be well protected from overload, contamination of Cerriumoxide and water.
  - It should be considered for mass production for a larger active polisher of, perhaps, 2.5 m in diameter, requiring about 600 force transducers.
  - It should be bi-directional in force sensing.
- **Economics**

The budgetary limit does not allow more than about £100 for each force transducer on average. To reduce the unit cost is important not only for the first installation but for the maintenance of the active lap. One way of reducing the overall cost for force sensing is to decrease the number of active transducers, using dummy transducers that are mechanically the same with the active one in all aspects but not producing a real signal.

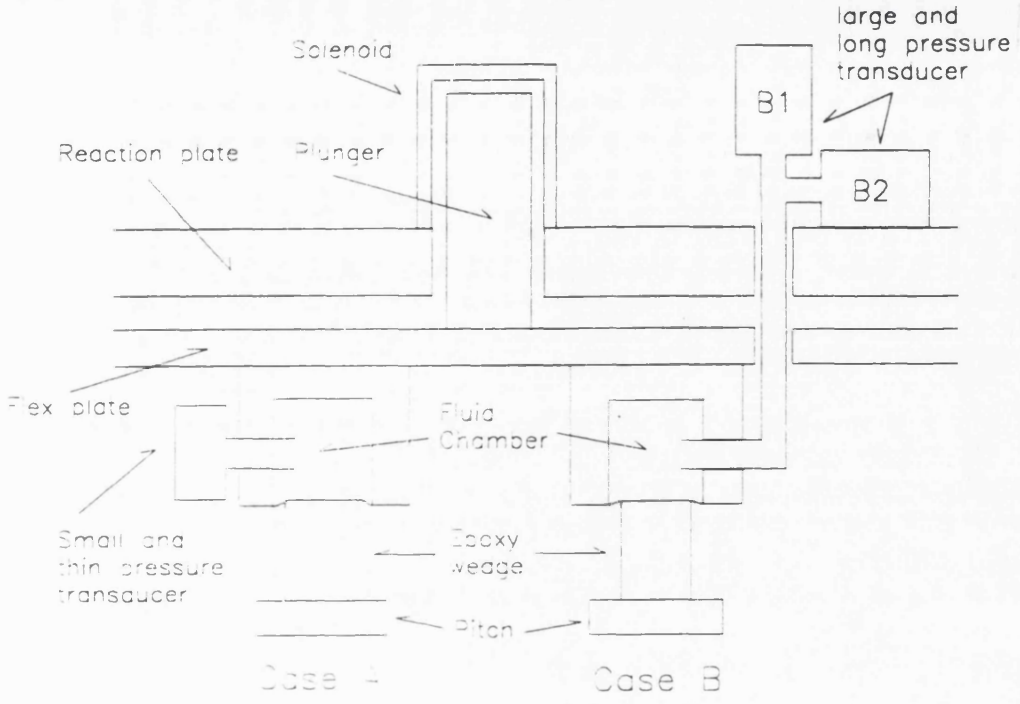

Figure 4.1: Two ways of using pressure transducers for the active lap

4.2.1.2 Transducer Survey

A number of transducer manufacturers were contacted [2] [20] [28] [33] [34] [39] [40] [65] [87] [104] [105] [108] and their products were compared. However, the survey showed that none of the existing force sensors can fully satisfy the requirements. Furthermore, in doing the survey, a question of what to measure arose. In general, there were two types of force sensor. One is the pressure transducer which is used for measuring pressure in fluids i.e. gas or liquid. The other is the load cell that is designed to sense force directly.

• Possible use of pressure transducer

The possible use of the pressure transducer is depicted in Figure 4.1. There would be a fluid chamber containing either air or water in between the epoxy wedge(or the thin shell) and the pressure transducer. The chamber could be a doughnut shaped rubber tube with the metal cylinder as enclosure. The pressure transducer would be plugged into it (case A in Figure 4.1) or a flexible pipe would be used to link the chamber and the transducer (case B in Figure 4.1). The former can be used if the transducer is small or low in profile whereas the latter would be suitable for the

larger or high in profile.

Advantages of pressure transducers:

The pressure transducer has many advantages in use.

- ability directly to sense the polishing pressure
- no damage caused by the off axis load
- freedom of choosing the place for accommodating the force sensor in the active lap (i.e. either on the reaction plate or on the flex plate)
- freedom of selecting geometry of the force sensor
- less expensive than the load cell

Disadvantages of pressure transducers:

Despite the advantage, the pressure transducer seems to have serious technical problems in use.

- The base pressure level should be high but the measuring range is very low i.e. 0.1-0.2 psi. This is to ensure the low compliance. The chamber might have to reach few hundreds psi and the transducer should be very heavy in duty and high in resolution. In addition, this model is normally expensive.
- If the transducer is not heavy duty enough, the fluid is free to move around inside the chamber. When the lap is overhung at the ends of each strokes, some pitch facets are partially contacted with the mirror surface. This gives localised force to the contact part of the chamber, pressing it harder than the non-contact part of the chamber. This can cause tilt of the pitch facet from the plain parallel geometry with the mirror surface, resulting in more abrasion at the edge of the mirror. This edge down effect cannot be fixed by any means.
- The volume of fluids such as air and water varies with temperature, thus altering the chamber pressure. This would requires frequent recalibrations or resupplies of the fluid for around 70 chambers. This could significantly reduce the efficiency of polishing work.

- If the water has to be used to fill the chamber, it must be boiled to remove soluble gas components prior to under water assembling the chamber and the transducer. The under water assembling is to make sure that no air bubbles enter into the chamber. Plugging the transducer into the chamber can easily be done for the active lap only if the transducer is small and water-proof.

  If it is long, the only way to mount the assembly onto the active lap would be to insert the transducers or the linkages through holes on the reaction and flex plates hanging in air. Then the under water assembling could be made. But in this case, they would take substantial area on the top surface of the reaction plate so there would be little space for force actuators. Another potential problem with water would be long term corrosion on the metal surface of the transducer which is in contact with it. However, the corrosion would not be a serious problem with stainless steel.

- Although there is no net change in fluid volume, there would be false pressure if the flexible tube linkage moves easily, thus altering slightly the volume inside it. This would be more serious if the chamber filling is water.

- Since the pressure transducer senses equal pressure inside the chamber, it would be impossible to monitor unequal force/pressure given to a pitch square when polishing. This means that there would be no way to know the unaveraged pressure distribution within a pitch square and also the spatial resolution of pressure sampling is low.

Choice of force sensor:

These support greatly the preference for the load cell. However, as seen from the survey, there are just a few flat line load cells and even they are of very much smaller diameter than the requirement. The way to use these miniature flat line load cells for the active lap is to attach them to common corners of the four pitch squares as seen in Figure 4.2. It would then be unavoidable for them to be exposed to a considerable amount of lateral and shear force as polishing is run. Unfortunately all the load cells surveyed have either a small load button/bar or load area in its centre. It is also warned that any off axis loads would substantially deviate the linearity and might cause damage to the load cell. Finally, these flat line load cells are particularly expensive i.e. £500-800 each which is much greater than the budgetary limit. Faced

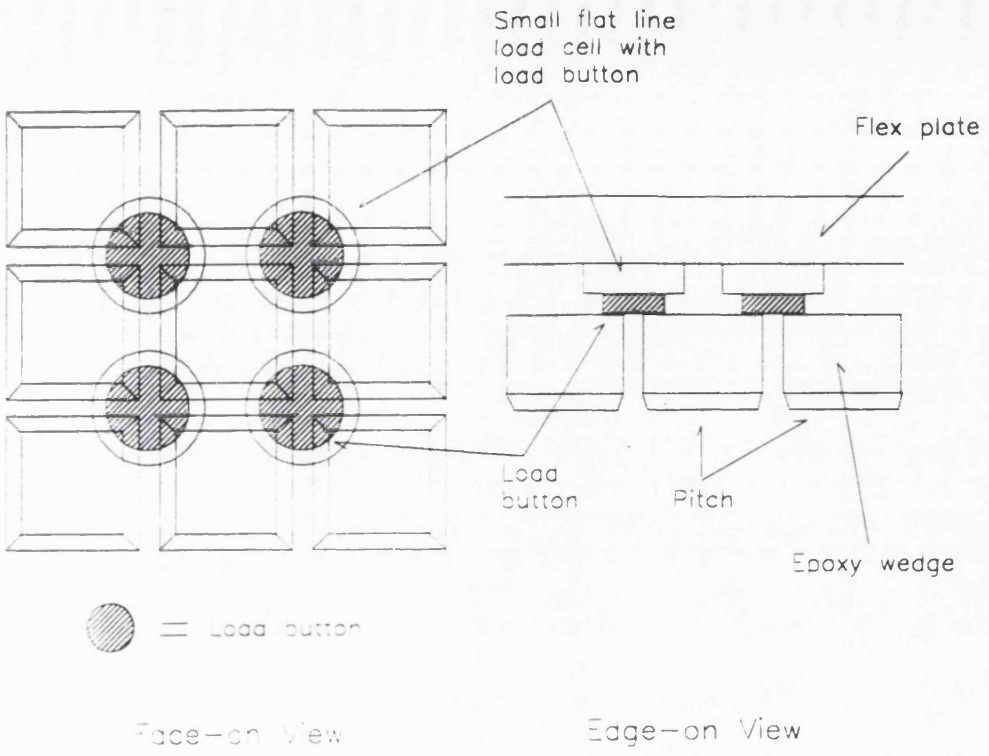

Figure 4.2: Use of the small flat line load cell

with these, the solution left was to develop a customised load cell that can fulfil the requirements.

4.2.1.3 Strain Gauge Selection

The development of the customised load cell starts with selection of strain gauge. There are two types of strain gauge widely used for tactile sensing.

• **Metal foil strain gauges**

The first are metal foil strain gauges such as RS stock 632-123 [91] and EA-XX-125AD [116]. Recently, they are commonly available with a large variety in resistance and size. The advantages are:

- robust and easy to handle when mounting, reducing manufacturing cost for the load cell.
- insensitive to the environment, such as temperature.

But they all suffer greatly from the low gauge factor which is typically about 2. The gauge factor is defined as the change in resistance corresponding to change in strain,

thus being unit-less but the higher value means higher sensitivity of the device to the strain. This implies that its sensitivity to the strain is low and therefore the span of the open circuit output voltage for the load range is very small, perhaps about less than 10 mV, which is closer to the background noise. The force sensors would work under electrically noisy environment due to active lap actuators, heavy industrial motors on the polishing machine, etc. Therefore it would require not only a good amplifier circuit but also a high resolution A/D converter. In order to push the open circuit output voltage up to the reliable level of a few hundreds milli-volts, the only way is to have high compliance of the structure, working at high strain level near the elastic limits of both the structure and the strain gauge.

• Semiconductor strain gauges

The second are semiconductor strain gauges made of either P or N type semiconductors. Examples include Entran ESU-025-1000 [33]. They have a number of disadvantages such as,

- little more expensive than the foil strain gauge, i.e. cost factor 1.2 (Hordesky, pp 113-127 [53]).
- fragile and easily broken while handling.
- more sensitive to environmental variables such as temperature, etc.
- small, i.e. less than 1 mm in length, so that they are difficult to mount precisely.

The advantages are that they are

- small, so that they can be used to measure highly localised strain.
- very high in gauge factor i.e. typically about 150. They can easily produce the open circuit output voltage of up to few hundreds milli volts so that even in some cases there is no need for amplification prior to A/D conversion. This can also ensure that the load cell works at low compliance and low level of strain far below the elastic limits of the structure and the strain gauge.

• Choice of strain gauge

Having considered these and the basic requirements, the semiconductor strain gauge

appeared to be more suitable for the load cell the active lap requires. Entran ESU-025-1000 was then chosen to be used since it was the cheapest off-the shelf item and reasonably high in resistance. Its gauge factor is 155, capable of producing the signal of about 233 mV with 300 μ strain when a half bridge is excited with 10 V. From the point of view for the open circuit output voltage, 233 mV with 300 $\mu strain$ is quite satisfactory. The strain is in fact 30% of the maximum useable strain (i.e. 1000 $\mu strain$) and 10% of its elastic limit (i.e. 3000 $\mu strain$) recommended by Entran.

The recommended wattage rating is 0-25 mW per gauge. Using its resistance of 1000Ω, the electric load was calculated as 5 mA and the excitation 5 V per gauge respectively. This gives the ideal excitation of 10 V for a half bridge load cell consisted of two strain gauges and two matched dummy resistors. (Note: In load cell terminology, the half bridge load cell means a bridge consisting of two active strain gauges and two dummy resisters.) Indeed, this was confirmed by the recommendation of Entran for the bridge excitation voltage.

4.2.1.4 Strain Elements

The strain gauge has to be mounted on the strain element where load i.e. stress causes strain through its structure. Numerous models for the strain element were considered but only some of them are discussed here just to show the progress toward the final model.

Vertical cylinder:

A cylindrical tube has been suggested as an example of how to use strain gauges to form a compression load cell [91]. The application of this for our load cell is depicted in Figure 4.3 . The compressive force to the cylinder can be regarded as the force given to the direction A, since the cylinder can be regarded as a bar. In this case, the same force would result in much less strain on the bar surface than given to the direction B. It seems likely that the necessary thickness to produce 300 to 400 μ strain under 5 kgf given to the direction A would be very thin so that it can be easily buckled when a substantial load, either axial or off-axial, is applied. For this reason, this model was not chosen.

Some other geometries:

Numerous geometries can be used if the strain gauge is allowed to be simply attached

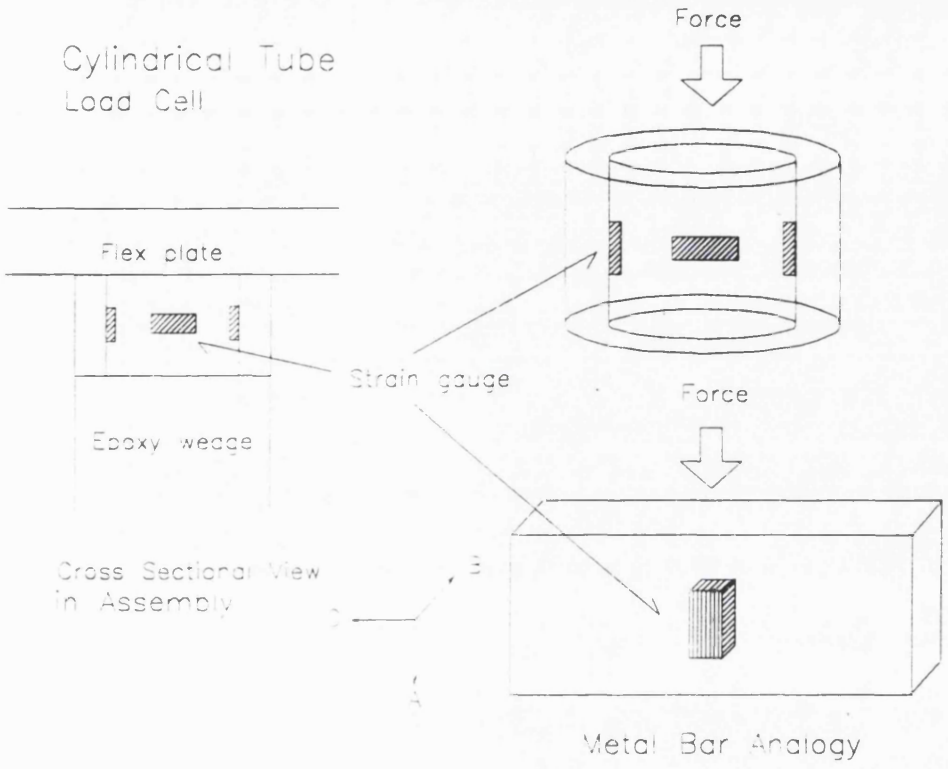

Figure 4.3: Cylindrical load cell and its bar analogy

at both its ends along the main axis to flexural structures. Some examples are shown in Figure 4.4. The strain gauges are fixed to the flexural structures at its both ends. When it is loaded, the deflection can give either tension or compression forces rather directly to the strain gauges but not via the fibre stress of the structure. Since this is to measure the load itself given to the strain gauges, the load-deflection relation of the flexural structure has to be carefully calculated to give the strain less than, perhaps, few microns to the strain gauge. The larger strain would be likely to cause buckling of the strain gauge. Entran suggested that it is suitable for measuring acceleration rather than the direct load [32]. For this reason, the models were not chosen.

Fixed diaphragm:

A load cell model using a metal diaphragm attached to the top surface of a fat cylindrical tube has been suggested [45]. The bottom face of the cylinder is covered with a thick metal plate, of which the centre is machined for slight depression. The diaphragm could be square or circular. The idea is to mount a strain gauge at the

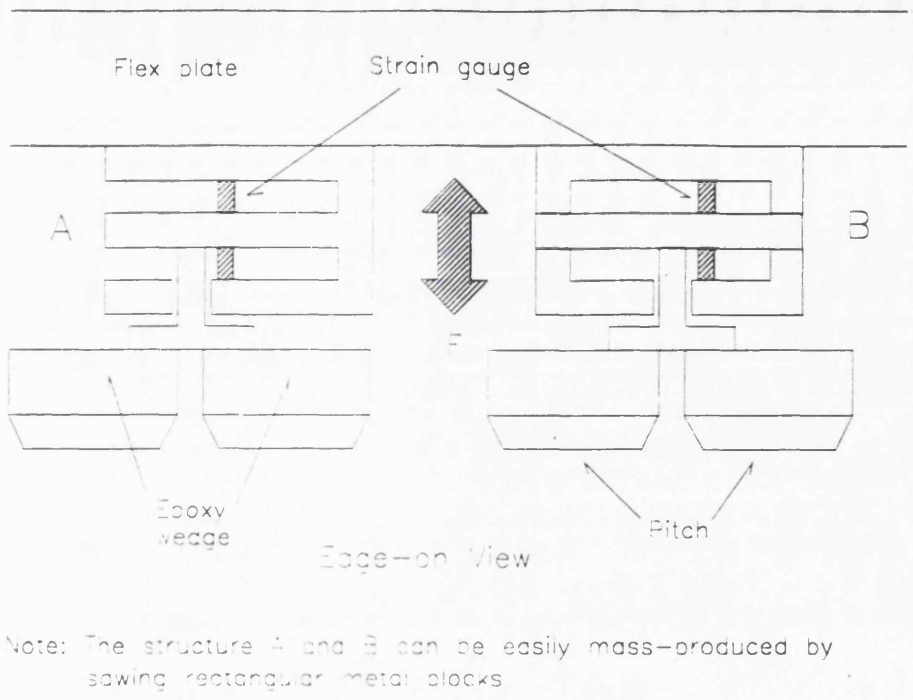

Figure 4.4: Two flexural structures for measuring direct load to strain gauge

centre of the diaphragm on its bottom surface. The load given to the top surface causes deflection of the diaphragm, producing tensile/compressive strain on the bottom surface and thus the strain gauge can alter its resistance responding to the fibre stress of the diaphragm. The overload protection is achieved by constraining the vertical deflection of the diaphragm with the height difference between the central depression and the surrounding high plateau in the thick bottom metal plate. However, it is intended to use the quarter bridge consisted of one strain gauge and three dummy resisters, of which the thermal susceptibility is suspected to be very large. The half bridge configuration cannot be used with this design since the centre of the top surface, where the second strain gauge should be placed, is already reserved for the load area. In addition, it uses a small load button where the axial load only is allowed to be applied. Thus it is not suitable for the active lap.

Although not actually used, this gave some useful ideas namely

- load is allowed to act at a right angle i.e. Z axis to the active axis i.e. X axis of the strain gauge, when placed in an XY plane.
- both ends of the strain element i.e. bar, diaphragm, etc. need to be firmly held by two rigid frames, one small and the other large in size.

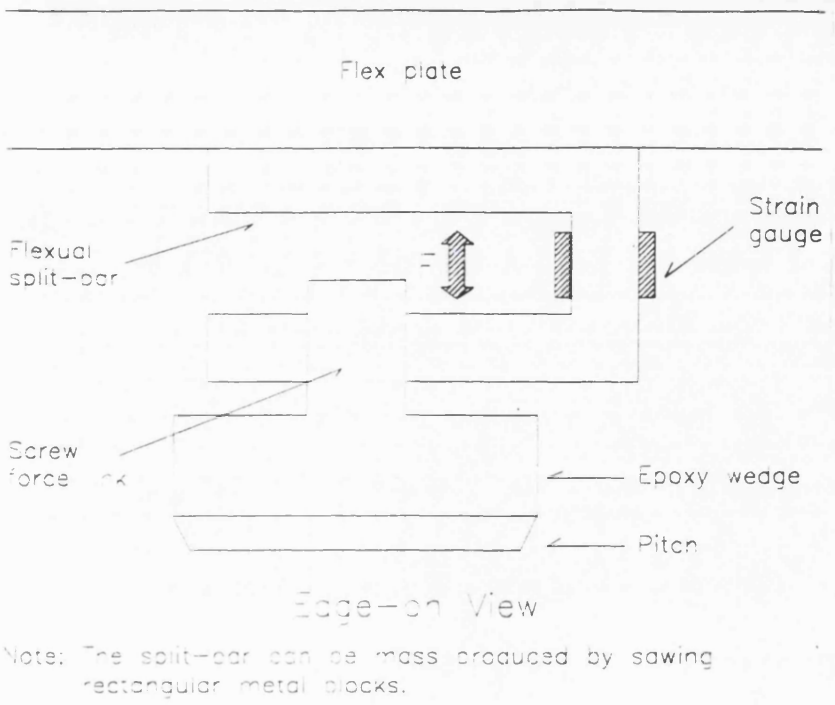

Figure 4.5: Flexural split-bar

- there should be a physical device for overload protection.

Flexural split-bar and cantilever:

A typical example of measuring the fibre stress can be found from the application of a metal bar of which one end is fixed on a rigid frame or wall and the other is free to move as seen in Figure 4.5. There are two ways of mounting strain gauges onto it.

The first is to glue them at the position A and B in Figure 4.5. When the load is applied, the gauge at the position A feels the compressive strain whereas one at the position B does the tensile strain. This can be called a flexural split-bar but it has the disadvantages given below.

- The strain gauges are pre-stressed by the weight of the flexural split-bar. This would permanently off-set the bridge balance but can be easily curable by calibration.

- There is no upgradability to compensate the off-axis force since its structure has no symmetry in XY plane.

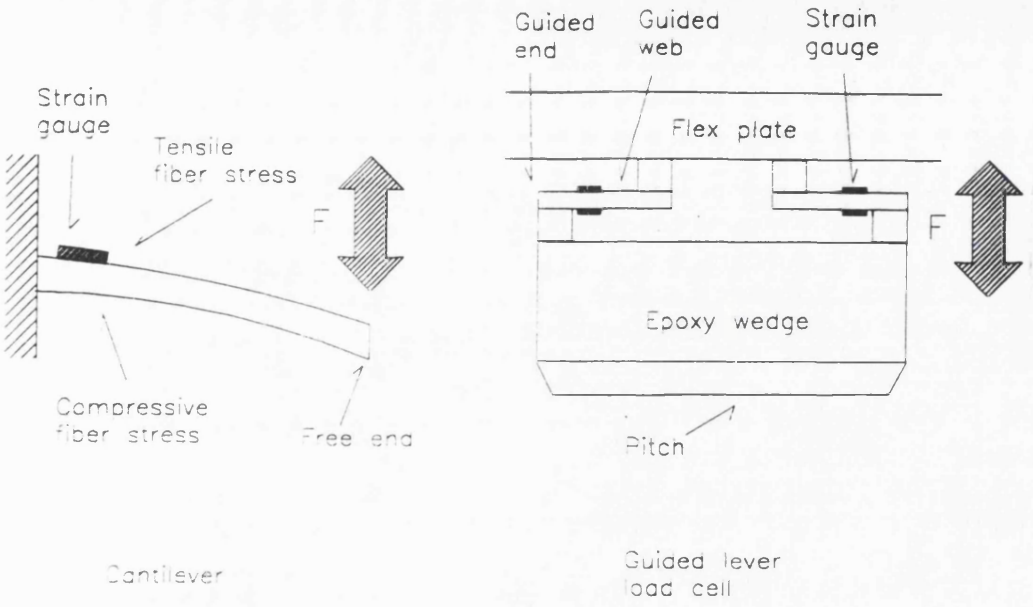

Figure 4.6: Cantilever and guided lever as strain element

The second called *'Cantilever'* is to mount them on the position C and D in Figure 4.6. When the load is applied vertically to one of its surfaces at the end, it can be deflected, producing the tensile strain on the surface of load and the compressive strain on the other surface. Then the two strain gauges would sense both the strains.

This Cantilever cannot be used directly for the active lap, unless the free end is fixed on a vertically movable guiding frame. This consideration leads to the final model described next.

Guided lever(i.e. Web):

The application of the guided lever i.e. web to the active lap is depicted in Figure 4.6. There are two frames of which the smaller is fixed to the flex plate and the larger is attached to the epoxy wedge, acting as the guiding frame. One strain gauge is mounted on the top and bottom surfaces of the webs respectably so that, when loaded, they can have opposite changes in resistance, corresponding to the tensile and compressive strains respectively. The structural symmetry in the XY plane can be achieved by placing 4 identical webs in the single structure as shown in Figure 4.6. This is to ensure that all in-plane components of the off-axis force give symmetrical effects to the stress-strain relation of the structure.

In fact, the same strategy of placing strain gauges can be applied to the circular

diaphragm which has also the symmetry in the XY plain. However, the main reason for not choosing it was that, firstly, the circular diaphragm has less strain than the web under the same load condition. Secondly, the inner and outer edges of the circular diaphragm do not have the same strain under the load condition whilst the web has. This means that the web is far easier to upgrade and to modify the dimensions for future optimisation of the load cell design. It also has more places to attach the strain gauges for the same strain to be experienced.

There are two possibilities to make the frames. One is the square frame of about $8cm \times 8cm$ in size with square cross-section and the other is the circular ring of about 8 cm in diameter with square cross-section. The later was chosen simply because the former requires higher machining cost and does not have circular symmetry in the XY plane. Because of the same radius of the ring frame, the same force always generates the same magnitude of torque any where on the ring but not every where on the square frame.

4.2.2 Structural Analysis and Design

4.2.2.1 Structural Analysis

As shown previously, the chosen load cell design consists of the two concentric rings and four webs and its size is around 8 cm in diameter. The precise dimensions for the rings can be determined based on the dimension of the web i.e. length, width and thickness. They are also affected by the manufacturing quality of the web since it affects the stress-strain relation of the web. Using ANSYS 4.4^{+}, FE analysis was carried out on numerous web designs with different dimensions and boundary conditions. The results of FE analysis were double checked with the solutions of the case equations for the bar structure.

• Choice of material

The FE analysis started with a bar of $2cm \times 1cm \times 0.1cm$. Stainless steel was regarded as suitable material. Though it is inferior to aluminium in terms of power dissipation in $watt/in^2$ [45], it still has many advantages over aluminium. It has a Young's modulus of about 215 GPa which is almost 3 times as much as that of aluminium i.e. about 70 GPa. Its thermal expansion coefficient is about $16PPM/°C$ which is

Case Number	ANSYS Data File *.DAT	Web Length mm	Web Width mm	Web Thickness mm	Load lbf	Stress Giga dyne/cm^2	Strain μ strain	Axial Sag mm
1	LO6345A	20	10	0.1	4	0.78	363.3	0.083
2	PLBMS1	20	10	0.1	4	0.86	400.1	0.062
3	PLBMS2	10	5	0.1	4	0.86	400.1	0.015
4	LO6345G	10	5	0.1	4	0.72	334.9	0.023
5	REBEM	10	5	0.1	4	0.76	353.5	0.014

Note: The calculated stress and strain are for the location of about 0.1 web length. The case 1 and 4 are the web of rounded edge to be fit with the supporting rings. The case 2 and 3 are the plain webs whilst the case 5 allows the rounded junction between the web and the supporting rings produced when macnining with a tool of finite thickness.

Table 4.1: The results of FE static analysis

smaller than aluminium's $23PPM/°C$ [45]. Among many variants of stainless steel, it has been reported that 314 and 600 series do not show good performance but 304 does with ESU-025- 1000 [32]. Thus, stainless steel 304 was chosen to be used.

• Results of FE analysis

Table 4.1 includes the results of only five among numerous web designs. The entire load cell structure was modelled and FE-analysed in cases 1 and 4, while the web only was FE-analysed in cases 2, 3 and 5. Specifically, cases 2 and 3 deal with the straight web, but the web of case 5 includes the rounded junctions between the web and the inner and outer rings, which is unavoidable due to the finite width of the machining tool. Figure B.1 B.2 B.3 B.4 and B.5 in Appendix B.1 are intended to show the fibre stress distributions and the deflections of the 5 web models. Figure B.6 in Appendix B.1 shows those of a notched web for comparison. The results of the ANSYS static analysis on the web models were compared with the solutions of the case equations. It was found that they agree well with each other within the accuracy of 10%. The method of the structural analysis using the case equations are also described in Appendix B.1.

• Some conclusions of FE analysis

Some conclusions drawn from the analysis are presented as follows.

- **Dimension of the web:**

In fact, the starting web model of $2cm \times 1cm \times 0.1cm$ produces the same stress distribution with the web of $1cm \times 0.5cm \times 0.1cm$ under the same load condition but gives an unacceptable level of compliance. It also requires a smaller inner ring of 3.4 cm in its outer diameter, giving only 0.4 as the ratio of the outer diameter of the inner ring to 8.6 cm i.e. that of the outer ring. Intuitively it is thought that the inner ring ideally needs to be around 2/3 of the outer ring to make the pitch facet mechanically stable against tilt when falling off at the edge of the mirror.

In this sense, the web is ideal with the dimension of $1cm \times 0.5cm \times 0.1cm$. It gives acceptable deflection and requires 5.4 cm as the outer diameter of the inner ring, thus making the ratio of 0.63 which is near to 2/3.

- **Location of the strain gauge on the web:**

  The maximum fibre stress appears at both ends of the web. However, the ideal location for the strain gauge is 1 mm apart from the ends, where the strain is 20% less than the maximum but still quite enough to produce the right amount of signal. The location provides enough space for the glue to be evenly spread over the strain gauge when mounted. If one end of the strain gauge is in contact with the wall of the ring it helps to form uneven thickness of the glue, influencing the strain gauge performance under stress.

- **Effects of notching the web:**

  It is found that the notched web gives greater strain than the non-notched web under the same amount of load. This is not helpful in practice. The plain web has already enough strain to give the right amount of signals and the notching removes the possibility of making various bridge configurations within the web which is still to be determined later.

- **Effects of rounded junction between the web and the ring:**

  The rounded junction caused by the finite thickness of the smallest NC cutter does not have significant effects on the stress-strain relation of the web. It can be explained by the fact that the fibre stress is linearly proportional to the width of the web and to the inverse cube of the thickness. Thus the strain

increases much less than about 10% of that of the ideal web which is less than the error involved in FE analysis with different elements.

- **Effects of the ring and the bottom plate:**

  The FE analysis with and without the rings and the bottom plate shows no noticeable effect on the stress distribution of the web.

- **FE frequency analysis:**

  Using the equation 4.1, the resonance frequency of the load cell is calculated to be about 6181 Hz, leading to the useful frequency of around 1236 Hz. This means that the load cell is able to respond linearly to the entire dynamic range within about 0.81 msec. It takes less than 1% of the intended pressure modulation time of 100 msec.

  If the epoxy wedge and the pitch facet are attached to the load cell, then the frequency decreases accordingly, since it contributes to increase of the movable mass. This gives an idea that the load cell needs to be separated from the epoxy wedge and the pitch facet in order to prevent the decrease of the response frequency. It is implemented by the Carbon fibre skin described in the next chapter.

4.2.2.2 Design and Considerations for Prototyping

The manufacturing design for prototyping the load cell is presented in Figure 4.7. Table 4.2 shows the operational characteristics of the load cell and compares them with those of Entran's ELF-1000 miniature flat line load cell.

In preparing the design, some more considerations were made.

Overloading and underloding protections:

Firstly, in order to protect the load cell from damage caused by overloading, there must be a physical overload protector. One way of doing this is to make the two circular frames with different heights. A simpler way is to have six metal shims of same thickness, three for the top surface of the inner ring and the other three for the bottom surface of the outer ring. The inner ring would be bolted to the flex plate with the three shims sandwiched in between them. The outer ring would also have the same way to hold a metal plate attached to the epoxy wedge.

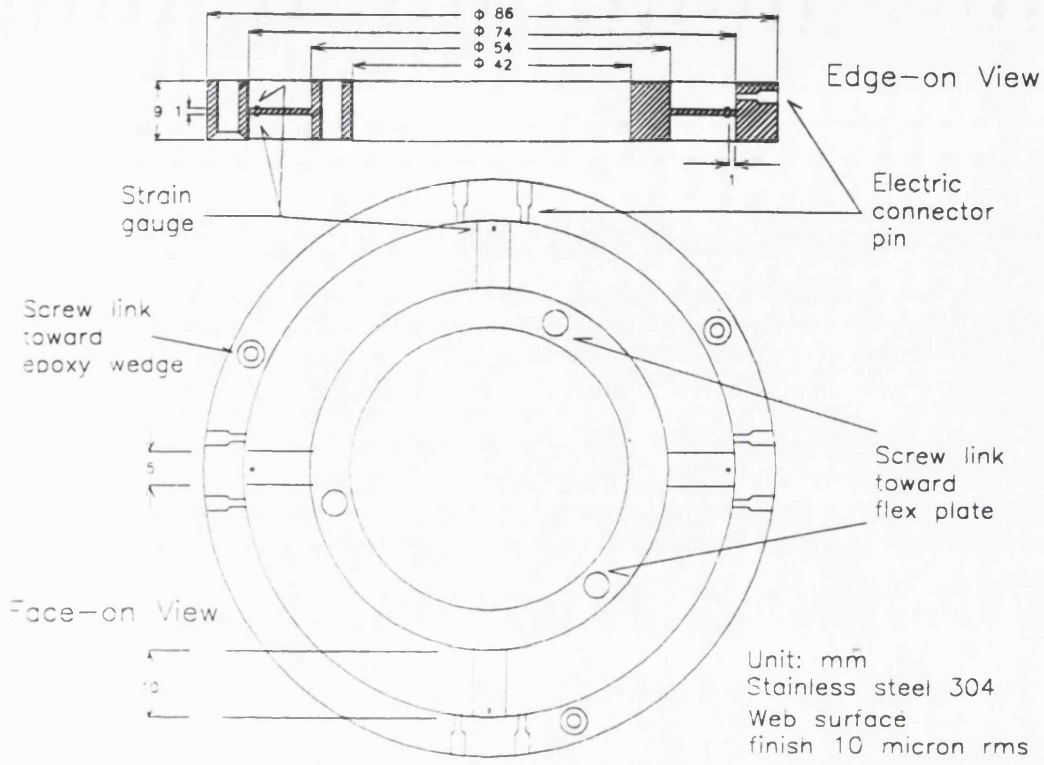

Figure 4.7: The manufacturing design for prototype load cell

Load Cell Model	Our Load Cell	Entran ELF-1000-10
Shape	Flat Concentric Rings linked with 4 webs	Flat Circular Disk
Dimension	86 mm outer diameter 9 mm thickness	25.4 mm outer diameter 3.81 mm thickness
Sensitivity	70.3 mV/lbf	25 mV/lbf
Load Range	16 lbf	10 lbf
Over Load Range	48 lbf (300 %)	25 lbf
Useful Frequency	0-1236 Hz	0-500 Hz
Excitation	10 V DC	15 V DC

Table 4.2: The comparison of the designed load cell to the ELF-1000 model

Since the recommended maximum strain is 1000 $\mu strains$ and the load of 4 lbf on each web gives about 363 $\mu strains$, it is acceptable to allow 11 lbf for each web as recommended maximum load. The deflection with this load was calculated as about 47 μm that serves as the thickness of the shim. Punching a thin metal sheet of about 50 μm in thickness would be the easiest way for mass producing them. About 10-20% tolerance for the shim thickness can be allowed. One potential problem can arise from the plates to which both sides of the load cell are mounted. Large

plates are not exactly flat. If the plate surface is too uneven, then some 50 micron shims have no effect, resulting in virtually dead load cells. This must be carefully investigated when installing the manufactured load cells to the main structure of the active lap. Underloading is unlikely to happen in any events of polishing so that there is no need to make a physical device to prevent it.

Surface finish for load cell structure:
Secondly, the surface finish for rings should be better than 20 μm rms. This is to secure the shim from deformation when screwed in on the ring surfaces. In particular, the webs should have the surface finish better than 10 μm rms for the strain gauges to be mounted ideally and to operate.

Methods of manufacturing:
Thirdly, if there is a difference in thermal expansion between the web and ring materials, it can certainly upset the load cell behaviour in operation. This means that the rings and webs should be made from the same material. If the load cell is assembled from separate webs and rings screwed together, there might be microscopic bows in the webs, permanently altering the stress-strain relation of the web from that analysed. The implication is that it would be better if the load cell is machined from a single piece of slice. This is very easy with NC milling and removes the need for precision assembling. However, machining the load cell structure was found to be rather costly. An alternative manufacturing process would be to laser-cut all components of the load cells i.e. webs, rings, etc. and to assemble them later. Modern laser-cutting can provide extremely good smoothness to the cutting surface with the minimum structural deformation in process. This would reduce substantially the magnitude of the microscopic bow within the load cell structure when assembled.

4.3 Force Actuator

4.3.1 Background

The force actuator is another active element working in collaboration with the load cell at the front end of the active lap. It is this element that actually modulates the pressure distribution as the lap moves across mirror surface.

When the basic concept of the full size active lap emerged in late 1989, use of a solenoid type actuator was initially suggested but with no technical details in the specification [112]. During 1990, two other types of actuators appeared to be of interest so that all the three types of actuator were subjected to a detailed comparison study in many respects. In early 1991, the design of actuator including the spring unit was finalised. This section describes its progress in detail.

4.3.2 Design Philosophy

Selection of actuator type would cause a large impact on designing the control electronics and system mechanics, since their design principles, operation environments and geometries differ from each other. The items listed below are the basic requirements to start up with.

4.3.2.1 Basic Requirements

- **Range of force**

  Since the weight of the instrumental lap would be about 80 kg and around 30 actuators are likely to be used, each actuator should be able to exert at least $\pm 2.7 kgf$. Thus $\pm 4 kgf$ is thought to be reasonable force.

- **Operation speed**

  The 1 m polishing machine rotates 1 revolution in 27 seconds. This gives a linear velocity of about 9.9 cm/sec at the radius of 42.5 cm of the 85 cm diameter mirror blank. It is intended to have the lap stroke of about 15 cm in 1 second. When combined, the two velocity components yield about 18 cm/sec as the maximum relative velocity between the lap and mirror. The force positioning accuracy should be within 1 cm or better for a cycle of force update. Ideally, then the force modulation should be made within about 55 msec i.e.18 Hz. However, since it is anticipated to exert half the total force range at a time on average, it is reasonable to expect the frequency of about 10 Hz for modulation of pressure distribution across the mirror surface. This of course is based on the assumption of the minimum level of the control overhead.

- **Impacts on other components**

  Several factors that can impact on other components and system performance, namely

  - stability in operation i.e. violent crashing, high frequency vibration noise, etc.
  - thermal dissipation
  - electro-magnetic field effect
  - direction of actuator movement
  - controllability

  These are discussed in the following subsection.

- **Mass and volume budgets**

  Once a type of actuator is chosen and the active lap is constructed, it cannot easily be replaced to control the total mass of the lap. However, there might be some cases where it is required to control over 50% of the total mass of the lap. Therefore the total mass of the actuators should not exceed about 25% of the lap mass, leaving more controllability for mass to the reaction and flex plates. This gives about 0.7 kg for the mass of the actuator.

  It is considered that the thinner the device through which the force is conveyed from the reaction plate to the flex plate, the more accurate the positioning of the force is achieved and the less coupling the active modules have. It is also to be short to lower the centre of mass of the lap. The height of the actuator is better to be about half of its width to lower the centre of mass for the lap. About 30 actuators would occupy the top face of the reaction plate so that each actuator is given about 189 cm^2 i.e. 15.5 cm in diameter, assuming that the actuator is cylindrical. This defines about $15cm \times 15cm \times 7.5cm$ as the volume requirement for each actuator.

- **Economics**

  It was considered that around £100 per unit, is within the budgetary limit. The actuators must be constructed in modular manner with standard units

so that they can be easily maintained and reused in a larger version of the active lap, when needed. These can reduce the construction cost for an active polisher for secondary mirrors of, perhaps, 2.5 m in diameter by a considerable amount.

4.3.2.2 Solenoid Actuator

The use of solenoids has long been considered since the first grant proposal for the active polishing lap was submitted [112]. The solenoid actuators have also been reported to be successfully used in real polishing work [66]. This led to exploring the solenoid in depth.

A number of solenoid manufacturers were surveyed. The survey showed, in general, that

- almost all the solenoids commercially available in market act in one direction i.e. push or pull
- there are special types of the solenoid which can move in bi-polar mode but very expensive
- some of the solenoids satisfy and few are indeed well over the some basic requirements such as the force range, the operational speed ,mass and volume budgets.

• Use of solenoid for the active lap

The starting point for the study was how to use the solenoid for the active lap, assuming a standard *pulling* one is used. The solenoid would be bolted on the top face of the reaction plate and the plunger would be attached to the flex plate via a hole in the reaction plate. When energised, the plunger is pulled up, resulting in attraction between the two plates. To extract adequate force with solenoids of suitable size and mass means that they have to be operated nearly bottomed i.e. with the plunger deep inside the solenoid within 0.5-1.0 mm of the end of its travel.

Unless the pull and push models are mixed in use, all the solenoids would act in the same direction. Moreover, the active lap is self-weighted so that there is no fixed point against which force is reacted against and thereby absolute force is controlled.

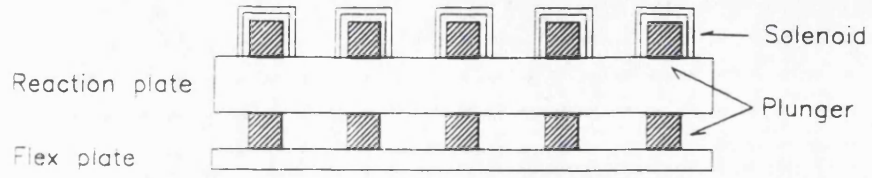

Figure 4.8: Solenoid as linking device of the two plates

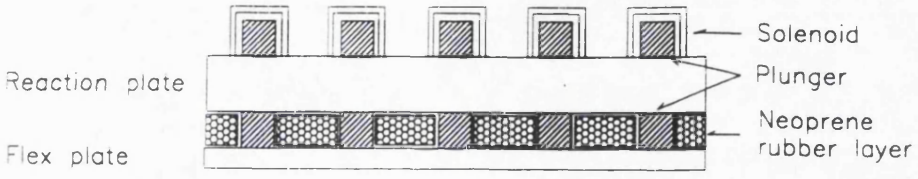

Figure 4.9: Neoprene rubber as linking device

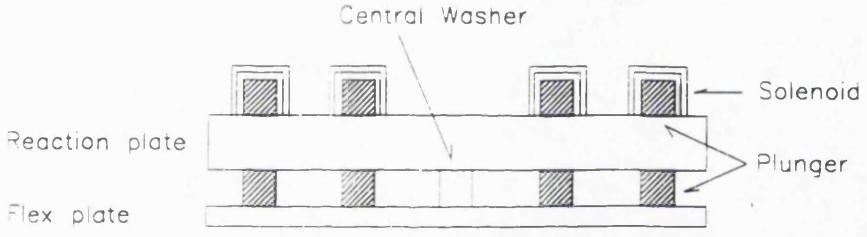

Figure 4.10: Central washer as linking device

It could then be possible that the net gain in pressure distribution is just a small fraction of what the solenoid can exert, if nothing, against which relative force is reacted, exists. For example, in an extreme case, energising all the solenoids with the same amount of current would not vary the existing pressure distribution at all.

Three possibilities are explored.

Solenoids as a linking device between the reaction and flex plates:
Firstly, an array of the solenoids only would be used to link the two plates with *nothing else*, as shown in the Figure 4.8. But this configuration would rather suffer from the strong lateral force in real polishing. The lateral force could be a source of perturbation of which the vector changes continuously as the lap moves on. The effect of the perturbation would be superimposed to the inherent instability of the solenoid, causing further complexity in control.

In this case, the net force gain is only the difference of the forces that the solenoids exert at a time, no matter how much they are. In order to maximise the net gain

across the mirror surface, either difference force solenoids are used or the solenoids at one end (i.e. near edge or centre remain deactivated while those at the opposite end exert suitable force). However, to use the different force models means that current scaling for each solenoids differ, resulting in additional complexity in the control system.

Uniform layer as a linking device between the reaction and flex plates: Secondly, a uniform layer of a compliant medium such as neoprene rubber could be used to fill the entire gap, holding the two plates as shown in Figure 4.9. Then each solenoid would squeeze the surrounded rubber when energised, reacting against the rest of the rubber. This could reduce the effect of the lateral force on the solenoids and ,therefore, the source of perturbation in strength but does not remove it completely. The problem of the net force gain still remains unsolved. Moreover, there are some more difficulties as follows;

- The force coupling between the solenoids is relatively strong so that force exerted by one solenoid can easily affect others.
- The solenoids have to overcome the internal strength of the rubber to reach a desired level of force, thus losing some of the force they exert. Because of the non uniform spring constants of most rubber layers, the amount of force that each solenoids loses varies, so that force/current scaling for each solenoid differs.
- Normally the rubber layer would work in one direction i.e. either in compression or in tension. But this can be managed with a precompressed layer.
- If part of the plunger in the gap is enclosed with the rubber, then it could slightly reduce the force to current ratio.

Central washer as a linking device between the reaction and flex plate: Thirdly, a central washer made of metal would be placed and bolted in between the two plates (Figure 4.10). The way that the solenoids are used is the same as the first idea. Unlike the two ways discussed above, this would provide a rigid platform against which all the relative force is exerted. The net force gain relative to the washer can be achieved to maximum level. It would resist against the lateral force

much better than the two others. This would give rise to reducing the perturbation. Since there is no medium surrounding the solenoids, no environments to change the solenoid characteristics would exist, as the force coupling between the solenoids would be relatively small. Thus, the use of the central washer would provide not only the rigid platform but less control overhead. From the above points of views, it was decided to use the central washer for the active lap.

• Problems with solenoid instability

The most fundamental problem with solenoid is its inherent instability, caused by the violent non-linearity of response when used almost bottomed to have enough force with relatively low current. For instance, a small external perturbation could cause the reaction plate to tip very slightly towards the flex plate on one side. The plunger on that side would be closer to the bottom of the solenoid and thus be provided with a very enlarged force. The solenoids on the opposite side would experience less force. If the servo system does not have a very fast time response, the two plates would simply clamp together on the near side until the next control cycle starts. It would then be impossible to modulate the force distribution during that time. There would always be a very strong positive feedback which the servo would have continuously to fight when a control cycle starts, even for an applied static force distribution.

• Potential solutions to this instability

There might be two solutions for this problem. One might be to use another type of actuator that is fully described in the next subsection. The other solution might be to use a pair of push-pull solenoids in adjacent places. The pair of solenoids would be bolted as close as possible so that any disturbances causing the pull solenoid to be clamped would also result in repulsion by the push solenoid. Thus any disturbances would be compensated by the pair. If they were equally energised, then there would be no net force gain. This could be solved by turning off one solenoid when the other is needed. For example, when pushing is needed to start a control cycle, the solenoid for pulling can be switched off. Immediately after the energization for the pull one is completed, the push one can be restored to the previous level of force and then the pair can wait for a new control cycle. An advantage of this is that the operation is inherently a bi-polar mode. However, this would double the actuator cost, making it comparable to the bi-polar solenoid.

• Few other problems with solenoid

There are few other minor problems. It has been well known that the solenoid is rather mechanically noisy in operation. It could produce high frequency vibration by which the load cell can fail to produce the right signal. The electromagnetic field of the solenoid could also affect the strain gauge of the load cell. Thermal dissipation of the solenoid would be a minor problem unless a significant amount of heat is transferred through the plunger to the load cell. It is quite likely that the heat would dissipate well above the reaction plate, with the ambient temperature controlled within a few degree in the optics shop.

• Proposed control system for solenoid actuators

In order to control about 30 solenoids, the control electronics would require a memory buffer, a digitally addressable 3 ways switch, three latched Octal DACs and 30 solenoid drivers. A control PC would provide control inputs consisted of addresses to specify solenoids and numerical values for equivalent currents. They are collected by the memory buffer. They are then serialised and down loaded through the switch to the Octal DACs all at once when the memory buffer is filled. A control input would be 14 bits i.e. 3 bits for the switch, 3 bits for the Octal DACs and 8 bits for the current scaling. Thus the buffer memory needs to be only about 420 bits, i.e. 52.5 bytes for 30 solenoids. With the digital control inputs downloaded, the Octal DACs would be able to rapidly distribute 30 analogue signals to the 30 solenoid drivers which scale the currents accordingly. The current levels once achieved would remain unchanged i.e. latched until the next control inputs are fed into.

• Disadvantage with the proposed control system

One potential disadvantage of this control system is that the solenoids might suffer from cross talk between the solenoid drivers and any other types of noise that can influence the current scaling. It is rather difficult to make noise immune analogue circuits when working in an noisy environment as the active lap does. Although Korhonen and Lappalainen [66] have pointed out that the solenoid can be used with force accuracy of 1% but only if proper calibration is made, it is doubtful if it can be applied to the active lap. Since the active lap is self-weighted, it would have more movements, such as XY movements, rotation and rocking, than that of their linear lap so that much more noise would be introduced to the control circuit. Together with a 2 dimensional array of 25 solenoids which is 4 times as many as their number,

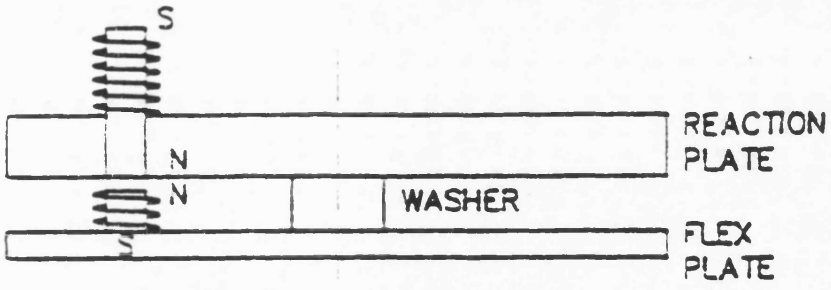

Figure 4.11: Use of the electro-magnetic coupling actuator

it would be much more difficult to achieve low noise level for the accuracy of 1% in real polishing even if static calibration guarantees the 1% accuracy. It would be nice if there could be found an actuator-control system with better noise immunity for the polishing environment.

• **Conclusion**

For the reasons described so far, it was decided not to use the solenoid actuator for the active lap.

4.3.2.3 Electromagnetic Coupling Actuator

One extreme method of utilising electromagnetic force rather directly for the active lap is to use either permanent magnets or electromagnets instead of the metal plungers on the flex plate. Examples of this are shown in Figure 4.11. Cylindrical metal rods would be attached underneath the reaction plate and naked cooper wire would be tightly wound around them, forming electromagnets at one side. There would be permanent (or electro) magnets with same size, geometry and magnetic characteristics at same positions on the flex plate i.e. opposite side. The gap between them would be about 1 mm. Assuming that the permanent magnet is used on the flex plate, when the electromagnet is energised, induced magnetic field is formed and causes either repulsion or attraction, depending on the direction of the current supplied to the coil.

• **Advantages of the electro-magnetic coupling actuator**

- One advantage seen immediately is that its operation is inherently bi-polar

and can easily switched to uni-polar operation. It is a matter of changing or maintaining the direction of current in the coil.

- The other advantage is its rapid response time in operation. In unipolar mode, the current scaling can be achieved by equal amounts of energization for the two electromagnets involved, not one magnet only. The time needed to scale up and down for the force level could be half of the time required for a single magnet (i.e. solenoid). When a relatively large amount of force swing from attraction to repulsion or vice versa is needed, the corresponding current scaling could be again halved with bipolarity, compared to unipolarity of the current supplied. This could improve the response time substantially. Realising this, unipolar operation can only be used for fine tuning of the force scaling while coarse force scaling is achieved by the bipolar operation.

- Thirdly, the violent non linearity seen from the solenoid is no longer a problem for this type of actuator. The actuator can operate in repulsion mode all the time as long as the unipolarity is maintained. Then any compressive disturbance would tend to be self-rectifying. In this case, all forces between the flex and reaction plate must act in the same repelling sense. This happens to be convenient for producing a primary mirror, where the net effect of pushing the lap down onto the edge of the mirror, accords with the turn-down asphericity at the edge of the primary mirror. However it is not satisfactory for the turn-up profile (with respect to the sphere) of a secondary mirror where the edge of the lap needs to be pulled up. It would be preferred to use bipolar operation because of the fact above. Even in the bipolar mode, the rapid response time and switching in polarity would be secure enough to protect the operation from the violent non linearity due to disturbances.

• Disadvantages of the electro-magnetic coupling actuator

However, the disadvantages are;

- Since the force/current relation is not linear even in the static case, accurate calibration needs to be made. In the dynamic state, as the two plates are bent slightly up and downward, relative positions of the two magnets would slightly vary and cause change in electromagnetic flux density to each other.

This would contribute to the non-linearity added onto the static non-linearity and thus slow down the control cycle.

- Cross talk could happen not only inside the control electronics but between the electromagnets through induced electromagnetic fields. This could cause more serious complexities. For example, if there is a large difference in the currents of both magnets to achieve repulsion, the one with the smaller current is likely to be overcome so that attraction could happen instead of repulsion.

- If one magnet is permanent, then demagnetisation could happen, even though it is slow in process. It is mainly caused by the induced electromagnetic field from the electromagnet than natural deterioration. This requires occasional recalibrations, but might not be a serious problem with modern rare earth magnets.

Jones [63] has also pointed out that some of these disadvantages foreseen could happen in real polishing.

• Proposed control system and disadvantages

The thermal dissipation would be similar to that of the solenoid and it may well be controlled by a control process to keep the room temperature constant. The control electronics is much like that of the solenoid. But if both magnets are to be electric, then The RAM memory size, the numbers of the addressing channels, the Octal DACs and of the solenoid drivers should be doubled. This would again lead to complicating the problem of the cross-talk and of the analogue noise discussed in the earlier section.

• Conclusion

Because of the complication of control electronics and other disadvantages described, it was decided not to use this actuator for the active lap.

4.3.2.4 Linear Motor-Spring Actuator

• Choice of linear stepping motor

Another actuator type is the linear motor-spring actuator. It is opposite to the electro-magnetic coupling actuator in the sense that the force scaling is entirely

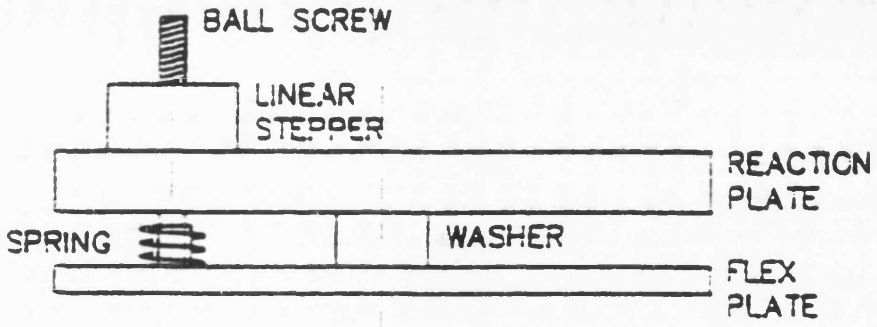

Figure 4.12: Linear motor-spring actuator

governed by mechanical coupling (i.e. spring), not by the electromagnetic coupling. The use of this actuator is depicted in Figure 4.12.

There are two types of the linear actuator i.e. DC servo motor and stepping motor. The trade-offs are extremely complex, but Digitron [28] have suggested that the stepping motor is the better solution if its application is cost-conscious, requires high torque and continuous duty at low speed and is short, rapid and repetitive motion. Fortunately, these are the conditions existing in our application. Thus, the stepping motor is chosen to be used.

• Use of stepping motor for the active lap

The stepping motor would be bolted onto the top face of the reaction plate whereas the spring unit is mounted onto the top face of the flex plate. There would then be used a type of lead screw to link both components. Hence, the force scaling can be achieved by defining a *spring constant*. The role of the stepping motor is to provide enough torque to move the lead screw up and down against the resistance of the spring. An example of using this type of actuator is the ESO VLT active mirror support system which is an array of stepping motor driven lead screws and load cells.

• Advantages of stepping motor-spring actuator

One distinctive advantage of this is that the electromagnetic force (i.e. torque of the stepping motor) is not used to directly generate the force for the pressure modulation. The force is generated by linear displacement of the lead screw multiplied by the spring constant. Therefore, the problems of the analogue control could be minimised and the control system would benefit from the ease of digital control. The other advantage is that the actuator operation is inherently bipolar. To move

both directions can easily be achieved with change of the direction signal from 1 to 0 or vice versa.

There would also be no problem of the non-linear violent response. Even if there were any external disturbances, it would affect only the spring (i.e. mechanical), not the electronic component. Of course, it can give rise in inaccuracy of force scaling but does not inherently lead to the violent over-shoot. This is because the spring tends to return back to its original position as the disturbance passes and the holding torque of the stepping motor would be much greater than the magnitude of the disturbance.

• Proposed control electronics

The control electronics would require a FIFO memory of 1000 Bytes, a stepping motor driver and two 16 channels Multiplexers for de-multiplexing about 32 channels. A control word would consist of 1 bit for direction, 1 bit for pre-set, 1 bit for full/half step and about 200 bits for step pulses. The control word is about 203 bits in length so that 750 Bytes memory is needed to store the control words for about 30 stepping motors. The control words would be collected by the FIFO memory. When it is full, the words are dumped to the stepping motor driver in First-In-First-Out manner. They are translated to equivalent analogue pulses and fed into the de-Multiplexer where appropriate channels are selected by separate control words from PC. The channel selection could be made either by fixed sequence of the selection words from control software or by a separate ROM where the sequence of the words are stored. With the fixed sequence of the control words, each block of the FIFO memory can always have the same 1-to-1 correspondence with stepping motors. Once the stepping motor finishes movement, it is latched naturally until the next control word is received.

• Advantages of the suggested control electronics

This control electronics, being purely digital, would operate with much higher noise immunity than the others. The use of the FIFO memory enables the provision of extremely small amounts of time delay in controlling the 30 stepping motors so that accuracy of force positioning in XY plane would be in few mm. With the aid of the de-Multiplexer (i.e. programmable switch), only 1 stepping motor driver can be used, but at the expense of slowing down the speed of the control cycle. This is

because the motor driver has to be engaged until a motor completes the movement and then starts controlling other. Alternatively, the total 30 stepper motor drivers can be used so that the control inputs can be rapidly downloaded to the 30 motors in parallel operation. This would increase the speed of the control cycle, taking full advantage of the FIFO memory. This electronic concept, the use of the FIFO memory, is directly derived from the mosaic CCD controller [47].

• Disadvantages of this type of actuator

One potential disadvantage is that the operation speed of stepping motor might be substantially slower than those of the solenoid and the electromagnetic coupling actuator. This can only be solved with a right choice for the stepping motor which falls into the limit of the specification discussed above. The lead screw of the stepping motor could be suffered from mechanical wear under continuous operation, worsening the backlash. Fortunately, it can easily be replaced when necessary.

• Conclusion

It seems quite natural to choose the stepping motor as an actuator for the instrumental active lap, since its advantages over two other actuators are evident as discussed above.

4.3.3 Design and Structural Analysis

4.3.3.1 Stepper Motor Selection

There are two models of the stepping motor considered; Parker A/AX 57-55R [84] and Sonceboz 7230 B linear actuator [101].

• Parker A/AX 57-55R motor

Parker A/AX 57-55R and the Parker electronics are designed to be used with micro step mode. At 1 micro step pulse, it can travel the distance of 0.127 μm. This gives the spring constant of $3.15 \times 10^9 N/m$ for the force scaling resolution of 0.4 N. This implies that the spring component should have the total compliance of 12.7 μm to exert 40 N (i.e. 100 steps). It is, indeed, relatively easy to achieve the compliance by a single sheet metal spring as shown later in this section.

If, on average, the maximum linear rate of travel is 5 rps (i.e. $125000 \mu steps/sec$

or 15.875 mm/sec) with the linear motor force of about 1600 N, it takes $800\mu sec$ (i.e. 1250 Hz) to exert 40 N when using the appropriate spring unit. As far as the operation speed is concerned, this is well over the specification. However, two problems exist. Firstly, the micro stepping controller is a analogue circuit which is rather difficult to control and therefore expensive. This may boost up the construction cost for the control electronics for the 30 motors running at micro stepping mode. Secondly, the frequency of 1250 Hz exceeds the useful frequency of the load cell i.e. 1236 Hz. It may then be quite possible that superposition of the 30 high frequency load pulses through resonances in the active lap structure, particularly the flex plate, could result in falsifying the load cell performance in a polishing run. It would lead to an incorrect pressure map being constructed, therefore an incorrect pressure error map and finally a wrong pressure modulation. An even more serious aspect is that there would be no way of verifying this happening during the polishing run.

Of course, the load cell has its own over load protection so that there would not be any serious damage to it. However, as the frequency of the external load pulse approaches the structural resonance frequency, there would be more likelihood of having the load cell malfunction. In order to prevent this, the half step rather than micro step mode can be used to slow down its operation speed.

Assuming that the motor rotor rotates 0.9° for a half step as most typical stepping motors do, then one half step equals about $63\mu step$ (i.e. about $8\mu m$) for 0.4 N. This leads to the spring constant of $5.04 \times 10^4 N/m$. The lead screw would travel about 0.8 mm in distance to exert 40 N. If, on average, the maximum travel rate is 5 rps (i.e. $125000\mu steps/second$), the operation speed to exert 40 N is $50\mu sec$ (i.e. 20 Hz) since $25000\mu steps$ are equal to 400 half steps needed to complete one turn of the motor. The operation speed seems to be still faster than the safe rise time of the load cell and therefore the problem of the load cell malfunction can not be solved completely. The compliance of 0.8 mm seems to be too large if the spring has to be made with a single sheet of metal. It would be quite likely that the principal stress for the spring may well exceed the elastic limit of typical industrial materials such as stainless steel 304. To use such a large compliance requires an alternative way to build the spring component.

The size of the Parker A/AX 57-55R is about $6cm \times 6cm \times 5cm$. It costs £400 per unit which is 4 times as much as the budgetary limits. This reduces very much the preference for the Parker A/AX 57-55R. For these reasons, this motor was not used.

• **Sonceboz 7230B motor**

The Sonceboz 7230 B linear stepping motor is designed to run with full/half step mode. The linear travel distance for a full step is 0.0254 mm i.e. 0.0127 mm for a half step. This gives the spring constant of $3.16 \times 10^4 N/m$. The lead screw must travel 1.27 mm to exert 40 N, meaning that the compliance of the spring unit is too large for a single sheet metal spring to take and an alternative way to design it has to be found. It is specified to be capable of running at around $380 steps/sec$ with the linear motor force of about 40 N. It would then need about 130 msec for 100 half steps, resulting in about 16 Hz and 8 Hz as operation speeds for full and half dynamic force ranges respectively. The speed is just about right and much slower than the safe rise time of the load cell. It does not seem likely for the signal falsification to happen during polishing.

Since the lead screw would tend to rotate when the motor is energised, an external anti-rotation device is required. The force required for the anti-rotation device depends on the screw friction. The anti-rotation device is discussed in the following subsubsection.

To control this motor is easier and less costly than that of Parker A/AX 57-55R in the sense that there is no analogue control element for micro stepping. A standard stepper motor driver IC which is widely available in the market can be used. This would contribute to reducing the construction and maintenance costs. The unit cost of Sonceboz 7230 B is about £80 which is within the limit of the budget. Its weight and volume are 450 gf and about $6cm \times 6cm \times 4cm$ respectively.

• **Choice of motor**

It was decided to use Sonceboz 7230 B for the instrumented active lap since it was economic as well as within the specification. An active lap of 2.5 m in diameter would use the same type of stepping motor although it requires about 9 times as many actuators as the instrumented lap uses.

4.3.3.2 Spring Unit Design

• Design requirements for spring unit

The force scaling for the stepping motor can be achieved by designing an appropriate spring unit. The spring unit should be designed to

- accommodate the spring constant of $3.16 \times 10^4 N/m$ and therefore the deflection of 1.27 mm for the force of 40 N.
- easily alter the spring constant for the lap to run with different force scaling when necessary.

• Spring of single metal sheet

Perhaps, the easiest and most economic way of making the spring would be to laser-cut a metal sheet to right geometry and dimension. But it requires the condition that the principal stress of the spring at the maximum load should be less than the yield strength of the material. There is a rising suspicion that for the large deflection of 1.27 mm, it may well be greater than the yield strength of typical industrial material, no matter what material, geometry and dimension are used. In order to confirm this, FE analysis was used to calculate the stresses and deflections of the three springs i.e. circular and square diaphragms and cross web. The results are summarised in the Figure 4.13, clearly showing that to achieve the deflection of about 1.2 mm for 40 N all the spring models have much greater maximum stresses than the yield strength of stainless steel and therefore rupture is likely to happen in use.

• Conventional helical spring

The conventional helical spring would not be a satisfactory solution. Of course, it can easily accommodate the spring constant. There are numerous models available in market. However since they have a rather fixed spring constant, the enclosure for the spring must be re-designed if the force scaling has to be changed as a result of polishing experiments. At the presence of overload, it tends to be buckled even inside the enclosure, thus ending up with another type of hysteresis. The spring rate also varies over its entire deflection range. Pre-loading can only improve the non-linear spring rate at the both ends of the spring.

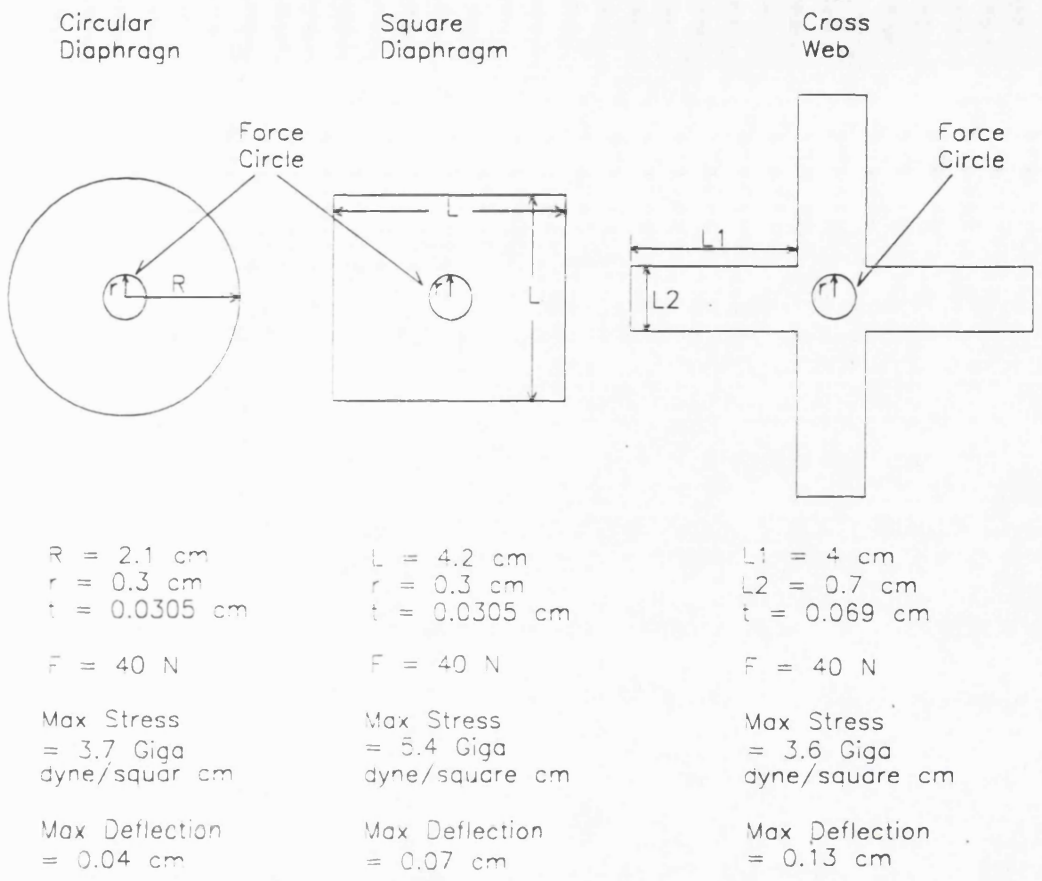

Figure 4.13: FE analysis results for the 3 spring models

• Disc Spring

The case of the single sheet spring above may suggest that if a number of the springs instead of just one are packed in the enclosure, then the maximum stress given to each springs for the total deflection of 1.27 mm does not have to exceed the yield stress, while their sum does. This would enable the spring unit as a whole to be compressed by a far greater range without the large stress given to individual springs. The single sheet spring discussed above can not be used directly for such packing because of its flat geometry. The conic geometry of the spring would be more suitable for packing. A commercial implementation of this is called the *'Disc Spring'*. They are widely available at a cheap price in the market.

The disc spring has a distinctive advantage in altering the spring constant. The spring constant decreases when they are packed in series, i.e. back-to-back. If they

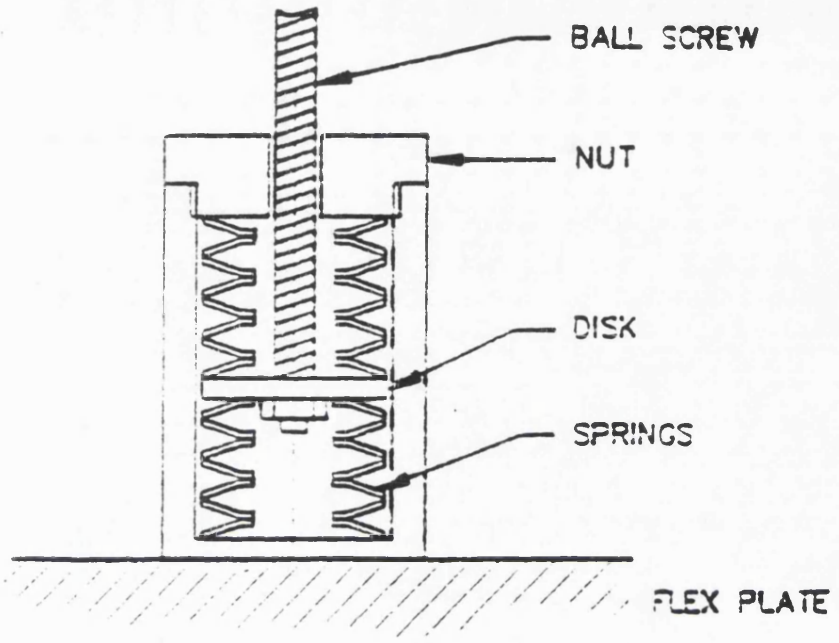

Figure 4.14: Use of the disk spring and design of the enclosure

are packed in parallel i.e. back-to-front, then it increases. So, in principle, it is possible to make virtually any spring constants with 3 packing strategies i.e. series, parallel and mixed. The disc spring of model C11608 [50] was determined to be used in series. It can deflect 0.38 mm with the maximum load of 154 N i.e. the spring constant of $405.3N/mm$. To pack 13 disc springs of model C11608 in series would give about $31.2N/mm$, which is similar to the spring constant of $31.5N/mm$ determined from Sonceboz 7230 B. With this spring constant, 1 half stepping would result in 0.3959 N instead of 0.4 N, thus leading to 101 half steppings for 39.99 N in one direction. Because of the bi-polarity discussed above, another 13 disc springs need to be placed in the opposite direction.

• Choice of spring

For the reasons described so far, the disc spring was chosen to be used for the active lap.

• Use of the disc spring for the active lap

The use of the disc spring is depicted in Figure 4.14. The enclosure for them should be designed to

- give and take the force at least greater than 40 N from the neutral position.

- withstand against lateral force caused by parallelogram when the lap is driven for polishing.
- form inherently the anti-rotational device with friction between the lead screw and the disk spring so that no extra device is needed.

The free height of a single disc is 0.9 mm so that the free height of 13 disc springs is 11.7 mm. The deflection for the preload of 74 N would be about 2.375mm to the top and bottom spring sets respectively. It gives 9.325 mm as the loaded height of a 13 disc spring set and leaves 80 N (i.e. about 2.56 mm for the two spring sets) that the spring can be further compressed. There is a stainless steel disc of 3 mm in thickness bolted at the end of the lead screw of the stepper motor. It is sandwiched between the top and bottom spring sets. Using the depth of the end cap of 17 mm, the depth of the inside cylinder, where the spring sets are accommodated, is calculated as 38.65 mm. The diameter of the inside cylinder of 16.2 mm is driven from the diameter of C11608 of 16 mm. The marginal diameter of 0.2 mm is to allow smooth vertical movement when loaded. There is about 5.5 mm as the marginal depth of the end cap that is for future adjustment of the spring constant. The enclosure design is also presented in Figure 4.14.

4.4 Active Polishing Module

4.4.1 Background

By February 1991, the design of the load cell and actuator was completed. It was then soon understood that

- it is imperative to find the best way to manufacture about 61 load cells and actuators in terms of cost, manufacturing period and ease of maintenance.
- it has to be checked if they work as designed and if there are anything to be modified for them to be used for the full size lap.
- it is needed to gather knowledge on how the active elements can be used for the full size active lap.

- it is necessary to check if active polishing results in an ablation pattern different from the passive polishing.

These motivated the building of an active polishing module which comprises the prototype load cells, the prototype actuator, the module controller and the active polishing software. Some findings from making the module were valuable in scaling up to the full size active lap. However, the module was not actually used for active polishing for the reasons described later in this section.

4.4.2 Active Polishing Module

4.4.2.1 Prototype Load Cells

• Manufacturing the load cell structure

A few discs of 5 mm in thickness were sliced from a cylindrical bar of stainless steel 304. This was the best way to reduce cost for the material and to ensure uniform granulity over the disc surface along its rotation axis. Non-uniform granulity would cause differences in deflections and therefore fibre stresses of each web. It results in different sensitivities in strain gauge operation even if they are precisely glued at the requested positions and the bridges are electrically well balanced with no weight.

They were NC-machined to make webs of 1 mm in thickness. The thinnest NC cutter was used to sharply cut the junction between the web and the rings. However the cutter was too flexible so that it was bent when machining. This caused somewhat smaller widths than were designed at both ends of the webs. Because of the diameter of the cutter, the junctions on the side surfaces became round at the ends of the webs. The top and bottom surfaces of the web have the surface finish of around 10 μm and they were then sand-blasted to ensure uniform smoothness. The surface finish of the side surfaces was allowed to be worse than that of the top and bottom surfaces. Variation of the web width would not have great effect on the fibre stress since the dominant factor is the thickness. It was found that it is a slow process to ensure the design tolerance even with the NC machine and in house manufacturing would be timely and costly.

• Strain gauge mounting

Strain gauges were mounted according to Entran's instruction [35]. The web was

first vigorously cleaned with solvent. Using a brush, a thin precoat of M-601 [115] was applied for electric insulation and then air-dried for about 30 min. It was then cured at 90° C for 1 hour. Using a microscope with cross-hair ruler, the strain gauge ESU-025-1000, with an additional thin coat of M-610, was applied at 1 mm distance from the end along the main axis of the web. Another film of M-601 with 30 minutes air dry was then applied to protect it from possible damage and environmental contamination. It was then cured at 125°C for 16 hours. It was post-cured at 150° C for 2 hours. In doing so, some difficulties were encountered.

- Since it is very small i.e. 0.65 mm in length, it took 1 hour to complete gluing 8 strain gauges with reasonable accuracy in positioning using a magnifier with ruler. This would lead to uneven air-drying for 8 strain gauges.
- The M-601 glue came as two separate chemicals and was mixed before use. Since it is liquid, it flowed when the web was inverted. This often resulted in change of the strain gauge position after it was glued.
- The strain gauge and its gold wire were extremely fragile so that it was easily broken while relocating them on the glue. As a result, one strain gauge was broken when gluing 8 strain gauges, indicating that 25 extra strain gauges would be needed if they were to be manufactured in house.

It was found that even with the best effort, it is extremely difficult to precisely locate the strain gauge with right orientation on the glue by the author's hand. This implies that in house gluing might ended up with strain gauges not precisely located at desired places, resulting in large differences in sensitivity.

• Two prototype load cells manufactured

Two prototype load cells were made. It was found that after baking one strain gauge on the prototype load cell 1 was broken again. Unfortunately, it was impossible, prior to baking, to check if they were glued properly and not broken, since they move very easily in the liquid glue. Using a temperature controlled soldering iron, the prototype load cell 1 was initially wired up to form 3 half bridges and a quarter bridge. Thin wires were glued on the outer ring and soldered to the gold wires of the strain gauges. But it was not good enough to ensure no movement of the wire coming out from the glue when the load cell moves. As a result of that, a gold wire

of a strain gauge on a web was again broken. It was realised that a robust device must be firmly attached to the load cell not to have the breaking and the prototype load cell 1 was unusable for the active module.

The prototype load cell 2 was modified to have two holes for each webs on the side surface of the outer ring along its neutral axis. A DIL pin was plugged into it and glued before the strain gauge was glued and baked. It was proved that this preparation is robust enough and the DIL pin was safe during baking. After soldering the DIL pins to the strain gauges, no short circuit was found. In the prototype load cell 2, there were 4 strain gauges used i.e. one on each web but two gauges on the top surfaces and the other two on the bottom surfaces. Load cell 2 was wired up to form a full bridge.

4.4.2.2 Prototype Actuator and Enclosure

The prototype actuator was built by linking the lead screw of the Sonceboz 7230 B to the spring unit. The components of the spring unit were machined and made of aluminium. The cylinder was made to have a hole on the body through which air can pass in and out when the disc springs were pressed.

Four Aluminium plates were used to form a square frame that has an extra Aluminium plate bolted horizontally at the middle inside the frame. The stepping motor was sited on the horizontal platform. The spring unit, the prototype load cell and the pitch were hanging on the motor by the lead screw. A thin metal lever was attached to the upper surface of the load cell and its four ends were bolted to the frame. It was used to prevent the lateral movement and rotation of the spring unit and the load cell with respect to the AL frame. All these are depicted clearly in Figure 4.15 which shows not only the prototype actuator but the active polishing module as a whole.

4.4.3 APOLO: Active Polishing Module Controller

The schematic diagram of the controller is presented in Figure 4.16. The four strain gauges were arranged to form a full bridge for the prototype load cell 2. Power supply A provides the OP-07 operational amplifier [92] and the bridge with $\pm 15V$.

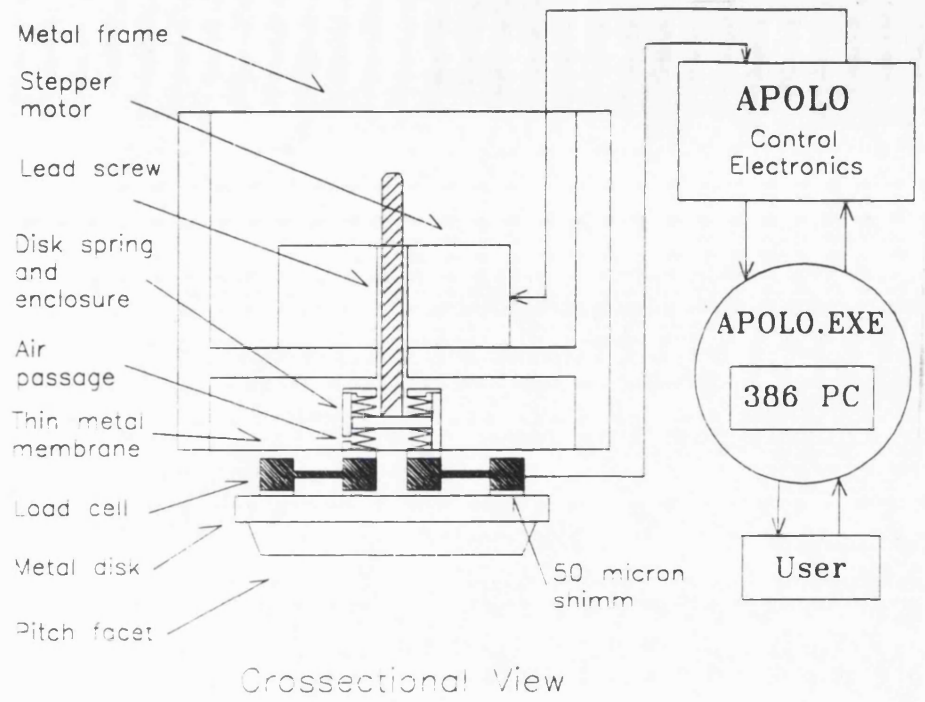

Figure 4.15: The active polishing module

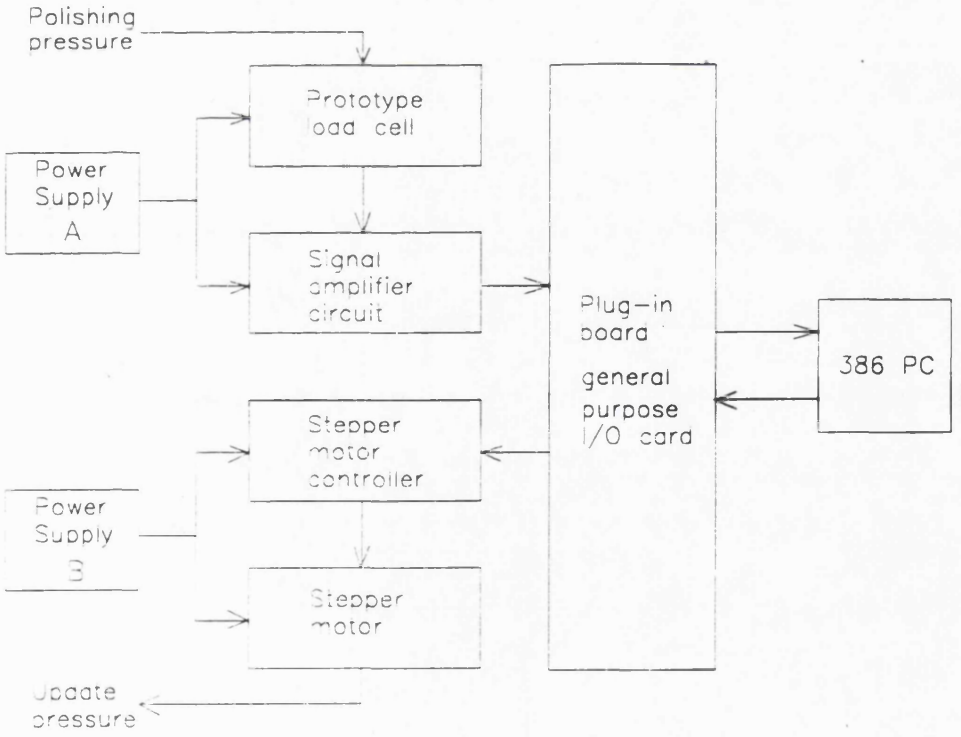

Figure 4.16: The active polishing module controller

A variable resister was used to convert $\pm 15V$ to $+10V$ for bridge excitation. The A/D conversion section of ADDA-8 card [42] was designed for bipolar input of ± 5 V. But it needs to be emulated as an unipolar A/D converter because the off-set

level of the amplified signal needed to be controlled within ±5 V. This was done by non inverted input biasing with another variable resistor.

Power supply B supplies $+15V$ to the 4 phase unipolar stepper motor driver board RS 322-098 [93]. It is then converted to +12 V via a fixed voltage diode MT78T12CT [94] for the motor. Major sources of current drain are the motor and the RS 322-098. They take about 1.02 *Amps* and the power dissipation would be around 5.8 W, which is about half of the power from the specification. The 8255 general I/O interface of ADDA-8 translates PC control commands and provides RS 322-098 with the four signals for stepper motor control.

4.4.4 APOLO.EXE: Active Polishing software

4.4.4.1 Control Elements

The number read from the channel 7 is in Analogue-Didital Unit(ADU) which has to be converted to a physical unit such as kg. The conversion needs the zero level of the load cell in ADU and its sensitivity in ADU/kg.

The prototype 2 load cell was not capable of compensating the effect of lateral force such as friction and shear force although the structural balancing was made. An unique solution for curing this would be to use, in the software, a tabular form of experimental data on the behaviour of the load cell under lateral force. (The experiments on this are presented in the next Section.)

Once the load is known in kg, conversions between load, pressure and friction are fairly straightforward, provided the friction coefficient is known. A calibration measurement showed that the sensitivity is about 55.5 ADU/kg and 2.2 ADU/stepping pulse. This gives an equation for calculating the pulse number for each force modulation.

$$P_N = \frac{L_R - L}{2.2} \tag{4.4}$$

where

P_N =pulse number.

L_R =required true load cell value in ADU,

L =observed true load cell value in ADU.

The vertical position of the lead screw has to be traced during either a polishing run, or any other operations. Otherwise, the spring would be left under either tensile or compressive stress until the next operation. During that period, with the prolonged stresses, the pitch would flow and its contact surface with the mirror would be deformed. This would cause a change in load cell readings for subsequent operations. Another serious problem would be that the deformed pitch surfaces of the full size lap;

- have a different contact area with the mirror surface from that of undeformed pitch surfaces.
- causes more rocking if the lap is initially tilted because of that.

There would be two solutions for this. The first is to use a hardware locking to which the lead screw would always be returned after operation. The second is to trace the lead screw position in the software in terms of the pulse number and direction. The screw position would be initially set as 0. It would be updated when a new pulse number and direction is calculated for the next movement. When the operation or the polishing run is finished, the final position is fed into the motion routine, activating reverse movement back to the initial position. The second solution is used for APOLO.EXE.

4.4.4.2 Overall Structure

The overall structure of APOLO.EXE is shown in Figure 4.17. It consists of Nine procedures which can be menu-selected. The module level interrupt always returns to the main menu while the procedure level interrupt ceases the operation but remains in the procedure.

Parameter Initialisation: This procedure is used to alter the operation parameters without modifying the source code. They are the zero level and the sensitivity of the load cell, the area of the pitch, the friction coefficient and the initial position of the lead screw.

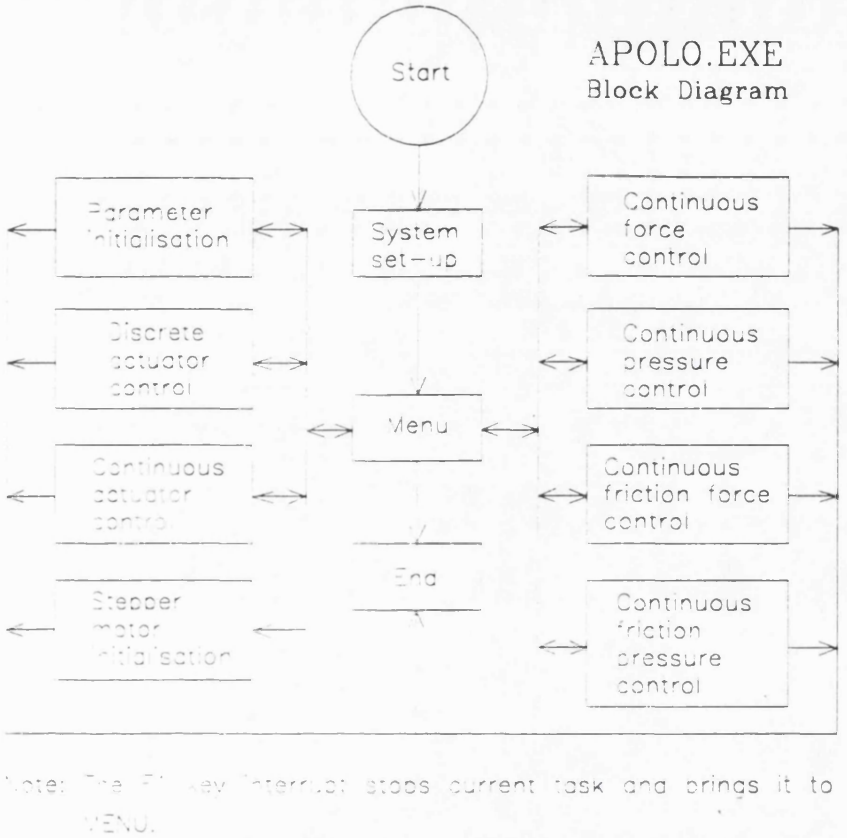

Figure 4.17: The structure of APOLO.EXE

Discrete Actuator Control: The user is prompted to input the pulse number and the direction. After a single operation, APOLO waits until new inputs are given.

Continuous Actuator Control: A required level of load is defined in ADU. Then APOLO operates the motor continuously to converge and to keep the level.

Four Other Procedures for Continuous Control: A required level of load is input according to the unit of the procedure names, for example, kg for the continuous force control. APOLO then converges and keep that level.

Stepper Motor Initialisation: The position of the lead screw is continuously monitored during operation. The procedure is used to return it to the defined position when the operation is finished. The procedure can be invoked from the main menu as a separate process. Ending without implementing this procedure

Bridge Number of Prototype Load Cell 1	1	2	3	4
Bridge	Compression Half	Compression Quarter	Tension Quarter	Compression Half
Observed Sensitivity (mV/lbf)	67.3	43.7	-39.9	64.3
Standard Deviation in Sensitivity (mV/lbf)	6.7	5.1	8.8	10.3

Note: The designed sensitivity of the half bridge is 70.3 mV/lbf with the standard deviation of 6.5 mV/lbf.

Table 4.3: The calibration of the prototype load cell 1

automatically activates it to ensure the initialisation.

4.4.5 Test and Optimisation

4.4.5.1 Calibration and Some Experiments

• Calibration of the prototype load cells

The prototype load cell 1 was used to see if the design sensitivity of $70.3 \pm 6.5(\sigma) mV/lbf$ is achieved for the half bridge with the excitation of 10 V. The load cell was placed on a cylindrical platform, supporting the outer ring of the load cell. The weight was altered from 0 to 8 kg with intervals of 0.5 kg and the open circuit output voltage was directly measured with a digital volt metre(DVM). A 9 V battery was used to simultaneously excite the half(1 and 4) and the quarter(2 and 3) bridges. The observed data were multiplied by 10/9 to be regarded as those obtained with the 10 V excitation.

The observed sensitivities for the 4 bridges are presented in Table 4.3. It is clear that the average sensitivity of the half bridge 1 and 4 of $65.8 \pm 1.4(\sigma) mV/lbf$ is in good agreement with the designed values and within the standard deviation of the FE model, which is about 10%. This implies that the FE analysis and the design principles worked correctly and the error in manufacturing must have been very small. It can be understood that the large differences in the zero levels of the bridges were caused mainly by poor bridge balancing. The dummy resistors used

to form the bridges are about 1000Ω whereas those of the strain gauges are around 850Ω. It also means that the sensitivity and the zero level of all bridges and hence of all load cells could be very closely matched if a better technique were employed in manufacturing.

• Magnetic effect

It has been suggested that the semiconductor strain gauge, such as ESU-025-1000, is sensitive to environment such as light and magnetic field [46]. A strong permanent magnet was moved around the load cell 1 to see its effects on the bridges. But no noticeable effects were observed from the DVM reading at all. It was thought that the cured M- 610 coat is good enough to protect it from the magnetic field. In the active lap, the magnetic field of the motor would not be greater than that of the permanent magnet used and there would be no magnetic disturbance in the load cell reading. This thought was proved right by the fact that, when APOLO energised the motor in air and hence no load was given to the load cell, no change in load cell readings was observed.

• Initial experiment for effect of off-axial load and sensitivity balancing

In a separate experiment with the prototype load cell 2, loads of 1 and 2 kg were applied in a place on the extreme periphery of the load cell. Initial results of the proportional error for each web were about ±5%. Fixed resistors were then placed in series with the individual gauges to adjust their sensitivities. The best result was obtained with a 60Ω resistor placed in series with the tension gauge Tb. It was ±2% of the output signal. In doing this, the resistors have much lower temperature coefficients than the gauges so temperature effect in the resistors is negligible. Although it can be reduced by this type of sensitivity balancing (not bridge balancing), the error of ±2% is still large enough to easily disturb the linearity of the output signal. This gives rise to use of extra measures for minimising the off-axis load .

4.4.5.2 Temperature Effect

• Thermal problems of strain gauge bridge

A semiconductor strain gauge is very sensitive to temperature change. It produces heat when excited and this changes its characteristics such as the Gauge factor. Therefore bridges must be left for at least two hours in excitation before attempting

any serious measurements [32]. Although individual strain gauges could reach thermal equilibrium sooner, the bridge still needs to be thermally compensated. The more strain gauges we use in a bridge, the better thermal insensitivity the bridge shows [107, 46]. However a full bridge requires four strain gauges while a quarter bridge does only one strain gauge. To use the full bridge would cost four times as much. Unlike any other commercial load cells, the author's load cell is designed to accommodate four separate bridges, whatever bridges they are. This means that a load cell would require 16 strain gauges for four full bridges, eight strain gauges for four half bridges, four strain gauges for four quarter bridges. A quality commercial one has only 2 strain gauges for a load cell and the unit cost is around £500. It would be ideal if the minimum number of strain gauges were used while satisfying the design principle.

• Industrial solution to the thermal problem

A typical industrial solution for this is to use the half bridge with an external thermal compensation module which is in fact a resistor circuit of which resistances are determined experimentally [86]. An advantage of using the external thermal compensation module is that the quarter bridge which is cheapest in manufacturing can be used, although it requires long and hard experimentation to determine the resistances. Specifically for the active lap, this would not only add further complications to the on lap electronics but requires such a long time to determine the resistances for 88 quarter bridges.

• Proposed two solutions, but subsequently rejected

Apart from that, two other solutions were explored. The first would be to stabilise the environmental temperature to ± a few degrees and to use either half or quarter bridges with software thermal compensation. There would be a look-up table containing calibration data for weight and temperature ranges used. This would be stored in a file and read when the control software runs. A number of temperature sensors would be attached near some load cells, providing temperature data. The unit conversion from ADU to kg could then be made accordingly. The second would be to emulate two quarter bridges as a half bridge in software. The idea is to take signals of a tension quarter bridge and of a compression quarter bridge separately but subtract them in the software. The detailed calculation on this software half bridge is presented in Appendix B.2. It requires no calibration data on temperature.

• Temperature experiments

No matter what solution was going to be used, it was imperative first to see how those bridges behave with temperature. While preparing an experiment, the gold wire on the tension side of the half bridge 1 was broken. It was then rewired to be a compressive quarter bridge. The load cell 1 and weights were placed on a wood plate of about 2 cm in thickness in an electric oven. The electric wires were fed through the ventilation hole on the top surface of the oven. They were baked until 30 minutes after the requested temperature inside the oven was reached. The power was then connected to the bridge before opening a door of the oven. Immediately after opening the door, a weight was put on the load cell and the door was closed. This series of actions i.e. opening the door, placing a weight and closing the door were required to be taken place in a very short time scale. That was the only way not to significantly alter the temperature inside the oven. In practice, it took normally about 3 sec and was short enough to restore the temperature in few minutes. However, at high temperatures, even the 3 seconds was too long not to severely disturb the temperature and it took 10 to 30 minutes to make it stable at the desired value. The power for the load cell was disconnected in that case until the measurement was about to be made.

The half bridge(4) and the tension quarter bridge(2) were used in the experiment. Measurements were made from 0 to 3 kg and from 22.5°C to 90°C. The results are as follows.

- For the quarter bridge, the sensitivity shift with temperature is 0.082 $mV/lb°C$ with the standard error of 0.191 $mV/lb°C$. The zero point shift is 10.183 $mV/°C$ with the standard error of 0.618 $mV/°C$.
- For the half bridge, they are 0.036 $mV/lb°C$ and 1.17 $mV/°C$ with the standard errors of 0.24 $mV/lb°C$ and 0.008 $mV/°C$ respectively.

It shows clearly that, in particular, the zero point shift of the quarter bridge is about 23% of the bridge sensitivity of 43.67 mV/lb. It implies that the temperature stabilisation within 0.1°C needs to be made if the measurement accuracy of 2% has to be achieved. This is almost impossible in practice. Despite the large zero point shift, the sensitivity shift is remarkably small i.e. 0.2% of the sensitivity. The only

practical way to use quarter bridge seems to be the software half bridge with strict control of temperature near the load cell. This method again requires more data on how the software bridge behaves under temperature variation.

The half bridge, however, shows that the zero point shift is about 1.8% of the sensitivity of 64.33 mV/lb. The sensitivity shift is only about 0.06% of the sensitivity. Thus, the half bridge is a much better solution than the quarter bridge i.e. factor of about 10 in the zero point and of about 3 in sensitivity. It is indeed usable without extra thermal compensation hardware if the temperature near the bridge is kept under $2°C$ in variation. This can be achieved without great difficulty.

• **Conclusion**

Strictly speaking, the ways that the signal is dealt with in the intrinsic half bridge and in the software half bridge are the same. The difference is where the compensation takes place; in bridge circuit or in software. It seems to be better not to use up software time since there are many time-consuming tasks such as calculations for pressure and ablation maps. This supported the intrinsic half bridge as a better choice.

4.4.5.3 Lateral Force Effect

• **Problem with lateral force effect**

As discussed in the early section, all commercial load cells suffer from sensitivity to off-axis loads, causing a departure from the calibration curve for axial load. The load-fibre stress relation of off-axis load in the load cell (i.e. web) differs substantially from that of the axial load. It also varies depending on off-axis load vectors i.e. directions and positions of the loads. The effect of the off-axis load is depicted in Figure 4.18. The transverse component $-F_x$ is mainly responsible for this, adding the negative strain CF to the existing strain TF_a of the axial force F_a. The tangential component F_z has little effect since it works on the inactive axis of the strain gauge.

Unfortunately, polishing is a frictional process where the kinetic energy of a polisher is dissipated mainly by friction, resulting in removal of material. For the active polisher, the friction plays a role of the lateral force as either the transverse force or the tangential force, depending on the off-axis load vector. As the lap moves, the fric-

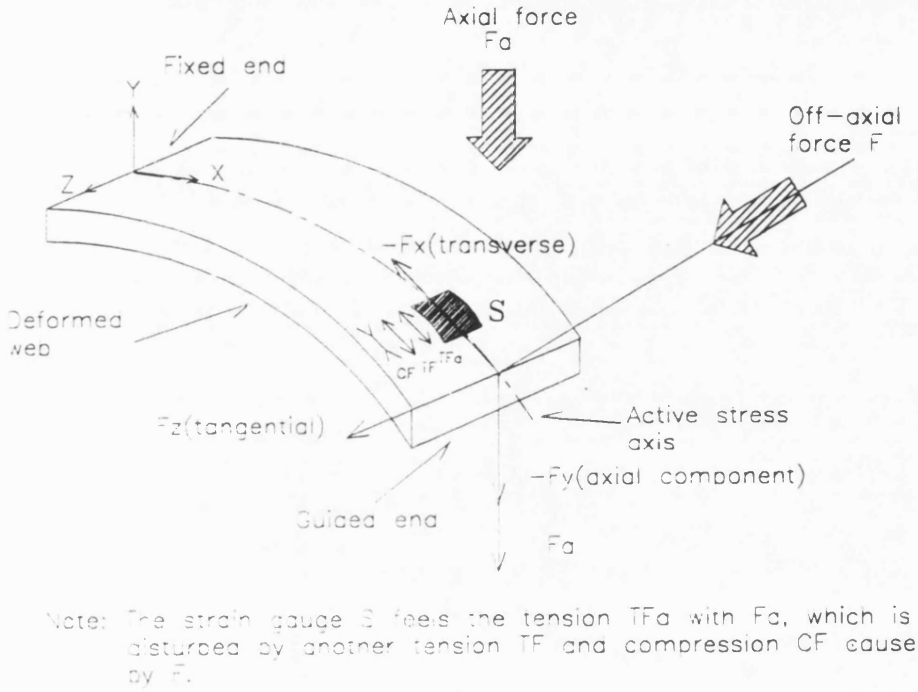

Figure 4.18: Effects of off-axis load to the web

tion acts against the pulling-pushing force, causing the parallelogram of the active lap structure and hence the lateral force on the load cell. The preliminary measurement of the friction showed somewhat larger friction than normally expected [6]. It would mean that the observed pressure map would be entirely unrealistic, unless the effects of the lateral force were at least separated from the signal or suppressed to a tolerance level.

• Proposed solutions to this problem

Solution for this can be found from three directions.

- Firstly, a series of detailed experiments should be made to provide calibration data of the behaviour of the load cell under the friction.
- Secondly, the load cell itself should be lateral-force-immune.
- Thirdly, external devices in the active lap should be designed to minimise the lateral force in the first place. (This is presented in Chapter 6.)

Software solution:

The first is again a software solution with the time consuming calibration, as is the

case of the temperature effect. For the full size active polisher, the friction for a load cell would be in any direction, depending on the way it is derived for polishing. A calibration for that would be a form of look-up table, containing the frictional behaviours of the load cell at least with the angular resolution of 22.5° in covering 360° C. This large data and its interpolation would take considerable software time.

But for the active polishing with only one test-module, the module is intended to be fixed at the end of the push-pull arm of the 1m polisher. It would then, unlike the full size active polisher, have one specific direction of the friction, i.e. the transverse force of a fixed direction given to the load cell. This could be calibrated and then used for the active polishing with reasonable accuracy in sensing the axial force.

• Lateral force experiments

Following up the first and second directions, two experiments were undertaken with the prototype load cell 2. The prototype load cell 1 was not adequate for the experiment because of its 4 webs having different bridges.

Friction measurements:

The first experiment was to measure directly the frictional behaviour of the load cell 2. Load cell 2 was disassembled from the module, including the spring enclosure, the lead screw and the circular pitch. It was placed on the polished surface of a soda lime glass with the abrasive film in between them. The abrasive film was in fact a mixture of Cerium Oxide of 80 mg and water of 500 ml. A thin cotton string was used to pull the load cell at the position P. The measurements were made from 0 kg to 3 kg with the interval of 0.5 kg in weight at every 22.5° clockwise, starting from the direction to the tension gauge Tb. A part of APOLO.BAS was separated from the source code and modified to sample the full bridge signal at 1 Hz. The room temperature varied within 21 ± 2°C and the room humidity was not checked. The apparatus is depicted in Figure 4.19.

Some sources of the measurement error were observed during the measurement.

- Twisting: Since the load cell was floating on the abrasive film, there was no way of stopping its twisting perpendicular to the pulling movement and it happened unpredictably. The data with the twisting were discarded and the measurement for a direction was made until no twisting was observed.

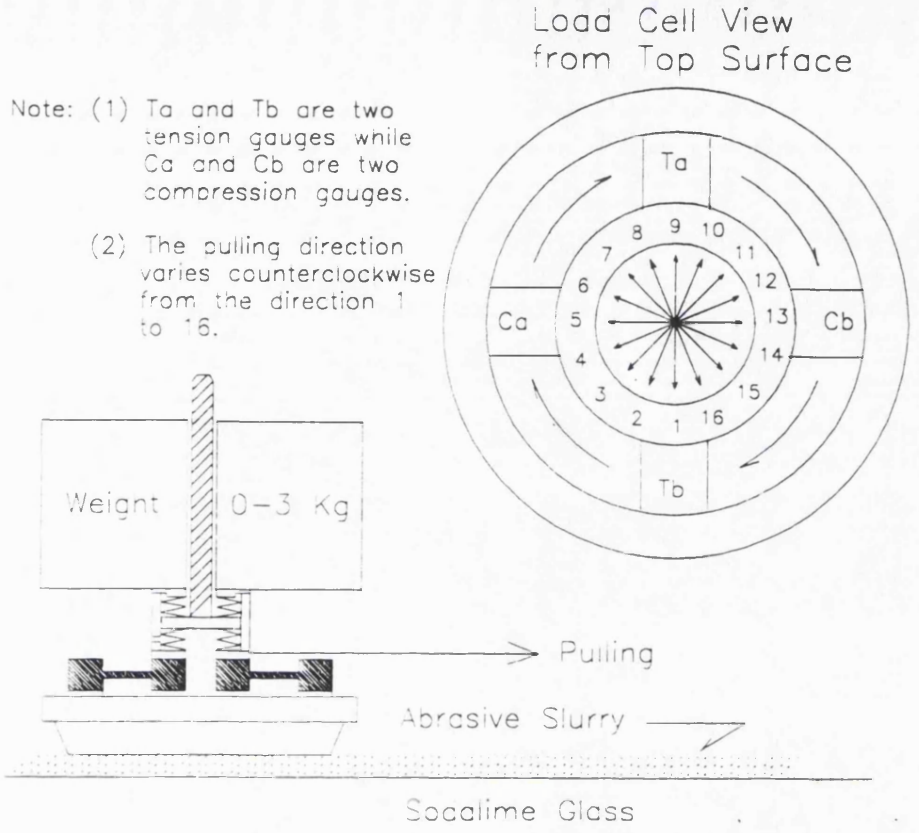

Figure 4.19: The apparatus for measuring the off-axis load

- Sticking: Sometimes, the load cell was not moved until the pulling force exceeded a certain level. It then surged to a position along the pulling direction at a faster speed than the pulling. This also happened unpredictably with lighter weights, but more frequently with heavier weights, causing spikes in the observed signals shown in Figure 4.20. For the data containing this, it was rational to take averages.

- Tipping: Small amount of tipping of the load cell toward the pulling was observed, meaning that the pulling side of the load cell was sinking deeper than the opposite side. This seemed to be natural since it was floating on the abrasive film. The axial component of the film resistance against the pulling at the rear edge of the load cell would be negligible. The dominant force would be its transverse component and the friction which is to be measured.

The friction measurement illustrated in Figure 4.20 means that the frictional effect increases with weights. It is also shown that with the weight of 1.5 kg the effect (i.e.

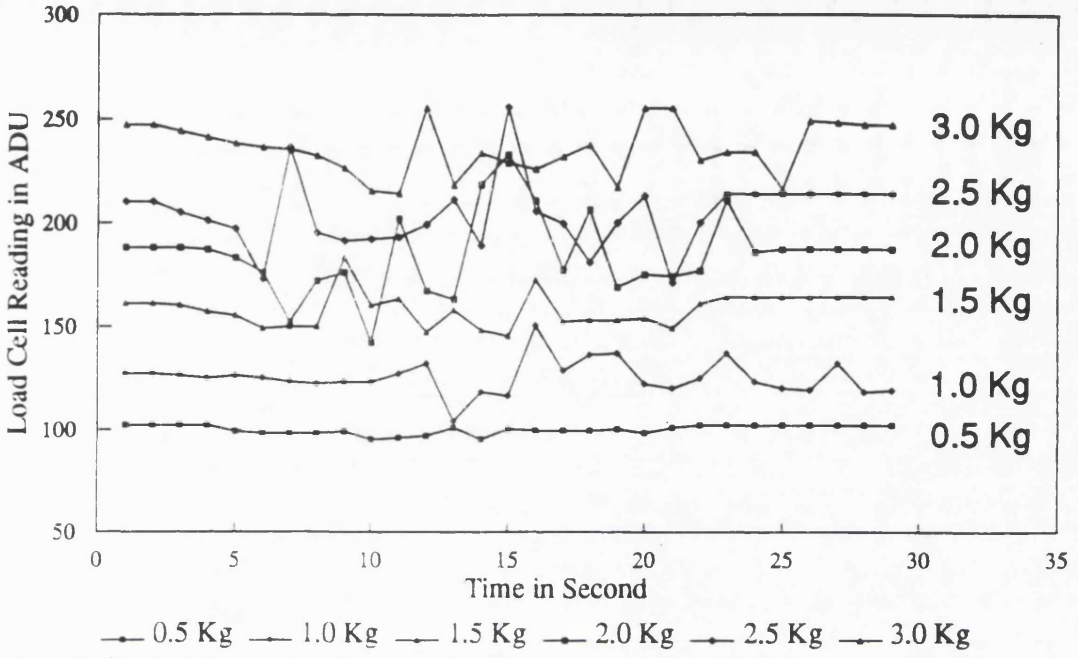

Figure 4.20: An example of friction force, showing spikes due to unpredictable sticking

the deviation from the base reading) is about 10 ADU, which is around 6% of the base reading of 160 ADU. This is not satisfactory at all. It can also be noticed that there is a sinusoidal variation with directions.

Forced tipping measurements:

The second was to measure the effect of forced tipping on the bridge output voltage. The load cell was clamped at the position A and B for the first measurement but at the position C and D for the second measurement as shown in Figure 4.21. This was to observe if the way of clamping the load cell causes any effects on the measurement. One end of a thin cotton string is holding the pulling point P and the other end is attached to the spring balance pulled with the force range of 0-2 kg. Using APOLO and APOLO.EXE, the measurements were made clockwise starting from the direction of Tb and continuing to cover 360^o with 16 directions. The bridge output voltage was recorded.

The two measurements plotted in Figure 4.22 look very similar, indicating that the measurements were not affected by the ways of clamping. It also shows similar behaviours to those of the friction tests but in greater magnitude. This means that

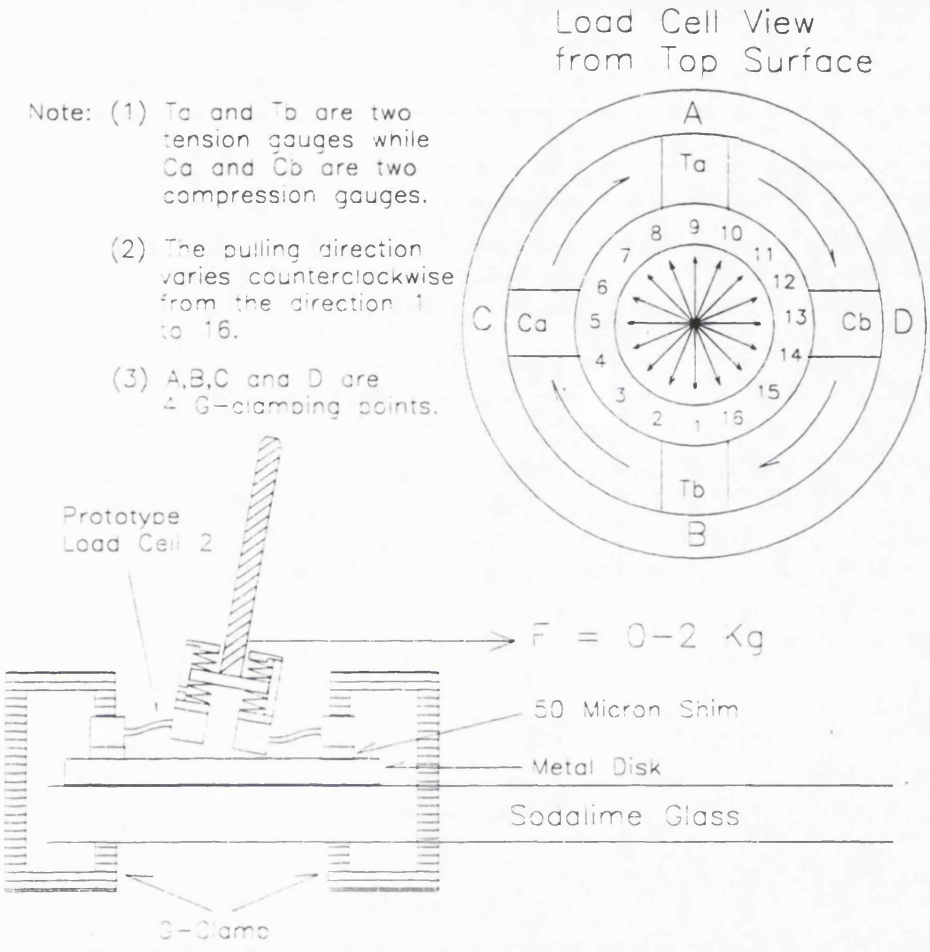

Figure 4.21: The experiment of the forced tipping

the structural behaviours of the load cell under friction and forced tipping are indeed identical and not distinguishable.

The sinusoidal pattern suggests two useful ideas for self-compensating the effect of the lateral components of any off-axis forces.

- Firstly, if a similar pattern shifted $\pi/2$ in phase is generated and added to the original pattern, then the effect could be removed. This second pattern could be generated by another full bridge of four strain gauges mounted at the same locations with those of the first four strain gauges but on the opposite faces of the webs. If the configuration of the first bridge is clockwise, then that of the second bridge must be anti-clockwise with a starting point rotated $\pi/4$ clockwise as seen in Figure 4.23. The data of the measurement 2 was used to simulate this and the result gave the effects of about ± 13 ADU with 2 kgf

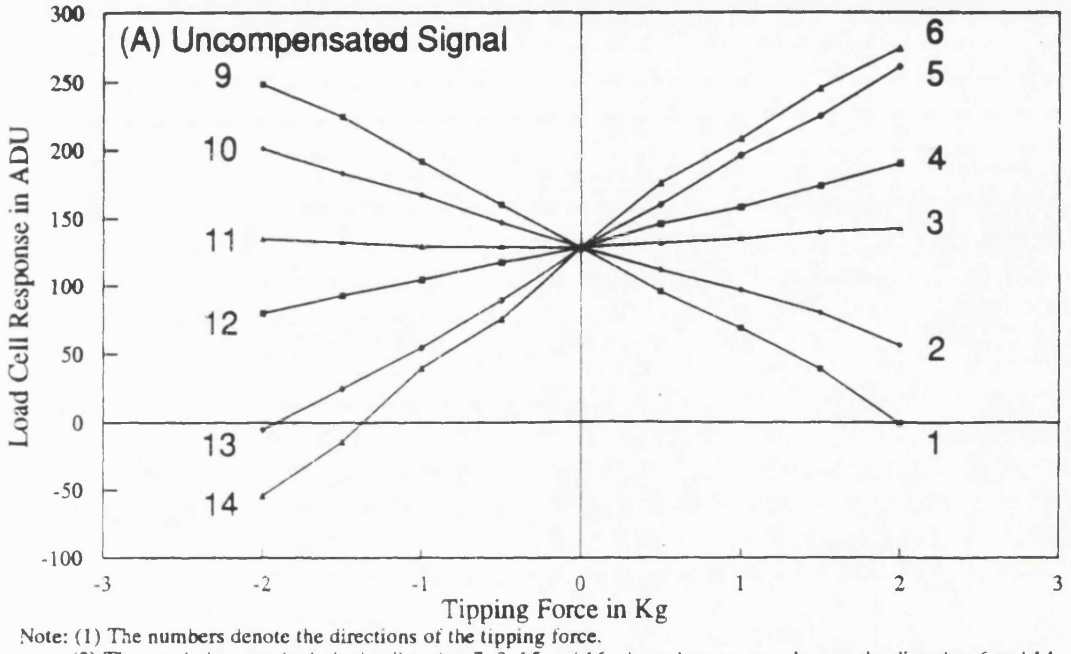

Note: (1) The numbers denote the directions of the tipping force.
(2) The graph does not include the direction 7, 8, 15 and 16, since they are too close to the direction 6 and 14.

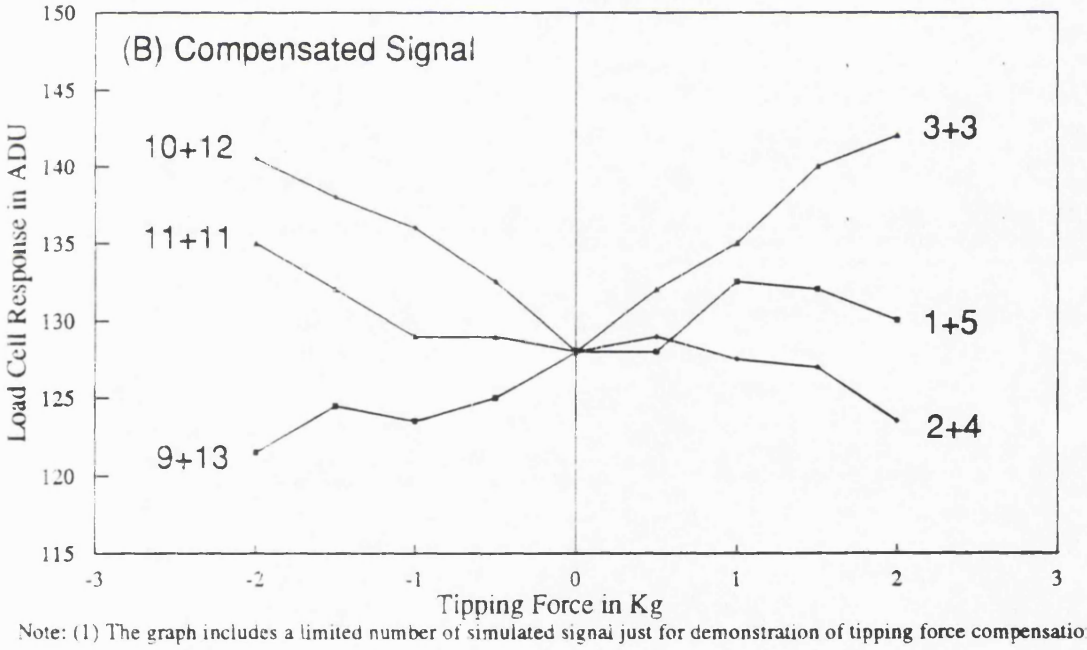

Note: (1) The graph includes a limited number of simulated signal just for demonstration of tipping force compensatio

Figure 4.22: The measurements of the forced tipping

which was only 7.6% of the uncompensated effects. Most of this residual effect would not be inherent. It would rather be caused by the different sensitivities among the four strain gauges and their environments on the prototype load cell 2. This means that it would ideally be possible to reduce the effect to

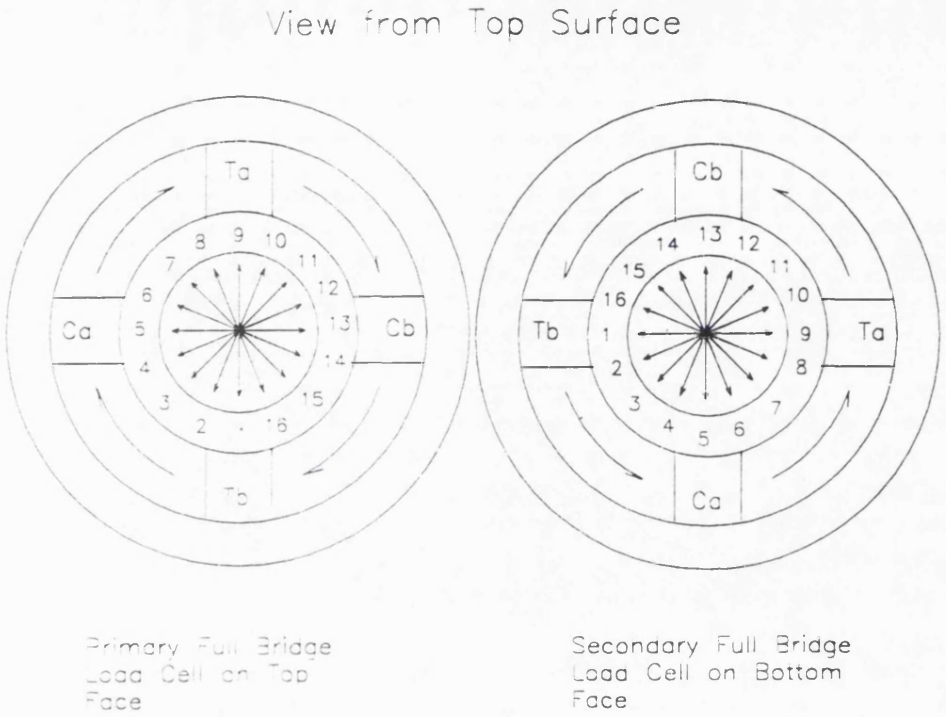

Figure 4.23: A second full bridge for self-compensating load cell

zero, if their Gauge factors, resistances and mounting locations were same and hence so the zero levels and the bridge sensitivities as well.

- Secondly, the previous idea suggests a total of 8 strain gauges for four webs (i.e. 2 per web). But in fact, they could then form four half bridges, producing four bridge output voltages, each of which acts separately under any loads and can be read separately. A lateral force giving positive maximum effect to a web would also give negative maximum effect to the opposite web at the same time. The remaining two web would have minimum effects since it is given along their inactive axis. Thus, averaging these four outputs would compensate the effect of the lateral force and the reading would represent only the axial force. Unfortunately, this could neither be simulated nor be experimented at

this stage because the prototype load cell 1 and 2 do not have complete 8 strain gauges on their four webs. Experiments for this were made when actual load cells were calibrated during manufacturing the active lap and are described in Chapter 6.

4.5 Discussion

In summarising the Chapter, first in static mode, it was observed that the module is able to converge and maintain a force level with the accuracy of 1% of the dynamic force range with just a few iterations. When a step pulse was generated downwards, the load cell output increased by about 2 ADU. This confirms that the force scaling of the stepper motor and the spring unit was achieved as designed. However, no further measurements and analysis for the module performances were made in detail because those of the real active lap depend largely on the lap control system. The module was used just to prove that the philosophy and the design are correct and active force modulation can be achieved with them. Thus, the fact that it is able to modulate force in real time is good enough to allow mass production to proceed.

• Implication of prototyping the active elements

The experience of producing the prototype module make it crystal-clear that

- bonding the strain gauges on the webs requires very much professional craftsmanship as well as proper hardware jigs which neither OSL nor the Departmental machining shop possess.
- in house NC machining for producing a single piece of load cell structure is not only time consuming i.e. costly but also likely to cause poor quality specifically in the web width at both the edges and in flatness of the load cell structure. The latter results from the prolonged axial force given to the load cell structure while being machined. This is serious because it widens the sensitivity distribution of all the webs. It also affect the thickness of the shim for overload protection.

It is crucial to find some other ways for mass-producing the 25 load cells as well as for ensuring identical characteristics among them. Ways were indeed found and

discussed later in Chapter 6.

• Considerations for electrical connection for load cell

The ideal number of strain gauges for a load cell would be 8 (i.e. two strain gauges on each web). This determines the minimum thickness of the outer and inner rings to accommodate connectors. The prototype load cell 2 has 5 mm in thickness and just two Dil pins for electric wiring to one strain gauge. If a web has two strain gauges with four gold wires, it then requires four Dil pins mounted through the outer ring. The vertical arrangement of the four pins (i.e. two on the upper half and two on the bottom half of the outer ring) would be better than the linear arrangement , since

- if the load cell is not a NC machined single piece, there would be no way to linearly locate the holes along the central line of the load cell.
- it can bring the ends of the pins closer to the strain gauges on the web and therefore the short and fragile gold wires have less risk of being broken.

This requires at least 4 mm at one side of the ring so the thickness would be 9 mm including the web thickness of 1 mm. It is still within the specification of 10 mm.

• Useful interim findings

There are some other interim findings, which are found to be valuable in the manufacturing and assembling stage of the active lap.

- The bridge selection is still to be solved but the possibility of the quarter bridge is firmly removed, even if the theoretical base for emulating it by software is established. Averaging 4 half bridge signals would be as good as averaging 2 inverted-phase shifted full bridge signals for lateral force compensating. However, as far as thermal immunity is concerned, the latter is the better solution.
- The offset level of the load cell varies depending on various parameters such as self heating, ambient temperature, structural biasing, etc. So in using them for actual polishing, the software might have to be adjusted every time a new polishing run starts. This again implies that it has little importance in calibration of the load cell.

- The gain (i.e. the sensitivity of the half bridge) is very stable and does not show any noticeable change under temperature variation over $70°C$. There is no need for the same kinds of adjustment as the offset needs. The calibration can be made once and for all. Therefore it should be calibrated with great care.

- The thermal compensation for zero offset can be made in software, e.g. two calibration data sets measured at two different ambient temperatures. The preliminary experiment showed that there is no noticeable difference in the sensitivity if the ambient temperature variation is kept under few degrees Celsius. The offset has a larger effect with the temperature variation but there is no need for concern since it can be re-established simply by pressing the lap.

- The thickness of the shim (i.e. 50 μm) is small, so that it can be easily overcome by roughness or bending of the flex plate. In addition, any manufacturing processes for the load cell can result in the inner ring either sagging or bending or tilting with respect to the outer ring. If these occur, some load cells would be pre-stressed after assembly to the flex plate is finished, so their offsets and gains would be very much different from those of the rest of the load cells. The calibration should be able to show this. The only way to correct this is to have greater shim thicknesses, which give at least 70 micron compliance. In that case, the corresponding increase in strain would not exceed the maximum allowed strain, with more than 200% overload capability.

• Method of lateral force compensation

When the frictional behaviour of the prototype load cell 2 was being measured, an interesting finding was observed that is rather natural but gives an important clue for the lateral force compensation. When the load cell was pulled at the position above the webs, a large frictional effect was seen. However, there was no observable frictional effect when pulled at the position below the webs. This can be explained by the force parallelogram within the load cell. It gave two very effective ideas for reducing the amount of the lateral force to the load cells.

- Firstly, any sort of thin membrane that is structurally linked to the reaction

plate should be underneath the load cells i.e. somewhere between the load cell and the upper surface of the pitch square.

- Secondly, it would be more effective to minimise the lateral force if the load cell is not physically clamped to the membrane so that there exists a sliding surface between them.

These ideas are practically implemented in building the active lap as the Carbon fibre membrane and described in Chapter 6.

• An accident on the module

Finally, later a short circuit developed in the module without apparent reasons. It was noticed that one of strain gauges was in contact with the load cell structure and also that the entire module made of metal is physically mounted on the metal push-pull arm of the 1 m polisher. However it is still not known why it happened some time later after the module was built and whether a Dil pin or a gold wire is linked to the metal structure. This shows the importance of industrial manufacturing, careful assembling and quality assurance for the load cells. If the module has to be used for real polishing, it can be solved by electrically insulating the module from the push-pull arm, using a plastic board.

Chapter 5

Sub-Diameter Tool Polishing and Polishing Variables

5.1 Introduction

The ultimate aim of the active polishing might be to control the amount of ablation at a specific location on a mirror, in real time. It requires not only the active lap hardware but also an ablation algorithm to be developed. The core of its development is the relationship between the ablation rate and the polishing parameters described in Chapter 3. Finding this relationship depends largely on our understanding about the physical nature of optical polishing.

A number of experiments were carried out with the aims of

- examining Preston's law (i.e. The instant wear rate is proportional to the polishing pressure and sliding velocity) [4], which all the existing polishing methods rely on
- finding an alternative relationship empirically for the active polishing,
- experiencing polishing with a sub-diameter tool,
- observing behaviours of the abrasive liquids under polishing
- developing testing methods suited for the 1m polishing machine OSL possesses.

In particular, the experiments with a pitch polisher were focused on the relationships between ablation rate and four parameters i.e. friction, pressure, velocity and water to abrasive content ratio. As far as real-time control of the active lap is concerned, the other parameters are not directly relevant so the experiments did not deal with them.

It was fully understood that when starting the experiments, the proper completion of the work described in this Chapter would deserve either one or two complete PhDs. Thus, the work was intended to provide a broad background understanding of physics of optical polishing, specifically sub-diameter tool polishing. It was also to provide the ablation algorithm of active polishing with necessary inputs to start up with. The author believes that it is a preparatory work for more proper experiments and can be regarded as the starting point of a long term programme that OSL will pursue in the future.

Section 5.2 deals with the experiments for the ablation rate. The friction coefficient is concerned with Section 5.3. The experiments for the behaviours of the abrasive liquid are presented in Section 5.4. These experiments include the development of the apparatus as required. The discussion in Section 5.5 contains

- addressing problems with the existing theories,
- implications of the results,
- summary of the findings from the experiments,
- suggestions for future trend of large optics polishing,
- suggestions for future experiments.

5.2 Ablation Rate

5.2.1 Experiment Programme

It was intended first to attempt the active polishing using a linear array of 3-4 active modules for the ablation rate measurement. However later on this never materialised, not even with the prototype active module, since

- the project budgetary limit and the time table did not allow enough room to manoeuvre.
- reference polishing with a passive sub-diameter lap had to be made prior to any active polishings, for comparison. It took almost five months to complete the experiments and data reduction, leaving no spare time for the active polishing.
- the reference polishing showed inherent large scale errors, so that the active polishing would suffer from an even worse scale of error, unless it can embody some kind of self-learning capability.
- it was impossible to compensate accurately the lateral forces such as friction for the prototype active module to be used for real polishing.

Thus, passive polishing using a sub-diameter pitch polisher was only made.

The experiment was aimed at measuring the removal rates of a soda lime glass at different sliding velocities and polishing pressures. A pitch polisher held by three cotton strings would be placed at predetermined radii on a rotating glass surface. The polishing pressure can be controlled by altering the weight on it. The rotation of the turn table of the 1m polishing machine would then produce a groove on the surface. By repeating the rotation with the pitch polisher at different radii, there could be about 3-4 concentric circular grooves generated on the surface. The volume removal rates, i.e. ablation rates, can be obtained by measuring the depths of the grooves. The sliding velocities at the locations of the grooves can be calculated using the radii of the centres of the grooves and the rotation period of the turn table.

The typical approach for measuring the ablation rate of material including glass has been to polish and then measure the weight of the specimen. This method is capable of measuring the volume removal rate rather directly. But it requires either weight measurement at very high precision or a considerable polishing time, so that it is costly and time consuming. Another approach is to polish and *optically* determine the depth profile across the groove. The volume removal rate can then be calculated by integration of the profile over the extension of the groove, i.e. 360^o, for circular groove. The second method was preferable since the optical testing facilities to be built for the 1m polishing machine could be used instead, so no extra testing facility is required and this would be more economic.

5.2.2 Apparatus

5.2.2.1 Scatter Plate Interferometer

For the optical testing facility, the scatter plate interferometry invented by Burch [15] has been favourably considered. De Witte [25] has explained its theoretical aspects in detail. Shoemaker *et.al.* [97] and Scott [96] have explored its practical use for large optics testing. Recently, Harmer *et al.* [48] has used this for the 3.5m mirror project in NOAO.

• Advantages of this method in general

Its advantages over other optical testing methods for large optics are summarised below.

- It is a common-path interferometry so has good vibration immunity in acquiring interference fringes. This is particularly useful for long-focus and large optics such as large mirrors for astronomical telescopes.
- It requires neither large nor quality optics to build the apparatus except the scatter plate that can be produced without difficulty. This contributes considerably to reducing the overall cost for testing and therefore producing large telescope mirrors.
- It uses a much smaller space than some other methods.

Hence OSL has used this method to test a f/3 concave spherical mirror of 85 cm in diameter which was figured in the OSL large optics shop and now serves as a test mirror. Burch's original configuration [97] for the scatter plate interferometry was used for this testing. Figure 5.1 presents a schematic diagram of the interferometry setup used.

• Practical disadvantages of this method found

In doing so, the disadvantages summarised below have been found.

- It generates a speckled image of the mirror when laser serves as a light source, degrading the entire fringes to an unobservable quality. This can be improved by employing an semi-transparent acetate sheet rotating in front of the laser as a de-speckle device. With the de-speckle device, the overall throughput

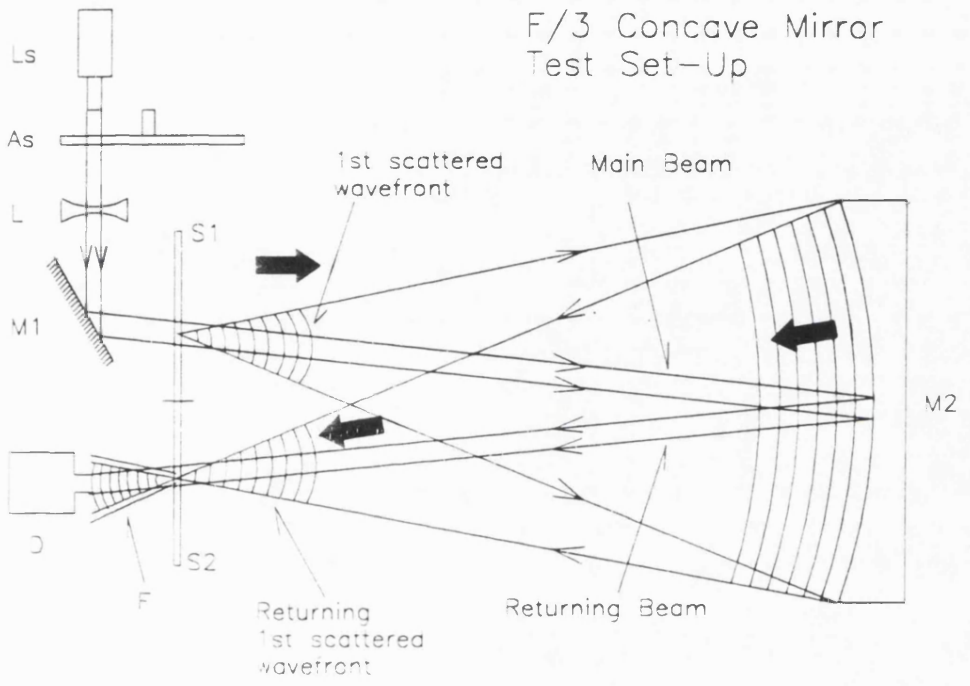

Note: Ls = He-Ne laser, 0.6328 micron wavelength,
As = Rotating Acetate Disk De-Specle Device,
L = Laser Expander Lens,
M1 = Reflecting Mirror,
S1 and S2 = Identical Scatter Plates,
M2 = f/3 Concave Mirror under Test,
D = CCD Camera, Photograph Plate or Naked Eyes
F = The returning beam produces the second scattered wavefront at S2, which interferes with the returning 1st scattered wavefront. This produces a fringe pattern representing the surface quality of M2.

Figure 5.1: The interferometry setup for testing the f/3 concave mirror with Burch's configuration of the scatter plate interferometry.

decreases and there still is a hot spot which makes a portion of the area on the unspeckled mirror image unobservable for the fringes.

- The fringe contrast produced by scatter plate interferometry is inherently lower than that of unequal path laser interferometry. There is no problem with the low contrast when they are photographed. However, if a frame grabber with a CCD camera had to be employed for digital fringe analysis, there can be a problem of not detecting the fringe pattern onto a buffer memory.

A simple experiment using the DT-2851 frame grabber [23] indicated that, with its default settings, for the input bias and the amplification, it is impossible to detect the fringe pattern clearly seen even with the naked eye. Fortunately, DT-2851 has potentiometers for manual adjustment for the input bias and the amplification. Even after adjusting these manually [41] and in the softwere, the fringes were still seen rather low in contrast. Part of the problem is that the CCD camera automatic gain control sets itself for the hot spot and then the comparatively faint fringes are hardly visible within the 8-bits data.

These advantages and disadvantages are in good agreement with Wyant's view [118] on scatter plate interferometry.

• Requirements for the ablation experiment

There are some aspects of the optical testing that the ablation experiment requires but which differs from those of the f/3 mirror testing.

- Unlike the OSL large optics shop, there is very limited space around the 1m polishing machine so it is impossible to accommodate Burch's configuration for the testing.
- It is to test a flat surface which does not naturally focus the reflected light as the f/3 concave does.
- The flat mirror under test is coated with Aluminium but transparent underneath the coating. The coating has to be removed to zero the reflectivity difference between the grooves and the rest of the flat surface. The f/3 concave mirror, made of Cervit, is opaque and has a higher reflectivity than the flat mirror.

• Optical test setup for the ablation experiment

With the first two items above in mind, the modified configuration that was implemented is presented in Figure 5.2, including the rest of the experiment setup.

The light of 632.8 *nm* from a He-Ne laser passes through the acetate de-speckle device and then the expander lens making it into a diverging beam. The beam is reflected 90° toward the first scatter plate S1 by a small reflector mirror. After the

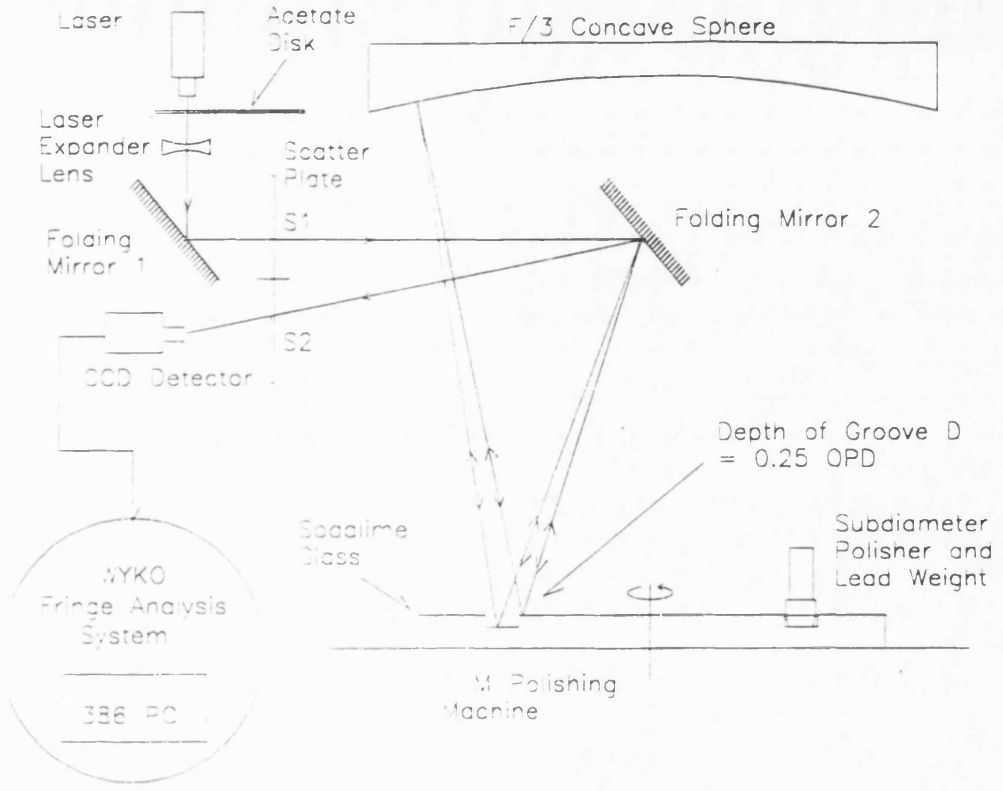

Figure 5.2: The ablation rate experiment setup including the modified configuration for scatter plate interferometry.

scatter plate S1, the scattered wavefront travels and hits a folding mirror, reflecting it to the test surface. The wavefront is again reflected toward the f/3 spherical concave mirror, producing the first set of optical path difference(OPD) between the groove surface and the adjacent-unpolished surface. The wavefront then hits the f/3 mirror surface, bouncing back to the test surface. This returning wavefront generates the second OPD when it is reflected by the test surface. It travels a very similar path back to the second scatter plate S2. The dark fringe pattern can then be observed by a detector i.e. the naked eye, photographic camera or CCD camera placed just after S2. The double OPD generation of this configuration is another difference from Burch's arrangement. It reduces the wedge factor from 0.5(Burch's configuration) to 0.25, meaning that 1λ OPD, i.e. a gap betweeen two fringes, corresponds to not two but four times the real height of a groove.

The fringe would be detected by the EEV CCD camera [30] and then analysed by the WYKO fringe analysis system that consists of the PC Vision 512-3-50 frame

grabber and DOS RTI software [119]. In fact, the WYKO system can detect the surface defect of down to $1/50\lambda$ (for Peak-to-Valley) when run with the phase shifting interferometry mode with the PZT aligner/translator from Burleigh Instrument [17]. But for the ablation experiment, the Video fringe analysis mode is good enough to determine the depth of the groove at reasonable accuracy if it is around $1/10-1/2\lambda$.

• Technical difficulties of using this test setup for the experiment

A number of difficulties were encountered when trying to acquire fringes on the flat mirror prior to polishing the grooves. They are briefly listed below, including the efforts made to cure the situations and to make it possible to use the configuration.

- An important condition of using interferometry for this experiment is that the fringes have to be aligned so that it crosses the grooves at a right angle. Otherwise, as their orientation becomes parallel to the grooves, the meniscus feature within the fringes representing the grooves slowly dies out. To analyse them would produce the totally wrong estimate about the depth, since they no longer represent the true feature of the grooves. To rotate the fringe for the alignment can be easily done once linear fringes are produced. However to control the fringe density in the image is very difficult.

- There is a great difficulty in handling the detector platform and the folding mirror to acquire observable fringes. Firstly, there is no stable platform for people to work. Users have to climb and work on a metal ladder and, up around the detector platform, there is not enough space for them to change their position. Secondly, there are too many reflecting surfaces i.e. 5 which alternates the orientation of the image. This makes it extremely confusing for even skilled optical technician to position the scatter plate and the folding mirror to acquire well-spaced straight fringes at the focus. As a result, it takes a considerable time, i.e. 2-3 hours, to recover the fringes, once it is lost for some reason. This reduces largely the efficiency of the testing.

- One of the problems with the optics available is that a too small area can be observed on the tested flat mirror. The observable area is just 2-3 times of the pitch in size and even then a low contrast fringe pattern appeared with a bright hot spot as a background, erasing almost half of the fringe in size at its centre. It results in a small fringe pattern of which size is comparable with

the width of the grooves, so there would be no observable features in fringe patterns caused by the grooves.

One of the reasons is that a detector is looking at a small area illuminated on the tested flat mirror via the folding flat mirror which is in fact an image of the folding flat mirror formed on the tested surface. Unfortunately, the size of the folding mirror cannot be increased freely because it also increases the blocked area on the f/3 concave by the folding mirror itself.

- Another fundamental problem is that, even with the aluminium coating of the tested flat mirror intact, the fringes are too low in contrast when observed with the CCD camera and acquired by the frame grabber. It is caused by
  - the inherent low contrast of the scatter plate interferometry
  - the high detection threshold and the low gain of the frame grabber

  This means that, after the grooves are made, a large difference in reflectivity between the groove and the rest of the mirror surface would affect the appearance of the fringe pattern. It could cause local errors in tracing the fringes so as in determining the depth of the grooves. In addition, if the coating is removed by using a corrosive chemical such as sodium hydroxide(NaOH), the overall reflectivity of the entire mirror surface decreases substantially, leaving just a small portion of the fringes near the hot spot, which is reduced in size, observable. Later, when the coating was removed, this was found to be the case, i.e. the overall brightness being greatly dimmed and there was no observable fringes left.

  In order to resolve this, several attempts were made as follows.

  - The WYKO DOS RTI software has a function called *'Gamma Function'* which controls the programmable gain amplifier and enhances image contrast. But, in practice, altering it to full range can only improve the contrast by the factor of about 2 which is not helpful.
  - A possibility was explored to build an external amplifier circuit between the CCD camera and the frame grabber [59]. However, the WYKO frame grabber has its own input control amplifier circuit which automatically

adjusts inputs to a predefined default range. This implies that, even if the external amplifier circuit alters the CCD output to the right level, it is readjusted back to the default range when entering the frame grabber. In this sense, there would be no use of the external amplifier circuit.

- Instead of losing the reflectivity from the tested flat mirror, it would be helpful if the f/3 concave is Al coated. Hence, the f/3 was Al-coated but it did not improve the contrast as much as the expected 10-20 times.
- Much of the laser power is lost due to the acetate de-speckle device. Several alternatives including tissue paper, tracing paper, white perspex, etc. have been tried but the acetate sheet appears to be the best choice [8].
- Brighter white light lamps were tried as alternative light sources. With a 50W white light lamp behind a pin hole, low contrast and faint fringes appears on a very small area near the reduced hot spot but larger area can be illuminated on the tested flat mirror than the 5 mW laser. No fringes are seen with a 150W white light lamp.
- A light guided diffuser is made according to Cullis *et al.* [21] to collect more laser light at the entrance and to more evenly emit it from the exit gate. Firstly it is experimented without Al coating over itself. It shows an even fainter image with highly localised illumination. It is found that there is a substantial leakage of the laser light through the cylinder wall of the diffuser. Although it is Al-coated, there is not much improvement but the leakage persists through the coating.

Despite the efforts made, the fringe contrast was not improved greatly so that the WYKO system was unable to properly trace and analyse them.

One last resort, that was not tried, would be to use a high power He-Ne laser such as 15-30 mW laser at the expense of a safety concern for operators. This was considered more and more attractive when testing the f/7 scaled secondary mirror of the Gemini telescopes is concerned. Using the scatter plate interferometry, the proposed method for the testing is to use a 45 inch meniscus lens in between the folding flat mirror and the secondary as shown in Fig. 5.3. The main disadvantage of this for light loss is that the final reflecting surface is not opaque, i.e. the mirror, but transparent, i.e. the lens. Therefore,

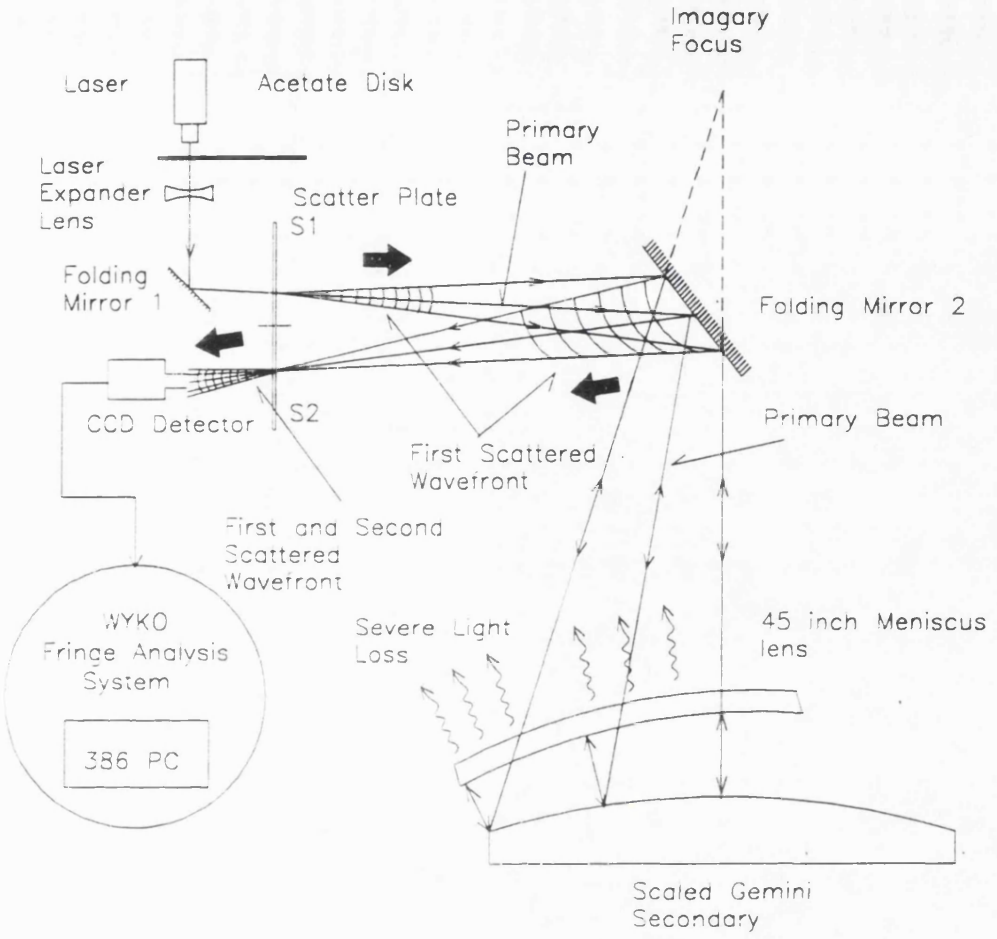

Figure 5.3: The proposed 'Modified Hindle Test' for testing the f/7 scaled secondary mirror of the Gemini telescopes, using scatter plate interferometry.

the overall light loss would be much more severe than the configuration for the ablation experiment. Hence, a high power laser would have to be used.

- The stability of fringe image is easily affected by change in environmental parameters such as air turbulence and vibration of the components involved. Unstable fringes would inevitably result in a larger error in fringe analysis. In particular, the air turbulence near the optical path is generated by the cooling fan of the PC and operator. This generates wavy movements of the fringe as well as high frequency ripples in the fringes. This can be improved with polythene cutain surrounding the optical path. The stability would become very much crucial if the phase shift mode is to be used.

• Conclusion and the reasons why this test method was not used

Thus, it can be concluded that the scatter plate interferometry with the WYKO fringe analysis system was not appropriate for the ablation experiment due to the small detection area combined with low light throughput. The further development of this method for testing the scaled Gemini secondary can be experimented only with a new high power laser.

5.2.2.2 Equal Thickness Interferometer

Pending the high power laser, since there was limited time and budget, it was decided to develop an alternative test which does not cause the difficulties described above. One of the simplest methods for testing the flatness of a glass surfaces would be to put an absolute flat on top of the glass surface to be examined. When a broad light source illuminates the glasses, a set of fringes appears, representing a height topography of the space gap, i.e. normally thin air film between the two surfaces. These fringes are called *'equal thickness fringes'* or often *'Fizeau fringes'*. Its theory and a schematic diagram of the experiment setup are well described by Hecht (p 351) [49]

Because of the ease in use, this method has been popularly used to test various small optical components. The most critical component for this is the absolute flat of right size. In most cases, this has not been a problem since the optical components to be tested are small and thus requires a small absolute flat. But, for the ablation experiment, it has to be at least greater than $15cm \times 10cm$ in size because of the pitch size of about 5-6 cm in diameter. Fortunately, OSL has two $\frac{\lambda}{10}$ flats of $30cm \times 20cm \times 2.5cm$. Therefore, the proposed method is to put an absolute flat on top of the grooves on the flat mirror to be tested. Then a set of meniscus fringes would appear when they are illuminated with a broad and bright white light. The fringes can of course have chromatic aberration, but it causes no serious problems in this case, as long as they are observable with the CCD camera.

• Advantages of this method for the ablation experiments

Just for the ablation experiment, this has a number of advantages over the suggested scatter plate interferometry setup as described below.

- It has a negligible optical path compared with the scatter plate interferometry

for generating fringes. Therefore, the fringes are much more stable against vibration of the components involved and the air turbulence along the optical path. This would contribute greatly to reducing the analysis errors.

- All the components used are much smaller and therefore the entire set up is smaller, which provides ease of accessibility from the ground. This would certainly increase the efficiency of testing.

- There is no need for adjusting the optical components for focusing, to acquire fringes. The size of the fringe image can be easily adjusted by altering the detector position and the focal ratio of the camera lens.

- The orientation of an entire image on detection frame can also be made with the ease of rotating the detector assembly.

- The orientation of the fringes with respect to the grooves can be easily made to 90°, by adjusting the thickness distribution of the air film. The fringe density in the image and therefore the fringe thickness can also be easily controlled by applying the same method.

- Since the method allows the use of an extended light source, a powerful lamp, e.g. 150 W mercury lamp, can be used without the aid of any auxiliary optics. Therefore there would be a substantial decrease in light loss. This would contribute enormously to increasing the brightness of the image, enhancing the contrast of the fringe image.

• Two set-ups of this testing method

Two setups were experimented with this method.

Setup with tilted detector angle:

Firstly, as shown with case (A) in Figure 5.4, a cardboard reflector covered with a section of large white drawing paper is behind the light source, which is a 30 W low pressure sodium lamp. The CCD camera looks at the absolute flat at about 45° tilted. An additional section of white drawing paper was inserted underneath the flat mirror to be tested in an attempt to increase the image brightness. This causes a number of problems.

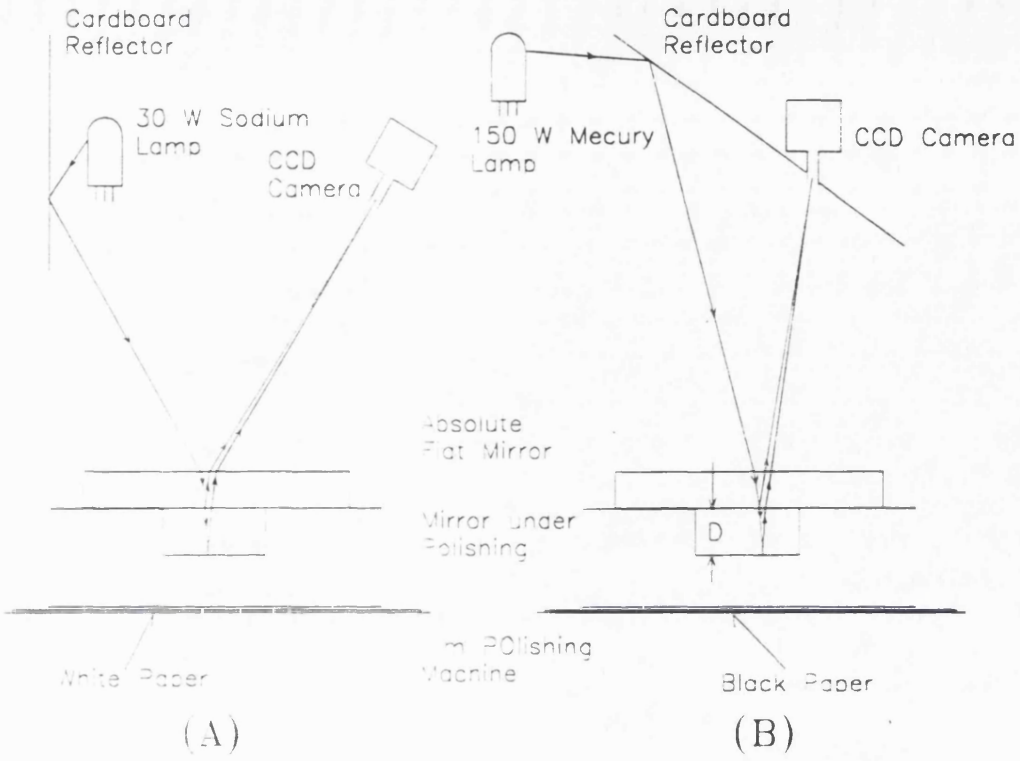

Figure 5.4: Fiezou fringe set-ups with the detector angle of about 45° and 0°

- The overall brightness is not high enough for the fringes to be traced and analysed.
- The CCD camera picks up the image of the lamp, confusing the surrounding fringes.
- A double crossed pattern of fringes is caused due to another OPD generation made at the gap between the flat mirror to be tested and the white drawing paper underneath it.
- It produces more prominent fringes nearer to the light source, leaving any images including the fringes impossible to observe at the far side of the absolute flat.

Setup with zero detector angle:

Secondly, as seen with the case (B) in Fig. 5.4, the sodium lamp is replaced with a

150 W mercury lamp. The cardboard reflector is placed in front of the light source with the tilt angle of about 45°. This is to direct the light toward the absolute flat directly from above. The black drawing paper was used instead of the white paper underneath the flat mirror to be tested. The CCD camera is set to look at the absolute flat directly from above, through a hole on the cardboard reflector. With this set up, the problems above disappeared. A minor problem was the saturation of the CCD image but was easily cured by moving the lamp away along the optical path. The fringes acquired with this setup had enough contrast to be traced and analysed by the WYKO fringe analysis system.

Choice of test setup:

Therefore, it was decided to use this setup, which is slightly modified from that of Hecht (p 351 [49]). It is to use the cardboard reflector instead of a large beam splitter which would otherwise have to be procured separately. Finally, for this interferometry, the wedge factor becomes 0.5 which is the default setting of the DOS RTI software.

5.2.3 Measurements, Data Reduction and Results

• **Measurements**

Since the ablation rate of the soda lime glass was not known, it was desirable to start polishing with 0.1 psi, this being the lowest limit of the polishing pressure that we understand Grubb-Parson typically used. An untrimmed pitch facet of about 5.3 cm in diameter and 154 gm in weight was used to generate a groove at the radius of 9.3 cm. The fresh abrasive used was the mixture of water (500 ml) and cerium oxide (80 gm) (hereafter called 'thin abrasive'). The glass was rotated to 1000 revolutions and the fringe was examined at 50, 150, 300, 500 and 1000 revolutions. No sign of polishing was observed at all and the polisher seemed to have floated over the abrasive slurry.

Hence, the polishing was re-run at the same radius with the new set of parameters below.

- polishing pressure: 0.61 psi (i.e. 682 gmf)
- pitch: trimmed pitch of about 4.5 cm in diameter

- abrasive: mixture of water (200 ml) and cerium oxide (100 gm) (hereafter called 'thick abrasive')

When the total revolution was 400, it was seen a shallow feature in the fringe, indicating a groove being generated. At the revolution of 500, there was a distinctive sign of the groove. The last 100 revolutions seemed to ablate much more than the previous 400 revolutions did. This gave rise to the suspicion that the bulk of the material inside the glass might be different in characteristics from the polished surface e.g. a non-uniformity in glass density or a hard 'skin'.

Keeping the polishing parameters unchanged, the grooves were made at the radii of 9.3, 16.7, 23.2 and 33 cm. At each radius, 3-5 fringe images were stored with the revolution of 500, 700 and 800. After completing 4 grooves, the pressure was altered on the fourth groove, polishing to 500 revolutions each with three different weights i.e. 334, 502 and 872 gm. This was to observe the ablation rate with different polishing pressures. As an example, a photograph of the fringe file TB800.VID is presented in Figures 5.5 and 5.6, showing the meniscus feature of the first three grooves along the fringes.

Unexpected features found during the measurements:

In doing this, a number of unexpected features appeared as follows.

- **Pitch:**

  The pitch area in contact with the glass is smaller than its actual size. In addition, it is not exactly circular, but regarded as a perfect circle for data reduction. The equivalent diameter of the circle is obtained by few measurements using a vernier calipers.

  Over the period of making the four grooves, the pitch grows in size (like a mushroom) due to the weight of about 682 gm. It started with about 4.5 cm in diameter when the first groove was about to be generated. It was then changed to about 4.9 cm when the second groove was completed. Since then, it was frequently checked and recorded. This is presented in Figure 5.7 which clearly shows the growth but, at the same time, it is rather premature to precisely determine the growth curve. Hence, the best way is to take average to estimate the responsible sizes of the pitches on the four grooves.

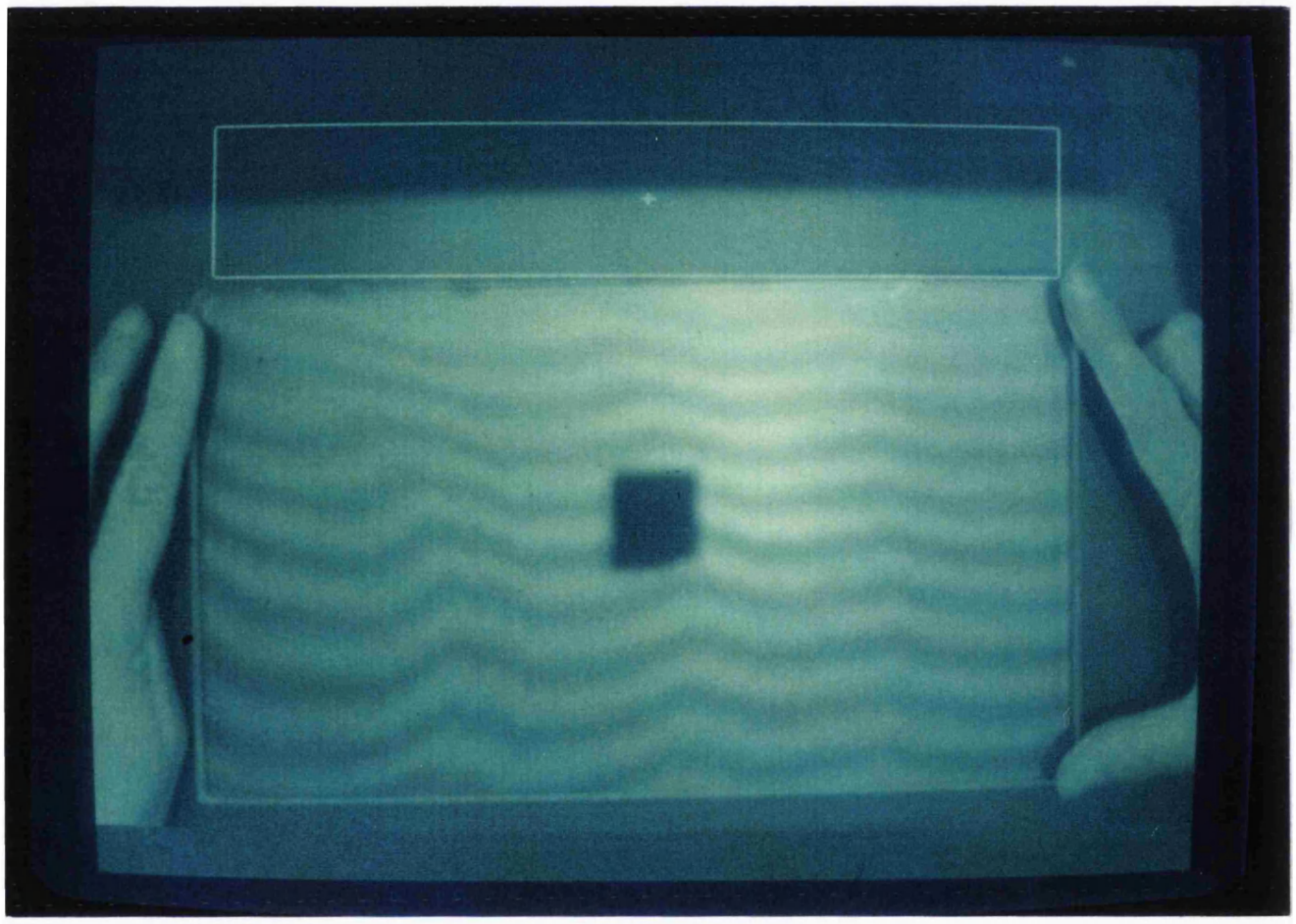

Figure 5.5: Photograph of fringe file TB800.VID, showing the first three grooves

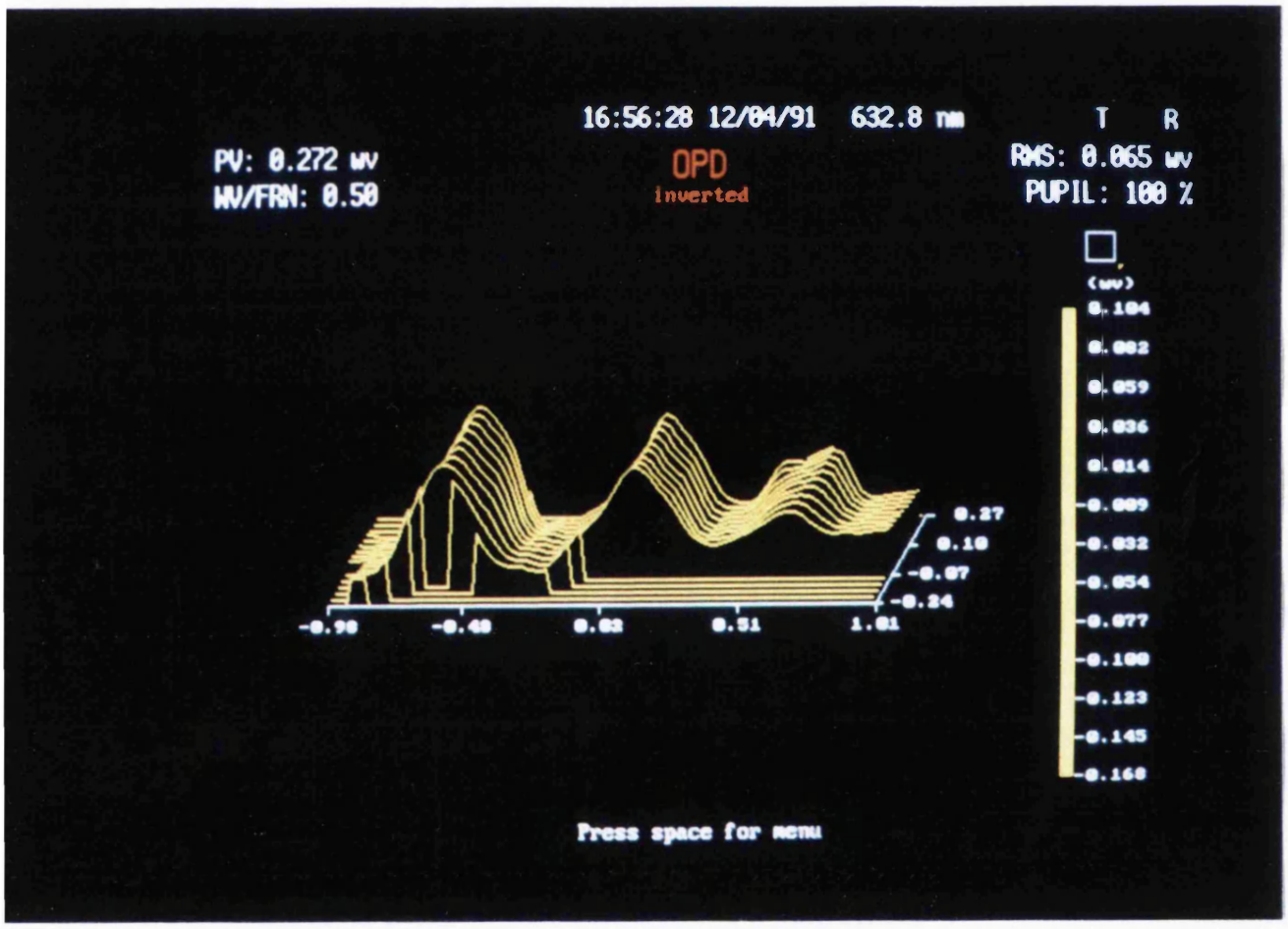

Figure 5.6: Resulting OPD display of the first three grooves

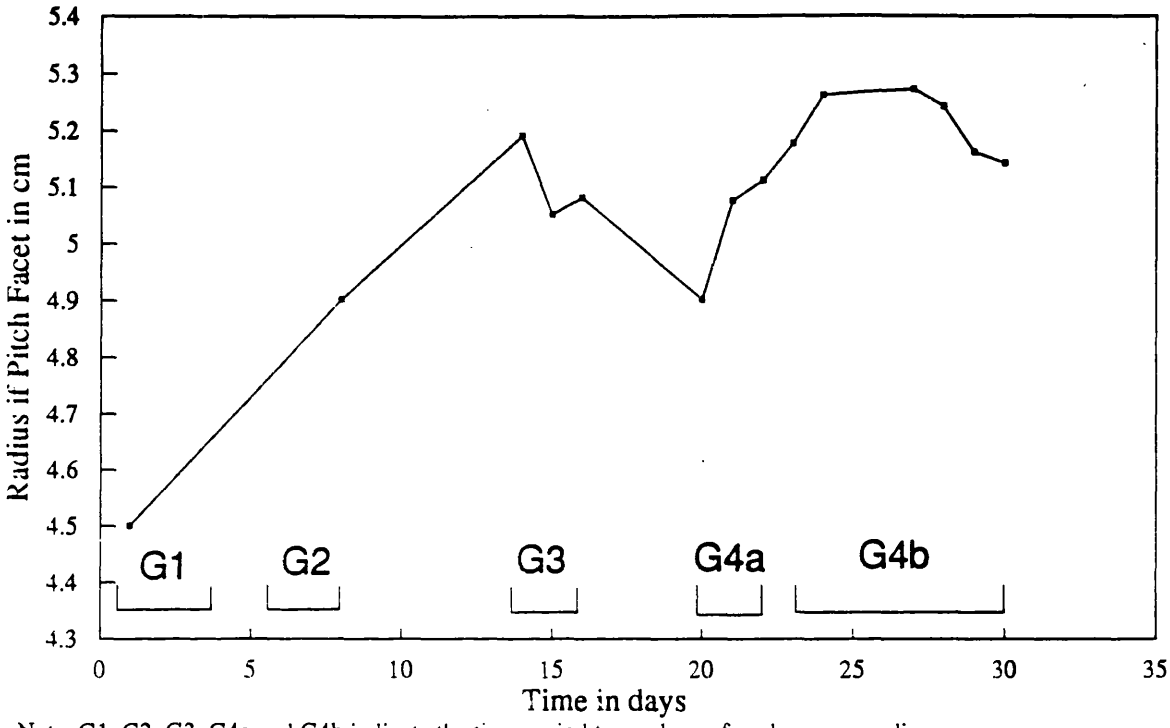

Note: G1, G2, G3, G4a and G4b indicate the time period to produce of each corresponding groove. The weight varies heavior and lighter for G4b whilst the constant weigt is used through G1 to G4a.

Figure 5.7: Growth of the pitch in size

When the polishing on the fourth groove was finished with the weight of 872 gm, the pitch surface developed a number of wavy-circular ripples transverse to the direction of the rotation. Few line scratches and broken areas were also found at the outskirt of the pitch as well.

This might be explained by the pitch used having a critical pressure above which its elasticity is weaker than its fluidity. The 872 gm weight might have produced localised pressures comparable to that. Then the friction energy combined with the enhanced fluidity can not only generate a surface flow of the pitch but, at the same time, enlarge the surface area of the pitch. The surface area would grow until the pressure comes down to a stable level. The surface flow could be stabilised in forming the wavy-circular ripples by an interaction with the abrasive slurry and the characteristics of the sliding motions. This theory can suggest the transverse wavy-circular ripples and the rapid growth of the pitch surface as its evidence.

Fortunately, the new size of the pitch surface was recorded and the ripples, the scratches and the broken area occupy just a small fraction of the total pitch

area. Therefore, it can be assumed that this does not affect the calculation of the polishing pressure.

When the ablation experiment was completed, the pitch seemed harder than it was before, i.e. the beginning of the experiment. This can be explained by the continuous evaporation of the pitch volatiles over the period. The hardening would results in an alteration of the friction coefficient and therefore the ablation rate over the period. However, there was, unfortunately, no way to avoid this, unless a fresh pitch was made and used for every polishing run. Thus, for the data reduction, it has reluctantly to be assumed that the hardening does not affect the friction coefficient. Several places on the outskirts of the pitch become broken as the experiment moved toward the end.

- **Abrasive slurry:**

  The water in the thick abrasive evaporates gradually as the polishing continues for the experiments, altering the friction conditions on the sliding surfaces. Two aspects of this were observed.

  Firstly, short term effect, a stable condition of an abrasive film applied for a polishing run can only last a few minutes to a few tens of minutes. The low humidity of about 30-35 % around the 1 m polishing machine and the frictional heating contribute highly to the rapid evaporation of the water from the abrasive. It may cause an instability condition for the abrasive film. Another cause of the instability may be the low surface tension inherent to the thick abrasive film. Once it runs away from the groove, mainly by the polishing pressure, it hardly returns back to the groove. This requires frequent resupplies of the abrasive to the groove being polished to maintain the stable film condition. The instability would certainly cause non-uniform friction and hence non-uniform ablation rates over the time span of a polishing run. The best effort was made for maintaining the stability during the polishings.

  Secondly, long term effect, when a fresh abrasive is left in a plastic container, a substantial amount of water evaporates within the next 5-7 days. The old abrasive would then have different friction coefficients and behaviours, from the fresh one, in polishing. It has never been a problem for the polishing conducted in the OSL large optics shop because a fresh abrasive is always

used for each new polishing. For the proposed experiments, a fresh abrasive is made and used at every 5-7 days.

- **Polishing behaviours:**

  Although an attempt at stabilising the pitch position is made with the three holding strings, there still exists oscillations and sticking of the polisher during the polishing. In most cases, they develop unpredictably, but with one condition for sure that the polisher is exposed to a sudden change in the abrasive film state. Examples include changes in film flatness, thickness, water to cerium oxide ratio, etc. and the abrasive being dried up.

  Stable polishing with no oscillation and sticking was very difficult to maintain. It starts unpredictably as the unstable polishing does and lasts for few minutes to 1-2 hours in polishing. No method of controlling instability was found despite considerable experimentation.

• Data reduction

Among many fringe files collected, TB800.VID, TC800.VID, FOC800.VID and FOD800.VI were chosen to be analysed for the ablation coefficient-velocity relation. The first two fringe files cover the first three out of the four grooves. The second two fringe files include the last three out of the four grooves. This means that the two grooves in the middle can be overlapped in analysis to make the comparison of the 4 depths consistent. For the ablation-polishing pressure relation, FOC800.VID, NE1B500.VID, NE2D500.VID and NE3D500.VID files were used in fringe analysis. The process of obtaining the depths of the grooves using the WYKO DOS/RTI software is as follows

- the fringes are traced and, if parts of the fringe tracing is made incorrectly, the FRINGE EDITION technique is used to correct it.

- Then, they are analysed as it appears. The resulting OPD data contain the depth of the grooves combined with the thickness of the air film which has to be removed. This is stored as the OPD file 1.

- The same fringes are again used and traced. The FRINGE EDITION technique is intensively used to edit and to remove the meniscus feature of the fringe, making them smoother.

- Then, they are analysed as it appears. The resulting OPD data represents just the thickness of the air film. It is stored as the OPD file 2.
- Finally, the OPD file 1 is subtracted from the OPD file 2, meaning that the air film thickness is removed, to generate an OPD data purely representing the depths of the grooves.
- The resulting OPD data is stored as the OPD file 3. This is indeed the *total integrated ablation at a location on the grooove.*
- The DATA LIST function is applied to the OPD file 3 to window and to separate the fringe area from the rest of the analysed area.
- Then, the OPD data of the separated area is exported to a text file for further data analysis outside the DOS/RTI software.

An example of the analysed OPD display is shown in Plate 3. The detailed calculation for the sliding velocity, polishing pressure and the integrated polishing time is described in Appendix C.

• Results of the ablation experiment

The analysis results are tabulated in Table. 5.1.

Looking at the following equation, if Preston's ablation theory were true, then there would be a single value of C with a reasonable error, for a given optical material and polishing conditions. If C either increases or decreases with P or V, it should no longer be regarded as valid theory.

$$W = CPV \tag{5.1}$$

where

W = instant ablation rate in cm/sec,

C = ablation rate coefficient in $cm^2/dyne$,

P = polishing pressure in $dyne/cm^2$,

V = sliding velocity in cm/sec

The results of the experiment suggest, firstly, that the average ablation coefficient is about $0.89(\pm 0.4\sigma) \times 10^{-13} cm^2/dyne$. In 1991, Brown has suggested about 2×10^{-13}

(A) Ablation Rate Coefficient vs Sliding Velocity

Groove	Radius cm	Pressure dyne/cm^2	Velocity cm/sec	Polishing Time sec	Groove Depth x10^{-8}cm	Ablation Rate Coeff. x10^{-13}cm	Ablation Coeff. Err Std x10^{-13}cm
1	9.3	42074.6	2.16	1667.5	1586.4	1.045	0.075
2	16.7	35485.6	3.89	1009.6	1108.3	0.796	0.039
3	23.2	32757.0	5.40	756.1	666.2	0.498	0.093
4	33.0	33809.4	7.68	523.1	903.3	0.665	0.132

(B) Ablation Rate Coefficient vs Polishing Pressure

Groove	Radius cm	Pressure dyne/cm^2	Velocity cm/sec	Polishing Time sec	Groove Depth x10^{-8}cm	Ablation Rate Coeff. x10^{-13}cm	Ablation Coeff. Err Std. x10^{-13}cm
4	33.0	39979.3	7.68	340.0	1083.1	1.038	0.268
4	33.0	33809.4	7.68	523.1	794.2	0.585	0.156
4	33.0	22666.9	7.68	342.6	478.8	0.803	0.369
4	33.0	15793.6	7.68	334.7	741.4	1.826	0.811

Table 5.1: The results of fringe analysis, showing the depths of the 4 grooves and the ablation rates with sliding velocity and fixed pressure(e.g. case A) and with pressure and fixed sliding velocity(e.g. case B).

and 5×10^{-13} for the fused silica and the zerodur ceramic glass respectably [13]. In a separate experiment, NOAO has found about $200\mu m/hr.psi.m.sec^{-1}$ i.e. $8 \times 10^{-13} cm^2/dyne$ [113]. Thus all the investigations are roughly in the same order of magnitude, i.e. 10^{-13}, as the ablation rate. It implies that the ablation experiment described in this Chapter is conducted with as much accuracy as the other two experiments. However, those other two experiments show the ablation coefficients about 3-11 times larger than that obtained here. An attempt to explain this discrepancy is described in Section 5.5

Secondly, in general, the ablation coefficient seems to decrease with the sliding velocity. It is not linear but rather more complicated. It decreases monotonically as the sliding velocity increases up to 5.3 cm/sec at the third groove. After that, it increases with the velocity at the fourth groove. There are several factors to be considered to validate this.

- The eye estimation on the fringe image shows the fourth groove deeper than the third groove, meaning that the integrated ablation on the fourth groove is

more than that on the third groove. This tendency seems to be reflected again in the ablation coefficient-sliding velocity relationship. This is in support of the fact that the relationship is a true feature.

- The polishing pressure on the fourth groove is slightly higher than that on the third groove whilst the integrated length of contact on the fourth groove is less than that on the third groove. However, the estimation of the polishing pressure and the integrated contacted length include a rather large error since it depends on the size of the pitch polisher, which was impossible to precisely determine. The error is estimated as only about $\pm 12\%(\sigma)$ on average. This supports the idea that the observed tendency of decrease in ablation coefficient with increased velocity may be a true feature, although it is contradictory to the original Preston's theory.

Thirdly, the C-V measurement gives the averaged C of $0.74(\pm 0.18\sigma) \times 10^{-13}$ whereas that of the C-P measurement is $0.92(\pm 0.27\sigma) \times 10^{-13}$. The fact that the separate two measurement series give similar averaged ablation coefficients gives rise in the reliability in controlling polishing variables throughout the measurements. Fourthly, as the polishing pressure increases, the ablation coefficient seems to decrease. This seems, again, contrary to Preston's theory. However, the large error of about $\pm 37\%(\sigma)$, on average, indicates that the tendency may well be not trustworthy. Thus, the inconclusive C-P relation found can support neither Preston's theory nor any possibility for alternatives.

• Concluding remarks of the ablation experiment

Having considered all these, the only way to validate it seems to be directly measuring the friction coefficient on those 4 grooves. It is quite natural to believe that the ablation coefficient is linearly proportional to the friction coefficient. This led to another experiment for direct measurement of the friction coefficient described in Section 5.3. Further discussion presented in Section 5.5 combines the implications of the ablation experiment with that of the friction experiment.

• Some features and errors of the WYKO fringe analysis system

A number of features and errors of the WYKO fringe analysis system were found during the fringe analysis. They were either properly dealt with in the analysis or reported to the supplier for repair. Some examples are listed below.

- At least 3-4 fringes have to be used to produce reliable analysis and, of them, 1 fringe has to cut across the groove to be analysed at the right angle.
- The ZERNIKE POLYNOMIAL fitting for the acquired fringes does result in topographies of saddle shape with no groove features. It is highly un-realistic. The analysis using the LINEAR POLYNOMIAL or SPLINE fittings show clearly the grooves within the analysis window.
- Even though the ANALYSIS MASK is applied, The DATA LIST function generates a set of data mixed, with a large array of (0,0) for the area outside the mask. This makes the data reduction very lengthy and inefficient.
- It can not trace and analyse diagonal fringes. This is why the fringe image has to be either vertical or horizontal.
- When the fringes are edited with the SQ/REC FIDUCIAL option, the MOVE command returns automatically to the Main Menu. This error is repaired with the DOS/RTI Version 4.26.
- Although an ELLIPTICAL FIDUCIAL is set, an analysis OPD display still looks like a circle. This is not used.

5.3 Friction Coefficient

5.3.1 Experiment Programme

This experiment is aimed

- to validate the ablation experiment.
- to generate friction data, to know how the ablation is linked to the friction, e.g. Is it proportional to the friction ?
- to investigate how the friction coefficient in polishing is related to other parameters such as pressure, sliding velocity, water to cerium oxide ratio for the abrasive.

- to know how the friction behaves with single supply of the abrasive liquid in polishing.

The results would be very helpful in controlling the polishing processes, whether they are active or passive.

The same pitch polisher would be held by the three cotton strings roughly angled 120° to each other on the glass surface. The central strings should be linked to a force sensor fixed to a reference point and have to be tangent to the circular grooves. The force sensor would then be able to measure a pulling force, i.e. the friction, when the glass is rotated away. The other two strings function to minimise the transverse oscillation of the polisher when the glass is rotated. The polishing parameters would be altered to cover its subset used for the ablation experiment as follows:

- Weight(gm): 154.11, 344.01, 519.99, 697.91, 888.73
- Radius(cm): 10, 12.8, 16.7, 19, 22, 27.7, 32, 38
- Abrasive(gm:ml): thin i.e. 80:500, thick i.e. 100:200

5.3.2 Apparatus

The key issue for setting up the apparatus was what kind of force sensor to use. The two possibilities explored are described in this subsection. The set up with the prototype load cell 2 was chosen for the reason described below.

5.3.2.1 Use of A Spring Balance Force Sensor

A home-made spring balance was tried, as a friction sensor, comprising tension spring, guide and graduated ruler. This is depicted in Figure 5.8.

A preliminary measurement for the friction with the thin abrasive is made by simply pulling a polisher of 230.12 gmf, in weight, on the glass, using a commercial spring balance. It showed a friction coefficient of about 0.44. This means that the total friction to be measured is less than half of the weight so that an ideal spring constant would correspond to 250-260 mm for about 450 gmf(about half of the maximum weight of 888 gmf). The measurement error could then be expected to be about ± 1

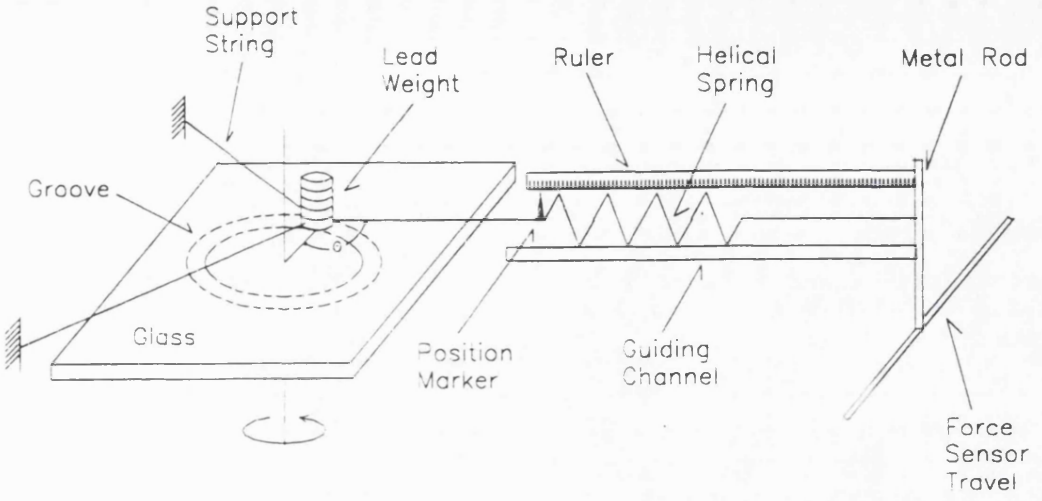

Figure 5.8: The apparatus using a spring balance force sensor.

mm, i.e. about ±1.8 gmf (±0.3 % of the total range), which is satisfactory for this experiment. The spring chosen had the spring constant of 1.7 gmf/mm.

However, when the polishing started with this set up, transverse and longitudinal oscillations developed in the polisher that were rather high in magnitude. The problem was that the excessive oscillation in longitude is caused by the weak spring constant combined with the different spring constants of the 2 other cotton strings. When the longitudinal oscillation become large, the spring tends to be bent very easily under transverse components of any external forces. This made measurements for the friction virtually impossible. It is mainly due to the low spring constant, but to increase it is not a solution either. With a higher spring constant, a more accurate ruler needs to be used and a smaller oscillation would produce the same level of error in measurement. For this reason, this apparatus was not used.

5.3.2.2 Use of The Prototype Load Cell 2

To use the prototype load cell 2 (decribed in Chapter 4) is more advantageous than the spring balance force sensor. It has the spring constant enormously greater than that of the spring balance. Its deflection is smaller than 1 micron under the force of about 500 gmf. Therefore, there would be virtually no longitudinal oscillation when polishing. This again helps greatly to reduce the transverse oscillation induced by it. Keeping the transverse oscillation down to an acceptable level can be achieved

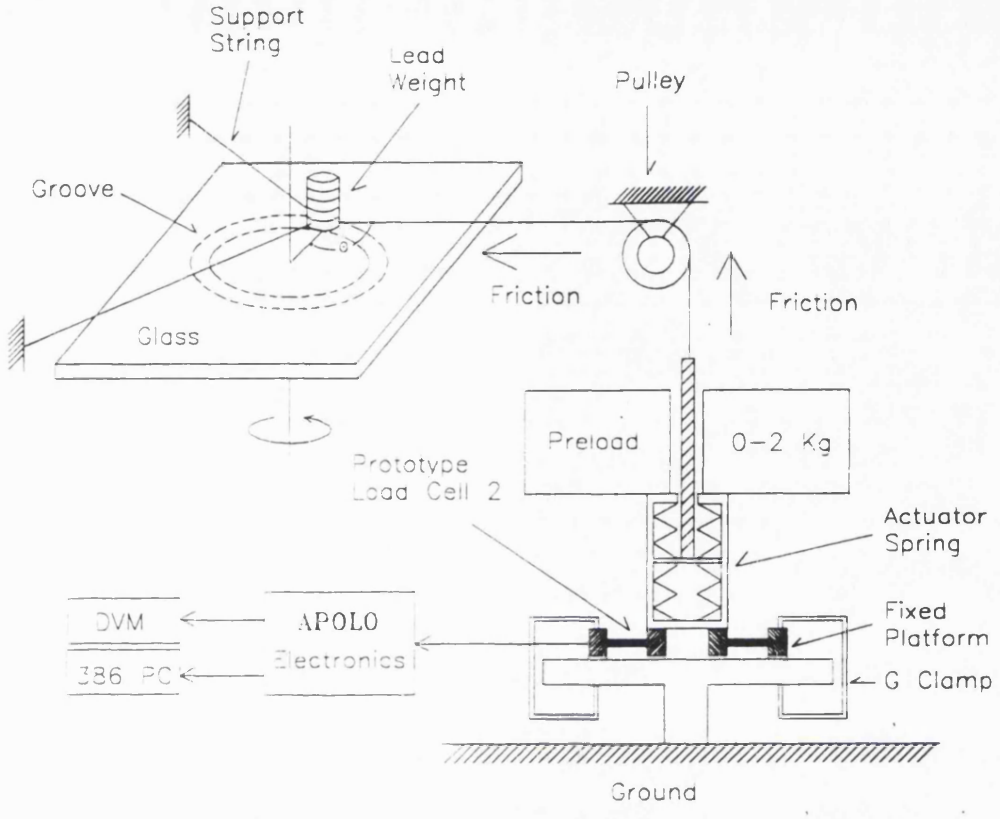

Figure 5.9: The apparatus using the prototype load cell 2.

by tightening the two side strings, with an appropriate level of tension.

The apparatus using the prototype load cell 2 is shown in Figure 5.9. A pulley is used to direct the friction in the XY plane to a Z axis force. The load cell is clamped to a fixed structure and the weight of about 2 kg is placed to preload it since it is a compressive load cell. Then the friction acts to reduces the load given to the load cell.

The APOLO electronics amplifies the load cell signal which is then directly read with a DVM. A preliminary measurement with the DVM gave the resolution of about 4.4 gmf which is close to about 1 % of the friction range to be measured. The A/D conversion using APOLO resulted in the resolution of about 18 gmf which is about 4 % of the friction range so it is 4 times worse than the DVM reading. Hence the DVM reading would be a better way for this experiment.

5.3.3 Measurement, Data Reduction and Results

• Measurement

For the friction coefficient, the measurement was made with the following sequence:

1. Find the centre of rotation and place the pitch to a position where the friction becomes a tangential force i.e. $\theta = 90^o$.
2. Tighten the two strings(Sa and Sb) while holding the pitch.
3. Position the pulley-load cell assembly to maintain $\theta = 90^o$ and then tighten the third string Sc through the pulley with $\pi = 90^o$ with the load cell.
4. Calibrate the load cell by cycling 4-5 times the weight on it from 0 to 2 kg with no load on the pitch and no tension on Sc.
5. Measure the friction by cycling 4-5 times the weight on the pitch from 154.11 to 888.73 gmf.
6. Repeat the previous two items 4-5 times and average the results.
7. The first and last measurements should always be the re-calibration for the load cell.
8. Repeat the sequence above for the other positions suggested earlier.
9. Repeat the steps above for another abrasive.

The way that the signal is dealt with was that

- the behaviour of the pitch and the signal on DVM are continuously monitored during polishing.
- the signal is read and stored only when
  - it is very stable for at least 10-15 seconds i.e. no oscillation of the pitch observed
  - it shows rapid fluctuation but its overall stability is well maintained for at least 10-15 seconds (the fluctuation amplitude is within ± 0.05 V due to small scale oscillations of the pitch)

For polishing at a given radius, 4-5 friction data sets are collected, each of which includes again 4-5 measurements of cycles with 5 weights. A data set takes 10-20 minutes to be completed. 5-6 calibration data sets are collected, each of which includes again 5-6 measurements of cycles with 5 weights. A calibration data set takes 2-4 minutes to be completed.

• Data reduction

The data reduction was made as below.

1. average the 5-6 consecutive measurements for one calibration data set and take the linear regression on the averaged calibration data
2. repeat it for all the calibration data sets
3. average the 5-6 consecutive measurements for one friction data set
4. average the results of the linear regression for the 2 consecutive calibrations that embraces a friction data set (It is not worth plotting the 5-6 results of linear regressions against time and reading values to know more precisely constants and coefficients at a given time.)
5. apply the averaged friction data to the resulting calibration curves
6. subtract the calibrated friction data from the Y intersections of the averaged calibrations i.e. zero levels of the calibration data to know the real friction
7. average the real friction data and estimate error.

• Results

The results are presented in Figure 5.10 and Figure 5.11, that show

- the friction coefficient increases as the normal load increases. There is shown some evidence for a non-linear increase of the friction coefficient with the normal load.
- A large standard deviation is observed in the individual and averaged friction coefficients. There is no doubt that some error originates from the experiment set up and the way in which it is carried out, including the control of polishing

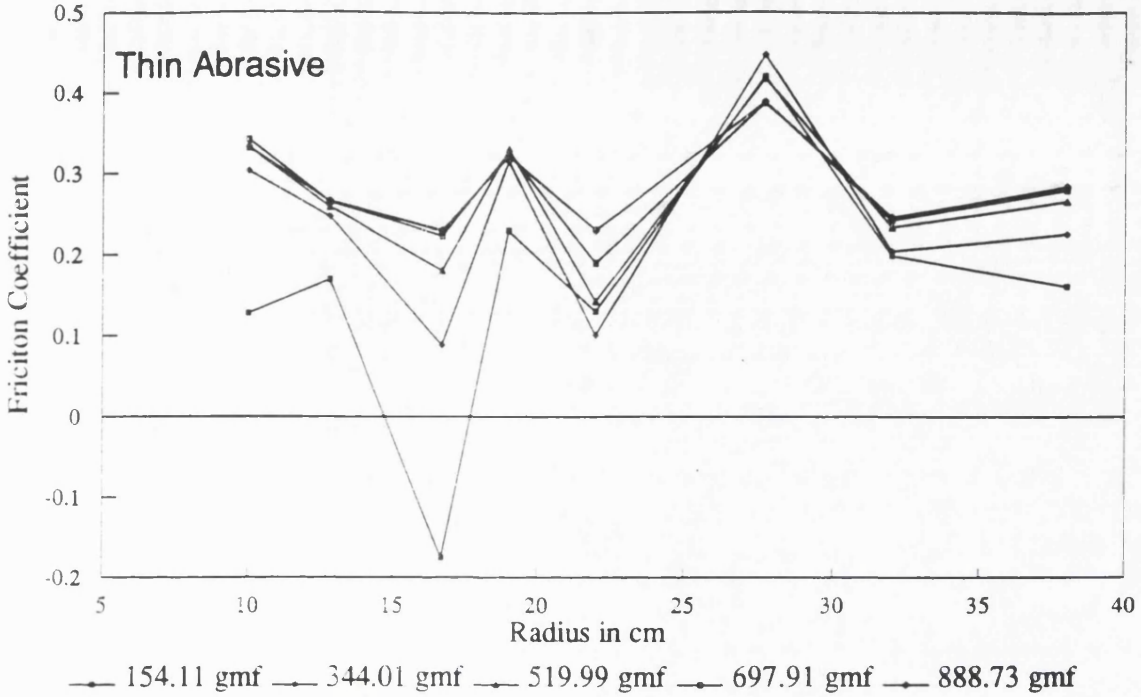

Note: The radius is equivalent to the sliding velocity.

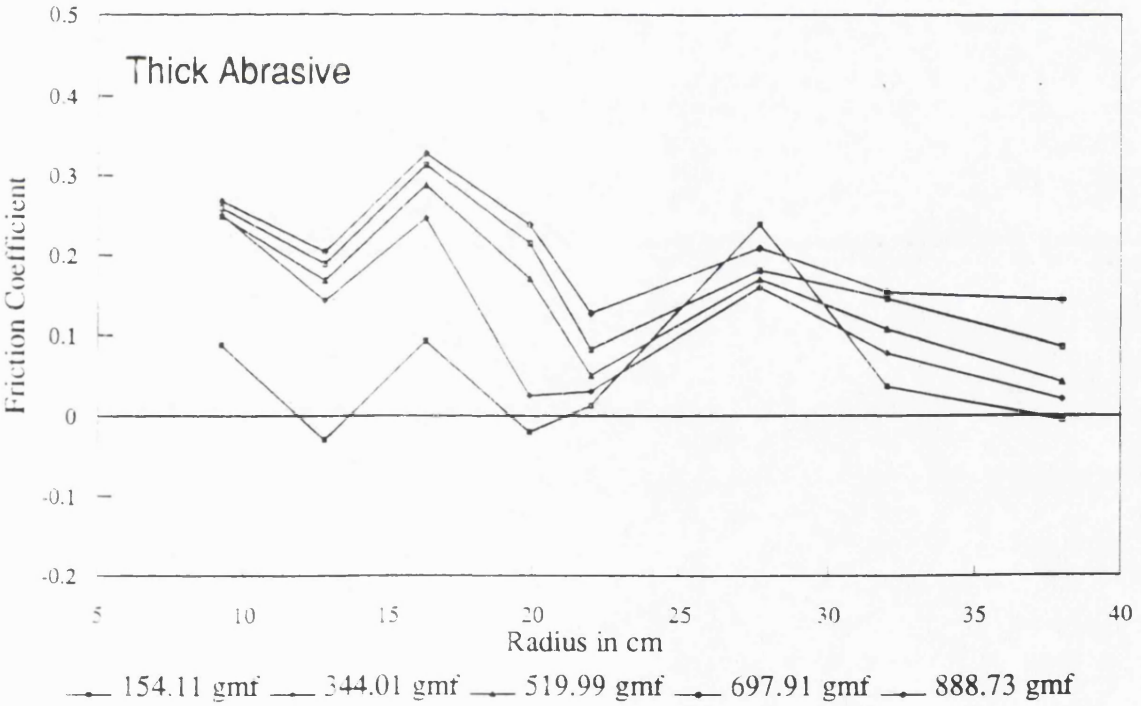

Note: The radius is equivalent to the sliding velocity.

Figure 5.10: Friction coefficients with different loads against sliding velocity for the thin and thick abrasive.

variables. However, it is believed that the undeterministic nature of polishing itself is responsible for the most of it.

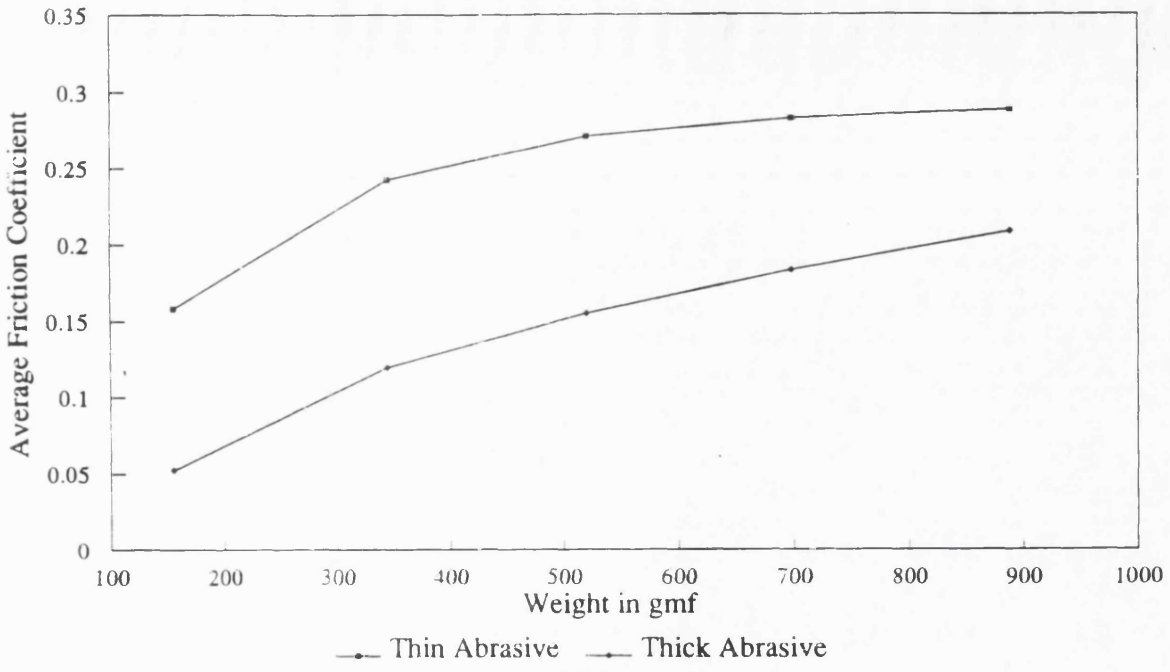

Note: The friction coefficient is averaged over the range of sliding velocity.
This graph shows a non-linear increase of the friction coefficient with the weight i.e. polishing pressure.

Figure 5.11: Average friction coefficient over the sliding velocity against different load

- as the velocity increases, it remains constant for the thin abrasive but decreases for the thick abrasive.
- in overall, it decreases as the water to curriumoxide ratio decreases.

• Additional measurement for friction stability

For the information of how friction behaves with a supply of the abrasives, the pitch polisher with the weight of 682 gmf was left as it polishes until the abrasive is almost dried out and the naked glass surface is about to appear. This information would be particularly helpful to know

- how long a supply of the abrasives lasted
- how well the frictional stability was maintained

in polishing for the ablation experiment. The friction signal was continuously monitored, read and stored, every 1 minute. Those experiments were made every time, after the friction measurements, for each groove on which the ablation rates were

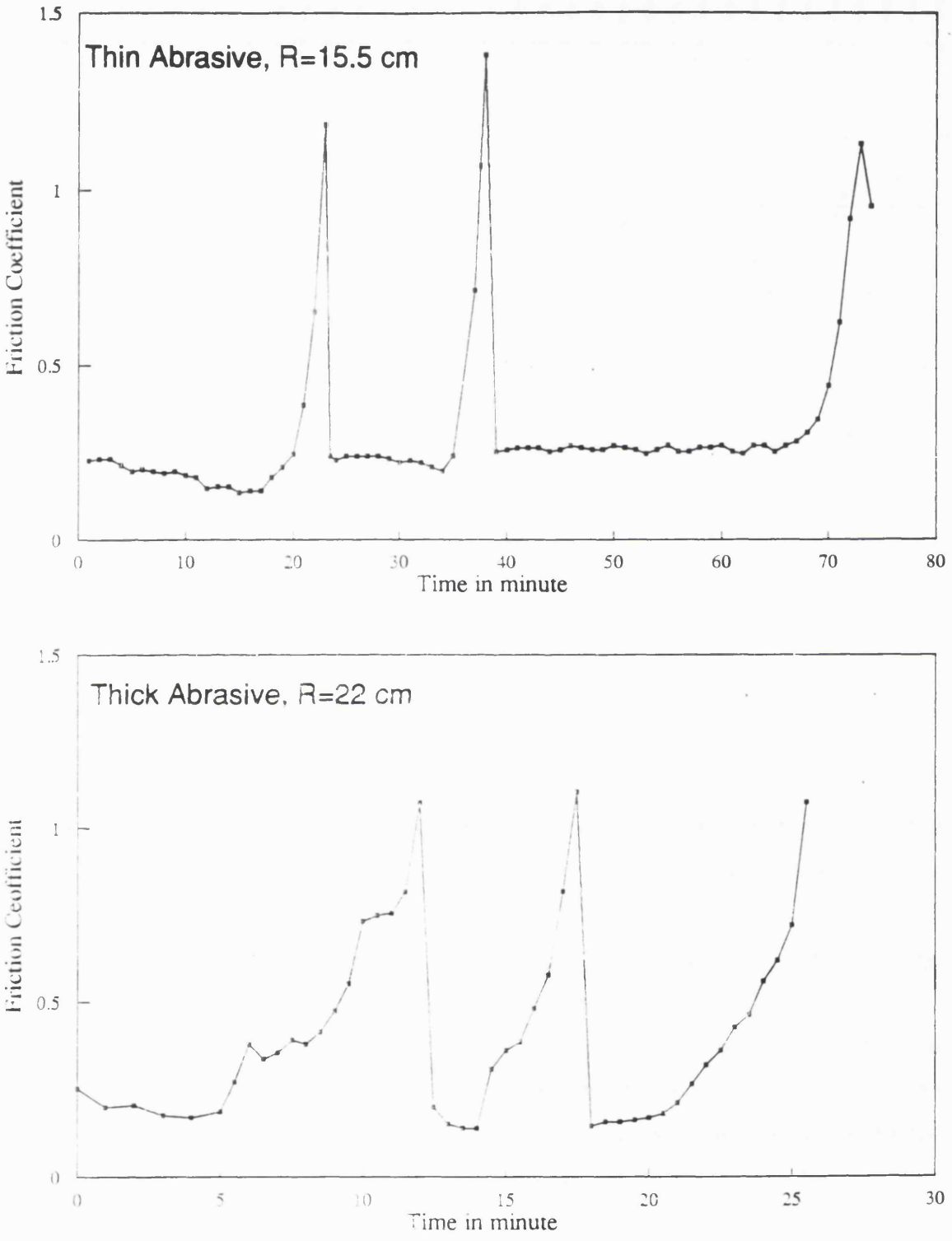

Figure 5.12: Examples of the friction stability with time for the two abrasives

measured. The calibrations were made before and after every measurement. Figure 5.12 shows an example of the friction signal plotted against time.

Thin Abrasive		Thick Abrasive	
Radius in cm	Friction Coefficient	Radius in cm	Friction Coefficient
10	0.431	9.2	0.425
15.5	0.273	15.5	0.283
22	0.163	22	0.178
32	0.290	32	0.185
Average	0.239	Average	0.268
Standard Deviation	0.095	Standard Deviation	0.010

Table 5.2: Friction coefficient against sliding speed for both the abrasives

Thin Abrasive		Thick Abrasive	
Radius cm	Friction Stability Time minute	Radius cm	Friction Stability Time minute
10	20.67	9.2	3.83
15.5	25.00	15.5	5.00
22	5.33	22	3.67
32	35.50	32	6.50
Average	21.63	Average	4.75
Standard Deviation	10.80	Standard Deviation	1.13

Table 5.3: Friction stability time against sliding speed for both the abrasives

Results of the friction stability measurement:

The results are as follows.

- In general, the thin abrasive has the friction stability time of about 21.6 mins with the standard deviation of 10.8 mins. The thick abrasive, however, shows 4.8 mins with the standard deviation of 1.1 mins. The stability of the thin abrasive lasts much longer than that of the thick. This implies that, firstly, the ablation experiment was made with rather poor friction stability since the thick abrasive was applied about every 10 mins, similarly as for the friction measurements for the thick abrasive. Secondly, the average time required for each friction measurement was about 5-10 mins. It is comparable to the stability time of the thick abrasive, meaning that the friction for the thick abrasive was measured with poor stability. Therefore, a large error in friction for the thick abrasive should not be a surprise.

- There seems no relation between the frictional stability time and the sliding velocity.

- In either case, the friction coefficient, sometimes, approaches quite close to 1 or indeed exceeds it. This could be the evidence of abnormal suction by air pocket formed between the pitch and the glass surfaces with a abrasive film.

- in most cases, the friction increases very rapidly when either most of the abrasive is pushed out of the tracks or dried out so the naked glass surface is about to be appeared.

- The friction coefficient shows a gradual decrease with time, even though small in magnitude, in two out of four measurements for the thin abrasive and four out of four measurements for the thick abrasive.

- Again, the friction coefficient seems to decrease with an increase of the sliding speed, for the both abrasives. But, at the highest speed, this tendency is reversed. The friction-speed diagram of this measurement looks very much like those plotted with the data chosen at the corresponding radii from the friction measurements. This confirms that the friction measurement was conducted in a correct way. However, it is also true that, since the stability measurement is made just after the friction measurement, the physical condition of friction (i.e. abrasives) would remain the same in both the measurements. Thus, it is no surprise that the same results are produced.

- At the slowest speed, the friction coefficients for the both abrasives are about 0.43 which is higher than those from the friction measurements. The friction coefficients for the rest of the speed range are in the same ranges of magnitude for the both abrasives.

• Some interesting features observed

During these experiments, a number of interesting features were observed by monitoring the friction with a DVM and the behaviour of the polisher. They are as follows.

- As already stated in the previous section, when the abrasive is squeezed with the polisher sliding over it, it is firstly pushed out from the polishing track and then, after the polisher moves to other places, tends to return back to where it was. The thin abrasive tends to have fast return, forming consistent film

all the time. The thick abrasive shows rather slow or no return at all, i.e. the abrasive removed from the track tends to stay at the new location. Thus the thick abrasive film on the track is under continuous change in its characteristics such as thickness, this being a non-consistent film. This may explain the higher stability of the friction and of the pitch with the thin abrasive, i.e. less oscillation and therefore a more stable signal on the DVM.

This is not relevant to the full-size polishing which OSL is practising. Firstly, OSL normally uses the thin abrasive that has the higher stability. Secondly, in the full-size polishing, the abrasive moved to other position encounters immediately polishing pressure from other pitches, this being re-positioned at another place. Thus, there is no place where the abrasive can stay for a period of time on the mirror surface as it does in this experiment.

- The transverse oscillation of the pitch delivers two aspects on the friction measurement. Firstly, the small oscillation forces the pulley to have the same sort of oscillation but in smaller magnitude and hence does not cause any harm to the stability of the friction signal on the DVM. Secondly, the large oscillation often causes tumbling of the calibration weights, re-positioning its centre of mass on the load cell. This results in alternation of the calibration, thus varying the friction signal accordingly so as to increases the measurement error if it is regarded as reducible data. The measurements that show this are discarded but the few undetected are likely to have entered into the data set to be reduced.

- The first out of the five measurement cycles for each grooves seems always be unstable, developing the transverse oscillation. The next four cycles go relatively quietly compared with the first, although from time to time oscillations take place during polishing. For this, no measurement is made for the first 5-10 minutes to allow this condition settled down when the first measurement starts.

- Tiny air bubbles are observed on the sliding track during polishing. The oscillations seem to be mainly responsible for this. It should inevitably lead to small scale jumping of the pitch up and down over the abrasive film. When it falls with air underneath it on the film, it can produce this air bubbles

distributed along the track. In some cases, the sliding motion can collect the bubbles, slowly building a larger bubble which can eventually become an air pocket between the pitch and the glass surfaces. When it happens, unpredictably, enormous suction is developed, pulling the pitch with a large force along the direction of friction. The friction signal on the DVM increases abnormally as this is introduced. When the suction is broken by the restoring force, a large oscillation in longitude takes place, sometimes causing tumbling of the pitch and, in most cases, the calibration weights re-positioned on the load cell. Hence the friction signal is affected accordingly. Any readings that show a sign of this are discarded but, as previously stated, it is likely that the undetected effect has entered into the data set exported to the data reduction.

- It is a big surprise to observe that, when the load increases to a certain amount on the pitch, the DVM signal rapidly drops down to a level (meaning rapid increase of the friction) and then slowly returns back to another level which is shallower than the first but still deeper than the level with no load (indicating slow decrease of the friction to a lower level). The term *'Abrasive Film Hysterisis(AFH)'* is coined

  - to describe this behaviour of the rapid increase to a higher friction and the slow decrease back to a lower friction when the load is given to the pitch and then left unchanged sometimes.
  - to underpin the thought that the abrasive film characteristics are basically responsible for it.

Since AFH is first noticed with the thick abrasive, some of its characteristics are unveiled by subsequent monitoring.

- AFH takes place unpredictably but in general more frequently with the thick abrasive than with the thin abrasive.
- Once AFH is triggered, the slow return takes about 15-25 seconds but sometimes longer than 30 seconds. After it reaches to the lower friction, it tends to stay there unless the load condition is subjected to a sudden change.

- With the thin abrasive, AFH is observed more frequently when it is about to be dried out, this being like the thick abrasive. Of course, this does not preclude AFH, unpredictably, and less frequently taking place when it is still fresh and contains plenty of water.

An immediate consequence of AFH gives rise in questioning what the DVM signals mean, which level of the signals represents the true friction, what impacts AFH can give to the ablation and friction experiments, etc. The ablation experiment is made without changing the load on the pressure during polishing i.e. no condition to trigger AFH exists for the experiment. Thus, it is undertaken without any effects from AFH. AFH seems to appear only with the change in load conditions and therefore the friction measurement can be easily contaminated with AFH. (If the true friction is defined as the friction without change in load conditions used for the ablation experiment, then it should be represented by the second-shallower DVM signal, i.e. lower friction.) Having understood this, three measures to stop the AFH contamination are used as follows.

- Wait for at least about 15-20 seconds during which the DVM signal is stable showing no gradual increase and decrease and then take reading.
- new abrasive is applied for each of the five measurement cycles on a groove.
- Using a rubber blade, the abrasives are forced to remain within the polishing track. This is to ensure a stable film condition.

5.4 Behaviours of Abrasive Films

5.4.1 Experiment Programmes

AFH was certainly unexpected and one of the most interesting findings from the previous experiment. It is of most interest to investigate this phenomenon in more details for hard and quantitative evidence. An experiment is proposed as follows.

The first is to collect the raw friction data plotted against time in order to estab-

lish the hard evidence of AFH. The friction signal would be continuously grabbed, digitised and stored at a high throughput rate during polishing. The experiment parameters used are

- Weight (gmf): 154.11 (O), 344.01 (W1), 519.99 (W2), 697.91 (W3), 888.73 (W4)
- Radius (cm): 27.7
- Abrasive (gm:ml): thin (80:500) and thick (100:200)
- Loading strategy: The weight would be altered every 20 seconds with the sequence of

  (A) O-W1-W2-W3-W4
  (B) O-W1-W2-W3-W4-W3-W2-W1-O
  (C) O-W1-O-W2-O-W3-O-W4-O
  (D) O-W1-O-W2-W1-O-W3-W2-W1-O-W4-W3-W2-W1-O
  (E) Combinations of (C) and (D)

The second is, by taking a closer look at the graphs, to find if there are any patterns in the response of the abrasives, i.e. how the friction under loads behaves. The third is to analyse the AFH phenomena as detail as possible, if they exist. The fourth is to investigate how fast the abrasive film responds to the force modulation in terms of the friction. The term *'Friction Response Time (FRT)'* is defined as the time required for the friction signal to move from a stable level to another stable level with a loading. It can be defined more specifically as the time required for the abrasive film to respond to the unit force modulation, i.e. 1 gmf. Thus, it would have the unit of sec/gmf. The friction data that does not show AFH can only be used for the FRT analysis.

The implication of FRT would also be of importance. For example it would give an important clue to find the optimum frequency of the force modulation, which was once derived from the force positioning accuracy and the kinematics of the active lap in polishing in Chapter 3.

5.4.2 Apparatus

The apparatus used for the friction experiment is again used but with little modifications. Instead of using a DVM, APOLO is employed so the amplified load cell signal, i.e. friction, is directly interfaced to a 386SX PC. The DATA acquisition routine of APOLO.EXE was modified for

- grabbing, digitising and storing the friction data in the PC Memory at 10 Hz
- writing them as a text file in a mass storage device with a single key stroke when necessary.

5.4.3 Measurement, Data Reduction and Analysis

• Measurement

The first set of measurements:

The loading strategy (A) was used for making the first three measurements with the thick abrasive. Each measurement showed large differences not only in the level of friction but in the pattern of the friction curves between the measurements. For example, the friction curve of the second measurements showed that the friction never be stable in a constant level even under the same load. The first and the third measurements have a similar appearance but very different friction levels under the same load condition. Although, in some parts of the graphs, the evidence of AFH expected was seen very clearly, the results were not good enough for quantitative analysis. They did not show any consistency in behaviour. It was realised that the thick abrasive used was a few days old, and much of the water had evaporated since then. Thus, the water to cerium oxide ratio became exceptionally low and it could influence its characteristics, leading to the inconsistency.

The second set of measurements:

The second set of measurements was made with the strategy (B), using the fresh thin and thick abrasives. Three measurements were made for each abrasives. The results were much more consistent and showed the following.

- In some cases, immediately after the load condition is altered, the friction responds sharply and linearly, moving to a certain level in the friction-time

diagram. However, in other cases, the friction responses have *'Shoulders'* at its both ends (see Figure 5.13). This happens with both the abrasives. It could mean that the abrasive film has linear and non-linear friction responses to normal loads, taking place unpredictably. This again requires a more specific definition of FRT; whether it should include the shoulders or not. One could argue that the shoulders taking place just after the change of load condition are not real features but more likely to be affected by duration of the load pulse. However, the presence of the second shoulder taking place without any change in load condition undermines the idea, while supporting it as a genuine feature, related to the physical nature of the abrasive film and the polishing action.

- In general, the friction curves shows asymmetry between their loading and unloading halves. The loading half appears to have smaller friction with the load cases of W1, W2 and W3, than the corresponding unloading half. In some cases, the load case W3 after W4 shows more friction than the corresponding W3 before W4. In most cases, the friction of the load case O in the unloading half tends to return back to the same level, with the load case of O in the loading half.

- AFH previously stated is not observed. Instead, the friction tends to stay in a stable level once it is reached.

The third set of measurements:

Thus, the previous two sets of measurements can neither positively confirm AFH nor provide an experimental basis for the FRT analysis. This led to the third set of measurements, being made with more precise control over the ways that the measurements were conducted. Table 5.4 shows how these measurements are conducted, including DATA file names. Figure 5.13 shows typical frictional behaviour of the thick abrasive as a demonstration.

• Data reduction

The data reduction was made with the criteria found after graphs of the friction data against time were carefully examined. They are summarised as follows.

- To study the items below is of the most interest.

Abrasive	Film Thickness	Loading Strategy	Data File NDECAY__DAT
Thin	Not Controlled	B	1A, 1B, 1C
		C, D	2A, 2B, 2C, 2D
	Controlled	B	3A, 3B, 3C, 3D, 3E
		C, D	4A, 4B, 4C, 4D, 4E
Thick	Not Controlled	B	5A, 5B, 5C, 5D, 5E
		C	6A, 6B, 6C, 6D, 6E
		D	7A, 7B, 7C, 7D, 7E
	Controlled	B	8A, 8B, 8C, 8D, 8E
		C	9A, 9B, 9C, 9D, 9E
		D	10A, 10B, 10C, 10 D, 10E

Note: (1) The abrasive is supplied when starting measurement of each data file.
(2) The controlled film thickness means that a rubber blade is used to stop the abrasive slurry escapingfrom the polishing track during measurement.
(3) The 'not controlled' film thickness means that a supply of abrasive is left uninterrupted until a measurement is completed. This allows the abrasive slurry to flow out of the polishing track during measurement.

Table 5.4: The third measurements for behaviour of abrasive films with sub-diameter tool polishing

- Case study: Percentage of specific phenomenon to total loading cases.
- AFH Time: Time required for the friction signal to increase back to a higher stable level after the end of the loading decrease.
- AFH Recovery Rate: Ratio of the signal increase to the decrease described above.
- FRT Time: Time required for the friction signal to decrease to a lower-stable level when the 1 gmf loading takes place.

The calibration measurement is not necessary since the absolute friction itself is not of interest.

- The whole set of friction data can be categorised into 4 groups called *'AFH group'*, *'FRT group'*, *'Shoulder group'* and *'Abnormal group'*.
- Each group except the Abnormal group can be divided into two subsets; *'Reducible'* and *'Un-Reducible'* sets. The Non-Reducible set is the data that can not be reduced due to various reasons stated below.

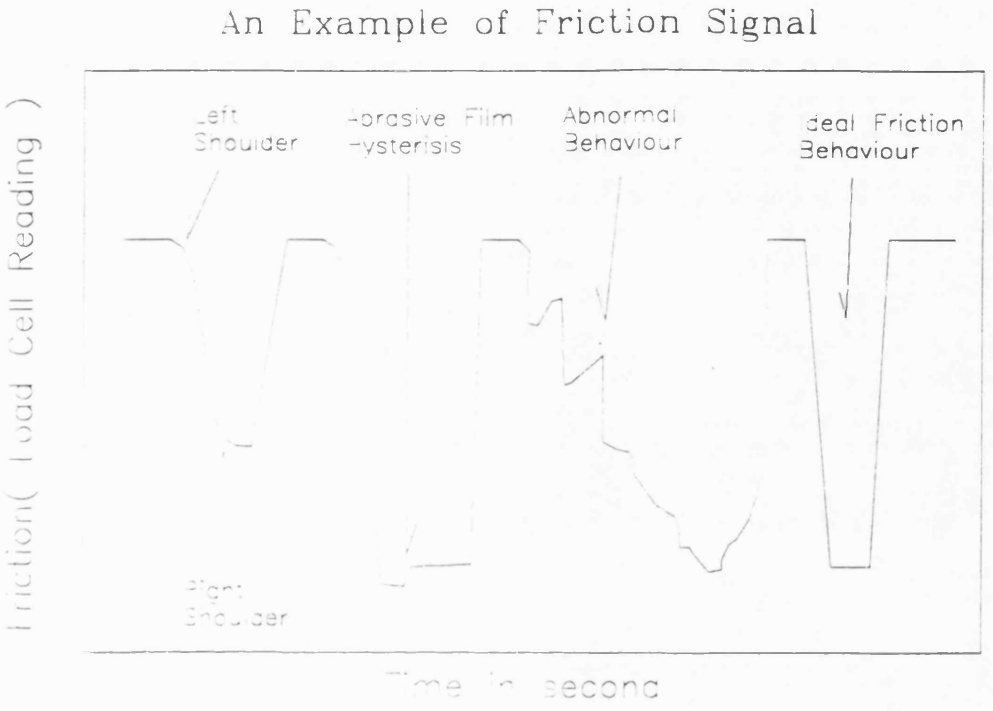

Figure 5.13: An example of typical frictional behaviour of the thick abrasive

- The AFH group covers the data showing AFH. Its frequency should be determined using the loading case, only excluding the unloading cases, because these cannot produce AFH. This group is excluded in the FRT analysis because it does not have a stable level of friction at the end of loading decrease, so that the time of loading decrease can not be determined. The Un-Reducible set of this group is generated with
  - multiple stepwise increase showing no dominant level of stable friction after the end of the loading decrease
  - large oscillation in friction signal
  - AFH longer than about 20 seconds and therefore interrupted with unloading.
- The data that shows sharp and linear responses of friction signal forms the FRT group. Unlike the AFH frequency study, the frequency should be derived

based on the total numbers of loading and unloading. It is used for the FRT analysis. The Un-Reducible set of this group is mainly caused by the same reasons listed above.

- The Shoulder group consists of data showing sharp and linear responses of the friction signal, but has non-linear ends. It has two subgroups called *'Left Shoulder'* and *'Right Shoulder'* groups according to where it takes place. The frequency study of these subgroups indicates whether or not the shoulder comes from the genuine nature of the abrasive film. The Shoulder group can be involved in the FRT analysis. The three reasons itemised above are mainly responsible for the Non-Reducible set within this group.

- The Abnormal group includes the data that can not be put into the three groups described above. The friction signals of this group have totally different responses from the rest of the data. Examples include

  - no response to loading and unloading at all
  - weights accidentally falling during loading or unloading
  - exceptionally large oscillation
  - large oscillation, combined with strong multiple step wise response during loading or unloading.
  - exceptionally long responses to loading and unloading

  This group is not involved in any of the analyses listed, but in the case study only.

5.4.3.1 Case Study

Table 5.5 presents the statistics for the categories mentioned, showing their percentages and availability in the total loading cases.

- Overall, about 28% of the loading cases appears to be Un-Reducible, on average. About half of this is taken by the Abnormal group. The data availability increases up to 89% with the thin abrasive, but falls down to 59% with the thick abrasive. The thicker the abrasive used, the more unpredictable the friction

Phenomena	Thin Abrasive	Thick Abrasive	Total
Number of Loading	244 (100.0 %)	300 (100.0 %)	544 (100.0 %)
Reducible AFH	39 (15.98 %)	47 (15.67 %)	86 (15.81 %)
Un-Reducible AFH	3 (1.23 %)	35 (11.67 %)	38 (6.99 %)
Reducible FRT	115 (47.13 %)	103 (34.33 %)	218 (40.07 %)
Un-Reducible FRT	0 (0 %)	19 (6.33 %)	19 (3.49 %)
Reducible Left Shoulder	3 (1.23 %)	0 (0 %)	3 (0.55 %)
Un-Reducible Left Shoulder	0 (0 %)	1 (0.33 %)	1 (0.18 %)
Reducible Right Shoulder	59 (24.18 %)	28 (9.33 %)	87 (15.99 %)
Un-Reducible Right Shoulder	7 (2.87 %)	13 (4.33 %)	20 (3.68 %)
Abnormal Data	18 (7.38 %)	54 (18.00 %)	72 (13.23 %)
Reducibility	216 (88.52 %)	178 (59.33 %)	394 (72.43 %)
Un-Reducibility	28 (11.48 %)	122 (40.67 %)	150 (27.57 %)

Table 5.5: The statistics of the cases and their reducibility

behaves, making active force modulation and friction, i.e. ablation, separate realities in polishing. It means that even if the active close-loop control from pressure sensing to force modulation is successful all the time, estimation of ablation rate becomes totally unrealistic, so as iteration of active polishing would fail to converge. Thus, the use of the thin abrasive is crucial to increase the availability for successful active polishing.

- The percentages of the AFH, in particular the Non-Reducible set, and the Abnormal groups are significantly higher and whereas those of the FRT and the Shoulder groups are lower with the thick abrasive, than with the thin abrasive. The thick abrasive has a much higher frequency of AFH and abnormality than the thin abrasive, this being the statistical evidence of AFH.

- In the Shoulder group, the Right shoulder is overwhelmingly dominant over the Left shoulder. This again greatly supports the idea that the loading and unloading pulses have nothing to do with this and it is indeed a genuine feature of friction in polishing with abrasive film.

Phenomena	Percentage of Thin Abrasive	Percentage of Thick Abrasive
Weak AFH	38 (97.4 %)	29 (61.7 %)
Strong AFH	1 (2.6 %)	18 (38.3 %)
Total Number of Load Case	39 (100 %)	47 (100 %)

Table 5.6: Frequencies of 'Strong' and 'Weak' AFHs in Reducible AFH data set.

5.4.3.2 AFH Analysis

As suggested earlier, if the percentage of AFH frequency has to be determined with half the number of loading and unloading cases, it is doubled up to about 34%(thin) and 55%(thick). It means that, even the thin abrasive has about 1 in 3 force(i.e. friction) increases that fails to reach a single true friction(but has a pair of friction levels). Thus the friction resulting from a force modulation has a wide band in real magnitude, increasing the error in friction measurement that was seen in the previous section. AFH would certainly be another reason why the ablation estimation in real time becomes unrealistic in optics polishing.

Two different types of AFH were observed; *'Weak'* and *'Strong'* AFHs. AFH, showing a shallow decrease after a rapid increase in friction, is called the *'Weak AFH'*, whereas that shows much decrease is named the *'Strong AFH'*. Table 5.6 shows the frequencies of the two AFHs in the Reducible AFH data set. It is clearly noticed that there is virtually no Strong AFH(only about 3%) with the thin abrasive but about 40% of AFH with the thick abrasive is Strong AFH. This Strong AFH is indeed the phenomenon that was ambiguously seen with DVM when the friction measurement was being undertaken.

AFH Time: The AFH time can be defined as the time required for the friction to move from the end of the rapid increase to a second stable level when AFH happens. Whilst Table 5.7 presents the averaged AFH times for the Weak and Strong AFHs with the 2 abrasives, the AFH time for different load cases with the 2 abrasives is shown in Table 5.8. It is clearly noted that

- there is not significant difference in the averaged AFH time between the Weak and Strong AFHs with an abrasive.

Phenomena	Thin Abrasive AFH Time in second	Thick Abrasive AFH Time in second
Weak AFH	2.72±1.57(σ)	7.03±4.03(σ)
Strong AFH	2.7(1)	8.93±3.22(σ)

Note: (1) The standard deviation σ is unavailable since the thin abrasive has only one case of the Strong AFH.

Table 5.7: Averaged AFH times for 'Strong' and 'Weak' AFHs for the thin and thick abrasives

- the AFH time seems to have no relation with load.
- however, in general, the thick abrasive produces much longer AFH times(i.e. 7.0-8.9 seconds), whereas the thin abrasive gives shorter AFH times(i.e. 2.7 seconds).

Apart from the qualitative description above, the numerical values of the AFH time for the thick abrasive is rather artificial. Because most of the AFH phenomena longer than 10 seconds, which happened mostly with the thick abrasive, have been interrupted by the loading and unloading and therefore classified as the Un-Reducible AFH data. This means that the AFH time of the thick abrasive is no longer valid for any further quantitative analysis on the property of the abrasives. In contrast, the thin abrasive has never exceeded 10 seconds and hence experienced the interrupt. Thus the AFH time of the thin abrasive can be used if further analysis is to be made.

Normal Load Increase gmf	Thin Abrasive AFH Time in second	Thick Abrasive AFH Time in second
190	1.47	6.53
176	2.6	11.5
178	2.13	8.68
191	3.23	8.1
366	2.57	7.64
544	3.26	7.54
735	2.05	6.71
Average	2.90±0.78(σ)	8.10±1.55(σ)

Table 5.8: AFH times for the different load cases

Phenomena	Thin Abrasive Recovery Rate in %	Thick Abrasive Recovery Rate in %
Weak AFH	11.69±8.83(σ)	28.58±15.02(σ)
Strong AFH	13.33(1)	61.84±21.74(σ)

Note: (1) The standard deviation σ is unavailable since the thin abrasive has only one case of the Strong AFH.

Table 5.9: Recovery rate for the Weak and Strong AFHs

Normal Load Increase gmf	Thin Abrasive Recovery Rate in %	Thick Abrasive Recovery Rate in %
190	14.48	62.59
176	25.00	52.18
178	23.33	34.33
191	33.33	33.48
366	9.50	35.71
544	7.44	39.24
735	5.42	18.09
Average	16.93±9.70(σ)	39.37±13.25(σ)

Table 5.10: Recovery rate for the different load cases

Recovery Rate: The recovery rate can be defined as the ratio of the second decrease to the first increase in friction when AFH takes place. Table 5.9 is intended to show the averaged Recovery rates for the Weak and Strong AFH with the 2 abrasives. The AFH time for different load cases with the 2 abrasives is given in Table 5.10. It is seen that

- On average, the recovery rates of the Weak and Strong AFH with the thin abrasive are very similar to each other. On the other hand, those with the thick abrasive look very different, i.e. 29% for Weak and 62% for Strong.

- The recovery rate appears to be a function of load, i.e. it decreases as the load increases. This is quite natural, giving no special meaning. The amount of recovery D2 is, in most cases, 1 ADU, whilst the initial increase of friction, i.e. D1 increases proportional to load.

- In general, the thick abrasive shows recovery rates much higher than those of the thin abrasive. This resulted not only from the existence of the Strong AFH, mostly happening with the thick abrasive, but also from the magnitude of the Weak AFH with the thick abrasive.

(A)	Thin Abrasive			
Load Case in gmf	Loading FRT FRT_l in msec	Unload Case in gmf	Unloading FRT FRT_u in msec	Difference FRT_l - FRT_u
190	4.08±2.07(σ)	-190	5.61±3.97(σ)	-1.53
176	7.20±6.43(σ)	-176	8.81±6.46(σ)	-1.62
178	1.69±0.56(σ)	-178	5.76±5.57(σ)	-4.08
191	3.40±3.32(σ)	-191	9.70±8.16(σ)	-3.30
366	4.67±2.75(σ)	-366	5.16±2.97(σ)	-0.49
544	1.81±0.97(σ)	-544	3.14±1.21(σ)	-1.33
735	2.11±0.12(σ)	-735	2.78±0.88(σ)	-0.67

(B)	Thick Abrasive			
Load Case in gmf	Loading FRT FRT_l in msec	Unload Case in gmf	Unloading FRT FRT_u in msec	Difference FRT_l - FRT_u
190	2.50±2.82(σ)	-190	1.99±3.63(σ)	+0.51
176	8.81±7.67(σ)	-176	2.93±4.50(σ)	+5.88
178	4.31±4.11(σ)	-178	8.56±12.6(σ)	-4.25
191	4.32±4.15(σ)	-191	6.56±7.65(σ)	-2.24
366	3.19±4.12(σ)	-366	2.02±1.94(σ)	+1.17
544	5.93±3.24(σ)	-544	4.60±3.13(σ)	+1.33
735	3.13± -(σ)	-735	2.04±1.32(σ)	+1.09

Table 5.11: Unit load FRTs for different load cases in separation of loading and unloading

5.4.3.3 FRT Analysis

The use of the FRT analysis is to give some estimations for the optimum frequency of force modulation in the active polishing. The active force modulation frequency of 10 Hz does not necessarily mean that the friction is modulated at 10 Hz on the mirror surface. The friction modulation frequency could indeed be entirely different from that of force. If it is assumed that any frequencies can be achieved in active lap control, then this is directly related to the question of how fast the abrasive film responds to load. The results of the FRT measurements are given in Table 5.11 and Table 5.12.

As observed in Table 5.11, the thin abrasive seems to have the loading FRTs shorter than the unloading FRTs whilst, for the thick abrasive, the loading FRTs are generally longer than the unloading FRTs, with two exceptions. If this is a true feature, the optimum frequency for loading would be slightly different from that of unloading, meaning that the active lap control should work at two different frequencies for loading and unloading, according to the abrasives used.

It is seen from Table 5.11 and Table 5.12 that, as the magnitude of loading and unloading increases, FRT of the thin abrasive seems to decrease from about 4.9-8.7 msec/gmf to about 2.5 msec/gmf. That of the thick abrasive tends to have no particular tendency. However, in general, the averaged FRTs over all the loading and unloading cases for both the thin and thick abrasives are about 4.1 msec/gmf and about 3.8 msec/gmf respectably. This means that there is virtually no difference between the two abrasives, as far as statistically averaged behaviour of their response speed to load is concerned.

• Implication of FRT to active lap control

As described in Chapter 4, the active lap actuator was designed to produce 40 gmf with 1 step pulses. Because of the averaged FRT, the force of 40 gmf requires about 160 msec to take effect of friction after loading, assuming that FRT for the both abrasives is about 4 msec/gmf. It means that, if the polishing pressure keeps being updated with 1 step pulses at 10 Hz, then just 25 gmf, i.e. 0.625 of a pulse, is spent to generate friction in 100 msec. Furthermore, the force modulation of about 400 gmf does require about 1.6 seconds to produce the intended friction. Hence, if the modulation frequency is 10 Hz, with 400 gmf, then there is only 25 gmf used to produce the friction in 100 msec. This suggests that there is only 25 gmf in effect, if the modulation frequency is 10 Hz, regardless of modulation amplitude. It also suggests that, at a given time, the active polishing can achieve the force modulation amplitudes entirely governed by the modulation frequency, e.g. 25 gmf at 10 Hz, 50 gmf at 5 Hz, 250 gmf at 1 Hz, 500 gmf at 0.5 Hz and so on. The more force the active polishing exerts, the slower control frequency it has to run under, in order to make the friction control consistent with the force modulation. Thus, the active polishing would have to control not only force magnitude, but also close loop control frequency

Combined Load Case in gmf	Thin Abrasive Combined Unit FRT in msec	Thick Abrasive Combined Unit FRT in msec
183.8	6.37±1.35(σ)	4.88±2.34(σ)
366	4.98±2.86(σ)	2.46±3.01(σ)
544	2.48±1.28(σ)	5.48±3.27(σ)
735	2.54±0.77(σ)	2.26±2.21(σ)
Averaged	4.07±1.65(σ)	3.77±1.43(σ)

Table 5.12: Unit load FRTs for different load cases in combination of loading and unloading data sets

to achieve a desired friction map i.e. pressure map. This discussion obviously relies on the assumption that FRT remains constant, no matter whatever magnitude the input load pulse is. Indeed, the case of the thick abrasive seems to be quite relevant to this. Unfortunately the data collected is small in number and large in error. More and better experiments need to be conducted to collect data to find an optimum frequency variation for the force range in active polishing.

Effect of increasing FRT

What effects are given to the active polishing, if FRT increases, although this seems rather unlikely, with magnitudes of input load pulses ? The same line of strategy with the above in active polishing has to be applied but with more emphasis on frequency control. The more the force needs to be exerted, the much slower, compared with the case above, the active force modulation has to run. At present, there is no experimental data, giving evidence for the existence of the FRT increase.

Effect of decreasing FRT

What does it mean to the active polishing, if FRT decreases with the magnitudes of input load pulses such as seen with the thin abrasive ? It would means that the more the force is exerted on the abrasive, the faster it responds to produce friction. Let's assume that FRT decreases inverse-proportionally with the input range of load pulses, such as seen in Fig 5.14; 5.8 msec/gmf with 250 gmf, 3.5 msec/gmf with 500 gmf, 2.5 msec/gmf with 750 gmf. If the force of 400 gmf(10 step pulses) is given at 10 Hz, that force needs, in fact, 1.7 sec to produce a corresponding friction. For the given 100 msec, only 23.5 gmf out of 400 gmf is capable of generating friction. Using the same argument, there are the effective forces of only 40 gmf in producing friction within the 100 msec interval, if 720 gmf(18 pulses, 1.8 sec needed) are given at 10 Hz. Fixing the modulation frequency at 10 HZ, the force modulation with 400 gmf and 720 gmf become the effective force modulation with 23.5 gmf and 40 gmf respectably. This means that, in principle, as far as the modulation frequency is set high such as 10 Hz, almost all the forces generated by the actuators disappear before the corresponding friction is generated and one never converted to an effective force, producing friction. In other words, the efficiency of friction generation and hence ablation is very low, perhaps less than 10% of all the forces used at a time.

Control of force modulation amplitude:

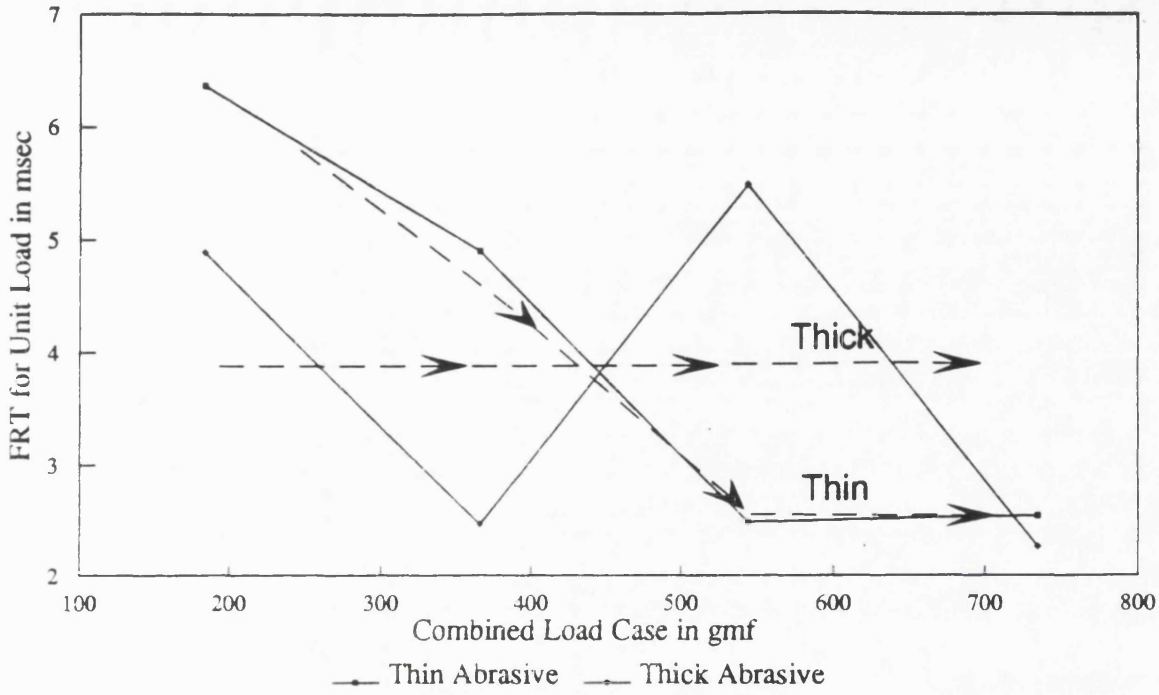

Note: The arrows are to show that assumed tendency of FRT with increase of load pulse.

Figure 5.14: Averaged FRT plotted against magnitude of load pulses for the thin and thick abrasives. The dotted arrow is assumed decrease of FRT of the thin abrasive for the discussion

However, despite this, it is also still true that the pressure map can be modulated as designed, if the active lap is capable of producing the force modulation amplitude somewhat 10 times larger than the designed one. This addresses the current limitations of the manufactured active lap at the time of writting this Chapter. It is capable of exerting only 31 pulses, i.e. 1240 gmf as a maximum force at a time. This leaves no room to improve the efficiency except to run the active polishing at a low frequency e.g. 0.5 Hz so that all the force exerted can take part in producing friction. To do that, some other polishing parameters have to be adjusted. For example, a shorter stroke and a much slower rotation of mirror than envisaged would have to be employed to keep the force positioning error down to about ± 0.5 cm. Unfortunately, active polishing can not employ these findings because the relationship between FRT and the input loads are not known at this stage. The FRT data collected for the thin abrasive is too coarse in interval and hence too small in number to be fitted into a mathematical function. The measurement error is also rather large. More and better experiments need to be made to collect enough data and to

reduce the measurement error.

Control of force modulation frequency:

There is an alternative way of achieving the desired friction map in real time. That is to control modulation frequency, only with a fixed force applied to all the actuators at all time. Assuming that 31 step pulses with the period of 100 msec are given to the actuators for every force modulations(in other word *'fixing force'*), they takes about 1.55 sec to produce corresponding friction. Assuming that the period of 100 msec is negligible compared with 1.55 sec, there would be a friction corresponding to about 10 pulses, if the friction generation process is interrupted by the next modulation after 500 msec instead of 1.55 sec. The next modulation would also start with the same pulse number but be interrupted with different time interval to give a friction of a different load. The whole active polishing would consist of a sequence of this type of force modulation.

With this way, the force command of the FIFO memory would always be same but not the sign command. Actual force is controlled with timing by interrupt for the next modulation. Therefore, the period of each force modulations varies each time from 50 msec to 1550 msec, if there is no control overhead. This method can be applied to active polishing under all the three cases of FRT above, since there is only one FRT curve used. The point is that it uses a single FRT characteristics and it is given up controlling friction with fixed frequency. But force modulation within the lap still runs at fixed frequency i.e. 100 msec as seen above. Friction is controlled with variable frequency from 50 msec to 1550 msec. Thus it also requires short stroke and slow rotation of mirror.

The control system currently manufactured can be experimented for implementing the methods suggested above. Two aspects are worth being mentioned in relation to this.

- With the earlier version of the active lap control electronics, the FIFO memory was able to accommodate a command for only 31 step pulses for each actuators maximum. The control system was unable to produce the aimed maximum force, e.g. 100 pulses, at a time. The actuator could not make the larger force necessary for generating the friction corresponding to the load of 4 kgf. In order to do that, the spring constant and the motor power of the actuator

needed to be modified. A larger FIFO memory would have to be used and the rest of the electronics needed to be modified accordingly. Since the time of writing this Chapter, the active lap control electronics has been improved. At the time of finalising this thesis, it can exert up to 100 step pulses at a time. This implies that the control of force modulation amplitude to achieve desired friction responses become even more attractive.

- The way that the FIFO memory works with is that a block of commands is output in sequence only after the memory is once filled with the step pulse and sign commands. There is no way of interrupting while the commands are being output e.g. the load pulse can not be interrupted within the control electronics. This also means that commands for each actuator cannot be output separately and hence each actuators cannot receive the next command immediately after the previous one is used. Even with this synchronisation in stepper motor operation, the force modulation frequency can be modified in real-time, using more complicated bitmap inputs than what is currently used to the FIFO memory.

5.5 Discussion

5.5.1 Implication of Ablation Experiment with Thick Abrasive

• Apparent contradiction to Preston's theory

The ablation coefficient decreases with the sliding velocity (error about 12%) and the load (error about 37%). The averaged ablation coefficient is 3-11 times smaller than others. This looks totally contradictory to the conventional Preston's theory [4] at a glance. However, as pointed out by NOAO [113] and Lindsey [70], there are two reasons that the direct comparison of the results with others would not be fruitful.

- The measurements of ablation and friction inherently suffer from large error.
- The experimental conditions and the way in which the polishing variables are controlled are not compatible each others.

• A hypothesis to explain this contradiction

In spite of these, the results obtained here are in the same order of magnitude in ablation coefficient as others. This encourages a hypothesis for a possible theory that can explain the contradiction as follows.

With continuous polishing, the wear at a point on the glass surface takes place continuously once accumulation of friction energy exceeds a threshold level of ablation after the starting of rubbing. Because the continuous rubbing keeps producing the same level of frictional energy on the glass surface, continuously, the ablation rate-time diagram of this case should look like (A) in Figure 5.15. However, with intermittent polishing, the wear takes place with a certain time interval for which rubbing contact is maintained. No ablation occurs for the remaining time period where the surface loses the frictional energy accumulated and eventually falls below the threshold. Looking at the single event of wear, each time a point on the glass meets the edge of polisher, it starts collecting frictional energy. Sometime later, when it exceeds the threshold, the molecules of the surface are able to separate themselves from the bulk of glass. Therefore, the ablation rate-time diagram should look like (B) in Figure 5.15. The integrated ablation over the polishing time, i.e. sum of the intermittent polishing times, could differ from that with the same amount of continuous polishing time. The averaged ablation rate of the intermittent polishing becomes smaller than that of the continuous polishing. This theory suggests the ablation coefficient as a function of the dwelling-indwelling time ratio. One characteristic of the function is that it decreases as the ratio goes toward zero.

The proposed theory explains why

- the averaged ablation coefficient obtained is smaller than those of others.
- the ablation coefficient at high speed is smaller than that of low speed.

The first is because of the low ablation coefficient of the intermittent polishing. The second is because the experiment set up reduces the dwelling to indwelling time ratio with an increase in the sliding velocity. It tends to decreases the ablation coefficient with high speed according to the suggested theory.

Thus, it implies that the results obtained here are not opposed to Preston's theory, but rather reveals a hidden variable, i.e. the dwelling-indwelling time ratio.

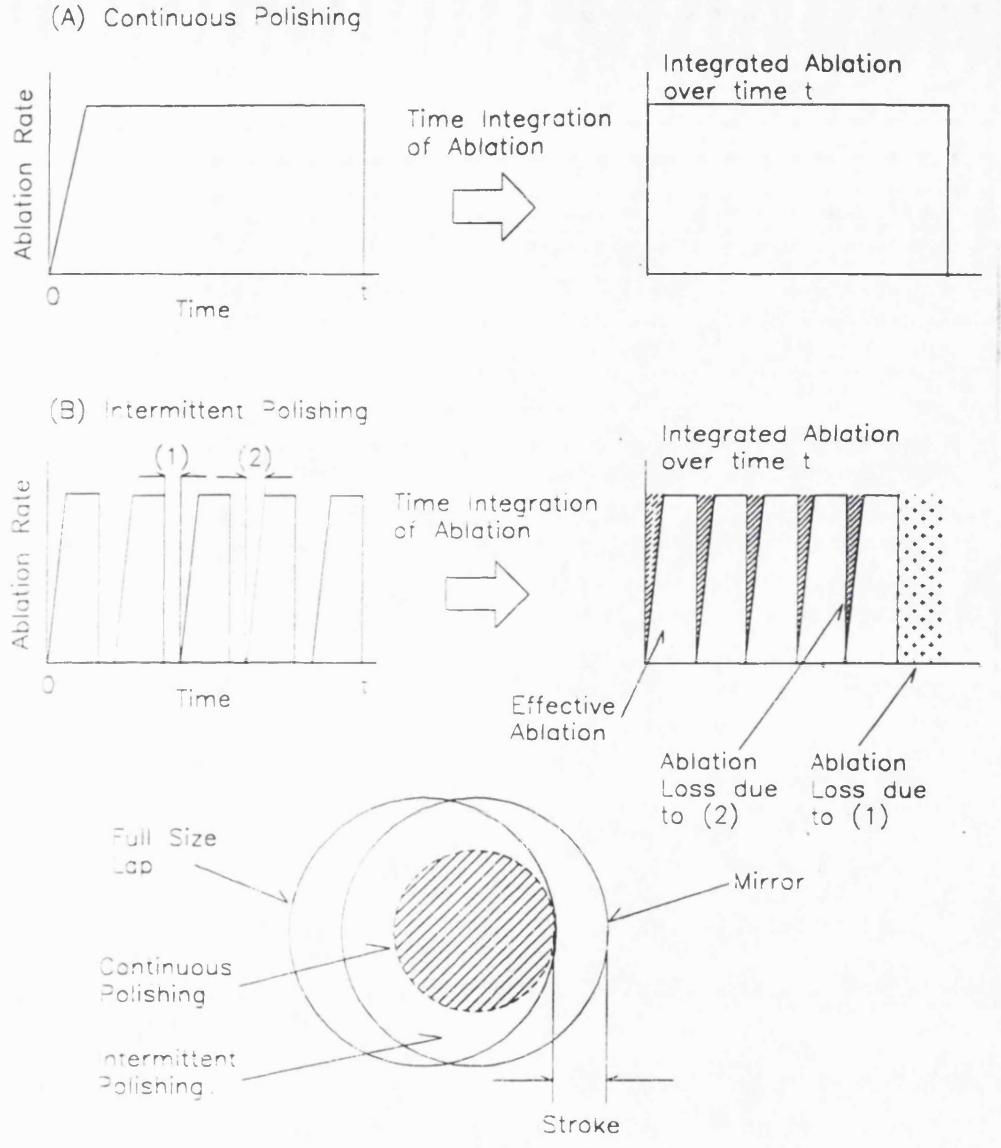

Note: (1) No polishing contact gives no ablation and the frictional energy is lost. This needs some of the frictional energy of the next polishing contact to be spent to re-energise the surface back to the same amount of ablation level.
(2) The (re)-energisation of the firctional energy needs a finite time span to be completed, for which the instant ablation rate increases titled in the ablation rate-time diagram.

Figure 5.15: Time variation of ablation rate in continuous polishing(A) and in intermittent polishing(B)

Preston's theory is that the ablation is directly proportional to the integrated polishing time. However, the experimental evidence obtained here suggests that the proportionality depends on the dwelling-indwelling time ratio. It seems a more gov-

erning variable than others in intermittent polishing. Preston's theory may well be found valid as long as this is kept constant in a polishing run. Examples include continuous polishing. It can be regarded as a subset of the intermittent polishing, of which the dwelling-indwelling time ratio becomes infinite. The behaviour of the ablation coefficient in intermittent polishing has to be thoroughly investigated by further experiments.

• Implication of the suggested theory to full/sub size tool polishing

Its implication to full/sub size tool polishing is that, when thinking about either the full size polishing or the local figuring using a sub-diameter polisher, there is always the intermittent polishing at the edge of the polisher. The area of the intermittent polishing depends on the stroke and size of the polisher. The central area of the stroke always have a continuous polishing and there is always a border between the intermittent and continuous polishings. The ablation rate patterns of these two regions with time differ considerably. The outer region of the stroke would be likely to have a much smaller ablation rate than the central area. This will be more enhanced if the full size polishing is made with the mirror rotating because of a smaller friction coefficient at the periphery. The ablation algorithm must take this into account in order to achieve successful ablation control over the whole work surface in either real time or integrated control modes.

5.5.2 Implication of Friction Measurement

The proposed theory suggests a validation experiment. No matter what physical process is involved in glass polishing, the instant ablation coefficient is believed to be proportional to the kinetic friction coefficient. If it is found, using the same experimental setup, that the kinetic friction coefficient also decreases with the sliding speed, it can proves the validity of the ablation coefficients and the proposed theory of the intermittent polishing. Two separate experiments were undertaken. One was to measure the kinetic friction coefficient with different loads at different sliding speeds. Another was to measure the friction stability over the time span for which a supply of abrasive lasts in polishing. The two abrasives -thin and thick- were again used in both experiments.

5.5.2.1 Friction Coefficient-Sliding Velocity-Pressure

The friction coefficient of the thin abrasive is higher than that of the thick abrasive. This agrees very well with the fact that the polishing rate is higher, with the presence of water, than its absence [19] [58]. Recently, Ahmed [1] has suggested that viscous lubricants form thick films into which the abrasive particles are suspended deep within. This leads to a smaller part of the abrasive grains exposed to surface contact. It lowers the cutting rate and makes shallow scratches. In contrast, low viscous lubricants tend to form a thinner film where more of the abrasive particles are allowed to be exposed. This produces a higher material removal rate and deeper scratches. This explains clearly the higher friction coefficient of the thin abrasive observed. Although the ablation experiment was not made with the thin abrasive, this provides a concrete support to the higher ablation coefficient of the thin abrasive.

Another thought about the higher friction coefficient of the thin abrasive is given to the air bubbles observed along the sliding track in polishing operation. More bubbles were observed with the thin abrasive than the thick abrasive. They are likely to form tiny air pockets between the two sliding surfaces, producing the suction force which acts as friction. This can give the thin abrasive a statistically higher friction coefficient than the thick abrasive. The presence of bubbles, i.e. air pockets, could lead to another process for ablation. When breaking the air pockets between the two rubbing surfaces, there might be enough energy produced for the abrasive particles to tear off molecules of the glass surface. The recent advances of the cavity theory in sonic waves explains how breaking air bubbles can release enough energy to ablate any metal and other solid surfaces such as glass [18].

The friction coefficient of both the abrasives increase with applied load. This feature is very distinctive with the thick abrasive but less with the thin abrasive. The friction coefficient of the thin abrasive remain rather constant, with the sliding speed. In 1957, Southwick (p 370 [52]) has shown that the kinetic friction coefficient on glass-glass polishing, with water flooded on, does not change over the wide range of sliding velocity and load. The result agrees well with this. However, the friction coefficient of the thick abrasive decreases with the sliding speed.

5.5.2.2 Friction Coefficient Stability-Sliding Velocity-Time

This independent measurement of the friction stability-velocity relation seems to repeatedly give evidence to the validity of the previous friction measurement. It also shows consistent results between the ablation and friction coefficients, supporting their proportional relationship. Thus it supports that the ablation rate-velocity relations obtained are a true feature.

The friction coefficient of the thin abrasive decreases with the sliding speed until the third groove and then increases a bit at the fourth groove. This appears to be contradictory to the result of the previous experiment. But the tendency of the friction coefficient at the four corresponding locations in the previous friction experiment looks very much similar, but with slightly less amplitude. The average measurement error of this experiment is also about 19% in standard deviation. Thus it is still reasonable to think that the friction coefficient of the thin abrasive does not vary with the sliding speed. However, the thick abrasive shows that it decreases with the sliding speed just as the previous experiment did.

In general, six out of eight measurements (i.e. two out of four for the thin and four out of four for the thick abrasives) show a gradual decrease of the friction coefficient until the abrasive is almost dried out. It then changes dramatically to rapid increase at the end of the gradual decrease. This may suggest that two different phases of friction exist. The transition between them takes place, depending on the property of abrasive and the wetting process of the glass surface.

This could suggest that there is a gradual decrease in friction coefficient over the period in which no abrasive is re-supplied in a polishing run. Since the ablation rate is proportional to the friction coefficient, as a polishing run progresses, the ablation coefficient used to estimate the ablation rate should differ, depending on time. This would become a source of error in ablation prediction, regardless of what algorithm is used. The ablation coefficient or friction coefficient as a function of time would have to be used to estimate the instant and integrated ablation maps in this case. Knowledge on this phenomenon is still to be understood in the future.

The gradual decrease in the friction coefficient can be explained using Ahmed's thought mentioned above. However, the rapid increase in the ablation coefficient,

when the two wet surfaces(i.e. glass and pitch) are rubbed with the abrasive slurry, that has almost dried, can not be properly explained with it. Nevertheless, our expectation of gradual increase in friction coefficient because of continuous evaporation of water, being closer to dry friction, is proved totally wrong. In fact, the truth is that the more water is present, the higher the friction coefficient that is produced.

Because of the continuous evaporation of the water in polishing, OSL has normally been adding a bit of water several times into the rubbed surfaces during a run of the full size passive polishing. This would result in dilution of the abrasive and therefore lead to gradual change, likely to increase, in the friction coefficient over the period of a polishing. This would compensate for the gradual decrease and keep the friction coefficient constant.

The friction stability time suggests that, if the thin abrasive is used, each polishing run of about 10-20 min for final figuring can be made with a single supply of the abrasive. This is based on the assumption that there is no external loss of the abrasive flown out of the mirror surface. However this is unrealistic, since the full size lap forces the abrasives to move out from the mirror surface. The loss of the abrasives would be more severe with the convex surface because, since unlike the concave surface, it does not have a natural reservoir of the abrasive slurry. Hence, the friction stability, with a single supply, would only last 5-10 min. If longer polishing has to be made, at least it must be given the abrasive supply at least 2-3 times to maintain the stability.

In concluding this subsection, the thin abrasive is better for the active polishing for the reasons that they have larger friction coefficient, better stability and predictability in friction behaviour, faster MTP and finally the ability to last longer.

5.5.3 Combined Implication of Ablation and Friction Experiments

The ablation experiment is conducted with the thick abrasive and the ablation coefficient decreases with the sliding speed. It is in good agreement with the kinetic friction coefficient of the thick abrasive which also decreases with the sliding speed.

In retrospect, would the ablation coefficient of the thin abrasive remain constant

with velocity just as the friction coefficient of the thin abrasive does ? Of course, the averaged ablation coefficient in this case is smaller than the others but kept constant over the speed range. The decrease in the dwelling-indwelling time ratio does not seem to affect the ablation and friction coefficients of the thin abrasive. If this is true, then it proves the validity of the original Preston theory, at least with the domain of thin abrasive (i.e. the ablation coefficient is constant). Here the dwelling-indwelling time ratio is not governing change in the ablation coefficient with the sliding speed. It functions only to keep the ablation coefficient of the intermittent polishing lower than that of the continuous polishing. Thus the validity of the Preston's equation would still be intact in either intermittent or continuous polishing with the thin abrasive. This allows for active polishing to use the Preston equation but only with the thin abrasive and large error. This is in good agreement with NOAO useing Preston's theory for their polishing work while allowing large errors.

The fact that the friction coefficient of thick abrasive increases proportionally with load implies that the ablation coefficient should also increase with the pressure. However, the observed ablation coefficient of thick abrasive decreases with the pressure. It might be a wrong impression caused entirely by the large error. Or as seen in Fig. 5.10, the ablation coefficient varies much more with the speed range than with the pressure range. The dwelling-indwelling time ratio might be playing a more powerful role than the polishing pressure during the measurement.

The friction coefficient of thin abrasive seems to increase with load but not distinguished as the thick abrasive. They seem to be distributed quite close together along the polishing pressure, even within the error of measurement. This is agreed with Southwark's view (Holland, p 370 [52]) that the kinetic friction coefficient is rather constant over a wide range of polishing pressure in glass-glass polishing with, flooded water. This result implies that the ablation coefficient would also remain constant over the wide range of polishing pressure with the thin abrasive. It underpins again the validity of Preston's theory with the thin abrasive.

In conclusion, the thin abrasive has a friction coefficient that does not change very much over wide range of the sliding speed and polishing pressure. The thick abrasive has friction and ablation coefficients that decrease consistently with sliding speed.

But despite the fact that the friction coefficient increases distinctively with the polishing pressure, the ablation coefficient decreases with it. The theory of dwelling-indwelling time ratio in intermittent polishing can be used to explain all the results of the ablation and friction experiments. This makes it viable to believe that the ablation coefficient of the thin abrasive would remain lower than that of continuous polishing, but rather constant over the wide range of sliding speed and polishing pressure.

The thick abrasive's strong tendency with the sliding speed and polishing pressure lowers the validity of Preston's theory with it. It is found that the dwelling-indwelling time ratio can be used to bring it up to a more reliable level. It seems to be valid with the thin abrasives. This allows for Preston's theory to be used for active polishing, but with a large error. The dwelling-indwelling time ratio could be a hidden variable in the use of Preston's theory, to explain various polishing phenomena. Preston's theory appears to be invalid in measurement, when the dwelling-indwelling time ratio is not kept constant in a polishing run. The continuous polishing can be regarded as a subset of the general intermittent polishing with the dwelling-indwelling time ratio of the infinite. Active polishing should make use of these findings.

5.5.4 Implication of AFH and FRT Analysis

The Reducible data set was about 89% for the thin abrasive and 59% for the thick abrasive. It means that the measurement of friction faces losses of 11% and 41% of the whole data set (i.e. the first undeterministic nature). Even with the Reducible data set, the friction measurement has large errors (see Section 5.3), this being second undeterministic nature. This indicates that any attempts for friction control, i.e. ablation control in real time, has large errors. The aim of ablation control should be given to control of the integrated-statistical behaviour of friction in glass polishing.

The thin abrasive has the AFH time of about 3 seconds and the recovery rate of about 12% on average for both Strong and Weak AFHs. The thick abrasive shows about 8 seconds and 29% (Weak AFH) and 62% (Strong AFH) for the AFH time and the recovery rate respectably. It means that, first of all, the thin abrasive must

be used in active polishing because of the better stability and therefore predictability in friction under force modulation. Secondly, the abrasive must not be left until it is dried in polishing. The thin abrasive must be re-supplied in every about $20 \pm 10(\sigma)$ mins in polishing (see previous Section).

For full size active polishing, the stroke tends to push the abrasive away from the mirror surface. This would require the abrasive more frequently re-supplied than 20 mins. In addition, convex surfaces have faster rates of loss for abrasives than concave or flat surfaces. It may require the re-supply time of, perhaps, 5-10 and 10-15 minutes for the convex and concave mirrors respectably in polishing. Because of the faster rate of abrasive loss, the convex mirror would be more difficult to maintain the friction stability than the concave mirrors. This leads to difficulty in measurement and hence control of friction and ablation.

The average FRT is 4 msec/gmf which means that the friction modulation of intended magnitudes at 10 Hz is impossible with the current active lap. FRT of the thin abrasive decreases whilst the thick abrasive shows no relation with applied load due to large errors in measurement. The emphasis in the current development of active polishing is to control force/pressure actively. Indeed, the traditional passive polishing has been trying to control force/pressure passively with no feed back control. These trends rely entirely on the assumption that the amplitude and frequency of the force/pressure modulation are those of the friction modulation in polishing. In other words, the transfer function from the force/pressure modulation to the friction modulation is 0 i.e. 100% transferable in amplitude and frequency.

What this evidence is leading to is a sort of *'Modulation Transfer Function (MTF)'* between force/pressure and friction modulations in polishing. This MTF seems to have following characteristics.

- There is a sort of statistical behaviour in force amplitude-friction amplitude transfer. It causes large spread in resulting friction level.
- In force amplitude-friction frequency transfer, the thin abrasive shows that the friction frequency increases with the force amplitude. The thick abrasive does not seem to show that particular tendency.
- In force frequency-friction frequency transfer, if the force frequency is com-

parable to the friction frequency, there exists a time delay between the force frequency and the friction frequency. If the force frequency is faster than the friction frequency, which is likely to be the case almost all the time, the faster force frequency chops off the slow friction respond to produce the same frequency in friction, but at the expense of reducing the friction amplitude.

- The second case in the previous item introduces the force frequency-friction amplitude transfer, which is an induced effect.
- The above is discussing the physics of polishing i.e. the core of the polishing algorithm. The MTF would also be affected by the hardware of the lap, itself, and how it works.

The mathematical expression of this MTF has still far to go. Many more precise measurements on the terms defined in this chapter have to be made in order to achieve that.

5.5.5 Criticism on The Existing Theories and Developments of Large Optics Polishing

The experiments made in this Chapter are entirely relevant to the sub-diameter tool polishing into which all the pseudo active polishing can be categorised. They have a common ablation pattern of the intermittent polishing, which seems to be neglected. The behaviour of the abrasive films such as FRT and AFH are also completely ignored in their polishing methods.

Except Preston's theory, most of early studies, reviewed by Cornish [19] on the polishing mechanism, are not in good use for controlling ablation. They are rather focused on the physical nature, than control of ablation in glass polishing. The recent studies made by Izumitani [58], Brown & Cook [14] and Silvernail [98] are no better than Preston's theory in any sense for the optician to control ablation during polishing operation. It has been known that more recent investigations have been made by some institutes such as NPL, LLNL, etc. Unfortunately, the exact nature and results of their experiment are veiled in commercial secrecy. There is still much argument in the public sector about what the relationship between the

ablation rate and the polishing variables is and the physics of optical polishing is still in an undeterministic realm.

In 1991, Norman J. Brown, one of the most renowned scientists in polishing science, admitted that he uses Preston's theory in quantifying ablation of material with the various polishing conditions. His ablation coefficients for fused silica and Zerodur to which my results were compared were obtained using Preston's equation. NOAO also uses Preston's theory with the ablation coefficient obtained by their own experiments, for their polishing work. Meanwhile, Lindsey [70] has concluded that optical polishing is a sort of *Addictive Process*. Among the three theories i.e. mechanical wear, plastic flow and chemical attack, no one is entirely responsible for a polishing run. It varies from one to another, responding to the set of polishing parameters and their magnitudes used. When a process takes responsibility for a certain stage of polishing, it becomes addictive. It means that controlling the polishing parameters, in small magnitude, does not trigger the replacement of the responsible process with others. However, if they are kept under continuous change, sometime later, its combination brings in another process to taking charge of the polishing. Unfortunately, how the transformation takes place is not well understood today. The ablation rate and, of cause, its relation to the polishing parameters would be totally different depending on which process is in charge.

Thus ablation in optical polishing does not seem to be linear process with the polishing parameters involved. In fact, NOAO and Lindsey have accepted that their experiments show a *large error* in estimating the ablation rate. The exact magnitude of the error is still not disclosed. The large error has been repeatedly observed from the experiments made in this Chapter. This non-deterministic nature of ablation, in polishing, could mean that control of the integrated ablation would be much more predictable than that of the instant ablation. This is because the statistical nature of the instant ablation rate would be reduced when integrated over a certain time period. This opens up a new way of updating the actuator in real-time operation. Instead of attempting control of the instant ablation rate with the fast frequency (e.g. 10 Hz) for actuator update, it is to update the actuators with low frequency throughout a polishing run. Examples include 10 mins polishing with a force modulation per every 1 minutes. An extreme end of this line would be, for example, a 10 mins polishing with a single force distribution defined. In this context, the

frequency of 10 Hz can be regarded as the opposite extreme end in the modulation frequency spectrum that can be used for the active polishing developed here.

The experiments made in this Chapter appear to give contradictory results unless the concept of dwelling-indwelling time ratio is applied to analyse them. The un-deterministic nature of polishing is well represented by the fact that a substantial amount of data becomes Un-Reducible and there is large errors involved in ablation, friction, FRT and AFT measurements. Preston's theory can be regarded as valid but with large errors if the thin abrasive is to be used. It becomes unclear if it is indeed correct for the thick abrasive. The contribution of the various polishing parameters including the dwelling-indwelling time ratio has to be investigated to clarify this.

In view of the suggested theory of the dwelling-indwelling ratio, Itek's CCOS approach, that controls primarily the dwelling time on the mirror surface, gives continuous polishing effect to the surface for the duration of dwelling. This is a better approach than other existing methods in the sense that only one type of polishing i.e. continuous polishing not intermittent is involved in the operation. Therefore, the ablation coefficient tends to be constant for a polishing run, assuming that all other variables remain constant and uniform over the mirror surface. However this is not in fact always the case. In addition, the dwelling time map has the spatial frequency of about the lap size, meaning that ablation can not be controlled in a higher spatial frequency. Due to these reasons, this approach is likely to produce a high frequency error of about the lap size.

In concluding this subsection, all the existing subdiameter tool polishings have the following disadvantages that should be improved for future developments in large optics polishing.

- The modulation of polishing pressure in open-loop with the absence of force sensor makes it impossible to reliably control the friction as intended.
- The behaviour of abrasives such as FRT and AFH are not taken into account.
- Therefore, the ablation coefficient at different zones differs from each others.
- This provides the inability to control the real friction precisely at different zones, causing zonal defects.

5.5.6 Some Guide Lines for Future Trends in Large Optics Polishing

The future development in large optics polishing would be greatly benefited from the following guide lines.

- **Full size-active close loop control of absolute pressure, velocity and dwelling time:**

  This method is actually an advanced version of the combination of 4 approaches from Draper's absolute pressure control, Grubb-Parson's full size polishing, Zeiss's pressure control, and Itek's dwelling time control with the closed-loop feed back control using load cells and position sensors.

- **Appropriate computer-based algorithm with learning ability:**

  The ablation algorithm should take the statistical behaviour of friction and therefore large errors into account when starting its development. The undeterministic nature of ablation gives a rise in the importance of employing fuzzy logic or a neural network in conjunction with parallel processing to find a necessary work functions for a polishing run. To precisely determine and to control the ablation in real time would not be achieved for the first time of use of the algorithm. Thus, it is crucial for the algorithm to be able to learn and evolve to a more matured form with time. This would inevitably involve a large amount of polishing data, that can be effectively processed only with the aid of modern microprocessors.

- **Variables embedded in algorithm must be found by experiments:**

  The ablation and friction coefficients have to be measured and optimised with the polishing conditions to institute's preference. In particular, an appropriate experiment is to be devised for measuring the variation of ablation coefficient with the dwelling-indwelling ratio in polishing. AFH, FRT, Availability, loss of abrasive, abrasive lasting time and friction stability have to be further experimented on by institutes, themselves. The results obtained here suggests that

- the large error in measurement of ablation and polishing variables must be allowed.
- the modulation of ablation variables do not have to be at high frequency such as 10 Hz, or faster.
- friction MTF of the abrasive film in terms of friction must be further investigated.
- the thin abrasive must be used and re-supplied in 5-10 minutes in operation.
- an international consortium can be established to collect and share the results of the ablation experiments conducted by each institute. This will provide, in the long term, the essential ground to solve the question about the nature of polishing.

5.5.7 Problems with The Experiments Made

A number of problems faced with the experiment described are summarised below.

Ablation Experiment

- The growth in pitch dimensions enlarges the error in calculating the polishing pressure.
- The results of the sub-diameter tool polishing are not relevant to the full size polishing. The results can not be directly used for the full size active polisher designed. The ablation coefficient of the continuous polishing is more important for the full size active polishing since most of the work piece surface is given the continuous polishing. However, the results obtained can be applicable to the edge of the mirror where intermittent polishing is made even with the full size polisher.
- The thick abrasive used actually decreases the ablation rate. The results are not relevant to the active polishing using the thin abrasive as OSL always does in polishing.

Friction Experiment

- Oscillation alters the position of the calibration weight on the load cell. This makes changes in the calibration data, resulting a larger error.

Behaviour of Abrasives

- Many of the Strong AFHs take longer than 20 seconds. These are often interrupted by the next loading. This causes an artificial decrease in data availability. There are found 5(thin) and 55(thick) cases, that are classified as Un-Reducible data but indeed triggered by the loading interrupt. However, it can not be sure that the loading interrupt is the only cause of that. If that can be assumed, then the data availability increases to 90.6% and 77.7% for the thin and thick abrasives respectably. It would be reasonable to think that some of them are caused by the loading interrupts but others by intrinsic causes e.g. oscillation, no-response, etc. Thus we can only say for now that the data availability is 88.5-90.6% and 59.3-77.7% for the thin and thick abrasives respectably.

- Because of the loading interrupts above, the AFH time for the Strong AFH is forced to be shorter than 20 sec.

- The weight should have been altered with an interval of about 30 sec. Longer interval takes longer e.g. 10-20 min to complete one measurement cycle. The abrasive must then be re-supplied within that time interval. This new abrasive changes the friction condition so as to affect the result.

5.5.8 Suggestions for Future Experiments

Experiments for the physical parameters introduced in this Chapter will continue with particular interest in their behaviour with different dwelling-indwelling time ratios. To experiment the ablation coefficient of the continuous polishing at different sliding speeds, and polishing pressure is crucial for validating the concept of dwelling-indwelling time ratio and for clarifying other issues discussed in this Section. A new

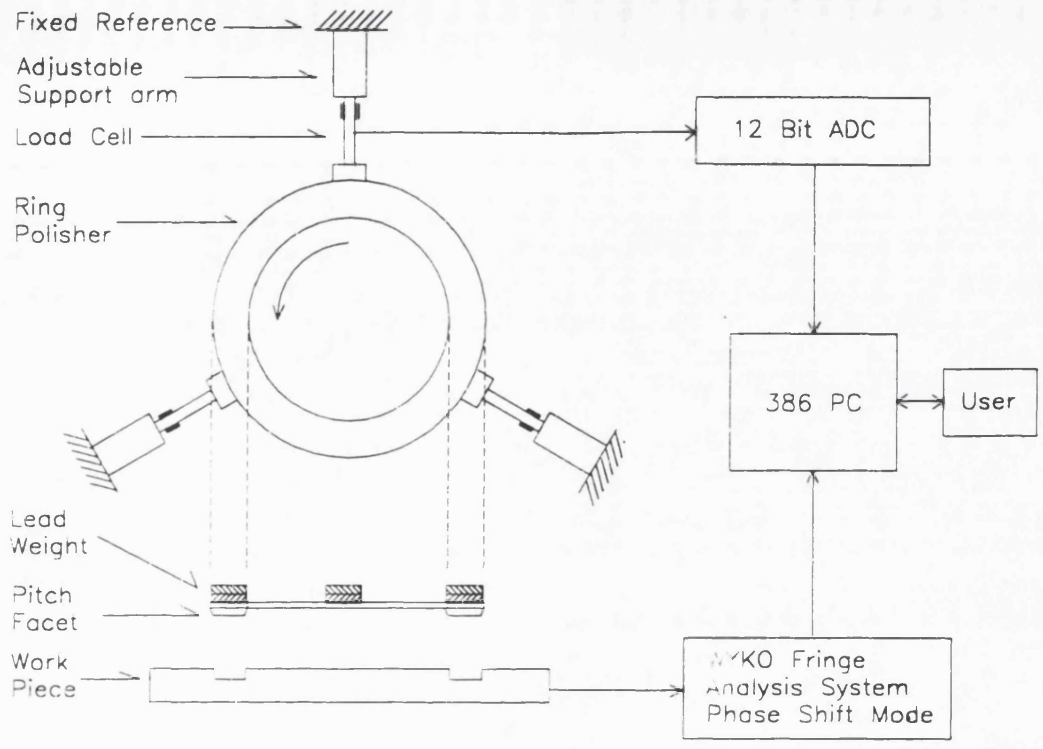

Figure 5.16: A proposed new experiment set-up

apparatus that does not suffer from most of the problems listed above is proposed for that as shown in Fig. 5.16.

It would at least include the modifications summarised below.

- Four annular ring polishers of about 5 cm in width would be used instead of the 5 cm diameter circular polisher. They can make the continuous polishing at four different radii. The intermittent polishing can be achieved by removing parts of the annular pitch so that the dwelling-indwelling time ratio can be controlled as requested.

- Instead of 3 pitch holding strings, 3 supporting arms, each spaced 120°, can be used to hold the annular polisher. The interface between the arm and the polisher would be a load cell that measures friction. A load cell can be mounted to each arm, to measure total friction. Alternatively, one active load cell is mounted to an arm and two other arms have a dummy load cell each, which has same dimension, weight and compliance as the active one.

- The polishing pressure can be controlled with lead weights placed on the top side of the polisher.

- Instead of the 8 bit A/D converter, a 12 bit A/D converter would be used to convert the analogue signal of the load cell to a digital number. This can provide higher resolution.

- All the axililiary polishing variables would have to be tightly controlled. Examples include the age of abrasive slurry, water to abrasive ratio, room temperature and humidity, etc.

- The dimension, weight and hardness of the pitch would have to be carefully monitored throughout the experiment.

- The phase shift fringe analysis would have to be employed instead of the static fringe analysis. It is capable of providing the analysis error of about 1/50-1/100 λ, which is impossible to achieve with the static fringe analysis due to the large error, from the manual fringe edition.

Chapter 6

85 cm Scaled Experimental Active Lap

6.1 Introduction

Following the initial design of the active lap and construction of the active module, further evolution and modifications of the active lap design were made in parallel with construction throughout 1991. In early 1992, the mechanical hardware of the active lap was assembled. The preliminary version of the control electronics and software became operational in the middle of 1992. These had been used for preliminary testing of the active lap before it was committed to any serious jobs. Findings from these early tests were used to improve the performance of the electronics and software. The second half of 1992 and almost three quarters of 1993 were spent upgrading every aspect of active lap performance, this indeed being a long and hard iterative process of 'test and fix'. In September 1993, at last, was introduced the first version of the operational active lap equipped with reliable calibration. Experiments in July and August 1993 showed that the active lap is able to detect correctly the pressure distribution throughout the lap stroke. This Chapter describes the progress made during this period.

Section 6.2 describes progress of the active lap design toward the final construction design, including specifications of active lap control software and ablation algorithms in detail. The technical problems foreseen and solutions are also addressed in this

Section. Various technical aspects of construction and installation of the active lap are discussed in Section 6.3. Technical problems with the initially assembled active lap and the solutions we found are concerned with Section 6.4. It includes FE analysis to find the coupling between the actuator and load cell arrays. Efforts for calibration of the active lap are also presented in this Section. Section 6.5 explains the performance of the assembled active lap in initial testing and the progress in production of the scaled Gemini secondary so far. Section 6.6 discusses the implications of the operational active lap, evaluation of its performance and the whole development, suggestions for improvement in the active lap performance and some future work.

6.2 Progress towards The Manufacturing Design

6.2.1 Mechanical Design

• Evolution towards An Interim Design

The developments made in Chapter 4 does not affect very much the overall design of the active lap described in Chapter 3, except that the solenoids were replaced with the stepping motor and spring actuator. Studying this design revealed another problem, that at the outer region of the lap, the load cells and thin plate would be several centimetres above the mirror surface. As seen in Chapter 5, the average friction coefficient of the thin abrasive was about 0.25 and 0.29 for the friction and its stability measurements respectively. This means that about 25-29 % of the axial load such of the lap weight would become the frictional force exerted to the pitch surface. Firstly, this would then exert a substantial moment that would tend to buckle the thin plate and twist the load cells. If the thin plate were thickened to avoid this, then it would introduce cross-talk between the load cells and reduce the precision with which the forces acting on the mirror would be known. Secondly, although the lateral force exerted onto the load cell can be compensated with reasonable accuracy by averaging the 4 bridge signals, its increasing magnitude would certainly enlarge the error.

For these reasons, a design modification has been proposed as drawn in Figure 6.1.

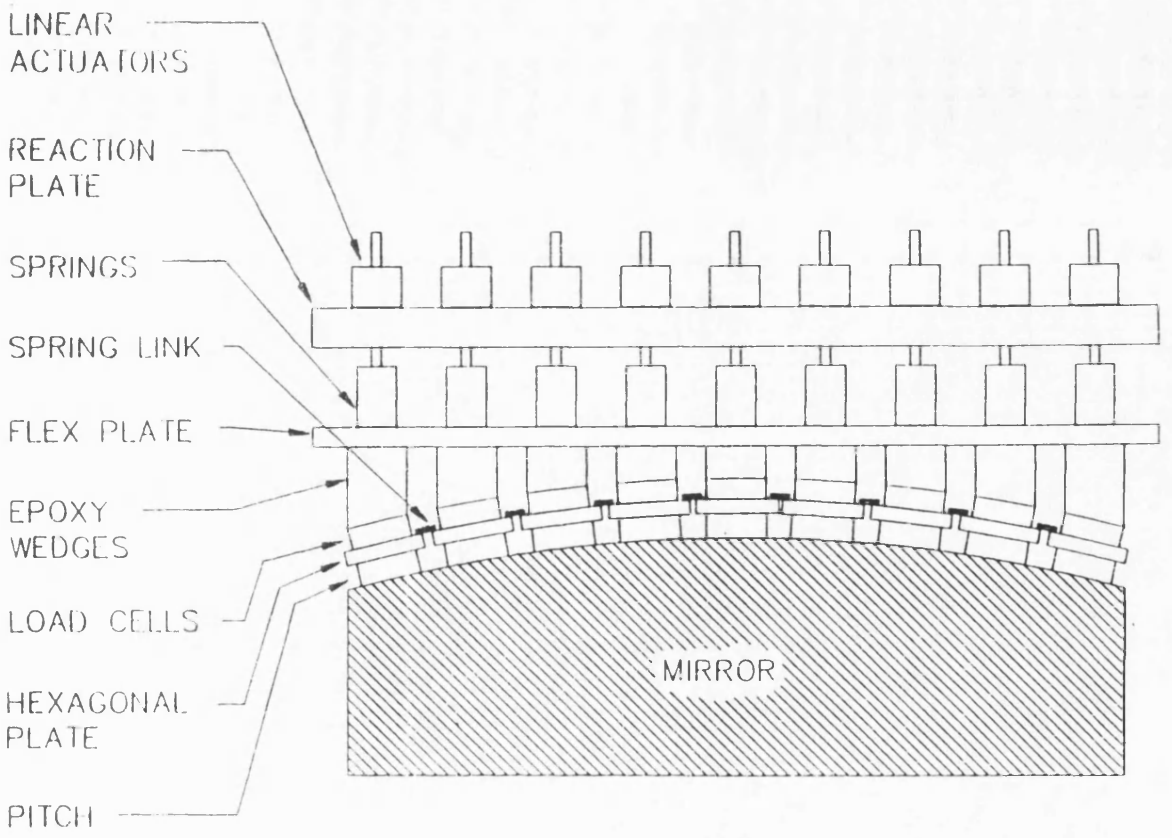

Figure 6.1: A modified design of the active lap

The thin plate is omitted and the load cells are located close to the work piece surface at the mirror-end of the epoxy spacers. The other ends of the spacers are mounted to the lower face of the flex plate. They can be NC-milled so that their height naturally accommodates the sag of the mirror profile. Separate hexagonal plates attached to the load cells carry the pitch. They are linked together with separate flexural links to emulate the effect of the thin plate. In practice, a water-proof membrane of continuous plastic film would be incorporated in-between the load cells and the hexagonal plates. This would protect both the load cells and the mirror surface from contamination. The plastic film would be larger than the lap, wrapped around the top of the reaction plate and clamped to enclose the delicate part of the assembly. If there are any problems with incorporating the flexural links, a thin (e.g. 1 mm in thickness) Aluminium shell would be used inbetween the hexagonal plates and the pitch. There would be no need to replace the main flex plate. The rest of the design remains the same.

• **The Final Overall Design:**

The interim design leaves two problems unsolved. Firstly, the load cells are inherently forced to work with the off-axis load. The off-axis load vector varies sys-

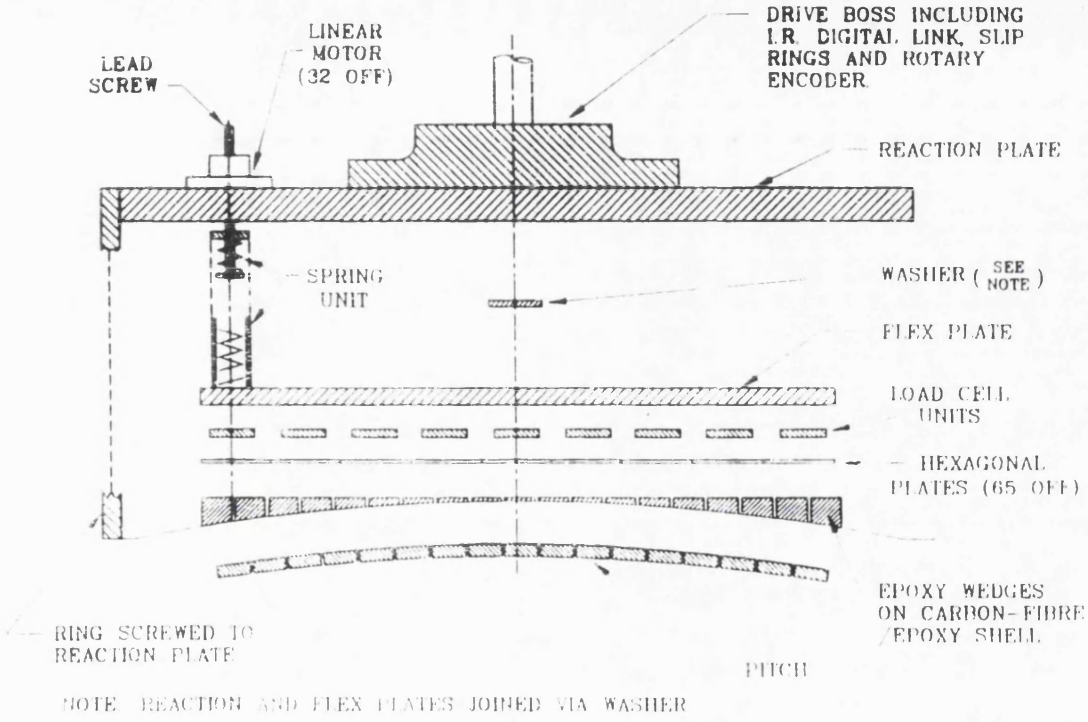

Figure 6.2: Exploded view of the active lap with the final design

tematically with the slope of the mirror profile. Secondly, this off-axial operation combined with the frictional force would certainly increase the error in the load cell performance even with the averaging technique. All non-axial loads would be better removed in the first place before they are transmitted to the load cells.

For this reason, the design finally settles to what is depicted in Figure 6.2. Here, the load cells are attached to the lower face of the flex plate just like the first design. A hexagonal plate is mounted at the mirror-end of each load cell and they are linked to each other by the flexural links as suggested in the modified design. If there exist any problems with the flexural links, they can be linked with a weak silicon cement. It is highly compliant so that one load cell does not piston the next and disturb its response. Its uneven height compared to the hexagonal plates can be trimmed after it has set. This provides a complete seal for the bottom face of the load cells. Underneath the hexagonal plates, there is an array of epoxy wedges whose height varies to accommodate the sag of the mirror profile. Their bottom faces are stuck onto the top surface of the cast thin metal shell which carries the array of pitch facets. The thin shell would be cast to fit with the desired mirror surface. The circumference of the shell is attached to the bottom end of the metal cylinder

whose top end is bolted to the edge of the reaction plate. There is a gap condition inbetween the hexagonal plates and the top surface of the epoxy wedges.

With this design, the load cells always work with axial forces. The lateral force generated by friction is transmitted through the thin shell to the reaction plate where the main driving force is exerted. Thus, the main structure with which the close-loop pressure modulation is achieved is virtually free from the disturbance of the lateral force. The delicate part of the lap is completely enclosed by the shell and the metal cylinder, this being a shield from any contamination. One condition though is that horizontal movements of the thin shell must be constrained while allowing vertical movements.

• Packing Strategy for Load Cells, Actuators and Pitch Facets:

General condition:

The dimension and shape of a specific component affect decisively the total number that can be mounted to the lap. The approximate size of 6 cm for the Sonceboz 7230B motor allows the lap to have about 13 motors at maximum across its diameter of about 80 cm. The link between the push-pull arm and the reaction plate would occupy the central area of the lap of about 15-20 cm in size. This leaves space for about 5 motors assembled very close to each others on one side of the lap. Allowing a gap between them gives about 3 motors mounted across the radius and approximately 28 motors in total for the entire lap surface. The size of the load cell of 8.6 cm in diameter allows approximately 9 to be mounted across the lap diameter of 80 cm diameter and roughly about 63 load cells in total distributed over the lap surface.

The flex plate smooths the force functions exerted by each actuator to a continuous function. The characteristics of the smooth force function depend on the flexibility of the flex plate which is again governed by its size and thickness and the presence of the central washer. The smoothing effect of the flex plate implies a complex relationship between pressures exerted by individual actuators and measured by the load cells (and so exerted on the mirror). The flex plate can be regarded as a medium that introduces 'cross-talk' not only between the actuators and load cells but also between the actuators themselves. Thus, operation of an actuator affects other actuators and all the load cells presented in the system. Knowledge on how

they are coupled together would play a crucial role for the success of closed-loop pressure modulation. This complex coupling exists whether the load cell are packed in the same way as the actuators or not. The technical difficulty of obtaining the knowledge would be the same regardless of similarity or difference in their packing strategies. This means that the load cells and the pitch facets can be distributed totally independently from the actuator packing. The spatial frequency response of the flex plate means that the pressure does not have to be sampled at every location of the load cells on the lap. This allows some load cells to be active with populated strain gauges while others are not.

Actuator packing:

The distribution of the actuator forces and the surface pattern of the pitch facets seriously affect the shape of pressure map on the mirror. For polishing mirrors with radial and circular symmetry, the packing of the actuators and the pitch facets should have the circular symmetry in shape. For 3 rings of the Sonceboz 7230B motors with the modified mounting flange, a total of 40 motors can be mounted with 8, 16 and 16 nodes on each ring. Then the total force of about 160 kg that they can exert is twice the lap weight initially designed. This is enough force to cause severe distortion of the flex plate. In order to avoid this, the 40 locations on the 3 rings are prepared for actuator mountings on the reaction plate but only 32 actuators actually be mounted for use with 8, 8 and 16 nodes. There is no active actuator at the centre of the lap but instead the central washer play a role of a virtual actuator with an extremely high stiffness. The mounting flanges of Sonceboz 7230B is removed and the motor body is directly bolted onto the channel which is attached to the upper face of the reaction plate. The channels have radial distribution to accommodate the 3 actuator rings.

Relation between actuator and load cell packings:

The actuator packing does not force the load cells to be packed in the same way. One condition though is that they must cover the entire surface of mirror with fine enough spatial frequency for pressure sampling. Since the load cell is similar to the traditional pitch facet in size but not in shape, they would be packed with very small gaps which are just large enough for electric pins and wires not to affect the load cell performance. In particular, at least one load cell must be located at the centre of the lap, since all the actuator forces react against the central washer. All the

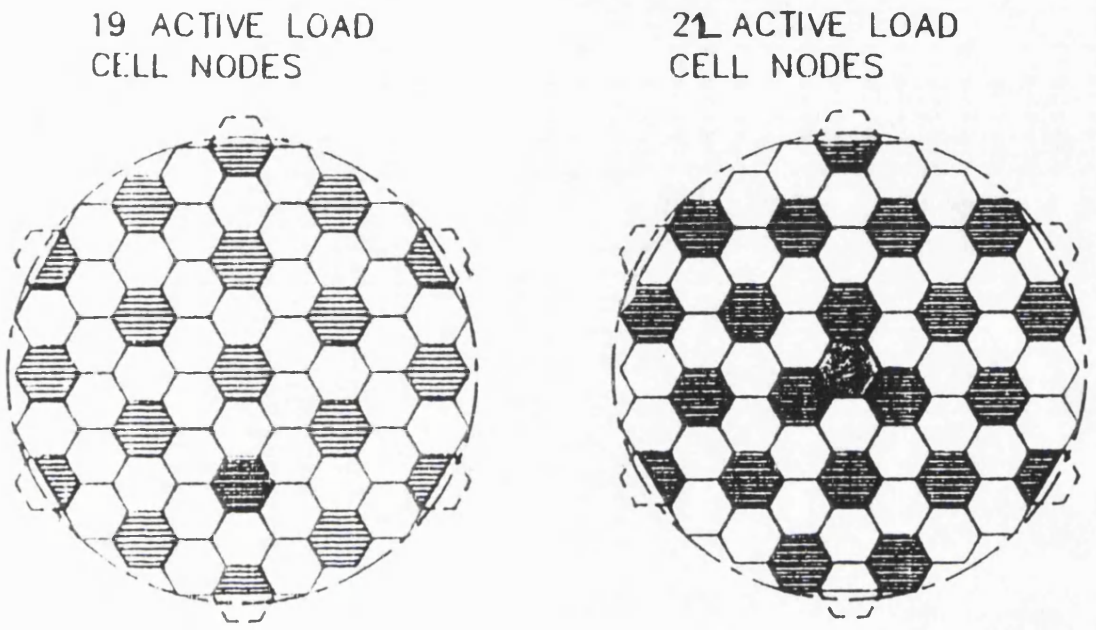

Figure 6.3: The hexagonal packing of 61 load cells has 2 modes in which the active load cells are configured.

other load cell readings can be compared to that of the central load cell, if required.

Load cell packing:

Detailed study reveals that, due to the gaps between the load cells, only 61 instead of 63 load cells can be mounted and there are two ways of doing that, as depicted in Figures 6.3 and 6.4.

Option1: Hexagonal packing

The first is the hexagonal packing where the load cells and their hexagonal shield plates are distributed with equal spacing in a large hexagon that covers the 85 cm work piece surface (Figure 6.3). The 6 ears of the hexagon are slightly larger than the work piece and therefore so is the flex plate in order to accommodate them. There are two ways of configuring the active load cells in this packing. One is to have active load cells every two hexagonal rings starting from the centre. In each hexagonal rings, the active one is in every second load cells. This leads to a total of 19 active with 1, 6 and 12 active nodes in 3 rings and 42 dummy load cells elsewhere. The other mode is to have an active load cell at the centre and three active load cells at the 3 nodes of the next ring. Then the active load cells are populated at the

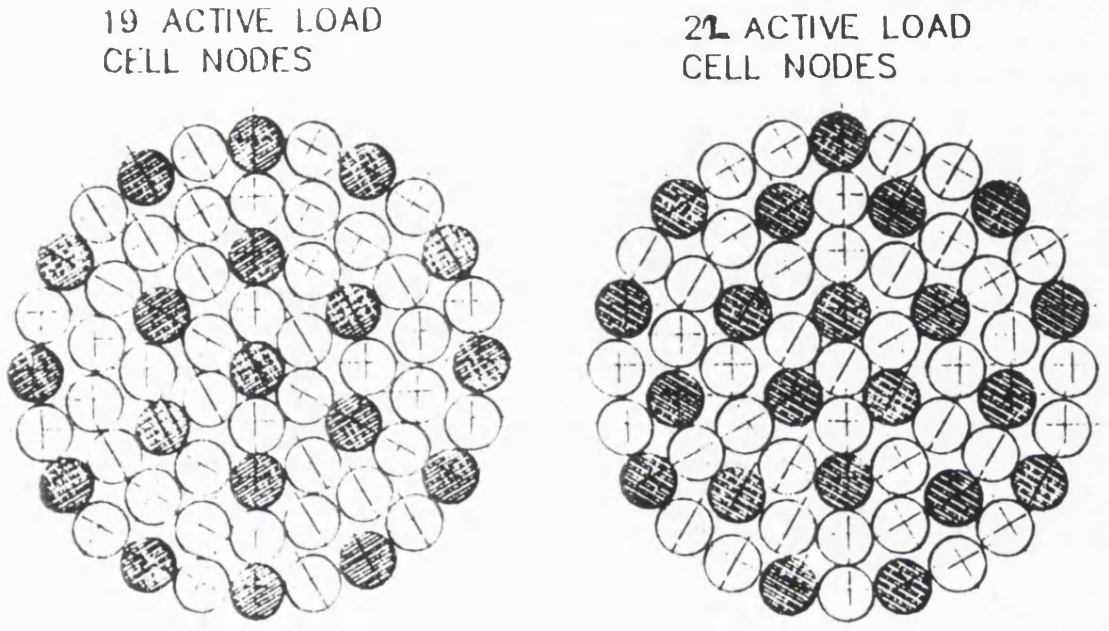

Figure 6.4: The circular packing of 61 load cells has 2 modes in which the active load cells are configured

3 vertices of every triangle within the large hexagon. This requires 22 active and 39 dummy load cells.

Option 2: Circular packing

The second is the circular packing. It was in fact found by slightly moving the relative locations of some load cell nodes from the hexagonal packing. The outer boundary of this packing can fit into the work piece size and the load cells have unequal spacing. The two modes of the active load cell configuration described can be applied to this packing in the same extent. The load cells are not equally spaced with the circular packing. Then the uneven support would cause a bending of the flex plate, which is totally unnecessary. In addition, some of the load cells(e.g. the central one) do not have enough space around them for the electric pins and wires to be placed. The 22 active load cell mode provides slightly finer spatial frequency than the 19 active load cell mode for pressure sampling.

Final choice for load cell packing:

For these reasons, the hexagonal packing with the 22 active load cells was chosen. Each load cell is attached to the lower face of the flex plate with a 3 point support of

about 50 μm metal shims. The orientation of the load cell is as random as possible.

Packing for pitch facets:

Since the active lap is designed to control the actual polishing pressure over the mirror surface, special patterns of pitch distribution were not needed for ablation control. The only condition is that it must cover the entire surface of the work piece. However, if the pitch surface is larger than the work piece, a height difference within each pitch facet at the edge of the lap can occur during pressing over night. This would cause damage to the mirror edge when polishing. For this reason, the pitch surface must fit within the mirror diameter and the peripheral pitch facets are trimmed to give an approximately circular outline to the riding surface.

The earlier interim design did not allow much freedom for the shape of pitch and its distribution. It is most likely to be hexagonal with each pitch facets stuck onto the load cell-hexagons assembly individually. However the final design provides the freedom to chose any shape and distribution of pitch, since they are stuck onto a single continuous shell. Thus it would not be a serious matter, as long as they are smaller than about 10 cm in length. Thus, to start with, it uses the traditional square pitch facets of about 8 cm in length in a 2-D linear array slightly decentred with trimmed periphery. Because they are glued onto the lower face of the thin shell, the replacement of the pitch facets, if required, can be easily made without causing significant down-time.

• Global Actuators

Problems with the initial design of global actuators:

The initial design of the global rocking actuators proposed in Chapter 3 would require either three pairs of actuator-load cell assemblies or three pairs of actuator-tilt angle encoder for rocking compensation. One additional pair of actuator-load cells, likely to be of different models, is attached to the supporting roller for the push-pull arms, would also be necessary for controlling global pressure. A number of disadvantages were found as listed below:

- The volume of the lap assembly would increase considerably. The resulting lap would hardly fit on to the 1 m polishing machine and its infrastructure.
- There is not enough space on the side of the two eccentrics of the 1 m polishing

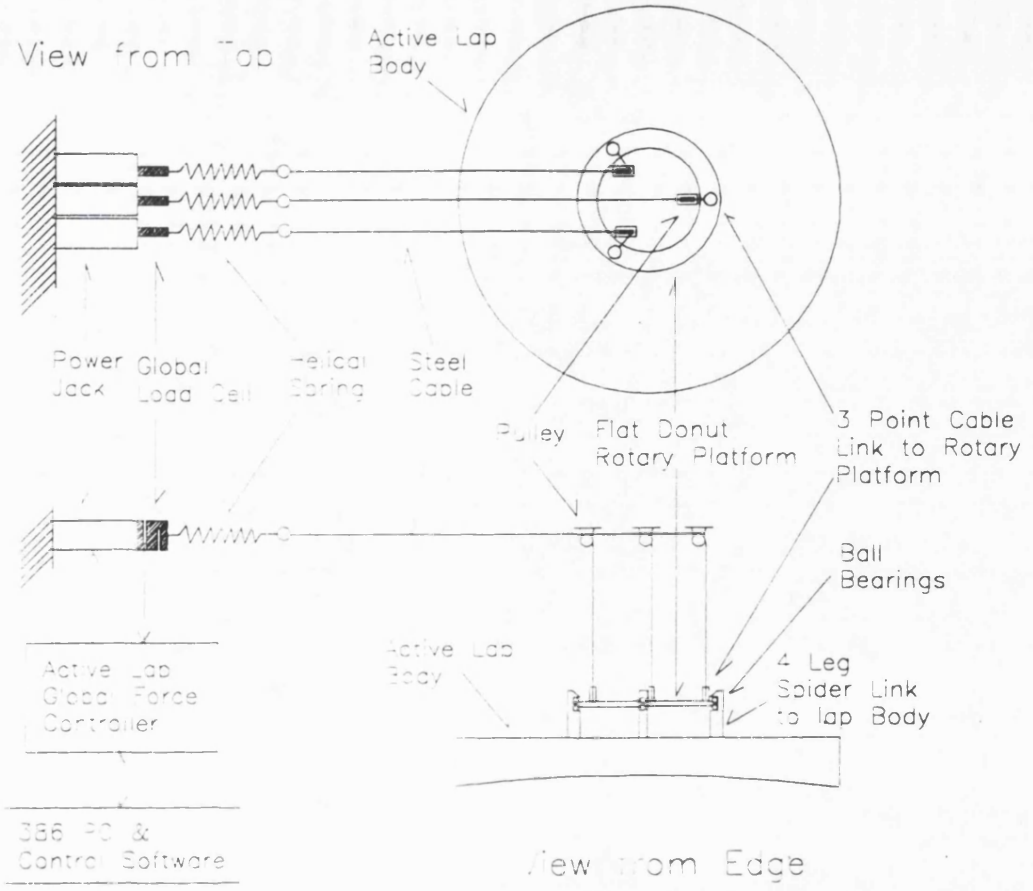

Figure 6.5: The new design of the global actuators for rocking compensation and global pressure control

machine. Extra mechanical hardware for the supporting roller would have no place to go.

- The rocking compensation would be controlled independently from the polishing pressure modulation. This could cause unforeseen complications in pressure modulation.

The final design of global actuators, as built:

A simpler but more effective design, as built, is presented in Figure 6.5. three power-jack actuators would be fixed to a reference point. They have three load cells at the opposite ends. The three helical springs link the load cells to three steel wires which holds a flat rotary ring. The ring slides to rotate freely, being sandwiched by 3 ball

bearings mounted on 3 metal legs angled 120° and attached on the reaction plate. As the lap strokes, the rocking increases tension on the steel wire of the rocking side. It is monitored by the load cells. A desired load level of the 3 load cells are pre-set for a global pressure control. The control PC keeps updating actuator forces to level the 3 forces sampled by the 3 load cells to the pre-set value.

Advantages of the final design of global actuators:

This concept, as built, has a number of advantages over the previous design.

- Instead of 4 pairs, only 3 pairs of actuator-load cell assembly are used for rocking compensation and global pressure control, which is cost-effective.
- The volume of the lap assembly increases at the minimal level. There are the 3 ball bearing-leg assembly and the flat donut platform on the lap. The current lap and its infrastructure designs are not affected by this.
- There is no need of space for the mechanical hardware for the supporting roller on the side of the 2 eccentrics.
- The 2 functions, i.e. rocking compensation and global pressure control, are dealt with the same hardware and controlled by a single control process of real-time pressure modulation.

Problems with the final design of global actuators:

Two technical problems were foreseen in relation to the lap stroke. Firstly, when the lap strokes, the three load cells are exposed to some degree of non- axial force which is undesirable. A solution would be to fold the 3 wires 90° using 3 pulleys and the load cells and the helical springs sit on the fixed metal channels. Any non-axial forces from the lap stroke are then separated when passing the pulleys. Secondly, the lap stroke varies the direction of the wire tensions in real time. Their vertical components, which vary accordingly, are the real forces that controls the global pressure exerted onto the mirror. The angles of the wires at a given time are slightly different from each other. The real forces that lift up the lap would always be smaller than the pre-set values by the factor of the cosine of the angle and they vary from one wire to another due to different angles. The difference in the real lifting forces between the 3 wires could still cause the rocking. However, if the wires

are long enough, the cosine factor and its effect on the difference between the three lifting forces is negligible. In principle, using the location of the lap on the mirror, the lap control software can correct it in real-time.

• Global Friction Load Cells

Functions of global friction load cells:

The arms provide the ideal and only place with which the side force given to the lap can be measured as a whole. Two other load cells of the same model, as the global force load cells, are attached to the eccentric end of the push-pull arms. These monitor the global force that the push-pull arms exert for lap strokes. The eccentric end of the arms is in fact the better place for the load cells to have less effects from the non-axial component of the force given to the opposite end of the arms throughout the stroke. The two eccentrics and the active lap are attached to the both ends of the push-pull arms in a manner that allows them to rotate freely in operation. This keeps the non-axial force to the load cells at a minimum. Two technical problems can be addressed in relation to the nature of the force measured by these.

Friction combined with the translational lap inertia:

Firstly, if the lap is pulled or pushed with a constant velocity using the push-pull arms, the load cells measure the kinetic friction force i.e. friction coefficient times the difference between the lap weight and the tension on the 3 global actuators. However, the lap stroke keeps changing the magnitude and direction of the velocity vector, and so the acceleration vector varies continuously in operation. The load cells would then measure the static and kinetic friction combined with the inertia of the lap mass. Fortunately, the inertia is related only to the mass and acceleration and has nothing to do with the normal load. Because the location of the lap, in an absolute coordinate system centred at the centre of rotation of the turn table, is monitored continuously, the acceleration of the lap movement can be calculated. This enables us to determine the time variation of the inertia of the lap. The real friction would be calculated by subtracting this from the measured force.

Friction combined with the rotational lap inertia:

Secondly, in spite of the stroke moving the lap only in translation, its rotation in the absolute coordinate system is almost always observed in practice. Depending

on the stroke parameter, it keeps either rotating in one direction or alternating the direction of rotation, synchronised with the stroke. One possible explanation on this phenomenon is that the kinetic friction force in translation varies on the lap. It is caused by combination of the instant lap stroke vector and the constant rotation of the mirror. Often, one side of the lap simply rides on the mirror of which angular velocity is in the similar direction with the stroke vector. The translation friction would be very little at this side. Whereas the other side of the lap faces the angular velocity headed in almost the opposite direction. This generates a considerable amount of translation friction toward the direction of the angular velocity of the mirror i.e. the mirror rotation. Thus the friction increases across the lap diameter. The shape of the friction map on the lap at a given time controls the rotation of the lap. If the lap rotation in the absolute coordinate system can be assumed to be entirely caused by this non-uniform map of the translation friction, the true friction is the observed load cell reading separated from the translation and rotational inertia. Because the lap rotation is monitored continuously in real time, the rotational inertia can be calculated. Thus the global friction force can be determined.

Use of this combined friction load cell reading, as it is:

Even if the pure friction force can not be separated from the load cell reading for some reason, they can still be used for controlling ablation. This can be achieved by means of inserting the load cell reading into the table of polishing variables for a polishing run, i.e. a specific ablation pattern. (This would work only with the data base approach for ablation algorithm described later in this Chapter.) The ablation algorithms can then be able to use them for control of ablation in polishing, no matter what nature it has.

• New Plate Specifications

The total weight of the lap is about 120 kgf, which exceeds the original design goal of about 80 kg due to the extra weight of the load cells, actuators, auxiliary components, and electro-mechanical components. The thickness of the two plates should be reduced to bring the total mass down. The thickness of the reaction plate would be reduced from 2 cm to about 1.5 cm, and that of the flex plate from 0.8 cm to 0.6 cm. This of course alters the stiffness of the lap, in particular the flex plate. Thus it would influences greatly the coupling, i.e. mechanical cross-talk, between load cells-actuators, actuators-actuators and load cells-load cells. This gives rise

to the necessity of FE analysis and appropriate experiments to determine those couplings.

• Link between The Push-Pull Arms and The Reaction Plate

The link is intended to provide three functions, which are transmission of the stroke force exerted by the two eccentrics motors, the slip ring mechanism for power supply, and a stable base for the bi-directional digital communications. The technical difficulty is compounded by the rotation of the lap with respect to the mirror-end of the push-pull arms. Brooks [11] has found a clever design for accommodating the three functions.

• Scalability

Problem with the current active lap structure:

The active elements can be simply mass-produced for a larger active lap for the 2.5 m Gemini secondary mirrors. In principle, those on the scaled active lap could be reused on the larger active lap. However, in practice, the 2 single plates approach of the lap make it difficult to reuse the components on a larger or smaller lap. The maintenance of the active elements, in case of malfunction, would be rather difficult because of poor accessibility. It would be a major engineering job to disassemble the load cells, actuators and auxiliary electronics from the scaled plates and to attach them onto larger plates.

An alternative structure for active lap:

One alternative is suggested as drawn in Figure 6.6. It is to use die-cast Al boxed frames instead of the reaction and flex plates. They are attached to each other to form the lap structure of appropriate shape and size. The actuator-load cell module can be plugged and bolted on to it from the top. Then the hexagonal plates attached to the mirror end of the load cells are linked with the flexural links. Underneath the hexagonal plate, there would be a thin metal membrane, much thinner than the original flex plate, mounted on an array of epoxy wedges that accommodate the mirror sag. The membrane would play a smoothening role which is very similar to that of the flex plate. The epoxy wedges would be attached to the upper face of the Carbon-fibre shell that carries the pitch facets. That shell would be held by the 3 metal rods of which the other end is firmly attached to the die-cast Aluminium boxed frame structure. All the components would be firmly bolted to each other so

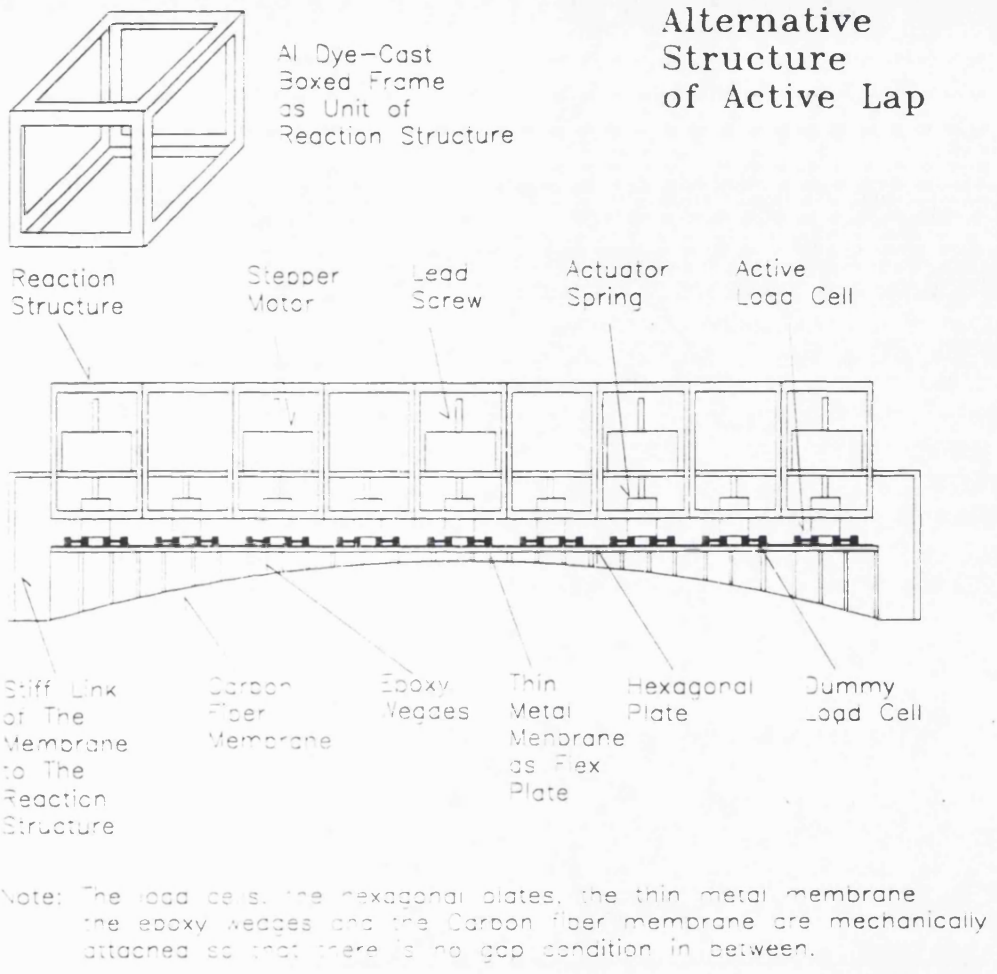

Figure 6.6: An alternative model of active lap, using dye-cast Al boxed frames.

that there would be no gap condition to link the membrane to the hexagonal plates. This, of course, allows more influence of the off-axial load to the load cell array than the original gap condition does. However, the bridge averaging and the mechanical link of the membrane to the reaction structure would be sufficient enough to reduce the effect of the off-axial load to an acceptable level. Attaching the Carbon-fibre membrane to the reaction structure provides a natural mean to stop rotation of the whole assembly underneath the stepper motors, which resulted from lead screw operation in an actuator update. All other aspects of the lap would be same as the existing design.

Advantages of this alternative structure:

One distinctive advantage of this is that the major components of the lap can be directly scaled to a larger lap without requiring a major engineering project. When

required, more dye-cast Aluminium boxed frames equipped with a load cell and actuator module would simply be attached to or detached from the existing structure and active modules. The lower structure beneath the load cells and hexagonal plates can easily be disassembled for replacement with a larger or smaller version. The maintenance of the active module would also be very easy, since they are accessible from the open space at the top. Mixed use of the active and dummy load cells can still be applied because of the membrane that smoothes the pressure sensed by the load cells. The actuator would be assembled in line with the active load cells so that the same number of the actuator and load cell are used in operation. In this case, the force exerted by an actuator is coupled to the actuator-load cell array via the membrane underneath. Thus the only difference between the flex plate and the membrane is their location on the lap. To this extent, the membrane can be regarded as the flex plate at the different location on the lap. This alternative lap would have different actuator-load cell coupling coefficients from those of the original lap structure. They can be found from an FE analysis and the active lap software can use them in much the same way as the original coupling coefficients.

Disadvantages of this alternative structure:

The three disadvantages of this approach and their solutions found are summarised below. Firstly, the four walls of a dye-cast Aluminium boxed frame do not keep the right angle with respect to the horizontal plane and the departures vary from wall to wall. This would result in a wavy surface at the top and hence the bottom of the assembly. It leads to difficulty in adjusting the absolute Z position of the active modules within the lap structure. Secondly, there would be the tilt of the module with respect to the thin membrane and its variation from module to module across the lap. The solution of these problems would be to place the actuator-load cell modules on the membrane first, lower the dye-cast Aluminium boxed frame assembly from the top using the global actuators and then bolt the modules onto the assembly when it reaches the right height from the membrane. Thirdly, it would cost considerably more than the single plate to build. The production cost of the scaled active lap would certainly rise, if this approach was to be taken. However, because of easy scaleability and maintenance and reuse of the same components, particularly the active modules, the overall cost of producing large optics in various sizes over years to come would actually be much smaller than the single plate approach.

The final choice for the active lap structure in view of scalability:
While the alternative structure remains very attractive, the construction of the 85 cm scaled active lap used the single plate approach due to budgetary limits.

6.2.2 Load Cells and Actuators

• Reduction of dummy resistors for load cells

To form a half bridge load cell means that two active strain gauges and two dummy resistors are wired up crossed in a Whetstone bridge. Because the active lap has 22 active load cells, each with 4 half bridges, for 88 bridges in total, an extra 176 dummy resistors need to be wired to the 176 active strain gauges. Wiring these would be extremely time-consuming, making the electronic circuit very complicated. A novel alternative is to use just two dummy resistors for the 88 half bridges. Because the same resistors are used for all the 88 bridges, their characteristics are expected to be more similar to each other and more reliable than using 176 separate resistors. The schematic diagram of this circuit is presented in Figure 6.7.

• Actuator mounting for reduction of overall lap thickness

The initial idea behind mounting the actuators was that they are attached directly to the upper face of the reaction plate. The plate has an array of small clearance holes through which the lead screws can pass. The flex plate would be several centimetres below the reaction plate so that the actuator spring assembly can be placed in between. But this makes the lap several centimetres thicker and hence increases the shear force within the lap structure. A better solution would be to make the clearance holes bigger so that the whole spring and its enclosure can be inserted in and out. This dramatically reduces the distance between the flex and reaction plates down to much less than 1 cm and hence lowers the centre of gravity of the lap. The motors would be attached on channels which are bolted radially to be the top face of the reaction plate. This allows almost all of the actuator well above the reaction plate. Thus, the driving force of the lap given to the reaction plate is closer to height of the centre of the gravity.

• Methods for actuator resetting There would be a reset position at which all the actuator operation start and end. There are two ways of doing this. The first is a software solution, where the location of the lead screw is traced throughout a

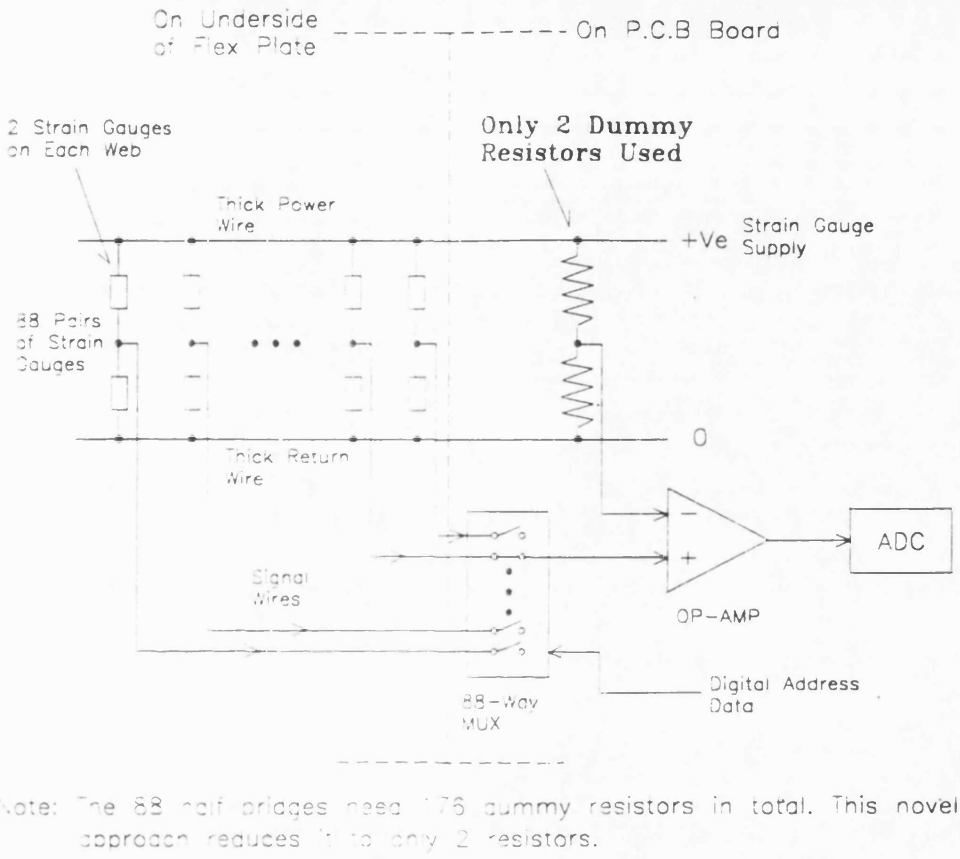

Figure 6.7: A modified circuit for 88 half bridges, using only 2 instead of 176 dummy resistors

polishing run in terms of pulse number and sign(i.e. - for UP and + for down) with respect to the reset position expressed as 0. When it finishes, the software automatically issues the reset command and then all the motors go to their reset positions. The second is to use micro switches mounted on top of all the actuators. When the lead screw touches the switch, the motor would be turned off. By using both methods in operation, resetting the motor position to a pre-defined zero position can be achieved within 1 stepper pulse, but only with no loss of stepping pulses during actuator operation.

• Suggested methods for calibration of active elements

The calibration of the active elements would be made in the following sequence. After the load cells are attached to the flex plate, reference weights are placed on individual load cells, ranging from 0 to about 8 kg. The digitised load cell values are then stored in the PC hard disk. This experiment enables us to examine if

they function properly as designed in terms of gain. The same experiment would be repeated after the hexagonal plates are attached to the load cells. This permits us to see if the hexagonal plates alter the absolute characteristics of the load cell. Once the carbon-fibre skin unit(comprising the epoxy wedges and pitch facets) is attached, it is impossible to precisely locate the weights on the load cell. A separate calibration for this entire lap use a water bag sitting on the mirror surface. The lap is fully relaxed on the water bag with no global force. Then it is lifted with increasing the global force until it is completely in the mid-air(i.e. the global tension equals the lap weight). The load cells are continuously monitored and the digitised responses are be stored. This provides a working calibration. It is expected that the working calibration would be a bit different from the absolute calibration.

• Necessity for absolute precision calibration

As far as use of the calibration is concerned, a precision calibration is not absolutely necessary for ablation control. Of course, the more precise the calibration, the more reliable the relation between the pressure modulation and the ablation data in absolute units. However, the active lap can still control the ablation as requested using less accurate or even relative calibration, but with a slower convergence factor until the ablation algorithm is fully matured. The real-time and global process algorithms can be adjusted and evolved for optimum ablation control according to a given calibration data. If an accurate calibration is input, the maturasation of the algorithm would take shorter. In contrast, it would take much longer if an inaccurate calibration is used. However, once the maturasation is completed, the final ablation algorithm can control ablation in no difference in convergence factor during successive polishing runs. The inconsistency between the pressure modulation and the ablation map come as the ablation error after optical testing. Thus, any inaccuracy in the calibration can be corrected by adjusting the entire set of polishing variables within the ablation algorithm as the polishing run continues.

6.2.3 Control Electronics

• Bi-directional Communication Link

Two possibilities were explored for bi-directional communication between the on-lap electronics and the PC.

Option 1: Remote radio digital links

Firstly, a pair of the remote radio digital links from LEX ltd [68] are able to communicate bi-directionally up to a few metres in distance. The normal direction of the lap centre tilts and rotates with the stroke process and results in a cone of line of sight in which the communication signal must travel. A few metres distance would certainly increase the area of intersection of the cone in which the receiver detects the signal from an emitter. However, it has a number of disadvantages. Only a particular wavelength band is allowed for individual users and it is under regulation. Even in this band, there would possibly be sources of interference, since the premises are in central London. The speed of communication is 9600 baud at maximum via RS232 and it is not upgradable. It is expected that the total amount of information to be communicated would be about 1000 bits for both directions. This includes 88 bridges, 1 temperature sensors, 4 encoders and 32 actuators each of which consists of 8 bits of data. It would take about 104.2 msec total, indicating that the communication alone needs about 10 Hz in which the control is aimed to cycle. This is not only unusable for the scaled active lap but also not upgradable to a larger active lap.

Option 2: Bi-directional IR digital link

Jamshidi [60] suggested an IR link for communication. The IR link can readily achieve a faster speed such as 19200 or 38400 baud rates. When used with a RS484 serial link, even 54000 baud rate would be possible. Thus data communication would take a small portion of the 10 Hz speed if the IR link is employed. In addition, there is no regulation to restrict the band and it is virtually free from external interference. One disadvantage though is that the link can only reach a few millimetres to centimetres in distance. This leaves a very small area of detection and rotation between the emitter and receiver. Hence a special enclosure is required for two pairs of emitters and receivers to be housed, in which the emitter and receiver are a few mm to cm apart and fixed in facing angle. The most likely source of interference would be the internal reflection of one emitter signal by the receiver and its surroundings, which can influence another receiver to the side of the original emitter. The link between the push-pull arms and the reaction plate includes the design of the enclosure mounted inside the hollow cylinder at the axis of rotation of the lap [11]. The cross-talk between the channels can be removed by optical baffling of the enclosure.

The link can be driven by universal asynchronous transmitter/receivers at each end.

Final choice for the bi-directional communication link:

For the reasons described above, the IR link was chosen for the communication link.

• Encoders

Use of potentiometers as encoders:

As earlier mentioned, four movements need to be encoded to display the pressure map in the absolute mirror coordinates. They are X, Y, θ (rotation of the lap) and ϕ (rotation of the mirror). Perhaps, the cheapest solution would be to use two potentiometers directly as rotary encoders to sense θ and ϕ. One is mounted on the lap and linked to the hollow cylinder with a tooth belt. The other is mounted near the rotation axis on the 1 m polishing machine and linked to it with a tooth belt. As the lap and the mirror rotate with respect to the central hollow cylinder and the lap, these two potentiometers alter their resistance which can be detected as a difference in voltage when energised with a fixed voltage. Two other potentiometers of the same model can be again used to monitor the X and Y coordinate of the lap in stroke. Each would be mounted to a hinge on a I-girder near the 1 m polishing machine. A friction wire surrounds the potentiometer. One end holds the central hollow cylinder while a lead weight is hung at the other end of the wire. The potentiometer functions like a pulley. As the lap strokes, the wire lifts the weight up and down and the potentiometer rotates accordingly. This changes its resistance and resulting voltage when energised with a fixed voltage.

Overcomimg the dead zone of potentiometer:

One drawback, though, is that there is a dead zone near the origin of the potentiometer rotation, where no signal is observed. However, this can be calibrated and used as the sign of next rotation. Thus the software can add up 360° from this point on.

Resolution of the encoders in use:

If the two rotary potentiometers are synchronised with the mirror and lap rotations, 8 bits A/D conversion for a full rotation provides the resolution of about 1.2 cm at the periphery of the 1 m turn table. For the other two potentiometer, if the typical stroke of about 30 cm, i.e. 1/3 of 1 m diameter gives a full rotation of the potentiometer, the 8 bits A/D conversion can give the resolution of 1.1 mm. These

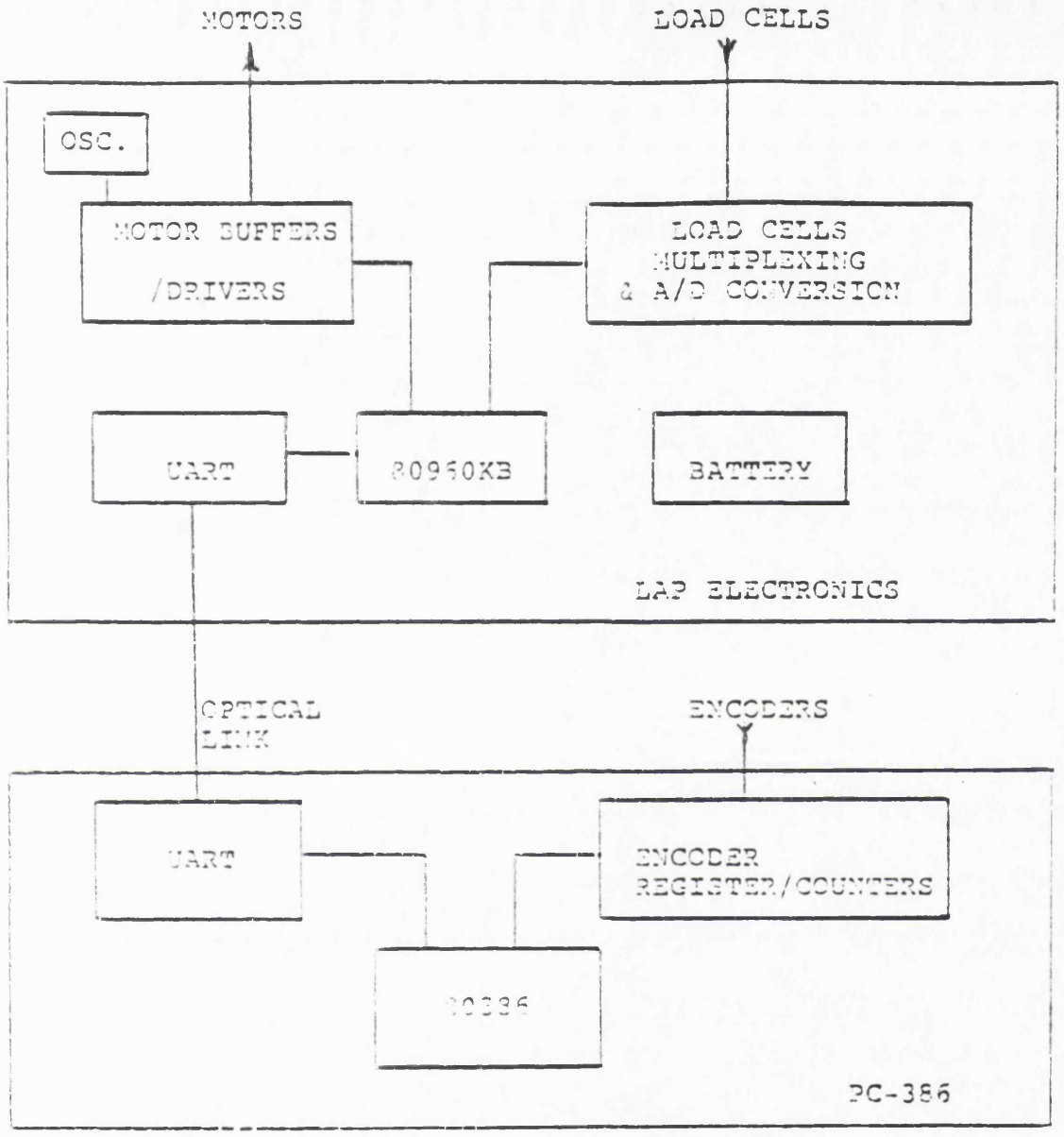

Figure 6.8: A block diagram of the active lap control system

resolutions are fine enough. If they rotate more than 1 revolution for the range of stroke and 1 rotation of the mirror or the lap, the resolutions increase accordingly.

• Overall Structure of The Lap Control System

Figure 6.8 shows a schematic diagram of the control system. Nixon [79] designed and built the lap control system. It is primarily for the 85 cm scaled active lap experiment. However, the choice of on-lap processor and the modularity of rest of the electronics are made with the 2.5 m scale lap in mind. Thus, scaling up to a 2.5 m lap would not need major development even for the control system.

Components and functions of the control system:

It may be divided into several blocks of functions:

- stepping motor buffers and drivers
- multiplexing and A/D conversion for load cell signals
- on-lap 32 bit processor Intel 80960KB
- bi-directional IR serial link
- encoder register/counters
- off-lap IBM PC 386/486(33 MHz)

The PC functions are to provide:

- a graphic control interface to the user
- accept input data-pressure, lap location and rotation, temperature, etc.
- use the real-time ablation algorithm to define and output the target pressure distribution for actuator update
- evaluate and adjust the real-time ablation algorithm using the Global- Process-Algorithm

The on-lap processor is to provide:

- polling of the load cells, multiplex and A/D convert their signals
- read the temperature sensors and encoders
- serialise and trigger the IR link to output the data to the PC
- accept the target pressure, compute the required adjustments for each stepper motors and update the actuators

On-lap microprocessor:

Choice for the on-lap intelligence is given to an Intel 80960 KB processor of which the speed is 7.5 MIPS, with a burst rate of 20 MIPS. The reason is that the more

powerful the slave intelligence is, the more work it can take over from the PC. Then the PC can be more dedicated to its primary function as GUI. Nevertheless, the main function of the on-lap processor in the current design is to provides bit-streams to update the actuators at 10 Hz frequency. This is achieved by generating arrays in memory and sending them via a serial link to a set of FIFOs (First-In-First-Out memories) on the lap circuit board.

Use of FIFO memory in driving actuators:

Each bit of the FIFO output passes through a standard stepping motor driver connected to stepper motor. The FIFO outputs are clocked at a constant speed to the motor drivers. A logical 1 in the FIFO memory generates a stepping pulse and a logical 0 becomes the absence of a pulse. The effect of a ramp, to accelerate and decelerate the motor at the beginning and end of the bit stream, can be generated by inserting 0s between the 1s. The use of the FIFO-memory and the single chip motor drivers reduces considerably the number of electronic components required per actuator. It contributes enormously to producing on-lap circuit boards that are very compact and reliable, leading to substantial savings in the design effort. One drawback is that the processor is faced with an intensive task of bit manipulation but this is no problem for a modern micro-processor of the correct type, such as the Intel 80960KB processor.

Handling the encoder signals:

A plug-in board has a set of registers where the encoders are connected. The board can be controlled by either the on-lap processor or the PC. The encoder signals is transmitted via the IR link if the former is used. Otherwise, the board is plugged into a 8/16 bit slot of the PC and the signals can be read directly by the PC.

Power:

Power is supplied to the rotating lap via the slip-ring mechanism. It is also restabilized and filtered.

• Mode of Operation and Initial Experiments

The active lap can be run in *static* or *dynamic* mode for polishing. The *static* operation uses a set of constant forces exerted by the actuators for the duration of the polishing run. Then, after optical testing, an updated set of constant forces is used for the next polishing run. An example of the constant force set would

be to pull up at the edge for polishing convex surfaces with turn-up asphericity. In the *dynamic* mode, a surface contour is provided from optical testing and then compared to the target surface profile. This gives an surface error contour that is used to update the actuator for pressure modulation in real-time. The instant target pressure is defined according to the relative rotation and translation of the mirror and lap.

This can be done only with the fully operational hardware and software of the active lap. But the first-installed hardware of the active lap needs to be tested and this requires an initial version of the software capable of doing simple tasks. A series of step-by-step experiments required for the testing is summarised as follows. Successful completion of each experiment provides essential background for undertaking the next experiment.

- **Experiment 1: Confirming that the all components work.**

  The lap sits on the mirror with no movement and the mirror does not rotate. Each actuator and load cell are tested. The graphic displays for various parameter including the pressure map in particular need to be checked. The pressure map is examined with various shapes of support underneath the lap to see if it looks sensible. The global and friction load cells and the encoders are tested with actual strokes and mirror rotation.

- **Experiment 2: Calibration of the load cells as integrated parts of the lap.**

  The lead weights are placed on individual load cells and their responses are stored in ADU (Analogue-Digital-Unit). Alternatively, the global actuators are used to lift the lap off from a supporting water bag. It is capable of calibrating all the load cells at one time and is the only method of calibration that can be made very easily just before beginning a polishing operation.

- **Experiment 3: Coupling map between actuators and load cells.**

  The coupling between the actuators and the load cells can be found theoretically from FE analysis. But it would be worth verifying it experimentally. The lap sits on the mirror with no movements. An observed pressure map is constructed. An actuator moves up and down to see how the load cell responds(in

other words how the pressure map varies). This provides the coupling map, showing how the load cells are coupled to the actuators through the flexible plate.

- **Experiments 4: Static close loop pressure modulation.**

  The lap sits on the mirror with no movements. A target pressure map is defined and the actuators are updated. The behaviour of displayed pressure map is then observed to see if it converges. This can give information on, for example, how fast the target pressure map is achieved, how many iterations of actuator update are required, etc.

- **Experiments 5: Dynamic close loop pressure modulation**

  The actual stroke is given to the lap with mirror rotation. Firstly, a target pressure map is defined across the mirror surface. The pressure map is observed to see if it is continuously achieved. Secondly, if the previous experiment is successful, then a target surface contour is defined instead and a run of active polishing follows. Optical testing afterward gives necessary data to see if it works, what error level it achieved, etc.

6.2.4 Software Specification

6.2.4.1 Functional Specification

The first version of the active lap software is used to undertake experiment 1 to 4. Its functional specification is summarised as follows:

- read load cell signals in arbitrary ADC units and convert to physical units
- monitor X, Y, ϕ and θ and use them to calculate the positions of each pitch facet or of each actuator and load cell
- calculate normal force/pressure on the mirror surface and construct a pressure map
- compare the observed pressure map to the target pressure map and construct a pressure update map

- calculate number of pulses for each actuator to achieve the pressure update map
- activate all actuators to give or take force
- read OPD file named *.OPD and determine ablation map for each polishing run

These are fundamental functions that every versions of the active polishing software have to use.

Some other functions for real time ablation rate control are

- calculation of frictional force at a position
- construction of a relative velocity map on the mirror surface
- construction of a real time ablation map at a given time
- construction of either a integrated friction map or an integrated ablation map

These do not have to be implemented in the first version but must be incorporated for experiment 5 and real polishing work.

Although the fundamental functions can be quite clearly understood, some aspects listed below remain still ambiguous.

- how those functions should be arranged to form a manageable code
- how the user works with the software when the experiments are performed in real situation

6.2.4.2 Ergonomic Specification

The ergonomic specification is defined to clarify the ambiguity risen above. It is as follows:

- The user should be able to select either a load cell (i.e. 4 consecutive half bridge/2 consecutive full bridge) or a number of load cells, or all load sells. Unselected load cells are not involved in monitoring force. Newly selected load

cells can be added up to or subtracted from those selected previously. The bridge signals for a load cell are averaged prior to being converted to physical units.

- Numerical values read from load cells are displayed and can be stored in a text file with appropriate name and extension when necessary.
- The force/pressure map can either be displayed as a coloured contour map or be stored as a text file with appropriate name and extension when necessary.
- The user should be able to select either an actuator or a number of actuator or all actuators. Unselected actuators do not take part in modulating the pressure map. Newly selected actuators can be added to or subtracted from those selected previously.
- The user should be able to control selected actuators either by sending pulse number and direction or by defining pressure values.
- The user should be able to define a desired pressure map as a function of radius of the mirror on the mirror coordinate system. The function is normalised to a pressure value at the centre of the mirror.
- The user should be able to
  - reset the origin of the mirror coordinates, i.e. coordinate of a starting point of movement in a fixed mirror coordinate system. (There is no need for this if absolute encoders are used.)
  - reset zero point and sensitivity of either each load cell or all load cells. (It is preferable if they can be traced and updated, say, every 10 min during a polishing run.)
  - trace vertical positions of each selected actuator lead screws whenever they move up and down and reset the positions after polishing run.
  - reset sensitivity of each actuator if it is found that they vary from one to another
- The user should be able to save, load and see look-up table data base files to determine polishing parameters for the next run.

- All unnecessary keys should be locked to prevent the software from crashing because of misuse of keys at any stage of running.

6.2.5 Ablation Algorithms

The ideas for the ablation algorithm described here are currently under software development at the time of submitting this thesis. The terms RTA and GPA were defined in Figure 3.1 as follow:

RTA is the real-time ablation algorithm which is entirely on-line.
GPA is the global process algorithm which includes off-line processes (e.g. optical testing to determine the observed integrated ablation map).

The brief descriptions of the ablation algorithms made in Chapter 3 need to be expanded in technical details to clarify the work necessary to perform each step of the algorithms. One should note that RTA can not be regarded as an independent algorithm but an integrated part of GPA and therefore any change in RTA influences the structure of GPA and vise versa. Figure 6.9 shows the definitions of various optical surfaces and errors used in the detailed structure of RTA and GPA.

As stated before, active polishing intends to control mainly polishing pressure, sliding velocity and polishing time(or in other words, dwelling time of friction contact). Therefore all other variables would remain constant throughout the polishing process. Examples of such variables include characteristics and distribution of pitchs and abrasive slurry, room temperature and humidity, etc. In Chapter 5, it was concluded that Preston's theory appears to be valid with the thin abrasive slurry which is in continuous use for polishing at OSL. However, for generalisation in algorithm development, a modified mathematical equation of Preston's theory is adapted.

$$W = CP^{\alpha}V^{\beta} \tag{6.1}$$

$$W_i = CP^{\alpha}V^{\beta}T \tag{6.2}$$

where
W = instant ablation rate at (X,Y) on the mirror,
W_i = integrated ablation at (X,Y) on the mirror,

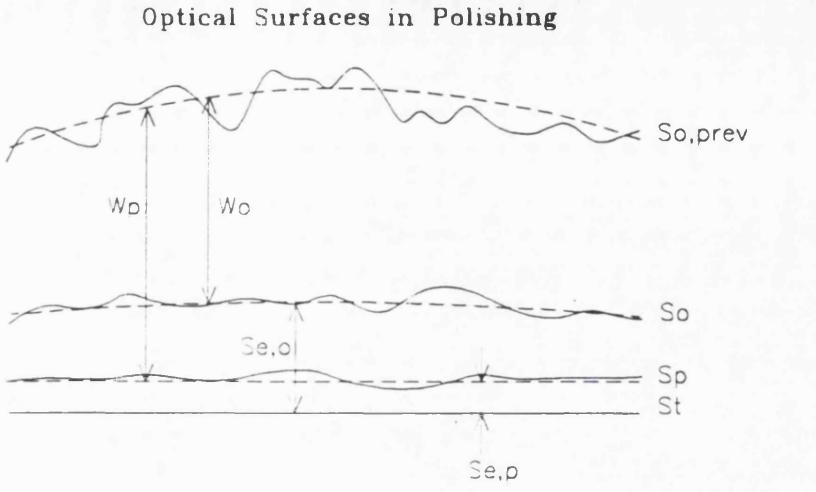

Figure 6.9: Definitions of various work piece surfaces in polishing

P = instant pressure at (X,Y) on the mirror,

V = instant sliding velocity at (X,Y) on the mirror,

C = ablation rate coefficient,

α = pressure power coefficient,

β = velocity power coefficient

6.2.5.1 Detailed Structure of RTA

• Variable to be controlled actively

The current 1 m polishing machine controls sliding velocity passively with the mirror rotation and the stroke of the push-pull arms driven by two rotating eccentrics. A polishing run is made with pre-set values for those variables. Throughout the polishing run, the stroke motion becomes a periodic pattern over the mirror surface. In addition, it is not directly measured but calculated from two coordinates sampled in successive control cycles. Thus, with the current hardware, it is impractical to

vary the sliding velocity as requested in real-time. In this context, RTA regards the sliding velocity not as a active control variable but just as a monitored variable. For a similar reason, the polishing time is also regarded as a monitored variable. This leaves the polishing pressure, alone, free to be actively controlled in real-time by RTA during a polishing run.

• RTA that suits the GPA strategy 1AaBa-2A-3A-4Aa

(Note: Two GPA strategies are mentioned in this section. There are coded as 1AaBa-2A-3A-4Aa and 1Bb-2B-3B-4B. The detailed explanation and classification scheme of various GPA strategies are presented in Table 6.1 in the following section describing GPA.)

As briefly introduced in Chapter 3, the main function of RTA is to estimate the integrated ablation map and update the actuators for pressure modulation in real-time. However, the functional requirement and therefore the structure of RTA vary depending on what strategy of GPA is to be used. For example, as explained with the second example of GPA in the next section, estimation of the integrated ablation rate in real-time does not have to be made if the data base approach (the strategy 1Bb-2B-3B-4B) is employed for GPA. In that case, RTA has only one function, to cycle controls to update the actuators to maintain a predefined pressure map. The structure of RTA would then be much simplified since it has only one major function rather than two. A design of RTA presented in Figure 6.10 is for the GPA strategy 1AaBa-2A-3A-4Aa that works with the full functional specification in its operation. (See the paragraph 6.2.5.2 for classification of GPA strategy.)

Work blocks in Figure 6.10 that have a capital letter enclosed by a circle are explained below in more detail:

• Block A: Observed pressure map

The 22 load cell readings are processed to generate an interpolated pressure map with finer pixels over the mirror surface. The main problem is to find a mathematical way of doing that based on the physics of the lap structure. The nature of the problem is discussed further and a solution is discussed in Section 6.4.

• Block B: Load cell update force

As stated earlier, each actuator has complicated coupling with the 22 active and 39 dummy load cells via the lap structure. This means that each of them should work

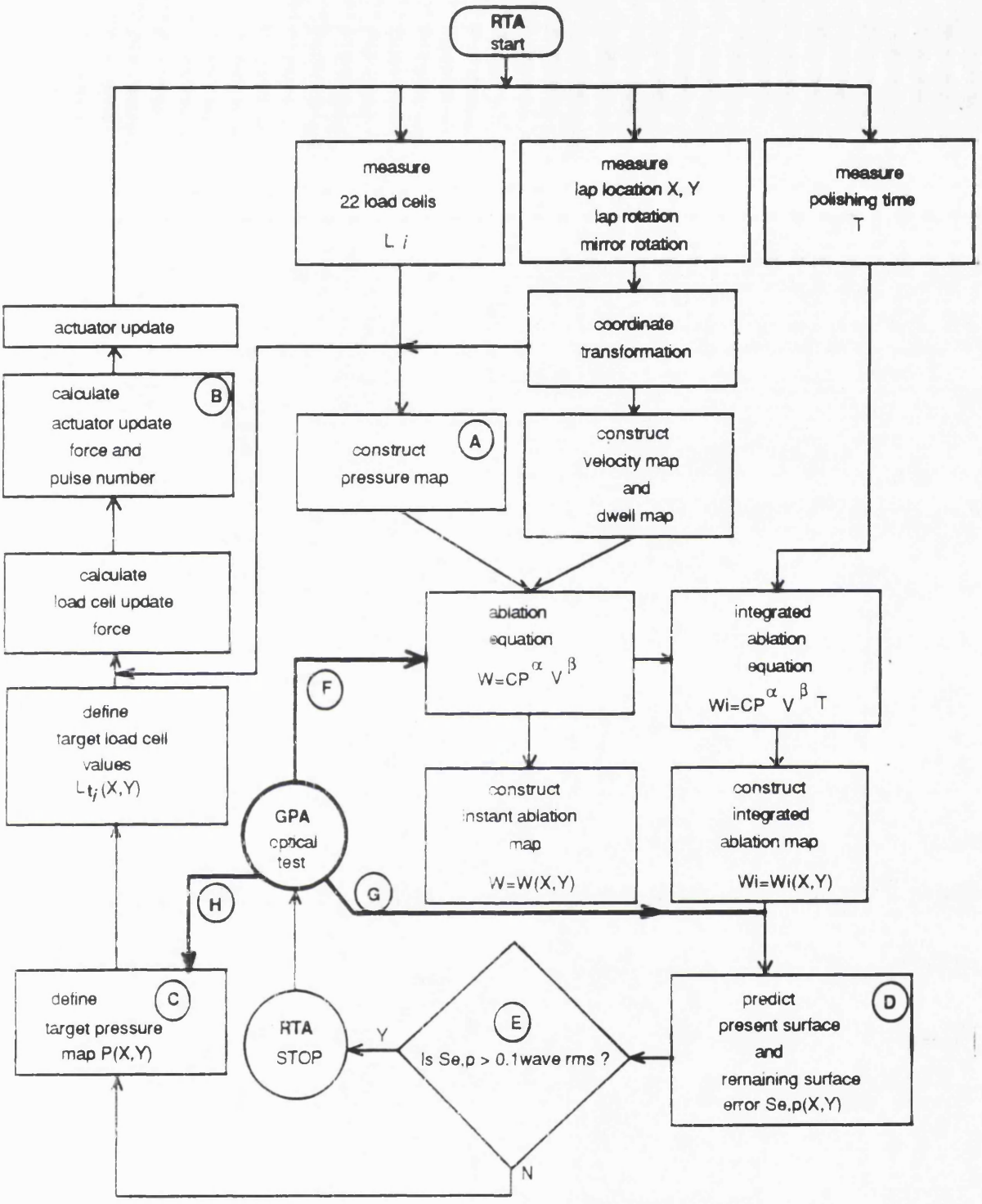

Figure 6.10: A work flow of RTA

not in isolation but as an integral part of the lap. Thus actuator operation has to be made in an integrated way in which all the 32 actuators are involved to achieve a pressure map that the 22 load cells sense. A solution is presented in Section 6.4.

- **Block C: Target pressure map**

There are many ways to determine the real-time target pressure map. It would be

ideal if the surface error map i.e. either observed or predicted is used in determining it. The next section describing GPAs in detail presents a practical implementation of this idea.

• Block D: Remaining surface error

Subtracting the predicted integrated ablation map from the observed (from the previous optical testing) mirror surface gives the predicted present mirror surface. The centres of the two surfaces should be coincident in doing so. Another subtraction of the predicted present mirror surface from the final target mirror surface with centre matching gives a predicted remaining surface error map.

• Block E: Comparision between predicted and target surface errors

There are two ways of controlling the polishing time. One is to continue the polishing, if it converges, until the predicted surface error becomes less than predefined. The other is to continue the polishing until the predicted surface error arrives at a minimum (in other word it starts diverging with more polishing action). This puts a decision making process into the control cycle and consumes more time for computation and comparison. This must be taken into account in writing the active lap software.

• Block F: GPA's correction of ablation equation

The ablation equation is best adjusted using the observed integrated ablation map made with two subsequent optical tests before and after a polishing run.

• Block G: GPA's influence to the block D by correcting the ablation equation

There are two optical surface profiles involved in this process. One is the observed mirror surface profile obtained from the optical testing of the previous GPA run. This is used to estimate the predicted present mirror surface in real-time. The other is the final target surface profile at which the polishing process is aimed to converge i.e. a theoretical or designed surface. This is known and is used for determining the predicted surface error in real-time.

• Block H: GPA's influence to the Block C

Two surface error maps could be used in determining the target pressure map. One is the observed surface error (i.e. designed surface-observed surface from optical testing of the previous GPA run). This would be used to estimate the initial target pressure

map when starting this polishing run. However, once it starts, the remaining surface error is predicted by subtracting the predicted present surface from the target mirror surface. Because the remaining surface error changes with the time in this polishing run, the target pressure is always kept under continued adjustment in real-time.

6.2.5.2 Detailed Structure of GPA

As stated in Chapter 3, one of the ultimate aims of GPA is to provide a way in which RTA is eventually equipped with reliable real-time target pressures and ablation equations for polishing operations. A number of different forms of GPA structure were envisaged and they needed to be classified. It is, of course, well understood that the structure of RTA varies depending on the sturcture of GPA that is actually implemented for the real polishing. In this sense, the RTA form described in the previous section is just one of many possible forms.

Table 6.1 summarises a classification scheme developed. The scheme has two code scheme in Table 6.1; columm and row codes. The columm code is denoted by numeric numbers enclosed by a bracket. Examples are (1), (2), (3) and (4). The row code is represented by upper case letters enclosed by a bracket. Examples are (A) and (B). The row code also has the sub-code of (a) and (b). In this classification scheme, for example, the GPA strategy 1AaBa-2A-3A-4Aa means that

- Column code (1): This GPA strategy intends to alter the ablation rate coefficient C in Preston's equation and to update continuously the target pressure map in real-time.
- Column code (2): In doing so, the data of polishing variables of the last polishing run is used.
- Column code (3): The ssame liding velocity (i.e. stroke parameters) and polishing time is always used for successive polishing runs and the polishing pressure is controlled in real-time.
- Column code (4): The target pressure is intended to be controlled at fast frequencies depending on the predicted remaining surface error in real-time during a polishing run.

<table>
<tr><th colspan="2">Classification[1]</th><th colspan="2" rowspan="2">Row Code (A)</th><th colspan="2" rowspan="2">Row code (B)[2]</th></tr>
<tr><th>Column Code</th><th>Meaning</th></tr>
<tr><td rowspan="3">(1)</td><td rowspan="3">Work block in RTA to control</td><td colspan="2">Ablation equation $W=CP^{\alpha}V^{\beta}$</td><td colspan="2">Target pressure map</td></tr>
<tr><td>(a)</td><td>(b)</td><td>(a)</td><td>(b)</td></tr>
<tr><td>C</td><td>α, β</td><td>Updated by an real-time ablation algorithm</td><td>Defined manually when starting a polishing run</td></tr>
<tr><td>(2)</td><td>Data to use</td><td colspan="2">Data of polishing variables of last polishing run.</td><td colspan="2">Data record of polishing variables of series of polishing run</td></tr>
<tr><td>(3)</td><td>Variable to control</td><td colspan="2">Vary pressure but fix all other variables including velocity and polishing time</td><td colspan="2">Vary pressure and velocity but fix all other variables including polishing time</td></tr>
<tr><td rowspan="3">(4)</td><td rowspan="3">Way of controlling the selected variables for a polishing run</td><td colspan="2">Alter the target value continuously depending on the remaining surface error</td><td colspan="2" rowspan="3">Do not alter the target value[3]</td></tr>
<tr><td>(a)</td><td>(b)</td></tr>
<tr><td>Fast and real-time during a polishing run</td><td>Slow and few times in a polishing run</td></tr>
</table>

Note: (1) This is a 2-dimensional classification with the vertical and horizontal classification codes.
(2) The horizontal classification has 3 possibilities; A, B and AB.
(3) The target values for the variables are preset and the real-time operation is to maintain the target values.
(4) Having ignored the sub-classification denoted by (a) and (b), there exist 3×2×2×2=24 different stratages for GPA.

Table 6.1: Classification scheme of various GPA strategies

One should note that, although the scheme is artificial, it covers almost all possible variants of GPA. Even with sub-classification ignored, the scheme indicates about 24 different forms of GPA. It could be few hundreds if all possible sub-classifications are combined into the scheme. It is anticipated that some of them would be operational, and others not, with the current active lap design. A few examples of possible GPA are presented in the following paragraphs.

1AaBa-2A-3A-4Aa Strategy This intends to adjust both the ablation equation and the real-time target pressure map together. The operational data of the last polishing run only is directly used, although it is stored in a format convenient to construct a data base for later use if necessary. The polishing pressure is actively-controlled in real-time whilst all other variables are frozen in operation. This means that the same values are always input for the polishing variables except the pressure.

Those include the stroke, abrasive slurry, temperature, etc. The target pressure map is to be updated fast, depending on the mirror surface predicted in real-time. Two crucial ideas form the foundation of this strategy:

- Only the ablation coefficient C is adjusted in the form of a 2D map over the mirror surface. The power coefficients α and β always remain constant.
- The initial and subsequent target pressures are defined real-time by applying the same sort of ablation equation with the adjusted C map, to actual observed or predicted surface errors

A schematic diagram of this is drawn in Figure 6.11. A polishing run would be made with a known value for the initial ablation coefficient C_{ini} of, for example, 200 micron per hour per psi per m/sec as NOAO found. It is initially assumed uniform everywhere on the mirror surface to start with. The power coefficients α and β are set to 1 if the thin abrasive slurry is used all the time (note that this is one of the conclusions from the experiments discussed in Chapter 5). Each work block is explained below.

• Block A: Subtraction of two observed surfaces

After a polishing run, the optical testing would give an observed-actual surface topography of the mirror S_{obs}. The centre of this is merged to the observed mirror surface S_{prev} previously obtained. The two surfaces are then subtracted to yield the observed integrated ablation map W_o. This process artificially creates no ablation effect at the centre of the mirror in spite of existence of real ablation in polishing. Using the optical testing does provide the integrated ablation map not in absolute sense but in an absolute unit relative to a reference point defined on the mirror surface. The centre of the mirror would be the best for this.

• Block B: Adjustment factor for ablation rate coefficient

The key idea for improving the ablation equation with this method is to adjust directly the ablation coefficient, instead of the power coefficients of the pressure and velocity, over the mirror surface for each polishing run. The integrated ablation W at (X,Y) is expressed in polishing operation as follows.

$$W = C \sum_{i=1}^{N} P_i V_i t_i \tag{6.3}$$

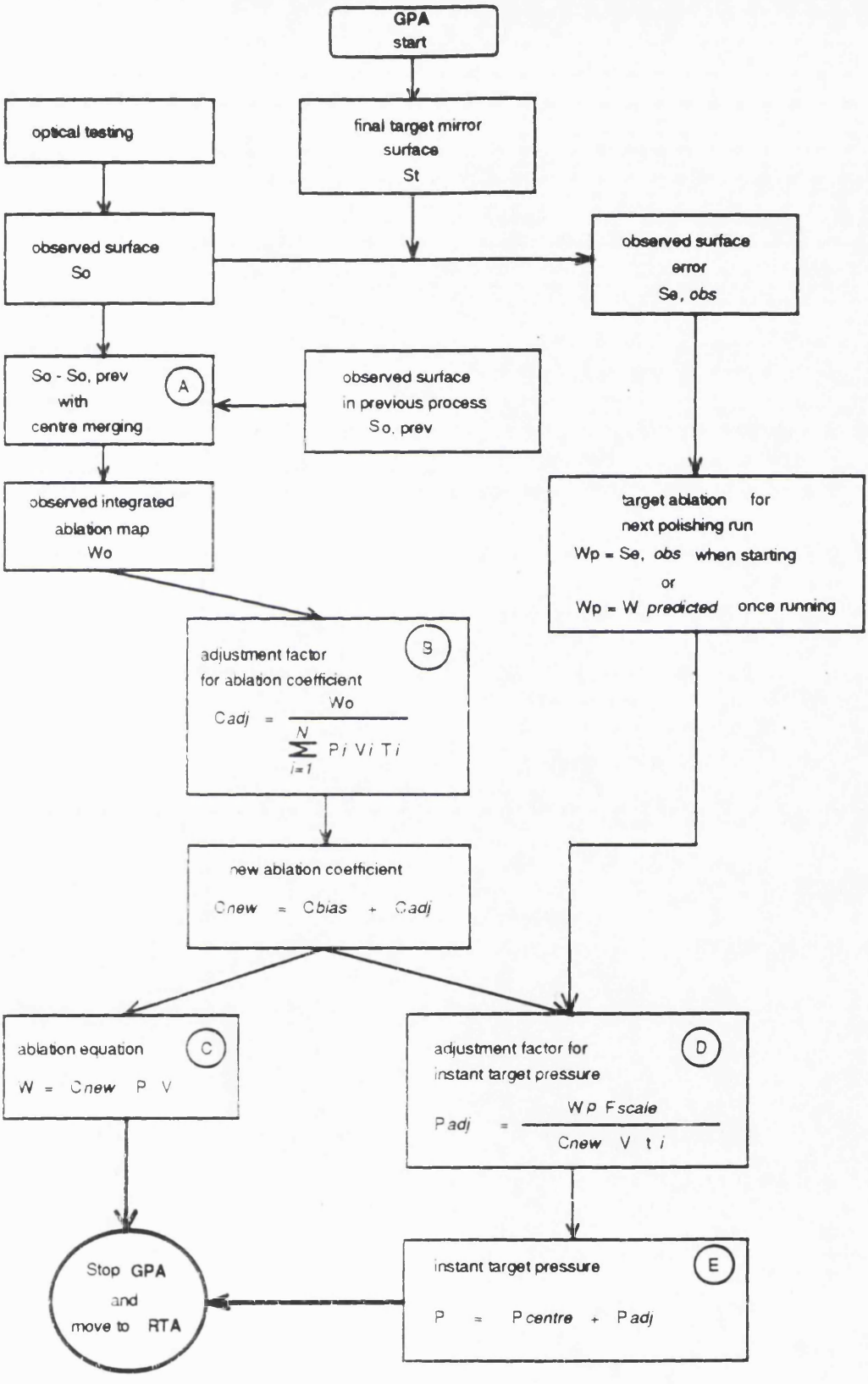

Figure 6.11: Flow chart of the 1AaBa-2A-3A-4Aa strategy of GPA, using the ablation coefficient map C(X,Y)

where

C = ablation coefficient at (X,Y),

P_i = pressure for the *ith* control cycle at (X,Y),

V_i = velocity for the *ith* control cycle at (X,Y),

t_i = duration time of the *ith* control cycle at (X,Y)

Substituting the observed integrated ablation W_o to the equation and rearranging for C gives the adjusted ablation coefficient C_{adj} for each location (X,Y) defined on the mirror.

$$C_{adj} = \frac{W_o}{\sum_{i=1}^{N} P_i V_i t_i} \tag{6.4}$$

This forms an ablation coefficient map, reflecting *all* the physical properties made over the mirror surface for the duration of this polishing run. For example, the different effects of intermittent and continuous polishing on ablation are automatically expressed as the C_{adj} map and therefore can be corrected in the next polishing run. In this context, any identified or unidentified effects in predicting (hence controlling) the ablation pattern over the mirror surface can be corrected with the C_{adj} map evolved during the course of the polishing process.

One difficulty is that since W_o is always 0 at (0,0), C_{adj} is always forced to be 0 at (0,0) as well. This causes no problem in estimating the ablation rate and integrated ablation using the ablation equation with C_{adj} for the next polishing run. However, it generates a singularity in calculating the target polishing pressure using the ablation equation as explained in the item below. A solution was found by understanding that the governing factor is not the absolute value of the ablation coefficient but relative shape of the ablation coefficient map with respect to that at the centre. It allows us to add a bias map C_{bias} to the C_{adj} map, bringing it to a new level C_{new}, where the C_{new} map has positive non-zero value everywhere on the mirror surface.

• Block C: New ablation equation

The old ablation coefficient C_{old}, but C_{ini} in this case, is replaced with the resulting C_{new} map for the ablation equation to be ready for use in the next polishing run.

• Block D: Adjustment factor, ablation scaling factor and the concept 'onion-peeling' for instant target pressure

The proposed idea is to use the same form of ablation equation to estimate target pressure real-time during polishing. Re-arranging the integrated ablation equation

with appropriate variables gives a general expression of the target pressure at (X,Y) below.

$$P = \frac{W}{C_{new} V t_i} \tag{6.5}$$

where

W = amount of (integrated) ablation to be removed during the time t_i

C_{new} = newly improved ablation coefficient

V = sliding velocity observed

t_i = dwell time of polishing contact.

When starting the first control cycle of the next polishing run, W is defined as the observed surface error Se_{obs} obtained from the two optical tests, each made from the last and this polishing runs respectably. Applying the scaling factor, as described below, to this equation makes it possible to 'onion-peel' the surface error map. The concept of onion-peeling is that although the surface error vaires over the mirror surface, it can be regarded as being consisted of a same number of error layers (i.e. therefore, the thickness within an error layer varies over the mirror surface.). An analogy of this is an onion, which consists of a same number of layer. Those layers covering the entire onion surface can be removed one by one by peeling actions. Just like this, the whole error layers over the entire mirror surface can be removed one by one by successive iterations of pressure map control in real-time.

Of course, W becomes 0 at (0,0) because of centre matching in subtraction of the two surfaces. Fortunately, this does not cause any singularities in the following processes. When starting the second control cycle of the next polishing run, W is defined as the predicted surface error Se_{pre}, varying in real-time as each control cycle is made.

The surface error ranges from about 20 μm (40 λ, where λ is about 5500 A^o, the central wavelength of the yellow light) to typically about 0.05 μm (1/10 λ). It is rarely required to go down to about 0.02 μm (1/25 λ). This means that the dynamic range of the integrated ablation that each polishing run attempts to remove varies within the factor of about 1000 between the loose abrasive lapping and the final polishing. Obviously, it is not possible for the current active lap, and unlikely with any plausible polishing lap, to achieve the differential polishing range of 1000

in the instant pressure distribution across the mirror surface. This differential pressure range of about 1000 in integrated ablation(i.e. integrated polishing pressure) distribution can only be achieved with time integration of instant ablation (i.e. polishing pressure) distribution over the entire polishing process (not a single polishing run). Thus, the instant target pressure that the active lap can exert needs to be scaled, not for the integrated amount of ablation, but for the instantaneous ablation to be removed in real-time. It can be regarded as either time scaling or ablation scaling since the integrated ablation to be removed(i.e. remaining surface error) is a function of polishing time in mirror fabrication. The solution for defining the instant target pressure is to slice the integrated ablation to be removed with the right scaling factor. The scaling is just to predefine the thickness of a error surface layer to be removed with a single pressure modulation on the mirrir surface. An analogy of this can be found from the concept of 'onion-peeling' already explained. Here, each complete layer of an surface error onion is peeled with a single action and accumulation of continuous peeling actions would eventually remove all error layers.

The discussion above leads to a more appropriate expression for the instant target pressure.

$$P_{form} = \frac{S_{oore} F_{scale}}{C_{new} V t_i} \tag{6.6}$$

where

P_{form} = instant target pressure with respect to zero pressure at the centre of the mirror

S_{oore} = observed or predicted remaining surface error

F_{scale} = ablation scaling factor

Roger Angel's ablation coefficient $C_{rni} = 200\mu m$ per $(psi)(\frac{m}{sec})(hour)$ can be used to estimate F_{scale} in the first approximation. It indicates the ablation rate of about $8.056 \times 10^{-5}\mu m$ per second when polishing with the typical polishing pressure of 0.15 psi and the sliding velocity of 1 cm/sec. This means that it needs 250000 seconds(about 70 hours) of continuous polishing to remove the optics material of about 20 μm. In retrospect, the polishing with P= 0.15 psi and V= 1 cm/sec for 1 sec can remove the material of the thickness of only $\frac{20}{250000}\mu m$. Thus if t_i= 1 second is used, the scaling factor F_{scale} can be around $\frac{1}{250000}$ for each pressure modulation.

P-V Surface Error in micron	Number of Polishing Actions[3] required at 0.15 psi, 1 cm/sec, 1 sec	Ablation Scaling Factor[4]	
		Control Cycle 1 Hz	Control Cycle 0.1 Hz
20 (36λ[1])	248262	248262^{-1}	2482620^{-1}
2 (3.6λ)	24826.2	24826.2^{-1}	248262^{-1}
0.2 (2.8^{-1}λ)	2482.62	2482.62^{-1}	24826.2^{-1}
0.05 (11^{-1}λ)	620.66	620.66^{-1}	6206.6^{-1}
0.02 (27.8^{-1}λ)	248.26	248.26^{-1}	2482.6^{-1}

Note: (1) 1λ = 550 nanometre, central wavelength of the yellow light band
(2) The NOAO ablation coefficient of 200 micron/psi. m/sec. hour gives 8.056×10^{-5} micron/0.15 psi. cm/sec. sec.
(3) This means the number of polishing contacts required to remove the surface error of the first columm with p = 0.15 psi, v =1 cm/sec and t = 1 sec.
(4) This means the fraction of the surface error that can be removed in each control cycle during an active polishing run.

Table 6.2: The ablation scaling factors for different magnitudes of surface error

If the pressure modulation frequency of 10 Hz (i.e. 100 msec) is used, the scaling factor can be about $\frac{1}{2500000}$. This is further expanded to other scales of surface error in Table 6.2, showing corresponding scaling factors. One interesting finding is that Table 6.2 indicates that about 625 seconds (around 10 minutes) of continuous polishing is required to remove the thickness of 0.05 μm (i.e. $\frac{1}{10}\lambda$). This is exactly what is normally practised for the final stage of large optics figuring in optics shops (e.g. iterative processes of about 10 minutes polishing followed by optical testing). This agreement gives firm support to validity of the scaling factors in use for active polishing. One more implication is that one should never allow a polishing run, either passive or active, longer than about 5 minutes, if a surface error of about 0.025 μm(i.e. $\frac{1}{20}\lambda$) is to be corrected.

The scaling factors look inverse-proportional to the remaining surface error to be corrected. Thus they can be stored either as a function or as a look-up table in memory and be used in conjunction with the surface error, observed or predicted, in real-time. The essence of the suggested method for defining the instant target pressure is to use the remaining surface error as the integrated ablation to be removed and the scaling factor to estimate the thickness of material that can be removed with a control cycle in active polishing. With this method, if a larger error is presented at a location on the mirror, the target pressure is automatically set to be higher and hence more material is removed there. Thus it is capable of onion-peeling an

amount of material proportional to the error magnitude and therefore the entire error surface over the mirror is corrected with an equal number of control cycles. This is applicable even to the intermittent polishing(i.e. discrete friction contact) when used in conjunction with the method of adjusting the ablation coefficient map over the mirror surface.

• Block E: Instant target pressure

In operation, the polishing pressure at the mirror centre is monitored and likely to be non-zero, whereas P_{form} is always set to be 0 there because of the centre matching. This discrepancy can be solved by levelling P_{form} according to the observed pressure value P_{centre} at the mirror centre in real-time. This gives the final expression for the instant target pressure at (X,Y) as below.

$$P_{target} = P_{centre} + \frac{S_{eoro} F_{scale}}{C_{new} V t_i} \tag{6.7}$$

where

P_{target} = instant target pressure calculated in real-time

P_{centre} = observed pressure at the mirror centre

S_{eoro} = observed or predicted surface error

F_{scale} = ablation scaling factor determined according to the remaining surface error

C_{new} = newly corrected ablation coefficient

V= observed sliding velocity

t_i= time of control cycle i.e. pressure modulation time = 0.1 sec

Advantages of this GPA strategy:

This strategy of GPA has a number of advantages listed as follows:

- It has a clear direction to which adjustments of the polishing variables such as the ablation coefficient map are to be made.
- Except the polishing pressure and time, almost all the polishing variables are fixed in use for the whole polishing process to figure a mirror. Opticians do not have to put enormous efforts to planning for a polishing run. All necessary adjustments are made by a computer-based GPA.
- The ablation coefficient map is adjusted using the observed integrated ablation, that is a collective representation of the behaviour of the active lap during a

polishing run. Thus the evolution of this between each polishing run is quite likely to converge to an optimum value that can give a fastest convergence factor in correcting the surface error in successive polishing runs.

Two variants of this GPA strategy:

Two close variants of this strategy exist. With the original strategy above, the adjustment of the ablation coefficient map relies entirely on the observed result of the previous polishing run. If this gives no more convergence towards a tolerable surface error range, a data base approach can be incorporated into this. Each record of the data base would consist of the observed integrated ablation map made and the ablation coefficient map used with a polishing run. The remaining surface error map to be removed with the next polishing run is compared to the records. Then perhaps 5-10 records showing similar observed integrated ablation map would be selected. Finally their ablation coefficient maps are interpolated to yield a new ablation coefficient map. It can automatically adjust to predict ablation and to define target pressure map in real-time. This can be called the 1AaBa-2B-3A-4Aa strategy according the classification scheme. (In fact, this is a simplified version of the data base approach, being combined with the primary strategy 1AaBa-2A-3A-4Aa discussed in this section.)

If the stroke is intended to be altered in series of polishing run, the data base approach can be ideal. Change in stroke causes alternations in the dwell time pattern between subsequent polishing runs. It would alter the ablation coefficient map unpredictably in subsequent polishing runs. **Thus estimating a new ablation** coefficient using the observed integrated ablation map is not relevant to another polishing run with a different dwell time pattern. The adjustment of the ablation coefficient map would not converge, so the surface error correction would not. This has one more variable to be filled in the record so that the estimation for not only the ablation coefficient map but also the stroke has to be made. It would be more difficult than the data base approach proposed in the previous item. It is called the 1AaBa-2B-3B-4A strategy according to the classification scheme.

1Bb-2B-3B-4B Strategy This approach is intended to plan and define the necessary variables prior to beginning a polishing run. Once the variables are set, they

are not changed throughout the polishing run. For example, GPA pre-sets a target pressure and then the polishing run keeps cycling the control to maintain the pressure distribution during the polishing run. The stroke and the polishing time are predefined as is the dwelling time. The prediction of integrated ablation in real-time does not have to be made in RTA at all and hence there is no need for a decision making process to define when to stop the polishing run. One advantage from this would be to remove considerable load of computation from the micro processor, giving it ability to speed up the real-time control cycle.

Figure 6.12 shows a flow chart of work blocks for the 1Bb-2B-3B-4B strategy which is at the opposite end from the 1AaBa-2A- 3A-4A strategy in the classification scheme. When starting the first polishing run, it would start with C_{ini}=200 μm per hour per m/sec per psi and $\alpha = \beta = 1$. The polishing pressure would be manually set constant everywhere on the mirror. The velocity and polishing time are defined manually by setting the stroke parameters on the eccentrics and a timer. All other variables remain constant throughout the whole process of polishing mirror.

• Block A: Subtraction of two observed surfaces

It provides the observed remaining surface error Se_{obs} and the observed integrated ablation W_{obs}. The mathematical process to obtain these is identical to what is explained in the Block A for the GPA strategy 1AaBa-2A-3A-4Aa. Se_{obs} then becomes naturally the integrated target ablation W_{tar} to be removed with the next polishing run.

• Block B: Target pressure, velocity, polishing time

It collects values of the polishing variables used for the current polishing run. The coefficients C, α and β are not involved in forming the data base since there is no use of the ablation equation due to no need for prediction of integrated ablation and definition of target pressure in real-time. The basic idea of this approach lies in an optimum- planning for the main polishing variables in advance rather than adjusting them in real-time during polishing. Once the variables are set, polishing would be made without any prediction for the resulting ablation. The pressure sensing is not to predict the ablation rate but to find out the update force - the difference between observed and target pressures - for the actuator to exert. The target pressure, sliding velocity(determined by the stroke and the lap rotation settings) and polishing time

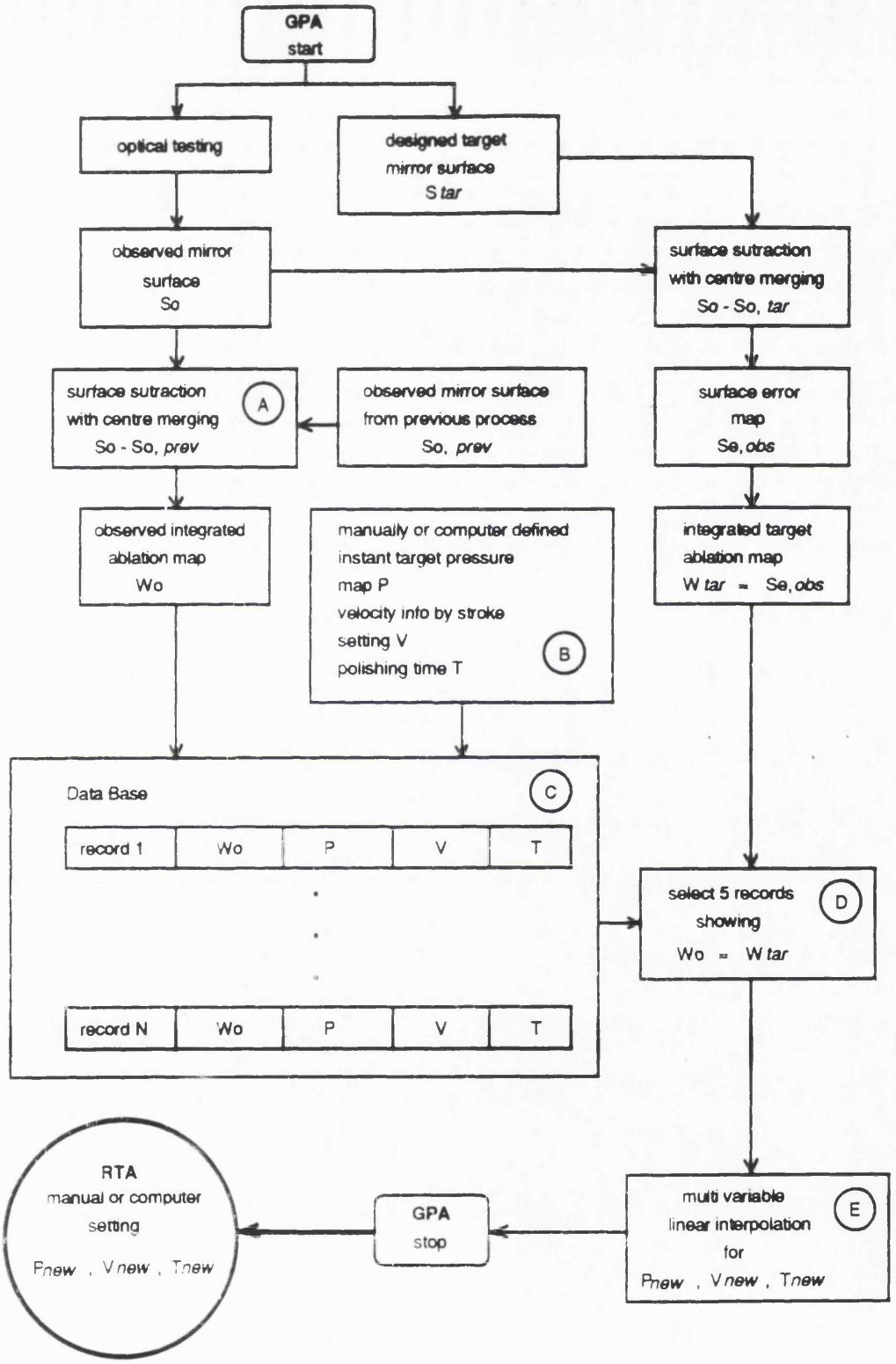

Figure 6.12: Flow chart of the 1Bb-2B-3B-4B strategy of GPA, showing data base approach to plan the polishing variables

are to be parts of a record in the data base.

• Block C: Data base for polishing operation

A record of the data base would consist of the observed integrated ablation W_{obs}, target polishing pressure P, sliding velocity V defined by the stroke setting and polishing time T. When each polishing run is completed, the resulting values of those variables are put in a record. For the first 10-20 polishing runs, the optician would vary P, V and T to alter or to correct the mirror surface to his/her preference. The aim is not to correct the surface error, but to construct the initial data base where different forms of integrated ablation map are stored beside the polishing variables that cause it. The more the polishing runs made, the more the records grow in number. The variables in a record are stored in a normalised format with respect to the size of the mirror and values of the variables at the centre of the mirror. With this normalisation, the strategy and the data-base are applicable to mirrors and full size laps in any size.

• Block D: Selection of relevent data records

When a data-base of about 10-20 records is initially constructed, they would be used in comparison with the target ablation map W_{tar} for the next polishing run. In fact, the comparison is made between Se_{obs} (to be removed) and a number of W_{obs} record to select, perhaps, 3-4 W_{obs} maps showing close resemblance to the Se_{obs} map.

• Block E: Multi-variable interpolation for a new set of values for polishing variable

An estimation for the target pressure, velocity and polishing time for W_{tar} (i.e. Se_{obs}) can be made by linear-interpolation of the variables of those W_{obs} maps selected. Then the estimated values of the variables are brought into the RTA run for the next polishing. Of course, it is likely that the polishing variables linear-interpolated would result in an integrated ablation W_{obs} somewhat different from that intended if variable spacing between records is too coarse. However, as more polishing runs are made with different sets of values for the variables, the spacing becomes finer and finer, gradually filling the entire data base space, whose limits are defined only by hardware limitations and optician's preference of polishing conditions. Then linear-interpolated values of the variables would be able to produce, to reasonable accuracy, the resulting integrated ablation very close to what is requested to be

corrected. When the data base evolves toward its full maturity(i.e. spacing and total number of records are good enough), as it would eventually be, it includes every possible form of integrated ablation map and the corresponding values for the polishing variables. No interpolation, but only selection of the integrated ablation map looking closest to the surface error map would then be necessary to plan the variables for the next polishing run.

Variants of this GPA strategy:

Perhaps, the closest variant of this GPA strategy would be the data base approach with one additional entity(i.e. the ablation coefficient map derived from the observed integrated ablation map over the mirror surface) in control during a polishing run. It can be classified as 1Bb-2B-3B-4A but would become operational only when the data base has fully matured. Here the integrated ablation map is predicted in real-time and the instant target pressure map is altered not in real-time but just a few times during a polishing run, depending on the remaining predicted surface error. The way to alter the pressure map is to compare the remaining surface error to the integrated ablation map record of the data base, select the closest one and use its pressure map, velocity(stroke) for the duration of the time record. If the polishing machine has a computerised stroke setting, this change in the variables would be made without interrupting the polishing operation. However, if it has not, the optician could alter the stroke setting after stopping the polishing and then start it again.

The two data base strategies introduced in this paragraph(i.e. 1Bb-2B-3B-4B and 1Bb-2B-3B-4A) would mature much faster if the same stroke setting is always used for a series of polishing runs.

Unclassified Breed of GPA Algorithm The most simple strategy with the data base approach would be to fix not only the stroke but also the actuator forces throughout a polishing run. A pressure map is achieved with pulse numbers to the actuators of the lap sitting stationary on the mirror. Examples include all the actuators at the outermost ring, pulling up the edge of the lap when polishing a turn-up aspheric mirror. The actuator forces are then locked during the polishing run. However, the pressure map would be changed continuously during the polishing run. The stoke and the polishing time are pre-set for this polishing run. The stroke

would have to be short, perhaps $\frac{1}{10}$ diameter of the work piece as must a passive full size tool, so that the force profile exerted by the actuators takes full effect on the required location. After the run is completed, the data base would have the actuator force map in the record instead of the pressure map used. Thus a record would consist of the observed integrated ablation map, the actuator force map, stroke setting and polishing time. The whole process of this strategy is same with the 1Bb-2B-3B-4B. The only difference in GPA is that it has the actuator force map, instead of the pressure map, in the data base record. An impact of this to RTA is that the actuators are not used to modulate the pressure map at fast speed e.g. 10 Hz in real-time, but to adjust the pressure once for a polishing run. In this context, this approach is outside the classification scheme suggested in Table 6.1.

One possibility is that, since there is no function to be achieved in real-time, RTA does not have to exist. An extreme possibility is that it could be operational only with proper calibration of the lap but without the pressure sensing ability, suggesting removal of the load cell and its related electronics from the lap. This approach would be attractive if extremely low cost has to be made in active lap construction. But this brings the whole approach back to the realm of pseudo-active polishing, which we want to supersede. Alternatively, this approach can utilise the load cells and their related electronics to predict the integrated ablation and the remaining surface error while the machine is running. The polishing continues until the predicted error is within the tolerance defined. The data record would have one more cell for the difference, if it exists, between the observed surface error and the final predicted surface error to be stored. This could be further investigated later to find what causes the difference and if they are systematic or random.

6.2.6 Optical Testing

The direct use of aperture synthesis for testing the 85 cm hyperbolic convex mirror has a problem of limiting precision. If either the static fringe analysis or knife edge image analysis have individual precision of about 0.1-0.05 λ for each measurement, then the combined surface topography would suffer from much worse precision e.g. the sum of individual precisions. Hence, the requirement is that individual tests have to achieve the precision of at least around 0.015-0.008 λ, if, for example, 6 sub-

apertures are to be combined for an whole aperture. In the interferometry regime, a solution would be phase-shifting interferometry using the PZT translator/aligner from Burleigh [17]. These are commercially available from WYKO and PhaseShift Inc., and their precision reaches up to 0.01-0.005 λ. For the quantitative knife-edge testing OSL has been developing [64], the current precision is about 0.1 λ which needs to be upgraded. Use of a precision motion control device for movements of the knife in X, Y and Z would improve the precision. The current motion control has the accuracy of about 2-3 microns which needs to be upgraded to at least about 0.5-0.2 micron.

OSL has 42 and 60 inch meniscus lenses. The 42 inch lens is used for testing the 85 cm scaled Gemini secondary by synthesising about 6 sub-apertures. Of course, the number of sub-apertures can vary depending the height of the lens from the mirror surface to be tested. The 60 inch lens would be used to test the real Gemini secondary of about 2-2.5 m in diameter with the aperture synthesis technique. Alternatively, the 60 inch lens can be used to test the scaled secondary, being placed closer to the mirror so that it can be tested with a full aperture. It is applied to the scatter plate interferometer in conjunction with the computerised knife edge testing. A possible experiment would be to make the full aperture and sub aperture synthesis tests on the 85 cm scaled secondary. These results can be compared to give rigorous assessment of propagation of errors in sub-aperture synthesis testing.

6.3 Construction, System Debugging and Calibration

6.3.1 Construction of The Lap

The hardware of the lap was constructed and satisfies almost all aspects of the final design. However, a few modifications were necessary to be made, mainly due to difficulty in actual production for some components and facts unforeseen.

• **Manufacturing load cells**

From the experience of construction of prototype load cells 1 and 2, it was understood that to NC-machine a single piece structure for each load cell was slow and

costly. In addition, the resulting structure became slightly bent, showing height difference between the inner and outer rings. This was due to the metal being relieved during machining. The degree of bending would vary from unit to unit. It would not be a serious problem for off-set and sensitivity, which can be calibrated individually. However, when they are mounted to the flexible plate, the load cells would have a bumpy surface toward the mirror, causing different characteristics when working collectively. A better way found was to laser-cut 1 mm thickness stainless steel plate for webs and then to bolt them between 2 pairs of inner and outer rings of about 4 mm in thickness. The mass production of the web plate and rings were sub-contracted to a laser-cutting company.

The first batch of the stainless steel web plate were in the incorrect state of hardness, showing large hysteresis. It was found accidentally that the web plate was distorted and never returned to the original form when pressed with a few kgf of force. The material cannot be hardened by heat-treatment but its surface can be work-hardened by machining. This is why the NC-machined web of the same thickness does not exhibit the hysteresis at all. The solution was to laser-cut temper-rolled stainless steel which has a hardened surface. The laboratory testing for the material showed satisfactory results and finally the assembled structures were sent to Entran in France for gauging i.e. gluing, trimming and terminating the strain gauges on them. The acceptance testing was satisfactory, showing the predicted sensitivity, linearity and no hysteresis.

• Concave nature of hexagon surface

The hexagon surface underneath the load cells proved to be milimetres away from flatness due to distortion of the flex plate in machining. In contrast, the mating top surface of the epoxy wedges is flat within the $\pm 30\ \mu m$ accuracy of the milling process using the profile generator developed in Chapter 2. If the lap had been assembled like this, there would have been arces of contact and voids between the hexagonal plates and the epoxy wedges. Some of the load cells would consequently not have worked. The solution was to fill the cavity with epoxy layer contained in a polythene bag which spreads to give even support to the hexagonal plates during the hardening process.

• PTFE skin on the hexagonal plates

Instead of using the flexural links, the hexagonal plates at the mirror end of the load cells were glued with silicone sealant and, after it hardened, the sealant height was trimmed to match the hexagon plates. The idea of wrapping the load cells, hexagonal plates and the reaction plate with a thin polythene aheet was replaced with the PTFE skin sprayed on the lower face of the hexagon plate surface. It's aim was to reduce friction between the hexagonal plates and the top surface of the epoxy wedges. However, the load cells and the hexagon plates are almost enclosed by the flex plate and the carbon-fibre membrane (described later) so that there is virtually no possibility of contamination. The PTFE skin actually proved to increase the friction between the hexagons and the epoxy wedges. Thus the skin was later removed completely.

• Carbon-fibre membrane

In the final design, the pitch facets and the epoxy wedges were going to be attached to a thin, perhaps 1 mm in thickness, cast metal shell, which is shaped to the 85 cm scaled Gemini secondary profile. The manufacturing was sub-contracted to a professional spinning company. However, the resulting shells were not acceptable at all. Their surfaces were covered with bumps of several centimetres in size and the manufacturing process can not produce a smooth surface as requested. Finally it was concluded that it is almost impossible to manufacture a cast metal shell of that shape in the thickness of 1 mm to the requested smoothness on the order of fractions of a milimetre. An alternative was to use carbon-fibre reinforced epoxy resin, cast using the generated 85 cm mirror as a mould. An important condition is that it provides enough axial compliance with high lateral stiffness to resist the polishing friction which tends to buckle the carbon-fibre membrane. The extended edge of the resulting carbon-fibre membrane is attached to the supporting ring mounted to the reaction plate. The membrane is free to move vertically but constrained laterally. Referring to the experiments using actuator movements and foam rings described in the next subsection, it proved to give enough axial compliance and a good quality surface finish with high lateral stiffness.

• Manufacturing other components of the active lap

The lap control electronics were designed and built by Nixon [79]. The low level software for controlling the electronics and the communication link was written by Jamshidi [61]. Rees [89] has been developing the high level software including

the GUI for controlling the active lap. Brooks [12] has manufactured the most of the mechanical components in house. The first active lap was finally assembled in October, 1992. The GUI software developed at that time was capable of sensing and displaying load cell values, displaying pressure map and controlling individual actuators by inputting pulse numbers.

6.3.2 System Debugging

In the following months, the initial system of the active lap constructed has been used for subsequent tests and modifications at the system and component levels. Much effort has also been made for calibration of the system and further development of the active lap software. These are described in this Section in detail.

6.3.2.1 Debugging for Electro-Mechanics

• **Performance of Load Cells and Related Electronics**

Accident on load cells:

When the load cells were delivered from Entran in France in August, 1992, the 88 half bridges were tested for continuity and bridge resistance balancing. It showed that they had no defects in continuity and were well balanced to 850Ω with trimming resistors. They are quite robust and have functioned very well for the subsequent testing and debugging process for the active lap system. However, when epoxy leakage accident described in the next paragraph happened in March, 1993, removal work must have damaged a strain gauge in the load cell 7. The strain gauge was found short-circuited, although visual inspection with a magnifier could not reveal any physical damage on the strain gauge. Fortunately, another strain gauge of the half bridge was intact so that it can still be used as a quarter bridge in hardware but a half bridge with the factor of 2 multiplied to its sensitivity in the software. Therefore, in the software, load cell 7 is still usable with the ability to compensate the lateral force. If the both strain gauges had been damaged, the entire load cell would have been replaced with a new unit and it could have delayed the debugging process by several months.

Testing for load cells:

When all the load cells and their electronics were assembled on the flex plate, their responses were thoroughly tested to ensure that they all showed the response to load similar to the designed values i.e. right sign (positive to increasing load) and sensitivity. The test showed some bridges cross-wired at the output terminals so that, for example, when the load cell 1 is given load, the load cell 7, instead of 1, shows the response. Some were short-circuited, not in the load cells, but in the electronics circuit board. Some have offset levels too high or low. All these were fixed as found and the tests continued until all the load cells worked well.

Removal of environmental contamination, relaxation of mechanical structure and test for hysterisis:

After that, a 50 μm slip gauge is used to double-check that no dust or micro-grains were between the outer ring of each load cell and the flex plate, since their presence would seriously disturb the sensitivity of load cells. Then a 3 kgf weight was placed on each load cell for about 10 seconds. It was to provide mechanical preloading of the load cell units, removing structural bias from the output signal. The load was cycled from 0 to about 17 kg on each load cell unit to see if there is hysterisis. No noticeable hysterisis was found, indicating that the temper rolled stainless steel works fine as the material for the load cell structure and the way that the load cell is assembled from the rings and web plates was satisfacory.

Validation for the idea of lateral force compensation

Two tests had been made before any serious calibration was attempted at this stage. The first was to prove experimentally that the suggested concept for lateral force compensation works in practice. The three experiments made are depicted in Figure 6.13. In the first experiment, a 1 kgf lead weight was placed at the 8 locations on the outer ring of the load cell. This simulates the 1 kgf off-axis force. The second experiment used a string to pull at the 8 locations on the outer ring with 1 kgf load, simulating pure lateral force. The signals were compared to that of 1 kgf axial load. The results showed that there is no noticeable difference within the range of signal noise of about ± 1 ADU (i.e. 0.009 kgf). The third experiment used the string to produce 1 kgf tangential load at the 8 locations on the outer ring. The signals were compared to that of 0 kgf axial load. It confirmed again no difference within the noise.

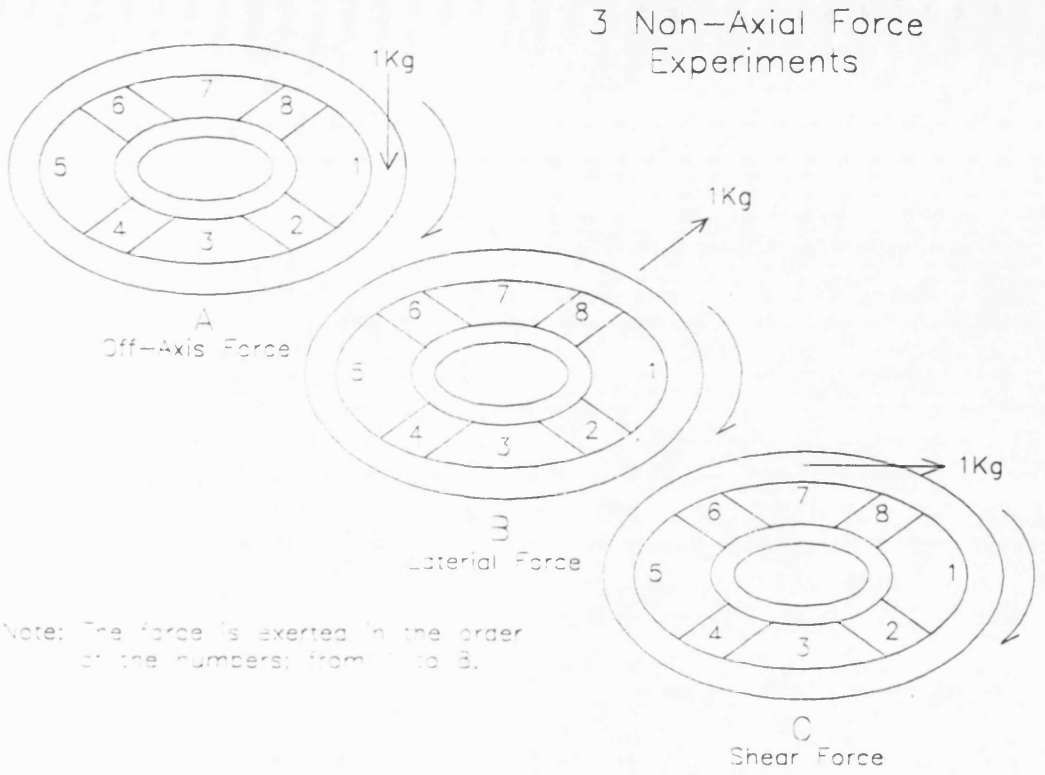

Figure 6.13: Experiments to give 3 different lateral forces to load cell

Test for temperature effect on the load cells:

The second was to investigate, once more, the temperature effect on the load cells, although experiments with the prototype load cells had shown that it is negligible. Since the load cells were already assembled to the flex plate, it was too large to be placed in a temperature controlled oven. The only practical way was to increase the room temperature using an electric fire. The first measurement was made in the completely sealed room at $21.8°C$. After 72 hours of heating, the second measurement was made at $24.4°C$. The difference in sensitivity of the 88 bridges measured at the two temperatures are presented in Figure 6.14. The average sensitivity of the both measurements were $0.1099 \pm 0.0076(\sigma) ADU/gmf$ and $0.1089 \pm 0.0072(\sigma) ADU/gmf$ at the low and high temperatures respectably. The average sensitivity difference is about $-0.001 \pm 0.0026(\sigma) ADU/gmf$. The decreases of about $-0.001 ADU/gmf$ with the temperature increase of $2.6°C$ is even smaller than the standard deviation of the measurement. Thus, the temperature effect on the bridge sensitivity is negligible since it is highly unlikely that the temperature change exceeds $2 - 3°C$ in a polishing run.

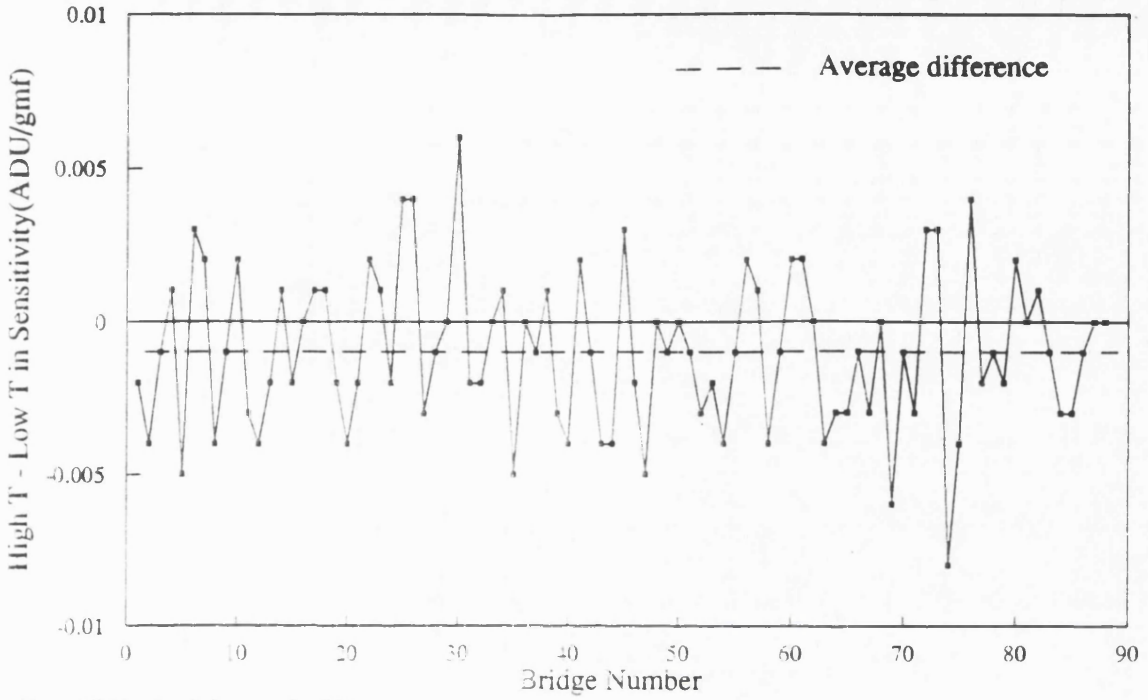

Note: ADU = Sensivity x gmf + Offset

Figure 6.14: Sensitivity difference (High-Low) against bridge number, measured at $21.8°C$ and $24.4°C$

Figure 6.15 shows the offset difference of the 88 bridges measured at the two temperatures. The average difference is about $-1.44 \pm 8.04(\sigma)ADU$, indicating no significant temperature effect on the offset. The only exception is the 4 bridges of the load cell 7 that show the abnormal increase of about 38 ADU on average. There was no obvious reasons found to explain this. However, because of its uniqueness, it seems more reasonable to think that it is caused by mechanical bias rather than temperature effect. In the worst case, even if there exists the temperature effect of some amount to the offset, it can be separated easily by taking bias frame of the 88 bridges when starting a polishing run. Thus it can be concluded that there is negligible effect of the temperature to the load cell characteristics.

• **Distorted Nature of Hexagonal Plates**

Polythene bag filled with epoxy resin as a solution:

As earlier mentioned, the distorted nature of the assembled hexagonal plates gives edge support preferentially, while leaving a gap condition at the central part of the lap. The only solution to this was to use a polythene bag of approximately work piece size, slightly larger than the entire hexagon plate, filled with epoxy resin. The

lap is inverted for the load cell side up in a support frame. The bag was filled with liquid epoxy resin. The epoxy was carefully spread over the surface and the bag was sealed afterward. Then the Carbon-fibre membrane unit was attached back to the lap. The entire lap was placed on the mirror and left for at least 24 hours until the epoxy hardened. Any gap condition was expected to be closed with this method.

Technical problems with the epoxy bag:

But in reality, there were a number of problems with the epoxy bag as discussed below. In the first few attempts to make the epoxy bag, the epoxy was pushed out to the periphery of the polythene bag and hardened there. This produced thick and hardened epoxy lumps at the periphery of the bag, pivoting the flex and reaction plates. This resulted in a serious disturbance of the load cell performance. The solution was to make the polythene bag of the right size. After several trials, the final bag size was determined so that the epoxy lumps at the periphery were not big enough to pivot the flex and reaction plates.

Although it was ensured that no air bubbles of significant size were present inside

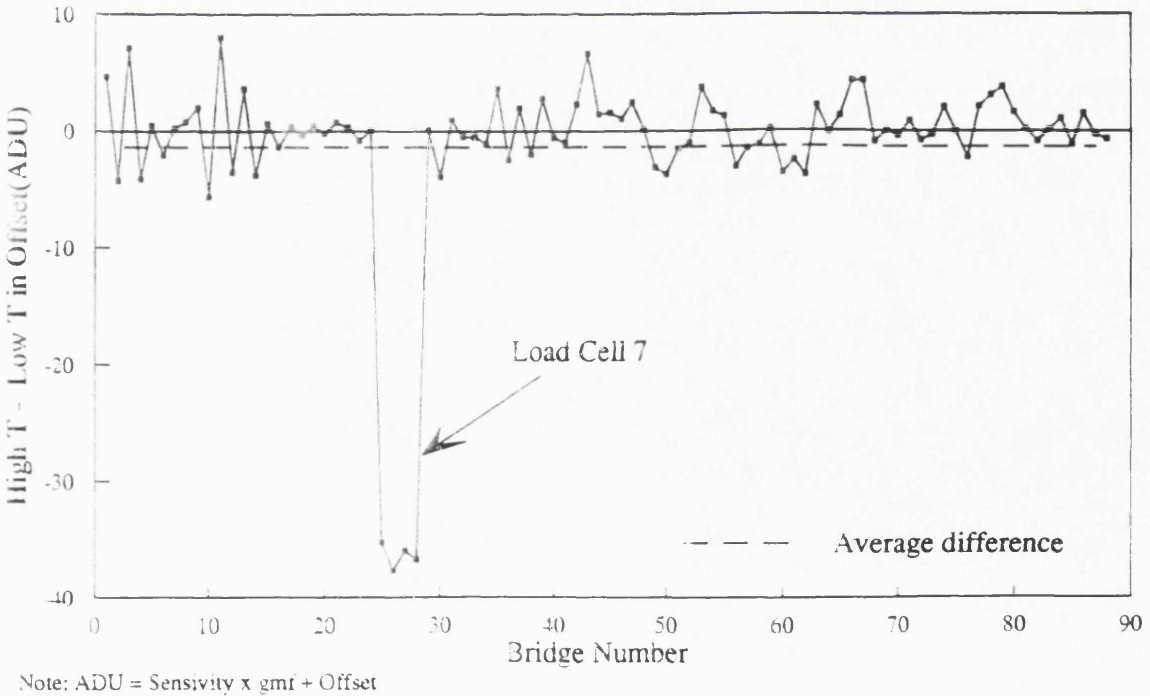

Note: ADU = Sensivity x gmf + Offset

Figure 6.15: Offset difference (High-Low) against bridge number measured at the 2 temperatures

the polythene bag before hardening, the resulting epoxy layers do have air bubbles of considerable size larger than that of a load cell. The presence of these bubbles would also disturb the performance of the load cell. It was traced that the polythene bag alone is unable to remove the large bubbles. Two sheets of coarse fabric cloth were placed at the both, top and bottom, sides in the polythene bag to stop flow of epoxy resin during hardening. The result proved that it is an effective way to remove large bubbles but it leaves enormous number of tiny bubbles across the hardened epoxy layer. It was decided to accept these bubbles since they were too small to disrupt the performance of the load cells.

Leakage of epoxy resin:

The double-layered polythene bag for the epoxy resin has two holes through which two rubber pipes pass from the reaction plate to the pitch surface. It is to supply the abrasive slurry while the machine runs. The edge of the holes of the polythene bag were completely sealed. No leakage was found when liquid epoxy resign was poured and spread inside. But during hardening process, due to the pressure of the lap structure, a substantial amount of epoxy escaped and sneaked through the silicon sealant between the hexagonal plates. Eventually, the load cells near to them and their electric pin connections were heavily contaminated with the hardened epoxy blocks. It was a painstaking process to remove this with precautions not to harms the load cells and bridges. As mantioned earlier, this seemed to cause a strain gauge on load cell 7 to short-circuit. This was solved by using the polythene bag without the hole when the liquid epoxy is poured and hardened. After it was cured, the holes were made by drilling from the reaction plate side.

Final epoxy bag used for the active lap:

A serious problem in the use of this bag is that it does not allow inspection of any method once it is made. For example, if the carbon-fibre membrane unit is disassembled and the hardened epoxy bag is taken out to be inspected, then the components may no longer be in the perfect registration needed. This is because even the slight change of the location of the epoxy bag, perhaps 0.1 mm from the original location, is big enough to disturb the performance of the load cells that work with a compliance of less than 50 μm. For this reason, the epoxy bag finally manufactured is currently used without inspection.

• Modification of Actuator Spring Assembly

Problems with the actuator spring initially designed and manufactured:

The initial experiment with the actuator unit revealed rather serious problems. The actuator spring has large backlash at the zero position, i.e. the middle of the spring stacks. It's magnitude is about 10 stepper motor pulses but it varies from unit to unit. Since the entire force range to be controlled was only about 100 step pulses, about 10 % backlash was unacceptable. It is also impossible to trace where the lead screw of the motor is, once it enters into the backlash region without use of a linear encoder to monitor it. The starting point of the backlash is also difficult to know with the accuracy of 1 step pulse, if calibration is not made with a precision micro-switch at the store position and the precision linear encoder.

If active polishing is intended use small strokes, then the change in pressure distribution to be compensated would also be small throughout stroke. Thus it was anticipated that the actuator would need to exert only 10-20 % of the full force range of ± 40 N (100 pulses designed) at any time during a polishing run, the actuator spring would normally work with the substantial influence of the backlash of unknown magnitude, which cannot be corrected. If the 10-20 % of ± 40 N is controlled for most of the polishing run, the force resolution is 0.4 N with one step pulse; in other words the spring constant designed is too coarse. In the mean time, it was later understood that, by stacking the two sets of 13 disc springs on the both faces of the lead screw, the movement of the lead screw is actually made with the spring constant twice as stiff as designed.

Cause of the problems and requirements for new actuator spring:

Most of the problems were caused by the principle of stacking two sets of disc springs for the actuator requirement for bi-directional movement. Thus it was necessary to make a new design for the actuator spring and its enclosure. The design requirements were that

- it must be able to make the bi-directional movement but normally work with no serious backlash.
- it must not work near the stall position
- the maximum force to be exerted does not exceed about ± 20-30 N so that the

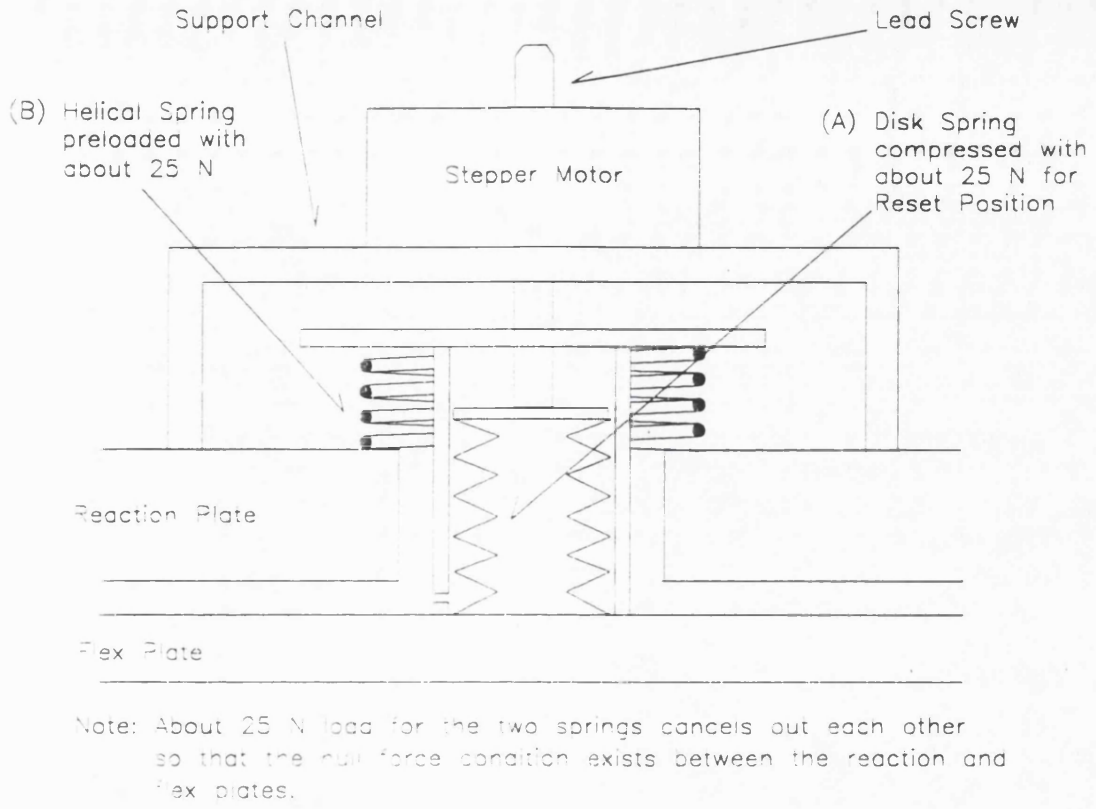

Figure 6.16: Schematic diagram of the new actuator spring.

spring constant is roughly halved, producing approximately doubled resolution of force control.

New actuator spring design:

A new design that satisfies the requirements above is presented in Figure 6.16. Here the spring set A alone is directly used to scale the actuator force at the flex plate side of the washer of the actuator lead screw. In contrast to the previous design, this spring set A works with the zero position at about 25 N in compression. The actuator works bi-directionally to add and subtract the force of 0 to 25 N from the zero position. This generates the compelling force of 0-50 N between the reaction and flex plates so that the two plates tends to become apart, thus being bent back-to-back with respect to the centre. Another spring set B is preloded with 25 N in compression which tends to remove the compelling force by pulling the flex plate with the same amount of force.

Disk spring set A in the new design:

For the spring set A, 23 disc springs of the same model give the total deflection of

8.74 mm with 154 N according to the specification, meaning the spring constant is 0.05675 mm/N. Therefore, a step pulse of 0.0127 mm corresponds to 0.224 N so that the total force of 25 N can be achieved with 112 step pulses.

Positioning error of force modulation with the new actuator spring:

If the Sonceboz 7230B motor speed is at 600 step pulses/sec with the motor force of about 55 N , it needs 0.187 seconds (i.e. 5.4 Hz) to exerts 25 N. The velocity of the periphery of the mirror is calculated as about 9.6 cm/sec at maximum in polishing operation which has the rotation period of 27 sec and the mirror radius of 41.5 cm. In practice, this varies from 0-9.6 cm/sec due to the frictional rotation of the lap caused by the mirror rotation and the stroke. The typical stroke is about 15 cm in length on the mirror, i.e. a total of 30 cm in 2 sec. This gives 15 cm/sec for the linear velocity of the lap with respect to the mirror. In the worst case, the combined velocity reaches about 17.8 cm/sec, meaning that there would be a force positioning error of about 3.33 cm for 0.187 sec to exert 25 N. In normal operation, the anticipated magnitude of force modulation is much less than 50 % of the full force of 25 N. Thus, the positioning error of the force modulation would be about 1 cm at maximum in practice, proving that the modulation speed with this spring constant is fast enough.

Helical spring B in the new design:

For the spring B, the helical spring(model Eurostock C1460-112-1500C) was chosen since it has a similar spring constant and right dimensions. This design brings the zero position of the force washer of the lead screw 11.675 mm(in case of 24 springs used) upward toward the reaction plate. Some lead screws were cut off so as not to contact with the pins of the on-lap control electronics. The designs for the enclosure and its cap were also modified to suit the new spring configuration.

Microswitches as reset device:

Because the new actuator-spring unit works always in compression as far as the spring is concerned, it is crucial to know the precise location of the zero point of the spring set A (i.e. 25 N in compression) for resetting all the motors after completion of a polishing run. Hence a micro switch was fitted to the store position, providing a reference point of no net force for each spring unit. The 25 N zero position can be reached with 112 step pulses exerted downward (according to the manufacturer's

specification). The micro switch also serves to turn power to the motor off as long as it is kept pressed so that no upward force can be exerted beyond this.

Anti-rotation device

Since this new actuator-spring unit works with a smaller force range that the original one, the friction between the force washer and disc springs would not be strong enough to stop the rotation of the lead screw and the force washer. The thin-flexible metal leaf was chosen as an external anti-rotation device. One end is attached to the motor mounting channel and other end is bolted onto the lead screw so that it provides high friction against the rotation of the lead screw. However, because of its high flexibility, it does not disturb the axial performance of the actuator-spring unit.

Experiments with the new actuator spring

A micrometer was used to measure deflection of the spring set A under varying loads cycled between 0 to 60 N. The results showed the hysterisis of about 3 % at maximum, which was quite acceptable, bearing in mind that it is a combined hysterisis of the micrometer and the spring unit. The observed spring constant is about 0.0336 mm/N which is about 1.7 times as much strong as the designed spring based on the manufacturer's specification. The observed spring constant of 0.0336 mm/N suggests that:

- since 1 step pulse equals to 0.378 N, the new zero position of 25 N would be achieved with 66 step pulses downward, instead of 112 as designed, from the stall position.
- the maximum force of about 50 N in compression is achieved with 132 stepper pulses.

• Stepper Motor and Performance

Lower graded version of the stepper motor delivered:

The stepper motor ordered was the Sonceboz 7230B model but the one actually delivered was the Sonceboz 7230R model. The model 7230R is identical to 7230B in most aspects but it is able to exert only 26 lbf of force at maximum i.e. 0 speed, which is much smaller than that designed and so the force-speed curve is downgraded. Because the motor can exert only about 26 lbf i.e. about 120 N at 0

Hz, the intended force control of about ± 40 N at 350 Hz is impossible to achieve. The speed requirement of about 350 Hz allows for the 7230R motor to control the force of about 60 N at maximum. This does not impact on the force positioning accuracy and the spring design described above, since 0 to 50 N force is intended to be controlled at maximum with the zero position of the 25 N compression.

Energisation of motors:

For energising the motor, the first approach was to supply continuously the power to the motors, even if they are in idle mode. This resulted in heat dissipation of considerable amount through the lap structure. After several hours of energisation, the whole lap was often found several degrees warmer than the room temperature but stable. The main concern was that it heats up the air column and the reference meniscus lens of th test setup above the lap, causing considerable time delay for optical testing after a polishing run, if the phase shifting interferometry was employed. The modified approach found was to cut off the power to the motors when they are in idle state. In practice, this was proved as a solution to reduce drastically the heat dissipation of the motor, and therefore, the load cells were not exposed to an external heat source in the vicinity.

Stepper motor performance as an intergral part of the active lap:

In an experiment, when the stepper motors updated continuously forces with pulses of random number on the lap, two problems were observed. Firstly, a considerable number of the motors lost some of the input pulses, and it was worse in compression than in tension. Secondly, some motors reached their store positions with much smaller displacement than others. A number of causes were found and fixed accordingly as follows.

- Some motors failed to operate as intended. These were replaced with healthy motors.
- Some motors had a broken plastic armature around the lead screw. These were replaced with new armatures.
- Dust inside the motors was vigorously cleaned.
- The motors were driven with 12 V power supplied, which does not seem to generate enough motor force. These were replaced with 24 V power supplied

for driving the motors.

- The tilted alignment of the lead screw with respect to the disk spring stack could increase side-way force while the axial force was decreased. Or the individual disk springs could be mis-aligned with respect to each other. These would give rise to friction between the spring stack and the inside wall of its enclosure, thus causing the loss of the pulses. All the motors and the springs were re-assembled with great care in view of this, but there is no practical way to inspect this happening inside the spring enclosure.

With these efforts, there was some success in reducing the number of bad stepper motors showing the loss of pulses.

Structural bias of the lap influencing the motor performance:
However, some motors still showed the persistent loss of the pulses and the problem with storing. Investigation revealed that, though a few bad performance motors were in the central area, the most of them were at the edge of the lap and systematically in one half of the lap. This could suggest that the problems are related to the tilt between the reaction and the flex plate and the bending of the two plates on the mirror. The tilt would make the actuator spring units compressed, being already deviated from the zero position even before starting any actuator operation. The uneven bending can be caused by the method of resetting the stepper motors. The assembled lap was placed on the mirror. Then all the actuators were pulled up until the micro switches closed. All the actuators were then screwed down by an equal amount of step pulses(i.e. 1 lead screw turn). In doing so, it could have been possible that, perhaps, half the motors were done in one day and the remaining half were completed the next day. Or the pitch facets might not have been fully pressed when resetting the motors. There were many possible reasons of structural biasing within the lap when the motors were reset to the zero position, since it was done in ignorance of this problem of storing and loss of pulses.

The solution would be to find a clever way in which the motors are reset without structural biasing during the course of resetting process and to limit the actuator operation in the software according to its store position. Rees [89] and Nixon [79] will describe this in more detail.

• **Tilt between The Flex and Reaction Plates**

Problems caused by the tilt between the two plates:

The reaction and flex plates are separated by the central washer, a circular disc of 5 mm thickness, bolted between them. Firstly, the separation was supposed to be same across the lap but in reality one side of the lap has considerably smaller separation (virtually no separation left) than that of the opposite side of the lap. It causes the motor operation to be severely limited at the side of no separation and this is introduced in the previous paragraph. Though no obvious reason that explains clearly this was found, the central washer and the way in which it is bolted onto the plates were suspected.

Domed head washer minimising the tilt:

A new washer with a domed head toward the reaction plate was tried to see how it work with the plates. Given the more point-like supporting at the centre, the tilt in separation was hoped to be self-rectified with even supporting forces from the new spring array. The result was much improved and acceptable.

Variation in the tilt magnitude and a experiment to validate the theoretical actuator-load cell and load cell-load cell coupling:

Secondly, even with the original flat-disc washer, it was reported that, when pressed at an edge of the reaction plate, the opposite side edge is lifted considerably. However a separate FE analysis predicted that when an edge of the lap is pressed so that it is displaced up or down by certain amount, the opposite edge moves to the opposite direction by about 1/5 to 1/6 of the displacement. An experiment was made to verify which is more realistic. Two micrometers were placed at the opposite edges of the lap and a couple of actuators very near to one of the micrometers updated force to give the edge displacement. Then the displacement at the both ends were measured with the micrometers. The result was that, while the actuator side edge has the deflection of about 200 μm down , the opposite edge shows the 50 μm displacement upward. Regarding the error in the FE analysis and with the micrometers, the experiment agrees very well with the prediction of the FE analysis. This suggests that

- the FE model of the active lap is valid and, hence, the A-L and L-L coupling coefficients, which is presented later in this Chapter, are too. Obviously, the

full validation of the theoretical A-L and L-L coupling coefficients can be made experimentally but with a precision calibration of the load cells.

- the operation of an actuator influences the rest of the actuator spring array, deviating their current position even if they do not exert any motor force.

Necessity of heaving a better motor resetting algorithm:
The experiment shows the non-negligible degree of Actuator-Actuator Coupling across the central washer. This supports even stronger Actuator-Actuator Coupling in the same side of the active lap. In view of this, it is quite clear that the actuator position, i.e. current and the zero positions in the spring assembly, is affected not only externally by the supporting condition to the lap structure but also internally by the actuator operation. In polishing operations, both conditions in continuous change would contribute to increasing rate of motor storing and therefore the loss of pulses. This indicates the necessity of having a clever algorithm for resetting the motors evenly within the active lap control software.

6.3.2.2 Active lap system calibration

The load cells have to be calibrated not in isolation but as an integral part of the active lap system. A number of calibration measurements were made and the results were very useful for improving the active lap system.

• First calibration
The reaction plate of the lap was supported by the flat platform and the lap was placed with the flex plate up, which is arrayed with the load cells. The lead weight of 0-8 kgf was cycled on the load cells with the interval of 0.5 kgf. A metal platform with 3 load cell holding legs was used to guide the weight along the central axis of the load cells. With this, it was ensured that 4 bridges of a load cell are received equal share of the lead weight. The weights of the force guide platform and the outer ring of the load cells were taken into account so that this became a precision-absolute calibration. The same measurement was made at two different temperatures as explained earlier. The results, as shown earlier, indicated that the thermal effect on the half bridge load cell is negligible. All 88 bridges showed very similar sensitivities in spite of the temperature difference. There was no systematic difference in the

bridge sensitivity across the active lap, although it was in the influence of the flex plate bowed under its own weight and the lead weights during the measurements.

• Second calibration

This is the same measurement but with the hexagonal plates on the load cells. It was not thermally cycled. The result showed that the average sensitivity of the bridges is about $0.104 \pm 0.0128(\sigma)$ in ADU/gmf. It is slightly less sensitive with larger measurement error than the first calibration in conversion of ADU to gmf. The smaller sensitivity of the load cells seems to be caused by the stiffness of the hexagonal plate as a whole. The larger standard deviation appears to result from larger errors in positioning the lead weights on the central axis of the load cell. This is mainly because the hexagons are linked with the weak silicon glue, leaving no space through which the force guide platform is used.

• Third calibration

A water bag is made and placed in between the assembled lap and the mirror. A cast epoxy bag is inserted to fill the concave gap condition in between the hexagonal plates and the epoxy wedges. The lap is first fully relaxed on the water bag with its own weight. The global actuators were then used to lift the lap with known forces and the response of the 88 bridges was recorded. The results were not useable beacuse

- the load cells in the centre have no response when the lap is almost lifted but surge in response when the global actuators release a considerable portion of the lap weight on the mirror.
- the load cells in the middle of the flex plate have no response for the full range of force exerted by the global actuators.
- the load cells at the edge of the flex plate shows pseudo-linear response in right sign i.e. signal increase in response to compressive force over the full range of the load exerted by the global actuators but much worse than the first and second calibration measurements in linearity.

Given the results above, the lap seems to be supported at the edge when almost lifted off and supported at the edge and the centre when almost relaxed on the water bag. The middle part of the flex plate, with the load cells distributed in

a ring shape there, seem to lose contact with the lower components such as the epoxy bag immediately after the pulling force of whichever magnitude by the global actuator is exerted. The centre of the flex plate seem to be in contact with the epoxy bag under the small pulling force of the global actuators but lost when the pulling force takes a substantial portion of the lap weight off. The worst fear is that there is no way of removing this behaviour as the gap condition exists in between the hexagonal plates and the epoxy wedges. Even if the epoxy bag is made to fill the gap in perfect sense, it would always be opened when the global actuators start lifting the lap, disturbing the load cell performance depending on varying support conditions.

The above feature was compounded with tilt of the lap on the water bag which is mainly due to inaccuracy of the global actuator-load cells servo. The size of the water bag is slightly smaller than the lap in diameter and amount of the water is not enough in volume. When it is placed on the convex mirror, the edge of bag sags down and the water flows down toward the edge. This leaves not enough water at the centre so that the lap centre is given mechanical support rather than fluid support. In particular, it was noted that this problem with the water bag is in good agreement with the behaviour of the load cells described above. This suggested another experiment to be made using an improved global actuator servos and the larger water bag, before attempting any further speculations on the behaviour of the flex plate in lifting. The third calibration gave at least firm evidence that;

- the gap condition could cause a major difficulty for precision calibration for the active lap.
- the disturbed behaviour of the load cells could be caused entirely by the inappropriate water bag.
- the cast epoxy bag might not be good enough to cure the concave nature of the gap, resulting in mechanical supports at the edge and the centre of the flex plate.
- the global actuator servos needs to be improved for better accuracy in control.

• Fourth calibration

The first water bag was replaced with the new and larger one and the same measure-

ment was repeated while the response of the 88 bridges were recorded. The results are shown below;

- The systematic difference disappears in the response of the three rings of load cells, which was observed with the third calibration. This proves that the inappropriate water bag played a considerable role in generating the systematic difference between the rings of load cells.

- Comparing the observed sensitivity and the offset to those of the first and second calibrations, the load cells respond less sensitively and suffer from larger variation in sensitivity from unit to unit. The flexibility of the components below the gap condition and the fluid support of the water bag seem to contribute enormously to this.

- Some bridges show hysterisis, whose magnitude cannot be neglected if the absolute precision calibration has to be made with respect to the load exerted by the global actuators. This does not seem to be an inherent characteristics of the load cells, themselves, but the active lap components below the gap condition is responsible for this. There seems no way to avoid it with the current active lap and the nature of the water bag calibration.

- In particular, load cells 1 and 2 do not seem to be properly supported with the water bag, showing extremely low sensitivity and large error. The edge of the water bag does not fully cover the edge of the lap at the side of load cells 1 and 2. In addition, the edge of the water bag is made with 2 sheets of polythene glued and clamped with the circular wooden frame. When it is filled with the water, the thickness of the water bag decreases rapidly around its edge, producing partial support to the load cells at the edge of the lap. Thus it needs a larger water bag, whose top and bottom surfaces are parallel with the water bag full.

- An error analysis shows the error decreasing towards the load cell 21 and 22 at the opposite end of the lap from the load cell 1 and 2. This is regarded as an evidence of lap tilt towards load cells 21 and 22. The load cells at the tilt-down side have a more consistent support whilst those at the tilt-up side

have irregular support during the measurement. This seems to be expressed by the larger error.

• Fifth calibration

The third water bag had a wooden circular frame and the two polythene sheets were glued and sealed on the both sides of the frame. This ensured a plane parallel geometry of the 2 polythene sheets of the water bag. The two wooden frames were again bolted onto the both side of the water bag, sandwiching the central wooden frame. The metal spacers were inserted in between the reaction and flex plates to ensure the flat and parallel geometry of the main structure. The results show much better linearity in sensitivity overall, but the load cells at the edge are still very non-linear. Two main problems come with this calibration.

- The plane parallel geometry forced by the metal spacer does not represent the real active lap, of which the both reaction and flex plates are flexible, thus never being plane-parallel in operation. Thus the calibration with the forced plane-parallel geometry is of no use for the polishing operation.
- More seriously, the polythene sheets has its own spring nature and it is quite high near to the bolted edge. This gives the load cells mechanical support instead of fluid support at the edge of the lap. Thus, the calibration can not be used for polishing since it is made with two different support conditions at one time; fluid support in the centre and mechanical support at the edge.

Water bags of various sizes were made and tested for their suitability for calibration. The result indicated that the third water bag was the best choice in size.

• Sixth calibration

The same measurement taken in the second calibration was made on the hexagonal plates but with the metal spacers inserted in between the reaction and flex plates. The load was cycled from 0 to 2 kgf with an interval of about 0.2 kgf. The results show that all the load cells have very good linearity, negligible hysterisis and similar sensitivities. The averaged load cell sensitivity is 0.0272 ADU/gmf with 0.0015 ADU/gmf as the standard deviation. This suggests very strongly that the load cells and the hexagonal plates work quite well when calibrated individually. From the experiments using foam rings described later in this section, it is clear that the

Carbon-fibre membrane and its associated units including the epoxy bag are flexible enough to transfer the force distribution to the hexagonal plates.

• **Seventh calibration**

The calibration was made using the third water bag but without the metal spacers in between the reaction and flex plates. The results are much worse than the fifth and sixth calibrations. Some load cells do not respond to the load at all while others have step-wise responses i.e. flat and jump up or down. They are totally unacceptable for use.

Findings from load cell calibrations:

The following three methods used to calibrate the active lap system were the absolute calibration for each load cell, the individual calibration with the hexagonal plates on the load cells, and the water bag calibration with the global actuator lifting the active lap. Specially, the main interest was given to the water bag calibration with the aim of using it regularly in polishing operation. However, the problems with the water bag calibration are substantial as summarised below;

- There is no way to take the gap condition into account in the calibration process. It is particularly hopeless when the lap is in the state of being pulled up by the global force actuators, widening the gap condition.
- The water bag calibration that has been believed to give the right calibration may not be appropriate since it works to increase the gap condition that is uncontrollable.
- The polythene sheets have their own spring constant, disturbing the load cell performance at the edge.
- The diameter of the water bag and the volume of water in it play a critical role in calibration. If it is too small, there would be no support at the edge. If it is too large, the edge of the lap would be given mechanical support rather than fluid support.
- The precision of calibration is limited very much by the accuracy of the global actuator servo.

- The tilt of the lap with respect to the water bag and the tilt between the reaction and flex plates due to imperfection of the central washer do not give uniform support to the lap.

- The resulting cast epoxy bag is by no means perfect and has different local spring constants across its diameter. This contributes greatly to producing non-uniform support to the lap.

Final calibration actually implemented:

Given the facts above, a practical method of calibration would be either to use the sixth calibration or to find an improved version. In fact, the main problem with the sixth calibration is that it does not take the characteristics of the Carbon-fibre membrane and its associated components into account. The improved version of this calibration would cycle the lead weight from 0 to about 4 kgf at each load cell location on the pitch facets of the assembled lap, inverted on the supporting frame. For the reasons summarised below, this method is believed not perfect but more realistic and hence reliable than any other methods used so far.

- The method allows the stiffness of the Carbon-fibre membrane and its associated components to be taken into account in calibration.

- The reaction and flex plates become concave toward the pitch facets when held by the support frame. This is very much similar to the mechanical bending when it is lifted by the global actuators. The load cells would then be calibrated in compression, mimicking the condition of the water bag calibration.

- Although the lead weights are placed on the concave surface, producing lateral force components, the load cell, as an average of 4 half bridges, is immune to the lateral force and furthermore the epoxy wedge and bag would tend to transfer only the axial component of the force.

During calibration, it was realised that the precision calibration would not be an absolute necessity for developing a fully matured algorithm for real-time ablation control. This is because all the errors in the active polishing system including the lap hardware and the polishing algorithm would eventually come out in the ablation error map whose precision is limited only by the precision of optical testing. Of

course, if the calibration is highly accurate, being capable of representing all aspects of the dynamic behaviour and support conditions of the lap in operation, a high degree of precision in force and ablation controls in real-time would be achieved very rapidly. The only drawback of using the less accurate calibration, for example the one not taking the behaviours of the Carbon-fibre membrane and its associated components into account, is that it takes much longer to reach the same degree of the precision.

It means that the maturation of the ablation algorithm would take longer if an inaccurate calibration is used. However, once it is done, there would not be any difference between the two calibrations in real-time ablation control. The use of an inaccurate calibration is in fact to correct the inaccuracy of the force control by modifying other steps within the algorithm so that the final ablation is controlled in a predictable way.

Realising these points, it was decided to use the sixth calibration to start up with when commencing the active polishing. The inaccuracy of calibration would then be expressed in the resulting ablation coefficient map with which the target pressure is defined in the next polishing run. Evolution of the ablation algorithm (i.e. RTA and GPA) based on this calibration would eventually be able to improve its accuracy, not by adjusting the spring constants but by operating the actuators with the target pressure defined using the evolving ablation coefficient map.

6.4 Real-Time Control of The Active Lap

RTA has two major functions for the active lap control; actuator update and construction of pressure map, both in real-time. The initial experience with the performance of some RTA functions lead to development of an active lap control theory for both functions. The essence of the theory is to use the physics of the active lap, i.e. Actuator-Load Cell and Load Cell- Load Cell Couplings, for the both functions. The ideas suggested in this Section are still under software development at the time of submitting this thesis. Experiments for verification of the theory are suggested.

6.4.1 Real-Time Actuator Update

• Initial method conceived

The method devised initially was to interpolate the 22 load cell readings to estimate the observed forces at the 32 actuator locations on the mirror. They are then compared to the target forces defined at the same locations to produce the magnitude and sign of the compensation forces. The compensation force is converted to stepper pulses which are sent to the actuator. This has some problems. Firstly, it assumes that a correct interpolation is used, this being expressed by the governing physics of the active lap. The accuracy of the calculated update force is critically dependent on that of the interpolation which unfortunately is not yet fully understood. Secondly, because of the complicated coupling between actuators and load cells, a force exerted by an actuator influences all the load cells as well as all the actuators on the lap. In this context, the suggested method for the compensation force is made in total ignorance of this influence. The update actuator force is derived from direct comparison of the observed and target forces only at its location without taking account of the force influence of other actuators on that location. Hence it would fail to achieve a global distribution of the update force required at one time.

• A new method: Actuator-Load cell coupling coeffieient method

Principle of the Actuator-Load cell coupling coefficient method:

Realising these points, a new method of actuator update was put forward. It is to use the Actuator-Load cell coupling coefficient(hereafter A-L coupling coefficient) derived from FE analysis on the whole structure of the active lap. Instead of compensating forces for 32 independent actuator locations, a pressure distribution represented with 22 load cell readings is made by the 32 actuators collectively working as a whole across the lap. The details are that the 22 load cell readings are directly compared to the 22 target forces at the load cell locations. The 32 actuators would then work together to produce the compensation force distribution which is the difference between the observed and target load cell values, while taking the coupling influence into account as the A-L coupling coefficient.

Here, the ith load cell reading L_i can be expressed as follows.

$$L_i = \sum_{i,j=1}^{i=22,j=32} C_{i,j} A_j \tag{6.8}$$

where

$C_{i,j}$ = coupling coefficient of the jth actuator to ith load cell,

A_j = force exerted by the jth actuator

In principle, this can be solved to obtain an optimum set of A_j as expressed in a form of matrix equation below:

$$A = C_{i,j}^{-1} L \tag{6.9}$$

where

A = matrix of actuator forces

$C_{i,j}^{-1}$ = inverse matrix of coupling coefficient matrix $C_{i,j}$

L = matrix of target load cell values.

In practice, the matrix inversion would be carried out off-line. The resulting inverse matrix of the coupling coefficients would be directly fed into the following equation which would be used repeatedly to determine the update actuator force for each control cycle.

$$A_j = C_{i,j}^{-1}(L_i^o - L_i^t) \tag{6.10}$$

where

A_j = update force for the jth actuator,

L_i^o = observed force of the ith load cell,

L_i^t = target force of the ith load cell

FE analysis to find the theoretical A-L coupling coefficients:

Thus, finding the coupling coefficient matrix $C_{i,j}$ is crucial to implement the suggested method for real-time actuator updates. The active lap was FE-modelled, including the reaction and flex plates, the central washer, the actuator springs and the load cells. The Carbon-fibre membrane and its associated components were excluded from the FE model for the following reasons:

- the aim is to find the coupling not between the actuator and the pressure underneath the pitch facets but between the actuators and load cells
- the Carbon-fibre membrane and its associated components are passive elements with a gap condition which can not be properly taken into account in

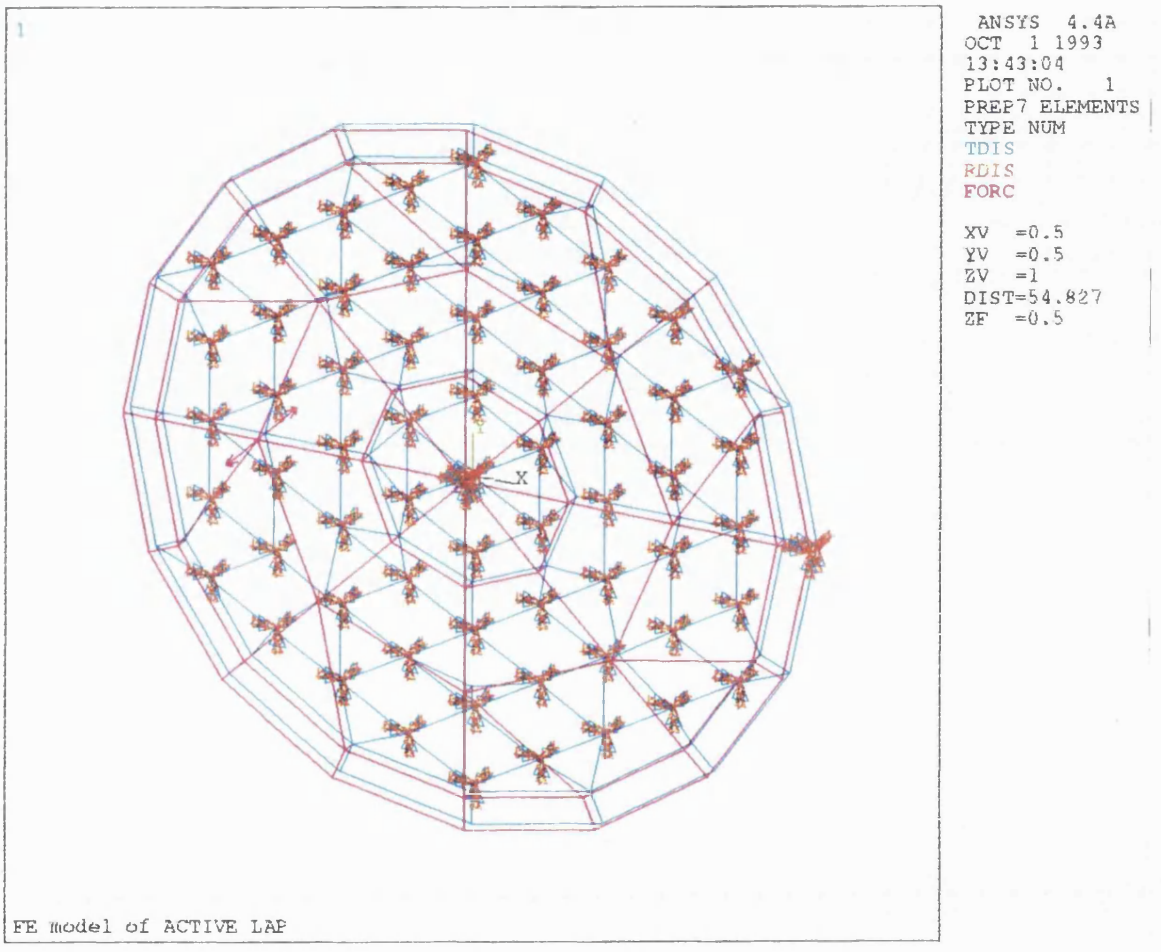

Figure 6.17: FE model of the active lap for A-L coupling analysis

the calibration. Hence it would make more sense if it was corrected not by the actuator-load cell coupling for real-time operation but by integrated variables as in the ablation coefficient map.

- the model would become too large for the ANSYS 4.4(+) educational version (which OSL had at that time) to solve.

Figure 6.17 shows a FE model of the active lap for the A-L coupling analysis. The analysis method is to apply a known force(i.e. 40 N in this case) to the actuator spring to simulate the actuator operation and find the reaction force at the bottom end of the load cell spring. Because of the symmetry of the load cell and actuator

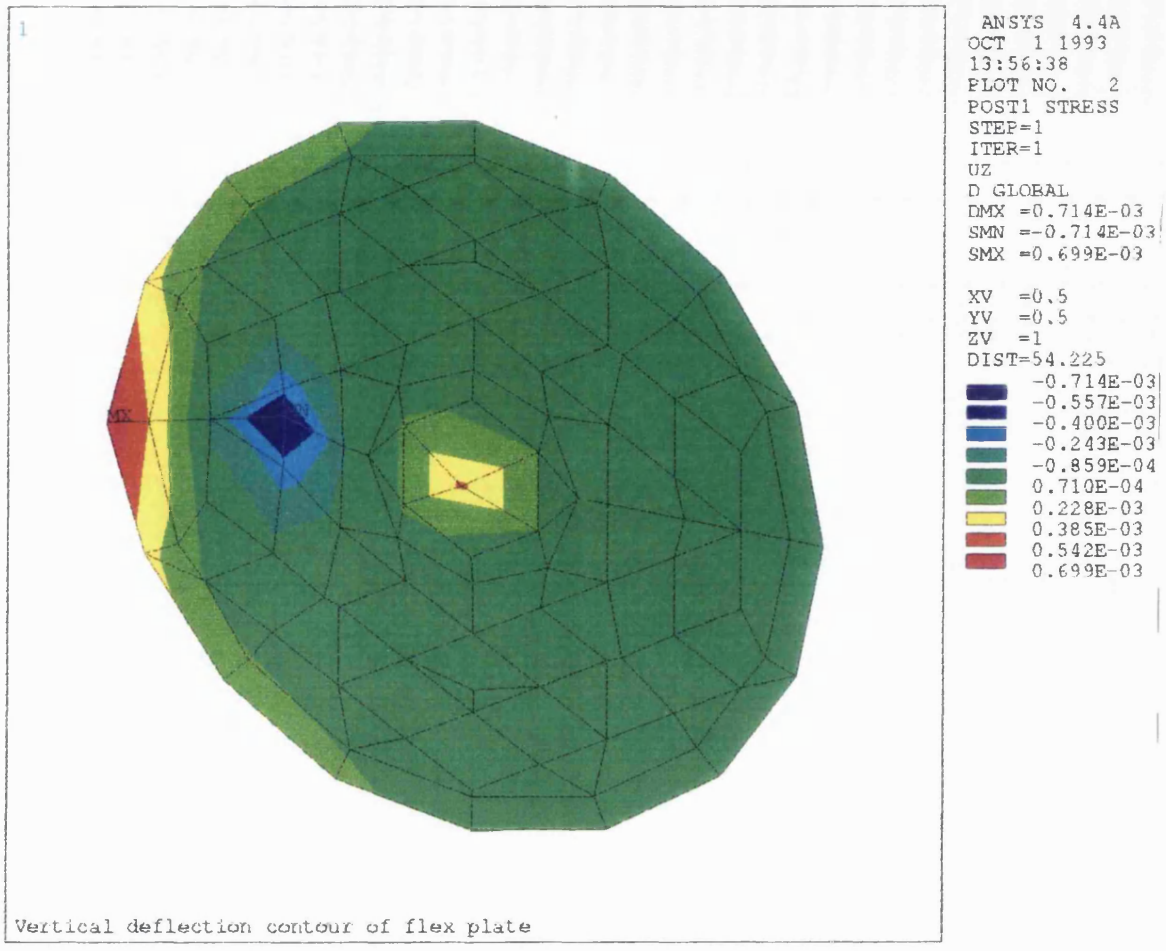

Figure 6.18: Vertical deflection of the flex plate as an illustration of A-L coupling coefficients with actuator 2 exerting 40 N repulsive force

distribution, the actual FE analysis was made only on the quarter of the actuators and the full set of the coupling coefficients would then be obtained by mirroring the resulting coefficient first in X and then Y or vice versa.

In illustration of the result of the FE analysis, Figure 6.18 shows a deformed contour of vertical deflection(UZ) of the flex plates when actuator 2 exerts a repulsive force Fz of 40 N. Appendix D.1 presents the resulting A-L coupling coefficients for a quarter of the actuators. The coefficient means the amount of the force that a load cell experiences when an actuator exerts +1 N on the mirror surface.

Implication of the result of the FE analysis:

The implication of the results of the FE analysis are briefly summarised as follows:

- The resulting coupling coefficients are made with the repulsive force between

the both plates i.e. increasing the pressure on the mirror. They would have the exactly opposite sign if it is made with the pulling force i.e. decreasing the pressure on the mirror.

- The operation of any actuators results in a force with the opposite sign at the centre of the lap. This is because any internal forces exerted by the actuators act against the central washer.

- The central washer plays a pivotal role in localising the influence of an actuator to the load cells, falling to a minimum across the central washer.

Validation of the FE analysis by passive polishing using the active lap:
In preliminary polishing run using the active lap in passive mode, an attempt to remove the central bump on the mirror by pushing the actuators near the centre downward failed, but worked in the opposite way. This is exactly what could be predicted by the coupling coefficients obtained by the FE analysis. It suggests that pushing actuators near the centre downward does not increase the pressure at the centre but decreases it. Thus the failed attempt proved, indirectly, the validity of the coupling coefficient and the FE analysis. In fact, the validity can be tested experimentally. Each actuator can be moved up and down to give known force. Then the sampled responses of the load cells are compared to the coupling coefficient to see how well they agree. However, one should be aware that the experiment would be trustworthy only when made with reliable calibration of the behaviour of the lap.

Practical complications of implementing the suggested A-L coupling coefficient method for actuator update:
The suggested method of actuator update has a practical complication in use due to mismatch in number of load cells and actuators. In the matrix equation, the number of unknown variable(i.e. 32 actuator forces) exceeds that of the known variables(i.e. 22 active load cell readings). This makes it impossible to solve the equation. Four solutions were explored in line with matching the number of the both variables.

- Rees [89] suggested that randomly generated small non-zero force could be defined for any 10 out of the 39 dummy load cells. This would give in total 32 load cell readings available for construction of the solvable 32 by 32 matrix equation. Selection of the 10 dummy load cells would be made randomly to

average out its effect over a polishing run. Or, alternatively, predefined 10 load cells always have the small non-zero pressure. At the time of submitting this thesis, Rees has confirmed that this method does not work as it is, simply because the zero pressures create singularities in the matrix inversion or the small non-zero pressures gives great influence to the resulting actuator forces from the matrix inversion. Rees is experimenting the method of *'singular value decomposition'* to solve the matrix with the zero pressures.

- 10 actuators are permanently dismounted so that the lap has the 22 load cells and 22 actuators. The matrix equation of 22 by 22 would then give a unique set of solution for the 22 actuator forces to be exerted. Of course, this method requires another FE analysis to produce a new set of coupling coefficient since it has only 22 actuator springs while the former coupling coefficient is made with the 32 actuator springs.

- If the pressure map is constructed in a reliable way, it could be used to extract 10 dummy load cell readings. They are then combined to the existing 22 active load cell readings to give 32 load cell values in total. This forms the 32 by 32 matrix equation that is solvable for the 32 actuator forces to be exerted. Success of this method is critically dependent on the reliability of the method used to construct the pressure map.

- Perhaps, the most simple solution would be to have 10 more active load cells i.e. 32 active load cells in total on the lap. This needs major re- engineering works for assembling, calibration, re-casting the epoxy bag, etc. Thus it is costly both in resources and in project time table..

- Rees, OSL software programmer, is also working on implementating *neural net computing* into this actuator update algorithm. In this approach, the 32 actuators update the pressure map randomly and the pressure map is stored. Applying a neural net to this data would idealy give an optimum way of updating the actuators for a specific pressure map at a given time.

Experimental validation of the theoretical A-L coefficients:

In addition to the validation of the FE analysis using the deflection of the reaction plate, it was necessary to see if the theoretical coefficients of A-L coupling agree well

with experiments. Each actuator updated a predefined force of about 30 stepper motor pulses and then the recorded responses of all the active load cells were devided by the force to obtain the observed A-L coupling coefficients of 32 by 22 points. These were then compared with the theoretical A-L coupling coefficients of 32 by 22 points. The detailed diagrammes of comparision and its full implications will be described by Rees [89].

From the experiment, we agreed that the results implies that the theoretical A-L coupling coefficients may be very accurate in representing the structural behaviour of the active lap comprising the two main plates, load cells and hexogonal plates and actuators. However, they do not represent the carbone-fiber membrane and its associated components including the epoxy bag quite well, beacuse they were not taken into account in the FE analysis. For this reason, it was decided that the observed A-L coupling coefficients can be used in practice.

6.4.2 Construction of Pressure Map

6.4.2.1 Linear Interpolation Method

Direct interpolation was applied to the 22 calibrated load cell readings for construction of a real-time pressure map. For a given location (X,Y) on the mirror, the 6 nearest load cells are selected and a 2D linear interpolation is applied to calculate the pressure. However, the resulting pressure map was quite unrealistic, showing a number of geometric features such as triangle, square, rectangle, etc overlaping each other. This was improved to a smoothened pressure distribution with the $1/r$ weighting function applied to the interpolation.

• Problems with the linear interpolation method

Four experiments were made to see if it produced a reliable pressure map.

- The lap was pressed for at least 24 hours with its own weight. The actuators were moved up and down. The load cells near to the actuator show more sensitively than those far from it in response to the load. This indicated that the Carbon-fibre membrane and its associated components were flexible enough to transfer the force function to the load cells. In the pressure map,

hot and cold spots appeared but their locations do not match precisely those of the actuator used.

- The lap was pressed by its own weight for about 72 hours on the mirror, allowing enough time for the pitch to flow and produce an even support condition on the load cells. Before pressing, there was a sharp central hot spot. After pressing, the central hot spot was still intact though more spread out.

- A thick foam plate was inserted to support the lap at the centre of the mirror. The four active load cells at the lap centre showed increase in signal as expected. However, a corresponding high pressure spot appeared slightly off the centre of the mirror. Next, foam rings were then placed on the mirror and the lap was put on top of the rings. There were very faint ring features which were indistinguishable in the full range display of pressure. With a zoom in range of pressure, the ring features turned up but with no sharp edge as expected.

- A three leg foam support, each angled 120° apart, was inserted in between the lap and the mirror. In the display of 22 load cell readings, the three leg feature was clearly shown. However, the pressure map showed the three leg feature not as distinctively as in the 22 load cell reading display. With the foam support was rotated about 60°, the display of the 22 load cell readings showed clearly the rotation of the foam support whereas it was not seen in the pressure map.

The results of the experiments indicated that the pressure distribution propagates from the pitch facets to the load cells correctly. However, the interpolation used for finer pixel pressure map does not seem to work quite well with the current active lap configuration, specially the distribution of the active load cells. This undesirable feature seemed to be caused by the problems listed below either solely or in combination.

- There are no physics supporting the $1/r$ weighted linear interpolation between the 22 active load cells mounted on the flex plate.

- Near the centre of the lap, the interpolation treats the load cells across the centre as if there is no central washer, which localises the deflection of the reaction and flex plates and hence the response of the load cells.

- The spacing between the active load cells is too coarse for the linear interpolation to be applied in between.
- Later it was found that numbering for some actuators is completely mixed up. This has been fixed.
- The lap may have non-uniform structural behaviour in response to various uniform support conditions.

• Suggested solutions to this problems

Five possible solutions to this problem were explored as follow:

- Firstly, the ideal solution would be to have the 61 load cells which are all active. Then the spacing between the active load cells is small enough for the linear interpolation to be used to calculate the pressure in between, when necessary. However, replacement of 39 dummy load cells with the active ones would be very time consuming and costly, not only for gauging but also for re-engineering the main components of the active lap. Considering a larger version of the active lap of 2.5 m in diameter, to use the load cells, all active, would be extremely costly, pushing production cost for a 2.5 m convex hyperbolic mirror such as the Gemini secondary.
- Secondly, realising the role of the central washer, the method of load cell selection could be altered. Rather than using the closest 4-6 active load cells in linear distance, all the active load cells within the angular distance of, for example $\pm 30^o$ or $\pm 45^o$, from the requested location (X,Y) would be chosen for interpolation. Furthermore, the four active load cells at the centre of the lap could always be added to those to form a full set of active load cells to be interpolated. This is depicted in Figure 6.19. The selection area in Fig. 6.19 rotates for interpolation for the different locations.

  One problem in realising this method would be the assumption that the propagation of all the physical events at one side of the lap reduces in magnitude to a minimum when crossing the centre of the lap, due to the central washer. However, as explained earlier, in the manufactured active lap, the reduction is not made down to a minimum. It was observed that when one side of the lap

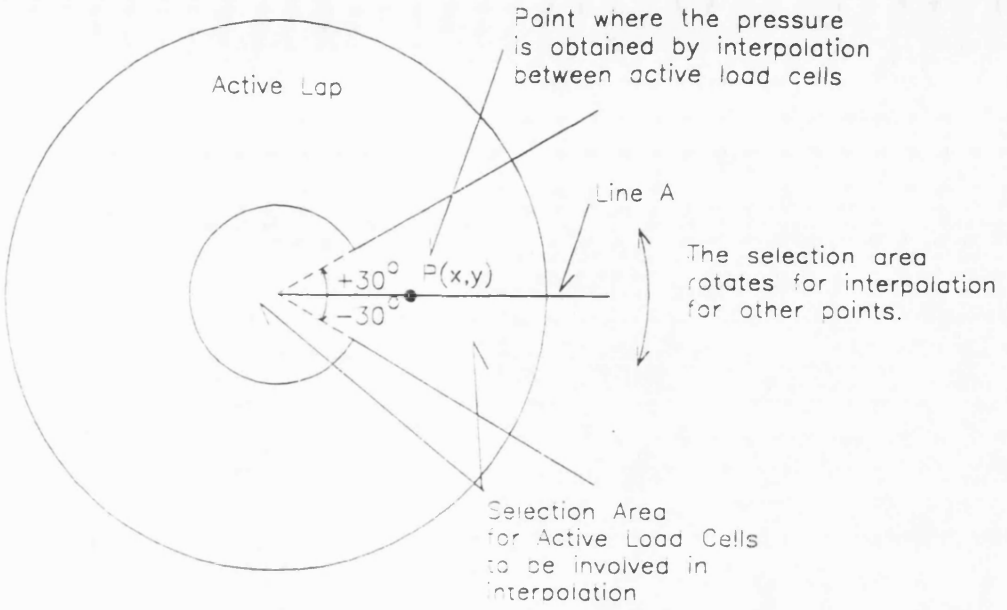

Note: All the load cells in the selection area are used in interpolation to calculate the pressure at P(x,y). The selection area is same for points along the line A. The selection area rotates as the line A rotates for other points where the pressure is calculated by interpolation.

(see Figure 6.3 for Load Cell Packing)

Figure 6.19: Conic selection area for the active load cells to be involved for interpolation

is pressed down, the other side is lifted to a non-negligible degree. Thus the underlying assumption may or may not be valid with the manufactured active lap in reality.

- Thirdly, instead of using the 2D linear interpolation, least square polynomial fitting could be used. Examples of such polynomials include *nth* order polynomials and Zernike polynomials. However, Rees [89] has found that *nth* order polynomial fitting does not work for data in 2D non-rectilinear spacing. Zernike polynomials with sufficient number of terms may be useful in fitting the 22 load cell readings, although their 2D distribution may have sharply turned feature in some cases.

- Fourthly, instead of directly attempting to find the response of the dummy load cells, the interpolation, using any load cell selection method for the active load cells, can be made with the 4-5 active load cells to predict an active load cell surrounded by them. The power coefficients of the weighting function is

adjusted until the prediction falls close to the observed response of the load cell. Continuation of this process for each active load cell would give a map of the power coefficient of the weighting functions to be applied. If they are quite similar to each other, an averaged weighting function would be applied to the interpolation for any locations(i.e. any dummy load cells). If they differ considerably from each other, they could be stored as a look-up table and the different power coefficients would then be used for the weighting function of interpolation for different locations on the mirror.

- Fifthly, a realistic interpolation, regardless how it is found, must be based on the physics of the lap behaviour, which are mainly related to deflection of the lap structure under various force conditions. It means that there must be a way of interpolation using the structural behaviour of the lap. In fact, it can be expressed in two different variables (Actuator-Load Cell and Load cell-Load cell coupling coefficients), these being the two sides of the same coin of the structural behaviour. Fortunately, they can be determined either theoretically from FE analysis for the lap model or experimentally.

• **Conclusion**

The fifth direction was of most interest since it uses the physics of the lap behaviour in construction of the finer pressure map. Two methods were developed along this line as described in the next two Sections.

6.4.2.2 A-L Coupling Coefficient Method

Previously, the actuator update and construction of the pressure map were to be made using two totally independent processes; the structural behaviour of the lap represented by the A-L coupling coefficient, and 2D linear interpolation between selected 4-5 active load cells. Use of the A-L coupling coefficients for construction of pressure maps means that both the actuator update and construction of the pressure map are made using the structural behaviour of the lap.

• **Clearer defination of actuator force**

The conceptual basis of this method lies in a clearer understanding of actuator force. In fact, the actuator force is not clearly defined so far. For this reason, it is

very easy to regard it as displacement of the lead screw times spring constant and each actuator works as if it is in isolation. However, its true definition is that it consists of the pure motor-spring force and the influence of the rest of the motor-spring actuators and support conditions. The validity of this definition has already been demonstrated with the Actuator-Actuator Coupling experimentally found and discussed in Paragraph 6.3.2.1. It is quite understandable for this definition, that even if there is no motor force exerted, the location of the lead screw in the spring with respect to the flex plate can vary with various support conditions. This is directly related to the pressure exerted on the mirror and the lap, which the load cells are supposed to sense. Since A-L coupling coefficients were derived with this definition of the actuator force taken into account in FE analysis, it does make sense to think that the actuator force distribution is another representation of the pressure map exerted on the flex plate and indeed the mirror surface.

• **Knowing the 39 dummy load cell readings**

The proposed method uses the equation 6.8 rewritten as

$$\begin{aligned}
L_1 &= C_{1,1}A_1 + \cdots + C_{1,22}A_{22} + \cdots + C_{1,32}A_{32} \\
&\vdots \\
L_{22} &= C_{22,1}A_1 + \cdots + C_{22,22}A_{22} + \cdots + C_{22,32}A_{32} \\
L_{23} &= C_{23,1}A_1 + \cdots + C_{23,22}A_{22} + \cdots + C_{23,32}A_{32} \\
&\vdots \\
L_{32} &= C_{32,1}A_1 + \cdots + C_{32,22}A_{22} + \cdots + C_{32,32}A_{32} \\
L_{33} &= C_{33,1}A_1 + \cdots + C_{33,22}A_{22} + \cdots + C_{33,32}A_{32} \\
&\vdots \\
L_{61} &= C_{61,1}A_1 + \cdots + C_{61,22}A_{22} + \cdots + C_{61,32}A_{32}
\end{aligned} \tag{6.11}$$

where

$L_1, \cdots, L_{22}$ = observed reading of active load cells,

$L_{23} \cdots L_{61}$ = response of dummy load cells,

$C_{i,j}$ = coupling coefficient of *jth* actuator to *ith* load cell,

$A_1, \cdots, A_{32}$ = actuator forces

Referring to the equation above, $C_{i,j}$ between the 61 load cells and the 32 actuators

are known from FE analysis made in the previous section. $L_1, \cdots, L_{22}$ are observed at a given time. Assuming that there are only 22 actuators mounted on the lap, the actuator force $A_1 \cdots A_{22}$ can be calculated. This involves a matrix inversion to find $C_{i,j}^{-1}$ (i,j = 0 to 22) and it can be done off-line. Once A_j (j= 0 to 22) are known, they are fed back to the equation 6.8 to calculate $L_{23} \cdots L_{61}$. This gives a pressure map for the entire lap surface with 61 pixels at the 61 load cell locations. From this, there are two ways to construct a pressure map with finer pixels, for example 100 by 100 pixels, if requested.

• First method to construct a finer pixel pressure map

Firstly, at the given location (X,Y) of each pixel, perhaps the 4-8 closest load cells are selected and then their A-L coupling coefficients are 2D linear- interpolated off line to give a set of A-L coupling coefficients for (X,Y). Doing this for all the pixel locations would eventually give a table of A-L coupling coefficient for, say, 100 by 100 pixel locations, including those for the original 61 load cells. In this case, those pixels except the actual 61 load cells are regarded as virtual load cells, having their own A-L coupling coefficients. The response of these virtual load cells would be determined by using the same procedure, just as that of the dummy load cells is calculated.

• Second method to construct a finer pixel pressure map

Secondly, alternatively the 4-5 closest load cells are selected and the 2D linear-interpolation is directly applied on-line to the 61 load cell values to predict the pressure at the location (X,Y) of each pixel. In either methods, to find the 61(22 active and 39 dummies) load cell values seems to be essential for constructing even finer pixel pressure maps(e.g. 100 by 100 pixel pressure map). This is because the current spacing between the 61 load cells is fine enough not to allow any complicated shape of pressure distribution between two adjacent load cells .

• Technical problems with the suggested method and solutions

The suggested method has a technical complication rising again from a mismatch in the number of load cells and actuators, just as the actuator update has. This makes it impossible to solve equation 6.11 for the 32 actuator forces. There are 4 directions for finding a solution to this problem.

- Firstly, the simplest way would be to build and use 10 more active load cells

so that the total 32 active load cells work on the lap. However, as explained earlier, this is costly and time consuming.

- Secondly, 10 actuators can be permanently dismounted from the lap and 22 actuators work on the mirror. The only minor problem induced from this would be to have the total controllable force 1/3 less than originally designed, but this is not seen as a major threat for operation. Of course, this requires another FE analysis to be made for the lap model with 22 actuators, to yield a new set of A-L coupling coefficients.

- Thirdly, 10 stepping motors can be disabled in the software, doing nothing but still mounted on the lap. The A-L coupling coefficients already obtained are still usable. However, according to the new understanding of the actuator force, disabling the stepper motors only does not mean that the actuator force for those actuators are always 0. The actuator springs are exposed to the influence forces from the 22 active actuators and thus a real force from the 10 disabled actuators exists. It would introduce unknown perturbations to the force modulation using the 22 active actuators. This could lead to a potential danger, that the lap would never be able to converge to the target pressure distribution.

- Fourthly, if it is proved that the actuator update works well with the Rees's method (singular value decomposition technique for matrix inversion) using randomly selected 10 dummy load cells with zero pressures as virtual active load cells, it can be used for solving the matrix equation 6.11 since it provides the 32 active load cell readings.

- Fifthly, if there are other ways apart from the A-L coupling coefficient to represent the structural behaviour of the lap, they can be used to predict the 39 load cell readings so that they can be again used to construct pressure map of finer detail.

6.4.2.3 L-L Coupling Coefficient Method

The load cell-load cell (L-L) coupling coefficient is the other variable that represents the structural behaviour of the lap. Thus, in principle, the L-L coupling coefficient

can also be used to determine the response of the 39 dummy load cells and indeed a pressure map of finer detail, using the observed response of the 22 active load cells.

• Knowing the 39 dummy load cell readings

The concept of this method is expressed as

$$L_j = \sum_{i=1,j=23}^{i=22,j=61} K_{i,j} L_i \tag{6.12}$$

where

L_i = true response of the *ith* active load cell,

L_j = true response of the *jth* dummy load cell,

$K_{i,j}$ = L-L coupling coefficient between the *ith* and *jth* load cells, meaning the response of the *jth* dummy load cell when the *ith* active load cell is given the unit force +1 N.

The equation means that the response of the *jth* dummy load cell is calculated by the response of the 22 active load cells and their L-L coupling coefficients to the dummy load cell. Just like the method using the A-L coupling coefficient, there are two ways to construct the pressure map. Firstly, once the response of the 61 load cells is obtained, they are then 2D-linear- interpolated for the locations between them. Secondly, the L-L coupling coefficients can be interpolated for the locations between them. Then the calculated L-L coupling coefficients would be imported the equation 6.12 above to yield the pressure map of finer detail.

• FE analysis to find theoretical L-L coupling coefficients

The active lap was again FE-analysed to find the L-L coupling coefficients. Forces of +40 N were given to the 19 load cells, iteratively unit by unit, in a quarter sector of the flex plate. The response of the rest of the load cells were then recorded and divided by the total sum of the response force to give a set of the coupling coefficients for the 61 load cells. Iteration for the 19 load cells resulted in the quarter (19) sets of the coupling coefficient. The full(61) set of coupling coefficient can be obtained by mirroring the results in X and Y axes. The FE model is presented in Figure 6.20. The resulting 19 sets of the coupling coefficient are tabulated in Appendix D.2. Figure 6.21 shows the resulting vertical deflection of the flex plate with +40N at load cell 7 as another representation of the L-L coupling coefficient of load cell 7 to the rest of the load cell array.

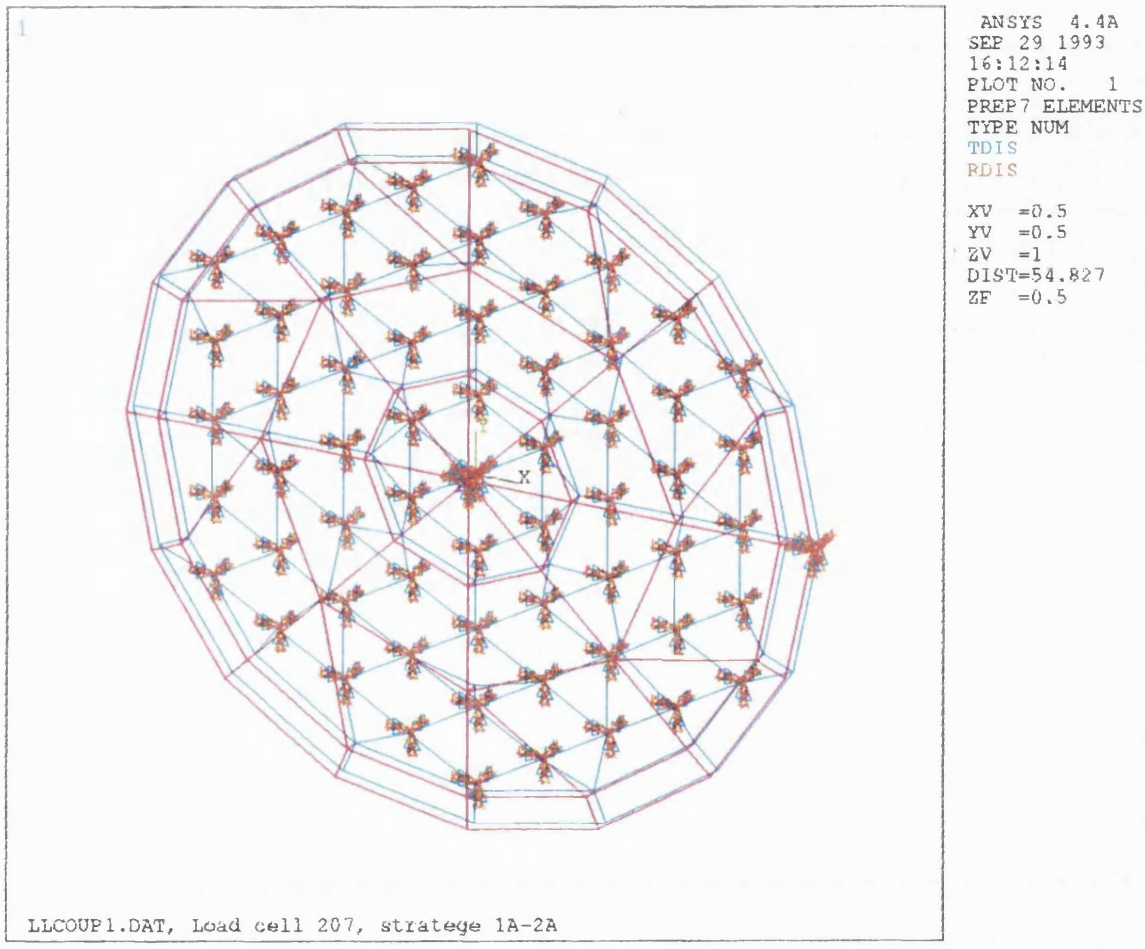

Figure 6.20: FE model of the active lap for L-L coupling analysis.

• Implication of the result of the FE analysis

The results of the FE analysis give the following implications.

Self L-L coupling:

A load cell senses only part of the total force exerted on it. This is because the undetected force bends the flex plate so that it influences the rest of the load cells. In practice, it defines a new variable called the *'L-L self coupling coefficient'*. It means that the observed response of an active load cell is the total force exerted on it times this L-L self coupling coefficient. Taking this into account, the true response

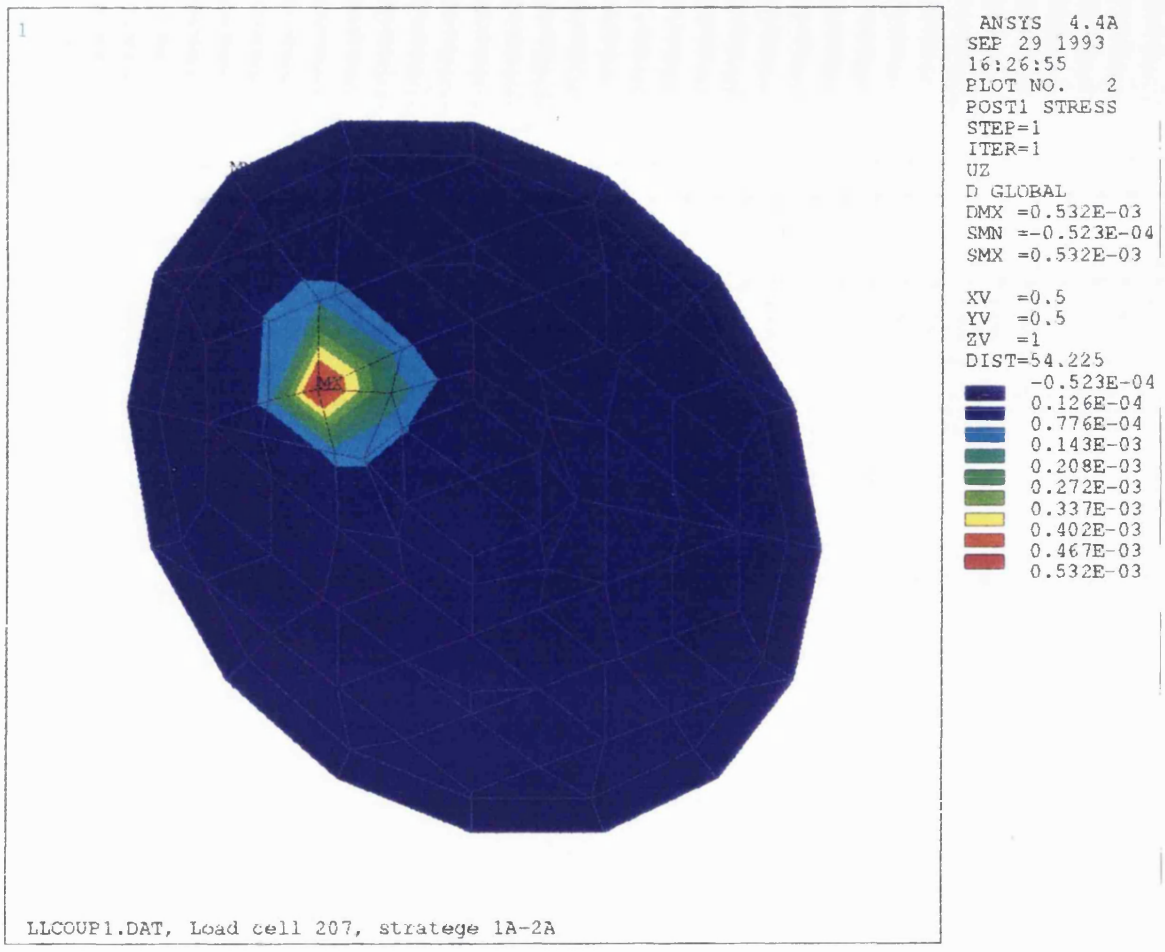

Figure 6.21: A vertical deflection contour map of the flex plate with +40N at load cell 7

of the *ith* active load cell is obtained by

$$L_i^{true} = \frac{L_i^{obs}}{K_{i,i}} \tag{6.13}$$

where

L_i^{true} = true response of the *ith* active load cell,

$K_{i,i}$ = L-L self coupling coefficient,

L_i^{obs} = observed response of the *ith* active load cell,

Relation between the self L-L coupling coefficients and the calibration methods:

In practice, whether equation 6.13 has to be used depends on how the load cells are calibrated. The L-L self coupling is caused by highly localised deflection in the flex plate. The water bag calibration gives equal force everywhere on the flex

plate so that it does not take the local deflection into account. In polishing, varying support conditions cause local deflection in the flex plate. This means that use of the water bag calibration inherently requires equation 6.13 to be used as well. However, the default calibration currently used, placing lead weights on individual load cells, naturally involves the self L-L coupling within the calibration process, since the flex plate deflects locally when the weights are given to a load cell. Thus, use of the default calibration does not need equation 6.13.

Complication in using the equation 6.12:

The coupling coefficients show that the adjacent load cells have a negative force when a load cell is given positive force. This is quite reasonable since the positive force at the load cell tends to lift the base of the adjacent load cells, reducing the deflection of the load cell structure. This means that direct application of equation 6.12 to those dummy load cells in between active load cells of positive axial force always give negative forces to them. The consequence of this could be a pressure map of 22 high pressure mountains surrounded by negative pressure valley, even though all 61 load cells sit on a uniform support. Thus the pressure map would become unrealistic. This raises doubt about the validity of equation 6.12.

One could argue that the dummy load cell would have negative influences from adjacent active load cells but also has positive influences from remote load cells such as those across the central washer. The sum of the influences, as calculated by the equation 6.12, could cancel out much of each other. The resulting pressure map would then be more realistic, not having the negative pressure valley surrounding the 22 positive pressure mountains. A simulation was made to see if the response of a dummy load cell calculated by the equation 6.12 was realistic. It assumes that the lap is pressed over a considerable time and that all the 61 load cells receive the same force of about 16 N, as the result of that. The calculated response of any dummy load cell should be very close to 16 N, if the equation 6.12 is valid for estimating the response of the dummy load cells. The simulated response of dummy load cell 29 is -3 N, proving the 22 high pressure mountains surrounded by negative pressure valley. This means that the equation 6.12 is not usable with the L-L coupling coefficients obtained. However, it does not preclude usefulness of the L-L coupling coefficients for construction of realistic pressure map.

Conceptional problem with L-L coupling coefficient:

The main problem is that there are two L-L coupling coefficients $K_{i,j}$ and $K_{j,i}$ between two load cells, depending on which load cell is given force. In practice, the response of the 22 active load cells does not tell which load cells are actually given true force. It could be caused by the force wholly given to the active load cells. Or it could be some influence from the force wholly or partially given to dummy load cells. This increases confusion about which coefficient has to be used for construction of pressure map using the observed response of the 22 active load cells.

In an extreme case where the lap is supported at 3 dummy load cells, the 22 active load cells would sense either extremely small positive or no/negative pressure. The resulting pressure map made with the proposed method would look rather flat, being centred at the zero pressure map, in spite of the presence of the 3 high pressure points in real terms. This raises a serious question about whether the current spacing of the active load cells is fine enough for the pressure distribution on the mirror to be adequately sampled.

Suggested experiments to validate the L-L coupling coefficients:

Some experiments would have to be made to verify the L-L coupling coefficient obtained by the theoretical FE analysis as follows. The lap would sit on the mirror stationary. A spacer of 10 μm in thickness would be placed underneath the 19 load cells in turn. This gives about +40N to the load cells. The responses of the 22 load cells would be stored and then divided by +40N to give the 19 sets of 22 observed L-L coupling coefficients. The full 61 sets of the 22 observed L-L coupling coefficients are obtained by mirroring the 19 sets in X and Y. They would then be compared with the corresponding values of the theoretical L-L coupling coefficient. This experiments requires a good precision calibration which has not been made yet. The theoretical L-L (and indeed A-L coupling) coefficients have rather high errors of up to 30% . This means that it would not be surprising if the experiments give up to 30% difference (with precision calibration) or more (with the inaccurate calibration currently used) from the theoretical coupling coefficients the FE analysis produced.

Conclusion of the L-L coupling coefficient method:

In practice, the error can be gradually removed as the ablation algorithm evolves

towards the full maturity, where all the errors such as that in load cell calibration, the both coupling coefficients, actuator spring constants, global actuators, encoder error, can be ultimately expressed in integrated ablation map of a polishing run. Adjustment of, for example, the ablation coefficient map using the integrated ablation map would be able to correct these as an integrated behaviour of the ablation error. At the time of this writing, it is inconclusive whether or not there exists a method using the L-L coupling coefficient that is capable of constructing realistic pressure map. It is one of the subjects to be further studied and will be described by Rees [89].

6.4.3 Control of Global Actuators

The theoretical foundation for using the A-L and L-L coupling coefficients in actuator updates and pressure map construction were explored in the previous sections. The advantage of these is to utilise the same physics of structural behaviour of the lap in both actuator update and pressure map construction. It means that the control cycle is made on a concrete basis of the lap physics. Concerning global force control, this method is to use a fixed global force manually defined prior to polishing run. A totally separate analogue close-loop servo control keeps updating the global force actuators and load cells to maintain the predefined level of tension lifting the lap.

• Problems with the current method of global force control

In fact, the pressure was originally thought to be controlled by the global force(3 pairs of global force actuator and load cell) and local force(32 stepper motor-spring actuator and 22 active and 39 dummy load cells) controls which in fact work in complete separation, i.e. ignorance of each other. This could impose a serious risk of conflict in control, that a target pressure distribution would never be achieved if the level of global force exerted at a time exceeds the range of force that the stepper motor-spring actuator and 61 load cells control can achieve. In other words, this assumes that the stepper motor-spring actuators and indeed the load cells have uniform(i.e. negligible) influence from the global force actuators in operation. It is in fact not realistic since they lift the lap from the three linkages on the reaction plate. This three point global force governs the overall shape of the lap in non-zero

tension and hence influences the stepper motor-spring actuators and the load cells.

• Suggested theory for global force control

For optimum operation of the active lap, the suggested theory of actuator update has to be modified to take the influence of the global force actuators into account. Assuming the 32 pairs of actuator-load cell are used, the matrix equation 6.8 can be expanded to include the three pairs of global actuator and load cell as follow.

$$\begin{pmatrix} L_1 \\ \vdots \\ L_{22} \\ \vdots \\ L_{32} \\ GL_1 \\ \vdots \\ GL_3 \end{pmatrix} = \begin{pmatrix} C_{1,1} & \cdots & C_{1,22} & \cdots & C_{1,32} & CG_{1,1} & \cdots & CG_{1,3} \\ \vdots & & \vdots & & \vdots & \vdots & & \vdots \\ C_{22,1} & \cdots & C_{22,22} & \cdots & C_{22,32} & CG_{22,1} & \cdots & CG_{22,3} \\ \vdots & & \vdots & & \vdots & \vdots & & \vdots \\ C_{32,1} & \cdots & C_{32,22} & \cdots & C_{32,32} & CG_{32,1} & \cdots & CG_{32,3} \\ 0 & & \cdots & & 0 & GG_{1,1} & \cdots & GG_{1,3} \\ \vdots & & & & \vdots & \vdots & & \vdots \\ 0 & & \cdots & & 0 & GG_{3,1} & \cdots & GG_{3,3} \end{pmatrix} \begin{pmatrix} A_1 \\ \\ \vdots \\ \\ A_{32} \\ GA_1 \\ \vdots \\ GA_3 \end{pmatrix} \tag{6.14}$$

where

L_i = Response of the *ith* load cell (i = 1 - 32),

GL_i = Response of the *ith* global load cell (i = 1 - 3),

A_i = Force exerted by the *ith* actuator (i = 1 - 32),

GA_i = Force exerted by the *ith* global actuator (i = 1 - 3),

$C_{i,j}$ = Coupling coefficient between the *ith* load cell and *jth* actuator,

$CG_{i,j}$ = Coupling coefficient between the *ith* load cell and *jth* global actuator,

$0_{i,j}$ = Zero coupling coefficients between the 32 on-lap actuators and the 3 global load cell,

$GG_{i,j}$ = Coupling coefficient between the *ith* global load cell and *jth* global actuator.

The equation has the three blocks of coupling coefficients sub-matrices added to the original coupling coefficient matrix $C_{i,j}$. They represent the influence of the global actuators on the global and flex plate load cells and that of the stepper motor actuators on the global actuators. No influence of the stepper motor-spring actuators on the global actuators is assumed as the zero matrix $0_{i,j}$, since the stepper motor force is exerted to the flex plate with respect the reaction plate, thus being

self-compensated to an external observer such as the global load cell in this case. Solutions of this equation obtained, using the procedure described in Section for actuator update, can then provide optimum update forces that the 35 actuators including the global force actuators exert in the next control cycle.

The influence(i.e. the three blocks of additional coupling coefficients) of the global force actuators can be determined either by lifting the lap using a global actuator each time with a known force using the real active lap on the mirror or by off-line FE analysis for the lap model. The 61 load cell and the 3 global load cell values are recorded in gmf (this unit is made using the default calibration with the hexagonal plates, if it is made experimentally). They are then divided by the force to determine the 64 (i.e. 61+3) coupling coefficients of each global actuator to the 64 load cells.

The coefficients are fed into the expanded matrix equation 6.14 above where the coupling coefficients to 10 dummy load cells are included to form a square matrix of 35 by 35. This expanded theory gives one more work block in the RTA work flow to define target global force in connection with the target pressure map in real- time operation.

• Implication of the suggested theory for global force contol

The calibrations with the water bags so far were attempts to implement this as calibration. This expanded coupling coefficient method takes the behaviour of the lap with the global force actuator into account, not as a calibration but as an influence function to the default calibration. It regards the behaviour of the lap under the global force as an influence of the global tension to the calibrated behaviour of the 61 load cells under compression. It combines the 2 independent control circuits into a single integrated control, where they form an inseparable control entity, working in harmony. Thus it provides the global force actuator and load cells with a way in which the global force is adjusted according to the observed and target pressure distribution in real-time. The beauty of this method is that the measurement for the coupling coefficients is made on the mirror so that the control cycle includes naturally the behaviour of the carbon-fibre membrane and its associated components in tension, i.e. partial compression. This is in fact what was wanted from the calibration made previously.

6.5 Work Progress for The Active Lap and The 85 cm Scaled Gemini Secondary

By August 1993, all the modifications the project team thought necessary for the active lap were completed and the lap control software became operational. Figure 6.22 shows the main hardware of the active lap. The five experiments suggested in Section 6.2.3 to ensure successful operation of the active lap in real polishing were undertaken throughout the year and some of them were already described earlier in this Chapter. The results can be summarised briefly.

• Experiment 1: Confirmation of component and system operationality

Finally, it can be confirmed that all the hardware components function well and the active lap software is marginally operational. In particular, the active lap shows its ability to monitor realistically the pressure distribution throughout the stroke and under various support conditions from the global force actuators.

Question of validity of the current spacing of the active load cells:

The question of validity of the current spacing of the active load cells has risen. The three methods discussed in Section 6.4 for construction of the pressure map are entirely based on the assumption that the current spacing of the active load cells is fine enough to adequately sample the pressure distribution throughout the stroke in polishing. In fact, this assumption has never been validated either experimentally or theoretically. The validation is related to not only the structural behaviour of the lap itself, but also the dynamic support conditions produced by surface contact between the lap and mirror during strokes.

Two experiments for the validation:

Two experiments were proposed for the validation. They are to examine the pressure map with various conditions of static support, which are in fact a series of time slices of the real-time pressure map during dynamic strokes. The first is to see if there are any effects on the pressure distribution, when the lap is placed at several different locations along the stroke on the mirror, starting from the centre to a 1/3 overhang. This measurement could be repeated for different position angles with respect to the array of load cells. It should be able to see the effect of the mis-match between the lap and mirror surfaces on the pressure map. The effect would be the low pressure

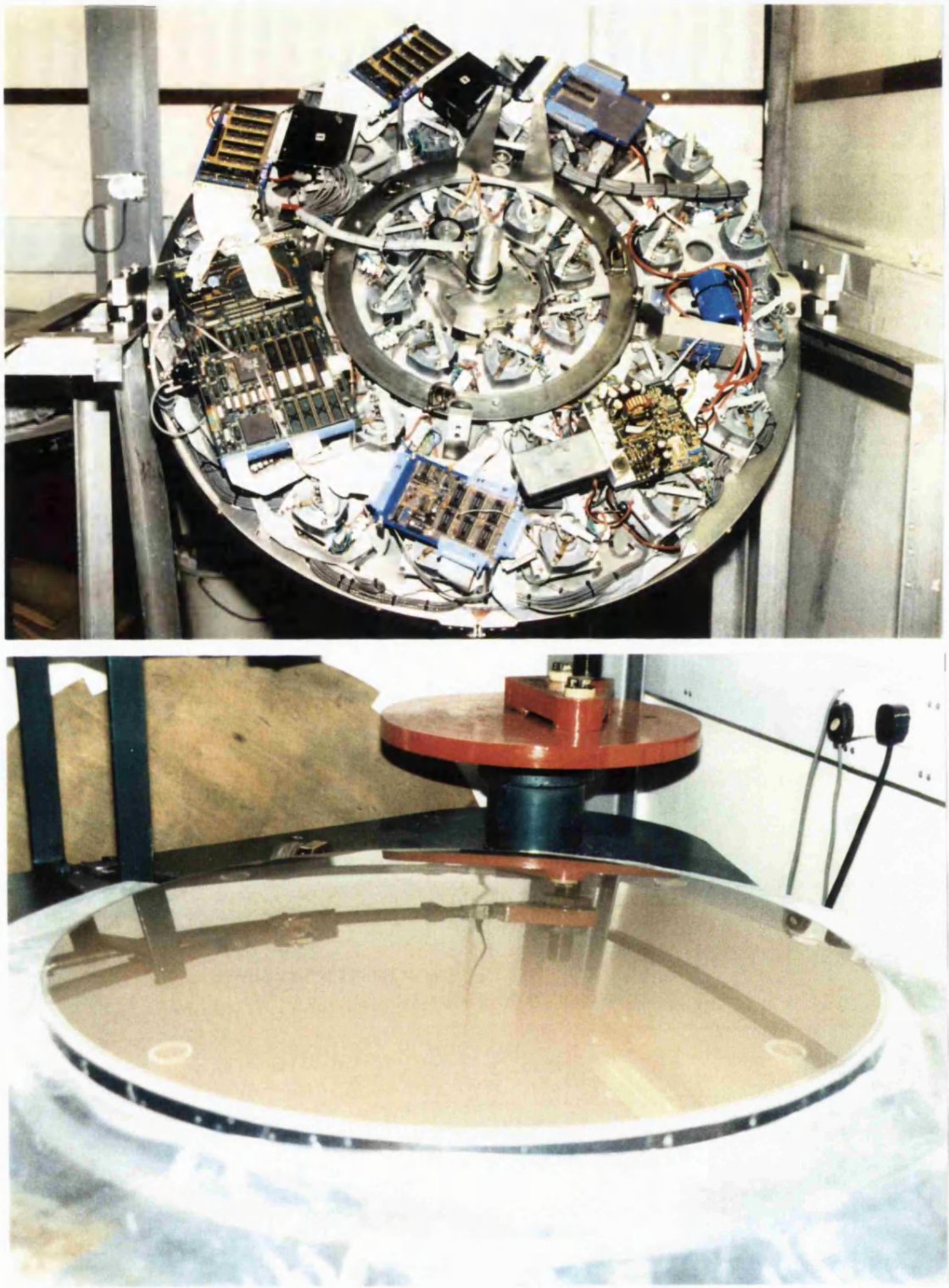

Figure 6.22 The main part of the active lap and the scaled 85 cm Gemini secondary mirror. The part of the global actuators are excluded from the picture due to limited angle of view.

at the mis-match and high pressure at the surface contact, this looking like the edge of an American foot ball under high pressure and its centre under low pressure. This is expected to move with strokes.

Secondly, one of the global force actuators pulls the lap up more than the other 2 while the pressure map is observed. It could be repeated again for different position angles and locations along the stroke from the centre to the 1/3 overhang. This should show slopes in pressure distributions across the mirror and indeed the active lap. One problem with this experiment is that, if it does not show what is expected, there is no way to clarify whether the spacing of the active load cells is too coarse or the lap is too flexible so that there is no mis-match throughout stroke. However, on the other hand, if it shows the expected, it proves that the spacing is fine enough and the flexure of the lap is finite enough to give a mis-match.

Results of the experiments:

The expected pressure maps are depicted in Figure 6.23. The results of both experiments, presented in Figures 6.24 6.25, were very satisfactory, showing the expected pressure distributions and slopes. This proves that

- the current spacing between active load cells is fine enough to realistically sample the pressure distribution when the active lap strokes to 1/3 of the diameter of the mirror.
- the mirror surface does not give the active lap highly localised support conditions which can easily be missed in pressure sampling with the current spacing of the active load cells.
- the lap is stiff enough to give a mis-match during strokes, which the actuator update algorithm must remove continuously while the machine runs. In other words, the lap is neither flexible enough for the lap to conform with the mirror surface, nor very rigid enough to have localised point-like support during strokes. The flexibility of the lap is quite acceptable in the sense that it can be corrected with real-time actuator update.

Implication of the experiments:

This provides a concrete foundation for the three suggested methods (1/r weighted 2D linear interpolation, use of A-L coupling coefficient, and use of L-L coupling

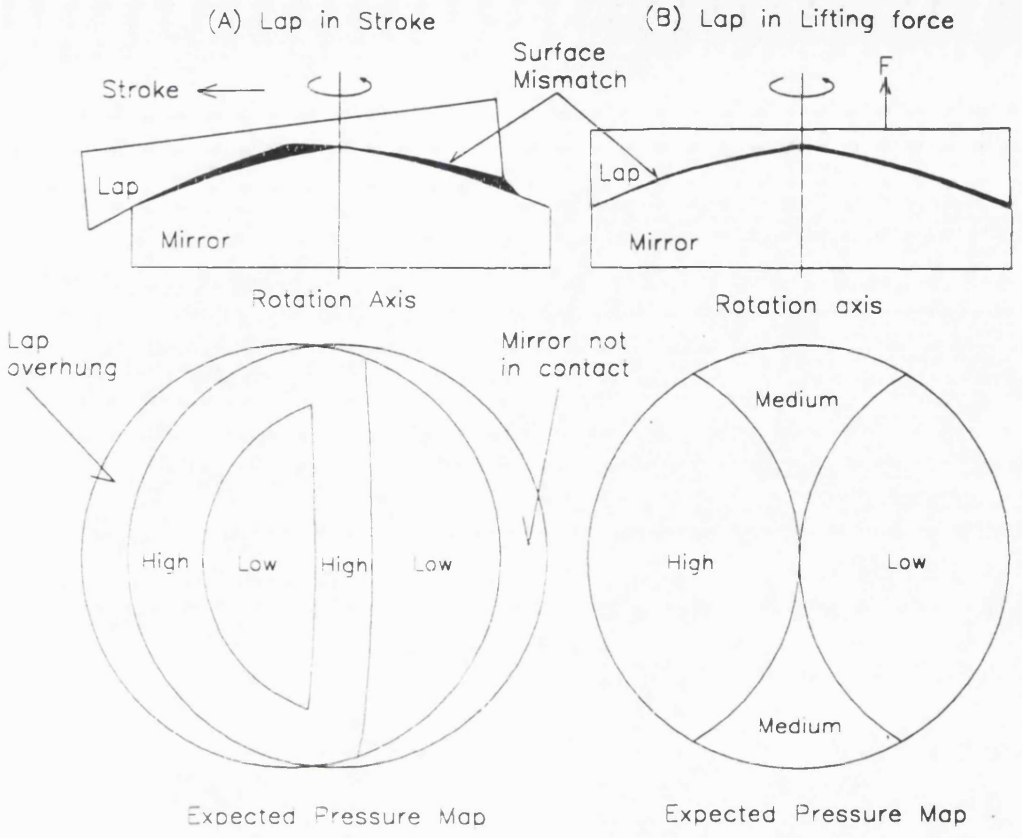

Note: In practice, the sharp-edge of pressure patterns such as drawn here is not expected because of coarse spatial sampling of pressure with the active load cells. However, the pressure map should look like what is shown in this diagram in general.

Figure 6.23: Expected pressure map with the active lap offset in stroke(A) and with one of the global actuator lifting the lap(B) on the mirror

coefficient) to be examined for construction of realistic pressure map. Not only can this give a realistic pressure map, but there is an additional benefit. If any of these is proved to be correctly working, the resulting pressure map using them can give a realistic estimate for response of 10 dummy load cells, making the A-L coupling method of actuator updates possible without the need to match the numbers of active load cells and actuators.

• Experiment 2: Calibration of the load cells as integrated parts of the lap

The active load cells are individually calibrated with lead weights on the hexagonal plate. The water bag calibration was proved unfruitful due to the various reasons already described. The gap condition between the hexagonal plates and the epoxy bag creates difficulty in achieving an absolute calibration of the load cells at the

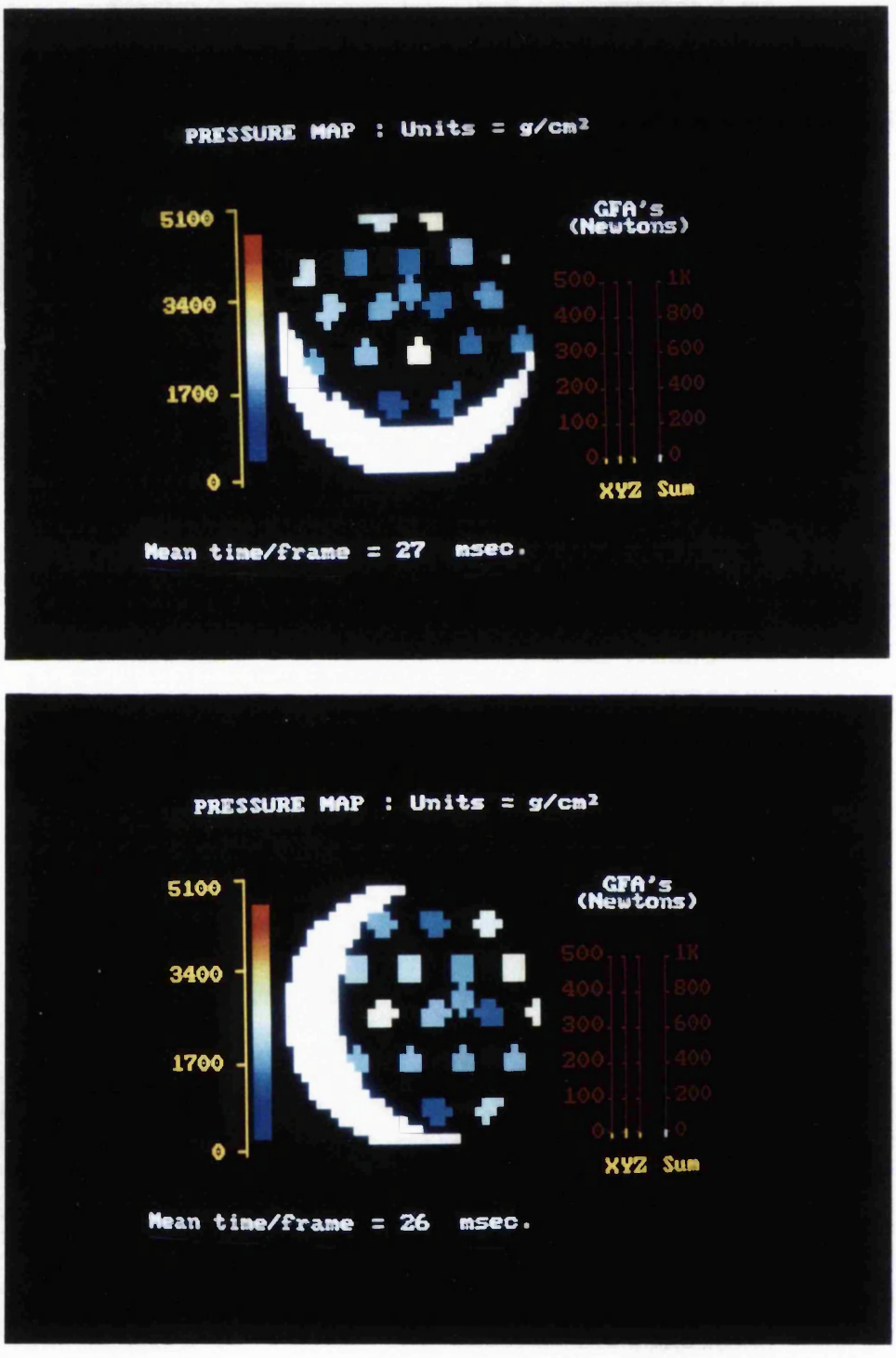

Figure 6.24: Observed pressure map with the active lap offset in stroke.

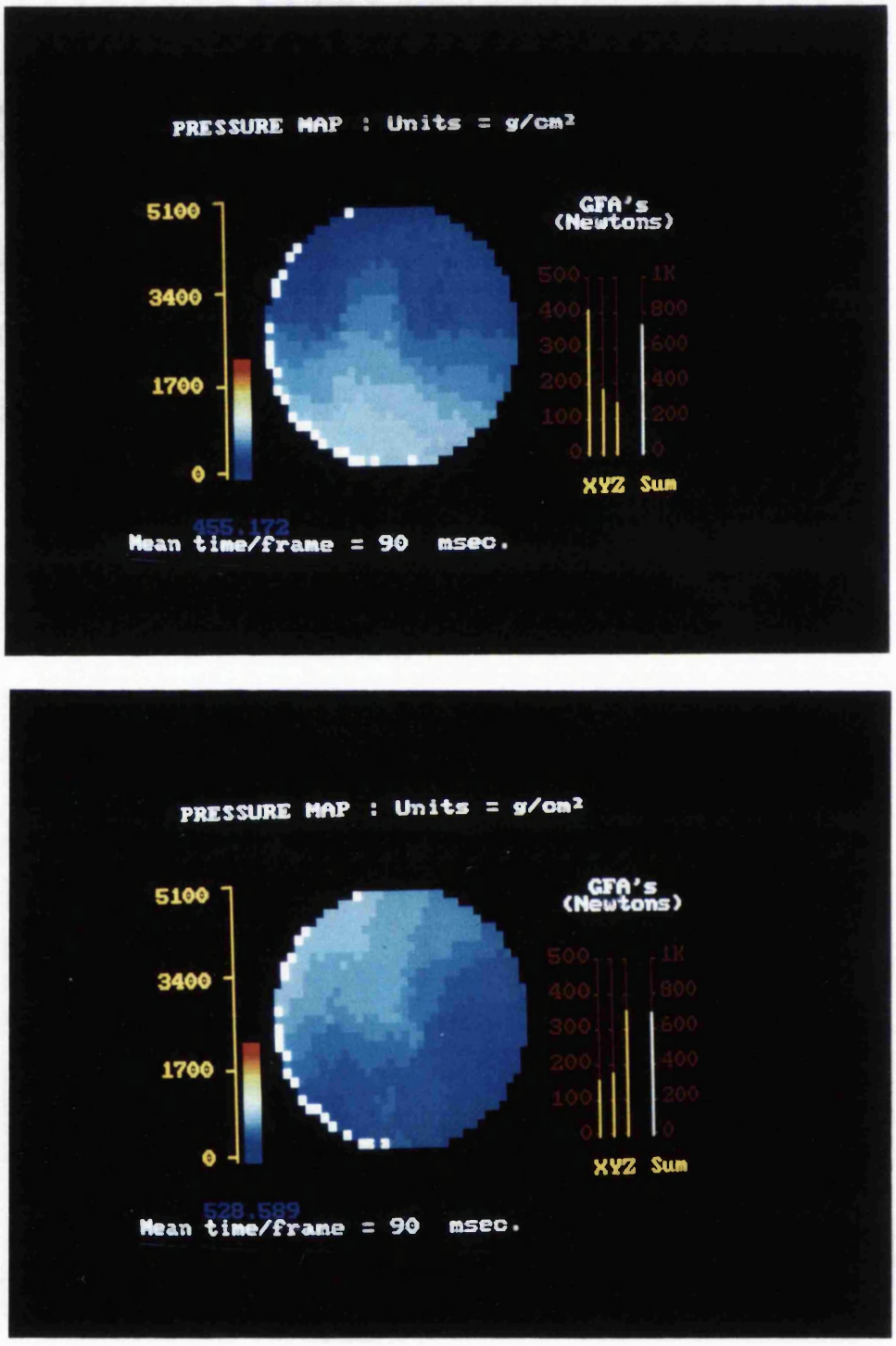

Figure 6.25: Observed pressure map with one of the global actuator lifting the lap on the mirror.

system level. Any differences between the current calibration and the true behaviour of the active lap in polishing can appear in the ablation and this would be corrected progressively in a series of polishing runs with the control-loop closed.

• Experiment 3: Coupling map between the actuators and the load cells

The A-L and L-L coupling coefficients were found from the FE analysis of the active lap model. Firstly, their validity was verified from the agreement of the expected movement of the reaction plate with the observed value when the stepper motor force pull or push the reaction and flex plates. Secondly, the however, the observed A-L coupling coefficients do not agree very well with the theoretical one. This is mainly due to the carbon-fibre membrane and its associated components which are not taken into account in the FE analysis. This also proved the existence of the Actuator-Actuator coupling that is one of the causes of the problem with resetting the stepper motor position, loss of step pulses and stalling. Another FE analysis of the existing active lap model can be undertaken to find the theoretical A-A coupling coefficients, if necessary.

• Experiment 4: Static close-loop pressure modulation

This is being undertaken at the time of submitting this thesis. Rees [89] will describe this in detail.

• Experiment 5: Dynamic close-loop pressure modulation

This has not been undertaken at the time of completing this thesis. Rees [89] will describe this in detail.

• Concluding remarks

There are still some stages to be passes through to reach the stage where the active lap can be actually used in real-polishing. Currently, the mirror is within 10 μm P-to-V error with respect to the theoretical hyperboloid. The error became worse than the best surface error of ± 4 μm P-to-V produced by profile generation (active NC-milling followed by the loose abrasive lapping). This is due to a year of *'test and fix'* procedures of the active lap on the mirror. There were also a couple of occasions of unsuccessful operation of a sub-diameter tool polishing on this convex hyperboloid since this was the first time OSL has attempted polishing a severe aspheric convex mirror of 85 cm in diameter. Most of the mirror surface is well polished but with still

a small zone to be polished. The OSL optician, David Brooks, thinks that, to speed the process, the mirror should be brought to at least 1-2 μm P-to-V error before any serious polishing using the active lap is attempted. Thus, a small sub-diameter tool has been used again to correct the profile rapidly. Once the error is achieved, the active lap, either in passive and semi-active modes or in active mode, will be continuously used for polishing the mirror. A number of sub-tasks left for further development of the active lap for fully operational polishing is described in Section 6.6 and in Chapter 7.

6.6 Discussion

• Lateral force compensation for load cell operation

As expected, the 88 half bridges on the 22 active load cells were found very susceptible to the off-axial load, thus being unreliable to sense the axial pressure while the active lap runs. However, with the averaging of four half bridge load cells, the influence of the non-axial force is almost removed from its characteristic curve. One limitation though, which is non-essential for the active lap, is that the averaged half bridge load cell can not distinguish pure lateral forces from torque.

• Gap condition between the load cells and the carbon-fibre membrane

It was understood that the gap condition between the load cells and the Carbon-fibre membrane causes enormous difficulties for calibration of the active lap. This revives the attraction for the pressure transducer as a pressure sensing device for the active lap. They need no gap condition when used for pressure sensing with the active lap. Of course. all the difficulties already addressed need to be solved prior to using them. The gap condition could be drastically reduced if the global actuator servo is used with either no or extremely small tension force. Alternatively, self weighted operation, as originally conceived, could be used to minimise this problem.

• Ablation algorithms

The variety of strategy for both RTA and GPA were found. The distinctions between RTA and GPA are purely artificial for convenience in understanding the active polishing algorithm. Both are in fact inseparable and each influences the other more or less in reality. According to the classification scheme developed for GPA, there

are a number of different GPA strategies. A full specification RTA was developed, which takes full advantage of the GPA strategy 1AaBa-2A-3A-4Aa. Another GPA strategy 1Bb-2B-3B-4B is explained in details. Some other GPA strategies briefly explained include 1Bb-2B-3B-4Ab, 1AaBa-2B-3A-4Aa, 1AaBa-2B-3B-4Aa. An example of a hybrid GPA, which is outside the classification scheme, is also briefly summarised.

The development of the polishing algorithm can be concluded as follows;

- The 1AaBa-2A-3A-4Aa GPA strategy embodying the full specification RTA is most attractive as the definitive algorithmic approach for active ablation control.
- The data base approach such as the 1Bb-2B-3B-4B strategy is very similar to the neural-net approach in the sense that more polishing experience can allow the active lap to control ablation with better accuracy.

However, only a few strategies are explained. These other GPA strategies need to be studied further in depth as well.

• Software development

The various ideas suggested in the previous sections for ablation algorithms (RTA and GPA), calibration, actuator update, pressure map construction, etc. were fed to the active lap software programmer, David Rees. The details of what and how to implement them in the active lap control software will be found in his PhD thesis [89]. At the time of this writing, the software development has reached to the stage where it is able to perform the following real-time tasks.

- Read and store all the readings from the load cells, encoders and thermal sensors.
- Display the load cell readings either in ADU or in calibrated unit such as gmf.
- Display the pressure map either in ADU or in gmf, with the interpolation using a selection of the nearest four active load cells and the $\frac{1}{r}$ weighting function.
- Display simultaneously the maps of pressure, velocity, instant ablation rate and integrated ablation rate.

- Update actuators with small force defined to the selected 10 dummy load cells. The update force is calculated by solving the 32 by 32 matrix equation with the known 22 active and 10 dummy load cell values.
- Independent close-loop control to maintain a predefined level of global force with which the lap is lifted.

This leaves more developments yet to be made as follows;

- For pressure map construction, experiments are to be made to see if the suggested method of using A-L and L-L coupling coefficients works for construction of the pressure map.
- For actuator update, the methods suggested in Section 6.4 need to be experimented to see how well they work.
- Combining the global force and pressure controls into one control process.
- The algorithms (RTA and GPA) have to be fully implemented in the software, especially defining the target pressure. The method of defining the target pressure, suggested in the full specification RTA, also needs to be examined how well it works in practice.

• Use of neural net approach for the active lap

Rees [89] has been developing the Neural Net approach for finding an optimum way of updating the actuator forces. It is a completely different from the deterministic algorithm approaches, which is one of the main subjects of development in Section 6.4. It would start with no algorithm for actuator update. The 32 actuators are moved with random magnitude and direction while the response of the 22 active load cells is stored. This actuator force and response of the load cells form the input parameter space for the Neural Net to process and yield an optimum algorithm of actuator updates as the output. The more actuator forces exerted and responses of the load cells collected, the better the resulting output. The Neural Net approach can be used for various subsets of the active lap. For example, the theoretical A-L and L-L coupling coefficients could be adjusted to satisfy the experimental behaviour of actuator update and pressure map construction. The relationship between the

polishing variables and the ablation rate coefficient map could ultimately be found by applying the Neural Net to the data collected from polishing runs over a long period.

• Active lap calibration

Concerning calibration of the active lap, it can be concluded that the water bag experiments are unable to give reliable calibration because of their own spring nature. However, it was realised that an absolute calibration would not be necessary. Because, firstly, the integrated ablation can only be known in relative terms with respect to the centre of the mirror. It means that, even if an absolute calibration is made, the ablation behaviour can not be quantified in absolute terms in polishing. Thus it would be wise to use the relatively inaccurate calibration and the work algorithms would be able to evolve toward the optimum with it. Secondly, as stated before, the proposed ablation algorithm, in particular RTA, uses the ablation rate coefficient map over the work piece that is adjusted by any errors in calibration, spring constant of actuator spring, servo, uncontrollable parts of active lap such as the Carbon-fibre membrane and its associated components, etc. Thus, the final calibration used is made with the lead weights placed on the pitch facets but at the load cell location of the inverted lap in the supporting frame.

• Importance of using software for managing the project

In the later stage of the active lap development, it was extremely painful to share available time and facility for two parallel tasks; test and fix for the active lap on the mirror and actual production of the mirror. Often each tends to delay the other for a considerable time. This gave rise in importance of careful planning for using available time, facility and resource to progress the project optimally. It is now understood that use of a commercial software for managing the future of this development would be beneficial to speed up the two parallel works.

Chapter 7

Conclusion

7.1 Summary

The development of the new active technology for large optics production has been an extremely ambitious and exciting project. In is indeed a long term project that OSL is committed to pursue to completion for years to come. The progress of the project that author has contributed is briefly summarised as follows.

• The diamond-milling facility of the former Grubb-Parsons's 8 ft grinding facility has been fully computer-controlled, this being able to generate directly optical surface profiles of any shape. The Mark 1 profilometer was developed to sample surface profiles and to give surface errors used for active-error compensation while generating profiles. Both facilities are now fully operational separately, but together forms into the 8 ft surface profile generation system.

• The load cells and actuators were designed, prototyped and experimented in house, specifically for full size active polishing. These were then used to design and build an active polishing module to access the technical problems of building the 85 cm full size active lap. Experience with this module has proved extremely valuable for construction of the active lap.

• The ablation rate and behaviour of abrasive film were investigated under different pressure, velocity and cerium oxide-water mixture ratio. The results were extremely influential to the active polishing. Implementation of these into the ablation algorithm to control ablation over the mirror surface using the active polisher is still

under software development.

• The 85 cm instrumented active lap was designed, constructed and then installed on the former Grubb-Parson's 1 m polishing machine. The functions of the components and of the whole lap were tested and the system was calibrated. The ablation algorithm consisting of RTA and GPA was developed and theories for actuator update and construction of pressure maps in real-time are suggested in detail.

• In preparation of full scale development for optical testing for the 85 cm scaled Gemini secondary, the scatter plate interferometry was experimented with the WYKO fringe analysis system.

7.2 Performance

The two static experiments were undertaken at the system level. Those were to demonstrate the ability of the active lap in sampling the correct pressure distribution throughout the stroke. The results described in the previous Chapter proved that the active lap is functional not only at the component but system level. These have been a significant step forward to the static and dynamic close-loop pressure modulation tests and its actual use in polishing, which are to be made in the near future. These are described in more detail elsewhere [89].

7.3 Implications

Increasing number of institutes which currently work on large optics production have been employing computerised grinding for surface profile generation. The modern machines such as one in Eastman Kodak are extremely stiff and the accuracy of machining is well within the sub-surface damage or the accuracy of profilometry used. In contrast, our development in this field is focused on converting the old Grubb-Parson's 8 ft machine, so that its performance is matched to that of modern machines. The resulting computer-controlled diamond-milling is extremely successful in generation of surface profiles of any shape. Provided the surface error data from profilometric measurement, with the ability of active error compensation in software, its performance is achieved to the level of those modern machines.

The full-size active polishing is developed and the preliminary experiments show that it has potentially superior ability in both smoothing actions and local figuring control. It differs inherently from other techniques in the sense that

- it has real-time close-loop control of polishing pressure and sliding velocity over the mirror surface.
- it is controlled by, for the first time in optics production history, an advanced computer based ablation algorithm.
- the algorithm has the ability to learn from the previous polishing runs and hence correct itself in evolution.

For these reasons, it is quite sensible to expect the fastest convergence factor of about 2-3 in correcting surface defects over the mirror surface, when the algorithm is fully matured.

The active production technique developed here will certainly benefit the astronomical community in the international context through superb quality of optical surface and substantial cost/time reduction in production of large telescope optics.

7.4 Applicability and Contribution

There are extremely wide prospects for the application of the facilities and underlying technology developed in this thesis. The author and OSL are confident that it will contribute to many international projects for large telescope optics production and related areas.

The computerised diamond-milling facility, when used with a new profilometer under development [55] [76], can be used to generate surface profile of any shape up to 2.5 m in diameter. The 85 cm scaled active lap can be used for

- full-size active polishing for any optics smaller than 85 cm in diameter.
- 1/3 sub-diameter active polishing for any optics up to 2.5 m in diameter.

The actual Gemini secondary of about 2.5 m diameter is just at the upper limit of the range that either the 1/3 i.e. 85 cm sub-diameter or 2.5 m full size active

polishing lap can figure on the existing 8 ft grinding and polishing machine OSL has.

The technology developed can be applied widely as described below.

- The experience gained from the modernization of the 8 ft diamond-milling facility and from developing the profilometers can be used for development of larger or smaller machines.

- The experience obtained from developing the active polishing module and the full size active lap can be used to develop a Computer-Controlled Polishing Machine (CCPM), both sub-diameter and full size, or an array of CCPMs for production of smaller optics.

- A full size active lap of up to 2.5 m in diameter could be built without requiring any further development in technology. This would reduce considerably the cost of polishing machines and therefore of the 2.5 m Gemini secondary mirrors.

- The experience of the Mark 1 and 2 profilometers leads to another project to develop a contact laser profilometer to measure up to 2.5 m in length with the accuracy of down to $\lambda/10$. This project is currently being undertaken at OSL and it would enormously benefit the testing of the actual Gemini secondary of about 2.5 m in diameter, if a contract is placed.

- The full size active lap is very similar to an active mirror support system in many respects. The technology obtained in mechanical system, pressure sensors, actuators, control electronics and software, and the algorithm of the active lap could be very useful for the development of advanced active mirror support systems. Examples includes the study for active support units - especially actuator, load cell and their calibration rig - for the ESO VLT active mirror support system. The work has been made in collaboration with British Aerospace Ltd. to prepare the bid for international tender.

- The in-house development of the load cells and actuators specially tailored to suit the active lap gave considerable amount of technological gain in designing, prototyping and mass-producing force/pressure transducers and actuators in general. The experiment and test of their performance as integrated parts of

the lap system delivered invaluable experience not only in building the same kind of polishing machines, larger or smaller, but also to develop active elements for different instruments for astronomy and other areas. Especially, there are good commercial prospects for flat-line load cell technology development.

- The principle of the ablation algorithm (RTA and GPA) developed here can be applied to polishing with any tool-to-mirror size ratios. This means that other techniques such as CCOS of Itek, stressed lap of University of Arizona, membrane tool of Zeiss, etc. will benefit from using either the principle of the ablation algorithm or some specific form of it in the algorithm classification scheme.

- The experience with the experiments to know the ablation rate and behaviour of Cerium oxide abrasive film will be valuable for future development of active ablation control using whichever polishing methods.

- All the technical problems with the active lap at the component and system levels are quite unique as the machine, itself, has several unique features explained throughout this thesis. The experience with solving these will be invaluable for future evolution of this type of polishing machine.

7.5 Future Work

Currently, the major improvements and modifications for all the hardware of the full-size active polisher are complete. This leaves mostly the software work to be done in the future.

- The experiment needs to continue in order to know the ablation rate and behaviour of abrasive film under different polishing conditions. The experiment described in Chapter 5 is made with a limited range of polishing variables and their magnitudes. The experiment with full extension of the variable space is necessary to understand physics of glass polishing and to achieve the fastest convergence in ablation control in polishing.

- The suggested A-L and L-L coupling methods (or improved versions of them) for construction of pressure map and actuator update need to be implemented in the software and be tested.

- A limited number of RTA and GPA forms are studied here. In fact, all the possible RTA and GPA forms in the classification scheme need to be studied in depth to find which is suitable for a specific method of polishing currently developed world-wide.

- Selected RTA and GPA forms need to be implemented in the active lap control software, specially the GUI part, and experimented to see how well they perform for active ablation control. Fast convergence is not anticipated in removing surface defects from the first time figuring for the scaled Gemini secondary. However, providing there is enough time, they will be fully matured through each polishing run toward completion of the mirror.

- The suggested sub-aperture synthesis technique with knife-edge and interferometric testing needs to be developed to an operational optical test procedure. No further development for the major hardware for both tests is required, but there are a few things to be done. Examples include incorporating the PZT translator/aligner into the WYKO fringe analysis system for phase shifting interferometry.

- The GUI software for active lap control should be able to read and process the optical surface height data generated by the WYKO fringe analysis system to produce the integrated ablation map of the previous polishing run and the current surface error. This will be used by RTA and GPA to adjust itself and to define target pressure map when starting the next polishing.

- It is intended to complete figuring the 85 cm scaled Gemini secondary mainly by using the full size active polishing. However, it could be possible to use a small sub-diameter passive tool from time to time for local touching, if the full-size active polishing proves ineffective for doing that. This will be a trade-off between motorising the full-size active polishing and the work time table for completion of the scaled Gemini secondary.

• Concluding remarks

In reviewing the progress of the active lap project over the past 3 years, it is felt that it took a much longer development time than expected. Its hardware was first assembled in January 1992, but became preliminarily operational in June 1993. Considerable time was spent in calibration, test and modification of the hardware of the active lap. Much work was also done on profilometric and optical testing facilities. In parallel, the software development has taken considerably longer than expected, this still being under development at the time of writing the conclusion. It is because the code can be written only when the work processes including ablation algorithm are clearly defined beforehand. Many aspects of the work process and technical problems with the active lap have been completely new and never introduced before in large optics production. These required a much longer time to solve than originally thought.

Recently, it has been noticed that Optical Science Centre in University of Arizona had a very similar experience, when developing the 60 cm diameter actively stress lap in late 1980s and early 1990s. It was first assembled, calibrated and then started polishing a 1.8 m f/1 ellipsoid mirror as a demonstration of their polishing method in November 1989 [71]. However, it took nearly 2 years to complete the mirror and to make the stress lap operational in November 1991. Even then, the mirror was completed not wholly by the stress lap polishing but with sometimes applying sub-diameter passive laps. They admitted that this period was very developmental in nature and much engineering work was necessary on both the stressed lap and test optics. However, they demonstrated, when the 3.5 m f/1.5 primary for the Phillips Laboratory was figured, that with the experience gained from the 60 cm stress lap polishing, the convergence factor of the 1.2 m stress lap is extremely fast [72].

Although the 60/120 cm stress laps are much simpler in many aspects than our 85 cm active lap, their work gives some useful extrapolations to the active lap polishing. According to this, the active lap would be much more operational when completing the 85 cm scaled Gemini secondary. Completion of active lap hardware and software (except the full maturisation of the ablation algorithm) would likely be around December 1993 or January 1994, about 2 years after its first assembly. By that time, all electro-mechanical hardware and software control functions will be fully operational. This will leave only the work algorithm i.e. selected RTA and

GPA to be fully matured and operational in another 1 or 2 years. It will be ideal if the maturation of the algorithm is made while a major astronomical mirror is figured by the active lap polishing developed.

In concluding this thesis, it is felt that the full-size active polisher is the most advanced polishing method to date in many respects. It will provide the three functions that large optics production has always wanted to have; fastest removal rate, overall smoothing action and local figure control in a predictable manner. Our method is, as far as we know, unique in measuring the real-time pressure exerted by the tool. It is an ambitious attempt to take the next step forwards in being to predict surface removal during polishing, with the ultimate goal of 'closing the loop'. The entire project is a long term programme and OSL is committed to take all necessary steps towards it's completion.

In practice, there may be several ways of using this new technology for large optics production. It can be used solely or in conjunction with other methods described earlier. Alternatively, an active sub-diameter polisher (the sub-set of the full-size active polisher), which runs under the same principle, can be used for local touching to remove highly localised surface errors left by polishing with other methods. No matter which way is used, the new technology developed here will be of enomours benefit to international astronomical communities through cost-effective production of superb quality large optics for astronomical telescope projects in the years to come.

Acknowledgements

It all started with the great storm in October 1987, in which two men, Dr. David Walker and Dr. Tu-Hwan Kim, happened to meet and had a chat in Hut 20 of UCL, OSL. Since then, it has been the most turbulent but, in contrast, most peaceful in mind and spirit 5 years I have ever had in my life. It would have been impossible to get through all these without *Thy Love and Mercy.* Thus, I feel most grateful and thankful for *Thy Guidance and Help* that has enabled me to meet numerous people who helped my study greatly in all respects for this period. It seems to me that there is no better alternative other than the traditional way to appreciate the help that they have given. Although it may look a mere list of names, it contains my most sincere thanks to all those whom I can and can not mention individually.

On a personal note, first of all, I would like to thank Jung-Sook Kim for her love, dedication and encouragement that has been the main driving force during the course of the study. I am grateful to Sae-Young Kim, my son, for his big smile that refreshes my tired soul and body and eases much of the load I have to withstand, particularly in this final stage of writing an PhD thesis. I specially thank my parents for their efforts in bringing me up in an honest and conscious way and for their share of all the problems we have tackled and solved in a collective way for the past 36 years.

My most sincere thanks should go to Dr. David Walker, the supervisor, who not only pioneered, for the first time in history, the full size active polishing lap, but also provided a number of innovative and ingenious solutions to the technical problems faced within it. Though he has an extremely busy time table with many commitments every day, he has always opened his door to numerous questions and discussions I had during the course of the project. It has been only his guide in enthusiasm, through which my journey from pure astronomy to a realm of instrumentation for astronomy has been made so safely and securely. I am also extremely thankful for the continuous help and encouragement from his family in walking toward *Thy Righteousness and His Kingdom.*

I surely feel extremely privileged to have been working with David Brooks, who has been eager to share his unique expertise in large astronomical optics production

within the UK. His practical experience with the facilities being developed and careful observation of their performance were essential throughout the project. I appreciate very much the technical advice of Dr. Hashmat Jamshidi when building the active polishing module and its electronics. His depth of knowledge in electronics and machine level software also played a pivotal role in his contribution to the active lap control system. Gil Nixon has designed and built the active lap control electronics that should be highly praised for its novel architecture and performance. The high level GUI software for active lap control was written by David Rees, with whom I have shared the same difficulties, feeling and length of time, discussing and experimenting various ideas for the main functions of the software. Much of the 'test and fix' work in the later stage of the project was possible only with the timely completion of a preliminary version of the software, which was of course a result of his hard work. I feel grateful to work in the project team of the highly motivated and talented individuals, from whom I have learnt much.

The continuous support from Andy Charalambous was a much needed help for me to undertake the FE analysis and the design study for various components and the whole system, for which I have special thanks. I appreciate very much Mark Dryburgh's help in using Auto CAD and he also produced many Auto CAD drawings for the active lap. His efforts in cross-validating some of FE calculations in the thesis must be appreciated as well. The success of the experiments for the ablation rate and the behaviour of abrasives in sub-diameter tool polishing must have been impossible if I did not have Brian Humm's timely assistance with his life-long expertise in setting up optical instruments and experiment apparatus. I am also grateful to David Mill for the help and advice, as a professional programmer, on data analysis that played an important role in completing PASS.EXE.

I thank sincerely Lee Hubbard for his technical supports in use of LaTeXand for detailed commenting upon much of the manuscript. I am also indebted to Dr. Adrian Fish for his kind help and advice in using STARLINK facilities. I am very grateful to Young-Soo Kim for his warm company and informative discussions on optical testing for the scaled Gemini secondary mirror. Bruce Bigelow's deep knowledge on the ANSYS package was particularly helpful in processing ANSYS outputs. I also appreciate greatly the detailed comments he gave on the manuscript. I hope that Byung-Jin Kim and Eel Kim will accept my thanks for their company in OSL. I am

also grateful to Dr. Francisco Diego, Alan Radley, Dr. Richard Bingham, Martin Clayton for their companionship for those years in OSL.

Special thank must be given to Dr. Tu-Hwan Kim, a former director general of ISSA (currently KAO), who initiated the ambitious project, in which I began to study in OSL, UCL, as a part. My deep gratitude goes to Dr. Wonyoung Han for his friendship and collaboration that enable us to sail the same boat through all those difficulties and finally to reach the safe and fruitful destination after 5 years or so. Special thanks should go to Drs. M.S. Chun, I.-S. Nha, S.H. Moon and H.S. Park for their concern and share of the feeling. I certainly owe much to Dr. John Parkinson's encouragement and effort to maintain an intergovernmental fund package between Korea and UK that generated some portions of the resources we needed. I must acknowledge the indebtedness to the programme officers of the British Council in Seoul and London for their effort to continue the financial support that was very helpful from July 1988 to early 1992. I also appreciate some portion of the financial support for the 1989/1990 academic year from the UCL Bursary. Some others parts of the resources for my study came from the ORS Award, ISSA and MOST(Korea) this I appreciate specially. The project, itself, was supported by SERC, this being the reason of special gratefulness to those who were involved in granting the resource to it.

I am specially thankful to those who gave helpful comments on the manuscript; Dr. D. Walker, Lee Hubbard, Bruce Bigelow, Gil Nixon, David Rees, Dr. Adrian Fish.

I want to thank all the servants of God I have met. They have given me so much help, making it possible to keep peace in spirit during the years. I also would like to thank Albert and Esther's family for friendship and hospitality. Finally, I must thank Mrs. S. Loizou and her family for their hospitality and company that helped me greatly to settle down well in the first year of my life in London.

Bibliography

[1] Ahmed, W. U., (1984), Effects of Various Polishing Conditions on The Surface Finish of Materials, *Techanical Digest: Topical Meeting on The Science of Polishing*, Optical Society of America, Vol. **84.3**, pp Tub-B3-1-4.

[2] Bailey & Mackey Ltd., (1990), *Pressure Transducer Catalogue*, Bailey & Mackey Ltd, Baltimore Road, Birmingham B42 1DE (Tel. 021-357 5351).

[3] Becker, J. M. and Tarenghi, M., (1992), ESO VLT Program Status Report, *Proceedings of ESO Conference on Progress in Telescope and Instrumentation technologies*, Ed. M.-H. Ulrich, ESO, Garching, pp 13-24.

[4] Beckstette, K., Küchel, M., Heynacher, E., (1989), Large Mirror Figuring and Testing, *Astrophysics and Space Science*, Vol. **160**, pp 207-214.

[5] Bevington, R.P., (1969), Propagation of Errors, *Data Reduction and Error Analysis for The Physical Science*, McGraw-Hill Book Company, New York, pp 56-65.

[6] Bingham, R.G., Walker, D.D. and Diego, F., (1990), Technology for Eight-Metre Primary Mirror, SPIE Vol. **1236**, Part **2**, pp 586-596.

[7] Bingham, R.G., (1990), *Written Communication* on Specification of the scaled Gemini secondary.

[8] Brooks, D., (1991), *Verbal Communication* on Laser Diffusing Materials.

[9] Brooks, D., (1992), *Verbal Communication* on Mark 1 Profilometer.

[10] Brooks, D., (1992), *Verbal Communication* on Work Comparision between the f/3 concave sphere and the scaled f/7 Gemini secondary.

[11] Brooks, D., (1992). *Verbal Communication* on The Link between The Push-Pull Arms and The Reaction Plate of The 85 cm Scaled Full Size Active Lap.

[12] Brooks, D., (1992). *Verbal Communication* on The 85 cm Scaled Full Size Active Lap.

[13] Brown, N. J., (1991), *Verbal Communication* on Ablation Rate Coefficient and Glass Polishing.

[14] Brown, N. J. and Cook, L. M., (1984), The Role of Abrasion in The Optical Polishing of Metals and Glass, *Techanical Digest: Topical Meeting on The Science of Polishing*, Vol. **84.3**, Optical Society of America, pp TuB-A3-1-3.

[15] Burch, J. M., (1953), Scatter Fringes of Equal Thickness, *Nature*, Vol. **171**, pp 889-890.

[16] Burge, J. H., (1992). Design and Analysis of Null Test Optics for Large Aspheric Mirrors, *Proceedings of ESO Conference on Progress in Telescope and Instrumentation technologies*, Ed. M.-H. Ulrich, ESO, Garching, pp 273-276.

[17] Burleigh Instruments, Inc., (1992), *PZT Aligner/ Translator Technical Memo*, Burleigh Instruments, Inc., Burleigh Park, Fisher, New York (Tel. 719-924-9355).

[18] Choi, M. J., (1993), *Verbal Communication* on Cavity Theory of Ultrasonic Wave Propagation.

[19] Cornish, D. C., (1961), *The Mechanism of Glass Polishing - A History and Bibliography*, B.S.I.R.A Research Report **R 267**, pp 1-70.

[20] Control Transducers, (1990), *Load Cell Catalogue*, Control Transducers, 25 Kimbolton Road, Bedford MK40 2NY (Tel. 0234-217-704/5/6)

[21] Cullis, A.G., Webber, H.C. and Bailey, P., (1979), A device for Laser Beam Diffusion and Homogenisation, *J. Phys. E:Sci. Instrum.*, Vol. **12**, pp 688-689.

[22] Czichos, H., (1978), *Tribology*, Elsevier Scientific Publishing Company, Amsterdam, pp 112-118.

[23] Data Translation Ltd., (1988), DT-2851 Frame Grabber. *1988 Image Processing Catalogue*, Data Translation Ltd., The Mulberry Business Park, Wokingham, Berkshire RG11 2OL (Tel. 0734-793-838), pp 2-23.

[24] Davis, R. L. and Raybould, K., (1990), Technical Description of The UK Large Telescope, *Advanced Technology Optical Telescopes IV*, Ed. Barr, L. D., SPIE Vol.**1236**, Part **1**, pp 26-41.

[25] De Witte, A. J., (1967), Interference in Scattered Light, *Am. J. Physics.*, Vol. **35**, p 301-313.

[26] 3D Digital Design and Development Ltd., (1988), *Technical Documentations for the 3D C6 and 3D C3 cards*, 3D Digital Design and Development Ltd., Interface House, Chelmsford Road, Southgate, London N14 4JN (Tel. 081-886-3668).

[27] 3D Digital Design and Development Ltd., (1991), *Technical Documentations for the LVDT*, 3D Digital Design and Development Ltd., Interface House, Chelmsford Road, Southgate, London N14 4JN (Tel. 081-886-3668).

[28] Digitron Instrumentation Ltd., (1990), *Pressure Transducer Catalogue*, Digitron Instrumentation Ltd., Mead Lane, Hertford, Herts SG13 7AW (Tel. 0992-587-441).

[29] Dressler, A., (1990), Progress Report on The Magellan 8-m Telescope Project, *Advanced Technology Optical Telescopes IV*, Ed. Barr, L. D., SPIE Vol. **1236**, Part **1**, pp 42-46.

[30] EEV, (1988), EEV P4314 CCD camera, *EEV Product Catalogue.* EEV, Waterhouse Lane, Chelmsford, Essex CM1 2QU (Tel. 0245-493-493).

[31] Enard, D., (1992), ESO VLT: A Status Report on Telescopes and Enclosures, *Proceedings of ESO Conference on Progress in Telescope and Instrumentation technologies*, Ed. M.-H. Ulrich, ESO, Garching, pp 25-34.

[32] Entran Ltd., (1990), *Verbal Communication*, Entran Ltd., 5 Albert Road, Crowthorne, Berks (Tel. 0344-778-848).

[33] Entran Ltd., (1990), *Loadcell Catalogue*, Entran Ltd., 5 Albert Road, Crowthorne, Berks (Tel. 0344-778-848).

[34] Entran Ltd., (1990), *Pressure Transducer Catalogue*, Entran Ltd., 5 Albert Road, Crowthorne, Berks (Tel. 0344-778-848).

[35] Entran Ltd., (1990), *Entran Gauging Instructions*, Entran Ltd., 5 Albert Road, Crowthorne, Berks (Tel. 0344-778-848).

[36] Entran Ltd., (1990), *Loadcell Instruction and Selection Manual*, Entran Ltd., 5 Albert Road, Crowthorne, Berks (Tel. 0344-778-848).

[37] Entran Ltd., (1990), *Pressure Transducer Instruction and Selection Manual*, Entran Ltd., 5 Albert Road, Crowthorne, Berks (Tel. 0344-778-848).

[38] Espiard, J., (1992), The Role Played by REOSC in the VLT programme, *Proceedings of ESO Conference on Progress in Telescope and Instrumentation technologies*, Ed. M.-H. Ulrich, ESO, Garching, pp 179-194.

[39] EuroSensor, (1990), *Pressure Sensor Catalogue*, Micro Pneumatic Logic, Inc., 20-24 Kirby Street, London SC1N 8TS (Tel. 071-405-6060).

[40] Farnell Electronic Components Ltd., (1985), *Technical note of the SX series pressure transducers*, Farnell Technical Data Service, Canal Road, Leeds LS12 2TU (Tel. 0532-310-160).

[41] Fish, A., (1990), *Verbal Communication* on DT-2851 Frame Grabber Input Bias Control.

[42] Flight Electronics Ltd., (1991), *FPC-023-8 Bit Digital/Analogue Card Manual*, Flight Electronics Ltd., Flight House, Ascupart Street, Southampton SO1 1LU (Tel. 0703-227-721).

[43] Geetron Systems Ltd., (1988), *Short Form Documentations for the Geetron System 83 encoder*, Geetron Systems Ltd., Carlton Road, Felmersham, Bedford MK43 7JL (Tel. 0234-720-977).

[44] Grassman, M., (1988), Deformable materials, *Tactile Sensors for Robotics and Medicine*, Ed. Webster, J. G., John Wiley and Sons, Inc., New York, pp 57-73.

[45] Hagner, D., (1988), Metal Strain Gages, *Tactile Sensors for Robotics and Medicine*, Ed. Webster, J. G., John Wiley and Sons, Inc., New York, pp 75-99.

[46] Hahm, G., (1988), Semiconductor Strain Gages, *Tactile Sensors for Robotics and Medicine*, Ed. Webster, J. G., John Wiley and Sons, Inc., New York, pp 101-124.

[47] Han, W-Y., (1993), New Developments for Mosaic CCDs, PhD Thesis, University of London.

[48] Harmer, C., Poczulp, G., and Stepp, L., (1989), *The 3.5 m Mirror Project Technology Development Programme Report No. 1*, NOAO, Tucson, Arizona.

[49] Hecht, E., (1987), *Optics*, 2nd Edtn., Addison-Wesley Publishing Company, Inc., Reading, Massachusetts.

[50] Herbert Terry and Sons Ltd., (1991), *SPEC-Stock Springs and Spring Washers*, Herbert Terry and Sons Ltd, Millsbro Road, Redditch, B98 7BU (Tel. 0386-833-377).

[51] Hiltner, W. A. and Shectman, S. A., (1989), Progress of The Magellan Project, *Astrophysics and Space Science*, Vol. **160**, pp 103-105.

[52] Holland, L. (1966). *The properties of glass surfaces*, Chapman and Hall, London.

[53] Hordeski, M. F., (1987), *Transducers for Automations*, Van Nostrand Reinhold Company, Inc. NewYork.

[54] Horne, D. F., (1972), *Optical Production Technology*, Adam Hilger, London.

[55] Hubbard, L., (1993), *Verbal Communication* on The OSL Mark 2 Profilometer.

[56] Humm, B., (1992), *Verbal Communication* on LVDT Probe Thermal Controller.

[57] Imaging Technology, Inc., (1990), **PC-VISION** *plus Hardware Reference Manual*, Document No. **47-h00010-03**, Imaging Technology, Inc., 600 West Cummings Park, Woburn, Massachusetts.

[58] Izumitani, T., (1984), Polishing Mechanism of Fused Silica Glass, *Technical Digest: Topical Meeting on The Science of Polishing*, Vol. **84.3**, Optical Society of America, pp Tub-A1-1-3.

[59] Jamshidi, H. O., (1992), *Verbal Communication* on an external Amp circuit for input bias ajustment for the PC-VISION frame grabber.

[60] Jamshidi, H. O., (1992), *Verbal Communication* on Digital Infrared Communication.

[61] Jamshidi, H. O., (1992), *Verbal Communication* on Low Level Software for Active Lap Control System.

[62] Jones, A. R. and Rupp, J. W., (1991), Rapid Optical Fabrication with Computer-Controlled Optical Surfacing, *Optical Engineering*, Vol. **30. No.12.** pp 1962-1967

[63] Jones, C. M., (1991), A Comparison Study of Actuator Designs for an Instrumented Mirror Polishing Lap, *OSL Project Report*, Department of Physics and Astronomy, University College London.

[64] Kim, Y. S., (1992), *Verbal communication* on Computerized knife edge testing.

[65] Kistler Instruments Ltd., (1990), *Catalogue for Loadcells and Pressure Transducers.* Kistler Instrument Ltd., Whiteoaks, The Grove, Hartley Wintney, Hants RG27 8RN (Tel. 025-284-3555).

[66] Korhonen, T. and Lappalainen, T., (1990), Computer-controlled Figuring and Testing, SPIE Vol. **1236**, Part **2**, pp 691-695.

[67] Kodaira, K., (1989), Outline of The JNLT Project, *Astrophysics and Space Science*, Vol. **160**. pp 137-144.

[68] LEX Ltd., (1992), *Verbal Communication* on Remote Digital Communication Link, LEX c/o Leadtrack Services, 595 Colonial Park Drive, Suite 302, Roswell, Georgia 30075-990, USA

[69] Lindsey, K., (1991), Tetraform Grinding, *NPL Technical Documentation 1001-119*, National Physical Laboratory, Teddington, England.

[70] Lindsey, K., (1992), *Verbal Communication* on Physics of Glass Polishing, National Physical Laboratory, Teddington, England.

[71] Martin, H. M., Anderson, D. S., Angel, J. R. P., Nagel, R.H. and West, S.C., (1990), Progress in The Stressed Lap Polishing of A 1.8 m f/1 Mirror, SPIE Vol. **1236** Part **2**, pp 682-690.

[72] Martin, H. M., Anderson, D. S., Angel, J. R. P., Burge, J. H., Davison, W. B., DeRegine, S. T., Hille, B. B., Ketelsen, D. A., Kittrell, W. C., McMillan, R., Nagel, R. H., Trebisky, T. J., West, S. C. and Young, R. S., (1992), Stress Lap Polishing of 1.8-m f/1 and 3.5-m f/1.5 primary mirrors, *Proceedings of ESO Conference on Progress in Telescope and Instrumentation technologies*, Ed. M.-H. Ulrich, ESO, Garching, pp 169-172.

[73] Mast, T.S. and Nelson, J.E., (1990), Fabrication of Large Optical Surfaces Using A Combination of Polishing and Mirror Bending. SPIE Vol. **1236** Part **2**, pp 670-681.

[74] Microsoft, (1990), *Microsoft Windows 3.0 user manual*, Microsoft, New York, p 485.

[75] Mills, D., (1991), *Written Communication* on Polynomial Fitting for The Calibration Data of The OSL Mark 1 Profilometer.

[76] Mohan, B., (1993), *Some Electrical and Mechanical Aspects of Measuring The Surface Profile and Roughtness of Large Optics*, MSc Thesis, School of Industries and Manufacturing Science, Cranfield University.

[77] Nelson, J. E. and Mast, T. S., (1992), Current Performance of The Keck Telescope, *Proceedings of ESO Conference on Progress in Telescope and Instrumentation technologies*, Ed. M.-H. Ulrich, ESO, Garching, pp 3-11.

[78] Nelson, J.E., Mast, T.S. and Faber, S.M., (1985), *Keck Obs. Report*, No. **90**, Keck Astronomical Observatory, P.O. Box 220, 65-1120 Mamalahoa Hwy., Kamuela, Hawai 96743 (Tel. 808-885-7887).

[79] Nixon, G., (1992), *Verbal Communication* on The Active Lap Control System.

[80] Oertel, G. K. H., (1989), The NOAO 8-m Telescopes; I Executive Summary and Scientific Programs, *AURA's Proposal to The NSF in USA*, pp 1-21.

[81] Osmer, P. S., (1990), NOAO 8-m Telescope Project, *Advanced Technology Optical Telescopes IV*, Ed. Barr, L. D., SPIE Vol. **1236**, Part **1**, pp 18-25.

[82] Osmer, P. S., (1992), Gemini Science Requirements Version 1.1, Gemini Telescope Project Office, Tucson, Arizona, pp 2-18.

[83] Osmer, P. S., (1992), The Gemini Project: Overview, *Proceedings of ESO Conference on Progress in Telescope and Instrumentation technologies*, Ed. M.-H. Ulrich, ESO, Garching, pp 35-37.

[84] Parker Digiplan Ltd., (1990), A/AX 57-55R Micro-Stepping Actuator, *Programmable Motion Control*, Parker Digiplan Ltd., 21 Balena Close, Poole, Dorset BH17 7DX (Tel. 0202-690-911).

[85] Parker Digiplan Ltd., (1990). *Digiplan Motion Control Handbook.* Parker Digiplan, Ltd., 21 Balena Close, Poole, Dorset BH17 7DX (Tel. 0202-690-911), p 79.

[86] Pierson, J. G., (1984), *Temperature Effects and Passive Compensation Techniques of Piezoresistive Semiconductor Strain Gage Installation*, Entran Device, Inc., 5 Albert Road, Crowthorne, Berks (Tel. 0344-778-848).

[87] Pioden Control Ltd., (1990). *Load Transducer Catalogue.* PIODEN Controls, Ltd., Graham Bell House, Roper Close, Roper Road, Canterbury, Kent CT2 7EP (Tel. 0227-463-641).

[88] Press, W. H., Flannery, B. P., Teukolsky, S. A. and Vettering, W.T., (1988), *Numerical Recipes: The Art of Scientific Computing*, Cambridge University Press, Cambridge, England.

[89] Rees, D., (1993), *Verbal Communication* on The Active Lap Control Software and Its Performance.

[90] Randall, L. K., (1992), The Gemini 8-m Telescopes Project: Current Activities, *Proceedings of ESO Conference on Progress in Telescope and Instrumentation technologies*, Ed. M.-H. Ulrich, ESO, Garching, pp 39-42.

[91] RS Components, (1990), RS stock 632-123 Strain Gauge, *RS Components Data Sheet E8155*, RS Components, PO Box 99, Corby, Northants NN17 9RS (Tel. 081-360-8600 for London).

[92] RS Components, (1990), OP-07 Operational Amplifier, *RS Components Data Sheet H/J16544*, RS Components, PO Box 99, Corby, Northants NN17 9RS (Tel. 081-360-8600 for London).

[93] RS Components, (1990), RS 322-098 Stepper Motor Controller, *RS Components Data Sheet B8199*, RS Components, PO Box 99, Corby, Northants NN17 9RS (Tel. 081-360-8600 for London).

[94] RS Components, (1990), MT78T12CT Fixed Voltage Regulator, *RS Components Data Sheet J6610*, RS Components, PO Box 99, Corby, Northants NN17 9RS (Tel. 081-360-8600 for London).

[95] Schlumberger Industeries, (1992), AG 2.5 LVDT, *Gauging Transducers Designer Handbook*, Schlumberger Industries Transducer Division, Steying Way, Southern Cross, Industrial Estate, Bognor Regis, West Sussex PO22 9ST (Tel. 0243-825-011), p G1.

[96] Scott, R. M., (1969), Scatter Plate Interferometry, *Applied Optics*, Vol. **8**, No. **3**, p 531-537.

[97] Shoemaker, A.H. and Murty, M.V.R.K., (1966), Some Further Aspects of Scatter Fringe Interferometry, *Applied Optics*, **Vol. 5, No. 4, p 603-607.**

[98] Silvernail, W. L., (1984), The Role of Cerium Oxide in Glass Polishing, *Techanical Digest: Topical Meeting on The Science of Polishing Vol.84.3*, Optical Society of America, pp Tub-B1-1-4.

[99] Sinnott, R. W., (1990), HST's Magnificent Optics ...What Went Wrong ?, *Sky & Telescope*, Vol. **80** No. **4**, pp 356-357.

[100] Smith, W. S., (1989), Large Mirror Polishing and Figuring, *Astrophysics and Space Science*, Vol. **160**, pp 215-219.

[101] SonceBoz UK Ltd., (1990), 7230B Linear Steppeing Actuator *SonceBoz Linear Actuator Catalogue*, SonceBoz UK Ltd., Victoria Road, Ruislip (Middx) HA4 0LL (Tel. 0211-453-474).

[102] Strittmatter, P. A., (1990), Columbus Project Telescope, *Advanced Technology Optical Telescopes IV*, Ed. Barr, L. D., SPIE Vol. **1236**, Part **1**, pp 71-85.

[103] Superior Electric Company, (1988), *Techanical Documentation for The SLO-SYN 3180-PTO Stepper Motor and Driver*, Superior Electric Company, 383 Middle Street, Bristol, Conneticut 06010 (Tel: 203-582-9561).

[104] Techni Measure, (1990), *Catalogue TLM PAM E-101 Z*, Techni Measure, Alexandra Building, 59 Alcester Road, Studley, Warwickshire B80 7NJ (Tel. 0527-854-103).

[105] Techni Measure, (1990), *PCB product catalogue*, Techni Measure, Alexandra Building, 59 Alcester Road, Studley, Warwickshire B80 7NJ (Tel. 0527-854-103).

[106] Texereau,J., (1957), *How to Make A Telescope*, Interscience Publishers, Inc., New York, pp 17-101.

[107] Open University, (1986), Measurement of Strain, *Instrumentation: Block 1.*, Ed. Loxton, R. and Pose, P., Open University Press, Milton Keynes. pp 44-85.

[108] TransInstruments, (1989), *TransInstruments Pressure Transducer Catalogue*, Hawco House, Cathedral Hill Industrial Estate, Guildford, Surrey GU2 5YB (Tel. 0483-606-06).

[109] Tyson, J. A., (1984), *P.A.S.P.*, Vol. **96**, pp 566-573.

[110] Walker, D.D., (1989), *Written Communication* on Specification for The Profile Generation Software.

[111] Walker, D.D., (1989), New Developments in Producing Astronomical Optics, *SERC Grant Proposal.*

[112] Walker, D.D., (1990), New Developments in Producing Astronomical Optics: Appendix, *SERC Grant Proposal.*

[113] Walker, D.D., (1992), *Verbal Communication* with NOAO about ablation rate.

[114] Walker, D.D., Brooks, D. and Jamshidi, H.O., (1992), *Verbal Communication* on The OSL Mark 2 Profilometer.

[115] Welwyn Strain Measurement, (1990), M-Line Strain Gauge Accessories, *M-M Catalogue A-110-4*, Welwyn Strain Measurement, Stroudley Road, Baingstoke, Hants RG24 0FW (Tel. 0265-462-131).

[116] Welwyn strain Measurement, (1990), EA-XX-125AD Strain Gauge, *Bulletin SFC-800-1*, Welwyn Strain Measurement, Stroudley Road, Basingstoke, Hants RG24 0FW (Tel. 0265-462-131).

[117] Wilson, J. T., (1991), Meeting New Challenges in Large-Optics Fabrication, *Photonics Spectra.* Vol. **25**, Issue **12**, pp 93-96.

[118] Wyant, J.C., (1991), *Scatter Plate Interferometer*, WYKO Corporation, 2650 E. Elvira Road, Tucson, Arizona 85706 (Tel. 602-741-1044).

[119] WYKO Corporation, (1991), *WYKO DOS/RTI Software Manual*, WYKO Corporation, 2650 E. Elvira Road, Tucson, Arizona 85706 (Tel. 602-741-1044).

[120] Zimmerman, J., (1990), Computer Controlled Optical Surfacing for Off-Axis Aspheric Mirror, SPIE Vol. **1236** Part **2**, pp 663-668.

Appendix A

Publications

A.1 ESO Conference Proceedings in 1992

THE PRODUCTION OF HIGHLY ASPHERIC SECONDARY MIRRORS
USING ACTIVE LAPS

D.D. Walker[1], R.G. Bingham[1,2], D. Brooks[1], F. Diego[1], B. Humm[1],
H. Jamshidi[1], S-W Kim[1], Y-S Kim[1], G. Nixon[1], D. Rees[1]
[1] University College London, [2] Royal Greenwich Observatory

1. INTRODUCTION

All eight-metre telescopes are being designed with fast primary mirrors. The aim is to reduce costs, a shorter tube leading to a smaller enclosure, higher stiffness and also a slightly smaller secondary mirror. However, the secondary mirror is then much more aspheric! The imaging performance now demanded compounds the problem of producing such mirrors. Success will demand advances in both figuring and testing. This paper summarises such research at the Optical Science Laboratory (OSL) of UCL.

We have taken the f/7 (nominal — recently changed to f/6) wide-field convex secondaries of the GEMINI eight-metre telescopes as a case for demonstration. Their diameter at f/7 is 2.13m, and the departure from the sphere which osculates at the vertex is about 2100 fringes (waves in reflection) at 500nm. We are producing an exactly-scaled prototype mirror of 85cm diameter using our new technique, which employs a full-size, active polishing lap.

2. CONTROL OF FIGURING

The special problems in figuring highly-aspheric surfaces are: i) preventing the surface from lapsing towards a sphere or toroid ii) avoiding "orange peel" or other small-scale ripples iii) measuring the result. The principal variables available in production are i) the pressure distribution exerted by the lap on the mirror, ii) the distribution of speed of the moving lap in relation to the mirror (stroke, rotation), and iii) the pattern of pitch on the lap. Of these, the first two are the most suitable for active control.

Our approach differs from others, first in using a full-size lap. We believe it has several advantages. For example, it tends to eliminate those types of error which have no circular symmetry. (It is possible to violate this constraint with our active lap, but under control.) In addition, a full sized lap gives the fastest overall polishing-rate for a given pressure, using a machine of the necessary power. Alternatively, much lower polishing pressures can be used than with a small lap, for the same polishing-rate. This could substantially reduce quilting with honeycomb substrates.

The natural smoothing action of the stroke minimises high-frequency defects at source. Martin et al.[1] use a sub-diameter lap whose *shape* is actively controlled so that throughout its wide

sweeping motion over the mirror, the lap profile conforms to the local target profile of the mirror surface. In our case, the aspheric profile is mainly accommodated by the natural flexibility of the lap which is used over smaller but significant strokes. This approach bears some resemblance to more traditional methods including the full-size and flexible petal-lap used during the figuring of the Keck secondary[2].

The most sophisticated part of our approach is the control of local figuring. This is achieved under computer control by modulating the *pressure* distribution in real-time using force actuators which are mounted within the mechanical structure of the lap. The true forces are monitored continuously by means of load cells.

A particular advance relates to superseding the classical open-loop nature of optical figuring. Historically, there has been no process-control feedback to the operator *while the machine is running*. Now we telemeter i) the pressure distribution, ii) the relative velocity distribution between lap and mirror and iii) the total lateral frictional force on the lap. To calibrate the telemetered data in useful terms, we undertook separate experiments to determine the ablation rates for different polishing variables. Those results enable us to interpret the telemetred forces and speeds in terms of the instantaneous ablation rate, which can be repeatedly calculated at each point on the mirror surface during polishing. The computed rates are numerically integrated in order to estimate, in real time, how the mirror profile is evolving. This is displayed, and the load pattern may be changed accordingly. At the end of each run, not only is the optical figure compared to that desired, but the predicted change is compared to the observed change. As the algorithm is also refined, so the system "learns".

3. CONSTRUCTION OF THE ACTIVE LAP

An exploded view of the 85cm prototype lap is shown in Figure 1, and a photograph of the OSL 1m polishing machine in Figure 2. The pitch is attached to a thin shell of carbon-fibre reinforced epoxy which was cast using the generated mirror as a mould. A grid of small square wedges of epoxy resin, cast on the upper side of the shell, matches the curve of the pitch to a plane interface with the active mechanism of the lap. The heart of the lap comprises two circular metal plates which are bolted together through a central spacer. The actuators are linear motors, attached to the upper 'reaction' plate and exerting variable forces via springs on the lower 'flex' plate. 65 load-cell flexures, each with a hexagonal load spreader, are attached to the lower side of the flex plate and bear directly onto the epoxy wedges. Of the 65, 22 are populated with strain gauges, and provide 88 load measurements.

The actuators provide differential control of the pressure distribution exerted on the mirror. A ring on the upper side of the lap is constrained so that it does not rotate with the lap. It

provides essential further live control, via three 'global force actuators' attached to the rigid test tower. They pull on the ring to vary the absolute overall polishing pressure, and to tilt the pressure distribution across the mirror. Thus although there is movement, the whole system is designed to modulate the *pressure* distribution, not to *distort* the flex plate.

Electronics for load cell digitisation, motor drivers and power conditioning are located on board the free-running lap, together with a single-board i960 computer. It is capable of sustained execution of 7.5 MIPs, and a burst rate of 20 MIPs, and also communicates with a host 386-PC in the laboratory. An infra-red data link is embedded within the central boss, through which the lap is pushed and pulled via the drive arms of the polishing machine. The central boss also houses slip-rings for power and an encoder for lap rotation.

The users' interface includes real-time maps of pressure, velocity and the computed glass removal. The maps are displayed, in colour, in fixed coordinates relating to the workpiece. The lap, the mechanical system, the load cells, electronics and software were all designed in house for this task.

At the date of the conference, the 85cm prototype mirror in Cervit had been generated with a diamond abrasive wheel on the OSL 2.7m machine, achieving an hyperboloid within $\pm 20\mu$m peak-to-valley. Experimental grinding with loose abrasives and tiles using the active lap had started.

4. TESTING

We propose to use two main testing methods. The first is contact profilometry, and developments are in progress in collaboration with 3D Digital Design and Development Ltd. The second is sub-aperture interferometry using a modified-Hindle null test as shown in **Figure 3.** We propose to use the 1.1m diameter lens we acquired from Grubb Parsons for testing the prototype, and the 1.5m lens for real secondary production. In both cases, we can cover about 65% of the mirror diameter at one time.

5. REFERENCES

1. 'Stressed lap polishing of 1.8m f/1 and 3.5m f/1.5 primary mirrors: H.M. Martin et. al.; in these proceedings.

2. 'Fabrication and testing of the Keck Telescope f/15 secondary mirror; J. Millar; in these proceedings.

FIG. 1 EXPLODED VIEW OF ACTIVE LAP

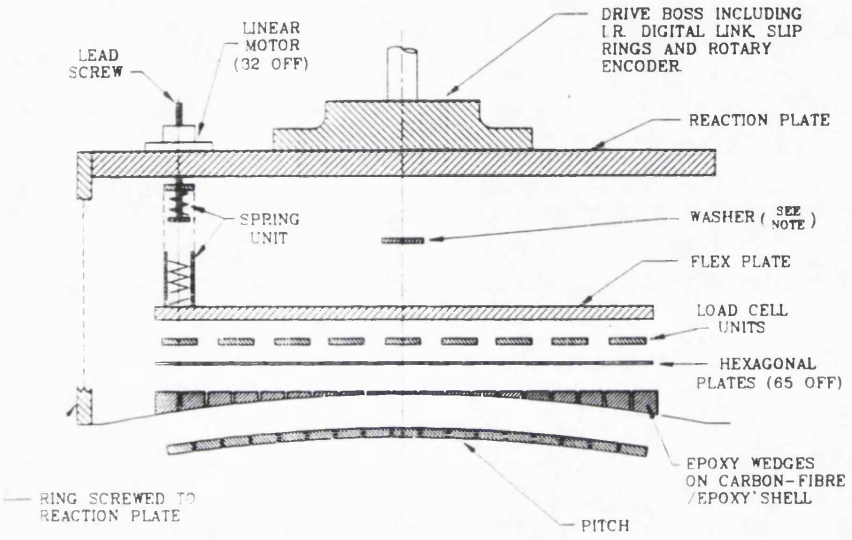

NOTE REACTION AND FLEX PLATES JOINED VIA WASHER

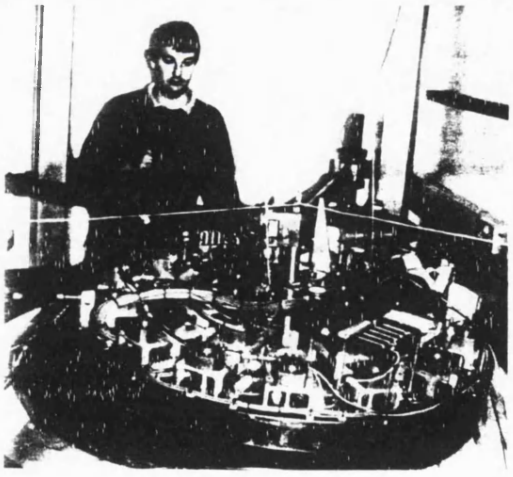

FIG 2 85 cm PROTOTYPE ACTIVE LAP

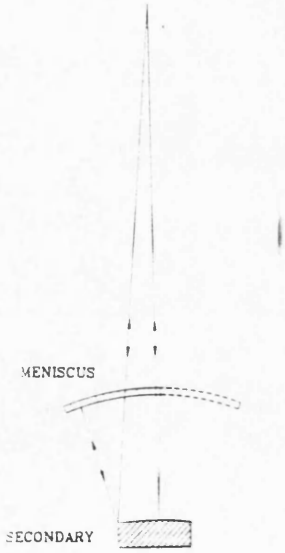

FIG. 3 MODIFIED SUB-APERTURE HINDLE TEST

Appendix B

Active Elements

B.1 FE Analysis for Various Web Models

The case equation of the plain guided web loaded at the guided end can be written as below.

$$Y = \frac{Wl^3}{Ebt^3} \tag{B.1}$$

$$S_x = \frac{3Wl}{bt^2} \tag{B.2}$$

$$\epsilon = \frac{3Wl}{Ebt^2} \tag{B.3}$$

where Y = Maximum deflection,

S_x = Fiber stress,

ϵ = Fiber strain,

W = Normal load,

l = length of web,

b = width of web,

t = thickness of web,

and E = Young's modulus of Stainless Steel = 215.3 GPa.

According to this, the web of l = 2.0 cm, b = 1.0 cm and t = 0.1 cm produces Y = 66.2 microns, $S_x = 1.07 \times 10^9 dyne/cm^2$ and ϵ = 496.5 microns at its ends. This web is clearly unacceptable due to its large compliance. On the other hand, the web of W = 4 lbf, l = 1.0 cm, b = 0.5 cm, t = 0.1 cm yields Y = 16.6 microns,

$S_x = 1.07 \times 10^9 dyne/cm^2$ and $\epsilon = 496.5$ microns at its ends. Comparing these to Table 4.1 can validate that the FE model with ANSYS 4.4 gives the correct answer. Table 4.1 includes, among numerous models analysed, the only 5 FE models, of which stress output of FE analysis are presented with the following color displays.

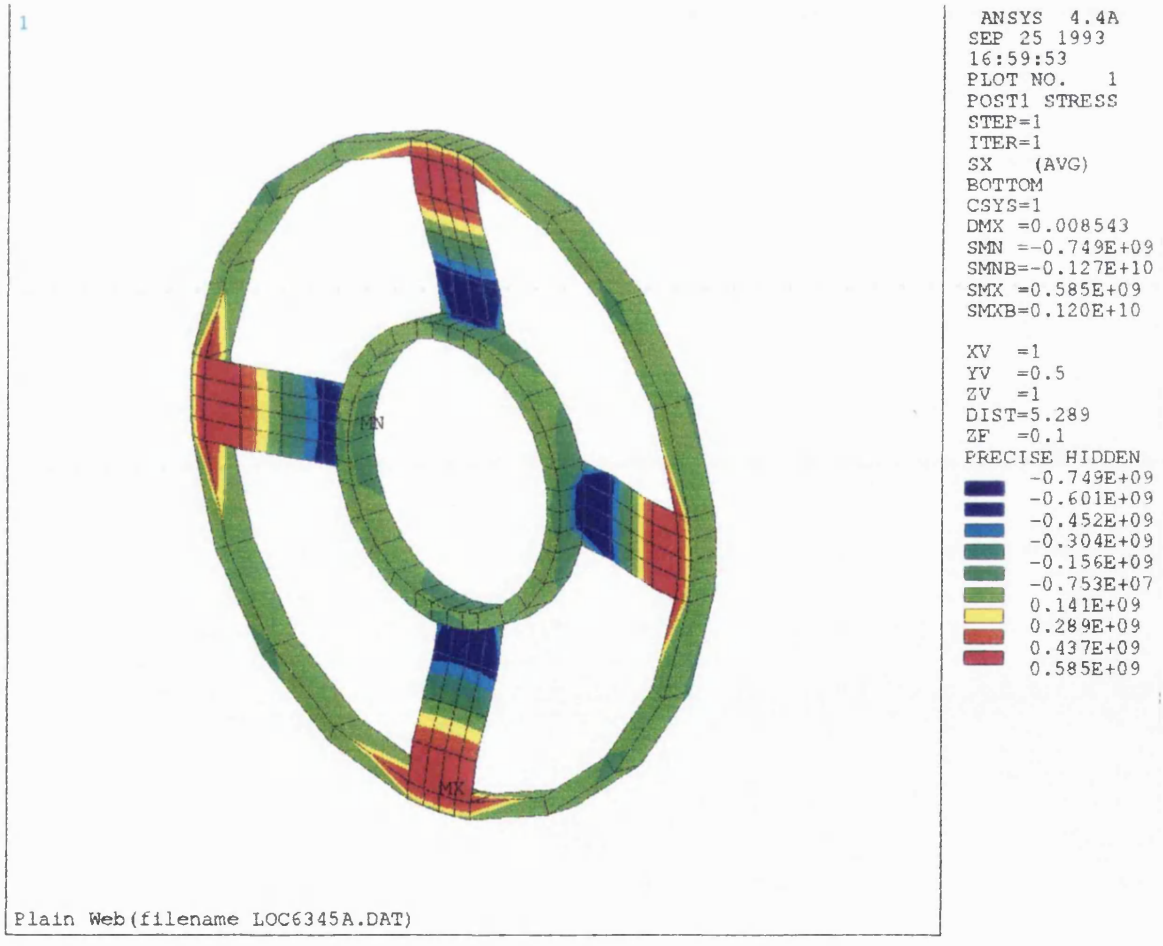

Figure B.1: Stress distribution of load cell with the web of $2cm \times 1cm \times 0.1cm$. data file LO6345A.DAT

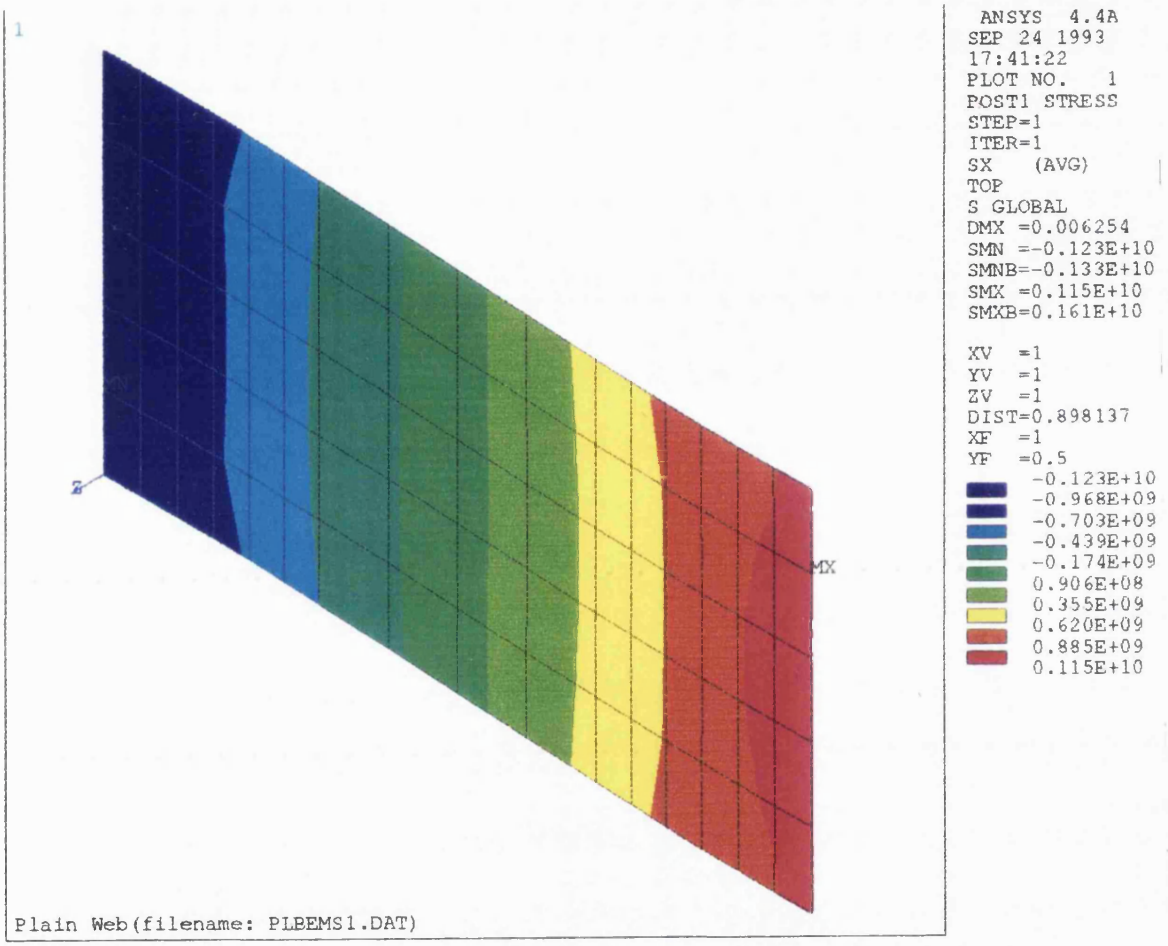

Figure B.2: Stress distribution of the web of $2cm \times 1cm \times 0.1cm$. Data file PLBMS1.DAT

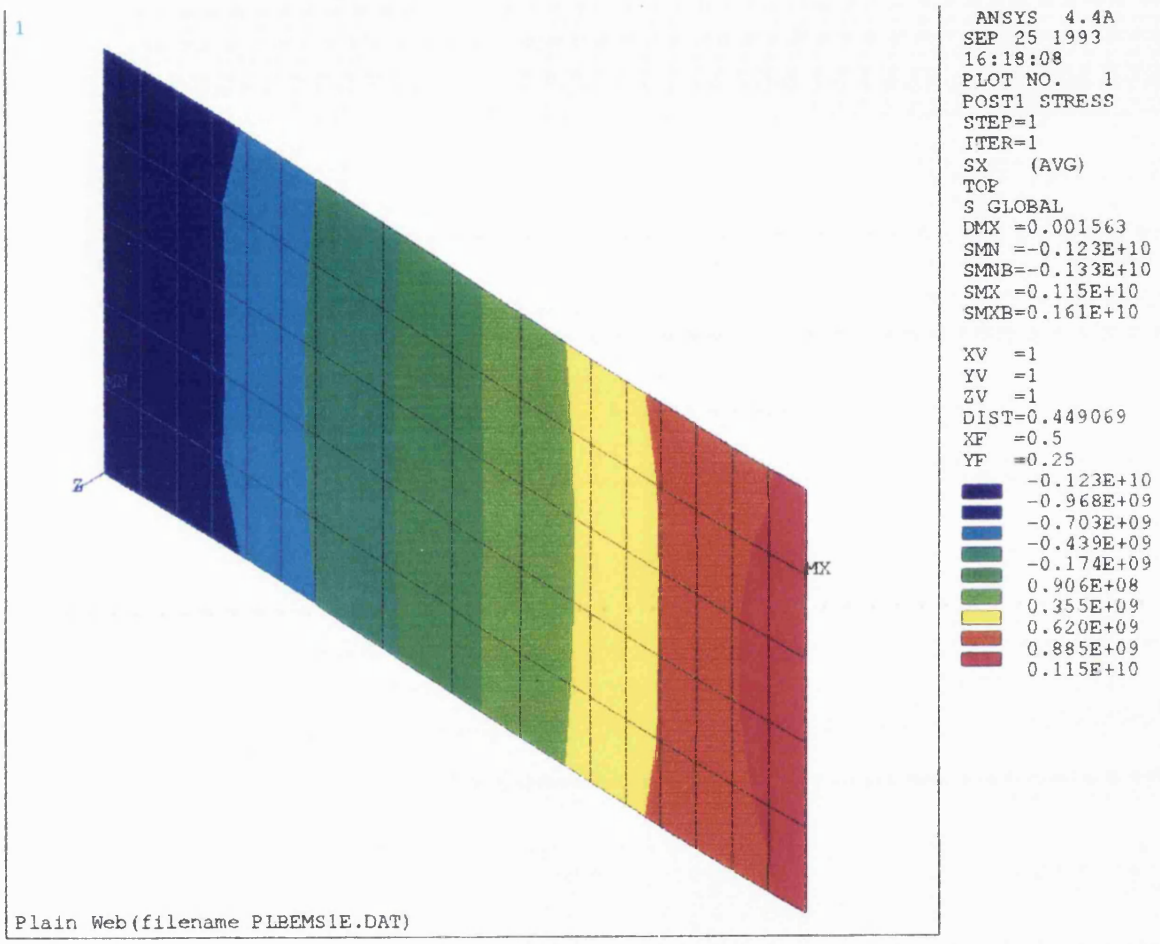

Figure B.3: Stress distribution of the web of $1cm \times 0.5cm \times 0.1cm$. Data file PLBMS2.DAT

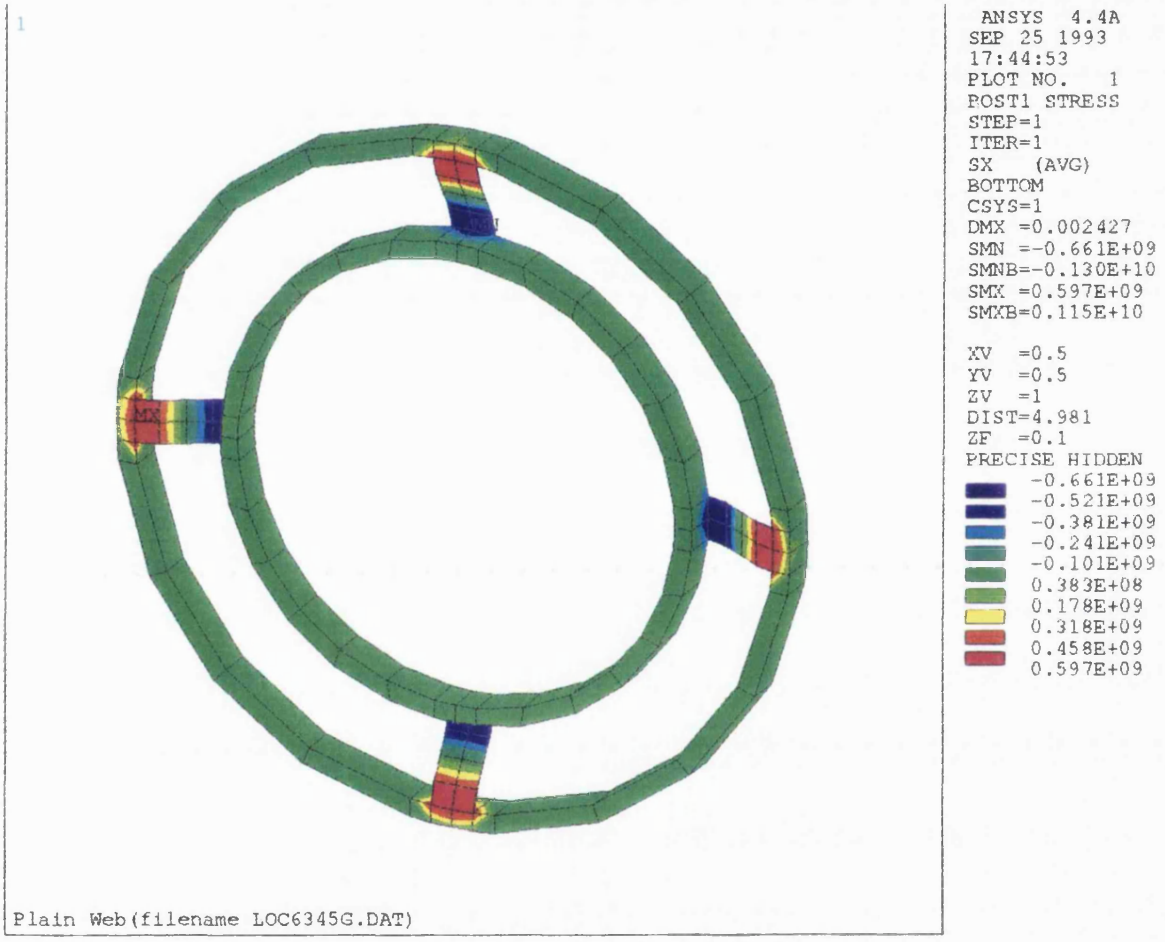

Figure B.4: Stress distribution of load cell with the web of $1cm \times 0.5cm \times 0.1cm$. Data file LO6345G.DAT

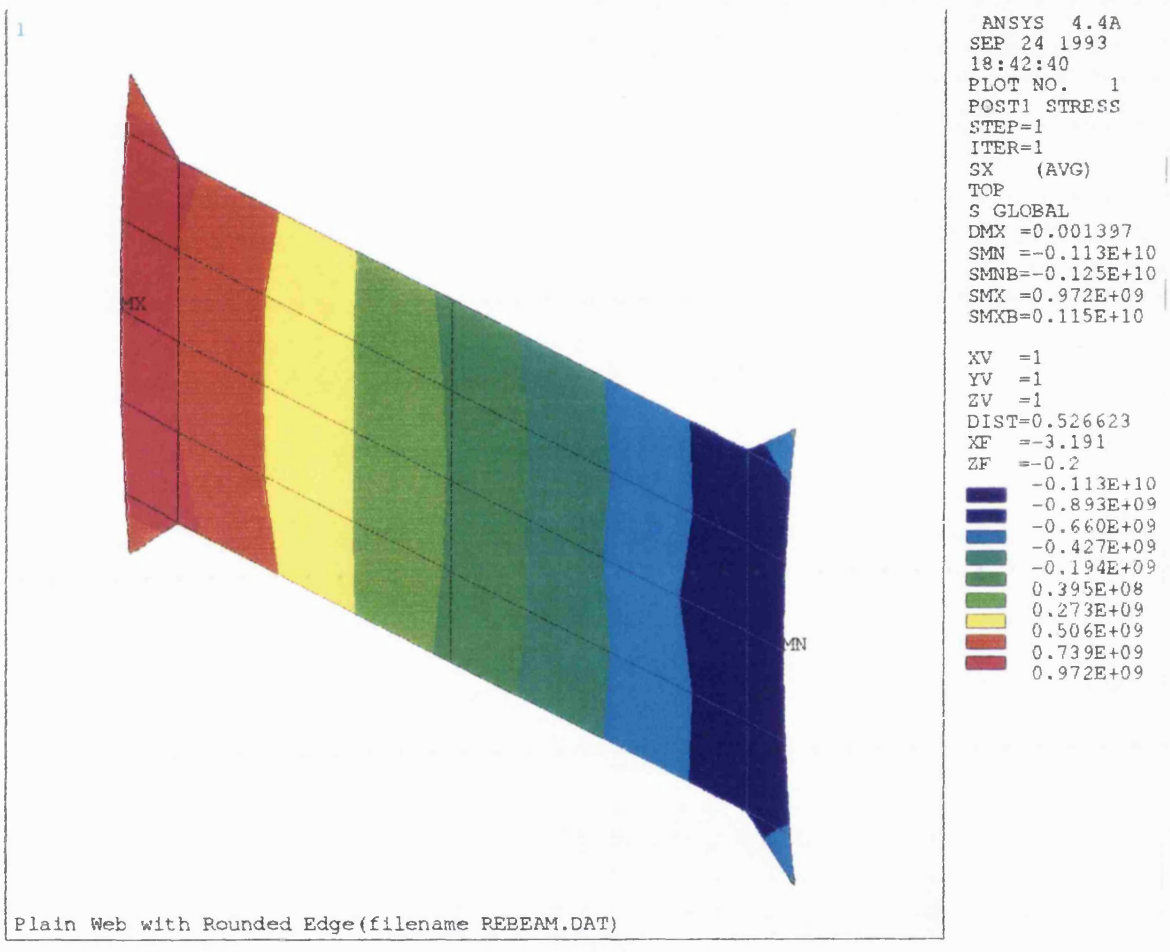

Figure B.5: Stress distribution of the rounded-edge web of $1cm \times 0.5cm \times 0.1cm$. The data file REBEM.DAT

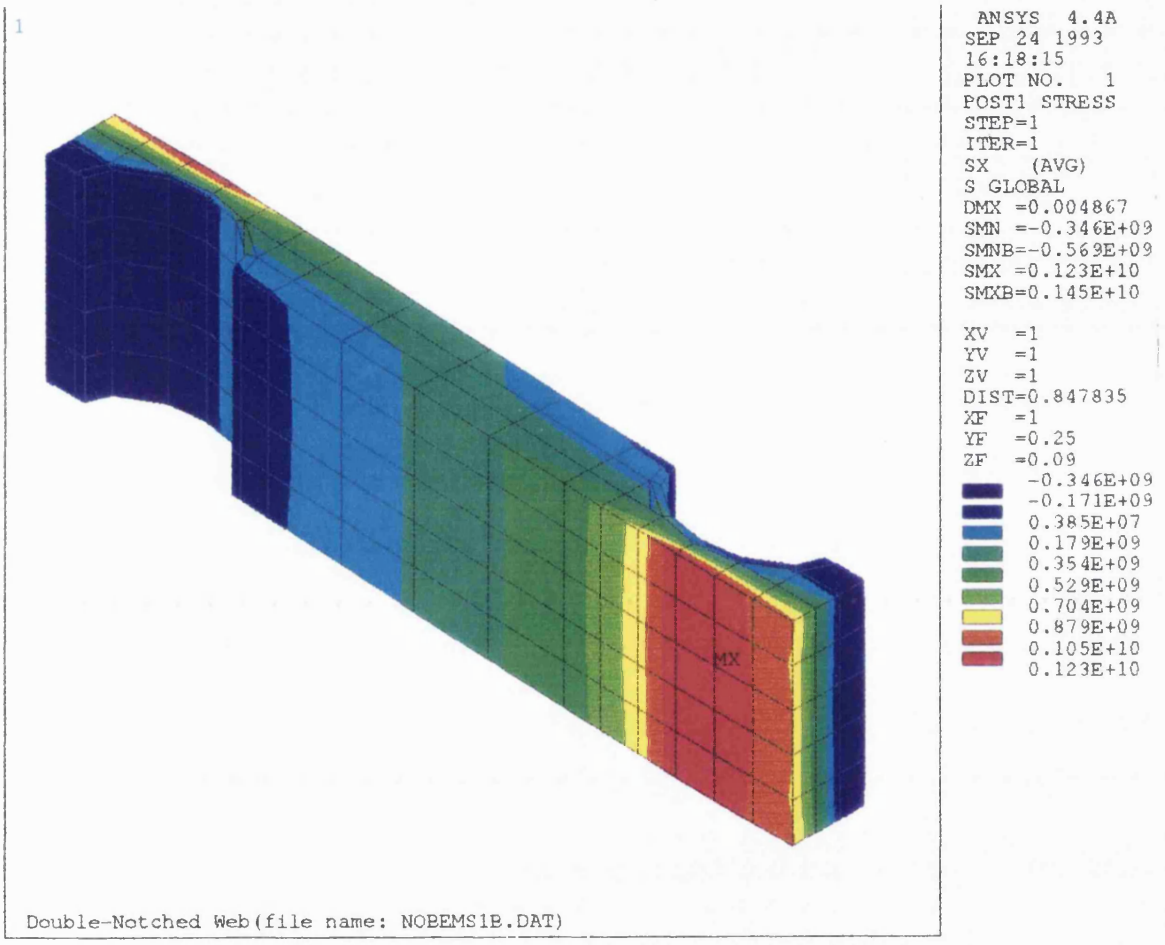

Figure B.6: The web is $2cm \times 0.5cm \times 0.18cm$. Data file NOCBEAM.DAT. The two semi-circle notches have the width of 4 mm and the depth of 1.2 mm. They have a fibre streess of 1.2×10^9 $dyne/cm^2$, giving a fibre strain of about 567 $\mu strain$ and a vertical deflection of 49 μm

B.2 Software Half Bridge

Figure B.7 shows two quarter bridges that can be used to form a software half bridge. Assuming no thermal effect i.e. T = 0, the compression and tension quarter bridges give the open circuit output voltage V_{oc} and V_{ot} respectably written as

$$V_{oc} = -\frac{1}{2}V_s x\frac{1}{2-x} \tag{B.4}$$

$$V_{ot} = \frac{1}{2}V_s x\frac{1}{2+x} \tag{B.5}$$

A half bridge open circuit output voltage can be emulated by subtracting V_{oc} from V_{ot} in the active lap control software.

$$V_o = V_{ot} - V_{oc} \tag{B.6}$$

Substituting the equation B.4 into the equation B.6 and re-arranging gives

$$V_o = \frac{1}{2}V_s x\frac{4}{4-x^2} \tag{B.7}$$

In the equation B.7, $\frac{4}{4-x^2} \approx 1$ since $x^2 \ll 1$. Thus the equation B.7 can be written as

$$V_o = \frac{1}{2}V_s x \tag{B.8}$$

This equation B.8 is identical to the open circuit output voltage of an actual half bridge.

Assuming existance of the thermal effect (i.e. $T \neq 0$), the open circuit output voltage V_{oc} and V_{ot} of the two quarter bridges are

$$V_{oc} = -\frac{1}{2}V_s\frac{x-T}{2-x+T} \tag{B.9}$$

$$V_{ot} = \frac{1}{2}V_s\frac{x+T}{2+x+T} \tag{B.10}$$

Subsituting the equation B.9 into the equation B.6 and re-arranging give

$$V_o = \frac{1}{2}V_s x\frac{4}{4+4T-x^2+T^2} \tag{B.11}$$

In the equation B.11, $x^2 \ll 1$ and $T^2 \ll 1$. Thus the equation B.11 can be written as

$$V_o = \frac{1}{2}V_s x\frac{4}{4+4T} \tag{B.12}$$

This equation B.12 serves as the open circuit output voltage of the software half bridge. It has an extra term of thermal effect when compared with the geneuin half bridge output voltage. If the temperatures of the strain gauge and of the surrounding material do not change significantly, then $T \ll 1$ and therefore $\frac{4}{4+4T} \approx 1$, leading to the geneuin half bridge output voltage $V_o = \frac{1}{2}V_s x$. However, as their change increase, $T \not\ll 1$ and $\frac{4}{4+4T} \not\approx 1$, deviating from the geneuin half bridge output voltage.

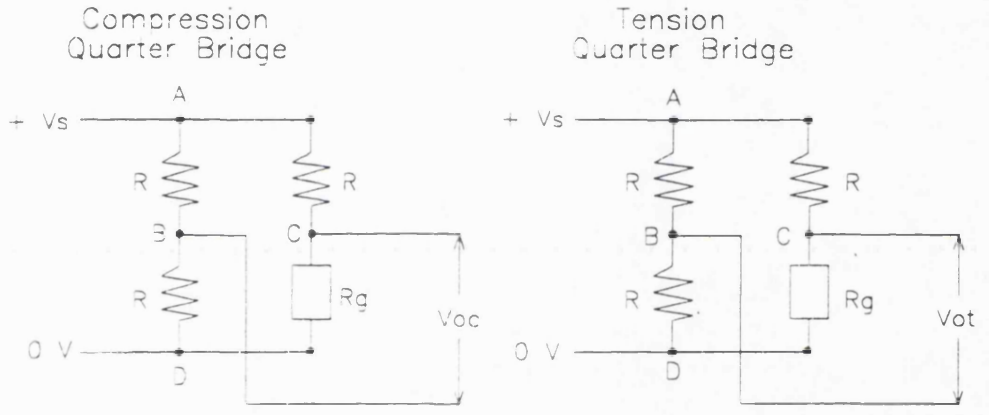

Note: R = Resistance of dummy resistors
Rg = Resistance of active gauge = R(1−x+T) for compression bridge
= R(1+x+T) for tension bridge
x = Fractional change in resistance of active gauge due to load
= Gauge Factor x Strain
T = Fractional change in resistance of active gauge due to temperature increase
Voc and Vot = Open circuit output voltage of compression and texsion briages

Figure B.7: Software half bridge consisted of two quarter briages

Appendix C

Calculation of Polishing Variables

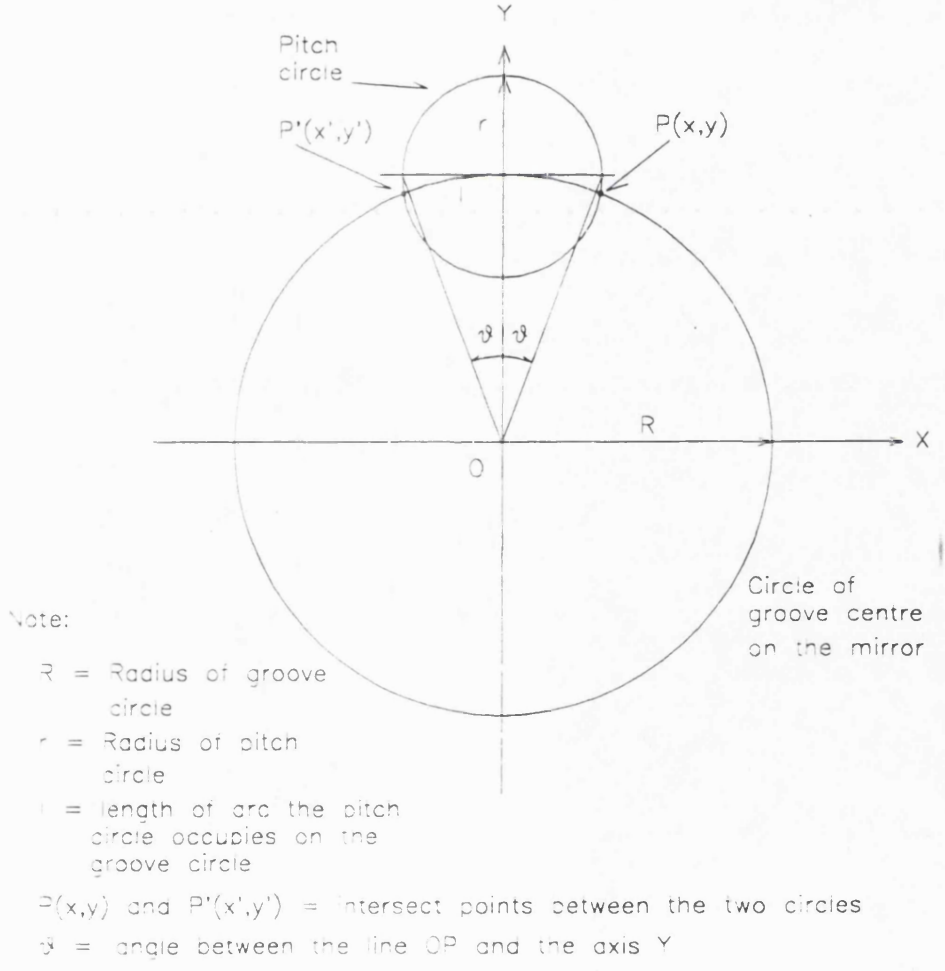

Figure C.1: This figure shows the geometry with a circular pitch tool sweeping along a circular track on the mirror surface.

The groove circle is written as

$$X^2 + Y^2 = R^2 \tag{C.1}$$

, while the pitch circle is expressed with

$$X^2 + (Y - R)^2 = r^2 \tag{C.2}$$

These two circles meet at the point $P(x, y)$, of which x and y values are solved as

$$y = \frac{2R^2 - r^2}{2R} \tag{C.3}$$

$$x = \pm\sqrt{R^2 - y^2} \tag{C.4}$$

$$or \tag{C.5}$$

$$x = \pm\sqrt{r^2 - (y - R)^2} \tag{C.6}$$

The angle θ between the line $\bar{OP}$ and the Y axis is then

$$\theta = \arctan\frac{x}{y} \tag{C.7}$$

This gives an expression for the length l between the two intesects P and P' on the groove circle.

$$l = 2\pi R\frac{2\theta}{360} \tag{C.8}$$

l is defined as the length of polishing contact at a given instance between the polishing tool and the mirror. Since the 1m polishing machine rotate 1 revolution every 27 seconds, the duration of the polishing contact and the sliding velocity V are written as

$$t = 27\frac{2\theta}{360} V = \frac{l}{t} = \frac{2\pi R}{27} \tag{C.9}$$

The total polishing time T for the duration of polishing with N revolutions of the polishing machine is

$$T = tN \tag{C.10}$$

In the mean time, the polishing pressure P is obtained,

$$P = \frac{W}{\pi r^2} \tag{C.11}$$

where W is the normal load.

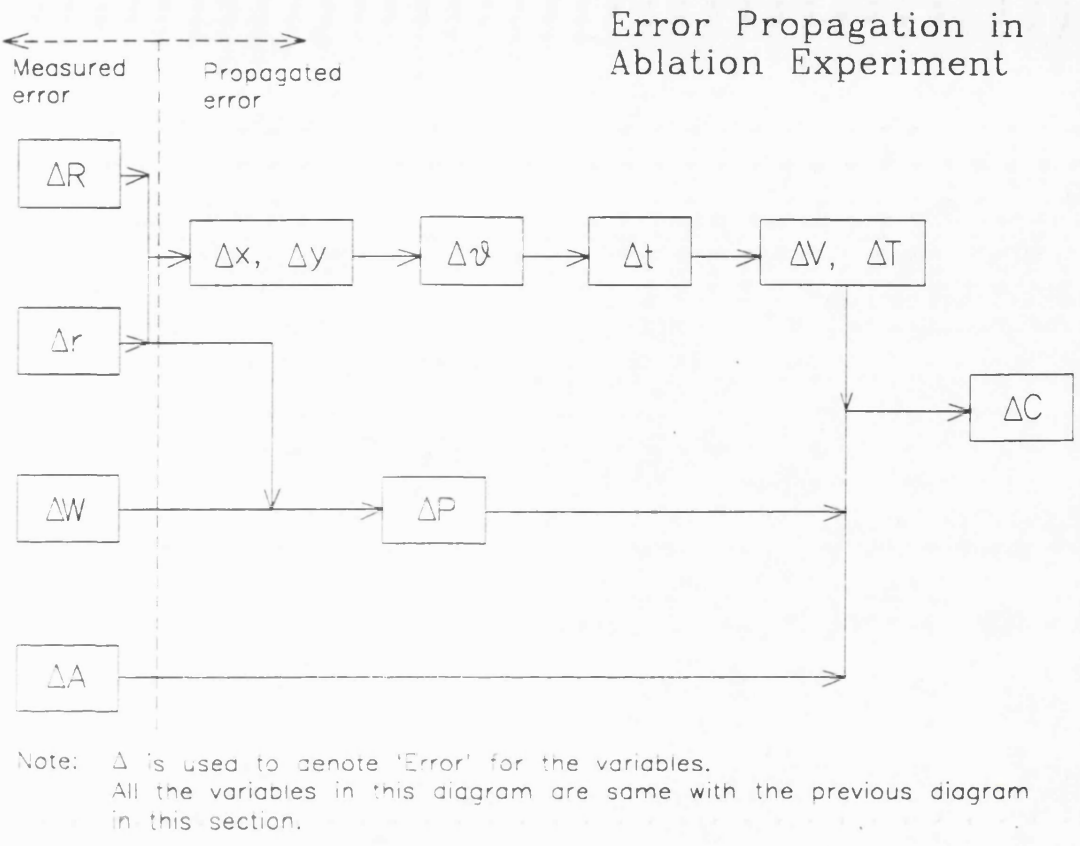

Figure C.2: Error propagation in claculation of ablation rate coefficient

Finally, according to the Preston's law, the ablation rate coefficient C is calculated with

$$C = \frac{A}{PVT} \tag{C.12}$$

where A is the total integrated ablation i.e. depth of the groove at R obtained from using the WYKO fringe analysis system.

The measurement errors in R, r, W and A are propagated and result in the error in the ablation rate coefficient C as shown in Figure C.2. Each step of the error propagation is estimated by using the standard technique for error estimation for multi-variable function [5]. This process demonstrates that the error in the integrated ablation rate plays the role of the dominent error source in estimating the ablation rate coefficient. This gives much rise in importance of analysing fringes with better accuracy. In this respect, use of phase-shift fringe analysis become even more attractive for the ablation experiment in the future.

Appendix D

Structural Coupling Coefficient of Active Lap

D.1 Actuator-Load Cell Coupling Coefficient

Load Cell	Actuator					
	1	2	3	5	6	7
1	-0.0023516	-0.0006916	0.00382481	-0.0215544	-0.0185409	-0.0460194
2	-0.0151872	-0.0257466	-0.0691398	-0.1334922	-0.0331341	0.04475633
3	-0.0015641	0.00251726	0.00728438	0.01235255	0.00458889	0.04769551
4	0.0008273	8.109E-06	-0.0012068	-0.0014478	-0.0065213	-0.0010727
5	0.00331041	0.00924418	0.01226415	0.01063162	-0.0030433	-0.0037409
6	-0.0258634	-0.0304744	0.18787652	0.34575266	-0.0196335	-0.0447083
7	0.08833206	0.01423532	-0.0151815	-0.0209925	0.19565199	0.10444893
8	-0.0754368	-0.0467719	-0.0242612	-0.0334639	0.04880949	-0.0561787
9	0.00647902	0.00479922	0.00319284	0.00353586	-0.0004712	0.00358667
10	0.00239896	0.00575047	0.00669068	0.00872435	0.00163511	0.00503921
11	-0.4526155	-0.3287331	-0.1793289	-0.2226053	-0.4602608	-0.3264343
12	0.01762048	0.31068073	-0.0935915	-0.0336874	-0.0066358	-0.0017039
13	0.14534947	-0.0668004	-0.0332826	-0.0396829	-0.075	-0.0576734
14	-0.0767695	-0.0495893	-0.0259656	-0.0317948	-0.0707326	-0.0489302
15	0.00300045	0.00280907	0.00220883	0.00266579	0.00281758	0.00244749
16	-0.0227317	-0.0681675	-0.0347381	-0.0481037	-0.0064926	-0.01043
17	-0.0098344	-0.0103054	-0.0037464	-0.0015291	-5.749E-05	0.00059832
18	-0.0043512	0.00250586	0.0023609	0.00358893	0.00418909	0.00461309
19	0.00353479	-0.00273349	0.00186709	0.00251977	0.00320217	0.00281702
20	0.0037953	0.00974435	0.01198009	0.01426191	0.00357703	0.00902054
21	-0.0062077	-0.0108321	-0.0103179	0.00343392	0.00163391	0.00582918
22	0.00215511	0.00696419	0.01010441	0.01345053	0.0036965	0.00833786
23	0.42259845	0.09645759	-0.038763	-0.0185346	0.05365802	-0.0129103

24	-0.0393259	0.09315821	0.45577135	-0.0150083	-0.0210317	-0.0439762
25	0.01831494	0.31153515	-0.0938576	-0.0439069	-0.0038733	0.00920148
26	0.14614257	-0.0668157	-0.0330114	-0.0448992	0.26759174	-0.0609863
27	-0.002744	0.0143672	-0.0560712	-0.0069341	-0.0024254	0.17706734
28	-0.0226737	-0.0679659	-0.0344635	0.45676285	-0.0272804	-0.0765169
29	0.0034733	-0.0084038	0.00114061	-0.0049324	0.31024082	0.04453125
30	-0.0099942	-0.0102351	-0.0038645	-0.025557	0.03541868	0.44555291
31	-0.0109377	-0.0180631	-0.0233395	-0.078127	-0.0300863	-0.0082234
32	-0.0061653	-0.0108117	-0.0102901	-0.0407483	-0.0215508	-0.057374
33	-0.0045013	0.00243225	0.002324	0.001488	0.02270427	-0.0056122
34	-0.0001967	0.00101163	0.00198415	0.00432802	-0.0091134	-0.006131
35	0.00215619	0.00694294	0.01008244	0.00659857	-0.0067398	-0.0055414
36	0.00272287	0.00797701	0.01111897	0.00699861	-0.0051027	-0.0071766
37	0.00151677	0.00287611	0.0019282	0.0010646	-0.0058606	-0.0029654
38	0.00359051	0.00276526	0.00187447	0.00221686	-0.0006654	0.00180765
39	-0.0762876	-0.049425	-0.0258815	-0.0330503	-0.0813076	-0.0524528
40	0.00075587	-0.0002398	-0.0007963	-0.0006715	0.00069453	0.00062308
41	0.00382241	0.009761	0.01198352	0.01368283	0.00001223	0.00341709
42	0.00295151	0.00278147	0.00219407	0.00275666	0.0029348	0.00284674
43	0.00150221	0.00397722	0.00356066	0.00422545	0.00256368	0.00340507
44	0.00376996	0.00897405	0.01048219	0.01297445	0.00239655	0.00747447
45	0.00238628	0.00573163	0.00667746	0.00794368	0.0015724	0.00474639
46	0.0064848	0.00481434	0.00320416	0.00414815	0.00643452	0.00488056
47	0.00076915	-0.0002286	-0.0007838	-0.0009747	0.00067473	-0.000156
48	0.00327151	0.00920979	0.01222828	0.01533106	0.0043315	0.00988066
49	0.00115149	0.00264476	0.00180101	0.00327641	0.00359499	0.00352024
50	0.002693	0.00797153	0.01112018	0.01510336	0.0042876	0.00969884
51	0.00084291	6.902E-06	-0.0012072	-0.0007508	0.00157966	0.0004376
52	-0.075492	-0.0466404	-0.0242183	-0.0284148	-0.0661983	-0.0418718
53	-0.0001753	0.00108978	0.00206345	0.00127296	0.00072419	0.0007735
54	-0.0024173	-0.0007288	0.00373333	0.01700562	0.00502236	0.01294221
55	-0.001597	0.00252996	0.00721006	0.00141255	0.00185279	0.00088877
56	-0.0110142	-0.0181295	-0.0232022	-0.0005184	0.00118013	0.0052785
57	0.00376669	-0.0081426	0.00118124	0.00037469	-0.0038905	0.00168879
58	-0.0152083	-0.0260467	-0.0686867	-0.0064149	0.00014449	0.0045613
59	0.08851026	0.01494427	-0.0151844	0.00012429	-0.0035057	0.00142942
60	-0.002383	0.01404647	-0.0556077	-5.329E-05	0.00058674	0.00415833
61	-0.0259763	-0.0300121	0.18669221	-0.0621419	-0.0108408	-0.0212112
Error%	0.39007775	14.1123165	45.654185	19.6736933	0.23663854	14.4027885

Load Cell	Actuator				
	8	10	11	12	13
1	-0.0602278	0.03178723	-0.0319726	-0.0830856	0.71399676
2	0.51030839	0.04628363	-0.0191593	-0.0458368	-0.0744498
3	-0.0488849	-0.067758	0.01796942	0.14169924	-0.0206975
4	0.00119918	-0.0043381	0.01786353	0.14143743	-0.0222112
5	-0.0010225	-0.0206185	-0.018053	-0.0434441	-0.070681
6	-0.122278	-0.0337871	-0.0028713	-0.0016909	0.00101975
7	-0.0242976	-0.0147481	-0.0023571	-0.0029712	0.00057668
8	-0.0318433	-0.0323151	0.35587376	-0.0577145	-0.0479719
9	0.00253584	0.00228148	-0.0023322	-0.0029311	0.00064509
10	0.00761692	0.00512707	-0.0026555	-0.0018867	-0.0008154
11	-0.1964461	-0.1860606	-0.464193	-0.3202782	-0.2619635
12	0.0065287	0.00170546	0.00131953	0.00077401	-0.0002332
13	-0.0324733	-0.02851	-0.0819015	-0.0495471	-0.0389451
14	-0.02814	-0.0271893	-0.0818715	-0.0498454	-0.039565
15	0.00215179	0.00142045	0.00115591	0.000865	0.00047878
16	-0.0095667	0.00713145	0.00288033	0.00904933	0.01927964
17	-0.0005164	0.00119704	0.00318699	0.00251459	0.00302418
18	0.00366599	0.00363293	0.00520718	0.00459977	0.00502193
19	0.00238067	0.00224094	0.00310789	0.00231094	0.00262704
20	0.01196055	0.00992137	0.00015758	0.00348368	0.00895225
21	0.00971171	0.01094797	0.00380256	0.00823947	0.01428784
22	0.01075479	0.00871892	0.00277645	0.00617509	0.01064821
23	-0.0017951	0.00056083	-0.0087829	-0.0001393	0.00062237
24	-0.0667352	-0.0164869	-0.0019874	5.645E-06	0.00590165
25	-0.008353	-0.0015049	-0.0012003	0.0019836	0.00273571
26	-0.0388322	-0.0345654	-0.0305582	-0.0591286	-0.0465963
27	-0.0537373	-0.0389111	-0.003161	0.00203787	0.00439388
28	0.17040121	-0.0600954	-0.0107966	-0.0199798	-0.0345712
29	-0.0213505	-0.0257714	0.14006897	0.00935642	-0.0083259
30	-0.0880424	-0.091643	-0.004507	-0.0061459	-0.0063642
31	0.14348368	0.36013997	-0.0251285	-0.0566737	-0.0884729
32	-0.0287701	0.39682239	-0.024061	-0.0087317	0.04223472
33	-0.0085891	-0.0272866	0.26287495	0.15733225	-0.0240642
34	-0.0241152	-0.0928573	-0.0054733	0.42714491	-0.001367
35	-0.0160591	-0.0994768	-0.0233428	-0.0070397	0.04413147
36	-0.006736	-0.0368752	-0.024245	-0.0552509	-0.0853684
37	0.00118716	0.00088126	0.14116042	0.00942187	-0.0083388
38	0.00348262	0.00974517	-0.0045481	-0.0057751	-0.006665
39	-0.0302634	-0.0304125	-0.0311765	-0.0592166	-0.0468111
40	0.00018815	0.0031308	-0.0032568	0.00211914	0.00472063
41	0.00750764	-0.0029418	-0.0097793	-0.0181682	-0.0324966
42	0.00242506	0.00214347	-0.0015149	0.00181485	0.00300244
43	0.00315216	0.00178101	-0.0090888	-0.0003672	0.00034374
44	0.01100662	0.00731937	-0.003189	-0.0027483	-0.0002735
45	0.00677038	0.00497807	-0.0014775	-0.0007283	0.00146899

46	0.0036391	0.00323638	0.00374173	0.0042884	0.00400367
47	-0.000731	-0.0004068	0.00128769	0.00060017	0.00014318
48	0.01260697	0.01083735	0.00274616	0.00702316	0.01318214
49	0.00327554	0.00307981	0.00261498	0.0031472	0.00381202
50	0.01248415	0.0105035	0.00313067	0.00717466	0.01280255
51	-0.0002303	0.00001876	0.00187985	0.00080285	0.00018556
52	-0.0240306	-0.022213	-0.0652193	-0.0406802	-0.0312296
53	0.00082989	0.00053126	0.00059344	0.00055086	0.0006298
54	0.018285	0.01652168	0.00582325	0.01219139	0.02051549
55	-0.0002964	-0.0005743	0.00164364	0.00033981	-0.0006147
56	0.00965454	0.01290461	0.00453479	0.00999504	0.01778645
57	0.00116794	0.0024031	0.00286982	0.00345664	0.00426002
58	0.00995866	0.01429281	0.00477235	0.01097143	0.02000006
59	0.00311756	0.0028737	0.00377578	0.0043766	0.0041237
60	0.00656143	0.00139615	0.00117902	0.00019002	-0.0009081
61	-0.0256367	-0.0041552	-0.0001401	0.00252167	0.00844052
Error(%	32.9245362	38.7585554	0.133123	16.5002828	1.22595175

D.2 Load Cell-Load Cell Coupling coefficient

Load Cell	1	2	3	6	7
1	0.32285109	0.00636024	0.0180792	-0.0006791	0.00003903
2	0.00903802	0.36775997	0.01260759	0.03606581	0.00562954
3	0.03010754	0.01477503	0.40214398	-0.0016939	-0.0002441
4	0.03119366	0.0006062	0.00088267	-3.568E-05	0.00077632
5	0.00873543	-0.0002505	0.00051915	0.00008249	-0.0001387
6	-0.0009283	0.03469221	-0.0013903	0.36475646	0.00544536
7	0.00006831	0.00693496	-0.0002566	0.00697367	0.3941263
8	0.00083319	0.00104197	0.00054874	-0.0002502	0.002536
9	0.00008328	-0.0001708	0.00082411	9.901E-07	0.00073087
10	-0.0008704	0.00007922	-2.966E-05	0.00005312	1.583E-07
11	-0.0031213	-0.0015917	0.00258912	-0.0014834	0.00530015
12	0.0000431	-0.0026774	0.00052641	0.01718005	-0.0001034
13	-0.0006827	-0.0001891	0.00149631	0.00106561	0.00062254
14	-0.0006827	-0.0002557	0.00044469	-0.0002629	0.00040162
15	0.00003451	0.00001926	-9.915E-05	0.00001316	-9.595E-05
16	0.00013132	-0.0006184	0.00002071	0.00642499	-0.0001003
17	0.00004381	-4.865E-05	-0.0001137	0.00005483	0.00184854
18	0.00006091	0.00001518	-9.086E-05	-0.0001618	0.00026638
19	0.00004427	0.00002181	-2.598E-05	0.00002454	-8.771E-05
20	0.00013025	0.00007853	9.230E-06	0.0000685	0.00003325
21	0.0001015	0.00008195	7.899E-06	-0.000203	-0.0001165
22	0.00010117	0.00005448	5.538E-06	0.00008378	0.00001284
23	-0.0004887	0.00295538	0.00342988	0.01125439	-0.0853628
24	-0.0003535	0.01621893	-0.0011903	-0.1802315	0.01205695
25	-0.0005088	0.00819703	0.00350883	-0.0730433	-0.0870827
26	-0.0013539	0.00390609	0.00584462	0.00333057	-0.0766765
27	0.00108894	-0.082984	0.00557253	-0.0902091	-0.0771337
28	0.00160284	-0.152996	0.00942509	-0.1470791	0.01308493
29	0.0071093	0.01482706	-0.0740876	0.0032355	-0.0830508
30	0.01510998	-0.0845582	-0.0976789	0.0104244	-0.0866603
31	0.01162107	-0.1679418	-0.0712957	0.01257396	0.01129456
32	-0.209994	0.0017606	-0.0583318	0.00053006	0.00509682
33	0.02222119	0.00653724	-0.0929304	-0.000585	0.0078109
34	-0.0676632	0.01102019	-0.1005417	-0.001486	0.00322394
35	-0.2102341	0.0009981	0.00905367	-0.0002162	-0.0005783
36	0.01111155	-0.0006565	0.00434983	0.00013147	-0.0004678
37	0.00725945	-0.0008767	0.00921867	-9.431E-05	0.00309223
38	0.01545258	-0.000449	0.00380564	0.00004976	0.00022658
39	-0.0013541	-0.0007314	0.0046535	-0.0003588	0.0038692
40	0.00119736	0.00003646	-0.0004504	-3.142E-06	-5.873E-05
41	0.00153234	0.00005018	-0.0004523	0.00006937	0.00002213
42	-0.000515	0.00004546	-0.0003846	0.00001244	-0.0001389
43	-0.0005062	3.088E-07	0.00012658	0.00002224	-0.0003377
44	-0.0003394	0.00007705	0.00002242	0.00007263	0.00002325

45	0.00004572	0.00005284	0.00001938	0.00005322	0.0000291
46	0.00004806	0.00003996	-0.0001028	0.00003756	-0.0003166
47	0.00005093	-2.284E-06	-1.818E-05	-1.642E-06	-2.476E-05
48	0.00013392	0.00007242	2.271E-06	0.00005499	0.00003196
49	0.00004556	0.00002644	-9.810E-05	-4.355E-07	-0.0001421
50	0.0001202	0.00006957	5.998E-06	0.00005676	0.00002477
51	9.627E-06	2.622E-06	-1.342E-05	0.00002436	-9.560E-05
52	-0.0004046	-0.0002983	0.00018393	-0.0005535	0.00279158
53	9.490E-06	5.953E-06	-2.583E-07	0.00004567	-0.0001014
54	0.00016827	0.0000948	5.557E-06	0.00003368	0.00002766
55	9.631E-06	0.00004999	-3.656E-05	-0.0002993	7.919E-06
56	0.00011948	0.00011753	8.570E-06	-0.0007612	-0.0003757
57	0.00004679	-4.878E-05	-0.0001345	-0.0003058	0.00279811
58	0.00013429	-0.0002955	0.00004246	0.00029849	-0.0005062
59	0.00004981	-0.0006348	0.00001001	0.00613057	0.00889854
60	0.00005232	-0.0017237	-5.465E-06	0.01057774	0.00304586
61	0.00004691	0.00031748	-0.0002459	0.00813377	0.0047768
Error (%)	34.3993234	6.78022915	9.24569829	10.3305802	14.8362841

Load Cell	8	11	23	24	25
1	0.00050103	-0.0018245	-0.0002807	-0.0002339	-0.000305
2	0.00089039	-0.0013221	0.00241248	0.01524837	0.00698177
3	0.00054952	0.00252031	0.00328114	-0.0013115	0.00350242
4	0.00064483	0.00253947	0.00011323	0.00002619	-0.0003805
5	0.00089891	-0.0013307	6.607E-07	0.00007252	0.00003856
6	-0.0002057	-0.0011852	0.00883707	-0.1629927	-0.0598447
7	0.00266957	0.00542332	-0.08584	0.013964	-0.0913717
8	0.41518306	-0.0705348	0.00827357	-0.000671	0.00389531
9	0.00254491	0.00548747	-0.0003433	0.00002737	-0.0001439
10	-0.0001985	-0.0011848	0.00001777	0.00006569	0.00001014
11	-0.0725636	0.41475719	0.00123194	-0.0016602	0.00315088
12	0.00154191	0.0031104	-0.0798569	-0.0823322	-0.0893342
13	-0.0067884	-0.0817441	-0.0823833	0.00374572	0.00590795
14	-0.0067792	-0.081724	0.00252456	-0.0003887	0.00034627
15	0.00154718	0.00311887	-8.172E-05	0.00001543	-1.527E-05
16	-0.0003259	-0.0017311	0.00464544	0.00690699	0.00900286
17	0.00021699	0.0033521	0.00793994	0.00404399	0.00316961
18	0.00125107	0.00461292	0.0046866	-0.0004678	0.00018912
19	0.00021117	0.00335744	-0.000291	0.00003289	-6.253E-05
20	-0.0003255	-0.0017302	0.00003808	0.00008173	0.00001286
21	-0.0001905	-0.0011349	-0.0003439	-0.0005562	-0.0002278
22	-0.00019	-0.0011337	-5.739E-05	0.00012038	0.0000237
23	0.00866093	0.00125356	0.40020415	0.00902744	-0.0832627
24	-0.0006098	-0.0014668	0.00783814	0.36872236	-0.0745826
25	0.003908	0.00307275	-0.0797978	-0.0823246	0.40186564
26	-0.0820993	-0.0812273	-0.0824248	0.00373942	0.00214033
27	0.00419308	0.00159432	0.00022975	0.01443247	-0.095376
28	-0.0006552	-0.0017292	0.00469098	0.00681975	0.01896647
29	-0.0794937	0.00188096	-0.0002504	0.00099929	0.00813257
30	0.00418162	0.00336034	0.00780706	0.00420763	-0.0009137
31	0.00270189	-0.0011951	0.00126412	0.00121161	0.0050043

32	0.00329268	-0.0011308	-0.0003445	-0.00056	0.00028146
33	-0.0800781	0.0044826	0.00468375	-0.0004751	0.00207646
34	0.00795464	0.0007252	0.00026047	-0.0002997	-4.648E-05
35	0.00326266	-0.0011383	-5.623E-05	0.00012159	-0.0001398
36	0.00270097	-0.0011958	-7.519E-05	0.00010181	-1.038E-07
37	-0.0794387	0.00220956	0.00072917	-4.308E-05	-4.549E-05
38	0.00425473	0.00341714	-0.0002887	0.00003297	-0.0001541
39	-0.0818587	-0.0814701	0.00245363	-0.0003852	0.00047432
40	0.00421852	0.0015908	-9.679E-05	-3.560E-06	-2.931E-05
41	-0.0006595	-0.0017332	0.00003807	0.00008152	0.00002284
42	0.00391395	0.00307253	-7.876E-05	0.00001516	-2.189E-05
43	0.00868041	0.00116537	0.00045082	0.00001372	-8.175E-05
44	-0.0006068	-0.0014644	0.00001203	0.00008948	0.00001371
45	-0.0004557	-0.0011782	0.00001761	0.00006557	0.00001066
46	0.00297872	0.00549616	-0.0003512	0.00002746	-9.979E-05
47	0.00011571	0.0015945	-9.909E-05	-3.340E-06	-1.100E-05
48	-0.0002548	-0.0013243	2.312E-06	0.00007234	0.00001587
49	0.00141479	0.00183648	0.00072738	-4.422E-05	-0.0001636
50	-0.0002526	-0.0011989	-7.212E-05	0.00010111	0.00001415
51	0.00018153	0.00254348	0.00010285	0.00002543	-9.654E-05
52	-0.0047529	-0.0704279	0.00835107	-0.0006695	0.00150967
53	-1.207E-05	0.00074326	0.00026399	-0.0002951	-3.884E-05
54	-0.0002434	-0.0018273	-0.0002911	-0.0002261	0.00002033
55	0.00018315	0.00254682	0.00335185	-0.0013118	0.00052684
56	-0.0002528	-0.0012021	0.00131806	0.00119184	-0.0009278
57	0.00145886	0.00205207	-5.184E-05	0.00098239	0.00394076
58	-0.000255	-0.0013285	0.00236738	0.01521459	-0.0022228
59	0.00297597	0.00549015	-0.085991	0.01378196	-9.882E-05
60	0.00011451	0.00159688	-0.0002516	0.01456862	0.00489946
61	-0.0004556	-0.0011775	0.00883334	-0.1627456	0.01385412
Error (%)	0.09043427	12.2283125	14.197965	0.84680638	9.44578391

Load Cell	26	27	28	29	30
1	-0.0007791	0.00069692	0.00156819	0.0042261	0.00868522
2	0.00319416	-0.0754704	-0.2127096	0.01252471	-0.0690673
3	0.00560103	0.00593924	0.01535637	-0.0733423	-0.0935004
4	0.00441371	-0.0004715	-0.0007456	0.00895376	0.00368271
5	-0.0005886	0.00003185	0.00006989	-0.0007339	-0.0003776
6	0.00261981	-0.0789167	-0.1966955	0.002629	0.00819038
7	-0.0772411	-0.0864167	0.0224104	-0.0864227	-0.0871983
8	-0.0785657	0.00446266	-0.0010661	-0.0785822	0.00399705
9	0.00379199	-6.365E-05	0.00003975	0.00323114	0.0002237
10	-0.0002708	-2.640E-06	0.0000931	-7.693E-05	0.00004006
11	-0.079967	0.00174563	-0.0028943	0.00191288	0.00330441
12	0.00605828	0.00507607	0.01475459	0.00396264	0.00285907
13	-0.0761643	0.0034295	-0.0012867	0.00812191	0.0042816
14	-0.0103823	0.00013638	-0.0004164	0.00086495	0.00022622
15	0.00032896	-1.184E-05	0.00002129	-0.0001656	-6.064E-05
16	-0.0007706	0.00064888	0.00113676	-0.0002999	-0.000358

17	0.00423849	-1.732E-05	-0.0006147	0.00008746	-0.0002306
18	0.0034411	-0.0001482	0.00003535	-3.625E-05	-0.0001833
19	0.00022981	-5.014E-06	0.00003341	-7.791E-05	-5.498E-06
20	-0.0002434	-4.053E-06	0.00012717	0.00002871	0.00001973
21	-0.0004728	0.00002689	0.00001501	-1.642E-05	0.0000197
22	-0.0002401	-1.099E-06	0.00009618	0.00001004	0.00001426
23	-0.0825702	0.00025597	0.00798952	-0.0002591	0.00781185
24	0.0032525	0.01396116	0.01008496	0.00089785	0.00365555
25	0.00205488	-0.1018386	0.03095883	0.0080655	-0.0008762
26	0.42172175	0.00516168	0.00087259	-0.0781268	-0.0004052
27	0.00464113	0.42060788	-0.0778296	-0.0006465	-0.0904775
28	0.00051324	-0.050912	0.3156621	0.00498637	0.02016817
29	-0.0756314	-0.0006961	0.00820689	0.39938983	-0.0838183
30	-0.0004057	-0.100741	0.03432869	-0.0866832	0.40242155
31	0.00342421	0.01255653	0.01666136	0.00649558	-0.0688877
32	0.00078053	0.00883094	0.00900256	0.00793615	0.01402002
33	-2.524E-05	0.00237265	-0.0006158	-0.0925891	0.00027807
34	0.00325996	-9.410E-06	-0.0003097	-0.0004296	0.00606162
35	0.00009972	-0.0016865	-0.0010841	0.00351522	-0.0023616
36	-0.0004292	-0.0002531	-0.0002327	0.00058687	-0.0013576
37	0.0054883	0.00054278	-0.0005652	0.00332243	0.0044805
38	0.00200282	0.00003351	0.00005932	0.00465404	0.00118004
39	-0.0062559	0.00038058	-0.000672	0.0060246	0.00201772
40	0.00034429	-1.119E-05	0.00004889	0.0004855	0.00003454
41	-0.000395	0.00003198	0.00012343	-0.0003506	0.00003326
42	0.00046201	-3.175E-05	0.0000367	-4.263E-05	-0.0001452
43	0.00250906	-0.0001102	0.00006351	0.00078294	-0.0002879
44	-0.0003356	-3.307E-06	0.00012079	-3.942E-05	0.00002885
45	-0.0002053	-1.465E-06	0.00009136	-7.904E-07	0.00001933
46	0.00041725	-2.734E-05	0.00005743	-0.0001511	-8.954E-05
47	0.00012314	6.587E-07	-6.056E-06	-4.815E-05	-4.882E-06
48	-0.0002085	-2.204E-06	0.0001092	0.00002257	0.00001791
49	0.00083399	-5.122E-05	0.00004686	-0.0001984	-7.512E-05
50	-0.0002231	-1.479E-06	0.00010252	0.00002234	0.00001908
51	0.00043753	-1.893E-05	0.00001515	-9.639E-05	-2.470E-05
52	-0.0006813	0.00010993	-0.0005276	0.00139868	0.00020631
53	0.00003997	-8.746E-07	0.00006262	-6.715E-05	-1.570E-05
54	-0.0003914	0.00003301	0.000128	0.00002762	0.00002551
55	0.00142804	-9.273E-06	0.00003179	-0.0001373	-0.0001099
56	-0.0003837	-0.0002722	-0.0002416	-8.550E-05	-1.424E-05
57	0.00764801	0.0002958	-0.0004873	0.00162604	0.00008698
58	-0.0001644	-0.001557	-0.0008584	-4.131E-05	-3.698E-05
59	0.00066421	0.00346559	-0.0001385	0.00293573	0.00184898
60	0.00306083	-0.0002353	0.00097173	0.00027497	-2.443E-05
61	0.00087452	0.00916581	0.00840824	-0.0002485	0.0000458
Error (%)	13.9969662	2.50045824	32.9496645	10.3558383	14.1278332

Load Cell	31	32	33	34
t	0.00799901	-0.1519809	0.01238764	-0.0417467

2	-0.1642665	0.00181068	0.00517863	0.00966181
3	-0.081724	-0.0703046	-0.086273	-0.1033028
4	0.00489111	0.01087997	-0.0863113	-0.1034203
5	-0.0006393	0.0010854	0.00529442	0.0097079
6	0.01183038	0.00052437	-0.0004458	-0.0012532
7	0.01360913	0.00645732	0.00762243	0.00348199
8	0.00309269	0.00396287	-0.0742357	0.00816147
9	-0.0005637	-0.0007438	0.00759523	0.00349398
10	0.00012261	-0.0002276	-0.0004472	-0.0012623
11	-0.0014073	-0.0014001	0.00427509	0.00076545
12	-0.0010785	-0.0002693	0.00016885	-4.042E-05
13	-0.0004693	-0.0006055	0.00340958	0.0000312
14	-0.0002673	-0.0003033	0.00333182	0.00002618
15	0.00001663	0.00002849	0.00017435	-4.115E-05
16	-0.0001715	0.00001033	0.00002031	0.00003943
17	-1.629E-05	0.00002509	-0.0001769	-1.643E-05
18	0.0000166	0.00002814	-0.0001218	-2.385E-05
19	0.00002262	0.00001769	-0.0001778	-1.646E-05
20	0.00007196	0.00007117	0.00002036	0.00004009
21	0.00005351	0.00004199	0.00002121	5.148E-06
22	0.00005421	0.00004747	0.00002124	5.186E-06
23	0.00151471	-0.000434	0.00454533	0.00027975
24	0.00126053	-0.0006126	-0.0004003	-0.0002795
25	0.00574678	0.00033986	0.00193124	-4.784E-05
26	0.00409578	0.00098164	-2.445E-05	0.00349515
27	0.01350447	0.00998634	0.00206667	-9.071E-06
28	0.01172178	0.00665949	-0.0003509	-0.0001953
29	0.00752134	0.00966226	-0.0868297	-0.0004459
30	-0.0824926	0.01765282	0.00026968	0.00650642
31	0.36540386	-0.170761	0.01257841	0.01397168
32	-0.162404	0.36558931	0.0044066	-0.0815254
33	0.01553084	0.0057209	0.39719297	-0.0837567
34	0.01558724	-0.0956324	-0.0756783	0.41607963
35	0.01373635	0.03905503	0.00414019	-0.0813043
36	0.00130187	0.01430584	0.01288646	0.01429968
37	0.00063803	0.00431536	-0.0869593	-0.0003499
38	-0.0016163	-0.0031484	0.00019024	0.00608531
39	-0.000524	0.0001177	-7.193E-05	0.00346318
40	-0.000271	-0.0019572	0.00202406	-9.834E-05
41	-0.0001664	-0.0007898	-0.000343	-0.000161
42	7.544E-07	-0.0001654	0.00190417	-5.077E-05
43	-8.936E-05	-6.946E-05	0.00457592	0.0002909
44	0.0001054	0.00013163	-0.0004024	-0.0002778
45	0.00005331	0.0000828	-0.0001247	0.00003845
46	0.00002989	0.00001642	0.00026666	-0.0001097
47	-1.549E-06	-1.367E-06	-0.0001257	-8.308E-07
48	0.00006792	0.00005579	0.00001187	5.025E-06
49	0.00002549	0.00001171	-2.710E-05	-6.935E-05
50	0.00006579	0.00005692	0.00001245	5.986E-06

51	6.831E-06	6.783E-06	-8.495E-05	4.051E-09
52	-0.0002853	-0.0002281	0.00115408	-1.412E-05
53	6.759E-06	6.216E-06	-2.214E-05	4.052E-06
54	0.00008285	0.00007319	0.00003358	5.702E-06
55	0.00001061	0.00001001	-8.517E-05	-9.096E-09
56	0.00009024	0.00005571	0.00001245	5.962E-06
57	-9.657E-05	-1.973E-05	-2.506E-05	-7.003E-05
58	0.00011322	0.00008331	0.000012	5.193E-06
59	-0.0004547	-0.0001483	0.0002663	-0.0001115
60	-0.0002934	0.00003025	-0.000127	-2.344E-07
61	-0.000698	-0.0001988	-0.0001261	0.00003671
Error (%)	4.69449458	9.35867294	17.675799	6.3258002